Renewable reducing agents for the use in ferroalloy industries

Gerrit Surup

Renewable reducing agents for the use in ferroalloy industries

Doctoral Dissertation for the Degree *Philosophiae Doctor (PhD)* at
the Faculty of Engineering and Science, Specialisation in Renewable Energy

University of Agder
Faculty of Engineering and Science
2019

Doctoral Dissertation at the University of Agder 238
ISSN: 1504-9272
ISBN: 978-82-7117-938-0

©Gerrit Surup, 2019

Printed by Media 07
Oslo

Contents

List of Figures

List of Tables

ACKNOWLEDGEMENTS

This work was carried out at the University of Agder (UiA), Faculty of Engineering and Science, Department of Engineering Sciences. I would like to express my gratitude to my supervisor Professor Henrik Kofoed Nielsen and my co-supervisors Tore Vehus and Per-Anders Eidem for the supervision of my work. I would also like to thank the local industry for giving me insight on the industrial application of reducing agents. Especially Jens Davidsen from the ERAMET group and Bertil Andre Johansen from Lindum AS for the supply of reference materials used in the electric arc furnace (EAF). I am very grateful for the support from Dr. Anna Trubetskaya for the fruitful discussions and advices, as well as the support for the external co-operations.

I would also like to thank the external researchers for the support to my research results, such as Professor Rüdiger Deike, Manuel Foppe, Daniel Schubert, Marius Großarth and Markus Heidelmann from University of Duisburg-Essen, Michael T. Timko from Worcester Polytechnic Institute, Andrew J. Hunt from the Materials Chemistry Research Center, Thomas Attard and Vitaliy L. Budarin from the University of York, Victor Abdelsayed and Dushyant Shekhawatf from the National Energy Technology Laboratory and Jan Van den Bulcke and Iván Josipovic from Ghent University.

I would also express my gratitude to my colleagues Lorenzo Riva, Johan Olav Brakestad, Peter Hugh Middleton and Antoine de Padoue Shyikira for the nice cooperation and support in the laboratories. Last but not least I would like to thank Reyn Joseph O'Born, Zbigniew Jakub Mikulski, Shaun Falconer, Shiplu Sarker, Ingrid Lande Larsen, Andreu Regue Barrufet, Vidar Hellum and Mohammad Ali Mahdavipour for the friendly discussions in room D3 074.

Abstract

This Ph.D. thesis describes the experimental investigations of the high-temperature heat treatment without oxygen (pyrolysis) of biomass. Charcoal is considered as an alternative feedstock in metallurgy to reduce the greenhouse gas emissions by substituting fossil fuels, i.e. coal, petcoke and metallurgical coke. High temperature pyrolysis plays an important role in ferroalloy industries since the feedstock composition, time-temperature history and reaction environment affect the properties of charcoal. The solid residue yield and the properties of charcoal, such as fixed carbon yield, reactivity and electrical resistivity are important parameters for the use of biomass as a CO_2 neutral reducing agent.

Biomass pyrolysis experiments were performed in a laboratory-scale slow pyrolysis reactor and high-temperature furnaces to investigate the effect of primary and secondary heat treatment, biooil conditioning and wood type on the charcoal yield, chemistry, morphology and reactivity towards CO_2 using thermogravimetric analysis (TGA). In the present study, Norway spruce and sessil oak were used as a feedstock.

The charcoal yield decreased with increasing heat treatment temperature, whereas the fixed carbon yield was nearly constant at temperatures up to 900°C. However, greater heat treatment temperatures led to the decrease in a fixed carbon yield. Likewise, the carbon content increased with increasing heat treatment temperature, indicating the removal of oxygen and hydrogen containing species. Spruce charcoal showed a greater fixed carbon yield than oak charcoal, due to the greater carbon content in original spruce. However, the spruce charcoal exhibited a greater oxygen content, whereas the ash content of oak charcoal was twice greater than that of spruce charcoal. Secondary heat treatment of charcoal samples further decreased the charcoal yield. The ash composition and residence time influenced the charcoal reactivity less than the heat treatment temperature.

The co-pyrolysis of biomass with biooil decreased the CO_2 reactivity approaching that of metallurgical coke. It was also shown that the reactivities of charcoal from high temperature pyrolysis (2400-2800°C) were similar to those of metallurgical coke emphasizing

the importance of graphitizing temperatures on the charcoal behavior. Graphitization of charcoal increased with the increasing heat treatment temperature, leading to formation of graphitizing carbon. Moreover, the heat treatment temperature and CO_2 concentration affected the biomass reactivity stronger than the feedstock origin and biooil conditioning. The influence of heat treatment temperature was less pronounced at temperatures less than 1600°C. Results showed that charcoal from pyrolysis of spruce and oak has a similar reactivity at all heat treatment temperatures. The oak charcoal prepared at 1600°C contained long and flat graphene layers and interplanar distance that is similar to graphite and thus, was more ordered than the spruce charcoal. The transmission electron microscopy (TEM) analysis showed that charcoal had structural characteristics of non-graphitizing carbon. Thus, increasing heat treatment temperature increases the graphitization of charcoal structure, leading to the reactivity that is nearly similar to that of low reactive metallurgical coke.

Pre-treatment of biomass can increase the efficiency of pyrolysis process. The supercritical CO_2 ($scCO_2$) extraction enables the extraction of more than half of value-added compounds without any significant influence on the physical properties of the charcoal. The $scCO_2$ extraction decreased the O/C ratio of wood, and thus, improved the structure ordering of charcoal. The decrease in oxygen content enhanced the coalescence of crystallites and thus, enhanced the charcoal graphitization, whereas the remaining oxygen-containing functional groups hindered the alignment of charcoal graphitic layers during the high temperature pyrolysis. Thus, the oak charcoal from pyrolysis at 1600 °C showed more graphitic structure with smaller interplanar distance and longer graphene layers compared to less ordered spruce charcoal. Based on the less graphitic structure of spruce charcoal, it was expected that the CO_2 reactivity of spruce charcoal was greater than that of oak charcoal. However, the reactivity of spruce and oak charcoal in CO_2 was similar.

In the present work, biooil was successfully used as a binding agent for the production of charcoal-based pellets. The separation of the water phase increased the organic fraction of the binder, resulting in an increased density of charcoal-based pellets. The weight ratio of 65:30 of charcoal to biooil without water was used to produce pellets with acceptable mechanical properties. The secondary heat treatment of the charcoal-based pellets improved its hardness, but decreased the durability. Biooil decomposed and formed a polyaromatic coke structure during high-temperature pyrolysis. The reactivity of charcoal-based pellets was similar to that of heat treated charcoal-biooil blend, indicating that pelleting does not affect the reactivity towards CO_2 due to the devolatilization of the light fraction and the pore growth inside the pellet. The mechanical stability of

manganese composite charcoal pellets decreased after the manganese-ore was reduced by the carbon in the pellet. A large internal area was formed in the pellet which contained carbonaceous charcoal matrix and metal slag after the high-temperature pyrolysis. That increases the value of renewable charcoal-based pellets for the use in ferroalloy industries.

Overall, the pelletizing with biooil had the greatest influence on the electrical resistivity at temperatures greater than 900 °C. The effect of heat treatment temperature on charcoal particles was stronger at low and intermediate heat treatment temperatures before the basic structural units reorganized and coalesced. Charcoal particles produced at heat treatment temperatures $\geq 1300\,^{\circ}\mathrm{C}$ showed a similar electrical resistivity to metallurgical coke ($10\,\mathrm{m\Omega m}$), in which the biomass origin showed no influence on the electrical resistivity. Likewise, dielectric losses were enhanced by increasing heat treatment temperature. The electrical resistivity was increased by pelletizing the comminuted charcoal with bioooil as a binder. The production of charcoal based pellets with biooil as a binder showed great promise for producing renewable reducing agents with a high electrical resistivity and low CO_2 reactivity.

Abstrakt

Avhandlingen beskriver biomasse behandlet ved høy temperatur. Trekull har blitt vurdert som et alternativt råmateriale innen metallurgi for å redusere klimagassutslippene ved å erstatte fossile brensler, dvs. kull, petroleumkoks og metallurgisk koks. I ferrolegeringsindustri vil pyrolyse ved høy temperatur være viktig siden råstoffsammensetningen, tid, temperatur og reaksjonsmiljøet på- virker egenskapene til trekullet. Faststoffmengde, og egenskapene til trekull, slik som andel fast karbon, reaktivitet og elektrisk resistivitet, er viktige parametere i forbindelse med anvendelse av biomasse som et CO_2-nøytralt reduksjonsmiddel.

For å undersøke effekt av primær og sekundær varmebehandling, bio-oljebehandling og treslag, ble pyrolyse av biomasse i forhold til trekullutbytte, kjemi, morfologi og reaktivitet mot CO_2 ved bruk av termogravimetrisk analyse (TGA) utført. Eksperimentene ble utført i laboratorieskala med en langsom pyrolysereaktor og høytemperaturovner. I denne studien er norsk gran og vintereik brukt som råstoff.

Trekullutbyttet ble redusert med økende varmebehandlingstemperatur. Fast karbonutbytte var tilnærmet konstant ved temperaturer opp til 900 °C. Imidlertid førte høyere varmebehandlingstemperaturer til en reduksjon i fast karbonutbytte. På samme måte økte karboninnholdet med økende varmebehandlingstemperatur, hvilket indikerer fjerning av oksygen og hydrogenholdige forbindelser. På grunn av at karboninnholdet var høyere karboninnholdet i originalgran viste grankull et større fast karbonutbytte enn eikekull. Trekull fra gran hadde et høyere oksygeninnhold og askeinnholdet til eikekull var to ganger større enn for kull fra gran. Sekundær varmebehandling av kullprøver reduserte trekullutbyttet. Askesammensetningen og oppholdstiden påvirket trekullreaktiviteten mindre enn varmebehandlingstemperaturen.

Kombinert pyrolyse av biomasse med bioolje reduserte CO_2 reaktiviteten slik at den nærmet seg metallurgisk koks. I tillegg viste det seg at reaktiviteten til kull fra høytemperatur pyrolyse (2400-2800 °C) ligner på metallurgisk koks, som understreker betyd-

ningen av grafittiserende temperaturer på reaksjonen til trekullet. Grafittisering av trekull økte med økende varmebehandlingstemperatur, som igjen førte til dannelse av grafittisk karbon. Varmebehandlingstemperatur og CO_2 konsentrasjon påvirket reaktiviteten til biomassen sterkere enn råvarens opprinnelse og kondisjonering med bioolje. Effekten av varmebehandlingstemperaturen var mindre tydelig ved temperaturer under 1600 °C. Resultatene viste at trekull etter fra pyrolyse av gran og eik har en lignende reaktivitet ved alle varmebehandlingstemperaturer. Eikekullet som ble produsert ved 1600 °C inneholdt lange og flate grafittlag med avstander mellom lag som ligner på grafitt. Med andre ord var eikekullet mer velordnet enn grankullet. Transmisjonselektronmikroskopi (TEM)-analysen viste at trekull hadde strukturelle egenskaper som ikke-grafittiserende karbon. En økning i varmebehandlingstemperaturen medførte en økning i grafitiseringen av trekullstrukturen. Dette ledet til en reaktivitet som var tilnærmet lik lavreaktiv metallurgisk koks.

Forbehandling av biomasse kan øke effektiviteten til pyrolyseprosessen. Superkritisk CO_2 ($scCO_2$) -utvinning gjør det mulig å utvinne mer enn halvparten av verdiøkende forbindelser, uten noen signifikant påvirkning på kullets fysiske egenskaper. $ScCO_2$-utvinningen reduserte O/C-forholdet i tre, og forbedret dermed strukturen til trekullet. Reduksjonen i oksygeninnhold økte koaliseringen av krystallitter og forbedret dermed trekullgrafitteringen, mens de gjenværende oksygenholdige funksjonelle gruppene hindret ordningen av kullgrafittlaget etter høytemperatur pyrolyse. Altså viste eikekullet fra pyrolyse ved 1600 °C mer grafittstruktur med mindre avstand mellom lagene, og lengre grafittlag sammenlignet med mindre ordnet grankull. Basert på den mindre grafittiske strukturen av grankull, ble det forventet at CO_2 reaktiviteten til grankull var større enn for eikekull. Imidlertid var reaktiviteten til gran og eikkull i CO_2 lik.

I dette arbeidet er bruken av bioolje som bindemiddel vellykket for produksjon av kullbaserte pellets. Separarering av vannfasen økte den organiske fraksjonen i bindemidlet, noe som resulterte i en økt tetthet for kullbaserte pellets. Trekull og tjære i forholdet (65:30) ble brukt til å produsere pellets med akseptable mekaniske egenskaper. Sekundær varmebehandling av trekullbaserte pellets forbedret hardheten, men reduserte den mekaniske holdbarheten. Bioolje ble brutt ned og dannet en polyaromatisk koksstruktur under høytemperatur pyrolyse. Reaktiviteten til trekullbaserte pellets var lik trekull-biooljeblanding, som indikerer at pelletering ikke påvirker reaktiviteten i forhold til CO_2 på grunn av devolatiliseringen av flyktige komponenter og poreveksten inne i pelleten. Den mekaniske stabiliteten til mangan-kompositttpellets ble redusert etter at manganmalmen ble redusert av karbonet i pelleten. Et stort indre område som inneholdt karbonholdig

karbonmatrise og metallslagg etter høy temperatur pyrolyse ble dannet i pelleten. Det øker verdien av fornybare kullbaserte pellets for bruk i ferrolegeringsindustrien.

Samlet sett hadde pelleteringen med bioolje størst innflytelse på den elektriske resistiviteten ved temperaturer over 900 °C. Effekten av varmebehandlingstemperaturen på trekullpartikler var sterkere ved lave og mellomliggende varmebehandlingstemperaturer, før de grunnleggende strukturelle enhetene i karbonet i pelleten ble omorganisert og sammenblandet. Trekullpartikler som er produsert ved varmebehandlingstemperaturer $\geq 1300\,^{\circ}\mathrm{C}$, viser at en tilsvarende elektrisk resistivitet som metallurgisk koks (10 mΩm). Biomassens opprinnelse ikke viste noen påvirkning på den elektriske resistiviteten. På samme måte ble det dielektriske tapet redusert ved å øke varmebehandlingstemperaturen. Den elektriske resistiviteten ble økt ved å pelletere det komprimerte trekullet med bioolje som bindemiddel. Produksjon av trekullbaserte pellets med bioolje som bindemiddel virker lovende for fremstilling av fornybare reduksjonsmidler med høy elektrisk resistivitet og lav CO_2 reaktivitet.

Chapter 1

Introduction

1.1 Background

Climate change caused by mankind is considered as one of the major issues of the 21st century. The global temperature increase is caused by anthropogenic CO_2 emissions [1], resulting in an advancement of spring events [2], changes in biodiversity [3–5] or increasing heatwaves which might lead to environmental disater [6, 7]. The concentration of CO_2 increased from 316 ppm in 1960 to 406 ppm in 2017 [8], in which the global average temperature increased by about 0.7 °C. More than half of the anthropogenic greenhouse gas emissions (aGHG) are emitted from transport, industrial processes or power stations [9], where about 20 % points of the anthropogenic CO_2 emissions are emitted from the industry. To reduce aGHG emission, the European Parliament and the council of the European Union passed the mandatory target of 20 % share from renewable energy sources in the final energy consumption by 2020 [10]. The Norwegian Climate Policy committed ambitious objectives to cut the global emissions of greenhouse gases equivalent to 30 % of Norway's emissions in 1990 and be carbon-neutral in 2050 [11]. Thus, the reduction of the anthropogenic greenhouse gas emissions is one of major tasks in the upcoming decades [12].

The metallurgical industry contributes to about 10 % of the total CO_2 emissions or 22 % of the total industrial CO_2 emissions worldwide [13]. To fulfill upcoming national regulation, metallurgical industry must reduce the total CO_2 emissions by more effective processes, carbon capture and storage (CCS) or renewable carbon sources. Biomass and its derivatives are considered as CO_2 neutral, because the regeneration time (< 100 years) has no net effect on the biosphere's carbon concentration, due to the closed carbon cycle without a disposal of additional CO_2 emissions. While charcoal is used in steelmaking industry in Brazil to replace about 11 % of mineral coke [14], most companies in the EU continue to rely on fossil based reducing agents due to the limited knowledge of biocarbon

properties and knowledge gaps in the process conditions required to produce biocarbon with acceptable reactivity at low costs. To retain the high throughput and quality of the products, specific properties are demanded for the fuels and reducing agents. Highly reactive and mechanically stable reducing agents are required in blast furnaces, while low reactive reducing agents are desired in iron sintering processes, whereas the mechanical strength is of less importance [15, 16]. In contrast to the metallurgical coke used in blast furnaces and ferroalloy production, renewable reducing agents produced from biomass contain less fixed carbon and provide a greater percentage of volatile matter, and thus, may need to be graphitized prior to its use as a reducing agent [17]. Metallurgical processes can require a minimum fixed carbon content of 90 to 95 % [18], while charcoal produced at temperatures between 450 and 550 °C provides fixed carbon contents < 85 % [19–21]. The increase in heat treatment temperature during pyrolysis results in the further char decomposition and volatile matter release, leading to the greater fixed carbon content [18]. A fixed carbon content of 86.6 % was reported for pinewood char pyrolyzed at 550 °C with 1 h of soaking [22], while heat treatment temperatures > 850°C lead to the fixed carbon content > 85 % for chars produced from agricultural residues [23].
The optimization of charcoal properties and the usage of renewable reducing agents in metallurgical industry has deserved much attention in the recent years, which are directed to an improved furnace operation, reduced power supply in electric arc furnaces (EAF) and a reduction of aGHG emissions. Through improved characterization of the charcoal properties and charcoal compacting, it will be possible to replace larger fractions of fossil fuels in metallurgy and enable the usage of renewable reducing agents in submerged-arc furnaces of the manganese production.

1.2 Project objectives and scope

The work presented in this thesis aimed to develop a novel scientific framework for the efficient conversion of woody biomass into renewable reducing agents used in submerged-arc furnaces. The aim of this PhD project has been 1.) to investigate the influence of a primary and secondary high-temperature heat treatment on the charcoal yield and properties, in particular at temperatures above 900 °C using lab scale reactors 2.) to improve the understanding of the CO_2 reactivity in dependence of the heat-treatment temperature and gas concentration 3.) to investigate the utilization of the liquid byproducts as efficient binder for charcoal pelletization and (4) to study the properties of charcoal-based pellets during the reduction of silicon oxide and manganese oxide. The following chapters of this thesis describe the main results.

- Chapter 2 is a brief literature review of different aspects related to charcoal production and application in metallurgical industry.

- Chapter 3 describes the lab-scale reactors and instrumentation for the product characterization (charcoal + biooil).

- Chapter 4 describes the major results of the present work, whereas sections specifically present the material that was published or submitted to journals:

  - Section 4.1 concerns the experiments performed in a slow pyrolysis retort with the aim of investigating the effects of primary and secondary heat-treatment and biooil conditioning on the product yields.

  - Section 4.2 describes the effect of heat-treatment temperature on the gasification reactivity, nanostructure and carbon chemistry of the charcoal produced at slow heating conditions.

  - Section 4.3 presents the morphology, organic structure and reactivity under oxidation and gasification conditions for heat treatment temperatures above 1300 °C.

  - Section 4.4 deals with the effect of an upstream supercritical carbon dioxide extraction on the charcoal properties.

  - Section 4.5 presents the experimental work on the properties of charcoal-based pellets during the reduction of silicon oxide and manganese oxide

- Chapter 5 discusses the main findings

- Chapter 6 summarizes the results of the preceding chapters.

- Chapter 7 gives suggestions for the future work.

The manuscript is based on five articles submitted to scientific journals which were sorted by the chapter thematically. The submitted articles are listed below. A graphical representation is shown in Figure 1.1.

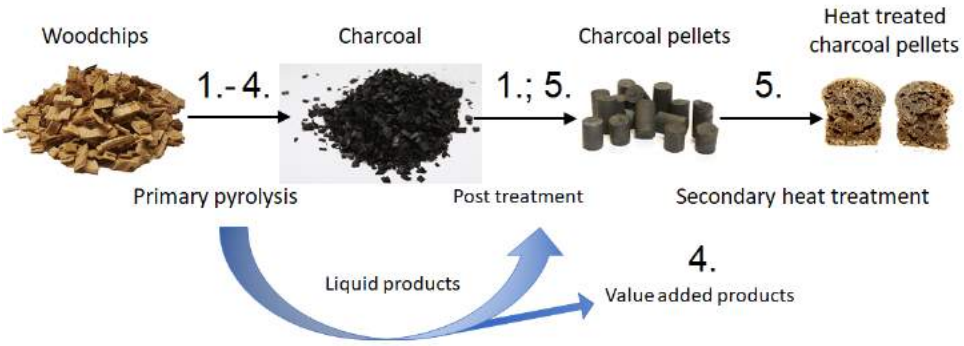

Figure 1.1: Process chain for charcoal pellet production

1. 'Characterization of renewable reductants and charcoal-based pellets for the use in ferroalloy industries' by Gerrit Ralf Surup, Tore Vehus, Per-Anders Eidem, Anna Trubetskaya and Henrik Kofoed Nielsen published in Energy (2019)

2. 'Characterization and reactivity of charcoal from high temperature pyrolysis (800-1600 °C)' by Gerrit Ralf Surup, Henrik Kofoed Nielsen, Markus Heidelmann and Anna Trubetskaya in Fuel (2019)

3. 'The effect of feedstock origin and temperature on the structure and reactivity of char from pyrolysis at 1300-2800 °C' by Gerrit Ralf Surup, Manuel Foppe, Daniel Schubert, Rüdiger Deike, Markus Heidelmann, Michael T. Timko, Anna Trubetskaya published in Fuel (2019)

4. 'The effect of wood composition and supercritical CO_2 extraction on biochar production in ferroalloy industries' by Gerrit Ralf Surup, Andrew J Hunt, Thomas Attard, Vitaliy L Budarin, Fredrik Forsberg, Mehrdad Arshadi, Victor Abdelsayed, Dushyant Shekhawat and Anna Trubetskaya submitted to Energy

5. 'Characterization of charcoal-based composite pellets for the use in ferroalloy industries' by Gerrit Ralf Surup, Henrik Kofoed Nielsen, Marius Großarth, Rüdiger Deike, Jan Van den Bulcke, Pierre Kibleur, Iván Josipovic, Elena Yazhenskikh, Sergey Beloshapkin and Anna Trubetskaya submitted to Energy

Bibliography

[1] M. Parry, O. Canziani, J. Palutikof, P. van der Linden, and C. Hanson. Climate Change 2007: Impacts, Adaptation and Vulnerability. Intergovernmental Panel on Climate Change; 2007 Contribution of Working Group II to the Fourth Assessment Report of the IPCC (978 0521 70597-4 Paperback).

[2] C. Parmesan and G. Yohe. A globally coherent fingerprint of climate change impacts across natural systems. *NATURE*, 421:37–42, 2003.

[3] O.E. Sala, F.S. Chapin III, J.J. Armesto, E. Berlow, J. Bloomfield, R. Dirzo, and et al. Global biodiversity scenarios for the year 2100. *SCIENCE*, 287(5459):1770–1774, 2000.

[4] C.D. Thomas, A. Cameron, R.E. Green, M. Bakkenes, L.J. Beaumont, Y.C. Collingham, and et al. Extinction risk from climate change. *NATURE*, 427:145–148, 2004.

[5] T.P. Hughes, A.H. Baird, D.R. Bellwood, M. Card, S.R. Connolly, C. Folke, and et al. Climate change, human impacts, and the resilience of coral reefs. *SCIENCE*, 301(5635):929–933, 2003.

[6] C. Schär, P.L. Vidale, D. Lüthi, C. Frei, C. Häberli, M.A. Liniger, and et al. The role of increasing temperature variability in european summer heatwaves. *NATURE*, 427:332–336, 2004.

[7] B.N. Goswami, V. Venugopal, D. Sangupta, M.S. Madhusoodanan, and P.K. Xavier. Increasing trend of extreme rain events over india in a warming environment. *SCIENCE*, 314(5804):1442–1445, 2006.

[8] E. Dlugokencky and P. Tans. Trends in Atmospheric Carbon Dioxide. noaa/esrl from www.esrl.noaa.gov/gmd/ccgg/trends/.

[9] O. Edenhofer, R.P. Madruga, Y. Sokona, K. Seyboth, P. Matschoss, S. Kadner, and et al. Renewable Energy Sources and Climate Change Mitigation: Special Report of the Intergovernmental Panel on Climate Change. Cambridge Universiy Press. 2011.

[10] European Parliament, Council of the European Union. Directive 2009/28/ec of the European Parliament and of the Council of 23 april 2009 on the promotion of the use of energy from renewable sources and amending and subsequently repealing Directives 2001/77/ec and 2003/30/ec. 2009.

[11] Norwegian Ministry of the Environment. Norwegian Climate Policy - Report No. 21 (2011-2012) to the Storting (white paper) Summary. 2012.

[12] Report on European Climate Foundation. Roadmap 2050 Volume 1: Technical and Economic Analysis. European Commission; 2010. pages 1–99.

[13] O. Edenhofer, R. Madruga, Y. Sokona, J. Minx, E. Farahani, S. Kadner, and et al. Climate change 2014 mitigation of climate change: Working group iii contribution to the fifth assessment report of the intergovernmental panel on climate change, 2014.

[14] R.G.D. Pinto, A.S. Szklo, and R. Rathmann. CO_2 emissions mitigation strategy in the Brazilian iron and steel sector–From structural to intensity effects. *ENERG POLICY*, 114:380–393, 2018.

[15] J.G. Mathieson, H. Rogers, M.A. Somerville, S. Jahanshahi, and P. Ridgeway. Potential for the use of biomass in the iron and steel industry. *Chemeca 2011. Engineering a Better World, Australia, 18-21 September*, pages 1–12, 2011.

[16] T. Miwa, H. Okuda, M. Osame, S. Watakabe, and K. Saito. Reduction in Steelmaking process by innovative technology for cool Earth 50: CO_2 emission reduction technology in Japan. *Metec InSteelCon, Proc 1st International Conference on Energy Efficiency and CO_2 Reduction in the Steel Industry in Düsseldorf, Germany*, 2011.

[17] H. Suopajärvi. *Bioreducer use in blast furnace ironmaking in Finland.* PhD thesis, University of Oulu, 2014.

[18] K. Weber and P. Quicker. Properties of biochar. *FUEL*, 217:240–261, 2018.

[19] Y. Lee, J. Park, C. Ryu, K.S. Gang, W. Yang, Y.-K. Park, J. Jung, and S. Hyun. Comparison of biochar properties from biomass residues produced by slow pyrolysis at 500 °c. *BIORESOURCE TECHNOL*, 148:196–201, 2013.

[20] M.J. Antal, E. Croiset, X. Dai, C. DeAlmeida, W.S.-L. Mok, N. Norberg, and et al. High-Yield Biomass Charcoal. *ENERG FUEL*, 10(3):652–658, 1996.

[21] M.J. Antal, S.G. Allen, X. Dai, B. Shimizu, M.S. Tam, and M. Grønli. Attainment of the Theoretical Yield of Carbon from Biomass. *IND ENG CHEM RES*, 39(11):4024–4031, 2000.

[22] M.J. Antal and M. Grønli. The art, science, and technology of charcoal production. *IND ENG CHEM RES*, 42(8):1619–1640, 2003.

[23] T. Griessacher, J. Antrekowitsch, and S. Steinlechner. Charcoal from agrocultural residues as alternative reducing agent in metal recycling. *BIOMASS BIOENERG*, 39:139–146, 2012.

Chapter 2

Literature research

This chapter is a brief literature review of different aspects for the usage of renewable reducing agents in the metallurgical industry. Section 2.1 gives an overview of the woody biomass structure, its composition and thermochemical conversion products. In section 2.2 the different types of metallurgical processes are discussed, while section 2.3 is dedicated to the reducing agents used in industrial furnaces for the production of pure metals. The charcoal production processes and mechanism are summarized in section 2.4 and section 2.5. The chapter summarizes the current state of knowledge of the charcoal used as a reducing agent in ferroalloy industries.

2.1 Definitions

The definitions of the feedstock and pyrolysis products used in the thesis are summarized in this section. Different definitions are used in literature for same products, since no precise definition exist for the products of thermochemical conversion processes. The solid product should be efficient to substitute highly carbonized materials, like coke used as a reducing agent in metallurgical industry. Therefore, the feedstock and solid product must provide specific properties, such as a high carbon content and low ash content. As a possible feedstock, only vegetable biomass was reviewed, in particular wood and residues from wood industry. Co-products from cereal production are considered as possible feedstock for thermochemical conversion processes, but the potential in Norway is small compare to the resources of wood.

2.1.1 Biomass

The chemical composition and structure of softwood and hardwood were reviewed in this chapter, since biomass type and its properties have an influence on the biomass conversion process, final product composition and properties. The biomass selection was based on

the available biomass potential and the findings from the literature review. Norway spruce (45 % of the forest), Scots pine (30 % of the forest) and birch tree (16 % of the forest) are the most dominant types of wood in Norway [1].
The chemical composition depends on several factors. Beside the type of biomass, distinct biological diversity, geographical origin, harvesting season and post-processing can have an influence on the properties of the biomass [2–4]. Vassilev et al. summarized that biomass is significant different from coal, where biomass ash is highly enriched in alkali and alkaline earth metal [3]. It will be shown in the following sections that the chemical composition of the biomass has a crucial influence on the pyrolysis process and properties of renewable reducing agents.

2.1.2 Composition of wood

There are different definitions to distinguish between softwoods (gymnosperms) and hardwoods (angiosperms). The botanical classification is based on the tree seed, in which the softwood seed is naked and hardwood seed is covered [2]. Hardwoods contain vessels, as shown in Figure 2.1, which do not occur in softwoods. A technical definition is executed by its gross density, in which wood species with a gross density less $550\,\mathrm{kg\,m^{-3}}$ are accounted for softwoods, respectively larger $550\,\mathrm{kg\,m^{-3}}$ for hardwoods [5]. By rule of thumb, softwoods are evergreen trees while hardwood trees shed their leaves.

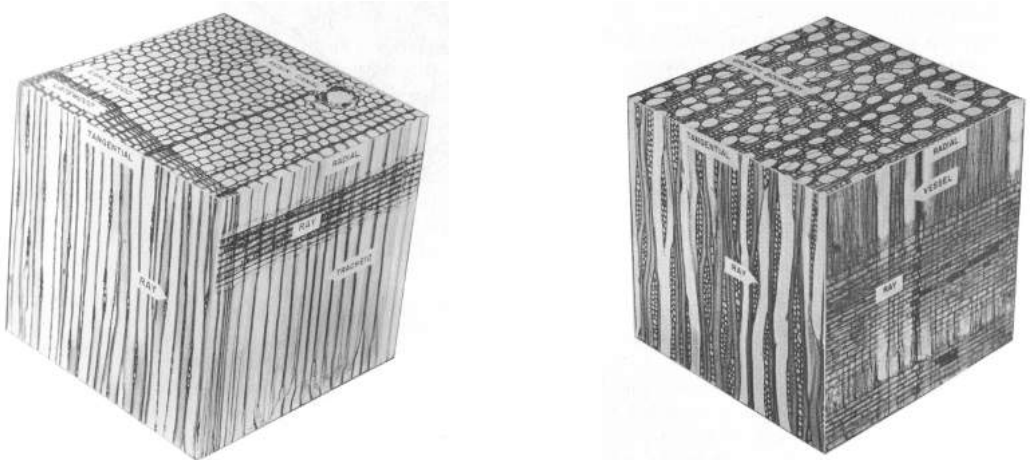

(a) Softwood (b) Hardwood

Figure 2.1: Schematic structure of (a) softwood and (b) hardwood [6]

The main structure of wood can be divided into heartwood, sapwood, cambium, phloem and bark, as shown in Figure 2.2. Heartwood is enriched in extractables and composed of dead cells, while the adjacent sapwood is build up of the main portion of

living cells. New wood is formed in the vascular cambium, and inner sapwood is converted to heartwood over time. Between 60 and 90 % of the wood volume are comprised by conducting and supporting cells, whereas 10 to 40 % of the volume are sapwood [2]. The phloem is a part of the inner bark. The outer bark is formed by cells which are impregnated with suberin, shortly dying after these are build [7].

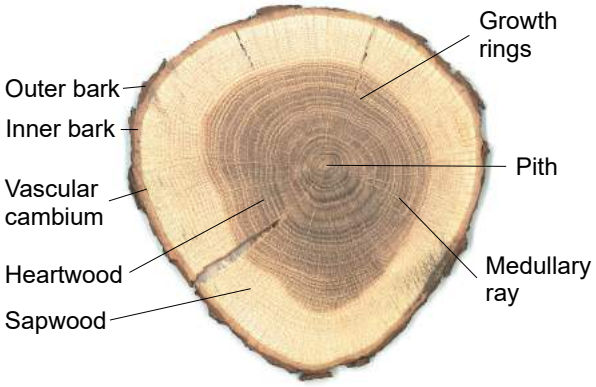

Figure 2.2: Cross section of sessile oak wood *Quercus petraea* [8]

The size of the annual rings varies and depends on the growth conditions [7]. This characterizes the early and late wood, in which the cells from early wood have a larger cross-sectional area with a thin wall and larger lumen compared to the late wood [2]. The early wood can be distinguished by its color, where the light portion is the early wood with a larger diameter in radial direction and thin walls, whereas the darker late wood is composed of cells with smaller diameter and thicker walls, leading to a less effective conduction, but a more stable structure which contributes to the stability of the stem [9]. Softwood and hardwood are classified by cell type and structure. Softwood is mainly composed of two cell types; longitudinal tracheids and transverse parenchyma, in which about 90 % of the volume is constituted to longitudinal tracheids, respectively 10 % to parenchyma cells [2]. The longitudinal tracheids are the largest cells in softwood, in which these cells are about 100 times longer than wide. The main purpose is the water conduction and the transport of dissolved minerals throughout the softwood, where the water passes from one tracheid cell to the next by pits. Due to the large proportion of tracheid cells in softwood, chemical and physical properties are mostly determined by this cell type [2].

In comparison, most hardwoods are comprised of vessel segments, fibers, transverse and axial parenchyma. Parenchyma cells are also called rays [7]. The largest cells in hardwood are vessel segments with a length of 8 to 10 times of its width, which perform the conduction of water. The transport from cell to cell is carried out in perforation plates between the cell walls. Fibers provide additional support to the mechanical stability of

the wood, in which an increasing percentage volume of fibers can result in a higher density of the wood [7]. Fibers are abundant in oak (*Quercus*), and parenchyma cells are used by the tree to store food in cells. A schematic structure of softwood and hardwood is shown in Figure 2.1. Due to the different cell types and growth direction, wood provides an anisotropic structure resulting in the up to 10^4 times higher permeability to gas flow along the grain than in the cross section of the grain [10].

The internal cell wall of softwood and hardwood is mainly composed of cellulose, hemicellulose and lignin, contributing to 95 to 98 % of it, whereas extractives account to 2 to 5 % [2]. Cellulose contains up to several thousand of linked β-(1→4)-D-glucose, as shown in Figure 2.3 (a) [7]. Hemicellulose contains multiple sugar units of xylan, glucuronoxylan, arabinoxylan, glucomannan, and xyloglucan. A partial structure of hemicellulose is shown in Figure 2.3 (b). The polysaccharides (cellulose and hemicellulose) in woods are also summarized as holocellulose [11]. Lignin consists of non-carbohydrate compounds or monolignols which include paracoumaryl alcohol, coniferyl alcohol and sinapyl alcohol. Lignins provide structural strength and sealing of the water-conducting system that links roots with leaves, and protect plants from degradation. Lignin occurs throughout the plant cell wall, yet is largely concentrated in the primary cell wall and middle lamella [7]. While hardwood lignins are produced from a similar portion of sinapyl alcohol and coniferyl alcohol, softwood lignins contain about 10 times more coniferyl alcohol than sinapyl alcohol precursors, leading to a more cross-linked and stable molecule [2]. The partial structure of the different components is shown in Figure 2.3.

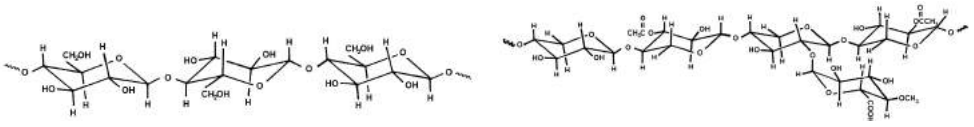

(a) Cellulose (b) Hemicellulose

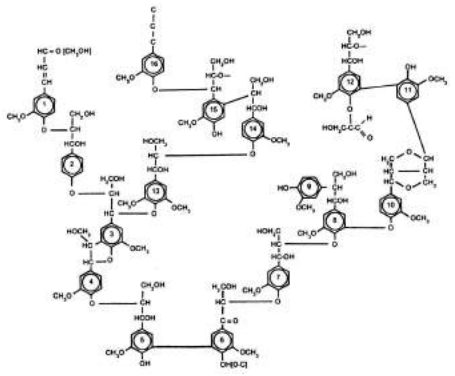

(c) Lignin

Figure 2.3: Partial molecule structure of (a) cellulose in the 1,4-β-D-glucopyranose form, (b) hemicellulose and (c) softwood lignin [11]

2.1.3 Charcoal

This section focuses on the definition and main properties of charcoal, whereas the production of charcoal is summarized in section 2.4. Charcoal is considered as the solid product of a partial or complete thermal decomposition of biomass and has been used by mankind since thousands of years [12]. It contains the unconverted organic solids, the carbonaceous products and the non-volatile mineral matter. In metallurgical industry, charcoal was used as the main reducing agent before the industrial revolution, and later it was replaced by fossil resources like coal and coke.

In literature, there is no precise definition of the term charcoal [13]. Emerich defined charcoal as the solid residue of non-agglomerating organic matter of biomass (both vegetable and animal origin) that results from thermal treatment at temperatures above 300 °C in the absence of air [12]. Other scientist defined charcoal as the solid residue from vegetable biomass [10, 14, 15]. However, these carbonaceous products are also called biochar [16], especially when they are used as a soil amendment or in the environmental application [17–20]. Biocoal, char or carbonaceous products are also synonyms found in the literature [21, 22]. The solid produced from pyrolysis of biomass-coal blend is called biocoke. [23–26]. Beside charcoal, soot, carbon black and pitch-coke can occur as solid residues from secondary reactions of the volatile matter. These products are considered as secondary charcoal in this thesis.

The charcoal yield is highly affected by the process conditions of the pyrolysis, like feedstock origin, heating rate, residence time, particle size, pressure and heat treatment temperature [27]. Charcoal yields at selected temperature are maximized at low heating rates, long residence times and high pressures [28, 29], where increased pressure leads to an increase in char yield (up to 50 %) with the decreased residence time [30]. Feedstock origin and pyrolysis operating conditions have a major influence on the physical, chemical and mechanical properties of the charcoal [31, 32]. Furthermore, the obtained structure of charcoal is defined by the morphology of the feedstock, as shown in Figure 2.4 [15]. The char structure is affected by high heating rates and small particle sizes, whereas slow heating rates and large particle sizes result in similar charcoal structure compare to the original biomass [32]. The charcoal produced from dense hardwoods, such as birch, beech and oak have a high mechanical strength that is desirable in ferroalloy industries [13]. An increase in heat treatment temperature and residence time results in an enhanced release of volatile matter, leading to a more carbonaceous charcoal with lower H/C and O/C ratios [16, 33]. Moreover, an increase in absolute pressure can decrease the O/C ratio due to the increased fixed carbon content [34]. The larger carbon content is coherent with larger carbon clusters and a higher degree of graphitization. However, classical pyrolysis temperatures at 500 °C do not lead to the formation of crystalline structure for the im-

provement of thermal and electrical conductivity [35].

Heat treatment temperatures in the range 2000 to 3000 °C are required to produce the crystalline char structure [36]. Chen et al. reported structural changes for coal graphitization in four temperature ranges: 1000-1500 °C, 1500-2000 °C, 2000-2500 °C and 2500-3000 °C, with a tendency of rapid ordering at 1800 °C [37]. Similar temperature ranges were reported by other scientists [38]. The basic structural units reorganize in the temperature range 800 to 1500 °C and coalesce in the temperature range 1600 to 2000 °C into disordered wrinkled layers [38]. Above 2100 °C these layers become more graphitic [39].

Charcoal produced from woodchips at temperatures above 1000 °C contains graphitized carbon that has a similar structure to the carbon in petroleum coke [40]. However, charcoal is very different from other highly carbonized compounds such as graphite, since it has larger surface area and greater absorptive capacity than graphite and carbon black [15]. An increase in graphitization of the charcoal carbon results in a loss of ohmic resistance [37], which can be disadvantageous for the use in electric arc furnaces. In addition, the electric conductivity is affected by the packing density, particle size and surface elements, such as oxygen groups of charcoal [41].

Thus, properties of charcoal can be designed by the selection of biomass type and process conditions. Charcoal produced for domestic cooking should provide a volatile matter content of at least 20-30 %, whereas charcoal for metallurgical application should should have a fixed carbon content of 85-90 % [13]. Low heat treatment temperatures, such as torrefaction, improve the specific density for transportation and storage. Byrne and Nagle showed that the carbonized wood is 28 % stronger than its biomass precursor [42], leading to the low production of small particles. However, an additional heat treatment of biomass samples did not have a significant influence on the final char yield [13].

The mineral matter content and its composition are mainly affected by the biomass origin and pyrolysis temperature. While most wood species are low in ash content, e.g. less 2 wt.% for spruce and oak, the ash content of herbaceous biomass can be greater than 10 wt.% [43]. With the increased heat treatment temperature, alkali metals (K, P, Ca, Mg) can accumulate in the charcoal matrix and thus, can increase the final ash content [44, 45]. These nutrients are also important for the plant growth.

Charcoal exhibits a higher reaction rate in CO_2 compared to fossil reducing agents. Xing et al. determined a 75 % greater reaction rate of charcoal in CO_2 compared to a biocoke [46]. The high reaction rate can be correlated to the formation of amorphous carbon structures, aliphatic side chains and the larger surface area of charcoal compared to biocoke [38]. The high surface area, pore volume and acidity of charcoal affect the catalytic ability of the charcoal for the different use in ferroalloy industries [47].

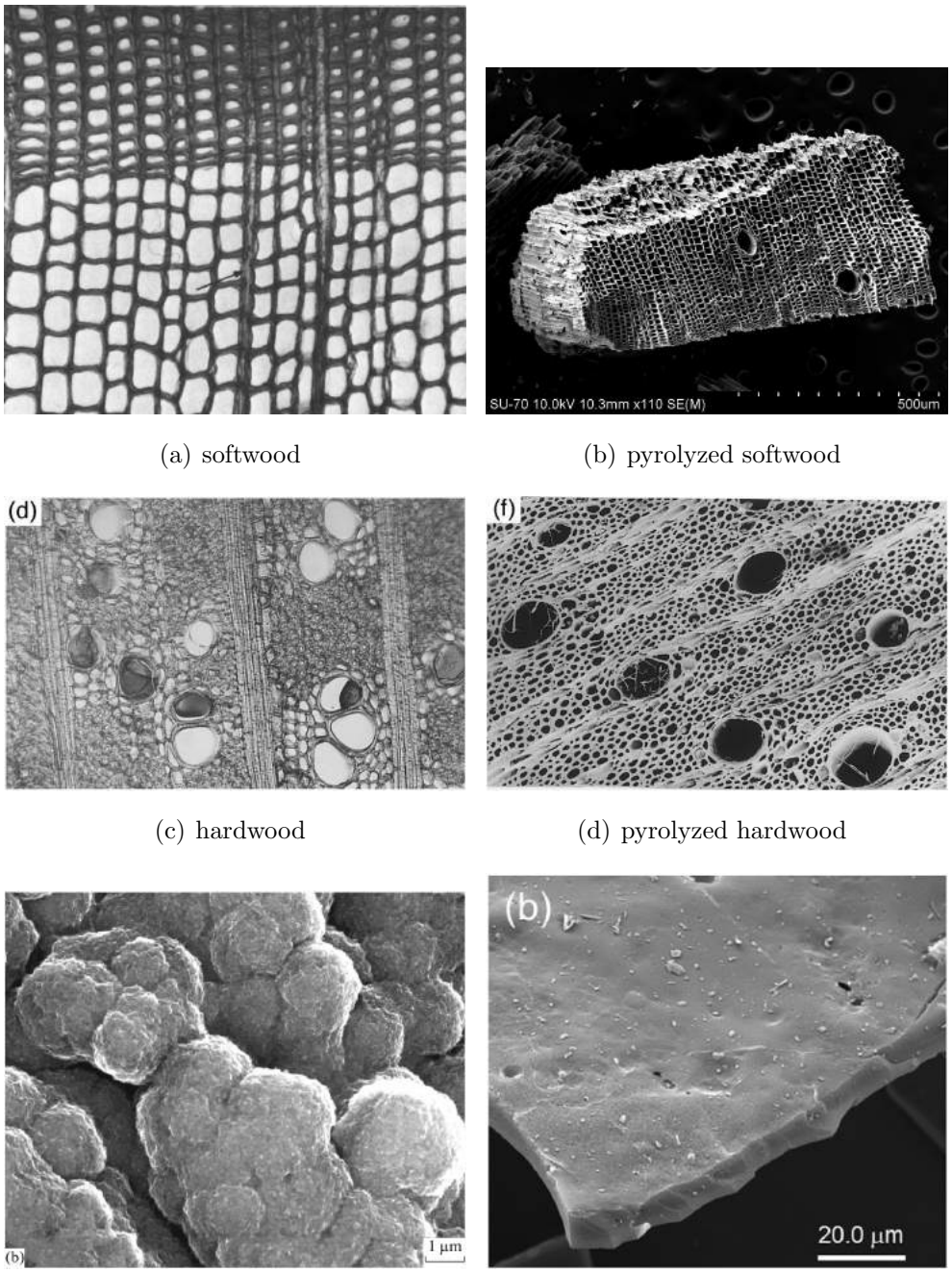

(a) softwood (b) pyrolyzed softwood

(c) hardwood (d) pyrolyzed hardwood

(e) soot (f) biooil pitch

Figure 2.4: SEM picture of (a) softwood [2], (b) pyrolyzed softwood [48], (c) hardwood [49], (d) pyrolyzed hardwood [49], (e) soot [50] and (f) biooil pitch [51]

2.1.4 Biooil

The condensed liquid products from pyrolysis of biomass are here called biooil. Other synonyms are bio-oil, pyrolysis oil, bio-crude, pyrolysis liqid, pyroligneous acid, wood liquid, wood oil and wood distillate [31, 52]. Biomass tar, biotar and pyrolysis tar are also synonyms for the condensed hydrocarbon fraction produced in biomass pyrolysis [53–55].

The yield of liquid pyrolysis products mainly depends on the heating rate, gas residence time and heat treatment temperature [52, 56, 57]. Particle size, moisture content and heating rate affect the yield of the biooil by secondary reactions [58]. The greatest yields of biooil were obtained at moderate and fast heating rates [52]. By the rule of thumb, the biooil yield is expected to be in the range 40-70 wt.% when small biomass particle sizes at short residence time are reacted in the temperature range 400 to 600 °C [27]. The biooil and charcoal yields varied from 62 to 68 % and from 11 to 14 % on dry basis, while the gas yields ranged from 20 to 26 % during the fluidized bed pyrolysis at 500 °C and residence time of 2 s [44].

Biooil is a complex mixture that consists of several hundreds to thousands of different organic compounds [52, 59, 60]. More than 300 organic compounds have been identified in biooil from fast pyrolysis [61]. More than 400 different compounds were analyzed by GC-MS and HPLC-Orbitrap MS with a molecular mass distribution between 100 and 400 Da [59, 62]. Gas chromatography has a recovery rate of 30 to 70 % of the condensate when these are revaporized [52]. Electrospray Ionization (ESI) and atmospheric pressure chemical ionization (APCI) were used by Staš et al. to identify compounds in the range of 100 to 450 Da, respectively 100 to 650 Da, in which up to 12 oxygen atoms were detected in molecules of the biooil [63]. Slow pyrolysis biooils provide a lower oxygen, water content and lower polarity due to secondary reactions, such as dehydration, decarboxylation and condensation [64].

The majority of the identified compounds are water, carboxylic acids, aldehydes, ketones, furfurals, sugar-like material, and lignin-derived compounds, like phenolic compounds [31, 33, 62, 65, 66]. Meier and Faix described biooil as a complex mixture of oxygenated aliphatic and aromatic compounds [67]. Biooils produced at fast pyrolysis conditions exhibit a 85 to 112 % higher molecular weight compared to that at slow pyrolysis conditions [68]. The composition is affected by lignocellulosic composition of the biomass and process conditions, in which heating rate has a greater influence than the biomass origin [64]. Secondary reactions of the biooil can form additional hydrocarbons like light olefins, cyclic hydrocarbons and aromatics [66, 69]. Levoglucosan for example, as a major product of cellulose pyrolysis, starts to decompose at temperatures above 500 °C [58, 70]. An increase in heat treatment temperature up to range between 700 and 900 °C can decrease the total biooil yield and the amount of phenolic compounds, while the amount of aromatic compounds can increase [33]. In contrast, Thangalazhy-Gopakumar et al. found that both phenols and toluene concentrations increase with increasing heat treatment temperature [71]. The condensable large molecular aromatic compounds are mostly considered as tertiary products [52, 58].

Due to the high water content and organic acids, biooils are acidic with a pH value in

the range 1.7 to 2.4 and with an estimated water content between 20 to 30 % [44, 64, 65]. Thus, the high water and oxygen content and high acidity of liquid products can hamper the use of biooil as transportation or boiler fuel [58, 65, 72]. The higher water content in biooil from fast pyrolysis gives a low viscous product compared to that from slow pyrolysis processes [64]. The influence of the average molecular mass is not as important as the biooil-water insoluble fraction in slow pyrolysis [72]. The formation of pyrolysis water depends on the feedstock type, and is greater in oak and eucalyptus than in pitch pine and Japanese cedar [44].

Furthermore, the high reactivity of the biooil can lead to a polymerization during storage or when heated [58, 65, 72, 73], which inhibits further upgrading due to coking [72, 74]. Atmospheric distillation, as a thermal separation technique, starts below 100 °C and continues to temperatures of about 280 °C [66], where up to 50 % solid residues are formed [73], referred to as distillate bottoms or bio-pitch. The thermal decomposition of the biooil over HZSM-5 catalysts results in a coke yield of about 10 to 20 wt.% [75, 76], which is mainly formed from large phenolic components and aldehydes [77, 78]. A coking value of about 29 and 34 % was analyzed for coniferous tree sawdust, respectively deciduous tree sawdust [39].

This bio-pitch can be utilized in other applications, for example as a binding agent and electrode production [51]. These calcined products are low in sulfur and metal contents and are superior to calcined petroleum coke [51], reducing the amount of emitted polycyclic aromatic hyrdocarbons in carbon-graphite technologies [39].

Biooil as binding agent enables the usage and separation of the coke forming compounds from the stable biooil by increasing the solid pyrolysis yield. Aqueous phase hydrogenation was used by Vispute at low temperatures to convert the remaining thermally unstable oxygen bonds (C=O bonds) to stable compounds [73]. A thermal polymerization of the biooil can assist to form graphitic structures on the charcoal structure to improve its properties. The biooil from pyrolysis of deciduous trees enhanced the char graphitization more than the biooil from pyrolysis of coniferous trees [39]. The polymerized bio-pitch exhibited a similar structure to coal tar pitch, whereas the bio-pitch contained less sulfur and ash than coal tar pitch [39].

In general, the H/C ratio of the heavy fraction of biooil is low and the biooil contains mostly large aromatic structures which are formed at temperatures above 600 °C [56, 66]. In addition, the biooil has value-added properties for a downstream processing, such as a binding agent for pelletizing or briquetting.

2.2 Metallurgical processes

The major technologies used in iron and steel industry are carbothermic processes, such as blast furnaces and electric arc furnaces. Electrolytic reduction is mainly applied for aluminum production. Alloying elements like silicon and manganese are mostly produced in electric arc furnaces. On the whole, metallurgical processes contribute to approximately 10 % of the anthropogenic CO_2 emissions [79], mainly from direct and indirect emissions. Direct emissions are emitted at the metallurgical plant and generated by reducing the metal-oxides or generating the heat required for the process, whereas indirect emissions are emitted by power plants and by transportation. The iron and steel industry emitted about 2.3 billion tons of CO_2 in 2007 and may increase to 3.0 billion tons of CO_2 in 2050 [24].

For the reduction of overall GHG emissions, new technologies and renewable reducing agents have been investigated in the last years. Electrolysis is an alternative technology to reduce metal-oxides [80]. Carbothermic reduction of alumina has been investigated as an alternative process for the production of aluminum [81, 82], shifting the indirect CO_2 emissions from its power input to direct ones.

The basic principle of carbothermal reduction processes is stated in equation 2.1 and 2.2, in which the oxidation state of the metal-oxide is reduced by one. Carbon and carbon monoxide act as a reducing agent in both solid and gaseous state. The reaction of the metal-oxides takes place at different temperature ranges, depending on the reactivity and free enthalpy of formation, dividing the furnace in different reaction zones. The main reactions for the reduction of manganese-oxides, silicon-oxides and iron-oxides are summarized in Table 2.1.

$$Me_xO_y + C \rightarrow Me_xO_{y-1} + CO \tag{2.1}$$

$$Me_xO_y + CO \rightarrow Me_xO_{y-1} + CO_2 \tag{2.2}$$

Carbothermal reduction requires large amounts of carbon at high temperature to reduce the metal-oxides. Based on the technology, metallurgical furnaces require the carbonaceous charge to provide the required temperature in the furnace. For example, the production of pure metals in blast furnaces requires about four times more metallurgical coke compared to electric arc furnaces [83]. The required process temperature for the reduction of metal-oxides by carbon, methane or hydrogen can be predicted by the Ellingham diagram. This diagram was developed in 1944 and is schematically shown in Figure 2.5 for several metals. The free enthalpy of formation is stated on the ordinate and the required temperature on the abscissa. This visualizes the stability of the metal-oxide relative to carbon, which can be reduced when the carbon line intersects the line of the metal-oxide. It is obvious that the reduction of metal-oxides, especially alumina, takes place at very

high temperatures.

The high process temperatures require a mass and energy flow analysis of the metallurgical process to avoid losses. Heat recovery and improvements of the available technologies have reduced the energy consumption in steel production by approximately 60 % in the last 50 years [79], resulting in an average energy consumption of $20\,\mathrm{GJ\,t^{-1}_{crude\ steel}}$ at $1.83\,\mathrm{t_{CO_2}\,t^{-1}_{steel}}$. The potential for the further improvement was estimated to be 15 to 20 % [79, 84], in which the blast furnace technology still has the largest energy saving potential [85]. The cumulative energy saving of 41 technologies used in China contributed to a saving of $4.63\,\mathrm{GJ\,t^{-1}}$ or $443\,\mathrm{kg_{CO_2}\,t^{-1}}$ [85]. Kuramochi assessed the best available technologies with the replacement of coke and an increased usage of steel scrap in a case study for Japan, in which 12 % of total emissions can be reduced by 2030 [86]. To further decrease GHG emissions, new technologies and processes must be developed, including the implementation of carbon capture and storage (CCS) [80].

For an integrated steelmaking operation in a blast furnace, approximately 350 to 400 kg of coke per tonne crude steel are used for sintering and cokemaking blend components, while approximately 200 to 250 kg of nut coke and tuyere injectant per tonne crude steel are used [87]. Smelting-reduction technologies (e.g. COREX) use approximately 900 kg of coal and 100 kg of coke per tonne hot metal, leading to direct CO_2 emissions of 2.3 t CO_2 per tonne crude steel [88], which would increase the charcoal demand in contrast to classical routes. The usage of biomass and charcoal in metallurgical industry is challenged by technical and economical aspects, in which the synergy between both sectors is required to overcome these obstacles [24]. Biomass and its derivatives have the potential to reduce the CO_2 emissions in the range of 6 to 12 % in the electric arc furnace (EAF), respectively from 32 to 58 % for integrated routes [87], illustrating the importance of selected processes.

Table 2.1: Reduction reactions of manganese-oxide, silicon-oxide and iron-oxide and free energy of formation and temperature ranges of these reactions

reaction	formation enthalpy [kJ mol^{-1}]	temperature range [°C]
manganese-oxides [89]		
$3Mn_2O_3 + C \rightleftharpoons 2Mn_3O_4 + CO$	-0.25–$0.17T$	25-1100
$3Mn_2O_3 + CO \rightleftharpoons 2Mn_3O_4 + CO_2$	-170.71–$0.004T$	25-1100
$Mn_3O_4 + C \rightleftharpoons 3MnO + CO$	110.96–$0.21T$	25-1244
	84.35–$0.20T$	1244-1700
$Mn_3O_4 + CO \rightleftharpoons 3MnO + CO_2$	110.96–$0.21T$	25-1244
	84.35–$0.20T$	1244-1700
$MnO + CO \rightleftharpoons 3Mn + CO_2$	$102.38 + 0.01T$	25-1227
	$116.73 + 0.01T$	1227-1727
$MnO + C = Mn + CO$	287.6–$0.16T$	25-1227
silicon-oxide [90–95]		
$SiO_2 + 3C \rightleftharpoons SiC + 2CO$	625	1250-2000
$SiO_2 + C \rightleftharpoons SiO + CO$	664	1500
$SiO_2 + 2C \rightleftharpoons Si + 2CO$	687	2000
$SiO + 2C \rightleftharpoons SiC + CO$	-74	1500
$SiO + 3CO \rightleftharpoons SiC + 2CO$	-397	1500
$2SiO_2 + SiC \rightleftharpoons 3SiO + CO$	1380 to 1416	1500
$SiO + SiC \rightleftharpoons 2Si + CO$	167	2000
$2SiO \rightleftharpoons SiO_2 + Si$	-599	2000
$2Si + CO \rightleftharpoons SiC + SiO$	166.3	1500
iron-oxide [96, 97]		
$3C(s) + Fe_2O_3(s) \rightleftharpoons 2Fe(s) + 3CO(g)$	$462 - 0.507T$	700-1200
$3CO(g) + Fe_2O_3(s) \rightleftharpoons 2Fe(s) + 3CO_2(g)$	$-26.37 - 0.004T$	700-1200
Boudouard reaction [89]		
$C(s) + CO_2(g) \rightleftharpoons 2CO(g)$	$170.82 - 0.18T$	25-1727

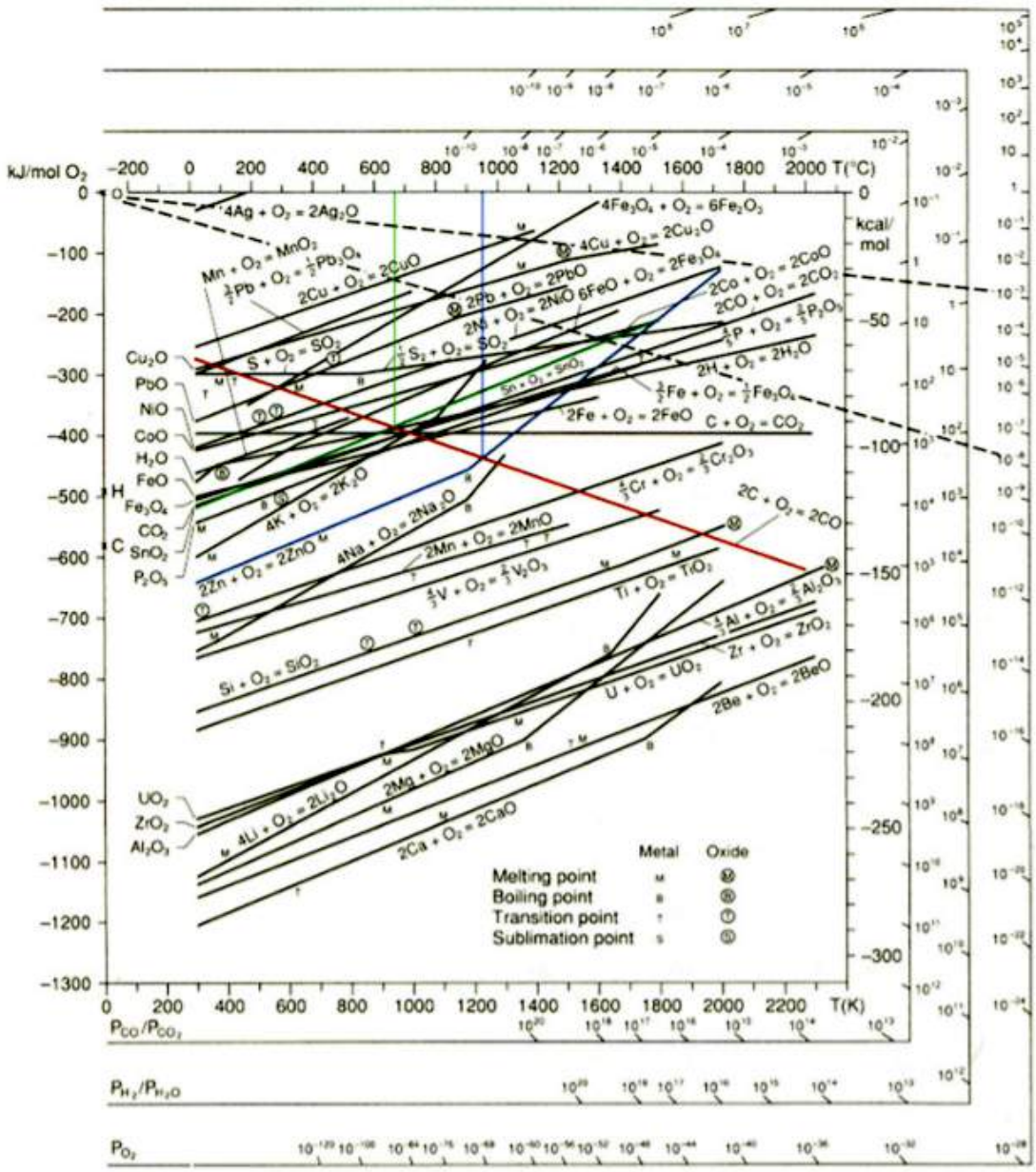

Figure 2.5: Ellingham diagram for several metals [98]

Aluminum is mainly produced in the Bayer process followed by an electrolytic reduction called Hall-Héroult process, as shown in Figure 2.6. The energy consumption of the primary production route is stated for cradle-to-gate between 188 and 211 $\mathrm{MJ\,kg_{Al}^{-1}}$ with a global-warming potential (GWP) of 22.4 $\mathrm{kg_{CO_{2,eq.}}\,kg_{Al}^{-1}}$, when power is provided by coal fired power plants [81, 99]. Considering a CO_2 neutral power production, the primary energy consumption for 1 kg aluminum can be reduced to $\approx 100\,\mathrm{MJ\ kg^{-1}}$ [82]. The direct CO_2 emissions in Hall-Héroult process are mainly formed by the anode consumption, in which an excess of 35 % compared to stoichiometric requirements was estimated by Choate and Green for the classical aluminum production [100]. The carbon source for electrode production may partly be replaced by calcined biooil pitch to reduce these emissions [51].

Several attempts were undertaken since 1962 to introduce the carbothermic reduction of alumina as an alternative to the energy intensive Hall-Héroult process [101]. The energy demand can can be reduced to about 136 MJ kg_{Al}^{-1} by carbothermal reduction processes, in which the CO_2 emissions decrease from $\leq 15\,kg_{CO_2}$ kg_{Al}^{-1} to $\leq 12\,kg_{CO_2}$ kg_{Al}^{-1} for indirect emissions and 3.8 to 2.6 kg_{CO_2} kg_{Al}^{-1} for direct emissions. Several drawbacks of this process, such as heat supply and slag transfer, have been solved with the ACT-ARP (aluminum carbothermic technology - advanced reactor process) developed by Alcoa-Elkem [102, 103], but industrial application has not been achieved for this type of process [81]. In general, recycling of metals is less energy intense than the primary production routes. The recycling of scrap requires about 4 to 6 GJ per tonnes of iron compared to the 13 to 14 GJ per tonnes iron in blast furnace basic oxygen furnace (BF-BOF) [84, 104]. The energy consumption for the recycling of aluminum is stated to about 5 to 10 % of the primary production route [105], illustrating the importance of metal recycling for the reduction of the energy input and GHG emissions.

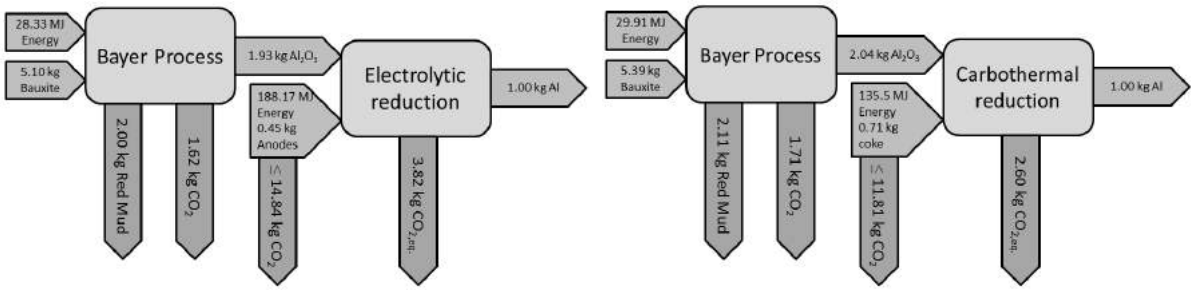

(a) electrolytic (b) carbothermal

Figure 2.6: Simplified mass and energy balance of primary aluminum production: left: electrolytic process; right: carbothermal process [81]

In general, the main products from metallurgical processes are the pure metal, gases such as carbon monoxide and carbon dioxide, and slag. Carbon monoxide is formed by the reaction of solid carbon with the metal-oxide, which also acts as a reducing agent according to equation 2.2. For high carbon ferro-manganese (HC FeMn) production, the partial pressure of CO is about 100 kPa in electric arc furnaces, respectively 35 kPa in blast furnaces [104]. Carbon dioxide reacts with the solid carbon, as shown in Table 2.1, forming additional carbon monoxide at the cost of solid carbon. The Boudouard reaction is a highly endothermic reaction with a reaction enthalpy of 172.5 kJ mol^{-1}, increasing the power requirement in the EAF. Almost 500,000 tonnes of the annually CO_2 emissions in FeMn and SiMn production are correlated to the Boudouard reaction, corresponding to approximately 30 % of the annual emissions [106]. The objective of the present work was related the reduction of CO_2 emissions by synergistic effects of renewable reduction agents in ferromanganese production.

2.2.1 Blast furnaces

Blast furnaces are the most common metallurgical furnaces in metallurgy to produce iron and steel and other pure metals. The basic oxygen furnace (BOF) accounted for about 74 % in steelmaking in 2014 [79, 84]. Beside pig iron, blast furnaces are also used to produce pure copper and lead. For steel production, 40 to 50 % of the energy requirement are related to metallurgical coke and coal [24], in which the properties of the metallurgical coke are essential for a stable furnace operation [107]. Based on the quality of the feedstock, plant size and heat recovery, the differences in energy efficiency between industrial and developing countries can be as high as 50 % [84].
The schematic of a blast furnaces is shown in Figure 2.7. It is operated as a counter-current furnace, in which ore and coke are charged in layers at its top, while the blast and oxygen are injected at the bottom of the furnace. This operation enables a high heat recovery from the produced gases within multiple temperature and reaction zones in the furnace. Initial reaction of hemantite can start at temperatures between 200 and 600 °C [108]. According to Geerdes, Chaigneau and Kurunov the first reduction reaction takes place at temperatures about 500 °C in the stack [109]. Reduction reactions can be divided into indirect reduction reaction below 1000 °C, where FeO is formed by the reduction of Fe_2O_3 and the consecutive direct reduction of FeO to Fe above 1000 °C [110]. With an increasing temperature above 1000 °C the ore starts to melt in the cohesive zone, creating voidage in the bulk. To this temperature, metallurgical coke lost about 2 wt.% by the release of remaining volatile matter [111]. The reaction between coke and CO_2 slowly starts after surpassing the threshold temperature at about 910 °C [112].

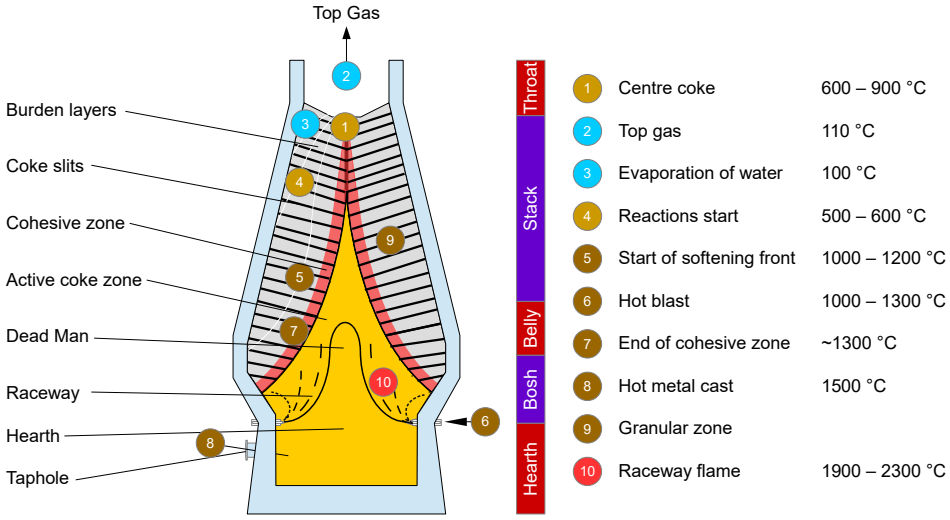

Figure 2.7: Schematic presentation of a blast furnace with the main reaction zones and temperature profile [109]

Oxygen and fuel are injected into the blast furnace by tuyeres at the bottom of the blast furnace. Coal, natural gas and oil are used as carbon sources in the blast, in which the coke in front of the tuyeres is also partly combusted to CO. The consumption of coke in front of the tuyeres creates voidage and weakens the bed structure. Depending on the size of the blast furnace, up to 12 tuyeres are installed in small blast furnaces, respectively up to 42 in larger ones [109]. The combustion and reaction of the blast takes place at the raceway, in which particle size distribution and the reactivity are key parameters on the flow and fuel combustion [110]. Previous studies have shown that conditions in the raceway are important for an effcient combustion of the blast [113].
Different carbon sources are charged into the blast furnace, namely metallurgical coke, coal, oil and natural gas. These carbon sources are used as reducing agents and energy carrier [114]. The main carbon source is metallurgical coke which is fed into the top of the furnace. For stable operation of the furnace, the metallurgical coke requires a high mechanical stability, low amounts of volatile matter, good gas permeability and low reactivity. On the other hand, the blast should provide a high heating value and high reactivity to form CO. Thus, the different carbon feedstocks used in the blast furnace require specific properties. The partial replacement of coke by the injected blast was found as the best available technique to reduce coke consumption [114]. Depending on the blast furnace type, maximum injection of 270 to 290 kg of pulverized coal per tonnes pig iron can be utilized [86, 115]. The pulverized coal injection (PCI) can replace coke at a rate of 0.85 to 0.95 kg of coke per kg pulverized coal for a PCI consumption of 180 to 200 kg per tonnes pig iron [86, 116]. A lower limit of 290 kg of coke per tonnes hot metal was assumed by Ribbenhed, Thoren and Sternhufvud [115]. Previous studies have shown that modern blast furnaces are operated with the metallurgical coke consumption of 286 to 320 kg per tonnes hot metal and a PCI of 170 to 220 kg per tonnes of hot metal [24].
A high gasification threshold temperature of the metallurgical coke is important to reduce the carbon consumption by the Boudouard reaction in the stack. On the other hand, a lower gasication threshold temperature can improve the blast furnace reaction effciency and reduce the coke consumption [112]. Thus, the replacement of metallurgical coke with renewable carbon sources such as charcoal, biocoke, charcoal-coke blends or charcoal pellets requires such properties as high mechanical stability and chemical resistance.

2.2.2 Electric arc furnaces

Electric arc furnaces (EAF) can be operated with an alternating current (AC) or a direct current (DC). In ferroalloy industries, electric arc furnaces have been operated with an alternate current since the beginning of the 20th century, whereas DC furnaces have been used only since the last 30 years [117, 118]. Nowadays, EAF are used in about 20 different

industrial fields [117]. While power rating of first EAF was about 1.5 MVA, maximum power rating reached 135 MVA with a power input of 100 MW in 2015 [117, 119]. In Norway, most metallurgical furnaces are electric arc furnaces operated with an alternate current. Especially in Southern Norway, where three of four metallurgical processes are operated as carbothermal processes, and the fourth as an electrolytic process. These processes comprise the production of silicon manganese (SiMn) by Eramet, silicon (Si) by Elkem and silicon carbide (SiC) by Saint-Gobain, as well as the production of aluminum (Al) by Alcoa.

In carbothermal processes operated as EAF, the heat is provided by electricity and reduction by carbonaceous materials [38]. Three electrodes installed in the most EAF processes are operated with the alternating current, while very large rectangular-shaped furnaces are operated with six electrodes [119]. The power input is at the highest capacity when a three electrode-circuit exhibits a similar impedance [120]. For submerged arc furnaces, the resistance of the burden, i.e. the carbon material, limits the allowable electrode penetration into the hearth [120].

The power rating of an EAF is limited by its electricity supply or by the furnace transformers [120]. For example, Eramet Norway Kvinesdal uses three 30 MW smelting furnaces for the production of 180000 tonnes of SiMn [121]. The power consumption for the production of 1 kg SiFe result for modern furnaces in about 3.4 kWh (Porsgrunn) and 4.2 kWh (Kvinesdal). Up to 35 % of the energy input was recovered from the CO gas in Porsgrunn. Silicon and ferrosilicon are mostly produced in submerged arc furnaces operated at 12 to 24 MW [119], resulting in a power consumption of 10 to 13 kWh kg^{-1} of silicon [37, 119, 122, 123]. This power input accounts for about 45 % of the required energy of the furnace [122], while remaining energy demand is provided by carbonaceous materials. The working principle of an EAF is schematically shown by the reduction pathway of manganese in Figure 2.8. Depending on the quality of the charge, the EAF emits several GHG emissions, such as volatile organic compounds (VOC), particulate matter, carbon monoxide, carbon dioxide, sulfur oxides, nitrogen oxides, dioxins and furans [124]. Demus et al. stated that a specific consumption of 12 kg coal and coke per tonnes of steel results in 40 to 70 % of the direct emissions of the EAF [125]. Biomass and charcoal can reduce these emissions by two effects: 1. the carbon dioxide emissions are accounted as CO_2 neutral, 2. a higher efficiency of the renewable reducing agents decreases the carbon demand of the process. Chen et al. investigated a synergistic effect between petcoke and woodchips, in which an increased reactivity improved the utilization of silica [126]. Similar results were observed by Demus et al. for steel production, in which no negative effects on the product quality were observed [125]. Woodchips improve the gas permeability of the burden and prevent charge crusting [38].

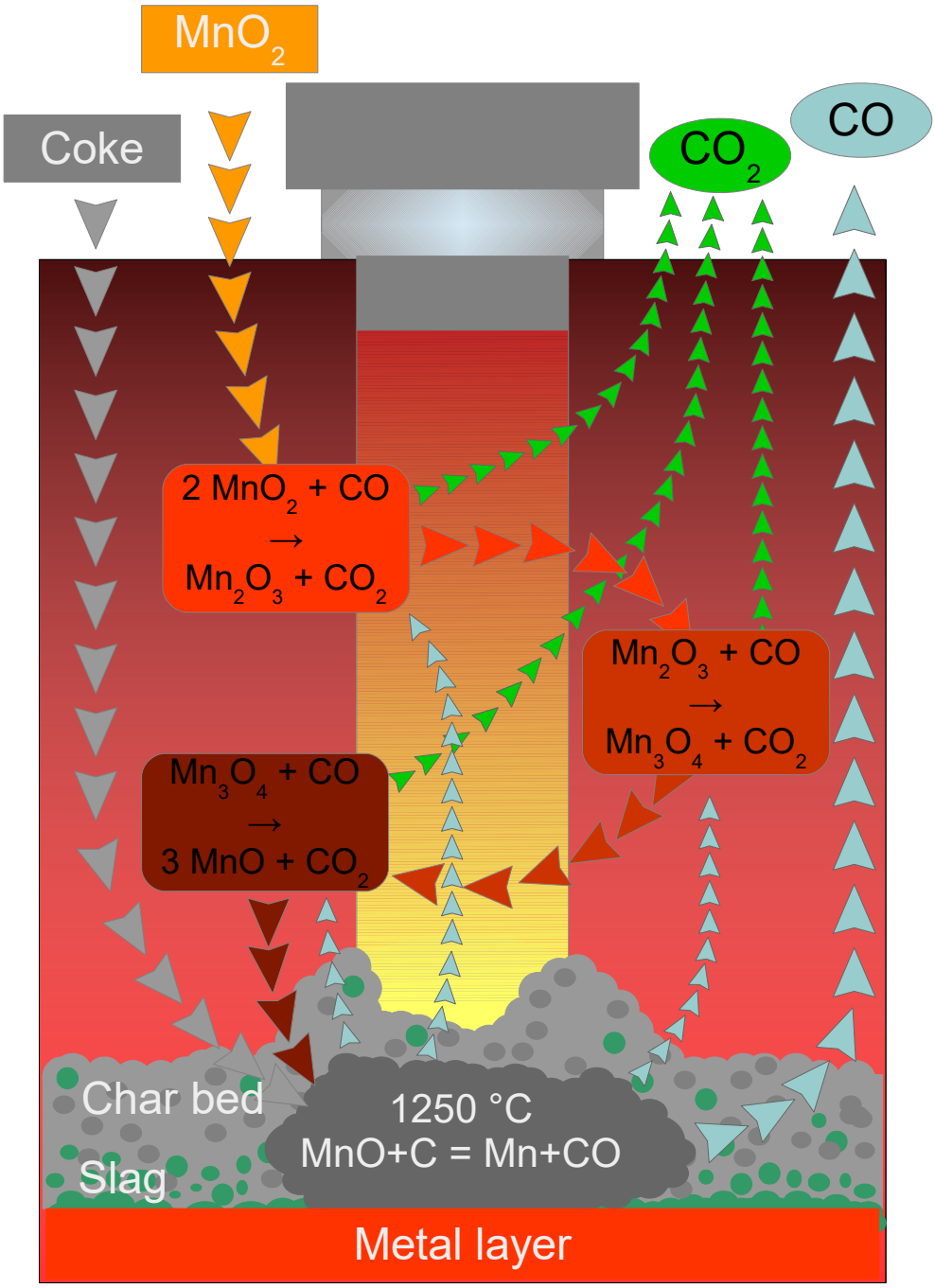

Figure 2.8: Schematic pathway for the reduction of manganese-dioxide in an EAF [127]

An important property of the reducing agent in EAF, especially in submerged arc furnaces, is the electrical resistivity. The total resistivity depends on the reducing agent, volume fraction, carbon content and particle size [38], in which the resistance of the reducing agent is influenced by its proximate analysis, ash distribution, microstructure, macroscopic cracks and graphitization [128]. A high resistivity is preferred due to an improved heat distribution in the furnace, resulting in a more efficient operation with

respect to energy and electrode consumption [38].
Carbonaceous materials for the reduction of metal-oxides are selected based on their properties and economics. Electricity and reducing agents account for more than 70 % of operating plant costs [37]. Blending of reducing agents can improve the operation by reducing the operational expenditure (OPEX). Thus, the properties of reducing agents are the most important parameter for an effective operation of the metallurgical furnace. Based on the feedstock, furnace size and furnace type, reducing agents must fulfill minimum mechanical and chemical requirements. In comparison to blast furnaces, the reducing agent does not require the high coke reactivity index (CRI) and coke strength after reaction (CSR), but a proper electrical resistivity by smaller particle size is important [38, 129]. Based on the formation of CO, a high reactivity is desirable in ferroalloy prodcution [130].

2.3 Reducing agents

The primary function of reducing agents is to provide the carbon in metallurgical furnaces to produce pure metals. In addition, the porous material enhances the permeability of the burden and improves the gas distribution, which also acts as a SiO gas trap in silicon production [38]. Based on the metallurgical process, reducing agents can be obtained from gaseous, liquid or solid sources, in which solid reducing agents are most abundant in carbothermal reduction processes. Gaseous reducing agents are summarized in section 2.3.7 and comprise mainly synthesis gas, hydrogen, methane or natural gas. Liquid fuels and its derivatives are stated in section 2.3.6. Solid reducing agents are examined in section 2.3.5. Metallurgical furnaces have been improved over decades and require specific properties of the feedstock to ensure a high production rate, a stable operation of the furnace and a great product quality [131].
Metallurgical coke is the main reducing agent used in blast furnaces and manganese production. Several standards have been developed to evaluate the quality of the reducing agents, such as the CSR, CRI, fixed carbon content or element analysis. The required properties of metallurgical coke used in blast furnaces are summarized in Table 2.2. In ferroalloy production the chemical composition, such as volatile matter content, ash content, ash composition and the reactivity towards CO_2 and SiO are the main criteria for reducing agents [38]. However, most of the standard tests are based on fossil fuels like coke and coal and may not be directly adopted to renewable reducing agents. Other important properties of the reducing agents used in EAF are the specific surface area and the electrical resistivity of the bulk layer, in which the surface area must be accessible for chemisorption of the gas-vapor phase [132].

Table 2.2: Required chemical and physical properties of blast furnace coke [133–138]

	European range	Australian BHP Port Kembla	American range	Japan range	limit
Proximate and ash compositional analysis					
Moisture (wt.%)	1 - 6	< 5.0	-	5.0	< 5
Volatile matter (wt.%,db)	< 1.0	1.5	0.7 - 1.1	1.0	< 1.5
Ash (wt.%,db)	8 - 12	< 12	6.6 - 10.8	7 - 11	< 9.0
Sulfur (wt.%,db)	0.5 - 0.9	0.5	0.54 - 1.11	0.7 - 0.8	< 0.82
Phosphorus (wt.%,db)	0.02 - 0.06	0.04	-	-	< 0.33
Alkalies (wt.%, db)	< 0.3	-	-	-	< 0.4
Particle size, mechanical strength and reactivity					
Mean size (mm)	47-70	50	50	45-60	
M_{40} (+60 mm)	> 78− > 88	85	n.a.	n.a.	
M_{10} (+60 mm)	< 5− < 8	6.5	n.a.	n.a.	
I_{40}	53-55	n.a.	n.a.	n.a.	> 57
I_{20}	> 77.5	n.a.	n.a.	n.a.	< 18
DI150/15	n.a.	84.4	n.a.	83-85	
ASTM stability	n.a.	63.6	60	n.a.	
CSR	> 60	74.1	61	60-65	> 65
CRI	20-30	17.7	23	n.a.	< 23

2.3.1 Mechanical stability and particle size

The most common analyses to evaluate the properties of metallurgical coke are the coke reactivity index (CRI) and coke strength after reaction (CSR). These two analyses represent the chemical and mechanical stresses in the shaft of the blast furnace. While minimum values are stated for blast furnaces, it is not evidence which coke reactivity index (CRI) and coke strength after reaction (CSR) are best for coke application in EAF [130].

Charcoal can be blended into the coal mixture to produce a biocoke with nearly similar properties to metallurgical coke. However, an addition of at least 5 wt.% of charcoal to coal can decrease the coke strength [139], whereas an addition of 2 % of high-density polyethylene (HDPE) can improve its mechanical strength [140]. These results indicate that only small amounts of classical charcoal can be added to coal blends without inducing negative effects on the properties of metallurgical coke.

A grain size of 40 to 60 mm is requested in blast furnaces for a good distribution of the gases. Up to 11 wt.% of the metallurgical coke can be charged into the furnace with a grain size less 25 mm, respectively up to 4 wt.% larger 100 mm for a stable operation of the furnace [134]. A coke with a grain size larger 25 mm results in a CRI between 30 and 40 and a CSR between 42 and 58 [141]. Bulaevskii and Shved pointed out that an increased coking period by 10 h increase the hot strength of the fossil coke by 4 to 6 % and decreased its reactivity by 1.2 %. However, a concentration of intermediate products larger 1 % led to a decrease in the CRI and CSR by 5 to 11 % [141].

2.3.2 Organic composition

Carbon is required to reduce metal-oxides in carbothermal processes. Beside its primary function as a reducing agent and carbon donator, carbonaceous feedstocks are process energy sources. For example, about 55 % of the total energy in silicon production are provided by the carbon materials with an exergetic efficiency of about 39 % [122]. Typical solid carbonaceous reducing agents are metallurgical coke, petroleum coke, coal, charcoal and woodchips. To increase the amount of renewable reducing agents in metallurgical industry, biomass and charcoal are blended at a higher ratio into the feedstock. The carbon content of reducing agents is greater than 80 % for coke and greater than 67 % for coal [142]. Metallurgical grade charcoal should have a fixed carbon content greater than 85 % [13].

Biomass is composed of about 50 % carbon, 6 % hydrogen and 40 % oxygen. The carbon content increases by removing oxygen containing compounds in temperatures above 250 °C. To obtain a metallurgical grade charcoal, heat treatment temperatures above 750 °C and slow heating rates are required [143, 144]. The carbon content is assumed to be equal to the fixed carbon content that is determined by sample heating up to 900 °C based on the DIN 51720 standard, respectively to 950 °C based on ASTM D3175 standard. To estimate the carbonization efficiency, Antal and Grønli combined the fixed carbon content with the charcoal yield according to equation 2.3.

$$\gamma_{FC} = \gamma_{\text{char}} * \left[\frac{\text{FC}}{100 - a_{\text{feed}}}\right] \tag{2.3}$$

where γ_{FC} is the fixed carbon yield, γ_{char} is the charcoal yield, FC is the fixed carbon content of the char and a_{feed} is the ash content of the original feedstock.

The high treatment at temperatures over 2000 °C can increase the degree of graphitization, but also increase the ash content of the final charcoal as nearly all original biomass ash remains in the charcoal. A higher degree of graphitization result in a decrease of the ohmic loss, which increases the electrical consumption in EAF [37]. The resistivity of materials used in electric arc furnaces for silicon production is shown in Table 2.3.

Table 2.3: Resistivity of the materials in the silicon process [90]

Material	Temperature	Resistivity ρ
Quartz	$T < 1800\,K$	$\rho > 10^4\,\Omega m$
	$1800\,K < T < 2000\,K$	$10^2\,\Omega m < \rho < 10^4\,\Omega m$
Carbon materials	$T < 1800\,K$	$\rho > 1 - 2\,\Omega m$
Silicon carbide	$T \approx 2000\,K$	$\rho \approx 10^{-4}\,\Omega m$

2.3.3 Inorganic compounds

The reactivity can be catalyzed by the ash composition of the charcoal. Biomass is low in ash content, especially sulfur, but often biomass has a greater alkali metal content than coal. The products with a high alkali metal content exhibit a greater CO_2 reactivity compared with the alkali metal lean carbon samples [145, 146]. Potassium is expected to increase the reactivity of carbon in CO_2 [147–149], increasing the energy demand of metallurgical furnaces. Monaghan et al. investigated the reactivity of cokes which were doped with specific minerals, in which the influence of the mineral matter was ranked as: $K_2CO_3 > Na_2CO_3 > CaCO_3 > MgCO_3 = MgO > FeCO_3 > FeS_2 > Al_2O_3 = SiO_2$ [150]. Alumina and silica showed almost negligible influence on the CO_2 reactivity of metallurgical coke samples. The biocoke with the high mineral matter content can decrease the threshold temperature and increase the CO_2 reactivity.
In addition, alkali metals can form deposits on furnace walls and thus, the mineral matter should be minimized in the feedstock [151]. Other critical ash constituents are sulfur and phosphorus, which can decrease the mechanical strength of the ferroalloy [152]. In addition, reactions of alkali metals with the carbon structure can alter the structural properties of coke [107]. This can be critical when the high mechanical stability is required for reducing agents.

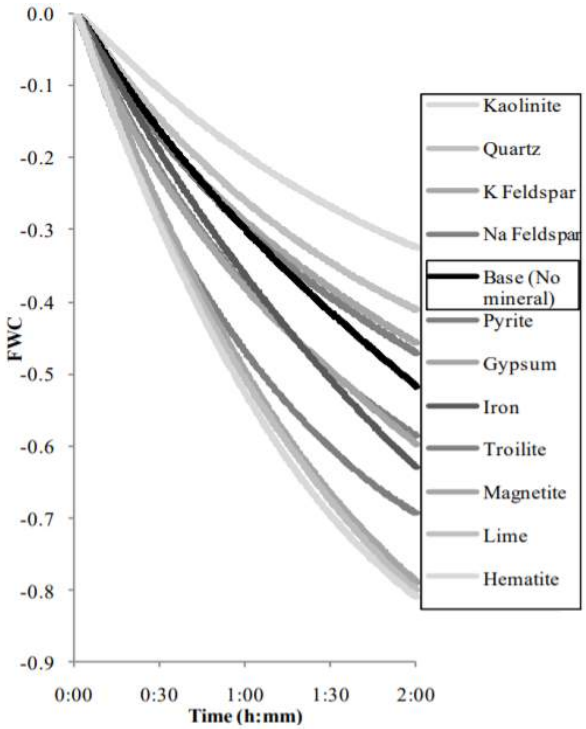

Figure 2.9: Changes in fractional weight change (FWC) over time for doped coke analogues according to CRI [150]

2.3.4 Reactivity

The coke reactivity index (CRI) is the common analysis to investigate the reactivity of metallurgical coke in CO_2. The analysis is carried out at 1100 °C according to ISO 18894:2018 and should be between 20 to 30 %. At the same time, the threshold temperature in CO_2 should be in the range 950 to 1000 °C [112]. Semi-cokes are products which are not fully carbonized. Due to the incomplete pyrolysis, an additional mass loss occurs at the beginning of the mass loss curve for steady and non-steady thermogravimetric measurements [111]. This thermal decomposition of the charcoal can mislead to a low threshold temperature and high reactivity in oxidizing and reducing atmosphere. Previous studies have shown that the blending up to 3 % of coarse charcoal to coal can lead to a similar CO_2 reactivity of the biocoke [112]. For coal samples, the CO_2 reactivities of pure coal and coal blended with 30 wt.% charcoal from pyrolysis in the temperature range 500 to 700 °C are similar [153].
A high reactivity of SiO is desirable in the silicon production, whereas charcoal and coke provide a greater reactivity of SiO than carbon black and coal [154]. Raaness, Kolbeinsen and Byberg investigated the SiO reactivity of several reducing agents by measuring the SiO gas after passing through a reducing agent bed, schematically shown in Figure 2.10. The low reactivity of coke and quartz mixture makes it a good adsorber for SiO gas [154].

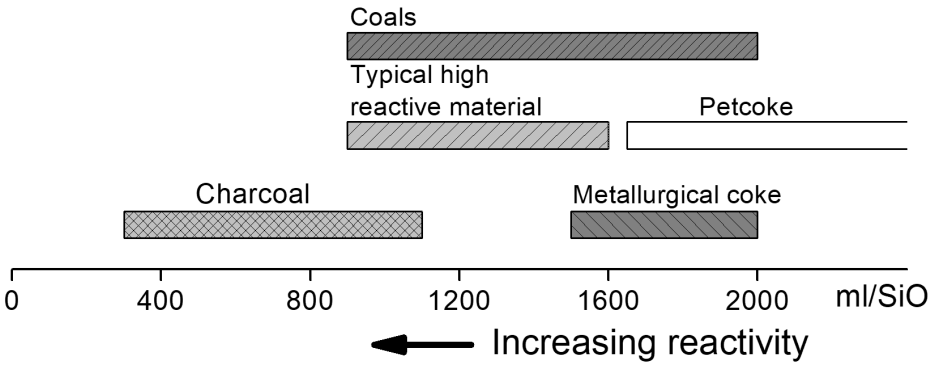

Figure 2.10: Expected SiO reactivity for various reducing agents [155]

Beside standard analysis, the texture of metallurgical coke is investigated by optical microscopy to identify the crystallinity of the coke and to correlate the structure to its physical properties [148, 156]. A greater content of amorphous carbon in charcoal can increase the reactivity in oxidizing gases [38]. By rule of thumb, a high reactivity can be correlated to a less ordered carbon structure. MacPhee et al. did not observe any changes in the texture of biocoke with a charcoal addition up to 10 % [139], whereas Gornostayev et al. reported visuable textural changes in for additions of 2.5 % of high-density polyethylene (HDPE) [140].

2.3.5 Coal and its derivatives

Fossil fuels are the main carbon source of the reducing agents used in metallurgical industry. Metallurgical coke, the main reducing agent in blast furnaces and manganese production, is produced in coke oven batteries in the temperature range 1100 to 1400 °C from specific coal blends [84, 133], in which approximately 1.25 to 1.65 kg of coal are converted to 1 kg coke. These coals are selected by their coal rank or physical and chemical properties, as shown in Table 2.3.5. Coal is classified according to ASTM D388-18 or DIN 22020 into its main coal rank: lignite, sub-bituminous coal, bituminous coal or anthracite coal. These ranks are further subdivided into characteristic subgroups. By the standards, coal is classified by its maceral analysis. The main maceral groups are inertinite, liptinite and vitrinite. Liptinites are divided into its primary liptinites: sporinite, sporangia, cutinite, resinite, alginite, suberinite and fluorinite and its secondary liptinites: exsudatinite and bituminite [157]. A higher coal rank can be correlated with an increased carbon aromaticity [158].

Table 2.4: Coal rank classification [157]

Rank	% carbon (daf)	% Volatile matter (daf)	Gross specific energy (MJ/kg)	Vitrinite reflectance (%)
Peat	60	> 60	14.7	0.2 - 0.26
Lignite	71	52	23	0.38 - 0.4
Subbituminous	80	40	33.5	0.42 - 0.6
High volatile bituminous	86	31	35.6	0.65 - 0.97
Medium volatile bituminous	90	22	36	1.47 - 1.5
Low volatile bituminous	91	14	36.4	1.85 - 1.92
Semianthracite	92	8	36	2.58 - 2.65
Anthracite	95	2	35.2	5 - 6.55

A common representation of the main organic composition of the coal, peat and biomass is the van Krevelen diagram, in which the molar ratio of hydrogen to carbon and oxygen to carbon are plotted on the y and x-axes. Both ratios decrease within the coalification, schematically shown in Figure 2.11.
The thermal heat treatment of biomass and coal results in a carbonization of the material. Increasing temperatures result in an additional mass loss, which can influence the physical and chemical properties of charcoal, semicoke and coke, e.g. its carbon structure and porosity. The thermal ordering decreases the amount of amorphous carbon by an increase of aromaticity and crystalline size [38]. The porosity is modified by pore growth and coalescence of pores, and changes in the carbon matrix can weaken the abrasion resistance, which has a strong impact on its degradation behavior [159]. Swelling and re-solidification from original coal affect strongly the porosity and porous structure of the coke [160, 161].

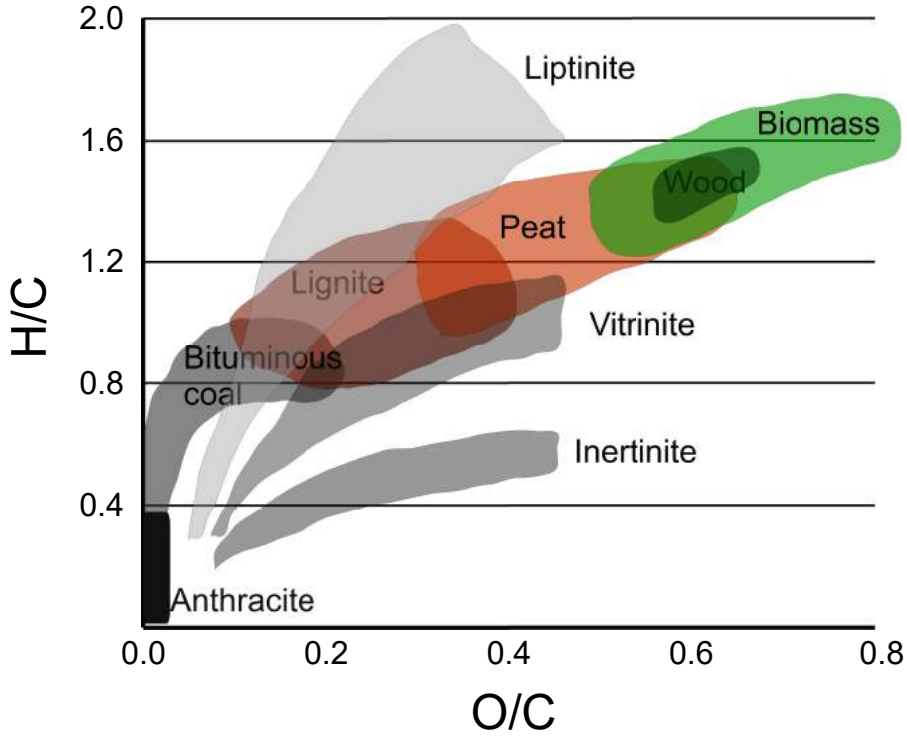

Figure 2.11: Van Krevelen diagram of biomass, coal and main coal maceral groups ([16, 162])

Differences in the carbon structure and changes in the surface area have an influence on the properties of the reducing agent. Especially low rank coal produces an isotropic porous coke which is very reactive in CO_2 [107]. The isotropic carbon and smaller anisotropic clusters form weaker structures and thus, increase the CO_2 reactivity [163]. Wilkinson reported that an increase in heat treatment temperature can improve the tensile and compressive strength [107].

The threshold temperature of solid reducing agents specifies the temperature at which the reducing agent starts to react with CO_2. This temperature can be correlated to the thermal reserve zone in the blast furnace shaft, which is typically in the range of 950 to 1000 °C [164]. The usual threshold temperature of metallurgical coke is about 910 °C [112]. A charcoal addition of 8 % to the coal charge results in a decrease of biochar threshold temperature of the biocoke to about 840 and 850 °C for fine and coarse charcoal. The high mineral content of biocoke corresponds to the decreased threshold temperature, in which the gasification characteristics can be well described by the alkalinity index [23]. This assumption is supported by results of other researchers after washing and acid leaching of charcoal samples, in which the post-treated samples provided a similar reactivity to coal chars after removal of the alkali and earth alkali metals [146, 165]. Fidel et al.

investigated the alkalinity of charcoal for soil processes, in which the charcoal alkalinity was not a simple function of ash composition, fixed carbon or volatile matter content [166]. Taking the alkalinity index (AI) as a guideline, it is defined as [167]:

$$AI = \frac{wt.\%\ Fe_2O_3 + wt.\%\ CaO + wt.\%\ MgO + wt.\%\ K_2O + wt.\%\ Na_2O}{wt.\%\ SiO_2 + wt.\%\ Al_2O_3} \cdot wt.\%\ ash \tag{2.4}$$

One issue is that alkali metals accumulate in metallurgical furnaces [148, 168]. Wilkinson demonstrated that the alkali metal vapors reacted with the carbon structure and formed intercalation compounds, which can decrease the mechanical stability of coke [107]. In contrast, Hilding et al. did not observe an influence of alkali metal on the graphitization behavior and mechanical strength of the coke [159]. A similar result was found by Trubetskaya et al. who investigated the interaction of potassium with high temperature soot and found no potassium incorporation into the soot matrix occurred during high temperature pyrolysis [169].

The reactivity towards SiO is crucial for silicon, silicon carbide and ferrosilicon production. The reactivity in SiO mostly decreases with increasing coal rank, whereas coke with isotropic carbon structures had a greater CO_2 reactivity compared to anisotropic carbon structures [38]. In detail, reactivity in SiO decreases with increasing vitrinite reflection and decreasing inertinite and liptinite maceral concentration [163]. In addition, the reactivity of the charcoal in SiO is affected by the specific surface area of the reducing agent [132]. Thus, the overall tendency of SiO reactivity is similar to that of the CO_2 reactivity.

In the hearth of the furnace, reducing agents require a high slag reactivity to dissolve into and react with the liquid metal. The dissolution rate of the carbon into the liquid metal is affected by the carbon structure and ash content [38]. Pistorius investigated the dissolution rate of ferroalloy production, in which a higher degree of crystallinity results in an increased dissolution rate of the carbon into the metal, whereas higher sulfur concentration resulted in a decreasing dissolution rate [130]. The increasing heat treatment temperatures also showed an improvement for the dissolution rate constants of charcoal samples [38]. Based on the carbon structure, graphite samples can dissolve faster into the melt than coal samples [170]. The carbon increase in the melt was assumed to follow a first-order rate, as shown in equation 2.5 [130, 170].

$$\frac{dw_C}{dt} = K\,(w_{C,sat} - w_C) \tag{2.5}$$

Where w_C is the carbon content in weight-%, $w_{C,sat}$ is the carbon solubility in the melt in weight-% and K is the apparent rate constant [130]. The coal rate constants are stated in the range from 0.0011 to 0.0036 s^{-1} [38]. Other metals like chromium, manganese and silicon can affect the dissolution rate, but the role of the coal structure is not well investigated [130].

Based on the chemical resistance, an increasing coal rank or higher heat treatment temperature can improve the quality of the reducing agents. However, an increasing coal rank and degree of graphitization result in a decrease of electrical resistivity, which is disadvantageous for the application in EAF [163]. These opposing trends require a certain understanding for the processing of biomass to provide the right reducing agent for the application in Norwegian EAF.

2.3.6 Oil and its derivatives

Fossil oil and biooil can be utilized as carbon and energy sources in metallurgical industry. Crude oil is a mixture of different hydrocarbons which can be refined to multiple products, schematically shown in Figure 2.12. The crude oil is mainly composed of alkanes, cycloalkanes and aromatics, with an oxygen content less than 1.5 % and sulfur content up to 8.0 % [171]. In contrast, biooil exhibits an oxygen content in the range 35 to 45 % [72], that makes it less suitable for the industrial use.

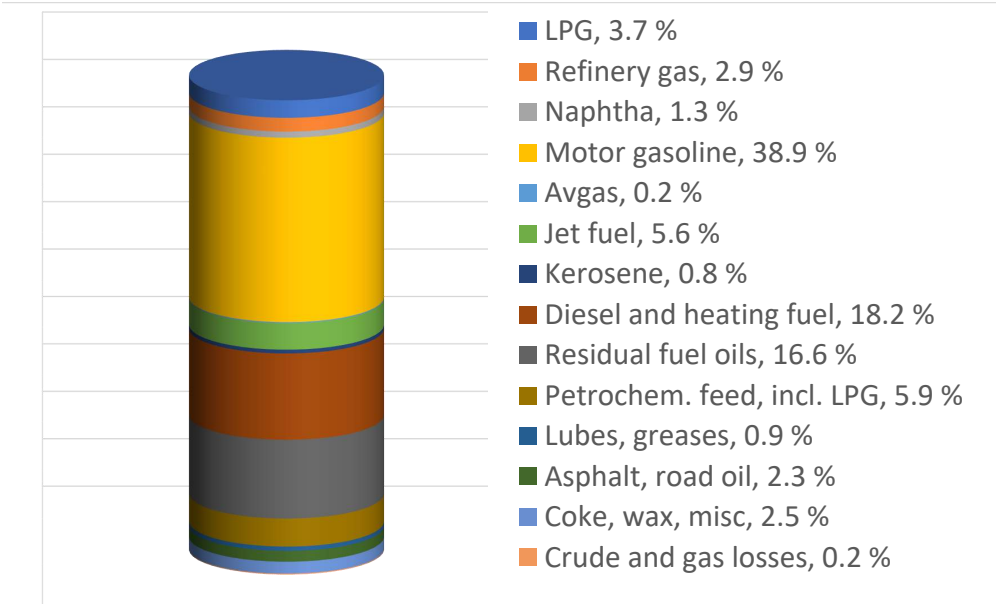

Figure 2.12: Refinery products from crude oil [172]

Oil and natural gas have been used in blast furnaces since the late 1950s to increase the productivity and control of a furnace [173]. Oil is also used as an energy carrier for the heat hardening of iron ore pellets and carbon sources to form CO in blast furnaces and direct reduced iron (DRI) [174]. A more common reducing agent used in EAF is petcoke that is the solid residue from oil refining process. Carbon anodes have been produced from calcined petroleum cokes since more than 120 years [175]. The oil pitch is a graphitic agent that has a similar reactivity to commercial graphite and with the coke reactivity index varying between 19 and 20 [111, 176]. Petcoke is used in Southern

Norway for silicon carbide production. The volatile matter content of petcoke is usually between 7 to 9.1 % [111], which is problematic for closed submerged arc furnaces used for manganese production.
Petcoke and biooil pitch calcined at 1200 °C have nearly identical composition and structure. However, biooil pitch is low in sulfur, nitrogen and metal content [51, 56]. The biooil conditioning may enhance the usage of bio-pitch in ferroalloy industries due to the similar chemical properties to metallurgical coke after calcining.

2.3.7 Gases

Methane, hydrogen and carbon monoxide are gases which are used as reducing agents in ferroalloy industries. Beside natural gas, reducing gases can be produced by pyrolysis and gasification of coal or biomass. Reducing gases can be also used in DRI plants. As mentioned in section 2.2, carbon monoxide occurs as a major product gas in carbothermic processes, especially in electric furnaces [104]. A recirculation of the CO gas can reduce the coke demand up to 45 % [177].
Hydrogen can be used to reduce iron-oxides at temperatures above 500 °C [178, 179]. It has been utilized to reduce nickel, copper, iron and zinc oxides [178]. Hydrogen can be provided from electrolysis and gasification, and no significant differences between fossil and renewable hydrogen are expected after gas cleaning.

2.4 Biomass and its derivatives

Biomass and charcoal are generally considered as CO_2 neutral reducing agents to reduce the levels of CO_2 and SO_2 emissions in metallurgy [38]. Brazil is the largest producer of charcoal with a global market share of 12 to 14 %, in which up to 75 % of the production are utilized in metallurgy [30, 180, 181]. About 8 million tonnes of Brazilian pig iron were produced in small blast furnaces with renewable reducing agents in 2002 [182]. Biochar was also used as a CO_2 neutral agent in ferrosilicon and silicon production [183]. In Norway, bio-based reducing agents are broadly used in silicon production by Elkem, whereas no substitution is implemented in silicon carbide and manganese alloy production. Biomass can be used as an effective reducing agent in the manganese oxide industries [184]. However, the installed furnaces cannot be operated at stable conditions due to the high volatile matter release in biomass pyrolysis.
In European silicon production between 800 and 1200 kg of wet woodchips and more than 10 % of charcoal are used, whereas charcoal has not been used in manganese and chromium alloy production [183]. Elkem intends to increase the percentage of biomass

and charcoal use up to 40 % in 2030 [185]. This indicates an increased interest in the use of renewable reducing agent in Norway.

2.4.1 Charcoal production

Charcoal is produced from woody biomass using thermochemical processes. The thermochemical production processes can be differentiated by heating rate, final temperature and gas atmosphere. Carbonization, torrefaction, slow pyrolysis and hydrothermal carbonization are processes used to produce solid residues as the main product, whereas gasification is used to produce synthesis gas and flash pyrolysis to produce biooil [186]. The charcoal can be produced in either batch or continuous multiple kilns and retorts [15], whereas the charcoal yields range from 10 to 30 wt.% [27]. The charcoal yield in kilns is as low as 5 to 20 % with an increased discharge of unburned methane and higher hydrocarbons, whereas the charcoal yield in retorts is in the range from 20 to 30 % [10, 180, 187]. The global charcoal production increased by 19 % in the last 10 years and by 46 % in the last 20 years. Most charcoal producers harvest and pyrolyze hardwood species to produce high quality charcoal with a high calorific value. The charcoal from hardwood consists of 80 % carbon with the ash content ranging from 1 to 3 % and with 12 to 15 % of volatile matter [15].

Chen, Aanjaneya and Atreya investigated the exergy efficiency for a pyrolysis of different wood components, in which woodchips can increase the charcoal yield and consume less forest area [40]. Brick-made hot trail kilns in Brazil have a conversion efficiency of 25-30 % [180], respectively a carbon conversion efficiency up to 69 % [188]. Most kilns are operated in the temperature range between 400 to 600 °C [12, 189–191]. As described above, a pyrolysis temperature of 500 °C is insufficient to change the crystalline structure and increase the thermal and electrical conductivity [41].

To improve the charcoal properties for the transportation and storage, charcoal particles can be pressed into pellets or briquettes to increase the bulk density of the material. Due to the low mechanical stability of charcoal, more than 20 % of fines can be generated during transportation and handling [192].

Charcoal from wood has a bulk density that is less than 600 $kg\,m^{-3}$ [193], whereas charcoal from wood sawdust has a density of less than 300 $kg\,m^{-3}$ [194]. The bulk density is constant in the temperature range 450 to 650 °C, whereas the true density increases with the heat treatment temperature [193, 194], leading to the greater BET surface area and greater porosity compared to the low temperature treated charcoal samples. On one side, the low specific energy density can lead to the increase in transportation costs, whereas on the other side it can increase the mechanical abrasion and CO_2 reactivity due to the high porosity and large surface area.

The material must be densified to increase the bulk density for the long distance transportation. The bulk density of charcoal can be increased up to 500 kg m^{-3} and the envelope density up to 870 kg m^{-3} after pelletilization [195]. The bulk density of charcoal can be increased up to 713 kg m^{-3} when torrefaction is as a pre-treatment [196]. However, the durability of torrefied pellets is low ranging from 80 to 90 %, whereas the amount of fines is high ranging from 20 to 30 % [196]. In general, the durability of charcoal pellets is lower than biomass pellets. Pellets produced from torrefied Norway spruce investigated by Larsson et al. provided a durability of less 90 %, while >95 % are required according to standard US Pellet Fuel Institute (PFI) grade [196, 197]. Binding agents can be used to improve the mechanical durability of charcoal pellets. For the cost reduction of binding agents, blends of 70 wt.% charcoal with raw sawdust as a natural binder can be used [195]. Possible binder, such as lignin, starch, $Ca(OH)_2$ and NaOH were investigated by Hu et al. for concentration up to 20 %, in which the increasing binding agent concentration resulted in an increasing volatile matter content [198]. The highest envelope density of 1163 to 1298 kg m^{-3} was measured for charcoal pellets with NaOH. Funke et al. successfully investigated molasse and water as binding agents for wheat straw char, in which the ash content, such as potassium, was increased [199]. This increase in alkali metals may inhibit the application in metallurgy. The high pressure of up to 250 MPa can increase the envelope density of charcoal [200].

The pyrolysis process should be carried out at temperatures above 800 °C to increase the cluster size of nanocrystallites and graphene layers [201, 202]. A homogeneous temperature profile of the biomass particles is desirable to avoid thermal stresses of the biomass, whereas a low heating rate is desirable for a homogeneous volatile release. Byrne and Nagle investigated the charcoal quality at different heating rates. To obtain a high quality charcoal without visible cracks at the surface, a heating rate as low as 5 °C h^{-1} is required, whereas heating rates of 20 °C h^{-1} already result in a crack development on all sides [42].

2.4.2 Pyrolysis

Pyrolysis is the thermal decomposition of biomass and coal in an inert atmosphere. Pyrolysis processes are used for the production of solid residues like coke and charcoal, and can be also conducted with the aim to produce liquid products (biooil) or pyrolysis gases. In general, solid pyrolysis products are rich in carbon, whereas volatile products from biomass have a greater oxygen content compared to volatiles from coal pyrolysis. The relative ratios of main products depend on the operational conditions and feedstock properties. Depending on the heating rate, pyrolysis process can be classified into slow (conventional), intermediate (fast) and flash [10, 27, 31].

Slow pyrolysis is the main conversion process to produce charcoal from biomass [13, 27,

203]. Biomass is heated up to temperatures in the range 300 and 700 °C at slow heating rates (up to 20 °C min^{-1}), forming up to 50 % of solid residues [10, 27]. Pyrolysis at temperatures below 1200 °C is defined as carbonization process [15], in whereas charcoal yields decrease with the increased temperature.
Intermediate pyrolysis are most common for the production of biooil and pyrolysis gas at temperatures between 400 to 600 °C, in which the heating rate reaches a few 100 °C s^{-1}. Flash pyrolysis have usually heating rates above 1000 °C s^{-1} and are considered as the initial step in entrained flow gasification and pulverized biomass combustion. The pyrolysis process is intended to produce charcoal with the carbon content greater than 85 % and volatile matter content less than 5 %.

2.4.2.1 Pyrolysis mechanism

In general, biomass pyrolysis follows a three-step mechanism; 1. dehydration, 2. primary reaction and 3. secondary reactions. The initial step in biomass pyrolysis is drying at about 100 °C. After dehydration, the biomass undergoes dehydrogenation, depolymerisation, and fragmentation of chemical bonds. The organic chemical bonds are ruptured and a semi-char, gases and smaller molecular fragments are formed [204]. Small molecular fragments, also called metaplast, are released as tar to the gas phase if they are vaporized and transported to the surface of the char particle [205]. The gases, such as CO_2, CO, CH_4 etc., are formed by the decomposition of functional groups of the origin biomass.
The reactions which are directly affected by the feedstock are defined as primary pyrolysis reactions, whereas secondary pyrolysis reactions include intermediate decomposition products and tertiary pyrolysis reactions, which include gas reactions of products from secondary pyrolysis [10]. The small molecular fragments can also undergo secondary pyrolysis reactions in the particle and are converted to char, light gas and soot [206]. These cross-linking reactions between the metaplast and the char and the re-condensed tar increase the final char yield, whereas the depolymerization reactions are responsible for the formation of larger aromatic tars [207]. Permanent gases and light aliphatic compounds are formed during the cross-linking and condensation reactions. A number of parameters can affect the final yield and quality of pyrolysis products, including the substrate composition, pretreatment, heat treatment temperature, heating rate, reaction gas atmosphere, particle residence time and alkali metals [13, 31].
The pyrolysis pathway is shown in Figure 2.13. By rule of thumb, primary products occur and are preserved at temperatures below 500 °C, whereas secondary reactions and tertiary reactions occur in the temperature range 500 to 750 °C and 750 to 1000,°C respectively [58].

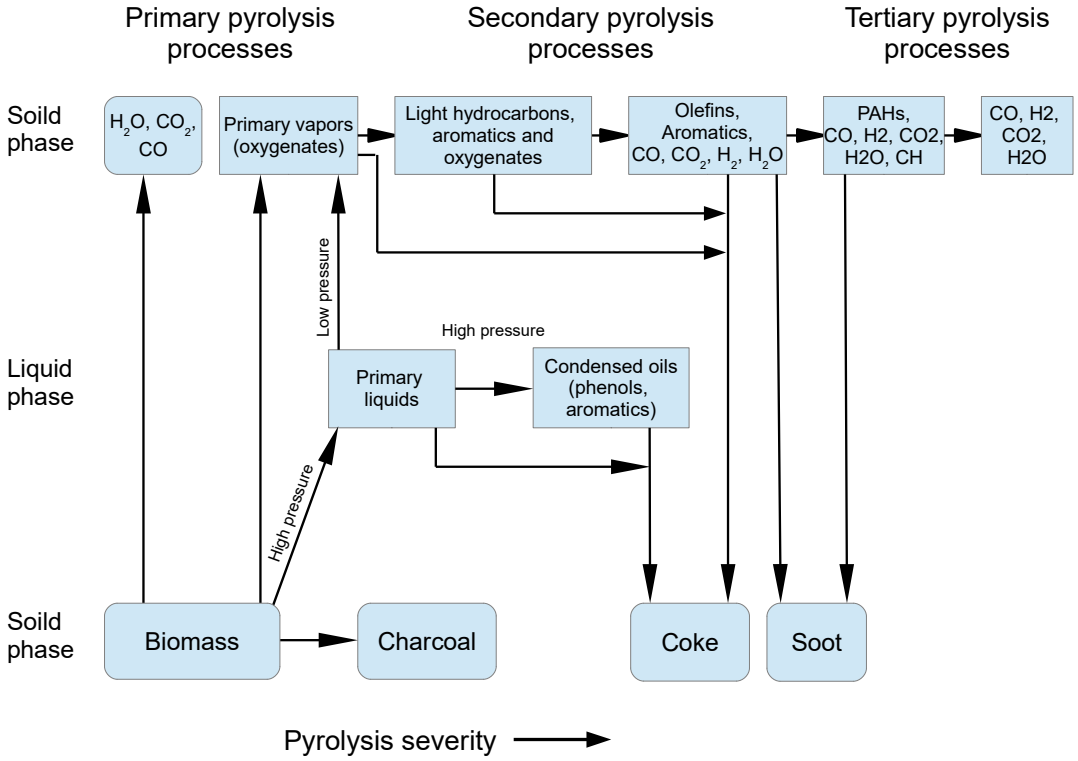

Figure 2.13: Possible pyrolysis pathways reported by Evans and Milne [52]

2.4.2.2 Primary pyrolysis processes

The main biomass compounds undergo different decomposition based on their original structure. Cellulose, hemicellulose and lignin decompose at different temperature ranges to monomer and monomer-related fragments which have characteristic mass spectral signatures [52]. Several authors have studied the thermochemical conversion of these constituents in thermogravimetric analysis (TGA). Pure cellulose shows a relatively narrow temperature range for the reactions. It is composed of crystalline and amorphous phases [208, 209], which randomely decompose into chains of about 200 anhydroglucose units before further decompose to levoglucosan [210]. Cellulose decomposes in the temperature range 280 to 380 °C with highest reaction rate at 350 °C [211].

Hemicellulose and lignin structures vary among the plant species and can highly affect the pyrolysis behavior and product compositions [212]. The primary pyrolysis of hemicellulose occurs mainly in the temperature range 190 and 380 °C with a maximum reaction rate at 310 °C [209, 213–215] and a local maximum at 260 °C. This wider temperature range indicates a lower thermal stability of hemicellulose compared to cellulose that is probably related to the lack of crystallinity in hemicellulose [216]. Xylan, which is often used as the representative of hemicellulose, provides a double peak at 246 and 290 °C [214], in

which the distribution of volatiles is similar to cellulose [52]. A mass loss occurring at temperatures greater than 350 °C is attributed to the char forming reactions. The char yield from xylan can be twice greater than that of cellulose and three times greater than that of glucomannan [217]. However, the large variation of the different hemicelluloses hampers the usage of a single representative [215]. Xylan as the least stable compound produces up to 20 % solid residue [218], whereas the fixed carbon content of pyrolyzed β-glucan can be as low as 1.3 % [215].
Lignin decomposes in the temperature range 200 to 500 °C with the maximum reaction rate at 360 and 400 °C [209, 214, 219]. The solid yield slowly decreases from 50 % at 500 °C to about 40 % at 900 °C [10, 218]. Similar to hemicellulose, the reactivity of lignin towards oxidative depolymerization varies among the different structural characteristics, leading to a specific monomer production [220].
The high oxygen content in biomass and its constitutes can result in the formation of oxygenates such as carboxyl and carbonyl groups, which are mainly products from decomposition of cellulose and hemicellulose. Pyrolysis of lignin results in the formation of phenolic and methoxy groups [64]. The condensate can separate into two phases: one phenolic oil phase that is mostly composed of phenols, ketones, aldehydes etc. and another phase mostly consists of acetic acid, methanol, acetone etc. [10]. The amount of pyrolysis water formed in pyrolysis can vary and depends on the biomass origin. Hardwood samples produce 2 to 3 % point more water than softwood in pyrolysis [44], that is attributed to the greater amount of acetylated hemicellulose in hardwood than in softwood.
High pyrolysis temperatures result in a more aromatic structure of the charcoal due to dehydrogenation and cross-linking reactions [32]. The reactions between gaseous species and the solid char matrix are defined as secondary pyrolysis processes. A portion of the cleaved bonds in the matrix undergo further reactions and form stable aromatic species [52].

2.4.2.3 Secondary pyrolysis processes

Primary biomass decomposition is followed by homogeneous gas phase and heterogeneous gas-solid reactions such as biooil cracking and reforming [221]. The biooil decomposition occurs mainly in the temperature range 600 to 850C °C [52] and can be simplified into three parallel reactions. Two species decompose, whereas the third specie remains thermally stable [222].
Aromatic species such as furan, benzene, toluene and phenol are mainly formed at temperatures above 700 °C by gas phase polymerization of unsaturated species such as propylene, butadiene and butene [52]. The light molecular aromatics are also formed in lignin de-

composition. An increase in heat treatment temperature can lead to the greater amount of aromatic components by tertiary reactions. However, at temperatures above 1400 °C the biooil components are converted to gaseous species [223].
An increasing absolute pressure in combination with a long vapor residence time lead to an increased solid yield by enhanced cross-linking reactions at relatively low temperatures [13]. In addition, the increased solid yield is accompanied by a shorter carbonization time [30], improving the throughput of pyrolysis facilities. Thus, an increase in pressure result in an overall decrease of the tar an gas yields [224]. At 450 °C, the higher heating value (HHV) of the char decreases with increasing pressure [30], indicating the cross-linking of oxygen compounds with the char matrix. This effect was reversed at temperatures of 600 °C [30].

2.4.2.4 Catalytic effect of alkali metals on biomass pyrolysis

The mineral matter of biomass can substantially affect primary and secondary pyrolysis pathways by accelerating the dehydration and char forming reactions [10, 225, 226]. An addition of 0.1 wt.% of potassium or sodium can inhibit the formation of levoglucosan and lead to high yields of aromatic hydrocarbons and charcoal [52]. Calcium and potassium similarly affected the char yields in lignite pyrolysis, whereas sodium had lower catalytic influence on the yield of char from bituminous pyrolysis than calcium and potassium [221]. For the decomposition of levoglucosan, the catalytic effect of cations follows the trend: $K^+ > Na^+ > Ca^{2+} > Mg^{2+}$, whereas anions follow the trend: $Cl^- > NO_3^- \approx OH^- > CO_3^{2-} \approx PO_4^{3-}$ [227].
Mueller-Hagedorn et al. [228] showed that sodium and potassium cations had a stronger catalytic effect on the softwood char yield than calcium cations in a slow pyrolysis. Nik-Azar et al. [229] also showed that at intermediate heating rate (1000 °C s^{-1}) in fast pyrolysis sodium and potassium cations have a stronger catalytic effect on the beechwood char yield than calcium cations. The investigations of Dall'Ora et al. [230, 231] at fast heating rates ($\approx 10^4$ °C s^{-1}) in an entrained-flow reactor and in a temperature range of 1000-1400 °C showed that Ca and K catalyze cross-linking, leading to higher char yields and less severe morphological changes of beechwood (high K content) compared to pinewood (low K content).

2.4.2.5 Classical charcoal production

Globally, about 51 million tonnes of charcoal from were produced in 2016, mainly in classical charcoal production facilities such as kilns and retorts [232]. About 32 million tonnes of charcoal (64 %) were produced in Africa using kiln furnaces. In general, these furnaces are thermodynamically ineffcient and require large amounts of fuel. The modern

charcoal production furnaces require 4 to 5 kg of air-dried wood to produce 1 kg of charcoal, whereas up to 12 kg of wood are required for the charcoal production in traditional furnaces [13, 233].
There is only a limited charcoal production in Europe. In Germany, about 25000 tonnes per year of charcoal are produced in a Degussa Retort at a mass conversion efficiency of about 25 % [234]. An annual sales volume of about 40000 tonnes of charcoal are traded by *Holzkohlewerk Lüneburg* [235]. The Lambiotte retort is capable to produce about 9000 tonnes per year of high quality charcoal with an effciency of 30 to 35 % [236].

2.5 Modeling of biomass pyrolysis

Despite the fact that numerous studies exist on biomass devolatilization in pyrolysis, gasification and combustion, no general accepted model is widely accepted to describe the final charcoal yield and its chemical composition at elevated temperatures. Several kinetic models and reaction pathways have been adopted from coal pyrolysis to describe the biomass decomposition. Recent models have been proposed to increase the accuracy and predict the main volatile compounds. However, the kinetic models are mostly based on experimental data obtained at low or medium final temperature (less 900 °C), which cause challenges for the data extrapolation to higher temperatures. In addition, the charcoal composition is mostly considered as a solid residue without any information about its chemical composition. The routes of the biomass pyrolysis modeling are shown in Figure 2.14. In general, the biomass kinetics is described by the Arrhenius equation [8, 40, 237–241] or rarely by the collision theory or density functional theory (DFT) [240, 242, 243]. The Arrhenius equation is defined as:

$$k = A\ exp\left(\frac{-E_a}{RT}\right) \tag{2.6}$$

where k is the rate constant, A is the pre-exponential factor, E_a is the activation energy, R the universal gas constant and T the absolute temperature. Most studies describe the biomass pyrolysis as a pseudo first order reaction, resulting in:

$$\frac{dm}{dt} = A\ exp\left(\frac{-E_a}{RT}\right)(1-m) \tag{2.7}$$

The simplest biomass pyrolysis model is the single first order reaction model (SFOR), in which the pre-exponential factor and the activation energy are constant values obtained from the kinetic study. Parallel reaction models use multiple kinetic parameter sets to improve the estimation of volatile species [244]. The consecutive reaction model uses the

approach that is based on the kinetic modeling of representative single lignocellulosic compounds such as cellulose, hemicellulose and lignin and the pyrolysis products are grouped as volatiles, gases and char [212, 245]. However, the consecutive models do not consider the possible interactions among single lignocellulosic compounds. Different kinetic models have been proposed using xylan, chlorogenic acid, d-glucose, pentose and hexose-based polysaccharides model units [33, 212].

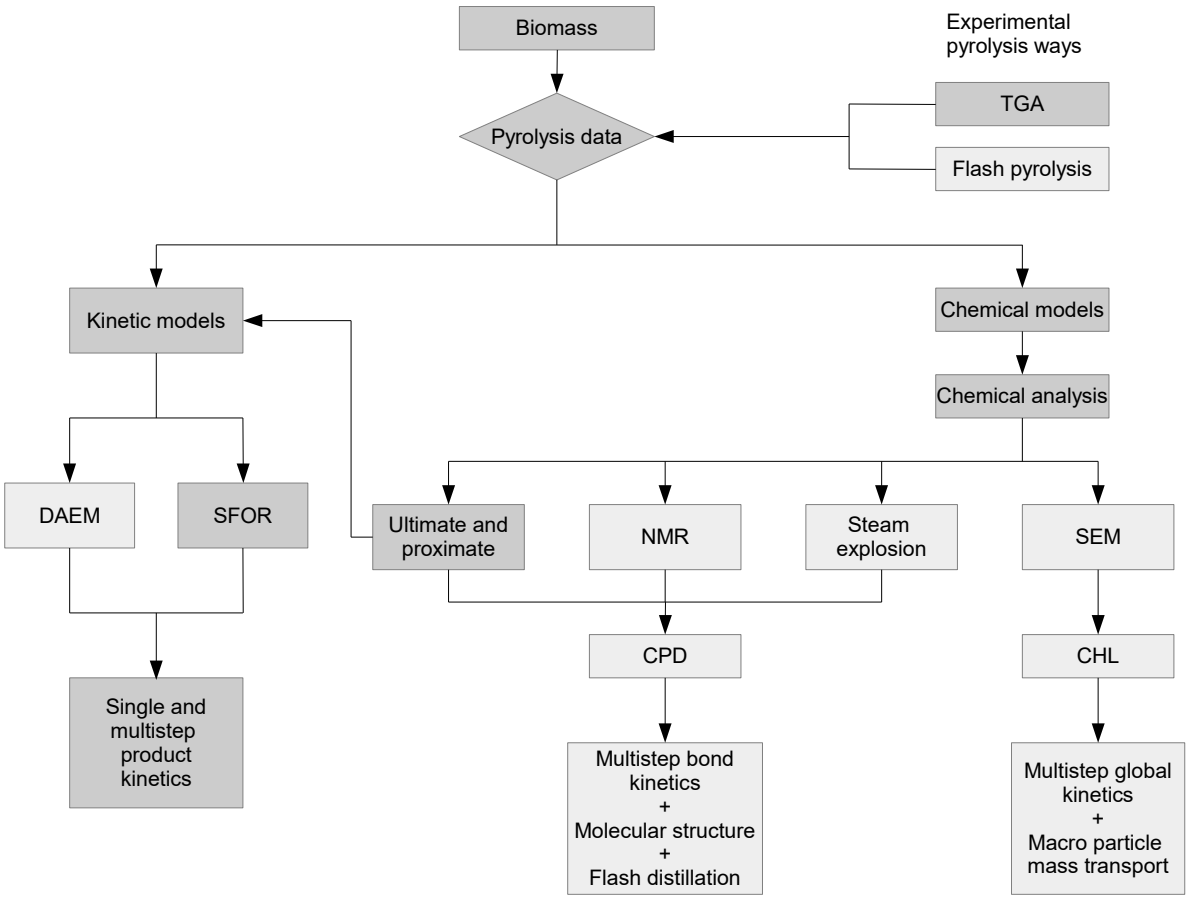

Figure 2.14: Methodological approaches for biomass pyrolysis [246]

To widen the activation energy range of the reaction rate, a distributed activation energy model (DAEM) can be used. The first DAEM was introduced in 1942 for the irreversible resistance changes of metallic films [247] and was later adopted to the problem of coal devolatilization [248]. In comparison to the SFOR model, the DAEM divides the decomposition mechanism into an infinite number of parallel reactions with different activation energies, reflecting the different bond strengths of molecules. Anthony assumed that the activation energy can be described by a Gaussian distribution with a mean activation energy $E_{a,0}$ and a standard deviation σ [249, 250]. Thereby, the reaction rate can be described as:

$$(m_0 - m) = \left[\sqrt{2\pi}\sigma\right]^{-1} \cdot m_0 \cdot \int_0^{\infty} exp\left(-\int_0^t A\, dt\right) \cdot exp\left(-\frac{(E_a - E_{a,0})^2}{2\sigma^2}\right) dE \quad (2.8)$$

This mechanism can be computed by a large amount of parallel reactions. An advantage of single and parallel reaction models is the low computing time.

More advanced models consider the chemical composition and lattice structure of the biomass, such as the chemical percolation devolatilization (CPD) model, functional group - depolymerisation, vaporisation and crosslinking (FG-DVC) model or flashchain model. These models are available as commercial software. The functional group - depolymerization, vaporization, and crosslinking (FG-DVC) model introduced by Solomon et al. [251, 252] was later adopted to lignin as the bio-FG-DVC model [253], whereas the bio-flashchain considers cellulose and pseudo-lignin compounds [254]. The chemical percolation devolatilization (CPD) model describes the devolatilization behavior of tar precursors on basis of the chemical structure of the feedstock [255], schematically shown in Figure 2.15. However, these models have some drawbacks, such as limited data in the supporting database, or absence of consideration of secondary reactions and catalytic effects of mineral matter [256]. The CPD model is implemented in the software FLUENT and can be described as:

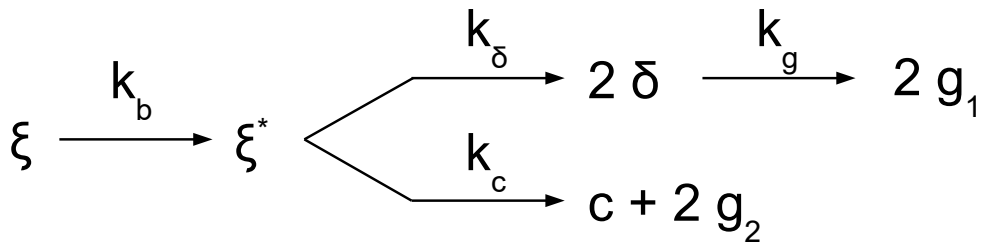

Figure 2.15: Reaction scheme to represent the devolatilization process [255]

where ξ is the labile bridge, ξ^* is the reactive intermediate bridge, k is the rate constant, δ is the side chain, g_1 and g_2 are the light gases and c is the stable char bridge. A common model used for the biomass pyrolysis includes the formation of an intermediate solid and secondary reactions, as shown in Figure 2.16.

This model was introduced by Park et al. [257]. A similar model that is known as the competitive biomass pyrolysis scheme includes secondary tar cracking [241]. A similar reaction scheme was proposed by Grieco and Baldi with different molecular weight tar species, as shown in Figure 2.17. This model considers the formation of charcoal by the crosslinking of tar precursors [239].

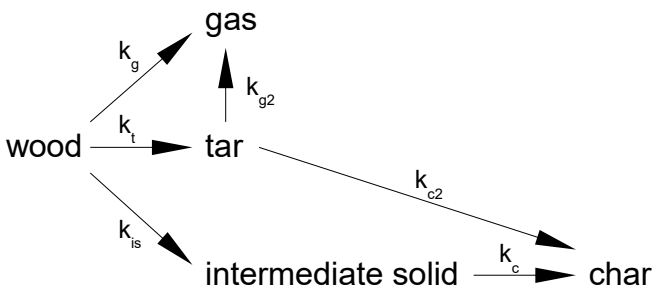

Figure 2.16: Model proposed by Park et al. [40, 241, 257]

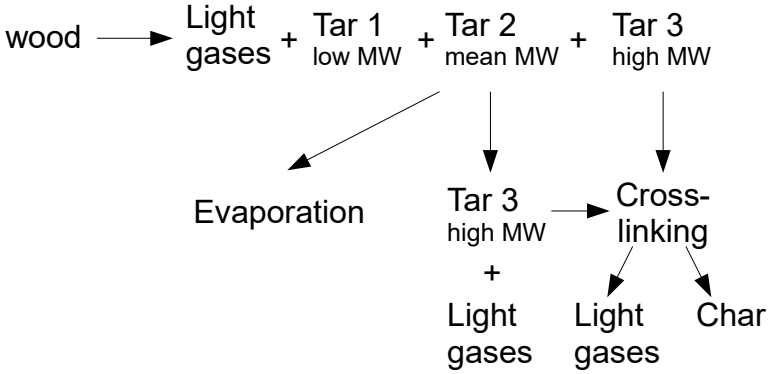

Figure 2.17: Reaction scheme proposed by Grieco and Baldi [239]

The fixed carbon content is generally measured for the charcoal samples and correlated to the molar H/C and O/C ratios [34] and thus, the fixed carbon yield can be estimated from the literature data for intermediate temperatures. However, the reviewed models do not include the elemental composition of biomass and the further decomposition at higher temperatures. The formation of an intermediate solid can be described by the formation of a metaplast observed at high heating rates.

2.6 Current state of knowledge

Charcoal has some drawbacks to replace metallurgical coke in ferromanganese production. The low mechanical stability of charcoal hampers the long distance transport and the charge into the closed furnace. In addition, the high volatile matter content and high reactivity towards CO_2 are technical risks for closed hearth electric arc furnace, whereas the low sulfur content and improved electrical resistance are advantageous. However, the charcoal properties in literature were mainly provided by heat treatment temperatures less 1000 °C or for high temperature post-treatment processes of undefined charcoals. Thus, it is not well investigated which effect a high primary and secondary heat-treatment on the final properties, especially the CO_2 reactivity have.

Charcoal pelletizing has been investigated with several binders to improve the specific density and the mechanical stability. However, the addition of different binder can increase the ash content of the pellets and decrease the overall economics. Biooil as a novel binder can improve the properties, such as the mechanical stability and electrical resistivity. Thereby, the unstable compounds of the biooil can be removed and the carbon yield increased. However, the volatile matter coming from the biooil content of the pellets must be decreased before the pellets are suitable for the closed hearth EAF. The secondary heat treatment and the biooil conditioning will be investigated on charcoal and charcoal composite pellets for the use in EAF.

Bibliography

[1] J. Dibdiakova, S. Gjølsjø, and L. Wang. Report on solid biofuels from forest-fuel specification and quality assurance. Norwegian Forest and Landscape Institute, Report 8/2014.

[2] R. J. Thomas. *Wood: Structure and Chemical Composition*, volume 43, pages 1–23. American Chemical Society, 1977. Irving S. Goldstein Wood Technology: Chemical Aspects.

[3] S.V. Vassilev, D. Baxter, L.K. Andersen, and C.G. Vassileva. An overview of the chemical composition of biomass. *FUEL*, 89(5):913–933, 2010.

[4] S.V. Vassilev, D. Baxter, L.K. Andersen, C.G. Vassileva, and T.J. Morgan. An overview of the organic and inorganic phase composition of biomass. *FUEL*, 94:1–33, 2012.

[5] S. Döring. *Power from Pellets: Technology and Applications*. Springer Berlin Heidelberg, 2012.

[6] A.J. Panshin and C. De Zeeuw. *Textbook of wood technology: structure, identification, properties, and uses of the commercial woods of the United States and Canada*. Number Bd. 1 in McGraw-Hill series in forest resources. McGraw-Hill, 1980.

[7] P.H. Raven and G.B. Johnson. *The Plant Body*. McGraw-Hill, 6th edition, 2002.

[8] Forest Products Laboratory. Wood Handbook - Wood as an Engineering Material. United States Department of Agriculture Forest Service; 2010 General Technical Report FPL-GTR-190.

[9] T. Higuchi. *Formation of Earlywood, Latewood, and Heartwood*, pages 291–307. Springer Berlin Heidelberg, 1997.

[10] C. A. Zaror and D. L. Pyle. The pyrolysis of biomass: A general review. *P INDIAN AS-ENG SCI*, 5(4):269, Dec 1982.

[11] R.C. Pettersen. *The Chemical Composition of Wood*, volume 207, chapter 2, pages 57–126. American Chemical Society, 1984.

[12] W. Emrich. *Handbook of Charcoal Making: The Traditional and Industrial Methods*. Solar Energy R&D in the Ec Series E. Springer, 1985.

[13] M.J. Antal, W.S.L. Mok, G. Varhegyi, and T. Szekely. Review of methods for improving the yield of charcoal from biomass. *ENERG FUEL*, 4(3):221–225, 1990.

[14] M.J. Antal, S.G. Allen, X. Dai, B. Shimizu, M.S. Tam, and M. Grønli. Attainment of the Theoretical Yield of Carbon from Biomass. *IND ENG CHEM RES*, 39(11):4024–4031, 2000.

[15] A. Demirbas, W. Ahmad, R. Alamoudi, and M. Sheikh. Sustainable charcoal production from biomass. *ENERG SOURCE PART A*, 38(13):1882–1889, 2016.

[16] K. Weber and P. Quicker. Properties of biochar. *FUEL*, 217:240–261, 2018.

[17] Z. Tan, C.S.K. Lin, X. Ji, and T.J. Rainey. Returning biochar to fields: A review. *APPL SOIL ECOL*, 116:1–11, 2017.

[18] F.R. Oliveira, A.K. Patel, D.P. Jaisi, S. Adhikari, H. Lu, and S.K. Khanal. Environmental application of biochar: Current status and perspectives. *BIORESOURCE TECHNOL*, 246:110–122, 2017.

[19] M. Tripathi, J.N. Sahu, and P. Ganesan. Effect of process parameters on production of biochar from biomass waste through pyrolysis: A review. *RENEW SUST ENERG REV*, 55:467–481, 2016.

[20] P. Debiagi, G. Gentile, A. Cuoci, A. Frassoldati, E. Ranzi, and T. Faravelli. A predictive model of biochar formation and characterization. *J ANAL APPL PYROL*, pages 326–335, 2018.

[21] G. Bensidhom, A.B. Hassen-Trabelsi, K. Alper, M. Sghairoun, K. Zaafouri, and I. Trabelsi. Pyrolysis of Date palm waste in a fixed-bed reactor: Characterization of pyrolytic products. *BIORESOURCE TECHNOL*, 247:363–369, 2018.

[22] P.E. Thoresen. Biocoal as an energy carrier. Symposium Paper, Energy from Biomass and Wastes. IGT Washington, Washington DC. pages 261–273, 08 1978.

[23] K.W. Ng, J.A. MacPhee, L. Giroux, and T. Todoschuk. Reactivity of bio-coke with CO_2. *FUEL PROCESS TECHNOL*, 92(4):801–804, 2011.

[24] E. Mousa, C. Wang, J. Riesbeck, and M. Larsson. Biomass applications in iron and steel industry: An overview of challenges and opportunities. *RENEW SUST ENERG REV*, 65:1247–1266, 2016.

[25] H. Suopajärvi, A. Kemppainen, J. Haapakangas, and T. Fabritius. Extensive review of the opportunities to use biomass-based fuels in iron and steelmaking processes. *J CLEAN PROD*, 148:709–734, 2017.

[26] H. Suopajärvi, K. Umeki, E. Mousa, A. Hedayati, H. Romar, A. Kemppainen, and et al. Use of biomass in integrated steelmaking - Status quo, future needs and comparison to other low-CO_2 steel production technologies. *APPL ENERG*, 213:384–407, 2018.

[27] J. Lehmann and S. Joseph. *Biochar for Environmental Management: Science, Technology and Implementation*. Taylor & Francis, 2015.

[28] L. Wang, M. Trninic, Ø. Skreiberg, M. Grønli, R. Considine, and M.J. Antal. Is elevated pressure required to achieve a high fixed-carbon yield of charcoal from biomass? Part 1: Roundrobin results for three different corncob materials. *ENERG FUEL*, 25:3251–3265, 2011.

[29] L. Wang, Ø. Skreiberg, M. Grønli, G.P. Specht, and M.J. Antal. Is elevated pressure required to achieve fixed-carbon yield of charcoal from biomass? Part 2. The importance of particle size. *ENERG FUEL*, 27:2146–2156, 2013.

[30] P. Rousset, C. Figueiredo, M. De Souza, and W. Quirino. Pressure effect on the quality of eucalyptus wood charcoal for the steel industry: A statistical analysis approach. *FUEL PROCESS TECHNOL*, 92(10):1890–1897, 2011.

[31] T. Kan, V. Strezov, and T.J. Evans. Lignocellulosic biomass pyrolysis: A review of product properties and effects of pyrolysis parameters. *RENEW SUST ENERG REV*, 57:1126–1140, 2016.

[32] M. Asadullah, S. Zhang, and C.-Z. Li. Evaluation of structural features of chars from pyrolysis of biomass of different particle sizes. *FUEL PROCESS TECHNOL*, 91(8):877–881, 2010.

[33] S. Yaman. Pyrolysis of biomass to produce fuels and chemical feedstocks. *ENERG CONVERS MANAGE*, 45(5):651–671, 2004.

[34] M. Azuara, B. Baguer, J.I. Villacampa, N. Hedin, and J.J. Manyà. Influence of pressure and temperature on key physicochemical properties of corn stover-derived biochar. *FUEL*, 186:525–533, 2016.

[35] E. Behazin, E. Ogunsona, A. Rodriguez-Uribe, A. K. Mohanty, M. Misra, and A. O. Anyia. Mechanical, chemical, and physical properties of wood and perennial grass biochars for possible composite application. *BIORESOURCES*, 11:1334–1348, 2016.

[36] G.S. Rellick. Carbon and Graphite Matrices in Carbon-Carbon Composites: An Overview of their Formation, Structure, and Properties. The Aerpace Corporation; 1992 Aerospace Report No TR-0091(6935-06)-3.

[37] Z. Chen, W. Ma, J. Wu, K. Wei, Y. Lei, and G. Lv. A Study of the Performance of Submerged Arc Furnace Smelting of Industrial Silicon. *SILICON*, 10(3):1121––1127, 2018.

[38] V. Sahajwalla, M. Dubikova, and R. Khanna. Reductant characterisation and selection - Implications for ferroalloys processing. *Infacon X,Cape Town, South Africa*, pages 351–362, 02 2004.

[39] T. Lis, N. Korzec, W. Frohs, J. Tomala, A. Fraczek-Szczypta, and S. Blazewicz. Wood-Derived Tar as a Carbon Binder Precursor for Carbon and Graphite Technology. *J WOOD CHEM TECHNOL*, 36(6):393–400, 2016.

[40] Y. Chen, K. Aanjaneya, and A. Atreya. A study to investigate pyrolysis of wood particles of various shapes and sizes. *FIRE SAFETY J*, 91:820–827, 2017.

[41] E. Behazin, E. Ogunsona, A. Rodriguez-Uribe, A. Mohanty, M. Misra, and A. Anyia. Mechanical, Chemical, and Physical Properties of Wood and Perennial Grass Biochars for Possible Composite Application. *BIORESOURCES*, 11(1), 2015.

[42] C.E. Byrne and D.C. Nagle. Carbonization of wood for advanced materials applications. *CARBON*, 35(2):259–266, 1997.

[43] Phyllis2, database for biomass and waste. ecn.tno, https://phyllis.nl/.

[44] K.H. Kim, T.-S. Kim, S.-M. Lee, D. Choi, H. Yeo, I.-G. Choi, and et al. Comparison of physicochemical features of biooils and biochars produced from various woody biomasses by fast pyrolysis. *RENEW ENERG*, 50:188–195, 2013.

[45] M.K. Hossain, V. Strezov, K.Y. Chan, A. Ziolkowski, and P.F. Nelson. Influence of pyrolysis temperature on production and nutrient properties of wastewater sludge biochar. *J ENVIRON MANAGE*, 92(1):223–228, 2011.

[46] X. Xing, H. Rogers, G. Zhang, K. Hockings, P. Zulli, A. Deev, J. Mathieson, and O. Ostrovski. Effect of charcoal addition on the properties of a coke subjected to simulated blast furnace conditions. *FUEL PROCESS TECHNOL*, 157:42–51, 2017.

[47] J. Lee, K.-H. Kim, and E.E. Kwon. Biochar as a Catalyst. *RENEW SUST ENERG REV*, 77:70–79, 2017.

[48] G.R. Surup, T. Vehus, P.-A. Eidem, A. Trubetskaya, and H.K. Nielsen. Characterization of renewable reductants and charcoal-based pellets for the use in ferroalloy industries. *ENERGY*, 167:337–345, 2019.

[49] P.A. Della Rocca, E.G. Cerrella, P.R. Bonelli, and A.L. Cukierman. Pyrolysis of hardwoods residues: on kinetics and chars characterization. *BIOMASS BIOENERG*, 16(1):79–88, 1999.

[50] D. Lugvishchuk, P. Kulchakovsky, E. Mitberg, and V. Mordkovich. Soot Formation in the Methane Partial Oxidation Process under Conditions of Partial Saturation with Water Vapor. *PETROL CHEM+*, 58:427–433, 2018.

[51] Y. Elkasabi, A.A. Boateng, and M.A. Jackson. Upgrading of bio-oil distillation bottoms into biorenewable calcined coke. *BIOMASS BIOENERG*, 81:415–423, 2015.

[52] R.J. Evans and T.A. Milne. Molecular characterization of the pyrolysis of biomass. 1. Fundamentals. *ENERG FUEL*, 1(2):123–137, 1987.

[53] M.G. Montiano, A.M. Fernández, E. Díaz-Faes, and C. Barriocanal. Tar from biomass/coal-containing briquettes. Evaluation of PAHs. *FUEL*, 154:261–267, 2015.

[54] W. He, Q. Liu, L. Shi, Z. Liu, D. Ci, C. Lievens, X. Guo, and M. Liu. Understanding the stability of pyrolysis tars from biomass in a view point of free radicals. *BIORESOURCE TECHNOL*, 156:372–375, 2014.

[55] N. Gao, S. Liu, Y. Han, C. Xing, and A. Li. Steam reforming of biomass tar for hydrogen production over Nio/ceramic foam catalyst. *INT J HYDROGEN ENERG*, 40(25):7983–7990, 2015.

[56] D.C. Elliott. Analysis and comparison of biomass pyrolysis/gasification condensates - final report, u.s. department of energy, de-ac06-76rlo 1830. 1986.

[57] J. Park, Y. Lee, C. Ryu, and Y.-K. Park. Slow pyrolysis of rice straw: Analysis of products properties, carbon and energy yields. *BIORESOURCE TECHNOL*, 155:63–70, 2014.

[58] R.J. Evans and T.A. Milne. Molecular characterization of the pyrolysis of biomass. 2. Applications. *ENERG FUEL*, 1(4):311–319, 1987.

[59] Y. Lu, G.-S. Li, Y.-C. Lu, X. Fan, and X.-Y. Wei. Analytical Strategies Involved in the Detailed Componential Characterization of Biooil Produced from Lignocellulosic Biomass. *INT J ANAL CHEM*, page 19 pages, vol. 2017.

[60] A. Krutof and K. Hawboldt. Blends of pyrolysis oil, petroleum, and other bio-based fuels: A review. *RENEW SUST ENERG REV*, 59:406–419, 2016.

[61] Q. Lu, W.-Z. Li, and X.-F. Zhu. Overview of fuel properties of biomass fast pyrolysis oils. *ENERG CONVERS MANAGE*, 50(5):1376–1383, 2009.

[62] G. Lyu, S. Wu, and H. Zhang. Estimation and Comparison of Bio-Oil Components from Different Pyrolysis Conditions. *FRONT ENERGY RES*, 3:28, 2015.

[63] M. Staš, J. Chudoba, M. Auersvald, D. Kubička, S. Conrad, T. Schulzke, and M. Pospíšil. Application of orbitrap mass spectrometry for analysis of model bio-oil compounds and fast pyrolysis bio-oils from different biomass sources. *J ANAL APPL PYROL*, 124:230–238, 2017.

[64] R. Maggi and B. Delmon. Comparison between 'slow' and 'flash' pyrolysis oils from biomass. *FUEL*, 73(5):671–677, 1994.

[65] C. Lindfors, E. Kuoppala, A. Oasmaa, Y. Solantausta, and V. Arpiainen. Fractionation of Bio-Oil. *ENERG FUEL*, 28(9):5785–5791, 2014.

[66] S. Wang. High-Efficiency Separation of Bio-Oil. In Miodrag Darko Matovic, editor, *Biomass Now*, chapter 16, pages 401–418. IntechOpen, Rijeka, 2013.

[67] D. Meier and O. Faix. State of the art of applied fast pyrolysis of lignocellulosic materials - a review. *BIORESOURCE TECHNOL*, 68(1):71–77, 1999.

[68] H. Ben and A.J. Ragauskas. Comparison for the compositions of fast and slow pyrolysis oils by nmr characterization. *BIORESOURCE TECHNOL*, 147:577–584, 2013.

[69] J.D. Adjaye and N.N. Bakhshi. Catalytic conversion of a biomass-derived oil to fuels and chemicals i: Model compound studies and reaction pathways. *BIOMASS BIOENERG*, 8(3):131–149, 1995.

[70] T. Funazukuri, R.R. Hudgins, and P.L. Silveston. Product distribution in pyrolysis of cellulose in a microfluidized bed. *J ANAL APPL PYROL*, 9(2):139–158, 1986.

[71] S. Thangalazhy-Gopakumar, S. Adhikari, R.B. Gupta, and S.D. Fernando. Influence of Pyrolysis Operating Conditions on Bio-Oil Components: A Microscale Study in a Pyroprobe. *ENERG FUEL*, 25(3):1191–1199, 2011.

[72] J. Meng, A. Moore, D.C. Tilotta, S.S. Kelley, S. Adhikari, and S. Park. Thermal and Storage Stability of Bio-Oil from Pyrolysis of Torrefied Wood. *ENERG FUEL*, 29(8):5117–5126, 2015.

[73] T. Vispute. *Pyrolysis Oils: Characterization, Stability Analysis, and Catalytic Upgrading to Fuels and Chemicals*. PhD thesis, University of Massachusetts Amherst, 2011. Open Access Dissertations. 349.

[74] R.S. Singh, A. Pandey, and E. Gnansounou. *Biofuels: Production and Future Perspectives*. CRC Press, 2016.

[75] S. Vitolo, M. Seggiani, P. Frediani, G. Ambrosini, and L. Politi. Catalytic upgrading of pyrolytic oils to fuel over different zeolites. *FUEL*, 78(10):1147–1159, 1999.

[76] J.D. Adjaye and N.N. Bakhshi. Production of hydrocarbons by catalytic upgrading of a fast pyrolysis bio-oil. Part i: Conversion over various catalysts. *FUEL PROCESS TECHNOL*, 45(3):161–183, 1995.

[77] A.G. Gayubo, A.T. Aguayo, A. Atutxa, R. Aguado, M. Olazar, and J. Bilbao. Transformation of Oxygenate Components of Biomass Pyrolysis Oil on a HZSM-5 Zeolite. ii. Aldehydes, Ketones, and Acids. *IND ENG CHEM RES*, 43(11):2619–2626, 2004.

[78] A.G. Gayubo, A.T. Aguayo, A. Atutxa, R. Aguado, and J. Bilbao. Transformation of Oxygenate Components of Biomass Pyrolysis Oil on a HZSM-5 Zeolite. i. Alcohols and Phenols. *IND ENG CHEM RES*, 43(11):2610–2618, 2004.

[79] World Steel Association. Steel's contribution to a low carbon future and climate resilient societies - worldsteel position paper. World Steel Association; 2017.

[80] M. Arens, E. Worrell, W. Eichhammer, A. Hasanbeigi, and Q. Zhang. Pathways to a low-carbon iron and steel industry in the medium-term - the case of Germany. *J CLEAN PROD*, 163:84–98, 2017.

[81] E. Balomenos, I. Gianopoulou, D. Panias, and I. Paspaliaris. Enexal: Novel technologies for enhanced energy and exergy efficiencies in primary aluminium production industry. *MJoM*, 15(4):203–217, 2009.

[82] E. Balomenos, D. Panias, and I. Paspaliaris. Energy and exergy analysis of the primary aluminum production processes: A review on current and future sustainability. *MIN PROC EXT MET REV*, 32:69–89, 2011.

[83] S.E. Olsen and M. Tangstad. Silicomanganese Production - Process Understanding. *Infacon X, Cape Town, South Africa*, pages 231–238, 02 2004.

[84] K. He and L. Wang. A review of energy use and energy-efficient technologies for the iron and steel industry. *RENEW SUST ENERG REV*, 70:1022–1039, 2017.

[85] Y. Li and L. Zhu. Cost of energy saving and CO_2 emissions reduction in China's iron and steel sector. *APPL ENERG*, 130:603–616, 2014.

[86] T. Kuramochi. Assessment of midterm CO_2 emissions reduction potential in the iron and steel industry: A case of Japan. *J CLEAN PROD*, 132:81–97, 2016.

[87] J.G. Mathieson, H. Rogers, M.A. Somerville, S. Jahanshahi, and P. Ridgeway. Potential for the use of biomass in the iron and steel industry. *Chemeca 2011. Engineering a Better World, Australia, 18-21 September*, pages 1–12, 2011.

[88] C. Hu, X. Han, Z. Li, and C. Zhang. Comparison of CO_2 emission between COREX and blast furnace iron-making system. *J ENVIRON SCI*, 21:S116–S120, 2009.

[89] F.E. Şeşen. Practical reduction of manganese oxide. *INT J CHEM ENG APPL*, 1(1):1–2, 2017.

[90] A. Schei, J.K. Tuset, and H. Tveit. *Production of High Silicon Alloys*. Tapir, 1997.

[91] M.V. Vlasova, N.G. Kakazei, V.N. Minakov, G. A. Puchkovskaya, V. S. Sinel'nikova, T. V. Tomila, and V. I. Shcherbina. Formation of silicon carbide in the reaction of reduction of silica by carbon. *POWDER METALL MET C+*, 28:718–723, 1989.

[92] M. Ksiazek, M. Tangstad, H. Dalaker, and E. Ringdalen. Reduction of SiO_2 to SiC Using Natural Gas. *METALL MATER TRANS B*, 1(3):272–279, 2014.

[93] K. Whitten, R. Davis, L. Peck, and G. Stanley. *Chemistry*. Cengage Learning, 2006.

[94] L. Nygård, B. Pachaly, H. Rong, M. Tangstad, H. Tveit, and I. Gamst. Silicon for the Chemical and Solar Industry XIII. NTNU, Kristiansand; 13.-16.06.2016.

[95] X. Li. *Effects of gas atmosphere on reduction of quartz and its reaction with silicon carbide for silicon production*. PhD thesis, School of Mechanical, Materials and Mechatronic Engineering, University of Wollongong, 2016.

[96] H.-b. Zuo, Z.-w. Hu, J.-l. Zhang, J. Li, and Z.-j. Liu. Direct reduction of iron ore by biomass char. *INT J MIN MET MATER*, 20(6):514–521, 2013.

[97] R.C. Nascimento, M.B. Mourão, and J.D.T. Capocchi. Reduction-swelling behaviour of pellets bearing iron ore and charcoal. *CAN METALL QUART*, 37(5):441–448, 1998.

[98] E. Longo and F. de Almeida La Porta. *Recent Advances in Complex Functional Materials: From Design to Application*. Springer International Publishing, 2017.

[99] T.E. Norgate, S. Jahanshahi, and W.J. Rankin. Assessing the environmental impact of metal production processes. *J CLEAN PROD*, 15(8-9):838–848, 2007.

[100] W.T. Choate and J.A.S. Green. U.S. Aluminum Production Energy Requirements: Historical Perspective, Theoretical Limits, and New Opportunities. ACEEE Industry. panel 1. industrial energy efficiency and sustainability, 2003.

[101] A. Russell. Pitfalls and pleasures in new aluminum process development. *METALL TRANS B*, pages 203–215, 1981.

[102] M.J. Bruno. Aluminum carbothermic technology comparison to Hall-Héroult process. *LIGHT MET*, pages 395–400, 2003.

[103] E. Balomenos, D. Panias, I. Paspaliaris, B. Friedrich, B. Jaroni, A. Steinfeld, E. Guglielmini, M. Halmann, M. Epstein, and I. Vishnevetsky. Carbothermic reduction of alumina: A review of developed processes and novel concepts. *EMC*, 3:729–744, 2011.

[104] S.E. Olsen, W. Ding, O.A. Kossyreva, and M. Tangstad. Equilibrium in production of high carbon ferromanganese. *Infacon VII, Trondheim, Norway*, pages 591–600, 06 1995.

[105] R. Quinkertz, G. Rombach, and D. Liebig. A scenario to optimise the energy demand of aluminium production depending on the recycling quota. *RESOUR CONSERV RECY*, 33(3):217–234, 2001.

[106] T. Lindstad, B. Monsen, and K.S. Osen. How the ferroalloys industry can meet greenhouse gas regulations. *Infacon XII, Helsinki, Finland*, pages 63–70, 06 2010.

[107] H.C. Wilkinson. The high temperature properties of coke. Commission of the European Communities; 1986 Synoptic Report EUR 10430 en.

[108] W.K. Jozwiak, E. Kaczmarek, T.P. Maniecki, W. Ignaczak, and W. Maniukiewicz. Reduction behavior of iron oxides in hydrogen and carbon monoxide atmospheres. *APPL CATAL A-GEN*, 326(1):17–27, 2007.

[109] M. Geerdes, R. Chaigneau, and I. Kurunov. *Modern Blast Furnace Ironmaking: An Introduction (Third Edition, 2015)*. IOS Press, 2015.

[110] J.M. Burgess. Fuel combustion in the blast furnace raceway zone. *PROG ENERG COMBUST*, 11(1):61–82, 1985.

[111] J.I. Rodero, J. Sancho-Gorostiaga, M. Ordiales Fernández, D. Fernández González, J. Mochón, I. Ruiz-Bustinza, A. Fuentes, and L. Verdeja. Blast furnace and metallurgical coke's reactivity and its determination by thermal gravimetric analysis. *IRONMAK STEELMAK*, 42:618–625, 2015.

[112] B.D. Flores, I.V. Flores, A. Guerrero, D.R. Orellana, J.G. Pohlmann, M.A. Diez, and et al. Effect of charcoal blending with a vitrinite rich coking coal on coke reactivity. *FUEL PROCESS TECHNOL*, 155:97–105, 2017.

[113] M. Helle and H. Saxén. Simulation of tuyere–raceway system in blast furnace. *IRONMAK STEELMAK*, 33(5):407–412, 2006.

[114] H. Suopajärvi. *Bioreducer use in blast furnace ironmaking in Finland*. PhD thesis, University of Oulu, 2014.

[115] M. Ribbenhed, M. Thorén, and C. Sternhufvud. CO_2 emission reduction costs for iron ore-based steelmaking in sweden. *J CLEAN PROD*, 16(1):125–134, 2008.

[116] K. Nozawa, A. Kasai, Y. Matsui, S. Kitayama, S. Kitano, and K. i. Shibata. Combustion Behaviors of Fine Coal and Its Impact on Gas Permeability at Lower Part of Blast Furnace under High Pulverized Coal Rate Operation. *ISIJ INT*, 51(8):1336–1343, 2011.

[117] J. Kunze and R. Degel. New Trends in Submerged Arc Furnace Technology. *Infacon X, Cape Town, South Africa*, pages 444–454, 02 2004.

[118] R.T. Jones. DC Arc Furnaces - Past, Present, and Future. In Phillip J. Mackey, Eric J. Grimsey, Rodney T. Jones, and Geoffrey A. Brooks, editors, *Celebrating the Megascale*, pages 129–139. Springer International Publishing, 2016.

[119] R. Dr. Degel, C. Dr. Fröhling, M. Köneke, E. Hecker, H. Oterdoom, and A. van Niekerk. Histroy and New milestones in submerged arc furnace technology for ferro alloy and silicon production. *Infacon XIV, Kyiv, Ukraine*, pages 7–16, 06 2015.

[120] A. De Waal, I.J. Barker, M.S. Rennie, J. Klopper, and B.S. Groeneveld. Electrical factors affecting the economic optimization of submerged-arc furnaces. *Infacon VI, Cape Town, South Africa*, pages 247–252, 03 1992.

[121] Eramet Norway. Eramet norway kvinesdal. (10.11.2018) from http://eramet.no/en/our-organization/kvinesdal/.

[122] Z. Chen, W. Ma, K. Wei, S. Li, and W. Ding. Effect of raw materials on the production process of the silicon furnace. *J CLEAN PROD*, 158:359–366, 2017.

[123] M.F. Johannessen. Sustainability report 2014, 2014. Elkem, https://www.elkem.com/.

[124] D.-A. Ilutiu-Varvara, C.M. Mârza, C. Aciu, A. Hădărean, F.V. Domnita, I.-M. Sas-Boca, and et al. An Assessment of Pollution with Volatile Organic Compounds in the Electric Arc Furnaces. *PROC TECH*, 22:452–456, 2016. 9th International Conference Interdisciplinarity in Engineering, INTER-ENG 2015, 8-9 October 2015, Tirgu Mures, Romania.

[125] T. Demus, T. Reichel, M. Schulten, T. Echterhof, and H. Pfeifer. Increasing the sustainability of steel production in the electric arc furnace by substituting fossil coal with biochar agglomerates. *IRONMAK STEELMAK*, 43(8):564–570, 2016.

[126] Z. Chen, W. Ma, S. Li, J. Wu, K. Wei, Z. Yu, and W. Ding. Influence of carbon material on the production process of different electric arc furnaces. *J CLEAN PROD*, 174:17–25, 2018.

[127] Eramet Norway. Sustainability report 2013, 2014.

[128] D.J. Dijs and H.M. Smith. Factors affecting the resistivity and reactivity of carbonaceous reducing agents for the electric-smelting industry. *J S AFR I MIN METALL*, 80:286–296, 1985.

[129] H.W. Jackman and R.J. Helfinstine. Coke Crushing Characteristics. State of Illinois Department of Registration and Education; 1964 illinois state geological survey, circular 375.

[130] P.C. Pistorius. Reductant selection in ferro-alloy production: The case for the importance of dissolution in the metal. *J S AFR I MIN METALL*, 102(1):33–36, 2002.

[131] S.E. Olsen, S. Olsen, M. Tangstad, and T. Lindstad. *Production of Manganese Ferroalloys*. Tapir Akademisk Forlag, 2007.

[132] V.P. Vorob'ev, A.D. Golunov, and A.V. Ignat'ev. Carbon Reductants for the Production of Manganese Ferroalloys. *RUSS METALL+*, 8:752–755, 2009.

[133] M.A. Díez, R. Alvarez, and C. Barriocanal. Coal for metallurgical coke production: Predictions of coke quality and future requirements for cokemaking. *INT J COAL GEOL*, 50(1):389–412, 2002.

[134] H.S. Valia. Coke Production for Blast Furnace Ironmaking. ispat inland inc; 2015.

[135] A. Babich and D. Senk. Chapter 12 - coal use in iron and steel metallurgy. In D. Osborne, editor, *The Coal Handbook: Towards Cleaner Production*, volume 2 of *Woodhead Publishing Series in Energy*, pages 267–311. Woodhead Publishing, 2013.

[136] United States International Trade Commission. *Metallurgical Coke: Baseline Analysis of the U.S. Industry and Imports : [investigation No. 332-342].* USITC publication. U.S. International Trade Commission, 1994.

[137] H. Schobert and N. Schobert. Comparative Carbon Footprints of Metallurgical Coke and Anthracite for Blast Furnace and Electric Arc Furnace Use, 2015.

[138] Metallurgical coke. Richa Refractories, from http://www.richarefractories.com/metallurgical-coke.php, url: 19.01.2019.

[139] J.A. MacPhee, J.F. Gransden, L.Giroux, and J.T. Price. Possible CO_2 mitigation via addition of charcoal to coking coal blends. *FUEL PROCESS TECHNOL*, 90:16–20, 2009.

[140] S.S. Gornostayev, J.J. Heino, T.M.T. Kokkonen, H.T. Makkonen, S.M.M. Huttunen, and T.M.J. Fabritius. Textural changes in metallurgical coke prepared with polyethylene. *INT J MIN MET MATER*, 21(10):969–973, 2014.

[141] B.Kh. Bulaevskii and V.S. Shved. Modifying CRI and CSR values of coke. *COKE CHEM*, 53(1):15–18, 01 2010.

[142] J. Lubetsky and B.A. Steiner. Industrial Processes and Product Use. IPCC; 2008 2006 IPCC Guidelines for National Greenhouse Gas Inventories - Volume 3.

[143] A. Adrados, A. Lopez-Urionabarrenechea, J. Solar, J. Requies, I. De Marco, and J.F. Cambra. Upgrading of pyrolysis vapours from biomass carbonization. *J ANAL APPL PYROL*, 103:293–299, 2013.

[144] J. Bourke, M. Manley-Harris, C. Fushimi, K. Dowaki, T. Nunoura, and M.J. Antal. Do All Charcoals Have the Same Chemical Structure? 2. A Model of the Chemical Structure of Carbonized Charcoal. *IND ENG CHEM RES*, 46(18):5954–5967, 2007.

[145] F. Kapteijn, G. Abbel, and J.A. Moulijn. Co_2 gasification of carbon catalysed by alkali metals: Reactivity and mechanism. *FUEL*, 63(8):1036–1042, 1984.

[146] A. Hussein, F. Larachi, D. Ziegler, and H. Alamdari. Effects of heat treatment and acid washing on properties and reactivity of charcoal. *BIOMASS BIOENERG*, 90:101–113, 2016.

[147] J. Kaczorowski, T. Lindstad, and M. Syvertsen. The influence of Potassium on the Boudouard Reaction in Manganese Production. *ISIJ INT*, 47(11):1599–1604, 2007.

[148] J. Kaczorowski and T. Lindstad. The effect of potassium impregnation on the Boudourd reactivity of selected single-source and commercial cokes. *Infacon XI, New Delhi, India*, pages 583–593, 02 2007.

[149] J. Kramb, N. DeMartini, M. Perander, A. Moilanen, and J. Konttinen. Modeling of the catalytic effects of potassium and calcium on spruce wood gasification in CO_2. *FUEL PROCESS TECHNOL*, 148:50–59, 2016.

[150] Monaghan B.J., Longbottom R.J., Reid M., Aladejebi O.A., Jayasekara A.S., and Panhuis M. A New Approach to Investigating Coke Reactivity. *In: Mackey P.J., Grimsey E.J., Jones R.T., Brooks G.A. (eds) Celebrating the Megascale. Springer, Cham*, pages 519–526, 2014.

[151] H.R. Kokal and M.G. Ranade. Metallurgical Uses - Fluxes for Metallurgy. *Society for Mining, Metallurgy & Exploration*, pages 661–675, 1994.

[152] D. Langberg, T. Norgate, M. Somerville, P. Fung, J. Bartle, and Giles, R. and et al. Biomass as Fuel and Reductant for Modern Smelting Processes. Usa: CSIRO; 2006 Report No. DMR-2941.

[153] L. Zhang, S. Xu, W. Zhao, and S. Liu. Co-pyrolysis of biomass and coal in a free fall reactor. *FUEL*, 86(3):353–359, 2007.

[154] F. Li, M. Tangstad, and E. Ringdalen. Carbothermal Reduction of Quartz and Carbon Pellets at Elevated Temperatures. *METALL MATER TRANS B*, 49(3):1078–1088, Jun 2018.

[155] O. Raaness, L. Kolbeinsen, and J.A. Byberg. Statistical Analysis of Properties for Coals Used in the Production of Silicon Rich Alloys. *Infacon VIII, Beijing, China*, pages 116–120, 06 1998.

[156] A. Moreland, J.W. Patrick, and A. Walker. The texture and strength of metallurgical coke. *J MATER SCI*, 24(12):4350–4354, 1989.

[157] S.N. Chaudhuri. *Coal Rank Classification*, pages 1–3. Springer Berlin Heidelberg, Berlin, Heidelberg, 2016.

[158] L. Lu, V. Sahajwalla, C. Kong, and D. Harris. Quantitative x-ray diffraction analysis and its application to various coals. *CARBON*, 39(12):1821–1833, 2001.

[159] T. Hilding, K. Kazuberns, S. Gupta, V. Sahajwalla, R. Sakurovs, B. Björkman, and et al. Effect of Temperature on Coke Properties and CO_2 Reactivity Under Laboratory Conditions and in an Experimental Blast Furnace. *AISTech 2005 Proceedings - Volume I*, pages 497–505, 2005.

[160] K.L. Smith, L.D. Smoot, T.H. Fletcher, and R.J. Pugmire. *The Structure and Reaction Processes of Coal*. Language of Science. Springer, 1994.

[161] H. Sato, J.W. Patrick, and A. Walker. Effect of coal properties and porous structure on tensile strength of metallurgical coke. *FUEL*, 77(11):1203–1208, 1998.

[162] R.E. Winans and J.C. Crelling. *Chemistry and Characterization of Coal Macerals: Overview*, chapter 1, pages 1–20. American Chemical Society, 1984.

[163] O. Raanes and R.J. Gray. Coal in the production of silicon rich ferroalloys. *Infacon VII, Trondheim, Norway*, pages 201–220, 06 1995.

[164] Masaaki Naito, Akira Okamoto, Kazuyoshi Yamaguchi, Takeshi Yamaguchi, and Yoshihiro Inoue. Improvement of Blast Furnace Reaction Efficiency by Temperature Control of Thermal Reserve Zone. NIPPON STEEL; 2006 NIPPON STEEL technical report No. 94.

[165] W. Zhu, W. Song, and W. Lin. Catalytic gasification of char from co-pyrolysis of coal and biomass. *FUEL PROCESS TECHNOL*, 89(9):890–896, 2008.

[166] R.B. Fidel, D.A. Laird, M.L. Thompson, and M. Lawrinenko. Characterization and quantification of biochar alkalinity. *CHEMOSPHERE*, 167:367–373, 2017.

[167] S. Pati, J. Drelich, A. Jha, N.R. Neelameggham, L.H. Prentice, and C. Wang. *Energy Technology 2013: Carbon Dioxide Management and Other Technologies*. Wiley, 2013.

[168] A.A. El-Geassy, K.A. Shehata, M.I. Nasr, and S.S. Fakhoury. Effect of Alkalies on the Performance of Blast Furnace. *T IRON STEEL I JPN*, 26(10):865–874, 1986.

[169] A. Trubetskaya, F.H. Larsen, A. Shchukarev, K. Ståhl, and K. Umeki. Potassium and soot interaction in fast biomass pyrolysis at high temperatures. *FUEL*, 225:89–94, 2018.

[170] C. Wu and V. Sahajwalla. Dissolution rates of coals and graphite in Fe-C-S melts in direct ironmaking: Influence of melt carbon and sulfur on carbon dissolution. *METALL MATER TRANS B*, 31:243—251, 2000.

[171] J.G. Speight. *Handbook of Petroleum Product Analysis*. Chemical Analysis: A Series of Monographs on Analytical Chemistry and Its Applications. Wiley, 2015.

[172] G.L. Borman and K.W. Ragland. *Combustion Engineering*. McGraw-Hill series in mechanical engineering. McGraw-Hill, 1998.

[173] J.G. Mathieson, J.S. Truelove, and H. Rogers. Toward an understanding of coal combustion in blast furnace tuyere injection. *FUEL*, 84(10):1229–1237, 2005.

[174] R.C. Gupta. *ENERGY AND ENVIRONMENTAL MANAGEMENT IN METALLURGICAL INDUSTRIES*. PHI Learning, 2012.

[175] L. Edwards. The History and Future Challenges of Calcined Petroleum Coke Production and Use in Aluminum Smelting. *JOM*, 67(2):308–321, 2015.

[176] X. Zhan, Z. Zhou, and F. Wang. Catalytic effect of black liquor on the gasification reactivity of petroleum coke. *APPL ENERG*, 87(5):1710–1715, 2010.

[177] A. Otto, M. Robinius, T. Grube, S. Schiebahn, A. Praktiknjo, and D. Stolten. Power-to-Steel: Reducing CO_2 through the Integration of Renewable Energy and Hydrogen into the German Steel Industry. *ENERGIES*, 10:451–471, 2017.

[178] G.B. Taylor and H.W. Starkweather. Reduction of Metal Oxides by Hydrogen. *J AM CHEM SOC*, 52(6):2314–2325, 1930.

[179] J. Bilik, P. Pustejovska, S. Brozova, and S. Jursova. Efficiency of hydrogen utilization in reduction processes in ferrous metallurgy. *SCI IRAN*, 20(2):337–342, 2013.

[180] J. Van Dam, J. Van Eijck, J. Schure, and X. Zuzhang. *The charcoal transition: greening the charcoal value chain to mitigate climate change and improve local livelihoods*. Food and Agriculture Organization of the United Nations, 2017.

[181] E. Vakkilainen, K. Kuparinen, and J. Heinimö. Large Industrial Uses of Energy Biomass. IEA Bioenergy; 2013 Task 40: Sustainable International Bioenergy Trade.

[182] J.-P. Birat, F. Hanrot, and G. Danloy. CO_2 mitigation technologies in the steel industry: A benchmarking study based on process calculations. *STAHL EISEN*, 123:69–72, 2003.

[183] B. Monsen, M. Grønli, L. Nygaard, and H. Tveit. The Use of Biocarbon in Norwegian Ferroalloy Production. *Infacon IX, Quebec City, Canada*, 9:268–276, 06 2001.

[184] H. Zhang, G. Zhu, H. Yan, T. Li, and Y. Zhao. The Mechanism on Biomass Reduction of Low-Grade Manganese Dioxide Ore. *METALL MATER TRANS B*, 44(4):889–896, 2013.

[185] Elkem. The road to climate neutral metal production. Elkem, https://www.elkem.com/.

[186] A.V. Bridgwater and S.A. Bridge. *A Review of Biomass Pyrolysis and Pyrolysis Technologies*, pages 11–92. Springer Netherlands, Dordrecht, 1991.

[187] M. Trossero, J. Domac, and R. Siemons. Industrial charcoal production. FAO; 2008 FAO TCP 3101.

[188] D.M. Pennise, K.R. Smith, J.P. Kithinji, M.E. Rezende, T.J. Raad, J. Zhang, and C. Fan. Emissions of greenhouse gases and other airborne pollutants from charcoal making in Kenya and Brazil. *J GEOPHYS RES-ATMOS*, 106(D20):24143–24155, 2001,.

[189] A. de Oliveira Vilela, E.S. Lora, Q.R. Quintero, R.A. Vicintin, and T.P. da Silva e Souza. A new technology for the combined production of charcoal and electricity through cogeneration. *BIOMASS BIOENERG*, 69:222–240, 2014.

[190] W.R. Smith, R. Peter, A.W. Toole, C. Arbogast, P.H. Lane, E.G. Lock, and et al. Production of Charcoal in a Masonry Block Kiln - Structure and Operation. US Department of Agriculture Forest Service; 1957 September Report No 2084.

[191] A. Saravanakumar and M.T. Haridasan. A novel performance study of kiln using long stick wood pyrolytic conversion for charcoal production. *ENERGY EDUC SCI TECH*, 31:711–722, 01 2013.

[192] P. Rousset, A. Caldeira-Pires, A. Sablowski, and T. Rodrigues. LCA of eucalyptus wood charcoal briquettes. *J CLEAN PROD*, 19(14):1647–1653, 2011.

[193] C.E. Brewer, V.J. Chuang, C.A. Masiello, H. Gonnermann, X. Gao, and Dugan, B. and et al. New approaches to measuring biochar density and porosity. *BIOMASS BIOENERG*, 66:176–185, 2014.

[194] Q. Hu, H. Yang, D. Yao, D. Zhu, X. Wang, J. Shao, and H. Chen. The densification of bio-char: Effect of pyrolysis temperature on the qualities of pellets. *BIORESOURCE TECHNOL*, 200:521–527, 2016.

[195] J. Peng, X.T. Bi, C.J. Lim, H. Peng, C.S. Kim, D. Jia, and H. Zuo. Sawdust as an effective binder for making torrefied pellets. *APPL ENERG*, 157:491–498, 2015.

[196] S.H. Larsson, M. Rudolfsson, M. Nordwaeger, I. Olofsson, and R. Samuelsson. Effects of moisture content, torrefaction temperature, and die temperature in pilot scale pelletizing of torrefied norway spruce. *APPL ENERG*, 102:827–832, 2013.

[197] S.H. Larsson, M. Thyrel, P. Geladi, and T.A. Lestander. High quality biofuel pellet production from pre-compacted low density raw materials. *BIORESOURCE TECHNOL*, 99:7176–7182, 2008.

[198] Q. Hu, J. Shao, H. Yang, D. Yao, X. Wang, and H. Chen. Effects of binders on the properties of bio-char pellets. *APPL ENERG*, 157:508–516, 2015.

[199] A. Funke, T. Demus, T. Willms, L. Schenke, T. Echterhof, A. Niebel, and et al. Application of fast pyrolysis char in an electric arc furnace. *FUEL PROCESS TECHNOL*, 174:61–68, 2018.

[200] W. Stelte, J.K. Holm, A.R. Sanadi, S. Barsberg, J. Ahrenfeldt, and U.B. Henriksen. Fuel pellets from biomass: The importance of the pelletizing pressure and its dependency on the processing conditions. *FUEL*, 90(11):3285–3290, 2011.

[201] L. S. Parfen'eva, T. S. Orlova, N. F. Kartenko, B. I. Smirnov, I. A. Smirnov, H. Misiorek, A. Jezowski, J. Muha, and M. C. Vera. Structure, electrical resistivity, and thermal conductivity of beech wood biocarbon produced at carbonization temperatures below 1000 °c. *PHYS SOLID STATE+*, 53(11):2398–2407, 2011.

[202] T. Griessacher, J. Antrekowitsch, and S. Steinlechner. Charcoal from agricultural residues as alternative reducing agent in metal recycling. *BIOMASS BIOENERG*, 39:139–146, 2012.

[203] M.J. Antal, E. Croiset, X. Dai, C. DeAlmeida, W.S.-L. Mok, N. Norberg, and et al. High-Yield Biomass Charcoal. *ENERG FUEL*, 10(3):652–658, 1996.

[204] P.R. Solomon, D.G. Hamblen, M.A. Serio, Z.-Z. Yu, and S. Charpenay. A characterization method and model for predicting coal conversion behaviour. *FUEL*, 72(4):469–488, 1993.

[205] P.R. Solomon, M.A. Serio, and E.M. Suuberg. Coal pyrolysis: Experiments, kinetic rates and mechanisms. *PROG ENERG COMBUST*, 18(2):133–220, 1992.

[206] G. Migliavacca, E. Parodi, L. Bonfanti, T. Faravelli, S. Pierucci, and E. Ranzi. A general mathematical model of solid fuels pyrolysis. *ENERGY*, 30(8):1453–1468, 2005. Dubrovnik Conference on Sustainable Development of Energy, Water and Environment Systems.

[207] Y. Zhao, M.A. Serio, and P.R. Solomon. A general model for devolatilization of large coal particles. *SYMP INT COMBUST PROC*, 26(2):3145–3151, 1996.

[208] D.K. Shen and S. Gu. The mechanism for thermal decomposition of cellulose and its main products. *BIORESOURCE TECHNOL*, 100(24):6496–6504, 2009.

[209] F.-X. Collard and J. Blin. A review on pyrolysis of biomass constituents: Mechanisms and composition of the products obtained from the conversion of cellulose, hemicelluloses and lignin. *RENEW SUST ENERG REV*, 38:594–608, 2014.

[210] A. Broido and F. J. Kilzer. A Critique of the Present State of Knowledge of The Mechanism of Cellulose Pyrolysis. *FIRE RES*, 1-5:157–161, 1959 to 1963.

[211] M.J. Antal, V. Gábor, and E. Jakab. Cellulose Pyrolysis Kinetics: Revisited. *IND ENG CHEM RES*, 37:1267–1275, 1998.

[212] K. Dussan, S. Dooley, and R. Monaghan. Integrating compositional features in model compounds for a kinetic mechanism of hemicellulose pyrolysis. *CHEM ENG J*, 328:943–961, 2017.

[213] Y. Peng and S. Wu. The structural and thermal characteristics of wheat straw hemicellulose. *J ANAL APPL PYROL*, 88(2):134–139, 2010.

[214] D.K. Shen, S. Gu, and A.V. Bridgwater. Study on the pyrolytic behaviour of xylan-based hemicellulose using TG–FTIR and Py–GC–FTIR. *J ANAL APPL PYROL*, 87(2):199–206, 2010.

[215] K. Werner, L. Pommer, and M. Broström. Thermal decomposition of hemicelluloses. *J ANAL APPL PYROL*, 110:130–137, 2014.

[216] R. Alén, E. Kuoppala, and P. Oesch. Formation of the main degradation compound groups from wood and its components during pyrolysis. *J ANAL APPL PYROL*, 36(2):137–148, 1996.

[217] T. Hosoya, H. Kawamoto, and S. Saka. Pyrolysis behaviors of wood and its constituent polymers at gasification temperature. *J ANAL APPL PYROL*, 78(2):328–336, 2007.

[218] H. Yang, R. Yan, H. Chen, D.H. Lee, and C. Zheng. Characteristics of hemicellulose, cellulose and lignin pyrolysis. *FUEL*, 86(12):1781–1788, 2007.

[219] C. Branca, A. Albano, and C. Di Blasi. Critical evaluation of global mechanisms of wood devolatilization. *THERMOCHIM ACTA*, 429(2):133–141, 2005.

[220] R. Ma, X. Zhang, Y. Wang, and X. Zhang. New Insights Toward Quantitative Relationships between Lignin Reactivity to Monomers and Their Structural Characteristics. *CHEMSUSCHEM*, 11(13):2146–2155, 2018.

[221] N.T. Weiland, N.C. Means, and B.D. Morreale. Product distributions from isothermal co-pyrolysis of coal and biomass. *FUEL*, 94:563–570, 2012.

[222] J. Rath and G. Staudinger. Cracking reactions of tar from pyrolysis of spruce wood. *FUEL*, 80(10):1379–1389, 2001.

[223] J.C. Mackie and K.R. Doolan. High-temperature kinetics of thermal decomposition of acetic acid and its products. *INT J CHEM KINET*, 16(5):525–541, 1984.

[224] C.W. Lee, A.W. Scaroni, and R.G. Jenkins. Effect of pressure on the devolatilization and swelling behaviour of a softening coal during rapid heating. *FUEL*, 70(8):957–965, 1991.

[225] K. Raveendran, A. Ganesh, and K.C. Khilar. Influence of mineral matter on biomass pyrolysis characteristics. *FUEL*, 74(12):1812–1822, 1995.

[226] C. Di Blasi, C. Branca, and G. D'Errico. Degradation characteristics of straw and washed straw. *THERMOCHIM ACTA*, 364(1):133–142, 2000.

[227] P.R. Patwardhan, J.A. Satrio, R.C. Brown, and B.H. Shanks. Influence of inorganic salts on the primary pyrolysis products of cellulose. *BIORESOURCE TECHNOL*, 101(12):4646–4655, 2010.

[228] M. M"uller-Hagedorn, H. Bockhorn, L. Krebs, and U. M"uller. A comparative kinetic study on the pyrolysis of three different wood species. *J ANAL APPL PYROL*, 68-69:231–249, 2003.

[229] M. Nik-Azar, M.R. Hajaligol, M. Sohrabi, and B. Dabir. Mineral matter effects in rapid pyrolysis of beechwood. *FUEL PROCESS TECHNOL*, 51(1-2):7–17, 1997.

[230] M. Dall'Ora, P.A. Jensen, and A.D. Jensen. Suspension combustion of wood: Influence of pyrolysis conditions on char yield, morphology, and reactivity. *ENERG FUEL*, 22(5):2955—-2962, 2008.

[231] M. Dall'Ora. *Reactivity and burnout of wood fuels*. PhD thesis, Technical University of Denmark, 2011. PhD thesis.

[232] Arvydas Lebedys. Global Forest Products Facts and Figures 2016. FAO Forestry Department; 2017 I7034EN/1/12.17.

[233] P. Girard. Charcoal production and use in Africa: What future? *UNASYLVA*, 53:30–34, 01 2002.

[234] P. Quicker, K. Weber, D. Blöhse, T. Echterhof, S. Eichenauer, S. Heger, C. Kammann, A. Kruse, M.A. Schulten, C. Sager, et al. *Biokohle: Herstellung, Eigenschaften und Verwendung von Biomassekarbonisaten*. Springer Fachmedien Wiesbaden, 2017.

[235] Holzkohlewerk Lüneburg; www.holzkohlewerk.de, url: 23.12.2018.

[236] L.A. Kristoferson and V. Bokalders. *Renewable Energy Technologies: Their Applications in Developing Countries*. Elsevier Science, 2013.

[237] C. Di Blasi. Modeling chemical and physical processes of wood and biomass pyrolysis. *PROG ENERG COMBUST*, 34(1):47–90, 2008.

[238] A.K. Sadhukhan, P. Gupta, and R.K. Saha. Modelling of pyrolysis of large wood particles. *BIORESOURCE TECHNOL*, 100(12):3134–3139, 2009.

[239] E. Grieco and G. Baldi. Analysis and modelling of wood pyrolysis. *CHEM ENG SCI*, 66(4):650–660, 2011.

[240] S. Wang, G. Dai, H. Yang, and Z. Luo. Lignocellulosic biomass pyrolysis mechanism: A state-of-the-art review. *PROG ENERG COMBUST*, 62:33–86, 2017.

[241] A. Anca-Couce. Reaction mechanisms and multi-scale modelling of lignocellulosic biomass pyrolysis. *PROG ENERG COMBUST*, 53:41–79, 2016.

[242] J. Bland and G. da Silva. A detailed chemical kinetic model for pyrolysis of the lignin model compound chroman. *AIMS ENV SCI*, 1(20140102):12–25, 2014.

[243] C. Liu, Y. Deng, S. Wu, M. Lei, and J. Liang. Experimental and Theoretical Analysis of the Pyrolysis Mechanism of a Dimeric Lignin Model Compound with α-o-4 Linkage. *BIORESOURCES*, 11(2):3626–3636, 2016.

[244] D. Merrick. *Metallurgical coke manifacture: A mathematical study.* PhD thesis, University of London, 1977.

[245] N. Mastorakis and J. Sakellaris. *Advances in Numerical Methods.* Lecture Notes in Electrical Engineering. Springer US, 2009.

[246] L. Tognotti E. Biagini, M. Falcitelli. Devolatilisation and pyrolysis of biomasses: development and validation of structural models. *29th meeting on combustion, Pisa, Italy*, pages IX6.1–IX6.6, 2006.

[247] V. Vand. A Theory of the Irreversible Elecrical Resistance Changes of Metallic Films Evaporated in Vacuum. *P PHYS SOC*, 55:222–246, 1942.

[248] M.J. Antal, E.G. Plett, T.P. Chung, and M. Summerfield. Recent Progress in Kinetic Models for Coal Pyrolysis. *Am Chem Soc Div Fuel Chem Prepr*, pages 137–148, 1977.

[249] D.B. Anthony. *Rapid Devolatilization and Hydrogasification of Pulverized Coal.* PhD thesis, Massachusetts Institute of Technology, 1974.

[250] D.B. Anthony, J.B. Howard, H.C. Hottel, and H.P. Meissner. Rapid devolatilization of pulverized coal. *Symposium (International) on Combustion*, 15(1):1303–1317, 1975.

[251] P.R. Solomon and H.-H. King. Tar evolution from coal and model polymers: Theory and experiments. *FUEL*, 63(9):1302–1311, 1984.

[252] K.R. Squir, P.R. Solomon, R.M. Carangelo, and M.B. DiTaranto. Tar evolution from coal and model polymers: 2. The effects of aromatic ring sizes and donatable hydrogens. *FUEL*, 65(6):833–843, 1986.

[253] Y. Chen, S. Charpenay, A. Jensen, M.A. Wójtowicz, and M.A. Serio. Modeling of biomass pyrolysis kinetics. *SYMP INT COMBUST PROC*, 27(1):1327–1334, 1998.

[254] S. Niksa. Predicting the rapid devolatilization of diverse forms of biomass with bio-flashchain. *PROC COMBUST INST*, 28(2):2727–2733, 2000.

[255] T. Fletcher, A. Kerstein, R. Pugmire, M. Solum, and D.M. Grant. A Chemical Percolation Model For Devolatilization: Summary. pages 1–66, 01 1992. Sandia report SAND 92-8207.

[256] A. Sharma, V. Pareek, and D. Zhang. Biomass pyrolysis - A review of modelling, process parameters and catalytic studies. *RENEW SUST ENERG REV*, 50:1081–1096, 2015.

[257] W.C. Park, A. Atreya, and H.R. Baum. Experimental and theoretical investigation of heat and mass transfer processes during wood pyrolysis. *COMBUST FLAME*, 157(3):481–494, 2010.

Chapter 3

Experimental study

This chapter describes the experimental investigation of the heat treatment of biomass and the analysis procedure to evaluate the produced charcoal. The initial heat treatment is defined as primary pyrolysis, while the consecutive is defined as secondary heat treatment. The used setups and analytical procedures are described in the following sections.

3.1 Selection of biomass

Different wood species were selected for the production of biochar, namely Norway spruce (*Picea abies*), sessile oak (*Quercus petraea*) and constituents of Scots pine trees (*Pinus sylvestris*). The samples were selected as local representatives of softwood and hardwood, which differ more in compositional analysis and ash content than within same group of plants. The spruce and oak samples were prepared from a whole tree, which were felled in Dømmesmoen, Grimstad, Norway in 2012 and 2016. The age of the trees was determined by the annual rings to 39 years for Norway spruce, respectively 46 years for sessile oak. Scots pine trees were harvested in northern Sweden with an average age of 147 years. Green needles, branches without needles and bark from basal log were investigated of Scots pine.

3.1.1 Sample preparation

Norway spruce and sessile oak samples were chipped by a disc chipper to a particle size less 20 mm. The complete samples were dried in a laboratory drier at 60 °C before storage. Prior to wood characterization, the biomass samples were divided into six equal fractions using a riffler. The particle size distribution was determined according to EN ISO 17827-1:2016 in a vibrating vibrating EFL2000 sieve shaker (ENDECOTTS, United Kingdom), comprising ten sieves ranging from 2 to 20 mm and a bottom pan (< 2 mm). Particles remaining on each sieve and in a bottom pan were collected and weighed using

an electronic top pan balance (readability ±0.01 g). Sieving was conducted for 15 min at 3 mm amplitude [1]. Two biomass samples were comminuted in a laboratory-scale mill POLYMIX PX-MFC 90 D (KINEMATICA, Switzerland) with a sieve size of 0.8 mm. The samples were divided into four equal fractions using a riffler.

3.2 Pyrolysis setup

The charcoal samples were generated in the slow pyrolysis reactor, as shown in Figure 3.1. The reactor can be operated at temperatures up to 1350 °C and heating rates up to 20 °C min^{-1}. A sample mass of 60 g wood chips was selected for each experiment, which was filled homogeneously into the pyrolysis retort. The retort has an inner diameter of 75 mm, a height of 150 mm, a wall thickness of 2 mm and is made of silicon carbide (SiC). The bulk temperature was monitored by a thermocouple type S (T_2, max. 1600°C). The pyrolysis setup encloses a two-stage cooling system with a condensate collector as described in section 3.2.1 and a pyrolysis gas sampling unit. The connection pipes between the retort and the condensation unit were made of quartz glass with an inner diameter of 16 mm. The connection pipes were heated up to 350 °C by a heating tape HBQ (Hillesheim, Germany) to minimize the condensation and thermal decomposition of tars. The temperature was controlled by a temperature regulator MC1 (HORST GmbH, Germany). The reactor retort was continuously purged by nitrogen at defined flow rate of 100 ml min^{-1}. The inlet flow was controlled by a flowmeter HFC-202 (Teledyne, USA). A similar flowmeter was used to measure the gas volumne flow after condensation. Data collection was based on the LabView software (version 8.6).
The wood samples in the retort were preheated in nitrogen at 10 °C min^{-1} to 160 °C with an residence time of 30 min. The dried wood was then heated at 10 °C min^{-1} to the primary pyrolysis temperature ranging from 500 to 1300 °C and kept at the final temperature for 1 h to ensure a complete conversion. After the heating program was finished, the furnace was turned off and the charcoal sample was cooled overnight in nitrogen (0.3 l min^{-1}). Samples were stored in sealed plastic containers.

3.2.1 Slow pyrolysis reactor

A modified SQ11 toploader furnace (Kittec, Germany) was used for the primary pyrolysis. An additional energy-saving package was installed to reduce heat losses and thermal wear of the furnace. The inner dimensions of the heated furnace chamber are 220 mm x 220 mm x 220 mm. A thermocomputer TC 505 (Bentrup, Germany) was used to control the heating program of the furnace.
A two stage condensation unit was used to separate the liquid fraction from the gases.

A 250 mm Liebig condenser with an inner diameter of 20 mm made of Duran glass was installed as condenser 1. The condenser was kept to 20 °C by tap water and connected to a 500 ml two-necked flask made of quartz glass, which was used to collect the liquid products. A consecutive 250 mm ball condenser with 5 balls (40 mm diameter) was cooled to 4 °C by a cryostat ECO RE 620 S (Lauda, Germany). A molecular sieve was installed downstream the second condenser to remove remaining liquids.

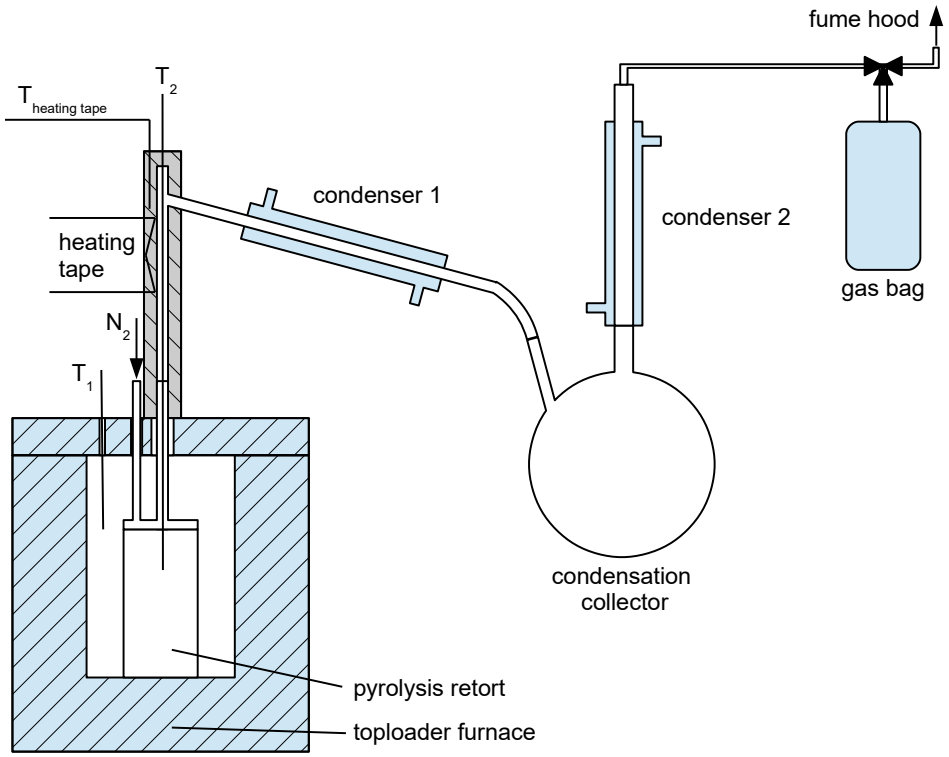

Figure 3.1: Slow pyrolysis reactor

3.2.2 High temperature furnace

The secondary heat treatment of the samples was carried out in high temperature reduction furnace LHTG 200-300/20-1G (Carbolite Gero, Germany) as shown in Figure 3.2. The furnace can be operated at temperatures up to 1800 °C and at heating rates up to 20 °C min^{-1}. 5 g of the char sample were loaded into a 70 ml alumina crucible (Almath Crucibles Ltd, UK) placed in middle of the graphite retort. The reduction furnace was completely evacuated and purged by argon before the experiment. The char sample was heated in argon at 10 °C to 700, 1000, 1300 and 1600 °C and kept at that temperature for 2 h to ensure complete conversion. After the heating program was finished the sample was cooled at a rate of 20 °C min^{-1} to room temperature. The samples were stored in sealed plastic containers.

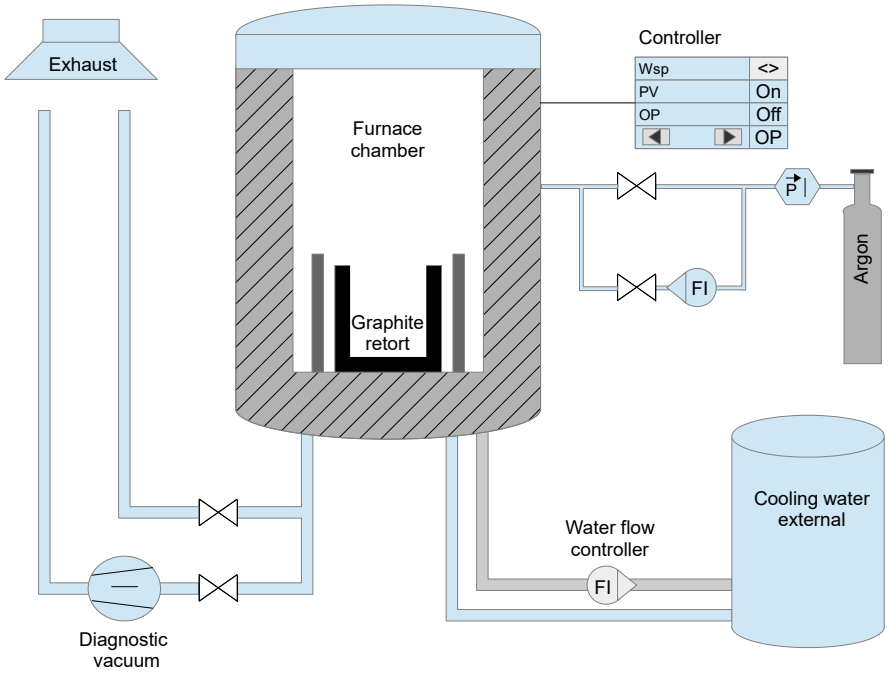

Figure 3.2: Schematic of the high-temperature reduction furnace at University of Agder

3.3 Liquid analysis

The biooil yield is comprised of the mass difference from the collection flask, condensers and connection pipe before and after the experiment. The condensed biooil in the connection pipes and the two condensers was dissolved in anhydous methanol (VWR chemicals, Norway) and mixed with the biooil collected in the flask. The sample was diluted by methanol by a factor of 2.5. The samples were stored in closed sample bottles in a freezer at -20 °C.

3.3.1 Determination of water content

The water content of the biooil was determined in a Karl Fischer KF1000 volumetric titrator (Hach, Germany). The experiments in the Karl Fischer titrator were conducted with the two component reagents titrant T5 (Merck, Germany). First, the dissolved biooil samples were homogenized and 1 ml of each sample was raised into a syringe. After stabilization of the measuring cell, about 0.1 g of the sample was injected into the solvent in the cell. The mass difference of the syringe was noted with a readability of 1 mg. The experiments were carried out at room temperature as a duplicate with a maximum error of $\pm 0.5\,\%$.

3.3.2 Gas chromatography

5 μl of an internal standard (Chlorobenzene, Sigma-Aldrich) were injected into the biooil-methanol mixture for semiquantification. Prior to a quantitative analysis in GC-FID, the biooil components were identified using a dual detector system GC-MS 5975C TAD Series / GC-FID 7890A (Agilent Technologies, USA). Nitrogen was used as a carrier gas with a constant flow rate of 1 ml min^{-1}. The column temperature program ran from 50 to 280 °C. The initial temperature of 50 °C was kept for the 2 min. Consecutively, the temperature was increased to 160 °C at a constant heating rate of 1.5 °C min^{-1}, following by a second ramp at a rate of 6 °C min^{-1} to 230 °C, and a third up to 280 °C at a heating rate of 8 °C min^{-1}, at which the temperature was kept for 5 min. The range from m/z 35 to m/z 250 was scanned by a quadrupolar type analyzer at a scan rate of 6.22 scans s^{-}1. 0.5,μl of sample were injected at a 4:1 split ratio as a triplicate. The collected spectra were exported from Chemstation E.02.00.493 (Agilent Technologies, USA) to NetCDF and further processed by the statistical software "R" 2.15.2 that can acquire and align the data, correct baseline, set time-window and perform multivariate analysis [2]. The multivariate analysis using MCR-AR algorithm yielded deconvoluted mass spectra with the well-resolved overlapping peaks [3], which were imported into the mass spectra library software NIST MS Search 2.0 [4]. The area of peaks was normalized to 100% within each sample and the mean of triplicate measurements was calculated. The peaks with mass spectra similarity higher than 80 % were used in the biooil quantification. The relative response factors (RRFs) were determined for each compound in tar samples using MatLab (version 8.6, MathWorks Inc.). The quantitative analysis of tar compounds was performed on a gas chromatograph 7820A (Agilent Technologies, USA) equipped with a flame ionization detector (GC-FID) and DB-EUPAH capillary column (30m length, 0.25 mm internal diameter, 0.25 μm film thickness) at University of Limerick, Ireland. The column temperature and carrier gas settings were programmed the same as those used in GC-MS analysis. The temperatures of the injector and detector were kept at 250 and 300 °C, respectively. Data acquisition and processing were performed using Agilent OpenLAB CDS EZChrom A.02.02 (Agilent Technologies, USA). Most probable species were calibrated at four levels with solutions of known concentration and 5 replicates per level.

3.4 Charcoal characterization

The charcoal samples were split into 4 fractions using a riffler. One fraction was crushed in a mortar with a ceramic pestle and sieved to a particle size < 0.25 mm. Proximate and ultimate analysis were carried out with the particle size $< 125\,\mu$m, whereas thermo-

gravimetic analysis was carried out with a particle size between 0.125 and 0.25 mm.

3.4.1 Standard analyses

3.4.1.1 Proximate analysis

The proximate analysis comprises the measurement of the moisture, ash, volatile matter and fixed carbon contents. Moisture content of fresh produced charcoal samples is inapplicable, but the moisture content was measured for the samples which were in equilibrium with atmospheric condition. The ash content was determined according to the standard test ISO 18122:2015. The fixed carbon content was determined according to the procedure described in BS ISO 15148. The fixed carbon yield of the charcoal samples was calculated according to equation 2.3.

3.4.1.2 Ultimate analysis

The ultimate analysis of the biomass and charcoal samples was performed on the Elemental Analyser 2400 CHNS/O Series II (Perkin Elmer, USA). The analyzer was operated in CHN mode with argon as the carrier gas. Each experimental point was carried out as a triple determination with about 1.5 mg of dried material. Acetanilide was used as a calibration and reference material. The ash content was taken from proximate analysis by parallel samples.

3.4.2 Solvent extraction

The amount of condensed biooil on the charcoal surface was investigated by Soxhlet extraction. 5 g of untreated charcoal were weighed in a quartz thimble with a readability of 1 mg and placed in the Soxhlet extractor. In the first extraction, 100 ml of distilled water were used as a solvent. The sample was dried at 106 °C before weigh out. The same sample was treated with a subsequent acetone extraction. The mass differences in the extraction stages were taken as water soluble and acetone soluble fraction.

3.4.3 Thermogravimetric study

The thermal decomposition of char samples was determined using an thermogravimetric instrument TGA/DSC 1 STARe System (Mettler Toledo, USA). 5 mg of the charcoal samples were loaded into an Al_2O_3 crucibles with a volume of 70 μl. The charcoal samples were firstly heated up to 110 °C and kept 30 min at the temperature for drying. The dried samples were subsequently heated up to 1100 °C at a constant heating rate of 10 °C min^{-1}

and kept at the final temperature for 15 min. A constant nitrogen volume flow of 100 ml min^{-1} was used to render the chamber inert and ensure pyrolysis conditions. After the heating program was finished the gas was switched to air to determine the not reacted organic content. The same heating program was used for parallel samples in CO_2, in which the reactivity of char was investigated in 10, 20, 60 and 100 % volume fraction of CO_2. The reaction threshold temperature is defined as the temperature that corresponds to the appearance of the sample mass decrease [5]. The reactivity in CO_2 was compared to the non-isothermal measurements in N_2 to deduct the mass loss by incomplete pyrolysis. The kinetic parameters of char samples were derived by the integral method presented by Coats and Redfern [6].

$$ln\left(-\frac{ln(1-X)}{T^2}\right) = ln\left(\frac{A_i R}{\kappa E_a}\right) - \frac{E_a}{RT} \tag{3.1}$$

Where X is the conversion, T is the thermodynamic temperature, κ is the heating rate and R is the gas constant. A plot of ln(-ln(1-X) T^{-2}) versus T^{-1} gives a straight line whose slope and intercept determine the values of the activation energy (E_a) and pre-exponential factor (A_i). The reactivities of charcoal samples were compared using the reaction rates calculated from the derived kinetic parameters (A_i and E_a) at a fixed gasification temperature of 1000 °C.

3.4.4 SEM microscopy

Scanning electron microscope (SEM) analysis were carried out on two systems. The overall structure of the charcoal pellets were investigated by a JSM-6400 Scanning Microscope (Jeol, Japan). SEM/EDS analysis of char was conducted on a high-resolution field emission microscope SU-70 (Hitachi, Japan) under high vacuum in order to understand char structural properties. Prior to the analysis by SEM/EDS, char samples were coated with a thin layer of gold (2 min, 20 mA) using an Edwards S150B Sputter Coater to avoid sample charging.

3.4.5 Electrical resistivity

The electrical resistivity was determined for the charcoal and charcoal based pellets. First, the electrical resistivity was investigated by the measurement of the electrical conductivity using a 34470A 7 1/2 Digit Multimeter (Keysight Technologies, USA). The sample was placed on a socket and connected to the four probes of the source meter and the microelectrodes. Two adjacent electrodes were connected to a multimeter 287 (Fluke, USA), whereas the other two electrodes were connected to the current source (ISO-Tech

IPS 3303) of the source meter, as it was reported by Sun et al. [7]. A charcoal pellet was connected by four different electrodes to the source meter based on the van der Pauw electrode geometry [8]. The electrical conductivity was determined according to equation 3.2:

$$\sigma = \frac{L}{R * A} \tag{3.2}$$

where σ is the electrical conductivity, A is the cross-sectional area, L is the length of the resistor, and R is the resistance between two Ti-Au electrodes. The electrical resistivity (ρ) is defined as:

$$\rho = \frac{1}{\sigma} \tag{3.3}$$

3.4.6 Particle shrinkage - heating microscope

The silhouettes of biomass cubes and charcoal pellets were investigated in inert atmosphere using a heating microscope EM-201-17 (Hesse Instrument, Germany). The heating microscope is schematically shown in Figure 3.3. The height, width, area and particle shape were analyzed at temperatures up to 1200 °C. Wood cubes and charcoal based pellets with an edge length of 3 to 4 mm were placed in a center of the sample plate above the tip of the thermocouple. The heating chamber was continuously purged by nitrogen at a constant rate of 500 ml min^{-1}, which was controlled by a flowmeter HFC-202 (Teledyne, USA).

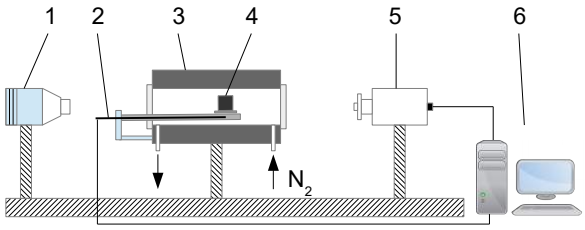

Figure 3.3: Schematic of the Hesse heating microscope. 1 Lamp, 2 Thermocouple S, 3 heating chamber, 4 sample, 5 CCD camera, 6 computer

3.4.7 External analysis

Some charcoal analyses were carried out in collaboration with University of Duisburg-Essen (Germany), National University of Ireland (Ireland), University of Limerick (Ireland), Materials Chemistry Research Center (Thailand), The University of York (UK), Luleå University of Technology (Sweden), Swedish University of Agricultural Sciences (Sweden), Eurofins Environment Testing (Sweden), National Energy Technology Laboratory (USA), Ghent University (Belgium) and GNF Berlin-Adlershof e.V. (Germany).

3.4.7.1 Raman spectroscopy

Raman spectroscopy was performed using an inVia Raman microscope (Renishaw, UK) operating with a 514 nm laser line at a power of 30 mW. The measurements were performed in static mode with a centre at 1600 cm^{-1} resulting in a 960-2200 cm^{-1} spectral region. The laser power was set to 100 % in the software and roughly 30 % in the hardware. 1 s exposure time was used in normal confocality mode. A 20x lens and 8-15 μm step size (X and Y directions) were used for mapping, and to generate 100-200 spectra/images for each charcoal sample. Cosmic rays were removed and the data was subjected to multivariate noise filtering using the WiRE chemometrics package version 3.0 (Renishaw, UK). Spectra were saved as text files and processed via the free, open-source MatLab script provided by the Vibrational Spectroscopy Core Facility at Umeå University (www.kbc.umu.se/english/visp/download-visp/). The following parameters were used for spectra pre-processing: asymmetrical least squares baseline correction with lambda = 20000000 and p = 0.001 [9]; Savitzky-Golay smoothing with the first polynomial order and frame rate of 3 [10]. Spectra were total area normalized in the entire spectral range. The corrected spectra from each mapping were then averaged to create a final composite curve for the peak deconvolution. No spectral scaling was performed. Deconvolution of the Raman spectra were conducted using the peak fit pro tool in the OriginPro software (OriginLab, USA) by combination of nine Gaussian-shaped bands (S_L, S, D_S, D, A_1, A_2, G_G, G_L, and D') following Smith et al. [11]. The mean crystal size in the a-direction (L_a) with the fitting constants C_0 = -12.6 nm and C_1 = 0.033, which are valid for the laser wavelength from 400 to 700 nm, is given by [12]:

$$L_a = \frac{C_0 + C_1 \lambda_L}{A_D / A_{G_L}} \tag{3.4}$$

3.4.7.2 N_2 adsorption analysis

The specific surface area (SSA) of biomass chars was determined based on N_2 adsorption at the boiling point (77 K). To remove remaining volatiles and possible adsorbate, the char samples were heated to 350°C in a dry N_2 flow prior to the measurement. The multipoint Brunauer-Emmett-Teller (BET) theory with seven points in the range of p/p_0 from 0.06 to 0.3 was applied on the NOVA 2000e instrument (Quantachrome, Germany). BET equation was used to determine the specific surface area [13].

3.4.7.3 Transmission electron microscopy

Prior to the microscopy, char samples were kept at 350°C for 6 hours in a thermogravimetric instrument to reduce the amount of volatiles. Samples were ground in a mortar to ensure a homogeneous particle distribution, sonified in deionized water for 30 min, wet

dispersed on a lacey carbon copper grid and dried at room temperature for 20 min. Char nanostructure was studied using a FEI Tecnai operated at 300 keV, equipped with an Oxford Instruments X-Max SDD EDS detector. The curvature of a single graphene sheet is defined in equation 3.5:

$$Curvature = \frac{Length}{Fiber\ \ length} \tag{3.5}$$

The length is a straight line that connects both ends of a graphene sheet. The fiber length is a contour or arc length (supplementary Figure S-1). Both length and fiber length were estimated by Gatan Digital Micrograph software according to method of Müller et al. [14]. The part of the image with the more visible graphene layers was magnified to a size of 10 nm x 10 nm, and both length and fiber length were manually determined by the software ruler which draws a straight or contour line to connect both ends of a graphene sheet.

3.4.7.4 Mercury intrusion porosimetry

The pore size distribution and porosity of char samples were determined by a Pascal mercury intrusion porosimeter system equipped with two instruments. Porosity in the ultramacro and macropore regions was measured by Pascal 140 porosimeter (Micromeritics, Germany) at the low pressures (up to 400 kPa). A Pascal 440 porosimeter equipped with a dilatometer (Micromeritics, Germany) was used to determine the pore size from 1.8 to 7500 nm at high pressures up to 400 MPa. To access the pores and voids within biomass particles, the samples were degassed at room temperature prior to the measurement. Prior to the porosity analysis, wood fractions were dried at 50 °C in an oven desiccator for 48 h.

3.4.7.5 Pore volume and size

The pore sizes in the char were distinguished into three categories: micropores (1.8-80 nm), mesopores (80-500 nm) and macropores (0.5-58 μm) [15, 16]. The pore volume can be derived from the quantity of intruded mercury. The pore size distribution is determined according to the Washburn equation [17]:

$$D_p = -\frac{4\gamma cos\Theta}{p} \tag{3.6}$$

In equation 3.6, Θ is assumed to be equal to 141° [18] and γ is equal to 0.48 N m^{-1} [15]. The median pore diameter (D_{md}) is defined as the pore diameter at which 50 % of total intrusion was reached. The average pore diameter (D_{pa}) is calculated, assuming that all pores are cylindrical, in equation 3.7:

$$D_{pa} = -\frac{4V_{cum}}{SSA} \tag{3.7}$$

The cumulative pore volume distribution is calculated in equation 3.8:

$$V_{cum}(D) = \frac{-dV_p}{dlogD_p} \tag{3.8}$$

3.4.7.6 Helium pycnometry

The skeletal density is defined in accordance with DIN 66137 (Part 2) standard by equation 3.9:

$$\rho_s = \frac{m_s}{V_s} \tag{3.9}$$

The calculation of skeletal density excludes the porosity within the particles and the interparticle voids. The skeletal density was determined using a helium pycnometer (POTOTEC GmbH, Germany) at room temperature.

3.5 Charcoal based pellets

Charcoal pellets were pressed from the milled charcoal and the biotar from the pyrolysis experiments on a single pellet press tool (Fistreem International Ltd, UK) similar to that described by Rudolfsson et al. [19]. The water fraction of the biooil was removed by vacuum distillation (300 mbar, 75 °C) by a rotary evaporator and the bottom product (biotar) was used as a binding agent. The pellet press tool comprises a metal cylinder with a press channel and a backstop, schematically shown in Figure 3.4. The press channel has an inner diameter of 12 mm and a maximum length of 40 mm. The charcoal was mixed and homogenized with the biotar as a binder and water in a mass ratio of 65:30:5. 3 g of the mixture were fed into the die of the pellet press. After pelletization of the material, the backstop was removed and the pellet removed from the steel die and stored for 24 h in an oven desiccator. A number of pellets were heat treated at 400 °C to remove the volatile fraction of the biotar and to study the influence of the heat treatment on the pellet hardness and durability.

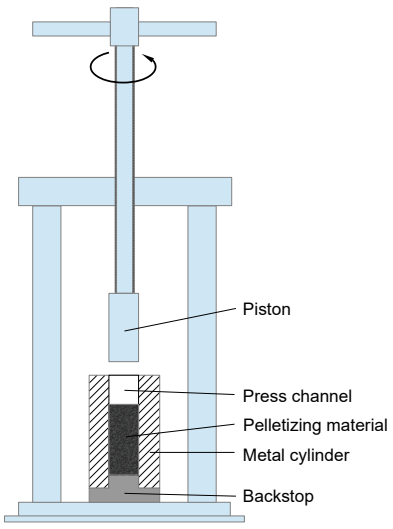

Figure 3.4: Manual single pellet press tool with 12 mm press channel at University of Agder.

3.5.1 Pellet hardness

The hardness of a single charcoal pellets were investigated using a pellet hardness tester (AMANDUS KAHL, Germany). A charcoal-based pellet was placed transverse between a die and a punch. The force was increased until the pellet broke, in which the applied force was reported as a destructive force in newton. The analysis was carried out as a triplicate.

3.5.2 Pellets ligno durability

The durability of the charcoal pellets was investigated in a Ligno tester (Borregaard, Norway) [20]. 100 g of pellets were treated for 60 s in a pressurized airstream with 70 mbar. The fine particles were separated by a 3.15 mm sieve and the ligno durability of charcoal pellets was calculated as the weight percentage of the remaining treated pellets.

3.5.3 Charcoal-manganese-oxide and silicon-oxide composite pellets

Charcoal produced at 900 °C in primary pyrolysis was mixed with biotar and manganese-oxide ore in a ratio of 1:2:4 (biotar:charcoal:ore), and 2.5 to 3 g of the mixture were compacted into pellets. The length and diameter were measured with the readability of 0.01 mm. The electrical resistivity of pellets was investigated before and after an additional heat treatment at 400 °C. The charcoal-manganese-oxide and silicon oxide pellets were reacted at 1600 °C in the high-temperature furnace and kept at that temperature for 2 h. The solid residue was was cooled overnight in nitrogen (0.3 l min^{-1}), cast in resin and used in the optical microscopy analysis.
The same mixture was pressed into small pellets using the hand press tools from the heating microscope. The charcoal-ore pellets had a diameter of 3 mm and a height of 3 mm. The pellets were heated up to 1200 °C in a nitrogen flow of 500 ml min^{-1} to investigate shrinkage and dilation of the mixture.

3.5.4 Industrial reduction agents

Three different reducing agents were selected as reference materials from Norwegian industry. A metallurgical coke used in manganese production, a petroleum coke (petcoke) used in silicon carbide production and an activated charcoal. The analyses comprises the proximate and ultimate analysis, ash analysis and reactivity in CO_2.

3.5.5 X-ray Micro-Computed Tomography

(XμCT) X-ray Micro-Computed Tomography (XμCT) was carried out on charcoal pellets before and after secondary heat treatment. The charcoal pellets were scanned using the HECTOR X-ray CT system [21, 22] by the Ghent University Centre for X-ray Tomography (UGCT, www.ugct.ugent.be). The HECTOR system has been developed and built by the Radiation Physics group of the UGCT in collaboration with TESCAN XRE, (www.XRE.be, part of the TESCAN ORSAY HOLDING a.s.), formerly known as XRE, a UGCT spin-off company. More specifically, a Region Of Interest (ROI) of an untreated and heat treated pellet was scanned without subsampling, thus avoiding any artifacts due to sample manipulation. The X-ray tube voltage and tube power were 70 kV and 10 W, respectively. 2401 projections were collected, with an exposure time of 1 s, over a sample rotation of 360°, resulting in a total scan time of 1 h. The volumes were reconstructed using the Octopus Reconstruction software [23], licensed by XRE, and the spatial resolution in terms of approximate voxel pitch was 3.5 μm. The reconstructed pellet structure corresponds to a cylinder with a diameter of 6.7 mm and a height of 5.9 mm. In order to calculate the porosity within the pellet volume, segmentation was carried out by thresholding using Otsu's method as a first estimate but further fine-tuned visually. Image analysis was carried out using Octopus Analysis, formerly known as Morpho+ [24], while the 3D visualizations were performed with VGStudio MAX3.2 (Volume Graphics GmbH).

Bibliography

[1] O. Williams, G. Newbolt, C. Eastwick, S. Kingman, D. Giddings, and Lester, E. et al. Influence of mill type on densified biomass comminution. *APPL ENERG*, 182:219–31, 2016.

[2] J. Tolu, L. Gerber, J.-F. Boily, and R. Bindler. High-throughput characterization of sediment organic matter by pyrolysis–gas chromatography/mass spectrometry and multivariate curve resolution: A promising analytical tool in (paleo)limnology. *ANAL CHIM ACTA*, 880:93–102, 2015.

[3] L. Gerber, M. Eliasson, J. Trygg, T. Moritz, and B. Sundberg. Multivariate curve resolution provides a high-throughput data processing pipeline for pyrolysis-gas chromatography/mass spectrometry. *J ANAL APPL PYROL*, 95:95–100, 2012.

[4] MS-SEARCH. Nist mass spectrometry data center: Nist/epa/nih mass spectral database. from http://chemdata.nist.gov.

[5] H. Suopajärvi, E. Dahl, A. Kemppainen, S. Gornostayev, A. Koskela, and T. Fabritius. Effect of Charcoal and Kraft-Lignin Addition on Coke Compression Strength and Reactivity. *ENERGIES*, 10:1–15, 2017.

[6] A.W. Coats and J.P. Redfern. Kinetic parameters from thermogravimetric data. *NATURE*, 201:68—-69, 1964.

[7] L. Sun, J. Wang, and E. Bonaccurso. Conductivity of individual particles measured by a microscopic four-point-probe method. *SCI REP*, 3:1–5, 2013. 1991.

[8] L.J. van der Pauw. A Method of Measuring the Resistivity and Hall Coefficient on Lamellae of Arbitrary Shape. *Philips Res Rep*, 20(8):220–224, 1958.

[9] P.H.C. Eilers. Parametric time WarpIng. *ANAL CHEM*, 76(2):404–411, 2004.

[10] A. Savitzky and M.J.E. Golay. Smoothing and differentiation of data by simplified least squares procedures. *ANAL CHEM*, 36(8):1627–1639, 1964.

[11] M.W. Smith, I. Dallmeyer, T.J. Johnson, C.S. Brauer, J.S. McEwen, J.F. Espinal, and M. Garcia-Perez. Structural analysis of char by Raman spectroscopy: Improving band assignments through computational calculations from first principles. *CARBON*, 100:678–692, 2016.

[12] M.J. Matthews, M.A. Pimenta, and G. Dresselhaus. Origin of dispersive effects of the Raman D band in carbon materials. *PHYS REV B*, 59(10):R6585–6588, 1999.

[13] S. Brunauer, P.H. Emmett, and E. Teller. Adsorption of Gases in Multimolecular Layers. *J AM CHEM SOC*, 60(2):309–319, 1938.

[14] J.O. Müller, D.S. Su, U. Wild, and R. Schlögl. Bulk and surface structural investigations of diesel engine soot and carbon black. *PHYS CHEM CHEM PHYS*, 9:4018–4025, 2007.

[15] M. Plötze and P. Niemz. Porosity and pore size distribution of different wood types as determined by mercury intrusion porosimetry. *EUR J WOOD WOOD PROD*, 69(4):649–657, 2011.

[16] J. Yin, K. Song, Y. Lu, G. Zhao, and Y. Yin. Comparison of changes in micropores and mesopores in the wood cell walls of sapwood and heartwood. *WOOD SCI TECHNOL*, 49(5):987–1001, 2015.

[17] E.W. Washburn. Note on a method of determining the distribution of pore sizes in a porous material. *PROC NATL ACAD SCI*, 7:115–116, 1921.

[18] K. Junghaus, P. Niemz, and F. Bächle. Untersuchungen zum Einfluess der thermischen Vergütung auf die Porosität von Fichtenholz. *HOLZ ROH WERKST*, 63(3):243–244, 2005.

[19] M. Rudolfsson, W. Stelte, and T.A. Lestander. Process optimization of combined biomass torrefaction and pelletization for fuel pellet production - A parametric study. *APPL ENERG*, 140:378–384, 2015.

[20] M. Temmerman, F. Rabier, P.D. Jensen, H. Hartmann, and T. Bohm. Comparative study of durability test methods for pellets and briquettes. *BIOMASS BIOENERG*, 30:964–972, 2006.

[21] M. Dierick, D. Van Loo, B. Masschaele, M. Boone, and L. Van Hoorebeke. A LabVIEW® based generic CT scanner control software platform. *J X-RAY SCI TECHNOL*, 18:451–461, 2010.

[22] B. Masschaele, M. Dierick, D. Van Loo, M.N. Boone, L. Brabant, E. Pauwels, V. Cnudde, and L. Van Hoorebeke. HECTOR: A 240kv micro-CT setup optimized for research. *J PHYS CONF SER*, 463:1–4, 2013.

[23] J. Vlassenbroeck, M. Dierick, B. Masschaele, V. Cnudde, L. Van Hoorebeke, and P. Jacobs. Software tools for quantification of X-ray microtomography at the UGCT. *NUCL INSTRUM METHODS PHYS RES*, 580(1):442–445, 2007.

[24] L. Brabant, J. Vlassenbroeck, Y. De Witte, V. Cnudde, M.N. Boone, J. Dewanckele, and L. Van Hoorebeke. Three-dimensional analysis of high-resolution X-ray computed tomography data with Morpho+. *MICROSC MICROANAL*, 17:252–263, 2011.

Chapter 4

Results

4.1 Primary and secondary heat treatment

Energy 167 (2019) 337–345

Contents lists available at ScienceDirect

Energy

journal homepage: www.elsevier.com/locate/energy

Characterization of renewable reductants and charcoal-based pellets for the use in ferroalloy industries

Gerrit Surup [a, *], Tore Vehus [a], Per-Anders Eidem [c], Anna Trubetskaya [b, **], Henrik Kofoed Nielsen [a]

[a] Department of Engineering Sciences, University of Agder, 4879, Grimstad, Norway
[b] School of Engineering and Ryan Institute, National University of Ireland Galway, Galway, Ireland
[c] Department of Material Sciences and Chemistry, SINTEF Helgeland, 8626, Mo i Rana, Norway

ARTICLE INFO

Article history:
Received 24 August 2018
Received in revised form
29 October 2018
Accepted 31 October 2018
Available online 5 November 2018

Keywords:
Ferroalloy industry
Charcoal
High temperature pyrolysis
Secondary heat treatment
Pelletization

ABSTRACT

This study investigates the effect of high-temperature pyrolysis and post-treatment processes on spruce and oak charcoal yields and CO_2 reactivity in a slow pyrolysis reactor. Post-treatment processes such as co-pyrolysis of biomass and recirculated tar mixture with that to the distillation of the charcoal-tar blend gave similar increase in charcoal yields. From a technological standpoint, co-pyrolysis of charcoal and tar mixture decreased the CO_2 reactivity of the charcoal approaching that of fossil-based coke. This emphasize the importance of tar addition and high temperature treatment on charcoal properties. Moreover, the findings of this work show the potential use of the tar organic fractions as a binder that can be used for the charcoal pellet preparation. The results are promising as they show that the charcoal-based pellets have comparable properties of pellets from herbaceous biomass leading to the cost reduction in charcoal transportation and storage.

© 2018 Elsevier Ltd. All rights reserved.

1. Introduction

The reduction of anthropogenic greenhouse gas emissions is one of the greatest challenges in coming decades [1]. Carbon dioxide is considered as the main source for anthropogenic climatic change. Metallurgy is one of the most energy intensive industries, which is responsible for about 10% of the global anthropogenic CO_2 emissions [2,3]. The use of biomass and its derivatives as CO_2 neutral reduction agents in metallurgical processes can be a possible solution to decrease emissions. However, the metallurgical production nowadays is based on the use of fossil-based fuels due to the limited knowledge of charcoal properties and its high costs.

Ferroalloys are defined as iron-rich alloys which contain high proportions of Si, Mn, C, Cr, etc. which improve tensile strength, wear, corrosion resistance and toughness [4]. Ferroalloys are mainly produced in submerged-arc furnaces at temperatures > 1500 °C. A three-phase electrode is inserted into a mixture consisting of ferroalloys and carbonaceous reductants [5,6]. The carbonaceous material acts as a reducing agent to form the base metal [7]. The most important properties of carbonaceous reductants are high reactivity, high conversion rates, low levels of impurities (such as sulphur and phosphorus), high bulk density and energy density [8,9]. The high reactivity of charcoal reductant may be advantageous in some cases within the ferroalloy industries. However, the use of a reductant more reactive than fossil-based coke may increase maintenance costs due to the decreased electrical conductivity [10,11]. Previous studies have examined distillation of bio-oil and charcoal blends which increased the char yields by over 15% and decreased the reactivity of remaining post-distilled solid residue [12–14]. Likewise, the low bulk density and energy density of charcoal necessitate relatively large equipment for handling and storage. Thus, the cost of charcoal reductants is not competitive with fossil-based coke [15]. Pelletization of charcoal using recycled tar as a binding agent has potential to increase the charcoal mechanical strength and bulk density leading to the reduction in transportation and storage cost [16]. However, there is little data in the literature that describes the effects of tar used as a binding agent on resulting charcoal pellet properties that impact metallurgical applications. This adds uncertainty to the use of recycled tar addition as an approach to increase the mechanical strength and decrease charcoal reactivity. In order to increase the

* Corresponding author.
** Corresponding author.
E-mail addresses: gerrit.surup@uia.no (G. Surup), anna.trubetskaya@nuigalway.ie (A. Trubetskaya).

https://doi.org/10.1016/j.energy.2018.10.193
0360-5442/© 2018 Elsevier Ltd. All rights reserved.

solid char yield and adjust the charcoal reactivity, metallurgical industries strive to understand how charcoal properties are correlated with heat treatment temperatures and composition of pyrolysis products.

In this study, the impact of heat treatment temperature, secondary heat treatment, feedstock origin, and co-pyrolysis with tar on the product yields, CO_2 reactivity and charcoal-based pellet properties were investigated. The specific objectives of this study were to: (1) determine the treatment conditions which decrease char reactivity and increase the yield of charcoal for the further use in pellets production and (2) understand the influence of post-pyrolysis processes on the charcoal properties.

2. Materials and methods

2.1. Raw biomass characterization

Norway spruce (*Picea abies*) and oak (*Quercus petraea*) from Dømmesmoen (Grimstad, Norway) were harvested in 2012 and 2016. The age of the Norway spruce was 39 years, whereas oak was 46 years. Feedstock selection was based on the differences in ash composition and plant cell compounds (cellulose, hemicellulose, lignin, extractives) of softwood and hardwood. Norway spruce is low in ash and with lower potassium and calcium contents than oak, whereas oak is low in lignin content. Both spruce and oak samples were chipped by a disc chipper to 5–20 mm and dried at 60 °C before storage. Prior to the wood characterization, biomass samples were divided into six equal fractions using a riffler. A vibrating EFL2000 sieve shaker (ENDECOTTS, United Kingdom) comprising ten sieves ranging from 2 to 20 mm in opening size and a bottom pan (< 2 mm) was used (EN ISO 17827-2:2016) to determine the particle size distribution.

2.2. Slow pyrolysis reactor

The charcoal samples were generated in the slow pyrolysis reactor, as shown in Fig. 1.

The reactor can be operated at temperatures up to 1350 °C and heating rates up to 20 °C min^{-1}, as reported by Surup et al. [17]. The pyrolysis retort (inner diameter: 75 mm, height: 150 mm, wall thickness: 2 mm) is made of SiC material. The sample temperature was monitored by a thermocouple type S (max. 1600 °C). The pyrolysis setup encloses a two-stage cooling system with a condensation collector and a pyrolysis gas sampling unit. The connection pipes (inner diameter: 16 mm) between the retort and the condensation unit were made of quartz glass. The connection pipes were heated up to 350 °C by a heating tape HBQ (Hillesheim, Germany) and a temperature regulator MC1 (HORST GmbH, Germany) to minimize the condensation and thermal decomposition of tars. The volume flow of the N_2 gas was measured by the flowmeter HFC-202 (Teledyne, USA). The reactor was continuously purged by nitrogen at a defined flow rate of 100 ml min^{-1}. The temperature control system was based on the LabView software (Version 8.6). A sample mass of 60 g for each experiment was selected. The wood sample was distributed homogeneously in the reactor's retort, preheated in nitrogen at 10 °C min^{-1} up to 160 °C and kept at that temperature for 30 min. The dried wood was further heated at 10 °C min^{-1} to temperatures ranging from 500 to 1300 °C and kept at the final temperature for about 1 h to ensure the complete conversion. After the heating program was finished, the furnace was turned off and the charcoal sample was cooled overnight in N_2 (0.3 l min^{-1}). Samples were stored in sealed plastic containers.

2.3. High-temperature furnace

The charcoal samples were further treated in the high-temperature furnace LHTG 200–300/20-1G (Carbolite Gero, Germany). The furnace can be operated at temperatures up to 1800 °C and at heating rates up to 20 °C min^{-1}. Prior to each experiment, 5 g of the char sample were loaded into the A_2O_3 crucible (Almath Crucibles Ltd, UK) placed in the graphite retort middle. Prior to pyrolysis, the furnace was repeatedly evacuated and purged by argon. The char sample was heated at 10 °C min^{-1} up to 700, 1000, 1300, and 1600 °C and kept at that temperature for 2 h. The sample was cooled to room temperature at a heating rate of 20 °C min^{-1} and stored in sealed plastic containers.

2.4. Pyrolysis product analysis

Sample preparation. The charcoal samples were crushed to a fine powder in a mortar with a ceramic pestle and sieved to a particle size ≤ 0.25 mm for the elemental and thermogravimetric analysis.

Fixed carbon yield. The fixed carbon yield of charcoal samples was determined in equation (1) [18]:

$$\gamma_{uc} = \gamma_{bc} \cdot \frac{FC_{biochar}}{1 - ash_{biomass}} \quad (1)$$

In equation (1), γ_{bc} and FC are the char yield and fixed carbon content as described in BS ISO 15148:2009.

Elemental analysis. The elemental analysis of raw biomass and charcoal was performed on Elemental Analyser 2400 CHNS/O Series II (Perkin Elmer, USA). Acetanilide was used as a reference standard. The ash content was determined using a standard ash test at 550 °C, according to the procedure described in DIN EN 14775.

SEM microscopy. SEM/EDS analysis of char was conducted on a high-resolution field emission microscope SU-70 (Hitachi, Japan) under high vacuum in order to understand char structural properties. Prior to the analysis, char samples were coated with a thin layer of gold (2 min, 20 mA) using an Edwards S150B Sputter Coater to avoid sample charging.

Thermogravimetric analysis. The reactivity of charcoal was analyzed by exposing samples to a reactive gas consisting of 100% volume fraction CO_2 in a thermogravimetric instrument TGA/DSC 1 STARe System (Mettler Toledo, USA). In each experiment, 5 mg of the crushed sample were loaded into an Al_2O_3 crucible. The charcoal samples were firstly heated up to 110 °C and kept for 30 min isothermally for drying. The dried samples were subsequently heated up to 1100 °C at a constant heating rate of 10 °C min^{-1} and kept at the final temperature for 10 min. The reaction threshold is the temperature that corresponds to the appearance of the sample mass decrease [19]. Simultaneous non-isothermal thermogravimetric measurements of char were carried out in N_2 to determine the mass loss.

Karl Fischer titration. Karl Fischer titration was carried out using a KF1000 volumetric titrator (Hach, Germany). Tar samples were first dissolved in anhydrous methanol and then injected into the titration cell. All titrations were carried out at room temperature and the experiments had an error of ± 0.5% water content.

Single pellet preparation. Prior to pelletization, the water fraction of tar was removed by distillation and the heavy fraction was used as a binding agent. A single pellet press tool (Fistreem International Ltd, UK) similar to that described by Rudolfsson et al. [20] was used, that consists of a metal cylinder with a press channel and a backstop, as shown in Fig. 2. The char particles were comminuted to a particle size of < 0.4 mm. A 3 g pellet with an diameter of 12 mm and a height of 20 mm was made from charcoal particles, tar binder and water in the wt. % ratio of 65:30:5. The mixture was dried for

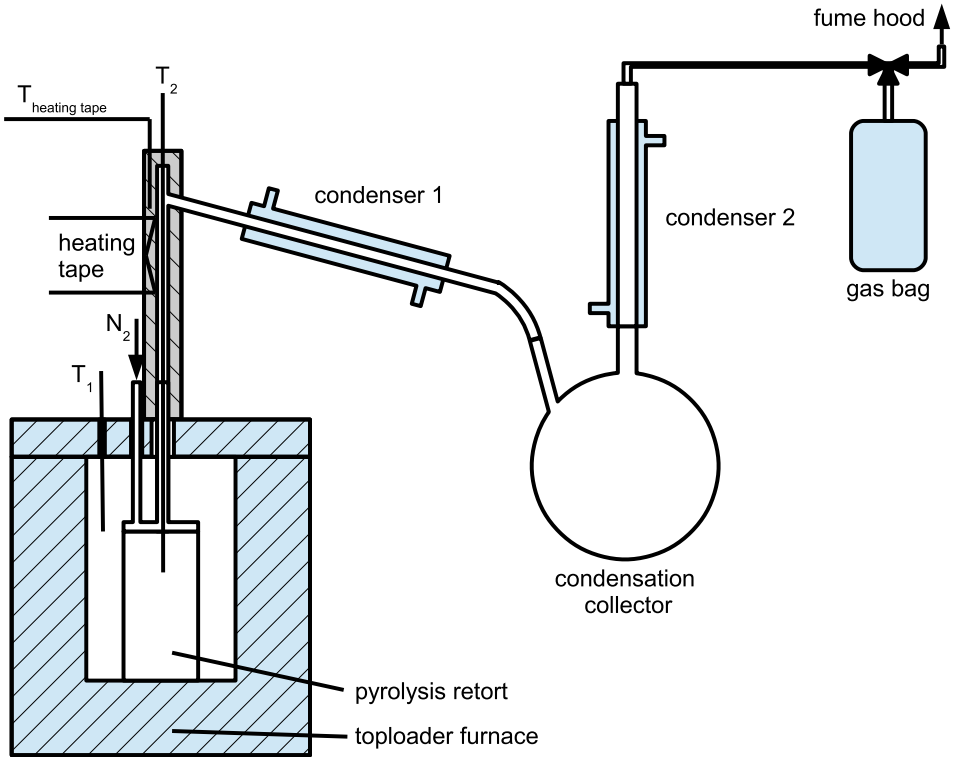

Fig. 1. Slow pyrolysis reactor.

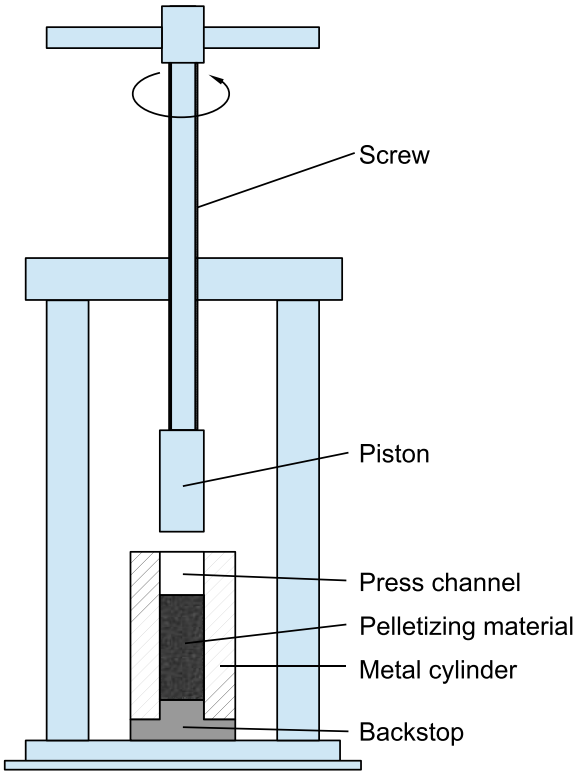

Fig. 2. Single pellet press tool.

30 min at room temperature before feeding into the mold of a single pellet press. Once the pellet was pressed, the backstop was removed and the pellet was extruded from the steel die. The charcoal pellets were dried for 24 h at 30 °C in an oven desiccator. In addition, a number of pellets were heat treated at 400 °C in a tubular furnace to study the influence of heat treatment on the pellet hardness and durability.

Pellet hardness. The hardness analysis of a single charcoal pellet was performed using a pellet hardness tester (AMANDUS KAHL, Germany). A charcoal-based pellet was placed between a die and a punch. The force was applied on the pellet until it breaks. The result was reported as a destructive force in newtons. The measurements were repeated three times.

Pellets ligno durability. Ligno durability of charcoal pellets was determined by treating 100 g of pellets for 60 s in a pressurized air-steam with 70 mbar in a Ligno tester (Borregaard, Norway) [21]. The fine particles were separated by a 3.15 mm sieve. The ligno durability of charcoal pellets was calculated as the weight percentage of treated pellets remaining on the sieve to the initial sample weight, as reported by Larsson et al. [22].

Electrical conductivity. Electrical conductivity measurements were performed using a 34470A 7 1/2 Digit Multimeter (Keysight Technologies, USA). The connection between the four probes of the source meter and microelectrodes was established using a socket. Two adjacent electrodes were connected to the voltmeter (Fluke, USA), whereas the other two electrodes were connected to the current source (ISO-Tech IPS 3303) (constant current) of the source meter, as it was reported by Sun et al. [23]. A charcoal pellet was connected by four different electrodes to the source meter based on the van der Pauw electrode geometry [24]. The electrical conductivity was determined according to equation (2):

$$\sigma = \frac{L}{R \cdot A} \tag{2}$$

In equation (2), σ is the electrical conductivity, A is the cross-sectional area, L is the length of the resistor, and R is the resistance between two Ti-Au electrodes.

3. Results and discussion

3.1. Biomass characterization

The ultimate and proximate analysis of metallurgical coke and wood was carried out at Eurofins Lidköping and shown in Table 1.

The compositional analysis of biomass (cellulose, hemicellulose, acid-soluble lignin, acid-insoluble lignin, and extractives) was conducted by Celignis Analytical according to NREL technical reports [25–27] and Thammasouk et al. [28], and is shown in Table 2.

3.2. Elemental analysis

Fig. 3 shows a Van Krevelen plot of original spruce and oak, their charcoals, and metallurgical coke.

The results indicate that the oxygen content in all char samples decreased with the higher heat treatment temperature. The spruce charcoal contained less carbon and more oxygen than oak charcoal. A point of note is that the elemental composition of oak samples obtained from pyrolysis at 1300 °C was comparable to the composition of metallurgical coke.

3.3. Product yields

The product yields from pyrolysis of spruce and oak with respect to char and major liquid products (water and organic fraction) are shown in Fig. 4.

The gas yield was determined by the difference between the total weight loss and the non-devolatized tar and solid fractions. The char yield from pyrolysis of both spruce and oak decreased with increasing heat treatment temperature, from about 29 to 22% for spruce and from 27 to 20% for oak in the temperature range from 500 to 1300 °C. The ash content remained only slightly changed with the increasing heat treatment temperature in pyrolysis of both feedstocks. The yields of tar organic fraction in pyrolysis of oak increased slightly from 33 to 38% in the temperature range from 500 to 900 °C and remained constant at higher temperatures. It was observed that almost similar yields of tar organic fractions were determined in pyrolysis of spruce, whereas the water content in spruce tar was 5% points greater than in oak pyrolysis. Spruce and oak charcoal samples were subjected to an additional heat treatment in the high temperature furnace. The fixed carbon content and volatile yield of non-treated charcoal and samples from pyrolysis in the temperature range from 500 to 1300 °C are shown in Fig. 5. The additional heat treatment led to the further decrease in fixed carbon content of both charcoal samples by about 1% point with the increasing temperature from 700 to 1600 °C. It was found that the fixed carbon content of spruce and oak charcoal samples produced at temperatures $\geq$ 700 °C increased after additional heat treatment at 700 and 1000 °C. The proximate analysis of charcoal samples showed that the mass loss in the additional high-temperature pyrolysis was mainly caused by the volatile matter release. The ash content of spruce and oak charcoal samples remained unchanged after additional heat treatment. The experiments in the slow pyrolysis reactor demonstrated that the maximum heat treatment temperature exerted greater influence on the solid product yield than the feedstock origin and secondary heat treatment. The solid product yield can be affected by differences in lignocellulosic composition of biomass, ash content, heat treatment temperature and secondary heat treatment. Proximate analysis of the solid residue showed that the ash content of spruce and oak char samples from pyrolysis in the temperature range from 500 to 1300 °C were not affected by the mass loss, whereas the yield of an organic matter decreased with the increasing heat

Table 1
Proximate, ultimate and ash compositional analyses of feedstocks.

Fuel	Norway spruce	Oak	Metallurgical coke
	Proximate analysis		
Moisture, (wt. % as received)	8.6	7.6	0.6
Ash at 550 °C, (wt. % dry basis)	0.8	1.6	11.8
Volatiles, (wt. % dry basis)	80.6	82.6	3
Fixed carbon content (wt. % dry basis)	18.6	15.8	85.2
HHV, (MJ kg^{-1})	20.3	19.3	27.9
LHV, (MJ kg^{-1})	18.5	17.5	27.8
	Ultimate analysis, (wt. %, dry basis)		
C	53.2	50.6	85.6
H	6.1	6.1	0.3
N	0.1	0.2	1.8
S	0.06	0.02	0.6
Cl	0.04	0.02	0.03
	Ash compositional analysis, (mg kg^{-1} on dry basis)		
Al	40	20	12000
Ca	2300	3600	6400
Fe	200	50	6300
K	800	1500	1700
Mg	250	300	1300
Na	< 50	< 50	1100
P	200	250	400
Si	550	550	27000
Ti	50	50	550

Table 2
Composition of Norway spruce and oak, calculated in percentage based on dry basis (wt. %).

Biomass	Cellulose	Hemicellulose	Lignin		Extractives
			acid insoluble	acid soluble	
Norway spruce	37.8	25	27.9	0.7	7.8
Oak	36.7	18.7	19.4	2.5	11

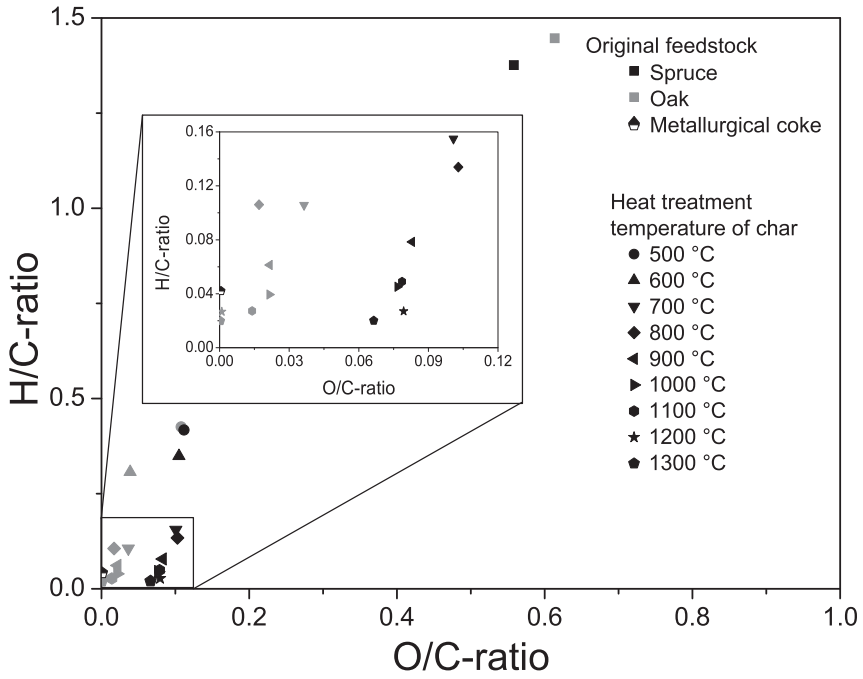

Fig. 3. Van Krevelen plot of metallurgical coke, original spruce and oak samples and their charcoals from pyrolysis in the temperature range from 500 to 1300 °C.

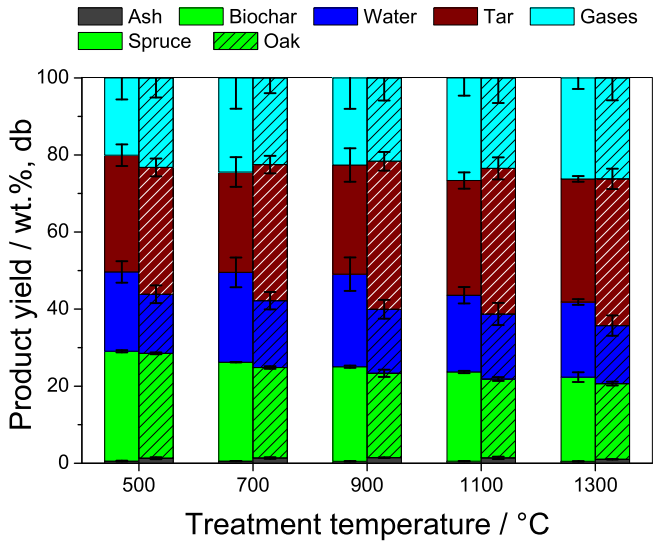

Fig. 4. Product yields of tar and char (wt. % relative to the original biomass) of spruce (left) and oak (right), reacted at 500–1300 °C in the slow pyrolysis reactor. The char yield is separated in ash and organic matters. The tar yield was separated in organic fraction and water content. The error bars characterize the standard deviations between the total yields of products.

treatment temperature. The ash content of the original spruce (0.8 wt. %) was half that in the original oak. Alkali metal ions (K^+ and Ca^{2+}) catalyze the conversion of bridges into char links and enhance cross-linking/polymerization, leading to the greater char yield [29]. Thus, based on ash content alone it might be expected that oak char yield should be greater than char yield from spruce pyrolysis. However, the yields of spruce and oak charcoal were similar. In addition, the yield of spruce char organic fraction was 2% point greater than that of oak char, whereas original oak contained less lignin and hemicellulose than spruce, indicating that lignocellulosic biomass composition had a minor influence on the biomass devolatilization. Spruce and oak char yields decreased by 7 wt.% in primary pyrolysis with the further char yield decrease during secondary heat treatment. The proximate analysis showed that after removal of volatile matter a fixed carbon yield was in the range from 20 to 23 wt.% and from 18 to 21 wt.% for spruce and oak charcoal, indicating only a minor influence of secondary heat treatment and feedstock origin on the char yield. In addition, the fixed carbon content of charcoal obtained at different temperatures in primary pyrolysis varied only slightly at 1600 °C of secondary treatment. The increase in heat treatment temperature during primary pyrolysis significantly decreased the char yield, emphasizing a key role of temperature on the biomass devolatilization.

3.4. Co-pyrolysis with liquid products

The char and volatile yields of co-pyrolysis of original feedstocks with recirculated tar and post-distilled residues are shown in Fig. 6. Co-pyrolysis of both original spruce and oak samples with recirculated tar increased the char yield by approximately 4% points at 700, 900, and 1100 °C, indicating that the feedstock had no influence on the product yields. The addition of recirculated tar to charcoal probably promoted secondary reactions which led to greater char yields than in primary pyrolysis. Moreover, the yields of remaining post-distilled solid product were similar to char yields from co-pyrolysis of original biomass with recirculated tar. The volatile matter content in the post-distilled product was 1–2% points greater than the amount of volatiles remaining in charcoal from co-pyrolysis. Temperatures greater than 700 °C in co-pyrolysis of charcoal with tar products led to the predominance of secondary reactions forming larger size tar products and more cross-linked char fractions with less volatile compounds than in distillation of tar and charcoal mixture at 450 °C. The fixed carbon yield obtained in co-pyrolysis of both charcoals with tar varied only slightly indicating that no tar decomposition occurs. In general, the differences in total char yields from both post-treatment processes were small. The increase in total solid yield of spruce charcoal from co-pyrolysis and distillation was nearly similar (≈ 4% points), whereas the increase in total solid yield from co-pyrolysis of oak

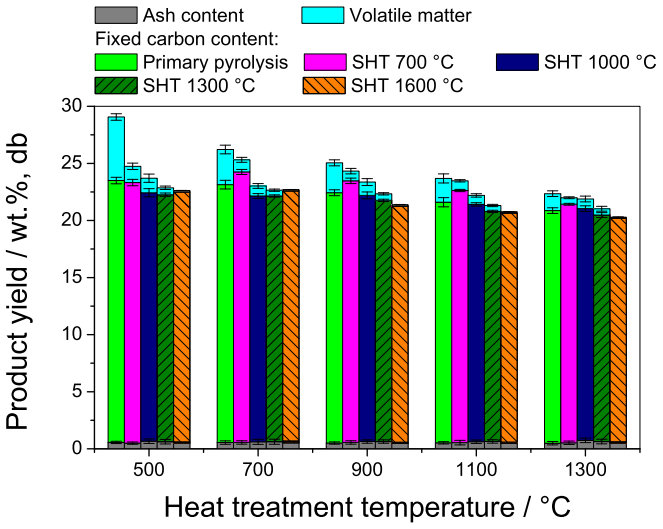

(a): Spruce

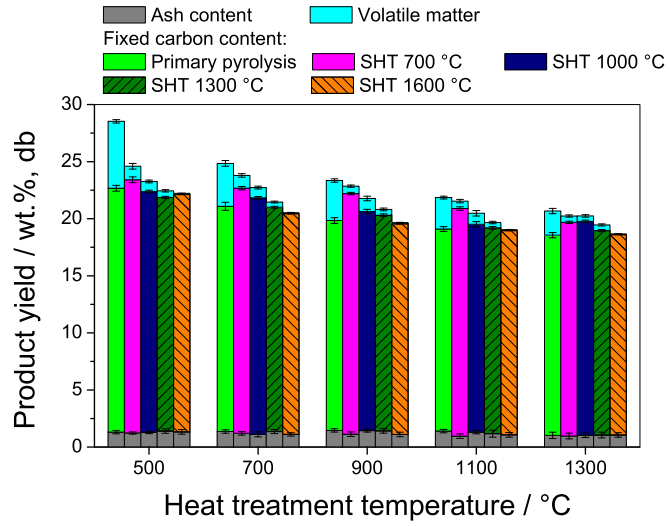

(b): Oak

Fig. 5. Char yields (wt. % relative to the original biomass) from pyrolysis of spruce and oak after secondary heat treatment at 700, 1000, 1300 and 1600 °C in the high temperature furnace. The total char yield is separated in ash, fixed carbon and volatile matter.

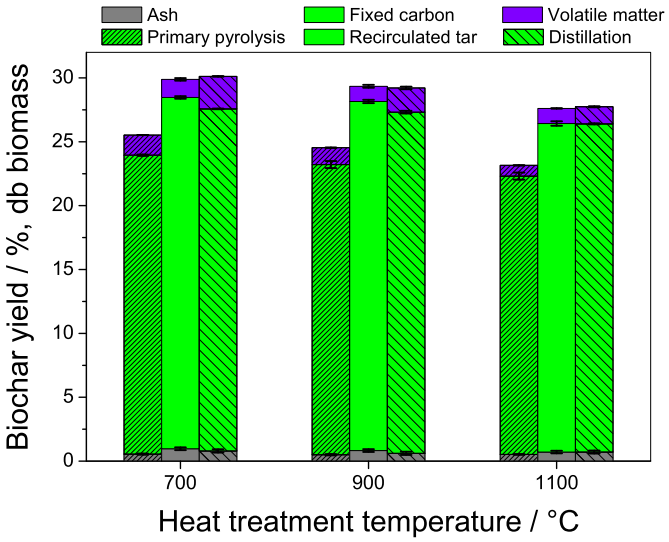

(a): Spruce

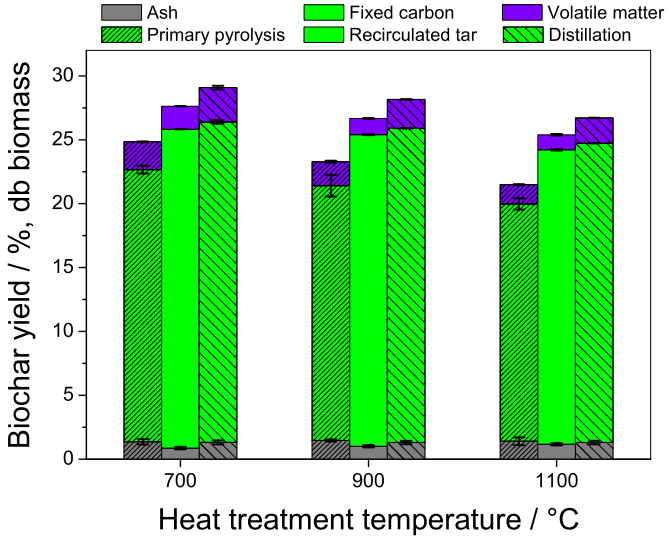

(b): Oak

Fig. 6. Char yields (wt. % relative to the original biomass) of spruce and oak from co-pyrolysis of charcoal with tar. The total char yield is separated in ash, fixed carbon and volatile matter.

charcoal with tar was 1% less than the yield after distillation.

Both post-treatment processes led to the formation of an additional carbon layer on the charcoal particle surfaces that had only small influence on the solid product yield, confirming the previous results of Elkasabi et al. [30]. In addition, an increase in the solid residue yield from both post-treatment processes varied only slightly between feedstocks suggesting that the additional carbonaceous layer was formed from tar with similar aromatic/phenolic composition [12]. The results showed that co-pyrolysis and distillation of charcoal with tar significantly increase the solid char yield in the entire process and thus, emphasize the potential use of biocarbon-based reductants in ferroalloy industries.

3.5. Charcoal reactivity

Fig. 7 shows the differential weight loss curves (DTG) for the 100% volume fraction CO_2 gasification of spruce and oak char samples. The DTG curves show a double peak in CO_2 gasification, indicating a heterogeneous char mixture with respect to the composition that leads to the differences in reactivity of two constituents with less reactive carbon structure that approaches the reactivity of metallurgical coke (maximal reaction rate is at 1220 °C) [31]. The maximal reaction rates of both woody chars varied from 800 to 1030 °C. The CO_2 gasification of spruce chars from pyrolysis ranging from 700 to 900 °C and oak chars generated from 700 to 1100 °C took place at nearly the same temperature of 960 °C, indicating a minor effect of feedstock origin on the char reactivity. The maximum reaction rates of spruce and oak chars reacted at 1300 °C were the highest and nearly identical. The results show that differences in heat treatment temperature have more influence on char reactivity than the residence time, feedstock composition or additional heat treatments.

Fig. S-4 from the supplemental material showed that spruce char samples exhibited a double peak, whereas oak char samples exhibited a triple peak after co-pyrolysis with recirculated tar and

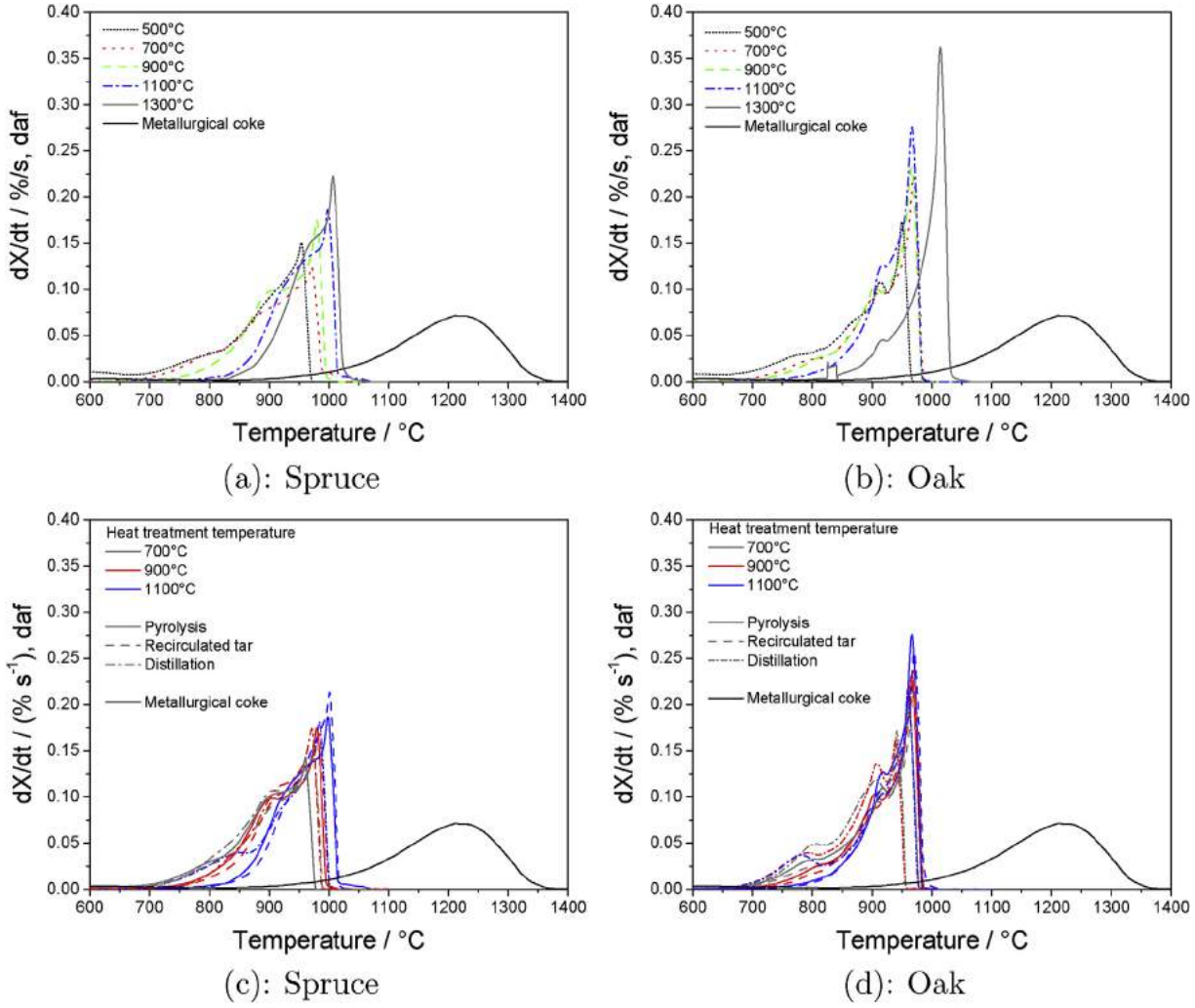

Fig. 7. DTG curves of spruce and oak charcoals from pyrolysis (a,b) at 500, 700, 900, 1100, and 1300 °C and (c,d) samples from co-pyrolysis of charcoal with recirculated tar and post-distillated solid fraction reacted in 100% volume fraction CO_2.

distillation. It was observed that the maximal reaction rate of spruce and oak charcoal after distillation shifted to the lower temperatures, indicating the increase in CO_2 gasification reactivity. In comparison, the maximum reaction rate of both charcoal samples from co-pyrolysis with the recirculated tar shifted to higher temperatures, indicating a decrease in CO_2 gasification reactivity. The reactivity of spruce and oak charcoal from co-pyrolysis at 1100 °C was similar to that of non-treated charcoal samples, whereas the maximum reaction rate of spruce and oak charcoal from co-pyrolysis with recirculated tar at 700 and 900 °C was about 50 and 20 °C lower than that of non-treated charcoal samples. This emphasizes that heat treatment temperature is the more important factor determining CO_2 gasification reactivity in co-pyrolysis with recirculated tar than the feedstock origin. The maximal reaction rate of spruce and oak chars from pyrolysis at 500 °C after additional heat treatment at 1000, 1300, and 1600 °C in a high-temperature furnace was about 60 °C greater than that of non-treated char samples. This is probably due to the further proceeded pyrolysis and catalytic effect of remaining alkali metals in the non-treated char structure. It was observed that the CO_2 reactivity of both charcoal samples remained unchanged at higher temperatures of additional heat treatment.

Figs. S-4 and S-5 from the supplemental material show that the additional heat treatment at temperatures > 1000 °C affected the reactivity of charcoal samples significantly less than the post-treatment using co-pyrolysis and distillation with tar, confirming the previous results of Hussein et al. [32]. It was found that the maximum reaction rate of charcoal from additional pyrolysis at 1300 and 1600 °C was shifted to temperatures about 40 °C lower than for charcoals from primary pyrolysis at 1300 °C. The TEM analysis showed that the mean separation distance of oak char graphene layers was similar to graphite, whereas spruce char contained different types of amorphous carbon structures [31]. However, in the present study the CO_2 reactivity of spruce and oak charcoal samples was similar after the additional heat treatment. Co-pyrolysis with tar and distillation of charcoal with tar showed a minimal influence on the CO_2 reactivity, confirming the results of Veksha et al. [33]. The post-treatment using distillation with tar slightly increased the reactivity due to the cross-linking of hydroxyl groups with carbonyls, increasing the molecular weight of solid residues [34]. The reactivity of charcoal after co-pyrolysis with tar remained similar to the non-treated charcoal due to the similar porosity and composition [33]. In addition, the CO_2 reactivity of charcoal after all post-treatment processes was about 250 °C lower than that of metallurgical coke.

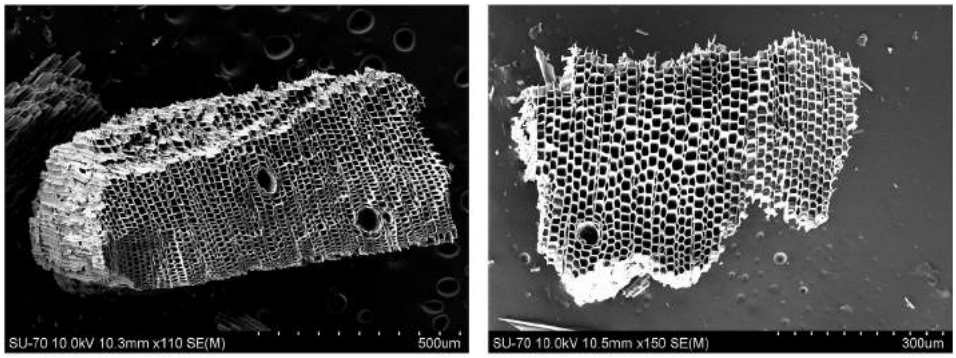

Fig. 8. SEM images of char from pyrolysis at 700 °C using (a) original spruce and (b) wood with the addition of tars.

3.6. Charcoal-based pellets

Fig. 8 illustrates the structure of a char particle from pyrolysis at 900 °C using original spruce and wood with the addition of tars. Both char particles preserved the structure of an original biomass particle with the longitudinal tracheids and resin vessels. Fig. 9 shows that the heat treated spruce char pellet obtained a structure with the visible cracks on the outer surface, whereas the non-treated spruce pellet exhibited a smooth external surface. The heat treatment increased the hardness of a spruce char pellet from 455 to 490 N, whereas the durability of the spruce pellet decreased from 98.4 to 95.7%. The previous studies showed that the durability of high quality pellets is required to be $\geq$ 97.5% [35]. The secondary heat treatment of charcoal pellets improved the hardness that was similar to that of alfalfa straw pellets using hydrated lime as a binding agent ($\approx$ 471 N) [36].

The increase in heat treatment temperature improved the hardness of charcoal pellets during pyrolysis, confirming the previous results of Li et al. [37]. The electrical resistivity of the heat treated charcoal pellets increased from 0.8 to 1.5 Ω·m, whereas the electrical resistivity of metallurgical coke and single spruce char particle was about 0.01 and 0.03 Ω·m, emphasizing the importance of tar addition on the charcoal pellet electrical properties. In addition, the electrical resistivity of metallurgical coke and single charcoal particle in the present study was similar to that of coke ($\approx$ 0.01 Ω·m) measured by the four-point-probe setting, as reported by Eidem et al. [38]. This indicates that the heat treatment improves the mechanical strength and electrical resistivity of charcoal pellets for the use in metallurgical processes. The improvement of charcoal pellet durability using other types of binding agents and different concentrations is a significant task that can be proposed for future studies.

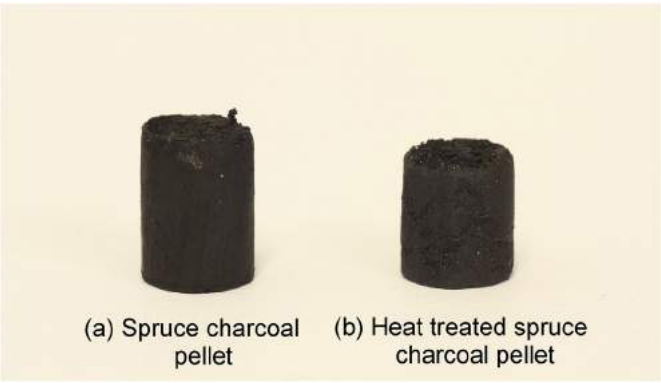

Fig. 9. Single spruce charcoal pellets (a) non-treated and (b) heat treated.

4. Conclusion

The novelty of this work relies on the fact that the reactivity, char yield and electrical resistivity of charcoal can be improved by the addition of recirculated tar. Softwood and hardwood were converted into renewable carbonaceous reductants using pyrolysis treatment. The experiments in the slow pyrolysis reactor showed that the char yield depends mainly on heat treatment temperature in primary pyrolysis and less on the feedstock origin and secondary heat treatments. The co-pyrolysis of charcoal with recirculated tar and distillation increased significantly the char yield. However, both spruce and oak charcoal samples remained more reactive than fossil-based coke after secondary heat treatment, co-pyrolysis with tar and distillation. In addition, the tar organic fraction showed properties of a binder that increase the electrical resistance and hardness of charcoal pellets. The findings of this study emphasize the potential use of biocarbon-based pellets in the ferroalloy industry with concomitant improvement in charcoal transportation and storage.

Acknowledgements

The authors gratefully acknowledge financial support from Elkem AS, Saint Gobain Ceramic Materials AS, and Eramet Norway AS. We acknowledge Raymond Mclnerney from University of Limerick for the article proof-reading.

Appendix A. Supplementary data

Supplementary data to this article can be found online at https://doi.org/10.1016/j.energy.2018.10.193.

References

[1] European Climate Foundation. Report on roadmap 2050 volume 1: Technical and economic analysis. 2010.
[2] Steinfeld A. High-temperature solar thermochemistry for CO_2 mitigation in the extractive metallurgical industry. Energy 1997;22(2):311–6.
[3] Balomenos E, Panias D, Paspaliaris I. Energy and exergy analysis of the primary aluminum production processes: a review on current and future sustainability. Miner Process Extr Metall Rev 2011;32(2):69–89.
[4] Holappa L. Towards sustainability in ferroalloy production. J South African Inst

Min Metal 2010;110(12):1–8.
[5] Liu J, Chen Z, Ma W, Wei K, Ding W. Application of a waste carbon material as the carbonaceous reductant during silicon production. Silicon 2018:1–9.
[6] Olsen SE, Tangstad M, Lindstad T. Production of manganese ferroalloys. Tapir Academic Press; 2007.
[7] Monsen B, Tangstad M, Midtgaard H. Use of charcoal in silicomanganese production. In: 10th int ferroalloys congress INFACON X. Transformation through technology, vol. 68; 2004. p. 155–64.
[8] Pistorius PC. Reductant selection in ferro-alloy production: the case for the importance of dissolution in the metal. J South African Inst Min Metal 2002;1:33–6.
[9] Kong L, Tian SH, Li Z, Luo R, Chen D, Tu Y, et al. Conversion of recycled sawdust into high HHV and low NOx emission bio-char pellets using lignin and calcium hydroxide blended binders. Renew Energy 2013;60:559–65.
[10] Yamagishi K, Endo K, Saga J. A comprehensive analysis of the furnace interior for high-carbon ferrochromium. In: 1th int ferroalloys congress INFACON 74. Transformation through technology; 1974. p. 143–7.
[11] De Waal A, Barker IJ, Rennie MS, Klopper J, Groeneveld BS. Electrical factors affecting the economic optimization of submerged-arc furnaces. In: 6th int ferroalloys congress INFACON 6. Transformation through technology, vol. 1; 1974. p. 247–52.
[12] Elkasabi Y, Boateng AA, Jackson MA. Upgrading of biooil distillation bottoms into biorenewable calcined coke. Biomass Bioenergy 2015a;81:415–23.
[13] Huang Y, Kudo S, Norinaga K, Amaike M, Hayashi I. Selective production of Light oil by biomass pyrolysis with feedstock-mediated recycling of heavy oil. Energy Fuels 2012;26(1):256–64.
[14] Suopajärvi H. Bioreducer use in blast furnace ironmaking in Finland. PhD thesis. University of Oulu; 2014.
[15] Diez MA, Alvarez R, Cimadevilla JLG. Briquetting of carbon-containing wastes from steelmaking for metallurgical coke production. Fuel 2013;114:216–23.
[16] Hu Q, Shao J, Yang H, Yao D, Wang X, Chen H. Effects of binders on the properties of bio-char pellets. Appl Energy 2015;157:508–16.
[17] Surup GR, Heidelmann M, Kofoed Nielsen H, Trubetskaya A. Characterization and reactivity of charcoal from high temperature pyrolysis (800–1600°C). Fuel 2019a;235:1544–54.
[18] Wesenbeeck SV, Higashi C, Legarra M, Wang L, Antal MJ. Biomass pyrolysis in sealed vessels. Fixed-carbon yields from avicel cellulose that realize the theoretical Limit. Energy Fuels 2016;30:480–91.
[19] Suopajärvi H, Dahl E, Kemppainen A, Gornostayev S, Koskela A, Fabritius T. Effect of charcoal and Kraft-lignin addition on coke compression strength and reactivity. Energies 2017;10:1–15.
[20] Rudolfsson M, Stelte W, Lestander TA. Process optimization of combined biomass torrefaction and pelletization for fuel pellet production - a parametric study. Appl Energy 2015;140:378–84.
[21] Temmerman M, Rabier F, Jensen PD, Hartmann H, Bohm T. Comparative study of durability test methods for pellets and briquettes. Biomass Bioenergy 2006;30:964–72.
[22] Larsson SH, Thyrel M, Geladi P, Lestander TA. High quality biofuel pellet production from pre-compacted low density raw materials. Bioresour Technol 2008;99:7176–82.
[23] Sun L, Wang J, Bonaccurso E. Conductivity of individual particles measured by a microscopic four-point-probe method. Sci Rep 2013;3:1–5.
[24] van der Pauw LJ. A method of measuring specific resistivity and Hall effect of discs of arbitrary shape. Philips Res Rep 1958;13:1–9.
[25] Sluiter A, Hames B, Ruiz R, Scarlata C, Sluiter J, Templeton D, et al. Determination of structural carbohydrates and lignin in biomass. Golden (CO). National Renewable Energy Laboratory; 2011 July. Report No. NREL/TP-510-42618. Contract No.: DE-AC36-08-GO28308.
[26] Willför S, Hemming J, Leppänen AS. Analysis of extractives in different pulps - method development, evaluation, and recommendations. Finland: Åbo Akademi University, Laboratory of Wood and Paper Chemistry; 2004-2009. Report No. B1 of the EU COST E41 action "Analytical tools with applications for wood and pulping chemistry".
[27] Hames B, Ruiz R, Scarlata C, Sluiter J, Sluiter A. Preparation of samples for compositional analysis. Golden (CO): National Renewable Energy Laboratory; 2011 June. Report No. NREL/TP-510-42620. Contract No.: DE-AC36-99-GO10337.
[28] Thammasouk K, Tandjo D, Penner MH. Influence of extractives on the analysis of herbaceous biomass. J Agric Food Chem 1997;45:437–43.
[29] Solomon PR, Best PE, Yu ZZ, Charpenay S. An empirical model for coal fluidity based on a macromolecular network pyrolysis model. Energy Fuels 1992;6:143–54.
[30] Elkasabi Y, Mullen CA, Jackson MA, Boateng AA. Characterization of fast-pyrolysis bio-oil distillation residues and their potential applications. J Anal Appl Pyrol 2015b;114:179–86.
[31] Surup GR, Heidelmann M, Deike R, Foppe M, Schubert D, Timko M, Trubetskaya A. The effect of feedstock origin and temperature on the structure and reactivity of char from pyrolysis at 1300–2800°C. Fuel 2019b;235:306–16.
[32] Hussan EB, Hussein AY, Steele PH, El-Gier E. Characterization of bio-oils from the fast pyrolysis of white oak and sweetgum. Energy Sources Part A Rec Utiliz Environ 2016;38(1):43–50.
[33] Veksha A, McLaughlin H, Layzell DB, Hill JM. Pyrolysis of wood to biochar: increasing yield while maintaining microporosity. Bioresour Technol 2014;153:173–9.
[34] Laurichesse S, Averous L. Chemical modification of lignins: towards biobased polymers. Prog Polym Sci 2014;39(7):1266–90.
[35] Abedi A, Cheng H, Dalai AK. Effects of natural additives on the properties of sawdust fuel pellets. Energy Fuels 2018;32:1863–73.
[36] Kaliyan N, Morey RV. Factors affecting strength and durability of densified biomass products. Biomass Bioenergy 2009;33:337–59.
[37] Li F, Tangstad M. Behavior of quartz and carbon black pellets at elevated temperatures. EPD Congr 2016:153–60.
[38] Eiden PA, Tangstad M, Bakken JA. Determination of electrical resistivity of dry coke beds. Mater Trans B 2008;39(1):7–15.

4.2 Gasification reactivity, nanostructure and carbon chemistry

Fuel 235 (2019) 1544–1554

Contents lists available at ScienceDirect

Fuel

journal homepage: www.elsevier.com/locate/fuel

Full Length Article

Characterization and reactivity of charcoal from high temperature pyrolysis (800–1600 °C)

Gerrit Ralf Surup[a], Henrik Kofoed Nielsen[a], Markus Heidelmann[b], Anna Trubetskaya[c,*]

[a] Department of Engineering Sciences, University of Agder, 4879 Grimstad, Norway
[b] Interdisciplinary Center for Analytics on the Nanoscale, University of Duisburg-Essen, 47057 Duisburg, Germany
[c] Mechanical Engineering Department, National University of Ireland Galway, Galway, Ireland

ARTICLE INFO

Keywords:
Charcoal
High-temperature pyrolysis
CO_2 reactivity
Non-graphitizing carbon
Low heating rate

ABSTRACT

This study presents the effect of wood origin and heat treatment temperature on the CO_2 reactivity, nanostructure and carbon chemistry of chars prepared at 800, 1200, and 1600 °C in slow pyrolysis reactors. The structure of charcoal was characterized by transmission electron microscopy, Raman spectroscopy, mercury intrusion porosimetry and N_2 adsorption. The CO_2 reactivity of char was investigated by thermogravimetric analysis. Results showed that spruce and oak chars have similar reactivity at all heat treatment temperatures. The oak char prepared at 1600 °C contained long and flat graphene layers and interplanar distance that is similar to graphite and thus, was more ordered than the spruce char. The TEM analysis showed that charcoal had structural characteristics of non-graphitizing carbon. Thus, increasing heat treatment temperature increases the graphitization of char structure, leading to the reactivity that is nearly similar to that of low reactive metallurgical coke. The wood origin, heat treatment temperature, nanostructure, differences in porosity and pore size of char influenced the CO_2 reactivity less than the differences in CO_2 concentrations.

1. Introduction

Ferroalloy production is energy-intensive, consuming large amounts of both electricity and coke. Coke is used in ferroalloy production to reduce metal oxides to the base metal. Development of cost-effective, renewable reductants is environmentally desirable because global ferroalloy production releases about 55 Mt of CO_2 emissions annually [1]. Using carbon sources from renewable, plant-based materials has potential to replace fossil-based reducing agents and effectively reduce CO_2 emissions. In recent years, much progress has been made on conversion of plant-based materials to carbonaceous char materials; some of these materials may have potential as reductants. However, metallurgical production continues to rely on fossil-based reductants due to limited knowledge of char properties and conditions required to produce chars with acceptable reactivity, and high costs.

Transportation of carbon reductants from Asia and South America creates additional economic and environmental challenges and thus, alternative options in Norway can be resorted [2]. In Norway, vast forest resources covering 12.8 million hectares with significant volumes of wood in the order of 6–8 million m^3 is harvested annually while wood growth increase by 25 million m^3 annually. This suggests that biomass can be an abundant source of carbon reductants in ferroalloy production [3,4]. Norway spruce, Scots pine and birch form 45%, 30% and 16% of forestry in Norway respectively [5]. There are different types of wood that can be converted into charcoal, of which wood residuals, consisting of limbs, tops, and stems are especially promising candidates for the use as carbonaceous reductants in ferroalloy industries because of low cost and high abundance [6]. The most important properties of the carbonaceous reductant are high reactivity, high conversion and low levels of impurities (such as sulphur and phosphorus) [7]. Low ash content is important, as each additional percent of ash in carbonaceous reductant increases slag volume by about 10–15 kg t^{-1} of ferroalloy, thereby increasing the electric power required for smelting [8]. Different types of wood contain various amounts of mineral compounds depending on the growth conditions. In general, hardwood ash contains a greater amount of K and P and less Ca and Si than softwood ash [9]. There are notable differences in the same genus of softwood, but less variation among hardwood species [10,11]. The distribution of lignocellulosic compounds shows significant variations between wood fractions (e.g. root, stem, and branch) [12]. The amount of extractives is greater in bark than in stemwood, whereas needles are rich in lipophilic extractives, especially in waxes [13–15]. Wood branches and roots contain a greater amount of galactan, xylan and lignin compared to glucomannan rich stemwood [16]. The high

* Corresponding author.
E-mail address: anna.trubetskaya@nuigalway.ie (Anna Trubetskaya).

https://doi.org/10.1016/j.fuel.2018.08.092
Received 4 April 2018; Received in revised form 23 July 2018; Accepted 21 August 2018
Available online 22 September 2018
0016-2361/ © 2018 Elsevier Ltd. All rights reserved.

Nomenclature

A	Relative area
A_i	Pre-exponential factor (s^{-1})
C	Constant
C_{fix}	Fixed carbon yield (wt% on dry basis)
D	Diameter (m)
E_a	Activation energy (kJ mol^{-1})
L_a	Mean cristal size in a-direction (Å)
R	Gas constant (J mol^{-1} K^{-1})
T	Temperature (K)
V	Pore volume (mm^3)
V	Volume (m^3)
X	Conversion
m	Mass (kg)
p	Pressure (Pa)
SSA	Specific surface area (m^2 g^{-1})

Greek symbols

γ	Surface tension (N m^{-1})
κ	Heating rate (K s^{-1})
λ	Wavenumber (cm^{-1})
ρ	Density (kg m^{-3})
Θ	Angle of contact (°)

Subscripts

a	average
cum	cumulative
md	median
p	pore
s	solid phase

reactivity of biocarbon-based reductant may be advantageous in some cases within the ferroalloy industries, however, the use of a reductant more reactive than metallurgical coke may increase maintenance costs due to the decreased electrical conductivity [17,18]. Therefore, reductant reactivity becomes a key variable that must be understood in potential replacements for metallurgical coke. Likewise, the effect of porosity and nanostructure in biocarbon-based reductants must also be considered. The increase in porosity of carbonaceous reductants increases the reactivity and thus the porous plant-based materials are advantageous in ferroalloy industries [19,20]. Charcoal porosity and pore size vary from 40 to 50% and from 20 to 30 µm [21]. In particular, charcoal from hardwood species is less porous than charcoal from softwood leading to the lower reactivity at high temperature pyrolysis [22]. Low interplanar distances (close to that of graphite) and high periodicity lead to lower oxidation of carbon materials, while the more bent graphene layers might enhance the reactivity [23,24]. The graphitizing carbons are non-porous with relatively high densities, whereas non-graphitizing carbonaceous materials have low density due to the high microporosity [25]. The non-graphitizability of charcoal is related to its porous structure [26,27]. The nanostructure of charcoal from pyrolysis at temperatures >2500 °C is observed to be similar to natural graphite, whereas charcoal prepared at lower temperatures exhibits a structure resembling glassy carbon [28,29]. Treatment at temperatures greater than 1250 °C will be required to produce non-graphitizing carbons suitable as metallurgical coke. Despite the arguments in favor of high temperature charcoal, the majority of previous investigations have studied charcoals produced at temperatures <1000 °C [30–33].

In summary, biocarbon-based materials have potential as environmentally benign replacements to fossil-based reductants, but knowledge of relationship between wood type, temperature and charcoal properties is limited. Therefore, in this study, the impacts of heat

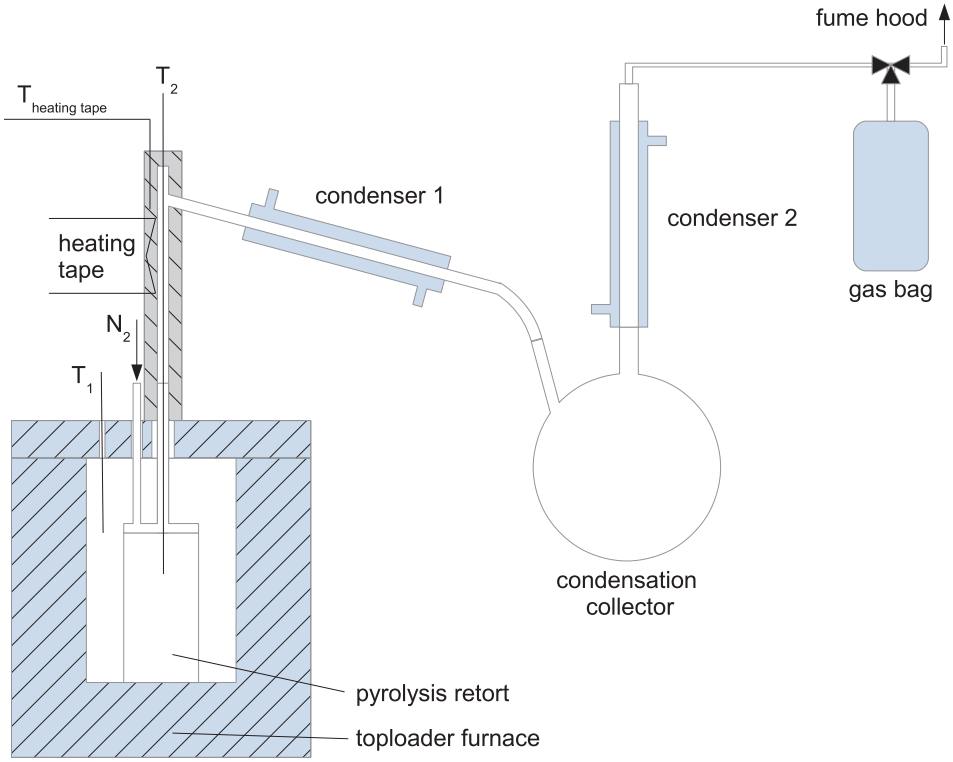

Fig. 1. Slow pyrolysis reactor at University of Agder.

treatment temperature (800–1600 °C), wood origin, porosity and nanostructure on the CO_2 reactivity were investigated in the slow pyrolysis reactor to simulate the conditions in industrial-scale coke production. The specific objectives of this study were to: (1) develop structure-property relationships governing the CO_2 reactivity of charcoal, and (2) determine the treatment conditions and wood composition which decrease char reactivity to levels that are suitable for application in ferroalloy industries.

2. Materials and methods

Norway spruce and oak were chosen for the charcoal study. Fuel selection was based on the differences in ash composition and plant cell compounds (cellulose, hemicellulose, lignin, extractives). Norway spruce is low in ash and with lower potassium and calcium contents than oak, whereas oak is low in lignin content. Char samples were generated in the slow pyrolysis reactor at 800 and 1200 °C. The char sample generated at 1200 °C was further heated to 1600 °C in the high-temperature furnace. The charcoal samples were crushed to a fine powder in a mortar with a ceramic pestle. The char samples were investigated under CO_2 gasification condition in a thermogravimetric analyzer. Reactivities of activated charcoal, metallurgical coke, and spruce and oak char samples were compared using reaction rates calculated from the derived kinetic parameters. Mercury intrusion porosimetry, N_2 adsorption, transmission electron microscopy (TEM) analysis and Raman spectroscopy were performed to characterize the effect of temperature and feedstock on the char carbon structure, surface properties and nanostructure.

2.1. Carbon material characterization

Norway spruce (*Picea abies*) and oak (*Quercus petraea*) from Dømmesmoen (Grimstad, Norway) were harvested in 2012 and 2016 respectively. The age of the Norway spruce was ≈39 years, whereas the oak was ≈46 years. Both the Norway spruce and oak trees were chipped by a disc chipper to 5–20 mm and dried at 60 °C. Metallurgical coke and activated charcoal were provided by Norsk Koksverk A/S (Mo i Rana, Norway). Prior to characterization, biomass samples were divided into six equal fractions using a riffler. The biomass samples were comminuted to <0.8 mm in a laboratory-scale mill POLYMIX PX-MFC 90 D (KINEMATICA, Switzerland).

2.2. Slow pyrolysis reactor

The charcoal samples were generated in the slow pyrolysis reactor, as shown in Fig. 1. The reactor can be operated at temperatures up to 1350 °C and heating rates up to 20 °C min^{-1}. The pyrolysis setup encloses a two-stage cooling system with a condensation collector and a pyrolysis gas sampling unit. The pyrolysis retort (inner diameter: 75 mm, height: 150 mm, wall thickness: 2 mm) is made of SiC material. The sample temperature was monitored by a thermocouple type S (max. 1600 °C). The connection pipes (inner diameter: 10 mm) between the retort and the condensation unit were made of quartz glass. The connection pipes were heated up to 350 °C by a heating tape HBQ (Hillesheim, Germany) and a temperature regulator MC1 (HORST GmbH, Germany) to minimize the condensation and thermal decomposition of tars. The volume flow of the N_2 gas was measured by the flowmeter HFC-202 (Teledyne, USA). The reactor was continuously purged by nitrogen at a constant flow rate of 100 ml min^{-1}. The temperature control system was based on the LabView software (Version 8.6). The sample mass of 60 g for each experiment was selected. The wood sample was distributed homogeneously in the reactor's retort, pre-heated in nitrogen at 10 °C min^{-1} up to 160 °C and kept at that temperature for 30 min. The dried wood was further heated at 10 °C min^{-1} up to 800 or 1200 °C and kept at the final temperature for about 1 h to ensure the complete conversion. After the heating program was finished, the furnace was turned off and the charcoal sample was cooled overnight in N_2 (0.3 l min^{-1}). Samples were stored in sealed plastic containers.

2.3. High-temperature furnace

The charcoal samples were further treated in the high-temperature furnace LHTG 200–300/20-1G (Carbolite Gero, Germany). The furnace can be operated at temperatures up to 1800 °C and at heating rates up to 20 °C min^{-1}. Prior to each experiment, 5 g of the char sample was loaded into the A_2O_3 crucible (Almath Crucibles Ltd, UK) placed in the graphite retort middle. Prior to pyrolysis, the furnace was repeatedly evacuated and purged by argon. The char sample was heated at 10 °C min^{-1} up to 1600 °C and kept at that temperature for 2 h. The sample was cooled to room temperature at a heating rate of 20 °C min^{-1} and stored in sealed plastic containers.

2.4. Char analysis

2.4.1. Elemental analysis

The elemental analysis was performed on Analyser Series II (Perkin Elmer, USA). Acetanilide was used as a reference standard. The ash content was determined using a standard ash test at 550 °C, according to the procedure described in DIN EN 14775.

2.4.2. Thermogravimetric analysis

The thermal decomposition of char samples was determined using an atmospheric thermogravimetric instrument STARe System (Mettler Toledo, USA). The reactivity of char in 20% or 100% volume fraction CO_2 (20 cm^3 min^{-1} of CO_2 and 80 cm^3 min^{-1} of N_2 or 100 cm^3 min^{-1} of CO_2 measured at 20 °C and 101.3 kPa) was determined by loading 5 mg of sample in Al_2O_3 crucible. The char samples were firstly heated up to 110 °C and kept for 30 min isothermally for drying. The dried samples were subsequently heated to 1100 °C at a constant heating rate of 10 °C min^{-1}. The kinetic parameters of char samples were derived by the integral method presented by Coats and Redfern [34]. Through integral transformation and mathematical approximation, the linear equation was expressed in the form:

$$ln\left(-\frac{ln(1-X)}{T^2}\right) = ln\left(\frac{A_i \cdot R}{\kappa \cdot E_a}\right) - \frac{E_a}{R \cdot T} \quad (1)$$

In Eq. (1), κ is the heating rate and R is the gas constant. A plot of ln (-ln(1-X) T^{-2}) versus T^{-1} gives a straight line whose slope and intercept determine the values of the activation energy (E_a) and pre-exponential factor (A_i). The reactivities of char samples were compared using reaction rates calculated from the derived kinetic parameters (A_i and E_a) at a fixed gasification temperature of 1000 °C.

2.4.3. Raman spectroscopy

Raman spectroscopy was performed using an inVia Raman microscope (Renishaw, UK) operating with a 514 nm laser line at a power of 30 mW. The measurements were performed in static mode with a center at 1600 cm^{-1}, resulting in a 960–2200 cm^{-1} spectral region. The laser power was set to 100% in the software and roughly 30 % in the hardware by using a filter. 1 s exposure time was used in normal confocality mode. A 20x lens and 8–15 µm step size (X and Y directions) was used for mapping, to generate 100–200 spectra/image for each char sample. Cosmic rays were removed and the data was subjected to multivariate noise filtering using the WiRE chemometrics package version 3.0 (Renishaw, UK). Spectra were saved as text files and processed via the free, open-source MatLab script provided by the Vibrational Spectroscopy Core Facility at Umeå University (www.kbc.umu.se/english/visp/download-visp/). The following parameters were used for spectra pre-processing: asymmetrical least squares baseline correction with lambda = 20000000 and p = 0.001 [35]; Savitzky-

Golay smoothing with the first polynomial order and frame rate of 3 [36]. Spectra were total area normalized in the entire spectral range. The corrected spectra from each mapping were then averaged to create a final composite curve for the peak deconvolution. No spectral scaling was performed. Deconvolution of the Raman spectra was conducted using the peak fit pro tool in the OriginPro software (OriginLab, USA) by combination of nine Gaussian-shaped bands (S_L, S, D_S, D, A_1, A_2, G_G, G_L, and D′) following Smith et al. [37]. The mean crystal size in the *a*-direction (L_a) with the fitting constants $C_0 = -12.6$ nm and $C_1 = 0.033$, which are valid for the laser wavelength from 400 to 700 nm, is given by [38]:

$$L_a = \frac{C_0 + C_1\lambda_L}{A_D/A_{G_L}} \quad (2)$$

2.4.4. N_2 adsorption analysis

The specific surface area (SSA) of biomass chars was determined based on N_2 adsorption at the boiling point (77 K). To prevent gas adsorption, the char samples were degassed under vacuum at 350 °C. The multipoint Brunauer-Emmett-Teller (BET) theory with seven points in the range of p/p_0 from 0.06 to 0.3 was applied on the NOVA 2000e instrument (Quantachrome, Germany). BET equation was used to determine the specific surface area [39].

2.4.5. Transmission electron microscopy

Prior to microscopy, char samples were kept at 350 °C for 6 h in a thermogravimetric instrument to reduce the amount of volatiles. Samples were ground in a mortar to ensure a homogeneous particle distribution, sonified in deionized water for 30 min, wet dispersed on a lacey carbon copper grid and dried at room temperature for 20 min. Char nanostructure was studied using a Jeol 2200 fs operated at 200 keV, equipped with an Oxford Instruments X-Max SDD EDS detector. The curvature of a single graphene sheet is defined in Eq. (3):

$$Curvature = \frac{Length}{Fiber\ length} \quad (3)$$

The length is a straight line that connects both ends of a graphene sheet. The fiber length is the contour or arc length, as shown in the supplemental material (Fig. S-1). Both length and fiber length were estimated by Gatan Digital Micrograph software according to the method of Müller et al. [40]. Portions of the image with visible graphene layers were magnified to a size of 10 nm x 10 nm, and both length and fiber length were manually determined by the software ruler which draws a straight or contour line to connect both ends of a graphene sheet.

2.4.6. Mercury intrusion porosimetry

The pore size distribution and porosity of char samples were determined by a Pascal mercury intrusion porosimeter system equipped with two instruments. Porosity in the ultramacro- and macropore regions was measured by Pascal 140 porosimeter (Micromeritics, Germany) at the low pressures (up to 400 kPa). The Pascal 440 porosimeter equipped with a dilatometer (Micromeritics, Germany) was used to determine the pore size from 1.8 to 7500 nm at high pressures up to 400 MPa. To access the pores and voids within biomass particles, samples were degassed at room temperature prior to the measurement. Prior to the porosity analysis, wood fractions were dried at 50 °C in an oven desiccator for 48 h.

2.4.7. Pore volume and size

The pore sizes in the char were distinguished into three categories: micropores (1.8–80 nm), mesopores (80–500 nm) and macropores (0.5–58 μm) [41,42]. The pore volume can be derived from the quantity of intruded mercury. The pore size distribution is determined according to the Washburn equation [43]:

$$D_p = -\frac{4\gamma cos\Theta}{p} \quad (4)$$

In Eq. (4), Θ is assumed to be equal to 141 ° [44] and γ is equal to 0.48 N m^{-1} [41]. The median pore diameter (D_{md}) is defined as the pore diameter at which 50% of total intrusion was reached. The average pore diameter (D_{pa}) is calculated, assuming that all pores are cylindrical, in Eq. (5):

$$D_{pa} = -\frac{4V_{cum}}{SSA} \quad (5)$$

The cumulative pore volume distribution is calculated in Eq. (6):

$$V_{cum}(D) = \frac{-dV_p}{dlogD_p} \quad (6)$$

2.4.8. Helium pycnometry

Skeletal density is defined in accordance with DIN 66137 (Part 2) standard by Eq. (7):

$$\rho_s = \frac{m_s}{V_s} \quad (7)$$

The calculation of skeletal density excludes the porosity within the particles and the interparticle voids. Skeletal density was determined using a helium pycnometer (POTOTEC GmbH, Germany) at room temperature.

3. Results

3.1. Biomass characterization

The ultimate and proximate analysis of metallurgical coke, activated charcoal, and wood was carried out at Eurofins Lidköping and shown in Table 1.

The compositional analysis of biomass (cellulose, hemicellulose, acid-soluble lignin, acid-insoluble lignin, and extractives) was conducted according to NREL technical reports [45–47] and Thammasouk et al. [48], and shown in Table 2.

Table 1
Proximate, ultimate and ash analyses of feedstocks.

Fuel	Norway spruce	Oak	Activated charcoal	Metallurgical coke
Proximate and ultimate analysis, (wt% on dry basis)				
Moisture[a]	8.6	7.6	3.8	0.6
Ash (550 °C)	0.8	1.6	8.6	11.8
Volatiles	80.6	82.6	10.3	3
C_{fix}	18.6	15.8	81.1	85.2
HHV[b]	20.3	19.3	30.5	27.9
LHV[b]	18.5	17.5	30.2	27.8
C	53.2	50.6	82.6	85.6
H	6.1	6.1	1.5	0.3
N	0.1	0.2	0.8	1.8
S	0.06	0.02	0.9	0.6
Cl	0.04	0.02	0.02	0.03
Ash compositional analysis, (mg kg^{-1} on dry basis)				
Al	40	20	4500	12000
Ca	2300	3600	4900	6400
Fe	200	50	3700	6300
K	800	1500	1900	1700
Mg	250	300	850	1300
Na	<50	<50	1100	1100
P	200	250	400	400
Si	550	550	31000	27000
Ti	50	50	200	550

[a] wt% (as received)
[b] in MJ kg^{-1}

Table 2
Composition of Norway spruce and oak, calculated in percentage based on dry basis (wt%).

Biomass	Cellulose	Hemicellulose	Lignin		Extractives
			Acid insoluble	Acid soluble	
Norway spruce	37.8	25	27.9	0.7	7.8
Oak	36.7	18.7	19.4	2.5	11

3.2. Char reactivity

Fig. 2 shows differential weight loss curves (DTG) for the 20% and 100% volume fraction CO_2 gasification of char samples, metallurgical coke and activated charcoal. The relative importance of external diffusion on the overall char gasification in the TG experiments was evaluated by comparison of the observed maximal reaction rate (r_{max}, % min^{-1}) with the calculated diffusion rate (r_{diff}, % min^{-1}) of CO_2 in the supplemental material (Eq. (1)). The calculated r_{max}/r_{diff} ratio showed that the gasification reaction in the TG analysis was influenced only by chemical kinetic limitations, as shown in the supplemental material (Table S-3). The DTG curves show both a single broad peak and a double peak in CO_2 gasification, indicating a heterogeneous char mixture with respect to the composition. A double DTG peak indicates a combination of two constituents with different reactivity [49,50]. The minor shoulder DTG peak at nearly the same temperature range from 810 to 825 °C was related to the reactivity of heavy hydrocarbon compounds [51]. The CO_2 gasification of most char samples and activated charcoal took place at nearly the same temperature range from 700 to 1200 °C, whereas metallurgical coke reacted at higher temperatures. The reactivities of char from spruce and oak were nearly identical, confirming previous results of Trubetskaya et al. [29].

The maximum reaction rate of oak char from pyrolysis at 1600 °C in 20% CO_2 gasification was about 100 °C greater than that of char produced at 800 °C. The maximum reaction rate of oak char at 1600 °C in 100% CO_2 gasification was about 20 °C lower than that of oak char produced at 800 °C. The maximal reaction rate of char samples reacted in 20% or 100% CO_2 changed significantly, based on the kinetic parameters in the supplemental material (Tables S-1 and S-2). The increasing CO_2 concentration led to the greater reactivity of both spruce and oak chars, confirming previous results of Cetin et al. [52]. Increasing heat treatment temperature resulted in a greater shift of maximum reaction rate from 50 °C at 800 °C to 70 °C at 1200 and 1600 °C. Interestingly, the reactivity of metallurgical coke in 20% and 100% CO_2 remained only slightly changed. The results show that differences in heat treatment temperature and feedstock origin have less influence on char reactivity than the CO_2 concentration, and will be discussed below.

3.3. Elemental analysis

Fig. 3 shows a Van Krevelen plot of original Norway spruce and oak and their chars, activated charcoal, and metallurgical coke. The results in Fig. 3 indicate that spruce char obtained from pyrolysis at 800 and 1200 °C contained more oxygen than oak char. The increased heat treatment temperature from 1200 to 1600 °C led to an increase in carbon content of both chars and thus the elemental composition of char samples was comparable to the composition of metallurgical coke. The activated charcoal contained more oxygen and hydrogen than chars obtained from pyrolysis at 1200 °C.

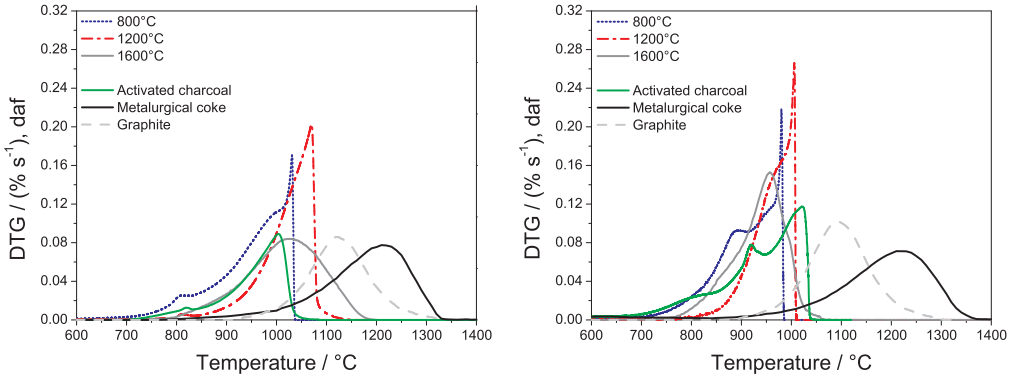

2(a): Spruce char (20 % CO_2 + 80 % N_2) 2(b): Spruce char (100 % CO_2)

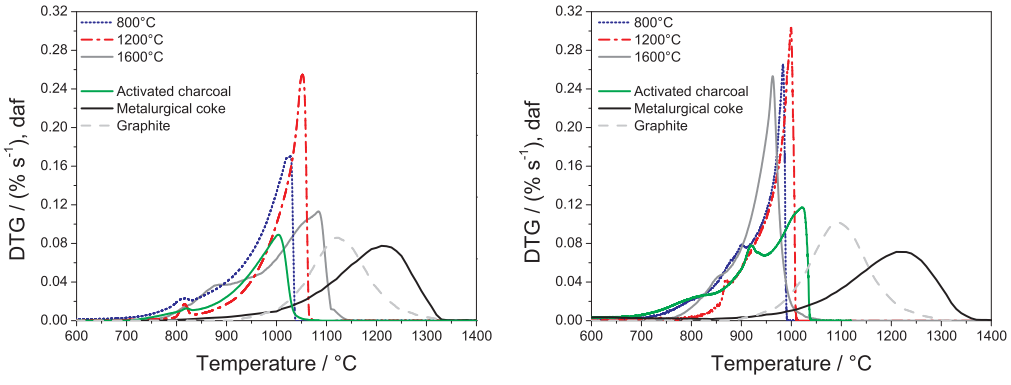

2(c): Oak char (20 % CO_2 + 80 % N_2) 2(d): Oak char (100 % CO_2)

Fig. 2. (a)-(d) DTG curves of metallurgical coke, activated charcoal, spruce and oak chars prepared at 800, 1200, and 1600 °C and reacted in 20% volume fraction CO_2 + 80% volume fraction N_2 and 100% CO_2.

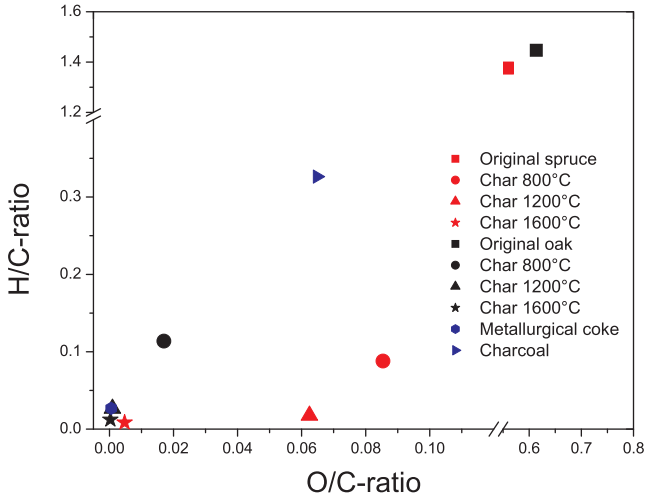

Fig. 3. Van Krevelen plot of metallurgical coke, activated charcoal, Norway spruce and oak chars prepared at 800, 1200, and 1600 °C.

3.4. Nanostructure

The nanostructure of the spruce and oak chars generated at 800, 1200, and 1600 °C was studied by TEM, as shown in Fig. 4. Both charcoal samples exhibited a common structure of amorphous carbon at 800 and 1200 °C, whereas a mixture of amorphous carbon and nano-crystalline graphite was observed at 1600 °C. In addition, spruce char showed two types of amorphous carbon structure at 1600 °C. The short graphene sheets of the spruce char merged, forming a continuous surface with a large number of crystallites, similar to the pyrolytic glassy carbon and lignin char, as shown in Fig. 4e [53,54].

Another type of amorphous carbon structure with more curved graphene layers was indicated on the spruce char surface and mixed with the nano-crystalline graphite. Fig. 4f shows the nanostructure of oak char generated at 1600 °C that mainly consists of nano-crystalline graphite with 22–26 layers of straight graphene layers arranged in an interconnected ribbon-like geometry [55]. The oak char nanostructure was similar to that of the crystalline carbon membrane [56]. The bent graphene layers of graphitized char contain carbon with hexagonal graphene layers [57] and a mean interplanar distance of 0.33 nm that indicates the highest degree of graphitization (graphite ≈0.335 nm) [58]. The spruce char generated at 1600 °C had a less ordered structure with the mean interplanar distance of 0.35 nm, as shown in Fig. 4. The differences in the nanostructure of spruce and oak chars generated at 1600 °C suggest that the feedstock composition has an influence on the char properties in high-temperature pyrolysis. The additional structures, detected by the TEM analysis of spruce and oak chars, were related to the presence of inorganic matter such as Al_2O_3 and Si [59,60]. In addition, TEM analysis showed that all char samples contained a small amount of SiC particles from the reactor's retort which could form the sp^3 diamond-like carbon in high-temperature pyrolysis [61,62].

3.5. Porosity and pore size

Table 3 summarizes the characteristics of spruce and oak chars generated at 800, 1200, and 1600 °C with regards to porosity, pore size and specific surface area. The porosity by skeleton density of spruce and oak chars measured by the mercury intrusion system was in the range from 70 to 78.8% and from 61.5 to 47.2%. Previous studies showed that the compositional differences led to lower porosity and greater apparent density of Eucalyptus charcoal compared to Acacia charcoal [63]. In the present study, the increase in porosity of spruce char is caused by the progressive removal of volatiles from pores, and the physical and chemical condensation of the remaining skeletal char structure with increasing heat treatment temperature, confirming previous results of Brewer et al. [32]. In contrast, the porosity of oak char samples decreased, probably due to the high alkali metal content in oak chars. The residual alkali metals (K^+ and Ca^{2+}) in oak char samples decreased the porosity to such extent that the active surface area was also decreased with increasing heat treatment temperature [64]. The greater alkali metal content in oak chars could also lead to the formation of charcoal with the different pore size and shape than during pyrolysis of low ash-containing spruce.

Table 3 shows that both spruce and oak chars possessed a high ratio of macropores. The macroporosity of the oak char (93–95%) was significantly greater than that of spruce char (57–60.3%). The micro- and mesoporosity of the spruce char ranged from 4 to 6%, whereas the oak char possessed greater proportion of micro- (23%) and mesopores (16.7–20%). The results also correspond to the greater total pore area of oak char samples (57.3–69.8 $m^2\ g^{-1}$) than that of the spruce char (10.7–11.8 $m^2\ g^{-1}$). In the present study, the formation of all pores in charcoal was a function of feedstock origin and less dependent on the heat treatment temperature respectively. The total pore area determined by mercury intrusion porosimetry was lower than that determined by N_2 adsorption because mercury porosimetry primarily determined macropores, whereas N_2 adsorption measured micro- and mesopores [65,66]. The results showed that the SSA of spruce and oak char samples determined by N_2 adsorption decreased significantly from 196 and 495 $m^2\ g^{-1}$ to 3 and 11 $m^2\ g^{-1}$ with the increased heat treatment temperature, as reported by Hussein et al. [67]. The reduction in the surface area was probably caused by the continuous growth of graphene sheets with the increasing heat treatment temperature, leading to the micropore coalescence [68]. The average pore size of the spruce and oak char samples varied from 0.7 to 2.3 nm using mercury intrusion porosimeter, whereas the average pore size of both spruce and oak chars varied only slightly from 0.6 to 1.3 nm when N_2 adsorption was used. This indicated no significant changes in all pore sizes. In addition, the pore size and specific surface area of oak char prepared at 1600 °C were similar to the values reported for metallurgical coke (0.9; 2.8 $m^2\ g^{-1}$).

3.6. Raman spectroscopy

Raman spectroscopy was carried out to examine primary differences in the carbon structure of char samples. The calculated integrated peak area ratio (A_{S_L}/A_{G_L}) in Fig. 5 and supplementary Table S-4 showed that spruce char samples obtained a greater amount of carboxylates than oak chars, whereas the A_{S_L}/A_{G_L} ratio of oak char generated at 1600 °C was the lowest (0.04) due to the low content of acetyl groups [69]. All char samples based on the A_D/A_{G_L} ratios exhibited a common structure of amorphous carbon and nano-crystalline graphite, as discussed by Ferrari and Robertson [70]. The pyrolysis at 800 and 1200 °C formed a less graphitic charcoal structure (A_D/A_{G_L}: 2.3–2.5) than the pyrolysis at 1600 °C (A_D/A_{G_L}: 1.7–1.9), corresponding to previous results of Trubetskaya et al. [22]. The average extensions of graphene stacks (L_a) from the Raman bands in spruce and oak chars generated at 800 and 1200 °C (1.7–1.9 nm) were less than those in the charcoal from pyrolysis at 1600 °C (2.3–2.6 nm). The size of one aromatic ring is 0.25 nm [71], and therefore, the size of PAHs in the char (800–1600 °C) is equivalent to approximately 7–10 aromatic rings. Moreover, the average extension of graphene stacks (L_a) in all char samples was quantitatively similar to that of commercial carbon black (Printex XE2: 2.5 nm) and biomass soot (2.1–2.6 nm) and different from the graphite structure (5.6 nm) [72,73].

4. Discussion

The thermogravimetric experiments demonstrated larger influence of CO_2 concentration on the intrinsic reactivity of char samples than the heat treatment temperature and feedstock origin. The reactivity of char

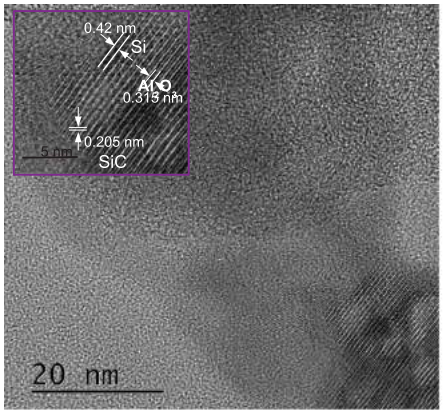

4(a): Spruce char (800°C)

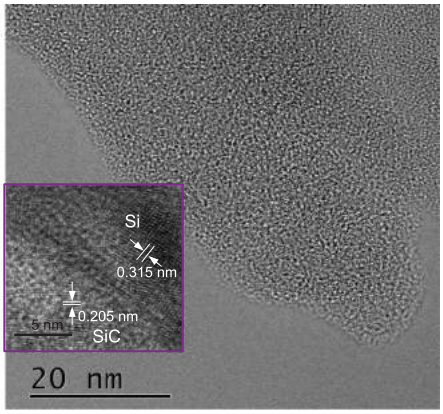

4(b): Oak char (800°C)

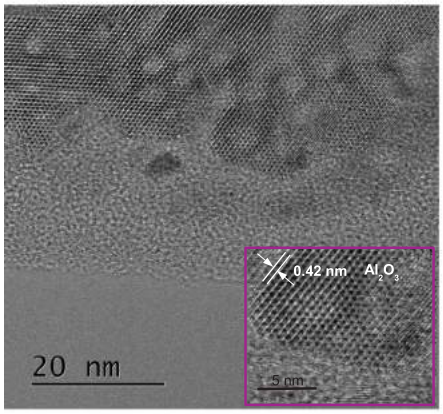

4(c): Spruce char (1200°C)

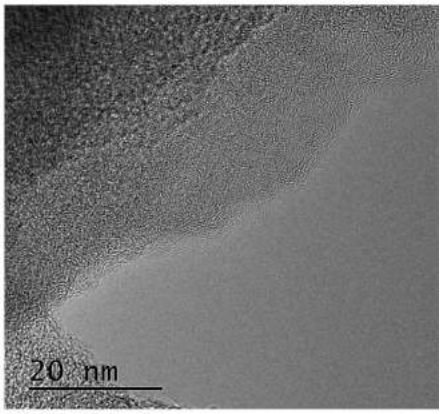

4(d): Oak char (1200°C)

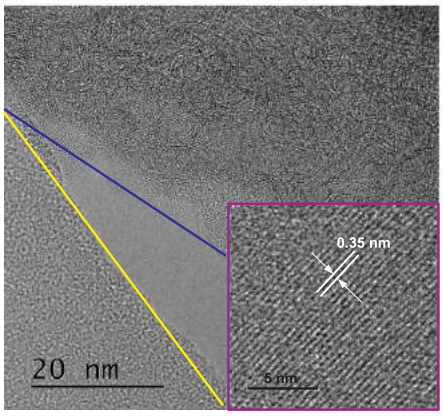

4(e): Spruce char (1600°C)

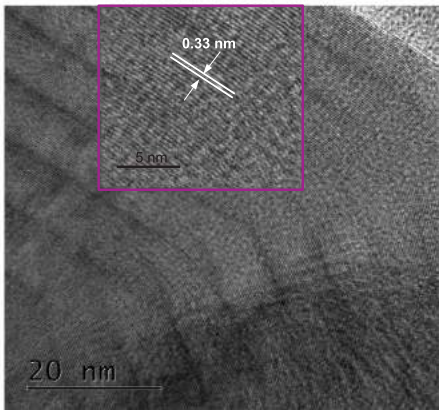

4(f): Oak char (1600°C)

Fig. 4. TEM images of char generated from spruce and oak. In (a)-(c), (e) and (f) the distance between graphene layers, Al_2O_3, SiC and Si was measured in the enlarged image (purple rectangle). In (e) the areas of different carbon types are marked with blue and yellow lines. (For interpretation of the references to colour in this figure legend, the reader is referred to the web version of this article.)

can be affected by differences in carbon chemistry, ash composition, nanostructure, heat treatment temperature and surface area characteristics of char samples. Raman spectroscopy results showed that char samples from pyrolysis at 800, 1200, and 1600 °C exhibited a structure resembling carbon black based on the A_D/A_{G_L} ratios (1.7–2.6). The ash content of original spruce (0.8 wt%) was twice lower than in the original oak. Thus, based on ash content alone it might be expected that spruce char should be less reactive than the oak char. However, the inorganic matter of both spruce and oak chars remained small, as shown in the supplemental material (Fig. S-23). Knudsen et al. [74] experimentally showed that at high temperatures, KCl sublimation and potassium silicates reactions are dominant during devolatilization, depending on the availability of Si, Cl, Ca and Mg in the original fuel. The lower Cl content in the wood might indicate that potassium was

Table 3
Porosity and pore size of spruce and oak char, characterized by mercury intrusion porosimeter and BET surface area (SSA) and pore size (DFT method) of chars, determined by N_2 adsorption $m^2\ g^{-1}$.

Parameter	Spruce			Oak			Metallurgical coke	Activated charcoal
	800 °C	1200 °C	1600 °C	800 °C	1200 °C	1600 °C		
Mercury intrusion porosimetry								
Porosity by Hg intrusion, %	70	74.5	78.8	61.5	58.2	47.2	39.7	14
Porosity by skeleton density, %	78.5	81.4	79.5	68.5	60.5	65.5	47.8	33
Inaccessible porosity, %	8.8	7	0.6	7.1	2.2	18.2	8.1	20
Macropores, %	93	95	93	60.3	57	57	87	97
Mesopores, %	6	4	6	16.7	20	20	10	3
Micropores, %	1	1	1	23	23	23	3	
V_{cum}, $mm^3\ g^{-1}$	1917	2636.8	2788.5	1163	1065	1232	403	146
Total pore surface area, $m^2\ g^{-1}$	11.4	11.8	10.7	57.3	69.8	65.3	5.9	0.2
Average pore diameter, μm	0.7	0.9	1	0.1	0.1	0.1	0.3	2.3
Median pore diameter, μm	6.9	7.7	6.9	1.1	0.9	0.9	16.2	21.8
N_2 adsorption								
BET surface area (SSA), $m^2\ g^{-1}$	196	97.2	3	495	80	11	2.8	0.3
Pore size, nm	0.6	0.7	1.3	0.6	0.7	0.9	0.9	0.9

released in the form of KOH or to a minor extent in the form of KCl [75]. The reactivities of spruce and oak chars remained similar at 800 and 1200 °C. This indicates that neither carbon structure nor ash composition had a strong influence on the observed differences in char reactivity.

Previous studies on charcoal from pyrolysis at temperatures <1000 °C showed that nanostructure and CO_2 reactivity are interrelated considerations. In the present study, all charcoal samples exhibited shorter and less curved graphene layers and less recognizable crystalline structure, indicating either greater porosity or larger fraction of amorphous carbon than in coal chars [76]. This indicates that biomass chars consist of non-graphitizing carbons [77–79]. The results showed that the differences in nanostructure of spruce and oak char samples from pyrolysis at 1600 °C were large. The oak char nanostructure was similar to that of glassy carbon, as reported by Jenkins et al. [80]. The TEM analysis of oak char graphitic ribbons from pyrolysis at 1600 °C showed that the mean interplanar distance of graphene layers (0.33 nm) was similar to graphite (0.335 nm). The spruce char samples exhibited heterogeneous structure of amorphous carbon and nano-crystalline graphite corresponding to the double DTG peak in Fig. 2. A double DTG peak in spruce char samples indicated the presence of a carbon constituent with similar reactivity to graphite and a more reactive carbon structure with similar reactivity to biomass soot samples [73]. The lower oxygen content in wood than that in herbaceous biomass inhibited the cross-linking and repolymerization reactions and therefore enhanced the coalescence of crystallites, leading to the charcoal graphitization [81]. The oxygen-containing functional groups remaining in charcoal are located at the edges of aromatic layers which hinder the alignment of graphene layers during pyrolysis [79]. Thus, based on oxygen content alone it might be expected that charcoal from softwood pyrolysis is more graphitic than hardwood charcoal. However, the nanostructure of oak char from pyrolysis at 1600 °C was more graphitic than that of spruce char. This is due to the catalytic effect of alkali on the oak charcoal graphitization that is especially pronounced at high temperatures (1000–1600 °C) [82,83]. Interestingly, the short graphene layers of spruce char could enhance the reactivity, whereas the straight and long graphene layers of oak char are expected to decrease the char reactivity. However, the reactivity of spruce and oak chars was similar.

The increased heat treatment temperatures led to greater char porosity in pyrolysis at temperatures 300–700 °C [32]. In the present study, the char porosity measured by mercury intrusion porosimetry varied among spruce and oak chars, but changed only slightly with the increased heat treatment temperature. Moreover, the spruce chars obtained less micro- and mesopores than the oak chars, indicating a strong influence of the feedstock origin on the char porosity. The specific surface area of spruce char prepared at 1600 °C was 9 times smaller than that of char from pyrolysis at 800 °C, whereas the spruce char prepared at 800 °C was 4 times more reactive than char from pyrolysis at 1600 °C in 20% CO_2 gasification. The oak char generated at 800 °C was twice more reactive than char from pyrolysis at 1600 °C, whereas the specific surface area of char from 800 °C pyrolysis was 8 times greater than the SSA of char prepared at 1600 °C. This indicates that the heat treatment temperature has a small influence on the CO_2 reactivity of charcoal samples determined by N_2 adsorption.

The oak and spruce chars prepared at 800 °C were 106 and 3 times more reactive respectively in 100% CO_2 atmosphere than the chars in 20% CO_2 gasification, indicating a major influence of CO_2 concentration on the char reactivity. The decrease in CO_2 concentration leads to the decrease in maximum reaction rate [84,85]. In the present work, the linear correlation between reaction rate and partial pressure could not be established based on the experimental results (Table S-4) and calculations in the supplemental material (Eq. 3). Moreover, as it was mentioned above, the gasification reaction in the TG analysis was influenced only by chemical kinetic limitations. Thus, the CO_2 concentration becomes the dominating factor governing gasification reactivity. The metallurgical coke in 20% CO_2 gasification was 5 times less reactive than spruce and oak char samples from pyrolysis at 1600 °C. The reactivity of metallurgical coke remained unchanged with increasing CO_2 concentration, whereas the reactivity of activated charcoal changed in a similar manner as the reactivity of spruce and oak chars from pyrolysis at 800 °C. This shows that the further increase in heat treatment temperature could increase the char graphitization, leading to the development of a structure that is more similar to low reactive metallurgical coke.

5. Conclusion

The novelty of this work relies on the fact that char from wood consists mainly of non-graphitizing carbon. The results indicated that both char samples from spruce and oak contained mostly nano-crystalline graphite at 1600 °C. However, the oak char was significantly more graphitic than the spruce char at 1600 °C. At lower temperatures, both chars formed less ordered structure that is similar to amorphous carbon. The major difference in the char morphology was related to the formation of a high ratio of micro- and mesopores in oak pyrolysis, whereas the spruce chars contained mainly macropores. The differences in micropore size of spruce and oak chars determined by N_2 adsorption were small. In contrast, the average pore size of oak char was 10 times

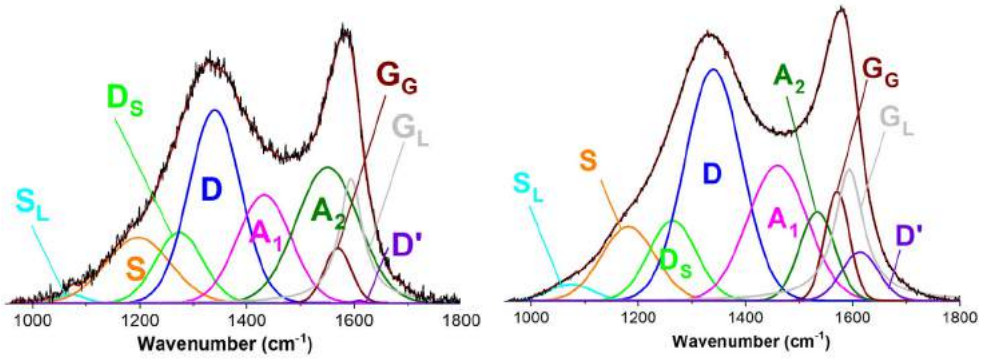

5(a): Spruce char (800°C) 5(b): Oak char (800°C)

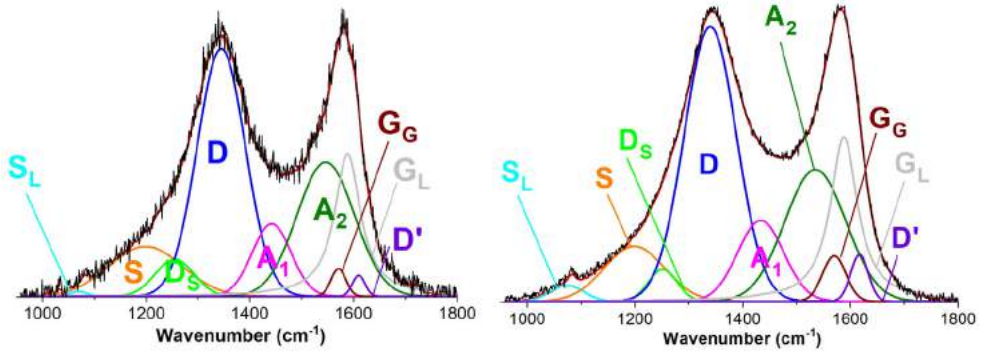

5(c): Spruce char (1200°C) 5(d): Oak char (1200°C)

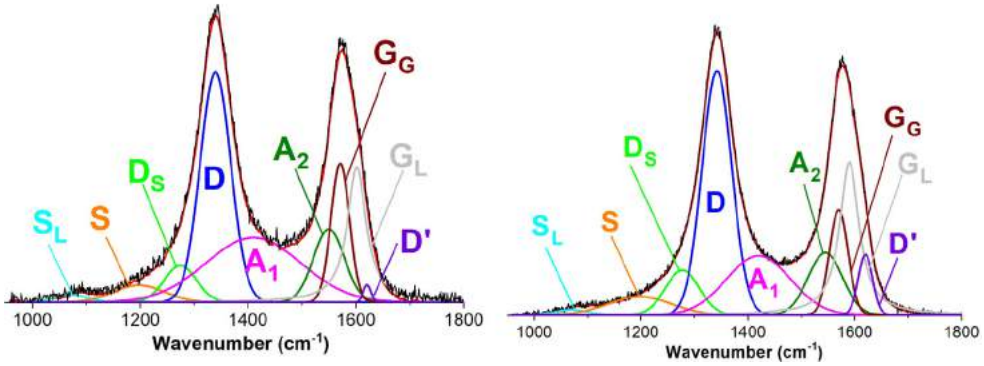

5(e): Spruce char (1600°C) 5(f): Oak char (1600°C)

Fig. 5. (a)-(f) Deconvolution of Raman spectrum of Norway spruce and oak chars from pyrolysis at 800, 1200, and 1600 °C.

smaller than that of spruce char using mercury intrusion porosity. The pore size analysis showed that the N_2 adsorption and mercury intrusion porosimetry methods are complementary for quantifying charcoal porosity characteristics at micro- to macropore scales.

The thermogravimetric analysis results showed that the char reactivity towards CO_2 depends mainly on the CO_2 concentration and less on the heat treatment temperature, ash composition and carbon structure. The more graphitic structure of oak char from pyrolysis at 1600 °C with a smaller interplanar distance, long and flat graphene layers showed a similar reactivity to the less ordered oak char. Both char samples were significantly more reactive in a 100% CO_2 atmosphere than in 20% CO_2 gasification emphasizing the role of CO_2 concentration on the char reactivity. The charcoal from pyrolysis at 800 °C showed a similar reactivity to the activated charcoal, whereas the charcoal prepared at 1600 °C was more reactive than metallurgical coke. This work indicated that the increase in a heat treatment temperature will lead to the further deactivation of char with the structure that is similar to low reactive metallurgical coke.

Acknowledgements

The authors gratefully acknowledge financial support from Elkem AS, Saint Gobain Ceramic Materials AS, Eramet Norway AS, Kempe Foundation, Björn Wahlströms, and Jernkontoret Stiftelsen. The authors acknowledge the facilities and technical support of Dr. Andras Gorzsas at Umeå University. The German Federal Government, Federal State of Nordrhein-Westfalen, Deutsche Forschungsgemeinschaft (DFG) are acknowledged for their contribution toward the establishment of the Interdisciplinary Center for Analytics on the Nanoscale in the University of Duisburg-Essen. Gundula Stein and Viktor Scherf from GNF Berlin-Adlershof e.V. are acknowledged for many discussions on N_2 adsorption analysis. We acknowledge Raymond Mclnerney from University of Limerick for the article proof-reading.

Appendix A. Supplementary data

Supplementary data associated with this article can be found, in the

online version, athttps://doi.org/10.1016/j.fuel.2018.08.092.

References

[1] Holappa L. Towards sustainability in ferroalloy production. J South African Inst Min Metal 2010;110(12):1–8.
[2] Monsen B, TangstadM,Midtgaard H, Use of charcoal in silicomanganese production. In: 10th Int Ferroalloys Congress INFACON X. Transformation through Technology 68 (2004) 155–64.
[3] Borrelli P, Panagos P, Langhammer J, Apostol B, Schütt B. Assessment of the cover changes and the soil loss potential in European forestland: First approach to derive indicators to capture the ecological impacts on soil-related forest ecosystems. Ecol Indic 2016;60:1208–20.
[4] Sjlie HK, Latta GS, Adams DM, Solberg B. Impacts of agent information assumptions in forest sector modeling. J Forest Econ 2011;17:169–284.
[5] Wang L, Dibdiakova J, Gjolsjo S. Report on solid biofuels from forest-fuel specification and quality assurance. Norwegian Forest Landscape Inst 2014;8:1–45.
[6] Wesenbeeck SV, Wang L, Ronsse F, Prins W, Skreiberg Ø. Charcoal mines in the Norwegian woods. Fuel 2016;30:7959–70.
[7] Pistorius PC. Reductant selection in ferro-alloy production: the case for the importance of dissolution in the metal. J South African Inst Min Met 2002;1:33–6.
[8] Sahajwalla V, Dubikova M, Khanna R, Reductant characterisation and selection: implications for ferroalloys processing. In: 10th Int Ferroalloys Congress INFACON X. Transformation through Technology 68 (2004) 351–62.
[9] Pitman RM. Wood ash use in forestry – a review of the environmental impacts. Forestry 2006;79(5):563–88.
[10] Naylor L, Schmidt E. Agricultural use of wood ash as a fertiliser and limiting material. TAPPI J 1986;69:114–9.
[11] Naylor L, Schmidt E. Paper mill wood ash as a fertiliser and limiting material. TAPPI J 1989;72:199–206.
[12] Gustafsson G. Heartwood and lightwood formation in Scots pine – A physological approach. Swedish University of Agricultural Sciences; 2001. [PhD thesis].
[13] Myeong S, Han SH, Shin SJ. Analysis of chemical compositions and energy contents of different parts of yellow poplar for development of bioenergy technology. J Korean For Soc 2010;99(5):706–10.
[14] Backlund I. Cost-effective cultivation of lodgepole pine for biorefinary applications. Swedish University of Agricultural Sciences; 2013. [PhD thesis].
[15] Koch P. Lodgepole pine in North America: Nonwood products characterization of tree parts. Forest Prod Soc 1996.
[16] Hakkila P. Utilization of residual biomass. Springer; 1989.
[17] Yamagishi K, Endo K, Saga J, A comprehensive analysis of the furnace interior for high-carbon ferrochromium. In: 1th Int Ferroalloys Congress IN FACON 74. Transformation through Technology (1974) 143–7.
[18] De Waal A, Barker IJ, Rennie MS, Klopper J, Groeneveld BS, Electrical Factors Affecting the Economic Optimization of Submerged-arc Furnaces. In: 6th Int Ferroalloys Congress INFACON 6. Transformation through Technology 1 (1974) 247–52.
[19] Pochart G, Joncourt L, Touchard N, Perdon C. Metallurgical benefit of reactive high grade ore in manganese alloys manufacturing. INFACON XI 2007:217–29.
[20] Longbottom RJ, Monaghan BJ, Chowdhury AA, Reid MH, Zhang G, Mahoney MR, et al. Effect mineral matter on the reactivity of coke and its replication in a coke analogue. ISIJ Int 2016;56(9):1553–8.
[21] Standish N, Tanjung AFA. Gasification of single wood charcoal particles in CO_2. Fuel 1988;67:666–72.
[22] Trubetskaya A. Fast pyrolysis of biomass at high temperatures. Technical University of Denmark; 2016. [PhD thesis].
[23] Hurt RH, Structure, properties, and reactivity of solid fuels. In: 27th Symposium on Combust (1998) 2887–904.
[24] Liati A, Eggenschwiler PD, Schreiber D, Zelenay V, Ammann M. Variations in diesel soot reactivity along the exhaust after-treatment system, based on the morphology and nanostructure of primary soot particles. Combust Flame 2013;160(3):671–81.
[25] Ion I, Kovalev Y, Banciu C, Pasuk I, Kuklin A. Structural studies of carbon materials by sans-technique. Rom J Phys 2006;51(7):783–9.
[26] Ishimaru K, Vystavel T, Bronsveld P, Hata T, Imamura Y, Hosson JD. Diamond and pore structure observed in wood charcoal. J Wood Sci 2001;47:414–6.
[27] Hata T, Yamane T, Kobayashi E, Imamura Y, Ishihara S. Microstructural investigation of wood charcoal made by spark plasma sintering. J Wood Sci 1998;44:332–4.
[28] Harris PJF. New perspectives on the structure of graphitic carbons. Crit Rev Sold State Mat Sci 2005;30:235–53.
[29] Surup GR, Timko MT, Deike R, Schubert D, Foppe M, Trubetskaya A, et al. The effect of feedstock origin and temperature on the structure and reactivity of char from pyrolysis at 1300–2800 °C. Fuel 2019;235:306–16.
[30] Antal MJ, Grønli M. The art, science, and technology of charcoal production. Ind Eng Chem Res 2003;42:1619–40.
[31] Bourke J, Manley-Harris M, Fushimi C, Dowaki K, Nunoura T, Antal MJ. Do all charcoals have the same chemical structure? 2 A model of the chemical structure of carbonized charcoal. Ind Eng Chem Res 2007;46(18):5954–67.
[32] Brewer CE, Chuang VJ, Masiello CA, Gonnermann H, Gao X, Dugan B, et al. New approaches to measuring biochar density and porosity. Biomass Bioenergy 2014;66:176–85.
[33] Griessacher T, Antrekowitsch J, Steinlechner S. Charcoal from agricultural residues as alternative reducing agent in metal recycling. Biomass Bioenergy 2012;39:139–46.
[34] Coats AW, Redfern JP. Kinetic parameters from thermogravimetric data. Nature 1964;201:68–9.
[35] Eilers PHC. Parametric Time Warping. Analyt Chem 2004;76(2):404–11.
[36] Savitzky A, Golay MJE. Smoothing and differentiation of data by simplified least squares procedures. Analyt Chem 1964;36(8):1627–39.
[37] Smith MW, Dallmeyer I, Johnson TJ, Brauer CS, McEwen JS, Espinal JF, et al. Structural analysis of char by Raman spectroscopy: improving band assignments through computational calculations from first principles. Carbon 2016;100:678–92.
[38] Matthews MJ, Pimenta MA, Dresselhaus G. Origin of dispersive effects of the Raman D band in carbon materials. Phys Rev B 1999;59(10):R6585–8.
[39] Brunauer S, Emmett PH, Teller E. Adsorption of gases in multimolecular layers. J Am Chem Soc 1938;60(2):309–19.
[40] Müller JO, Su DS, Wild U, Schlögl R. Bulk and surface structural investigations of diesel engine soot and carbon black. Phys Chem Chem Phys 2007;9:4018–25.
[41] Plötze M, Niemz P. Porosity and pore size distribution of different wood types as determined by mercury intrusion porosimetry. Europ J Wood Wood Product 2011;69(4):649–57.
[42] Yin J, Song K, Lu Y, Zhao G, Yin Y. Comparison of changes in micropores and mesopores in the wood cell walls of sapwood and heartwood. Wood Sci Technol 2015;49:987–1001.
[43] Washburn EW. Note on a method of determining the distribution of pore sizes in a porous material. Proc Natl Acad Sci 1921;7:115–6.
[44] Junghaus K, Niemz P, Bächle F. Untersuchungen zum Einfluss der thermischen Vergütung auf die Porosität von Fichtenholz. Holz Roh Werkst 2005;63(3):243–4.
[45] Sluiter A, Hames B, Ruiz R, Scarlata C, Sluiter J, Templeton D et al., Determination of Structural Carbohydrates and Lignin in Biomass. Golden (CO): National Renewable Energy Laboratory; 2011 July Report No. NREL/TP-510-42618. Contract No.: DE-AC36-08-GO28308.
[46] Willför S, Hemming J, Leppänen AS, Analysis of extractives in different pulps - Method development, evaluation, and recommendations. Finland: Abo Akademi University, Laboratory of Wood and Paper Chemistry; 2004–2009 Report No. B1 of the EU COST E41 action Analytical tools with applications for wood and pulping chemistry.
[47] Hames B, Ruiz R, Scarlata C, Sluiter J, Sluiter A, Preparation of Samples for Compositional Analysis. Golden (CO): National Renewable Energy Laboratory; 2011 June Report No. NREL/TP-510-42620. Contract No.: DE-AC36-99-GO10337.
[48] Thammasouk K, Tandjo D, Penner MH. Influence of extractives on the analysis of herbaceous biomass. J Agric Food Chem 1997;45:437–43.
[49] Abian M, Jensen AD, Glarborg P, Alzueta MU. Soot reactivity in conventional combustion and oxy-fuel combustion environments. Energy Fuels 2012;26(8):5337–44.
[50] Russell NV, Beeley TJ, Man CK, Gibbins JR, Williamson J. Development of TG measurements of intrinsic char combustion reactivity for industrial and research purposes. Fuel Process Tech 1998;57(2):113–30.
[51] Zhang D, Ma Y, Zhu M. Nanostructure and oxidative properties of soot from a compression ignition engine: The effect of a homogeneous combustion catalyst. Proc Combust Inst 2013;34:1869–76.
[52] Cetin E, Moghtaderi B, Gupta R, Wall TF. Biomass gasification kinetics: influences of pressure and char structure. Comb Sci Tech 2005;177(4):765–91.
[53] Jurkiewicz K, Pawlyta M, Zygadlo D, Chrobak D, Duber S, Wrzalik R, et al. Evolution of glassy carbon under heat treatment: correlation structure-mechanical properties. J Mater Sci 2018;53:3509–23.
[54] Li Y, Hu YS, Chen L, Li H, Huang X. A superior low-cost amorphous carbon anode made from pitch and lignin for sodium-ion batteries. J Mat Chem A 2016;4:96–104.
[55] Jenkins GM, Kawamura K. Polymeric carbons – Carbon fibre, glass and char. Cambridge University Press; 1976.
[56] Wollbrink A, Volgmann K, Koch J, Kanthasamy K, Tegenkamp C, Li Y, et al. Amorphous, turbostratic and crystalline carbon membranes with hydrogen selectivity. Carbon 2016;106:93–105.
[57] Welz S, McNallan MJ, Gogotsi Y. Carbon structures in silicon carbide derived carbon. J Mat Proc Tech 2006;179:11–22.
[58] Zhang ZL, Brydson R, Aslam Z, Reddy S, Brown A, Westwood A, et al. Investigating the structure of non-graphitising carbons using electron energy loss spectroscopy in the transmission electron microscope. Carbon 2011;49:5049–63.
[59] Gogotsi Y, Welz S, Ersoy DA, McNallan MJ. Conversion of silicon carbide to crystalline diamond-structured carbon at ambient pressure. Nature 2000;411:283–7.
[60] Aramesh M, Tran PA, Ostrikov K, Prawer S. Conformal nanocarbon coating of alumina nanocrystals for biosensing and bioimaging. Carbon 2017;122:422–7.
[61] Kiselev NA, Hutchison JL, Roddatis VV, Stepanova AN, Aksenova LL, Rakova EV, et al. TEM and HREM of diamond crystals grown on Si tips: structure and results of ion-beam-treatment. Micron 2000;36:81–8.
[62] Ischenko V, Jang YS, Kormann M, Greil P, Popovska N, Zollfrank C, et al. The effect of SiC substrate microstructure and impurities on the phase formation in carbide-derived carbon. Carbon 2011;49:1189–98.
[63] Kumar M, Gupta RC. Influence of carbonization conditions on physical properties of Acacia and Eucalyptus wood chars. Trans Ind Inst Met 1993;46(6):345–52.
[64] Branca C, Iannace A, Di Blasi C. Devolatilization and combustion kinetics of Quercus Cerris. Energy Fuels 2007;21:1078–84.
[65] Illingworth J, Williams PT, Rand B. Characterisation of biochar porosity from pyrolysis of biomass flax fibre. J Energy Inst 2013;86(2):63–70.
[66] Giesche H. Mercury porosimetry: a general (practical) overview. Part Syst Charact 2006;23(1):9–19.
[67] Hussein A, Larachi F, Ziegler D, Alamdari H. Effects of heat treatment and acid washing on properties and reactivity of charcoal. Biomass Bioenergy 2016;90:101–13.
[68] Kercher AK, Nagle DC. Microstructural evolution during charcoal carbonization by X-ray diffraction analysis. Carbon 2003;41:15–27.

[69] Sun Y, Cheng J. Hydrolysis of lignocellulosic materials for ethanol production: a review. Biores Tech 2002;83:1–11.
[70] Ferrari AC, Robertson J. Raman spectroscopy of amorphous, nanostructured, diamond-like carbon, and nanodiamond. Phil Trans R Soc Lond 2004;362:2477–512.
[71] Hayashida K, Nagaoka S, Ishitani H. Growth and oxidation of graphitic crystallites in soot particles within a laminar diffusion flame. Fuel 2014;128:148–54.
[72] Jawhari T, Roid A, Casado J. Raman spectroscopic characterization of some commercially available carbon black materials. Carbon 1995;33(11):1561–5.
[73] Trubetskaya A, Brown A, Tompsett GA, Timko MT, Umeki K, Kling J, et al. Characterization and reactivity of soot from fast pyrolysis of lignocellulosic compounds and monolignols. Appl. Energy 2018;212:1489–500.
[74] Knudsen JN. Volatilization of inorganic matter during combustion of annual biomass. Technical University of Denmark; 2003. [PhD thesis].
[75] Dayton DC, Milne TA. Laboratory measurements of alkali metal containing vapors released during biomass combustion. Baxter L, DeSollar R, editors. Application of Advanced Technologies to Ash-Related Problems in Boilers Plenum Press; 1996.
[76] Beeley T, Crelling J, Gibbins J, Hurt R, Lunden M, Man C et al. Transient high-temperature thermal deactivation of monomaceral-rich coal chars. In: 26th Symp Comb Inst (1996) 3103–10.
[77] Franklin RE. Crystallite growth in graphitizing and non-graphitizing carbons. Proc R Soc A Math Phys Eng Sci 1951;209:196–218.
[78] Oberlin A. Carbonization and graphitization. Carbon 1984;22(6):521–41.
[79] Kurosaki F, Ishimaru K, Hata T, Bronsveld P, Kobayashi E, Imamura Y. Microstructure of wood charcoal prepared by flash heating. Carbon 2003;41(15):3057–62.
[80] Jenkins GM, Kawamura K, Ban LL. Formation and structure of polymeric carbons. Proc R Soc Lond A 1972;327:501–17.
[81] Trubetskaya A, Jensen PA, Jensen JD, Steibel M, Spliethoff H, Glarborg P. Influence of fast pyrolysis conditions on yield and structural transformation of biomass chars. Fuel Process Tech 2015;140:205–14.
[82] Hata T, Ishimaru K, Fujisawa M, Bronsveld P, Vystavel T, De Hosson J, et al. Catalytic graphitization of wood-based carbons with alumina by pulse current heating. Full Nano Carbon Nano 2005;13:435–45.
[83] Johnson MT, Faber KT. Catalytic graphitization of three dimensional wood-derived porous scaffolds. J Mater Res 2011;26(1):18–25.
[84] Gomez A, Silbermann R, Mahinpey N. A comprehensive experimental procedure for CO_2 coal gasification: Is there really a maximum reaction rate? Appl Energy 2015;137:126–33.
[85] Gomez A, Mahinpey N. A new model to estimate CO_2 coal gasification kinetics based only on parent coal characterization properties. Appl Energy 2015;137:126–33.

4.3 Heat treatment temperatures above 1300 °C

Fuel 235 (2019) 306–316

Contents lists available at ScienceDirect

Fuel

journal homepage: www.elsevier.com/locate/fuel

Full Length Article

The effect of feedstock origin and temperature on the structure and reactivity of char from pyrolysis at 1300–2800 °C

Gerrit Ralf Surup[a], Manuel Foppe[b], Daniel Schubert[b], Rüdiger Deike[b], Markus Heidelmann[c], Michael T. Timko[d], Anna Trubetskaya[e,*]

[a] Department of Engineering Sciences, University of Agder, 4879 Grimstad, Norway
[b] Chair of Metallurgy for Iron and Steel Production, University of Duisburg-Essen, 47119 Duisburg, Germany
[c] Interdisciplinary Center for Analytics on the Nanoscale, University of Duisburg-Essen, 47057 Duisburg, Germany
[d] Chemical Engineering Department, Worcester Polytechnic Institute, 01609 Worcester, MA, USA
[e] Mechanical Engineering Department, National University of Ireland, H91TK33 Galway, Ireland

ARTICLE INFO

Keywords:
Biomass char
High-temperature pyrolysis
Reactivity
Biooil
Metallurgical coke

ABSTRACT

This study reports the effect of feedstock origin, residence time, and heat treatment temperature on CO_2 and O_2 reactivities, nanostructure and carbon chemistry of chars prepared at 1300, 1600, 2400, and 2800 °C in a slow pyrolysis reactor. The structure of char was characterized by transmission electron microscopy and Raman spectroscopy. The CO_2 and O_2 reactivity of char was investigated by thermogravimetric analysis. Results showed that the ash composition and residence time influence the char reactivity less than the heat treatment temperature. The heat treatment temperature and co-pyrolysis of pinewood char with biooil decreased the CO_2 reactivity, approaching that of metallurgical coke. Importantly from a technological standpoint, the reactivities of char from high temperature pyrolysis (2400–2800 °C) were similar to those of metallurgical coke, emphasizing the importance of graphitizing temperatures on the char behavior. Moreover, graphitization of chars from wood and herbaceous biomass increased with the increasing heat treatment temperature, leading to formation of graphitizing carbon.

1. Introduction

Ferroalloy production is energy-intensive, consuming large amounts of both electricity and coke. Coke is used in this process to reduce metal oxides naturally present in ores to produce the base metal. Development of cost-effective, renewable reductants is environmentally desirable because global ferroalloy production releases about 55 Mt of CO_2 emissions annually [1]. Using carbon sources from renewable, plant-based feeds has potential to replace fossil-based reducing agents and effectively reduce CO_2 emissions. In recent years, much progress has been made on conversion of plant-based materials to carbonaceous char materials; some of these materials may have potential as reductants. However, metallurgical production continues to rely on fossil-based reductants due to limited knowledge of char properties, knowledge gaps in the conditions required to produce chars with acceptable reactivity, and high costs.

Ferroalloys are defined as iron-rich alloys which contain high proportions of Si, Mn, C, Cr, etc. which improve tensile strength, wear, corrosion resistance, and toughness [1]. Ferroalloys are produced in submerged-arc furnaces at temperatures > 1500 °C. Within the furnace, a three-phase electrode is inserted into a mixture consisting of metal oxide and carbonaceous reductants, typically metallurgical coke and coal [2]. The carbonaceous materials serve many roles, with the primary function being to reduce the metal oxide to form the base metal [3]. Additionally, the carbonaceous materials improve gas distribution during the reduction process, trap SiO gas, and enhance electrical resistance of the reaction mixture [4,5]. The most important properties of the carbonaceous reductant are high reactivity, high conversion, and low levels of impurities (such as sulphur and phosphorus) [6]. Low ash content is important, as each additional percent of ash in carbonaceous reductant increases slag volume by about 10–15 kg t^{-1} of ferroalloy, thereby increasing the electric power required for smelting [5].

In recent years, many studies investigated production and/or co-production of carbonaceous solids by pyrolysis treatment of wide variety of renewable feedstocks [3,5,7–11]. In comparison with the metallurgical coke traditionally used in ferroalloy production, carbon produced from renewable feedstocks contains less fixed carbon and a greater percentage of volatile components and may need to be

* Corresponding author.
E-mail address: anna.trubetskaya@nuigalway.ie (A. Trubetskaya).

https://doi.org/10.1016/j.fuel.2018.07.093
Received 8 June 2018; Received in revised form 14 July 2018; Accepted 20 July 2018
0016-2361/ © 2018 Elsevier Ltd. All rights reserved.

graphitized prior to use as a reductant [11]. Although different types of biomass can be converted into biochar, herbaceous biomass species are especially promising candidates for the use as carbonaceous reductants in ferroalloy industries because of their high growth rate and relative ease of harvest [7]. Despite these arguments in favor of herbaceous biochars, the majority of previous investigations have studied charcoals produced at temperatures < 1000 °C [12–18]. Thus, the effects of feedstock composition, treatment at temperatures greater than > 1250 °C, and residence time on the char reactivity and structure have not been studied in depth. In particular, herbaceous feedstocks contain high amounts of alkali metals which promote faster devolatilization rates and suppress tar formation, leading to higher char yields and higher CO_2/O_2 reactivity than charcoals produced from wood [19]. The high reactivity of biochar reductant may be advantageous in some cases within the ferroalloy industries. However, the use of a reductant more reactive than metallurgical coke may increase maintenance costs due to the decreased electrical conductivity [20,21]. Therefore, reductant reactivity becomes a key variable that must be understood in potential replacements for metallurgical coke. Likewise, the effect of residual alkali metal content in biochar produced from pyrolysis of herbaceous biomass must be considered. Previous studies report that nearly 50% of the potassium in the herbaceous biomass is released in the temperature range from 900–1250 °C, with residual potassium likely being present as counter ions in phenolate groups [22,23]. In addition, alkali metal ions (K^+ and Ca^{2+}) promote catalytic conversion of tars to small molecule products in a temperature range from 700 to 900 °C [24]. However, treatment at temperatures greater than 1250 °C will be required to produce graphitic or turbostratic carbons suitable as metallurgical coke, and the fate of potassium at these temperatures is not clear. In addition to knowledge gaps in reactivity and composition, the cost of biochar reductants is not competitive with metallurgical coke, in part due to low biochar yields. Previous studies have examined deposition of biooil and tar recycling to increase char yields and to decrease char reactivity [11,25]. For example, impregnating biooil within an existing char increased the total char yield with minimal effect on char microporosity and adsorption properties [26]. Similarly, deposition of biooil on biochar prior to pyrolysis promoted formation of oxygen-containing functional groups and transformation of small aromatic rings to larger aromatic rings [27]. However, literature data are scarce that describe the effect of biooil deposition on resulting char properties that impact metallurgical applications, adding uncertainty to the use of biooil impregnation as an approach to increase char yields and decrease char reactivity.

In summary, renewable feeds have potential as environmentally benign replacements to fossil-based reductants used in ferroalloys production, but knowledge of relationships between feedstock, operating conditions, and biochar properties is limited. In this study, the impacts of feedstock, heat treatment temperature (from 1600 to 2800 °C), residence time, and nanostructure on the CO_2/O_2 reactivity of woody and herbaceous biomass were investigated. The specific objectives of this study were to: (1) develop structure–property relationships governing the CO_2 and O_2 reactivity of biochar at high-temperatures, and (2) determine the treatment conditions and feedstock composition which decrease char reactivity to levels that are suitable for application in ferroalloy industries.

2. Materials and methods

Pinewood, beechwood, wheat straw, leached wheat straw and alfalfa straw were chosen for the fast pyrolysis study in a drop tube furnace (DTF). The low-ash containing wood (pinewood, beechwood) of syringyl (S) or guaiacyl-syringyl (GS) lignin types and herbaceous biomass (wheat straw, alfalfa straw) of hydroxy phenol-guaiacyl-syringyl (HGS) lignin type, which are rich in K, Ca and Si elements, were selected to investigate the effect of differences in ash composition and organic matter (cellulose, hemicellulose, lignin, extractives) on the char structure and reactivity. The wheat straw was leached in deionized water (room temperature) by continuous stirring for 12 h, followed by drying at 30 °C in an oven desiccator without any ventilation. Due to leaching of wheat straw, the metal content was reduced to ≈60% of the original value and the Cl, S, K, Na and P contents were strongly reduced. Char samples were generated in the drop tube reactor at 1250 °C, as described in detail by Trubetskaya et al. [28]. The temperature of 1250 °C that is the wall temperature of the DTF was selected to ensure the complete pyrolysis. The reactor consists of an alumina tube (internal diameter: 54 mm, heated length: 1.06 m) heated by four heating elements with independent temperature control. The experiments were conducted by feeding ≈5 g of biomass at a rate of 0.2 g min^{-1}. Both primary (0.18 l min^{-1} measured at 20 °C and 101.3 kPa) and secondary (4.8 l min^{-1} measured at 20 °C and 101.3 kPa) feed gases were N_2. The residence time of fuel particles was estimated to be about 1 s, taking into account density changes during pyrolysis. The char samples generated at 1250 °C were further heated up to 1300, 1600, 2400, and 2800 °C in high-temperature furnaces. The effect of residence time on the char properties was studied by keeping samples at 1300 or 1600 °C for 2 or 12 h.

Pinewood biooil was supplied by BTG BioLiquids. When used, 10 g of pinewood char mixed with 20 mL of biooil were stirred at 40 °C for 5 days and further reacted at 1600 °C in a high-temperature furnace. The CO_2 and O_2 reactivity of all char samples was investigated in a thermogravimetric analyzer. Reactivities of biomass chars and metallurgical coke were compared using reaction rates calculated from the derived kinetic parameters. TEM analysis and Raman spectroscopy were performed to characterize the effect of temperature, residence time, and feedstock on the char carbon chemistry and nanostructure.

2.1. Raw biomass characterization

The ultimate and proximate analysis of pinewood, beechwood, wheat straw, leached wheat straw, alfalfa straw, metallurgical coke and pinewood biooil is shown in Table 1.

The fuels were milled on a Retsch rotor mill RZ200 and sieved to a particle size fraction of 0.2–0.425 mm. The analysis of biomass constituents (cellulose, hemicellulose, acid-soluble lignin, acid-insoluble lignin, and extractives) was conducted according to NREL technical reports [29–31] and Thammasouk et al. [32], and shown in Table 2.

2.2. High-temperature furnace (1300–2400 °C)

The char samples were further treated in the high-temperature furnace LHTG 200–300/20-1G (Carbolite Gero, Germany), as shown in Fig. 1. The furnace can be operated at temperatures up to 1800 °C and at heating rates up to 20 °C min^{-1}. Prior to each experiment, 5 g of the char sample was loaded into the A_2O_3 crucible (Almath Crucibles Ltd, UK) placed in the graphite retort middle. Prior to pyrolysis, the furnace was repeatedly evacuated and purged by argon. The char sample was heated at 10 °C min^{-1} up to 1300 and 1600 °C and kept at that temperature for 2 h. The sample was cooled to room temperature at a rate of 20 °C min^{-1}. Another high-temperature furnace 200–300/30-1G (Carbolite Gero, Germany) was used to heat the char sample to 2400 °C. Samples were stored in sealed plastic containers.

2.3. High-temperature furnace (2800 °C)

The biochar was treated in a vacuum induction furnace (max. 60 kW, max. 10 kHz) with a chamber volume of 0.5 m^3, as shown in Fig. 2. The heating vessel consists of a three-part crucible with an outer alumina crucible (outer diameter: 130 mm, inner diameter: 110 mm, height: 300 mm), a middle carbon crucible (outer diameter: 90 mm, inner diameter: 50 mm, height: 145 mm) and an inner glass carbon crucible (outer diameter: 50 mm, inner diameter: 38 mm, height: 125 mm). The three-part crucible was positioned in an induction coil.

Table 1
Proximate and ultimate analysis.

Fuel	Pinewood	Beechwood	Wheat straw	Alfalfa straw	Leached wheat straw	Metallurgical coke	Pinewood biooil[a]
Proximate analysis							
Moisture, (wt.% as received)	5.1	4.5	5.5	5.2	4.3	0.6	25
Ash at 550 °C, (wt.% dry basis)	0.3	1.4	4.1	7.4	2.1	11.8	0.01
Volatiles, (wt.% dry basis)	86.6	79.4	77.5	75.9	82.2	3	-
HHV, (MJ kg^{-1})	21.6	20.2	18.8	19.7	19	27.9	18.5
LHV, (MJ kg^{-1})	20.2	19	17.5	16.9	17.2	27.8	16
Ultimate analysis, (wt.%, dry basis)							
C	53.1	50.7	46.6	42.5	46.2	85.6	46
H	6.5	5.9	6.1	6.7	6.8	0.3	7
N	0.06	0.13	0.6	0.3	0.05	1.8	0.01
O	40	41.9	42.5	43.1	44.8		47
S	< 0.01	0.01	0.1	0.03	0.02	0.5	0.01
Cl	0.01	0.02	0.1	0.5	0.01	0.03	0.003
Ash compositional analysis, (mg kg^{-1}, dry basis)							
Al	10	10	150	600	100	12000	550
Ca	600	2000	2500	12900	1300	6400	500
Fe	20	10	200	-	350	6300	200
K	200	3600	11000	28000	1200	1700	850
Mg	100	600	750	1400	350	1300	550
Na	30	100	150	1000	50	1100	200
P	6	150	550	1900	80	400	10
Si	50	200	8500	2000	6200	27000	1800
Ti	2	< 8	10	30	10	550	10

[a] Kinematic viscosity at 40 °C: 13 cSt; pH: 2.9; density: 1.2 kg lt^{-1}; solid content: 0.04%.

The gap between the alumina crucible and the carbon crucible was filled up with a carbon felt. A carbon felt disc (diameter: 110 mm, height: 30 mm) between the bottom of alumina and carbon crucibles was used for the high-temperature protection. The sample was placed in the glassy carbon crucible. The sample temperature was measured by a non-contact thermometer (Cyclops 100L 2F, LAND AMETEK) through a borosilicate glass tube (diameter: 180 mm, height: 20 mm) at the upper part of the vacuum chamber. The non-contact thermometer was calibrated against Pt, Al_2O_3, and Mo. Prior to the experiment, the chamber was evacuated and filled with argon. The chamber was continuously purged by argon at a defined flow rate of 10 l min^{-1}. The sample was heated at 3 °C s^{-1} up to 2800 °C and kept at that temperature for 2 h. The sample was cooled to room temperature at a heating rate of 30 °C min^{-1} and stored in sealed plastic containers.

2.4. Char analysis

2.4.1. Elemental analysis

The elemental analysis was performed on Analyser Series II (Perkin Elmer, USA). Acetanilide was used as a reference standard. The ash content was determined using a standard ash test at 550 °C, according to the procedure described in DIN EN 14775.

2.4.2. Thermogravimetric analysis

The char samples were crushed to a fine powder in a mortar with a ceramic pestle. The reactivity of char was analyzed by exposing samples to a reactive gas consisting of 40% volume fraction CO_2 and 5% volume fraction O_2 in a thermogravimetric instrument Q600 (TA Instrument, USA). In each experiment, 4 mg of sample were loaded into an Al_2O_3 crucible and heated from 30 to 1500 °C in CO_2 at a constant heating rate of 10 °C min^{-1}. The kinetic parameters of char samples were derived by the integral method presented by Coats and Redfern [33]. Through integral transformation and mathematical approximation, the linear equation was expressed in the form:

$$ln\left(-\frac{ln(1-X)}{T^2}\right) = ln\left(\frac{A\cdot R}{\kappa\cdot E_a}\right) - \frac{E_a}{R\cdot T} \quad (1)$$

In Eq. (1), κ is the heating rate and R is the gas constant. A plot of ln(-ln (1-X) T^{-2}) versus T^{-1} gives a straight line whose slope and intercept determine the values of the activation energy (E_a) and pre-exponential factor (A). The reactivities of char samples were compared using reaction rates calculated from the derived kinetic parameters (A and E_a) at a fixed gasification temperature of 1000 °C.

2.4.3. Raman spectroscopy

Raman spectroscopy was performed using an inVia Raman microscope (Renishaw, UK) operating with a 514 nm laser line at a power of 30 mW. The measurements were performed in static mode with a center at 1600 cm^{-1}, resulting in a 960–2200 cm^{-1} spectral region. The laser power was set to 100% in the software and roughly 30% in the

Table 2
Lignocellulosic composition of woody and herbaceous biomass.

Biomass	Cellulose	Hemicellulose	Lignin		Extractives	Protein
			acid insoluble	acid soluble		
Pinewood	38.3	17.8	29.6	1.8	8.8*	0.6
Beechwood	35	19.2	32	1.5	7.5*	1.9
Wheat straw	35.9	18	19.2	6.5	10.1**	6.3
Leached wheat straw	32.1	23.5	13.8	2	13.3**.	1.3
Alfalfa straw	18.8	12	14.7	6.8	39.6**	5.1

* Acetone extraction.
** Ethanol–water extraction (room temperature).

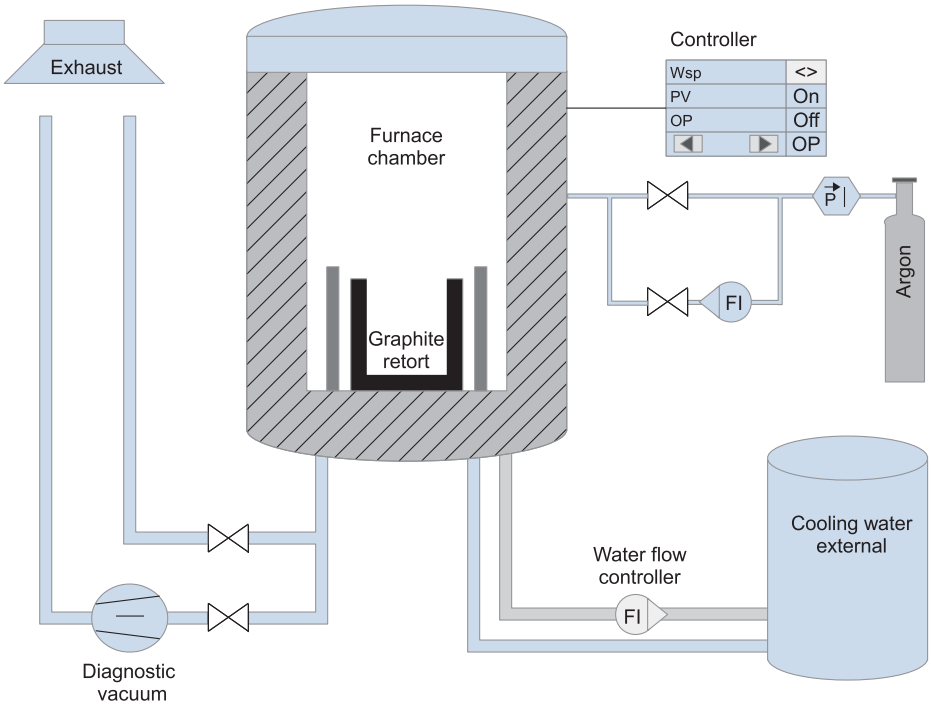

Fig. 1. High-temperature furnace at University of Agder.

hardware by using a filter. 1 s exposure time was used in normal confocality mode. A 20x lens and 8–15 µm step size (X and Y directions) was used for mapping, to generate 100–200 spectra/image for each char sample. Cosmic rays were removed and the data was subjected to multivariate noise filtering using the WiRE chemometrics package version 3.0 (Renishaw, UK). Spectra were saved as text files and processed via the free, open-source MatLab script provided by the Vibrational Spectroscopy Core Facility at Umeå University (www.kbc.umu.se/english/visp/download-visp/). The following parameters were used for spectra pre-processing: asymmetrical least squares baseline correction with lambda = 20,000,000 and p = 0.001 [34]; Savitzky-Golay smoothing with the first polynomial order and frame rate of 3 [35]. Spectra were total area normalized in the entire spectral range. The corrected spectra from each mapping were then averaged to create a final composite curve for the peak deconvolution. No spectral scaling was performed. Deconvolution of the Raman spectra was conducted using the peak fit pro tool in the OriginPro software (OriginLab, USA) by combination of seven Gaussian-shaped bands (D_4, D_3, D, D_2, D_5, G, and D_6) following Sadezky et al. [36]. The mean crystal size in the *a*-direction (L_a) with the fitting constants $C_0 = -12.6$ nm and $C_1 = 0.033$, which are valid for the laser wavelength from 400 to 700 nm, is given by [37]:

$$L_a = \frac{C_0 + C_1 \lambda_L}{A_D / A_G} \quad (2)$$

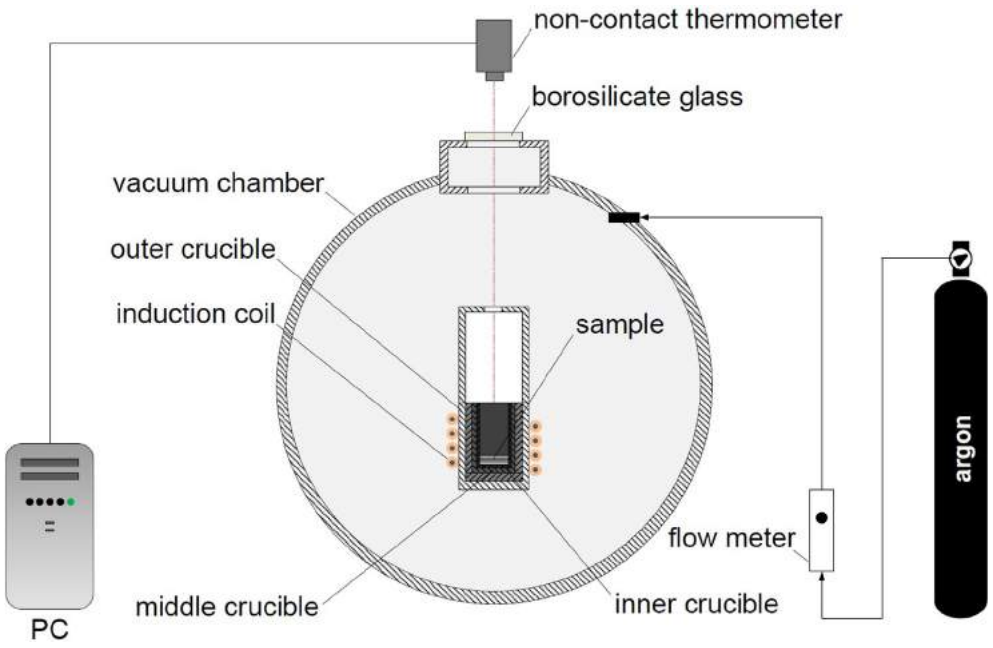

Fig. 2. High-temperature furnace at University of Duisburg-Essen.

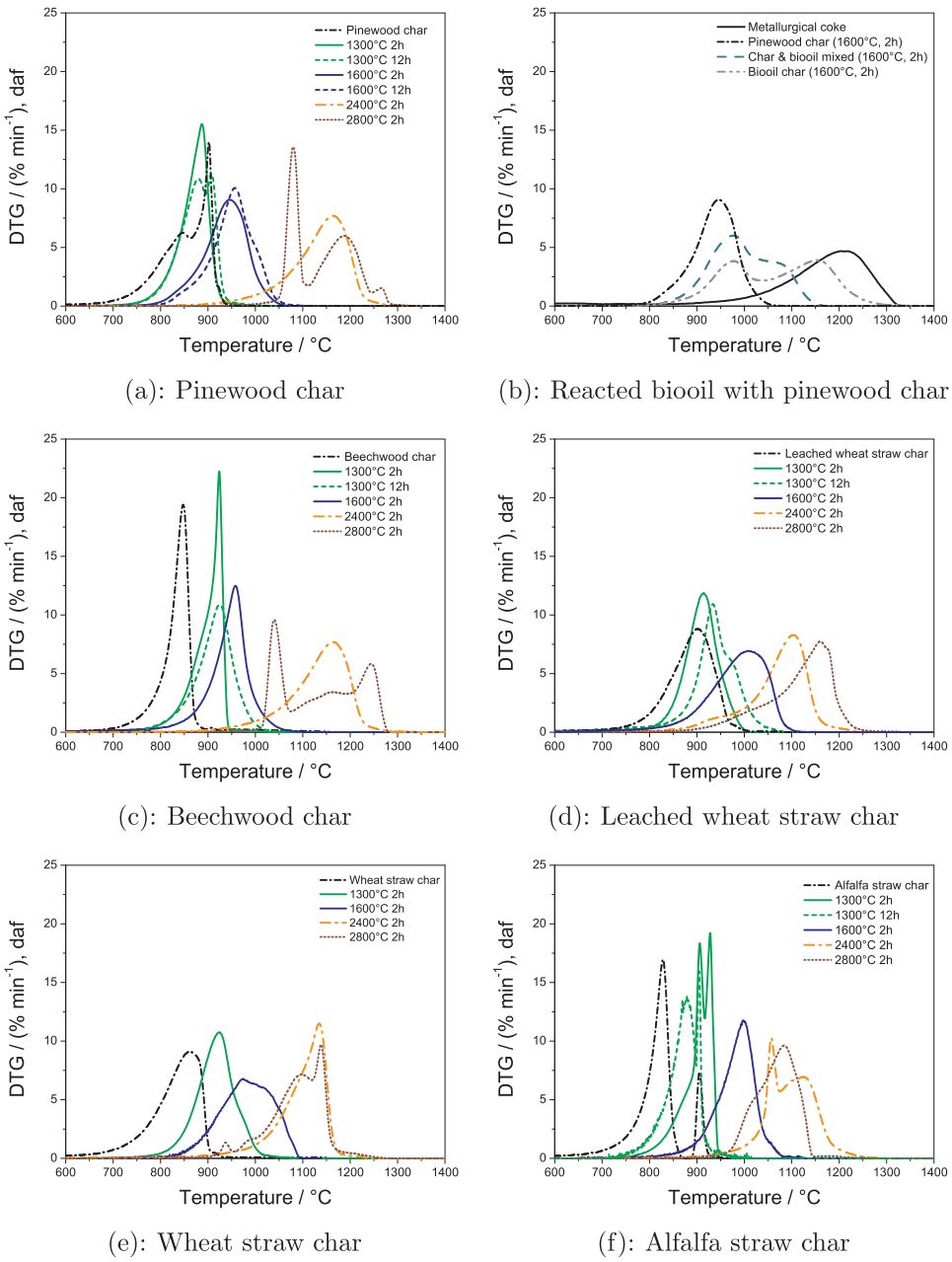

Fig. 3. (a), (c)–(f) DTG curves of pinewood, beechwood, leached wheat straw, wheat straw, alfalfa straw char from pyrolysis at 1300, 1600, 2400, and 2800 °C for 2 and 12 h and (b) DTG curves of pinewood char, co-pyrolysis of pinewood char with biooil at 1600 °C for 2 h, biooil char from pyrolysis at 1600 °C for 2 h, and metallurgical coke reacted in 40% volume fraction CO_2 + 60% volume fraction N_2.

2.4.4. Transmission electron microscopy

Prior to microscopy, char samples were held at 350 °C for 6 h in a thermogravimetric instrument to devolatize the samples. Samples were ground in a mortar to ensure a homogeneous particle distribution, sonified in deionized water for 30 min, wet dispersed on a lacey carbon copper grid and dried at room temperature for 20 min. Char nanostructure was studied using a Jeol 2200 fs operated at 200 keV, equipped with an Oxford Instruments X-Max SDD EDS detector. The curvature of a single graphene sheet is defined in Eq. (3):

$$Curvature = \frac{Length}{Fiber\ length} \quad (3)$$

The length is a straight line that connects both ends of a graphene sheet. The fiber length is the contour or arc length, as shown in the Supplemental Material (Fig. S-1). Both length and fiber length were estimated by Gatan Digital Micrograph software according to the method of Müller et al. [38]. Portions of the image with visible graphene layers were magnified to a size of 10 nm × 10 nm, and both length and fiber length were manually determined by the software ruler which draws a straight or contour line to connect both ends of a graphene sheet.

3. Results

3.1. Char reactivity

Fig. 3 shows differential weight loss curves (DTG) for CO_2 gasification (40% by volume) of wood and herbaceous biomass char samples, metallurgical coke, biooil char, and the reacted mixture of biooil with pinewood char at 1600 °C. Depending on the sample, the DTG curves show both either a single broad peak or a double peak, both of which

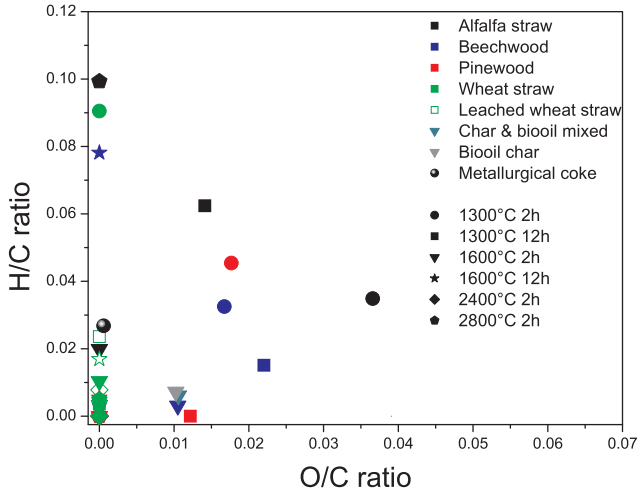

Fig. 4. Van Krevelen plot of pinewood, beechwood, leached wheat straw, wheat straw, and alfalfa straw chars from pyrolysis at 1300 and 1600 for 2 and 12 h, 2400 and 2800 °C for 2 h, metallurgical coke, biooil char and mixed biooil with pinewood char reacted at 1600 °C for 2 h.

indicate a heterogeneous char mixture with respect to reactivity [39,40]. The maximal reaction rates of chars produced in the drop-tube furnace varied significantly from 800 to 900 °C, whereas the wheat and alfalfa straw chars were more reactive than the pinewood, beechwood, and leached wheat straw chars [41]. In contrast, CO_2 gasification of all char samples from pyrolysis at 1300 °C for 2 and 12 h took place at nearly the same temperature range from 700 to 1050 °C. The maximum rate of all chars treated at 1600 °C in the CO_2 was about 100 °C greater than that of char samples from pyrolysis at 1300 °C, confirming the previous results of Trubetskaya [42]. The reactivities of chars from pyrolysis at 2400 and 2800 °C were nearly identical. Similar tendencies were observed for the oxidation reactivity of char, as shown in the Supplemental Material (Fig. S-2). The pinewood, beechwood and wheat straw chars obtained from pyrolysis at 2800 °C exhibited a triple peak, indicating the development of three main components: a reactive carbon constituent, a carbon constituent with intermediate reactivity, and a less reactive carbon structure with reactivity that approaches that of commercial graphite and metallurgical coke. The reactivity of metallurgical coke was similar to that of pinewood char from pyrolysis 2800 °C. The results show that differences in heat treatment temperature have more influence on char reactivity than the residence time and feedstock composition, and will be discussed below.

Fig. 3b shows that the maximum reaction rate of biooil char obtained from pyrolysis at 1600 °C was about 100 °C greater than that of pinewood char reacted under the same operating conditions, based on the kinetic parameters in the Supplemental Material (Table S-4). Additional heat treatment of mixed biooil with pinewood char at 1600 °C decreased the CO_2 reactivity. The results showed that the maximal CO_2 gasification rate of reacted biooil and pinewood char was about 50 °C lower than of metallurgical coke, emphasizing the importance of biooil addition on the char reactivity.

3.2. Elemental analysis

Fig. 4 shows a Van Krevelen plot of char derived from wood and herbaceous biomass, metallurgical coke, biooil char, and mixed biooil with pinewood char. The results contained in Fig. 4 indicate that the oxygen content in all char samples decreases with the higher heat treatment temperature. The alfalfa straw char obtained from pyrolysis at 1300 °C contained less carbon and more oxygen than chars obtained from other feedstocks. Interestingly, the elemental composition of all char samples obtained from pyrolysis at 2400 and 2800 °C was comparable to the composition of metallurgical coke.

3.3. Nanostructure

The nanostructure of pinewood char treated at 1300 and 1600 °C for 2 and 12 h, 2400 and 2800 °C for 2 h was studied by TEM, as shown in Fig. 5. The pinewood char exhibited a common structure of amorphous carbon at 1300 °C, whereas a mixture of amorphous carbon and nano-crystalline graphite was observed at 1600 °C. The graphene layers of pinewood char from pyrolysis at 1600 °C for 12 h and 2400 °C for 2 h were arranged in onion rings and straight ribbon structures. With increasing residence time, the onion-like carbon structures becomes more prevalent. Increasing the heat treatment temperature up to 2800 °C led to the gradual elongation of graphene-like layers and an increased number of graphene segments in the stacks, as shown in Fig. 5f. The pinewood char reacted at 2800 °C formed a nanostructure similar to a crystalline carbon membrane [43]. The bent graphene segments of graphitized char contain carbon with hexagonal graphene segments [44] and a mean separation distance of 0.33 nm that indicates the highest degree of graphitization (graphite spacing ≈0.335 nm) [45]. The pinewood char generated at 1600 and 2400 °C had a less ordered structure with mean separation distance of 0.35 nm. The differences in the nanostructure of pinewood chars generated at 1600 and 2800 °C suggest that heat treatment temperature influences char properties. The long residence time of 12 h at 1600 °C led to the formation of ring graphitic structures in pyrolysis of pinewood and beechwood char, as shown in Fig. 5d and Supplemental Material (Fig. S-21(c)). Less ordered, straight graphitic structures were formed at shorter residence times in high-temperature pyrolysis. Fig. 6 shows that the biooil char consisted of an amorphous carbon structure, whereas the reacted pinewood char with biooil contained a mixture of amorphous carbon and nano-crystalline graphite structures. The nanostructure of reacted pinewood char and biooil consists of nano-crystalline graphite with 30–50 layers of straight graphene segments. Fig. 7 shows the differences in nanostructure of beechwood, leached wheat straw, wheat straw and alfalfa straw chars obtained from pyrolysis at 2800 °C.

High heat treatment temperature of pinewood and beechwood chars led to the formation of nano-crystalline graphite with more than 100 layers of straight graphene segments arranged in an interconnected ribbon-like geometry [46]. The leached wheat straw char showed a well-ordered graphitic structure at 1300 °C, whereas the wheat straw char exhibited a similar graphitic structure at 2400 °C, as shown in the Supplemental Material (Fig. S-22).

Differences in carbon structure suggest that leaching of original wheat straw has an influence on the char properties, when the material is treated at temperatures ranging from 1300 to 1600 °C. However, Fig. 7b and c show that leaching does not affect the char nanostructure at 2800 °C, suggesting that temperature becomes the dominant variable at these conditions.

Both non-treated wheat straw and leached wheat straw chars contained a mixture of an amorphous carbon and a nano-crystalline graphite that was arranged in onion ring structures, similar to the pristine wood and lignin chars [47,48]. The alfalfa straw char contained a large number of pores up to around 10 nm long and 5–10 layers thick. The alfalfa straw char structure is mainly composed of curved and faceted nano-crystallites, similar to glassy carbon [49]. The wood chars exhibited a well-ordered graphitic structure, whereas the nanostructure of alfalfa straw char was more porous, containing random fragments with 30–50 layers of straight and long graphene segments.

3.4. Raman spectroscopy

Raman spectroscopy was carried out to examine primary differences in the carbon structure of char samples, as shown in the Supplemental Material (Figs. S-15–S-20). Based on estimated A_D/A_G ratios, all samples exhibited a common structure of amorphous carbon and nano-crystalline graphite, as discussed by Ferrari and Robertson [50]. Pyrolysis at 1300 and 1600 °C resulted in a less graphitic char structure (A_D/A_G: 1.1–2.5)

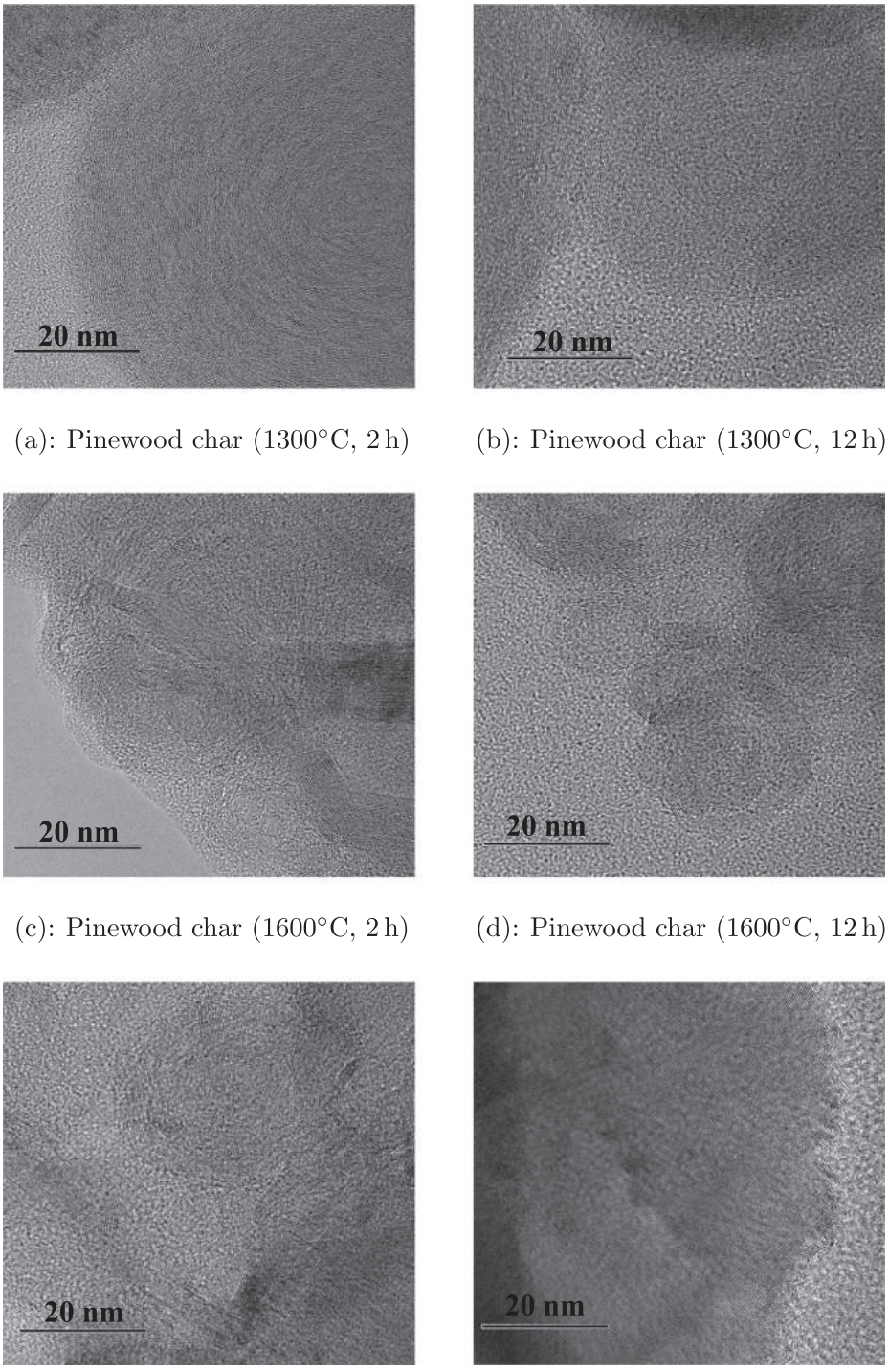

(a): Pinewood char (1300°C, 2 h) (b): Pinewood char (1300°C, 12 h)

(c): Pinewood char (1600°C, 2 h) (d): Pinewood char (1600°C, 12 h)

(e): Pinewood char (2400°C, 2 h) (f): Pinewood char (2800°C, 2h)

Fig. 5. TEM images of pinewood char reacted at 1300 °C and 1600 °C for 2 and 12 h, 2400 and 2800 °C for 2 h.

than pyrolysis at 2400 and 2800 °C (A_D/A_G: 0.4–0.9). The A_D/A_G ratios of pinewood and leached wheat straw chars reacted for 2 or 12 h varied only slightly at 1300 and 1600 °C, indicating that the residence time had less influence on the char graphitization than the heat treatment temperature. The biooil char obtained a similar structure to pinewood char and mixed biooil with pinewood char reacted at 1600 °C for 2 h with the A_D/A_G ratio of 1.1. The average extension of graphene layers (L_a) in the char reacted at 1300 and 1600 °C (2.2–4 nm) was less than those in chars from pyrolysis at 2400 and 2800 °C (4.8–10.9 nm). The size of one aromatic ring is 0.25 nm [51], and therefore, the size of PAHs in the char (1300–1600 °C) is equivalent to approximately 9–16 aromatic rings and at higher temperatures the amount of aromatic rings increases up to 19–44. The average extension of graphene stacks (L_a) in char samples obtained from pyrolysis at 1300–1600 °C was quantitatively similar to that of commercial carbon black (Printex XE2: 2.5 nm; Vulcan XC72: 2 nm; Printex L: 1.4 nm). Treatment at higher temperatures led to the formation of more graphitic char structure with an average extension similar to graphite (5.6 nm) [52].

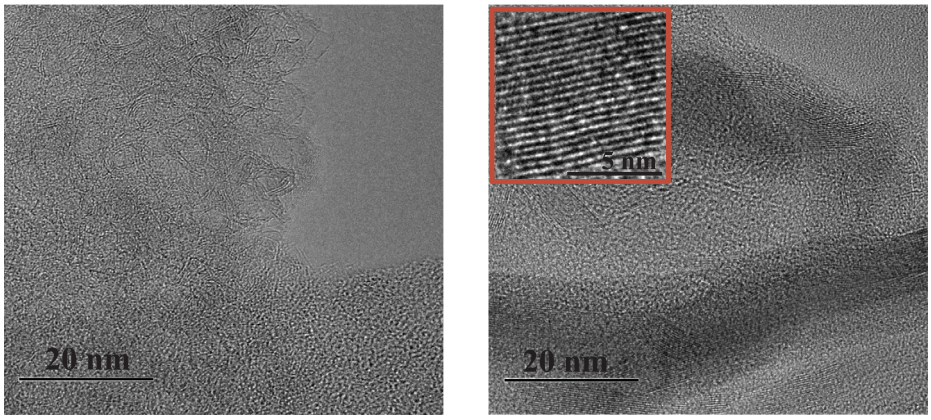

(a): Biooil char (b): Reacted pine char with biooil

Fig. 6. TEM images of pyrolyzed biooil and mixed pinewood char with biooil reacted at 1600 °C for 2 h. In Fig. 6b the nano-crystalline graphitic structure is enlarged in the red rectangle.

4. Discussion

Thermogravimetric experiments showed that heat treatment temperature exerted greater influence on the intrinsic reactivity of char samples than either residence time or feedstock origin. In principle, the reactivity of char can be affected by differences in ash composition, residence time, carbon chemistry, nanostructure, and heat treatment temperature. The ash content of native wheat straw (4.1 wt.%) was 20 times higher than that of native pinewood (0.3 wt.%). Thus, based on ash content alone it might be expected that wheat straw char should be more reactive than the pinewood char. However, differences in reactivity were observed only for chars reacted in the drop tube furnace,

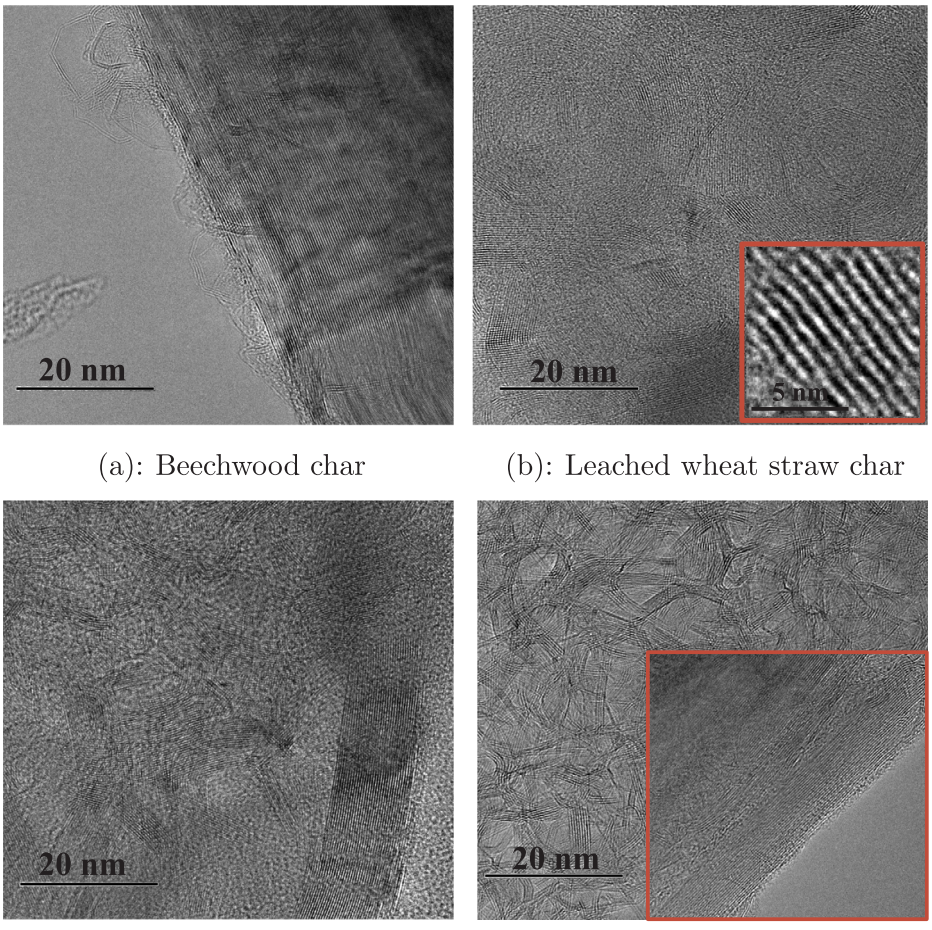

(a): Beechwood char (b): Leached wheat straw char

(c): Wheat straw char (d): Alfalfa straw char

Fig. 7. TEM images of beechwood, leached wheat straw, wheat straw, and alfalfa straw char reacted at 2800 °C for 2 h. In Fig. 7b and d the nano-crystalline graphitic structure is shown in the red rectangle.

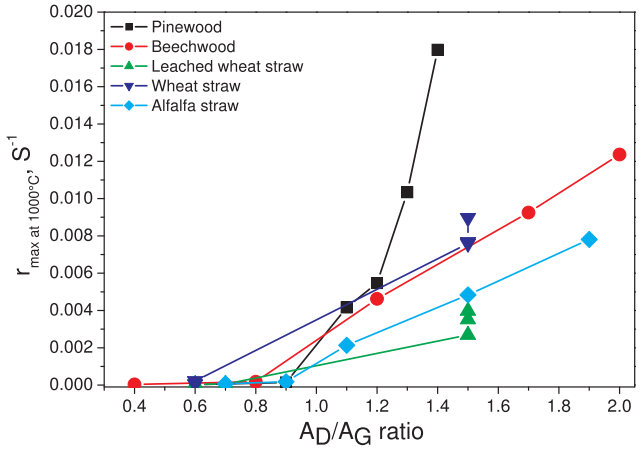

Fig. 8. Maximal reaction rate at 1000 °C (results from Tables S-4–S-6) during CO_2 gasification versus A_D/A_G ratio of pinewood, beechwood, leached wheat straw, wheat straw, alfalfa straw chars from pyrolysis at 1300, 1600, 2400, and 2800 °C for 2 or 12 h (results from Figs. S-15–S-20).

whereas the reactivities of all chars remained similar at both temperatures (1300 or 1600 °C) reacted for 2 and 12 h. This indicates that neither ash composition nor residence time has a strong influence on the observed differences in char reactivity.

Heat treatment temperature, carbon chemistry, and nanostructure of char samples were the main factors influencing the reactivity during CO_2 gasification and oxidation. Raman spectroscopy results showed that all char samples obtained from pyrolysis at 1300 and 1600 °C for 2 and 12 h exhibited a structure similar to carbon black based on their comparable A_D/A_G ratios (1.7–2.6). Treatment at higher heat treatment temperatures decreased the integrated peak area ratios to lower values (0.4–0.9) due to the effects of increasing carbon graphitization. Previous studies showed that low separation distances (close to that of graphite) and high periodicity lead to lower oxidation of carbon materials, while the more bent graphene layers might enhance the reactivity [53,54]. The char samples exhibit shorter and less curved graphene layers and less recognizable crystalline structure than coal char, indicating either higher porosity or larger fraction of amorphous carbon [55,56]. This indicates that biomass chars might consist of non-graphitizing carbons [57,58]. The present results showed that the graphitization of all char samples increases significantly with increasing heat treatment temperature, whereas the CO_2 and O_2 reactivity decreases. The TEM analysis showed that the mean separation distance of graphene segments of chars from pyrolysis at 2400 and 2800 °C was similar to graphite (0.335 nm), whereas char samples reacted at 1300 and 1600 °C mostly contained an amorphous carbon with a minority component of nano-crystalline graphite. The short graphene layers of chars from pyrolysis at 1300 and 1600 °C were associated with higher CO_2 and O_2 reactivity, whereas straight and long graphene segments, which are arranged in more than 100 layers in the char samples from higher temperature pyrolysis, decreased the char reactivity. The results indicated that the composition of original feedstock has an influence on the formation of nano-crystalline carbon in char samples. The nanostructure of alfalfa straw char obtained from pyrolysis at 2800 °C was less graphitic and more porous with 30–50 layers of graphene segments than the pinewood char. The long and straight graphene layers of alfalfa straw char at 2800 °C suggest that an increase in heat treatment temperature might lead to further char graphitization and formation of additional graphene segments, as shown in Fig. 7d. Both pinewood and beechwood chars contained a nano-crystalline graphite with more than 100 layers of straight graphene segments, forming a continuous surface merged with the small fraction of remaining amorphous carbon. The TEM results showed that both woody and herbaceous biomass chars most likely exhibit a graphitizing carbon structure, based on the comparison with the carbon structures proposed by Franklin [55].

The pinewood char obtained from pyrolysis at 1600 °C was 59 times more reactive than metallurgical coke in CO_2 gasification. The pyrolysis of biooil led to the formation of less reactive char than pinewood char under similar operating conditions, but still more reactive than metallurgical coke by factor of 27. The reaction rate of the biooil and pinewood char mixture reacted at 1600 °C was 15 times greater than that of metallurgical coke, consistent with previous results of Veksha et al. [26]. According to previous reports, the addition of biooil to the pinewood char leads to the formation of carbon deposits during pyrolysis [59,60]. Thermal decomposition generates H/O/OH radicals that penetrate deep into the char structure, promoting condensation reactions between the PAH rings, forming small ring structures (3–5 fused rings), and later transforming into larger PAH compounds [61,62]. Carbon deposits consisting of large PAH compounds are difficult to be cleaved during CO_2 gasification, decreasing the char reactivity as observed here and elsewhere [27]. This indicates that both heat treatment temperature and addition of biooil decrease CO_2 gasification reactivity. The elemental composition of metallurgical coke and chars obtained from pyrolysis at 2400 and 2800 °C was similar, yielding pinewood char with reactivity comparable to metallurgical coke. This emphasizes that heat treatment temperature is the most important factor determining CO_2 gasification reactivity. The reaction rates of all char samples treated at 2400 and 2800 °C were of the same order of magnitude in CO_2 gasification due to the extent of graphitization of char structure. Raman data were examined to understand the relationship between char reactivity and structure. As shown in Fig. 8, the A_D/A_G ratios estimated from Raman spectroscopy were correlated with the CO_2 gasification reactivity.

Ragardless of source, A_D/A_G ratios are greater than 1 and reactivity is greater than $0.002\,s^{-1}$ for samples treated at temperatures < 2400 °C. For A_D/A_G ratios greater than 1, the relationship between A_D/A_G ratios and reactivity is weak, with feedstock showing a clear impact on reactivity. On the other hand, pyrolysis of all tested materials at temperatures > 2400 °C leads to A_D/A_G ratios less than 1 (0.4–0.9) and reactivity less than $0.002\,s^{-1}$. This result clearly demonstrates that heat treatment temperature becomes the dominating factor governing reactivity when it is greater than 2400 °C, with chars obtained from all sources approaching a similar graphitic structure.

5. Conclusion

Various types of biomass were converted into renewable carbonaceous solids by pyrolysis treatment. The resulting materials were studied for reactivity and structure. Thermogravimetric analysis results showed that the CO_2 and O_2 char reactivities depend mainly on heat treatment temperature, and less on the ash composition of the original feedstocks and residence time. Differences in reactivity were ascribed in part to differences in char nanostructure, as evaluated by Raman spectroscopy. Treatment of biochar samples at temperatures greater than 1300 °C clearly showed that residual alkali metals have significantly less catalytic influence on char properties than observed at treatment temperatures less than 1300 °C. Under properly selected treatment conditions (e.g. > 2400 °C), chars can be produced from renewable sources with reactivity approaching that of fossil-based metallurgical coke. Co-pyrolysis of biomass with biooil also shows promise for producing carbons with reactivity comparable to metallurgical coke. The findings of this study emphasize the potential use of biocarbon-based reductants in the ferroalloy industries, with concomitant reduction in CO_2 emissions.

Acknowledgements

The authors gratefully acknowledge financial support from the Björn Wahlströms, Kempe Foundation, and Jernkontoret Stiftelsen. M.T. Timko thanks the U.S. National Science Foundation (Grant CBET-

1605916). The authors acknowledge the facilities and technical support of Dr. Andras Gorzsas and Dr. Markus Broström at Umeå University. The German Federal Government, Federal State of Nordrhein-Westfalen, Deutsche Forschungsgemeinschaft (DFG) are acknowledged for their contribution toward the establishment of the Interdisciplinary Center for Analytics on the Nanoscale in the University of Duisburg-Essen. BTG Bioliquids in Netherlands is acknowledged for the pinewood biooil supply. Professor Manuel Garcia-Perez is acknowledged for the many fruitful discussions.

Appendix A. Supplementary data

Supplementary data associated with this article can be found, in the online version, athttps://doi.org/10.1016/j.fuel.2018.07.093.

References

[1] Holappa L. Towards sustainability in ferroalloy production. J South African Inst Min Metal 2010;110(12):1–8.
[2] Liu J, Chen Z, Ma W, Wei K, Ding W. Application of a waste carbon material as the carbonaceous reductant during silicon production. Silicon 2018:1–9.
[3] Monsen B, Tangstad M, Midtgaard H, Use of charcoal in silicomanganese production, 10th Int Ferroalloys Congress INFACON X. Transformation through Technology 68 (2004) 155–64.
[4] Raanes O, Kolbeinsen L, Byberg JA. Statistical analysis of properties for coals used in the production of silicon rich alloys, 8th Int Ferroalloys Congress INFACON X. Transformation through Technology (1998) 116–20.
[5] Sahajwalla V, Dubikova M, Khanna R. Reductant characterisation and selection: implications for ferroalloys processing, 10th Int Ferroalloys Congress INFACON X. Transformation through Technology 68 (2004) 351–62.
[6] Pistorius PC. Reductant selection in ferro-alloy production: The case for the importance of dissolution in the metal. J South African Inst Min Met 2002;1:33–6.
[7] Yoshida T, Turn SQ, Russell SY, Antal MJ. Banagrass vs Eucalyptus Wood as Feedstocks for Metallurgical Biocarbon. Ind Eng Chem Res 2008;47:9882–8.
[8] Lundgren M. Blast Furnace Coke Properties and the Influence on Off-gas Dust Licentiate thesis Luleå University of Technology; 2010.
[9] Wesenbeeck SV, Wang L, Ronsse F, Prins W, Skreiberg Ø. Charcoal Mines in the Norwegian Woods. Energy Fuels 2016;30:7959–70.
[10] Wiklund CM, Pettersson F, Saxen H. Optimal resource allocation in integrated steelmaking with biomass as auxiliary reductant in the blast furnace. ISIJ Int 2012;52(1):35–44.
[11] Suopajärvi H. Bioreducer use in blast furnace ironmaking in Finland PhD thesis University of Oulu; 2014.
[12] Antal MJ, Grnli M. The art, science, and technology of charcoal production. Ind Eng Chem Res 2003;42:1619–40.
[13] Bourke J, Manley-Harris M, Fushimi C, Dowaki K, Nunoura T, Antal MJ. Do All Charcoals Have the Same Chemical Structure? 2. A Model of the Chemical Structure of Carbonized Charcoal. Ind Eng Chem Res 2007;46(18):5954–67.
[14] Griessacher T, Antrekowitsch J, Steinlechner S. Charcoal from agricultural residues as alternative reducing agent in metal recycling. Biomass Bioenergy 2012;39:139–46.
[15] Wang L, Skreiberg Ø, Grønli M, Specht GP, Antal MJ. Is elevated pressure required to achieve fixed-carbon yield of charcoal from biomass? Part 2. The importance of particle size. Energy Fuels 2013;27:2146–56.
[16] Brewer CE, Chuang VJ, Masiello CA, Gonnermann H, Gao X, Dugan B, et al. New approaches to measuring biochar density and porosity. Biomass Bioenergy 2014;66:176–85.
[17] Zeng K, Minh DP, Gauthier D, Weiss-Hortala E, Nzihou A, Flamant G. The effect of temperature and heating rate on char properties obtained from solar pyrolysis of beechwood. Biores Tech 2015;182:114–9.
[18] Smith MW, Dallmeyer I, Johnson TJ, Brauer CS, McEwen JS, Espinal JF, et al. Structural analysis of char by Raman spectroscopy: Improving band assignments through computational calculations from first principles. Carbon 2016;100:678–92.
[19] Niksa S. Predicting the rapid devolatilization of diverse forms of biomass with bio-Flashchain. Proc Combust Inst 2000;28(2):2727–33.
[20] Yamagishi K, Endo K, Saga J. A comprehensive analysis of the furnace interior for high-carbon ferrochromium, 1th Int Ferroalloys Congress INFACON 74. Transformation through Technology (1974) 143–47.
[21] De Waal A, Barker IJ, Rennie MS, Klopper J, Groeneveld BS. Electrical Factors Affecting the Economic Optimization of Submerged-arc Furnaces, 6th Int Ferroalloys Congress INFACON 6. Transformation through Technology 1 (1974) 247–52.
[22] Zhao Y, Feng D, Zhang Y, Huang Y, Sun S. Effect of pyrolysis temperature on char structure and chemical speciation of alkali and alkaline earth metallic species in biochar. Fuel Process Tech 2016;141:54–60.
[23] Trubetskaya A, Hofmann Larsen F, Shchukarev A, Ståhl K, Umeki K. Potassium and soot interaction in fast biomass pyrolysis at high temperatures. Fuel 2018;225:89–94.
[24] Feng D, Zhao Y, Zhang Y, Sun S. Catalytic effects of ion-exchangeable K^+ and Ca^+ on rice husk pyrolysis behavior and its gas-liquid-solid product properties. Energy 2018;152:166–77.
[25] Huang Y, Kudo S, Norinaga K, Amaike M, Hayashi I. Selective production of light oil by biomass pyrolysis with feedstock -mediated recycling of heavy oil. Energy Fuels 2012;26(1):256–64.
[26] Veksha A, McLaughlin H, Layzell DB, Hill JM. Pyrolysis of wood to biochar: Increasing yield while maintaining microporosity. Biores Tech 2014;153:173–9.
[27] Feng D, Zhao Y, Sun S. Effects of H_2O and CO_2 on the homogeneous conversion and heterogeneous reforming of biomass tar over biochar. Int J Hydrogen Energy 2017;42:13070–84.
[28] Trubetskaya A, Brown A, Tompsett GA, Timko MT, Umeki K, Kling J, et al. Characterization and reactivity of soot from fast pyrolysis of lignocellulosic compounds and monolignols. Appl Energy 2018;212:1489–500.
[29] Sluiter A, Hames B, Ruiz R, Scarlata C, Sluiter J, Templeton D, et al. Determination of Structural Carbohydrates and Lignin in Biomass. Golden (CO): National Renewable Energy Laboratory; 2011 July Report No. NREL/TP-510-42618. Contract No.: DE-AC36-08-GO28308.
[30] Willför S, Hemming J, Leppänen AS, Analysis of extractives in different pulps - Method development, evaluation, and recommendations. Finland: Abo Akademi University, Laboratory of Wood and Paper Chemistry; 2004–2009 Report No. B1 of the EU COST E41 action Analytical tools with applications for wood and pulping chemistry.
[31] Hames B, Ruiz R, Scarlata C, Sluiter J, Sluiter A, Preparation of Samples for Compositional Analysis. Golden (CO): National Renewable Energy Laboratory; 2011 June Report No. NREL/TP-510-42620. Contract No.: DE-AC36-99-GO10337.
[32] Thammasouk K, Tandjo D, Penner MH. Influence of extractives on the analysis of herbaceous biomass. J Agric Food Chem 1997;45:437–43.
[33] Coats AW, Redfern JP. Kinetic parameters from thermogravimetric data. Nature 1964;201:68–9.
[34] Eilers PHC. Parametric time WarpIng. Analyt Chem 2004;76(2):404–11.
[35] Savitzky A, Golay MJE. Smoothing and differentiation of data by simplified least squares procedures. Analyt Chem 1964;36(8):1627–39.
[36] Sadezky A, Muckenhuber H, Grothe H, Niessner R, Pöschl U. Raman spectroscopy of soot and related carbonaceous materials: Spectral analysis and structural information. Carbon 2005;43:1731–42.
[37] Matthews MJ, Pimenta MA, Dresselhaus G. Origin of dispersive effects of the Raman D band in carbon materials. Phys Rev B 1999;59(10):R6585–8.
[38] Müller JO, Su DS, Wild U, Schlögl R. Bulk and surface structural investigations of diesel engine soot and carbon black. Phys Chem Chem Phys 2007;9:4018–25.
[39] Zolin A. Reactivity of solid fuels PhD thesis Technical University of Denmark; 2001.
[40] Meszaros E, Jakab E, Varhegyi G, Bourke J, Manley-Harris M, Nunoura T, et al. Do All Carbonized Charcoals Have the Same Chemical Structure? 1. Implications of Thermogravimetry – Mass Spectrometry Measurements. Ind Eng Chem Res 2007;46(18):5943–53.
[41] Trubetskaya A, Jensen PA, Jensen AD, Steibel M, Spliethoff H, Glarborg P, et al. Comparison of the high temperature chars of wheat straw and rice husk with respect to chemistry, morphology and reactivity. Biomass Bioenergy 2016;86:76–87.
[42] Trubetskaya A. Fast pyrolysis of biomass at high temperatures PhD thesis Technical University of Denmark; 2016.
[43] Wollbrink A, Volgmann K, Koch J, Kanthasamy K, Tegenkamp C, Li Y, et al. Amorphous, turbostratic and crystalline carbon membranes with hydrogen selectivity. Carbon 2016;106:93–105.
[44] Welz S, McNallan MJ, Gogotsi Y. Carbon structures in silicon carbide derived carbon. J Mat Proc Tech 2006;179:11–22.
[45] Zhang ZL, Brydson R, Aslam Z, Reddy S, Brown A, Westwood A, et al. Investigating the structure of non-graphitising carbons using electron energy loss spectroscopy in the transmission electron microscope. Carbon 2011;49:5049–63.
[46] Jenkins GM, Kawamura K. Polymeric carbons – carbon fibre, glass and char. Cambridge University Press; 1976.
[47] Dufour A, Celzard A, Fierro V, Broust F, Courson C, Zoulalian A. Catalytic conversion of methane over a biomass char for hydrogen production: deactivation and regeneration by steam gasification. Appl Cat A: General 2015;490:170–80.
[48] Li Y, Hu YS, Chen L, Li H, Huang X. A superior low-cost amorphous carbon anode made from pitch and lignin for sodium-ion batteries. J Mat Chem A 2016;4:96–104.
[49] Jurkiewicz K, Pawlyta M, Zygadlo D, Chrobak D, Duber S, Wrzalik R, et al. Evolution of glassy carbon under heat treatment: correlation structure-mechanical properties. J Mater Sci 2018;53:3509–23.
[50] Ferrari AC, Robertson J. Raman spectroscopy of amorphous, nanostructured, diamond-like carbon, and nanodiamond. Phil Trans R Soc Lond 2004;362:2477–512.
[51] Hayashida K, Nagaoka S, Ishitani H. Growth and oxidation of graphitic crystallites in soot particles within a laminar diffusion flame. Fuel 2014;128:148–54.
[52] Jawhari T, Roid A, Casado J. Raman spectroscopic characterization of some commercially available carbon black materials. Carbon 1995;33(11):1561–5.
[53] Hurt RH, Structure, properties, and reactivity of solid fuels, 27th Symposium on Combustion. (1998) 2887–904.
[54] Liati A, Eggenschwiler PD, Schreiber D, Zelenay V, Ammann M. Variations in diesel soot reactivity along the exhaust after-treatment system, based on the morphology and nanostructure of primary soot particles. Combust Flame 2013;160(3):671–81.
[55] Franklin RE. Crystallite growth in graphitizing and non-graphitizing carbons. Proc R Soc A Math Phys Eng Sci 1951;209:196–218.

[56] Bar-Zic E, Zaida A, Salatino P, Senneca O. Diagnostics of carbon gasification by Raman microprobe spectroscopy. Proc Combust Inst 2000;28:2369–74.
[57] Oberlin A. Carbonization and graphitization. Carbon 1984;22(6):521–41.
[58] Kurosaki F, Ishimaru K, Hata T, Bronsveld P, Kobayashi E, Imamura Y. Microstructure of wood charcoal prepared by flash heating. Carbon 2003;41(15):3057–62.
[59] Appleby W, Gibson J, Good G. Coke formation in catalytic cracking. Ind Eng Chem Pro Des Dev 1962;1:102–10.
[60] Coll R, Salvado J, Farriol X, Montane D. Steam reforming model compounds of biomass gasification tars: conversion at different operating conditions and tendency towards coke formation. Fuel Process Technol 2001;74:19–31.
[61] Tay HL, Kajitani S, Zhang S, Li CZ. Effects of gasifying agent on the evolution of char structure during the gasification of Victorian brown coal. Fuel 2013;103:22–8.
[62] Keown DM, Hayashi JI, Li CZ. Drastic changes in biomass char structure and reactivity upon contact with steam. Fuel 2008;87:1127–32.

4.4 Supercritical carbon dioxide extraction

The effect of wood composition and supercritical CO_2 extraction on biochar production in ferroalloy industries

Gerrit Ralf Surup[a], Andrew J Hunt[b], Thomas Attard[c], Vitaliy L Budarin[c], Fredrik Forsberg[d], Mehrdad Arshadi[e], Victor Abdelsayed[f,g], Dushyant Shekhawat[f], Anna Trubetskaya[i,h,*]

[a]*Department of Engineering Sciences, University of Agder, 4879, Grimstad, Norway*
[b]*Materials Chemistry Research Center, Department of Chemistry and Center of Excellence for Innovation in Chemistry, Faculty of Science, Khon Kaen University, 123 Mittraparb Road, 40002, Khon Kaen, Thailand*
[c]*Department of Chemistry, The University of York, Heslington, York, YO10 5DD, UK*
[d]*Department of Engineering Sciences and Mathematics, Luleå University of Technology, 97187, Luleå, Sweden*
[e]*Department of Forest Biomaterials and Technology, Swedish University of Agricultural Sciences, 90183, Umeå, Sweden*
[f]*National Energy Technology Laboratory, Morgantown, WV 26507, USA*
[g]*AECOM, Morgantown, WV 26507, USA*
[h]*School of Engineering and Ryan Institute, National University of Ireland Galway, Galway, Ireland*
[i]*Department of Chemical Sciences, University of Limerick, V94 T9PX, Limerick, Ireland*

Abstract

This work demonstrated that the coupling of supercritical carbon dioxide extraction with slow pyrolysis is effective to remove over half of extractives from low quality wood and to generate biochar from remaining solid wood fractions. The high yields of extractives from supercritical carbon dioxide extraction illustrates the potential utilizing of low quality wood as an alternative feedstock for the sustainable production of value-added chemicals. Results showed that supercritical carbon dioxide extraction has neither a

*Corresponding author. anna.trubetskaya@nuigalway.ie

Preprint submitted to Energy *October 15, 2018*

strong impact on the physical properties of original wood nor on the yield of solid biochar. These results are promising as they show that the biochar obtained for this renewable feedstock could be used as an alternative to fossil-based coke in applications including ferroalloy industries. Moreover, the heat treatment temperature and supercritical carbon dioxide extraction had a significant impact on the tar yields, leading to the increase in naphthalene, polycyclic aromatic hydrocarbons, aromatic and phenolic fractions with the greater temperature. The differences in gasification reactivity and dielectric properties of solid biochars, composition and yields of liquid products of non-treated pinewood and extracted wood fraction emphasize the impact of supercritical carbon dioxide extraction on the pyrolysis process.
Keywords: biochar reductants, high-temperature pyrolysis, supercritical CO_2 extraction, XμCT, dielectric properties

1. Introduction

Wood for energy purposes represents about 9 % of the total wood utilization in Sweden [1, 2]. Pelletized softwood such as Scots pine and Norway spruce are major solid feedstocks for energy production in Sweden [2]. The separation of extractives from the wood provides a valuable feedstock for the energy sector and metallurgical industries [3]. The extracted fatty/resin acids can be utilized as primary feedstocks for chemicals and biorefinery applications [4–7], whereas the wood fraction after extraction is of high importance as a source of green carbon that could be utilized in metallurgical industries. Supercritical carbon dioxide ($scCO_2$) extraction of fatty/resin acids has been shown to improve the off-gassing of wood pellets, thus reducing the

potential for uncontrolled auto-oxidation, while maintaining pellet properties [3, 8]. Supercritical fluid extraction increases the bending strength and stiffness of residual wood and, thus, decreases the cost of process scaling up, wood storage and transportation [9]. Little is known about the effect that $scCO_2$ extraction has on the various physicochemical properties of different wood fractions in terms of the yields and characteristics of pyrolysis products used as biocoke reductants in metallurgical industries.

Utilization of the forest residues is constrained and frequently prevented by economic, technical and ecological challenges, which are related to anisotropic properties of wood [10]. The physical and chemical properties of lignocellulosic materials depend on structural (e.g. knots and grain deviation) and environmental (e.g. moisture and temperature) interactions during tree growth [11]. The mineral content and distribution of lignocellulosic compounds show significant variations between tree part (root, stem and branch) [12]. Needles are rich in lipophilic extractives, especially in waxes [13, 14]. Spruce needles have high phosphorus, sulfur, potassium and calcium contents, whereas the spruce bark contains high amounts of calcium and magnesium [15, 16]. The ash and extractives contents are higher in bark compared to stemwood [17], branch and root wood samples contain more minerals, galactan, xylan and lignin compared to glucomannan rich stemwood [10]. The physical properties such as moisture content, shrinkage, density and permeability are affected by the chemical composition of wood. Understanding the properties of wood fractions (bark, stem, needles, branches) is important for: (1) optimizing solvent extraction processes leading to maximal yields of extractives and (2) optimizing the biochar production in metallurgical properties. The combination

of biochar production from biomass with $scCO_2$ pre-treatment will provide a cost-efficient biocoke reductant for the metallurgical industries and improve the quality of a value added by-product for further application in chemical industries.

The main objective of this work is to demonstrate that the removal of extractives from low value forest residues using $scCO_2$ treatment provides a valuable feedstock in addition to biochar production. The differences in properties of original wood fraction and samples after $scCO_2$ extraction will be studied using X-ray microtomography, 2D dynamic imaging, helium pycnometer and mercury intrusion porosimeter. The product mass balances of non-treated wood fractions and samples after supercritical extraction will be established in high-temperature slow pyrolysis and the tar compounds will be characterized using GC-FID and GC-MS systems. The effect of feedstock origin and $scCO_2$ extraction on the biochar characteristics will be investigated using a thermogravimetric analyzer and microwave network vector analyzer.

2. Materials and methods

2.1. Supercritical CO_2 extraction

The $scCO_2$ extractions were conducted using a supercritical extractor SFE 500 (Thar technologies, USA). Supercritical fluid grade carbon dioxide (99.99 %, dip-tube liquefied CO_2 cylinder obtained from BOC) was used in the extractions. The CO_2 supplied from a cylinder as a liquid was maintained in this state through a cooling unit (-2°C) to avoid cavitation in the high pressure pump. $ScCO_2$ extractions of the different biomass types were optimized using a two-level factorial design [8]. Evaluation was made by determination

of the extracts' weight in the different experiments. Approximately 180 g of biomass was placed into the 500 mL extraction vessel. The reaction vessel was heated to the required temperature and was equilibrated for 5 min. An internal pump was used in order to obtain the required pressure. The system was run in dynamic mode, in which the carbon dioxide containing the extractives was flowed into the collection vessel. A flow rate of 40 g min^{-1} of liquid CO_2 was applied and the extraction was carried out for 2 h. On completion the system was depressurized over a period of 60 min. Eight extractions were carried out at various pressures (200, 300 and 400 bar) and temperatures (40, 50 and 60°C).

2.2. Slow pyrolysis reactor

The biochar samples were generated in the slow pyrolysis reactor, as shown in Figure 1. The reactor can be operated at temperatures up to 1350°C and heating rates up to 20°C min^{-1}. The pyrolysis setup encloses a two-stage cooling system with a condensation collector and a pyrolysis gas sampling unit. The pyrolysis retort (inner diameter: 75 mm, height: 150 mm, wall thickness: 2 mm) is made of SiC material. The volume flow of the N_2 gas was measured by the flowmeter HFC-202 (Teledyne, USA). The reactor was continuously purged by nitrogen at a constant flow rate of 100 ml min^{-1}. The temperature control system was based on the LabView software (Version 8.6). The sample mass of 20 g for each experiment was selected. The wood sample was distributed homogeneously in the reactor's retort, pre-heated in nitrogen at 10°C min^{-1} up to 160°C and kept at that temperature for 30 min. The dried wood was further heated at 10°C min^{-1} up to 900, 1000, and 1100°C and kept at the final temperature for about 1 h to ensure the

complete conversion. After the heating program was finished, the furnace was switched off and the biochar sample was cooled overnight in N_2 ($0.3\,l\,min^{-1}$). Samples were stored in sealed plastic containers.

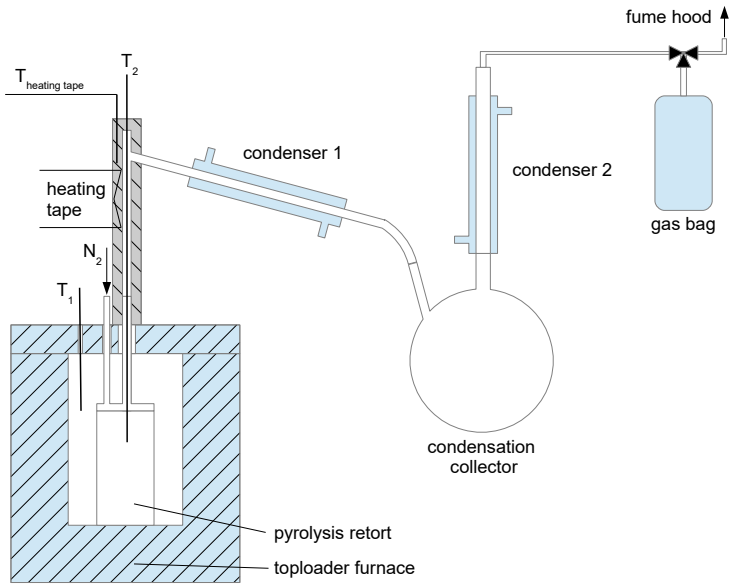

Figure 1: Slow pyrolysis reactor setup.

2.3. Original biomass and char analysis

Elemental analysis. The elemental analysis was performed on an Analyser Series II (Perkin Elmer, USA). Acetanilide was used as a reference standard. The ash content was determined using a standard ash test at 550°C, according to the procedure described in DIN EN 14775.

Ash compositional analysis. The ash compositional analysis was performed by an X-ray fluorescence instrument (Shimadzu, model EDX 800-HS) at TU Munich. Prior to the XRF analysis, char samples were pre-heated in

oxygen at 5°C min^{-1} up to 550°C and kept at that temperature for 7 h. The generated ash (about 100 mg) was initially mixed and then pressed with a special wax (mixture ratio 1:5). The Cl and S content in the ash was analyzed by ICP-OES/IC at ASG Analytics. The ash sample was dissolved in ultrapure water at 120°C for 1 h, and then the solution was filtered and analyzed by ICP-OES/IC.

X-ray microtomography. The full 3D microstructure of the wood samples was scanned using x-ray microtomography (XMT, μCT) [18–20], and characterized quantitatively using 3D image analysis. Wood particles, of approximate mass 10 g, were placed in a Kapton tube and scanned using the XMT instrument Zeiss Xradia 510 Versa (Carl Zeiss X-ray Microscopy, Pleasanton, CA, USA). No compression was used in order to prevent any artificial modification of the wood particles [21]. The field of view was 3.96 x 3.96 mm^2 and the spatial resolution in terms of voxel size was 1.96 μm. The x-ray tube voltage and tube power was 50 kV and 4 W, respectively. 3201 projections (radiographs) were collected, with exposure time 2.5 s, over a sample rotation of 360°, resulting in a total scan time of 5 h. The reconstructed wood structure corresponds to a cylindrical region of diameter 3.8 mm (top), 3.6 mm (bottom) and height 3.96 mm, as shown in Figure 2. 3D quantitative analysis of each wood sample was carried out in three subregions of similar shape, spacial scale and with geometrical location described in Figure 2. The size of each subregion, denoted Part 1-3, was 2.35 x 2.35 x 1.17 mm^3 (1200 x 1200 x 600 voxels). The segmentation was carried out by thresholding, using Otsu's method [22], and quantities such as porosity, number of particles, and volume-to-area ratio were calculated [19, 20]. The porosity was studied

on both global scale (entire ROI), as well as on particle scale. The particle porosity was calculated as the original binary mask (after segmentation) divided with the corresponding data where all the grains are filled, using a morphologic closing procedure, as described in the supplemental material (Figures S-12-14).

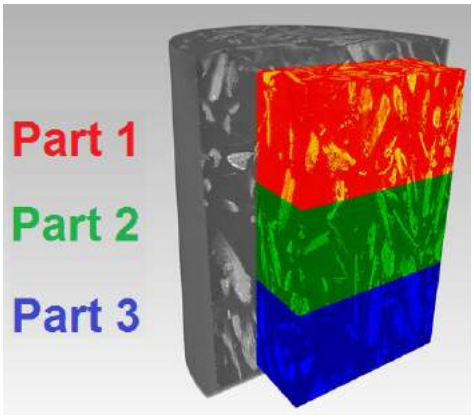

Figure 2: The 3D reconstructed wood samples scanned by x-ray microtomography, were each divided into three subsection, denoted Part 1-3, in which the quantitative analysis of the microstructure was carried out.

Moreover, the volume-to-surface area ratio (V/S) is the total evaluated volume divided by the sum of surface areas from all particles in a volume. The 3D quantitative image analysis and visualizations were carried out using Dragonfly Pro 2.0 software (Object Research Systems, Canada). Additional 2D analysis was carried out for comparison using MatLab R2017a software (MathWorks Inc., USA), and the image processing toolbox.

Mercury intrusion porosimetry. The pore size distribution and porosity of biomass samples were determined by a Pascal mercury intrusion porosime-

ter system equipped with two instruments. Porosity in the ultramacro and macropore regions was measured by Pascal 140 porosimeter (Micromeritics, Germany) at the low pressures (up to 400 kPa). The Pascal 440 porosimeter equipped with a dilatometer (Micromeritics, Germany) was used to determine the pore size from 1.8 to 7500 nm at high pressures up to 400 MPa. To access the pores and voids within biomass particles, the samples were degassed at room temperature prior to the measurement. Prior to the porosity analysis, wood fractions were dried at 50°C in an oven desiccator for 48 h. The porosity determined with mercury intrusion porosimetry only includes the percentage of open pores that are mercury accessible [23]. The pore sizes in the wood were distinguished into three categories: micropores (1.8-80 nm), mesopores (80-500 nm) and macropores (0.5-58 μm) [23, 24]. The definitions of porosity can be found in the literature [25].

2D dynamic imaging analysis. The particle size and shape of the original biomass were measured using the CAMSIZER XT (Retsch Technology, Germany). The particle size distribution, based on the volume, is represented by the $x_{Ma,min}$ diameter. For the particle size analysis, ca. 100 mg of a sample was used. All measurements were conducted in triplicate to establish sufficient reproducibility within $< 0.5\,\%$. The Martin minimal ($x_{Ma,min}$) and Feret maximal ($x_{Fe,max}$) diameters are suitable parameters to represent the biomass particle width and length in combustion [26]. The particle shape is characterized by sphericity/circularity (SPHT) and aspect ratio (b l^{-1}) in the present study [27].

Soxhlet extraction. The extractive fractions were removed by loading 3 g in a Soxhlet apparatus B-811 (Büchi Labortechnik AG, Switzerland) with a mixture (90/10 % v/v) of petroleum ether (Merck, bp 40 to 60°C) and acetone (AnalaR Normapur, VWR Chemicals, 100 %) for 1 h [8].

Karl Fischer titration. Karl Fischer titration was carried out using a KF1000 volumetric titrator (Hach, Germany). Tar samples were first dissolved in anhydrous methanol and then injected into the titration cell. All titrations were carried out at room temperature and the experiments had an error of ± 0.5 % water content.

Tar analysis. For the semiquantification of annotated substances, 5 μl of an internal standard (Chlorobenzene, Sigma-Aldrich) was injected in the whole volume of tars dissolved in methanol. Prior to the GC-FID analysis, a 1.5 ml aliquot was pipetted into the autosampler screw cap vial and stored in the freezer at -20°C. The quantitative analysis of tar compounds was performed on a gas chromatograph 7820A (Agilent Technologies, USA) equipped with a flame ionization detector (GC-FID) and DB-EUPAH capillary column (30 m length, 0.25 mm internal diameter, 0.25 μm film thickness). The temperatures of the injector and detector were kept at 250°C and 300°C, respectively. The column temperature program ran from 50 to 280°C. After holding the oven temperature at 50°C for the first 2 min the temperature was increased to 160°C at a rate of 1.5°C min^{-1}, then to 230°C at a rate of 6°C min^{-1}, and then to 280°C at a heating rate of 8°C min^{-1} and it was held at this temperature for another 5 min. Nitrogen was used as a carrier gas with a constant flow rate of 1 ml min^{-1}. Data acquisition and processing were performed us-

ing Agilent OpenLAB CDS EZChrom A.02.02 (Agilent Technologies, USA). Certain species were calibrated at four levels with solutions of known concentration and 5 replicates per level. Prior to the quantitative analyses in GC-FID, the tar compounds were annotated using a dual detector system GC-MS 5975C TAD Series / GC-FID 7890A (Agilent Technologies, USA). The column temperature and carrier gas settings were kept the same as those used in GC-FID analysis. The mass spectrometer with a quadrapolar type analyzer scanned the range from m/z 35 to m/z 250 resulting in a scan rate of 6.22 scans s^{-1}. The mass spectrometer was operated at unit mass resolution. A 0.5 μl of sample was injected at a 4:1 split ratio. The collected spectra were exported from Chemstation E.02.00.493 (Agilent Technologies, USA) to NetCDF and further processed by the statistical software "R" 2.15.2 [28] that can acquire and align the data, correct baseline, set time-window and perform multivariate analysis [29]. The multivariate analysis using MCR-AR algorithm yielded deconvoluted mass spectra with the well-resolved overlapping peaks [30], which were imported into the mass spectra library software NIST MS Search 2.0 [31]. The area of peaks was normalized to 100 % within each sample and the mean of triplicate measurements was calculated. The peaks with mass spectra similarity higher than 80 % were used in the tar quantification. The relative response factors (RRFs) were determined for each compound in tar samples using MatLab (version 8.6, MathWorks Inc.).

Thermogravimetric analysis. The char samples were firstly crushed to a fine powder in a mortar with a ceramic pestle. The thermal decomposition of char samples was determined using a thermogravimetric instrument STARe System (Mettler Toledo, USA) by loading 5 mg of sample in Al_2O_3 crucible.

Dielectric measurements. A microwave network vector analyzer N5231A PNA-L (Keysight, USA) was used to measure the dielectric properties of original biomass and char samples at room temperature. To avoid air gaps induced errors during measurements and to obtain comparative results, all samples were grinded, pressed to the same thickness before they were placed in a sample holder. Each measurement was repeated at least three times to ensure accuracy. The dielectric measurements were made with a high-temperature dielectric probe (Agilent 85070) connected via a coaxial cable to the network analyzer. The complex permittivity was measured in the frequency range between 1 and 5 GHz at room temperature. The permittivity (ε) and the loss tangent (tan δ) of the sample are given as [32]:

$$\varepsilon = \varepsilon' - i\varepsilon" \tag{1}$$

$$tan\ \delta = \frac{\varepsilon"}{\varepsilon'} \tag{2}$$

Where ε' is the real part and represents the ability of the dielectrics to store the microwave electrical energy, and ε" is the imaginary part and represents the loss of microwave electrical energy in dielectrics. The loss tangent, which is their ratio, measures the magnitude of the microwave electric field loss in the process.

3. Results

3.1. Biomass characterization

Scots pine trees, with an average age of 147 years, were harvested from a forest stand in northern Sweden. Fractions from harvested trees were green needles, branches without needles, and bark from the basal log with a

mean cross-sectional diameter of 210 mm. Prior to the feedstock characterization, wood fractions were comminuted on a hammer mill (MAFA EU-4B manufacturer, Sweden) with an operating speed of 60 Hz sieved to particle size fractions of 0.05-0.2 mm. Fuel selection in this study was based on the differences in the ash composition and plant cell compounds (cellulose, hemicellulose, lignin, extractives). The proximate and ultimate analysis of non-treated wood fractions and samples after $scCO_2$ extraction is shown in Table 1. The ash compositional analysis was determined for the non-treated Scots pinewood fractions. In supplementary Table S-1, the ash content of non-treated bark and bark after $scCO_2$ extraction remains unchanged, and thus, no differences in the ash composition are expected in other wood fractions. The compositional analysis of biomass (cellulose, hemicellulose, acid-soluble lignin, acid-insoluble lignin, protein and extractives) was conducted according to NREL technical reports [33–35] and Thammasouk et al. [36], and shown in Table 2.

Table 1: Proximate, ultimate and ash analyses of non-treated Scots pinewood fractions and samples after $scCO_2$ extraction.

Fuel	**Needles**		**Bark**		**Branches**	
	original	$scCO_2$ extracted	original	$scCO_2$ extracted	original	$scCO_2$ extracted
Proximate and ultimate analysis (% on dry basis)						
Moisture[a]	2.5	2.7	2.3	3.1	0.9	1.1
Ash (550 °C)	2.2	2.3	0.6	0.5	0.8	1
Volatiles	80.8	78.8	71.6	70.9	80.6	70.9
HHV[b]	22.4	21.3	21.8	21.3	21.7	20.9
LHV[b]	21	20	20.6	20.1	20.4	19.6
C	53.7	51.8	54.7	54.5	53.5	51.4
H	6.5	6.3	5.5	5.4	6.2	5.9
O	36.1	38.2	38.8	39.4	39.0	41.2
N	1.3	1.4	0.3	0.2	0.4	0.5
S	0.1	0.1	0.02	0.02	0.03	0.04
Ash compositional analysis (mg kg^{-1} on dry basis)						
Cl	0.02		< 0.01		< 0.01	
Al	250		250		150	
Ca	2450		1200		1300	
Fe	70		60		60	
K	5600		800		2000	
Mg	750		200		400	
Na	25		10		<10	
P	1500		150		400	
Si	400		350		400	
Ti	4		2		6	

[a] wt. % (as received) [b] in MJ kg^{-1}

Table 2: Composition of non-treated Scots pinewood fractions and extractives yield after $scCO_2$ extraction, calculated in percentage based on dry basis (wt. %).

Biomass	**Cellulose**	**Hemi-cellulose**	**Lignin**		**Extractives (raw wood)**	**Extractives (after $scCO_2$ extraction)**
			acid insoluble	**acid soluble**		
Needles	23.4	15.1	26.5	0.5	12.1	7.9
Bark	19.5	15.1	45.9	0.5	3.9	2.0
Branches	25.3	19.4	28.0	1.0	8.0	4.4

3.1.1. X-ray microtomography

Figure 3 shows the 3D cross-sectional slices obtained from XμCT measurements for non-treated pinewood needles and fraction after $scCO_2$ extraction. The spacial resolution of 1.96μm is sufficient for observing most features of the needles fibrous network and yielding physically reasonable structural assessments. The characteristic features of milled wood particles such as tracheids, vessels, and pits are observed for both non-treated and extracted samples. Figure 3(a) shows the higher level of voids in the non-treated needles than in the extracted wood fraction. The segmented tomography images of both pinewood needles in the Supplementary material (Figure S-37) show a wide particle size distribution from 0.01 mm to 12 mm. The XμCT images indicate that the milled pinewood needles are elongated and cylindrically shaped. The width to length ratio increases with the larger particle size of pinewood needles, confirming previous results of Trubetskaya et al. [26]. As seen in the supplemental material (Figure S-32(a)), the global porosity of non-treated and extracted pinewood needles is similar. Thus, the bulk den-

sity of non-treated needles (0.3 g cm^{-3}) is only slightly higher than that of the fraction after $scCO_2$ extraction (0.29 g cm^{-3}).

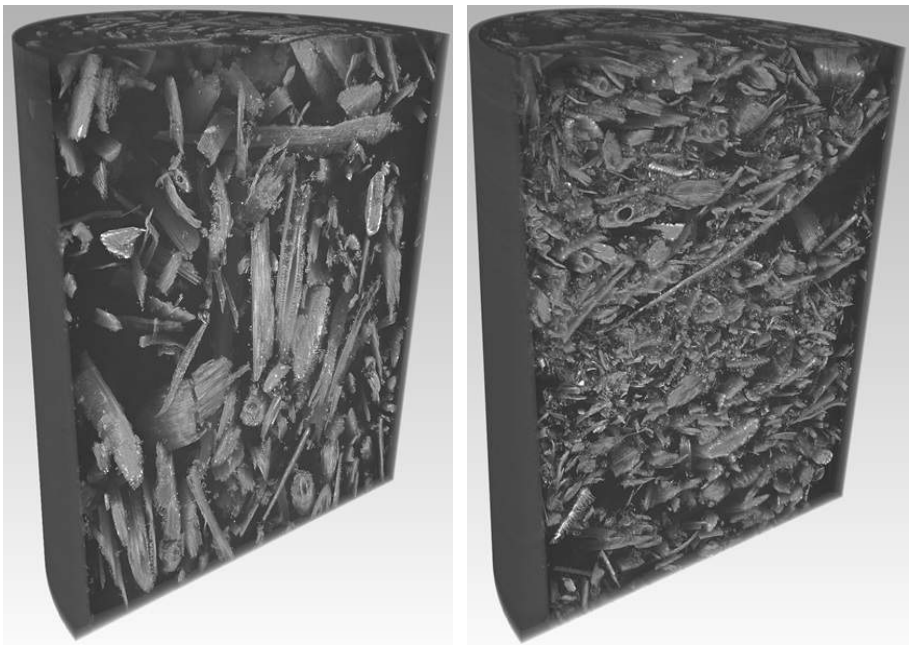

3(a): Non-treated needles

3(b): Needles after $scCO_2$ extraction

Figure 3: XμCT imaging analysis of non-treated pinewood needles and fraction after $scCO_2$ extraction.

Moreover, the bulk density determined using the global porosity from the XμCT analysis is comparable with the value determined for both samples using the pycnometer method as shown in Figure 4(a). The non-treated pinewood needles exhibited a lower porosity than the extracted wood particles, confirming the results in section 3.1.3. However, the porosity of needles determined by XμCT was on average 45 % lower than the porosity measured by the mercury intrusion porosimeter and calculated by skeletal density. This

is because the mercury intrusion porosimeter measures pores down to 3 nm compared to the 1.96 μm resolution of XμCT instrument as reported by Weber et al. [37]. The volume-to-surface area ratio were calculated using the 3D data from XμCT for both non-treated and extracted needles. The results showed that the volume-to-surface area ratio determined using the 2D dynamic imaging analysis (non-treated needles: 0.0037 mm; extracted needles: 0.0056 mm) was lower than the ratio calculated from XμCT data (non-treated needles: 0.003 mm; extracted needles: 0.0057 mm). In the 2D dynamic imaging, a particle is represented as an ellipsoid with the thickness assumed to be equal to the width. The previous microscopy results showed that the particle thickness of woody and herbaceous feedstocks can be estimated to be 1/2 of the particle width [26]. In 2D dynamic imaging, the shape of irregular biomass particles is commonly quantified by using equivalent shape models (i.e. a sphere, an ellipsoid, a cuboid), leading to the underestimation of the real particle surface area [38]. Three-dimensional image analysis using the XμCT enables the characterization of the true physical size of irregular biomass particles based on the results of Hamdi et al. [39].

3.1.2. Biomass density

The bulk densities of original bark, needles, and branches and samples after supercritical CO_2 extraction are shown in Figure 4(a). The bulk density of original wood fractions is in the range of 0.25-0.34 g cm^{-3}. The scCO_2 extraction of wood fractions does not affect the bulk density significantly, except for the increased bulk density of bark. The results show overall the bulk density decrease with increasing particle length.

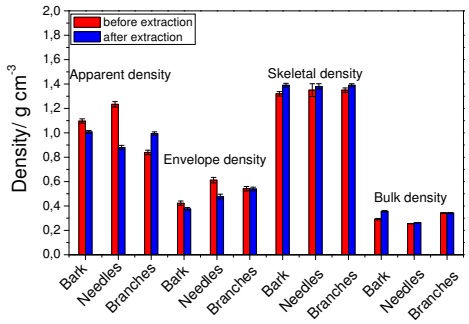

4(a): Densities

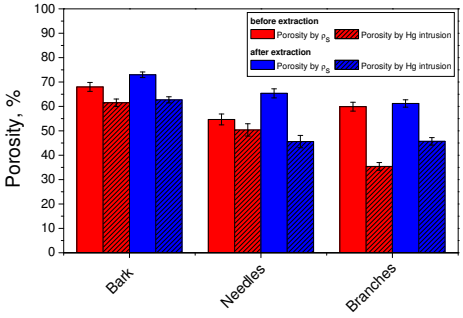

4(b): Porosity

Figure 4: Bulk, skeletal, envelope, and apparent density and porosity by skeleton density and Hg intrusion of original bark, needles, and branches and samples after supercritical CO_2 extraction.

The skeletal density of wood fractions is in the range of 1.4 g cm^{-3}, that increased slightly after $scCO_2$ extraction. Brewer et al. [40] reported that the envelope density varies substantially with feedstock due to the differences in cell shape and size distribution. Thus, the porosity of biomass fractions might be affected by the removal of extractives leading to the lower density. The apparent density of bark and needles decreases during the supercritical CO_2 extraction. This could be due to the increased micropore content [41]. Interestingly, the reduction of lignin content in branches via $scCO_2$ extraction might cause the apparent density increase, corresponding to results of Pfriem et al. [42, 43]. Figure 4(b) demonstrates large differences in porosities determined by skeletal density and mercury intrusion for the original wood fractions and samples after supercritical CO_2 extraction. For the non-porous samples, the skeleton and apparent densities are equal. The large differences in porosity determined by skeletal density and mercury intrusion might be

attributed to the presence of micropores in the wood fractions. In addition, the variations in plant cell wall composition (cellulose, hemicellulose, lignin, extractives) and the pore geometry might lead to the differences in porosity among the wood fractions [44, 45].

3.1.3. Pore size and porosity

Table 3 shows that untreated needles, bark, and branches and samples after $scCO_2$ extraction possess a high ratio of macropores in the range of 90-96 % owing to the occurrence of tracheids, with diameter ranging from 18 to 54 μm for earlywood and from 12 to 25 μm for latewood [46].

Table 3: Pore size and pore size distributions of original bark, needles, and branches and samples after $scCO_2$ extraction characterized by mercury intrusion porosimeter.

Fuel	**Bark**		**Needles**		**Branches**	
	Original	$scCO_2$	Original	$scCO_2$	Original	$scCO_2$
Macropores, %	90	96	97	95.3	93	94.7
Mesopores, %	7	3.8	3	3.3	5	3.7
Micropores, %	3	0.1	2	1.4	2	1.6
V_{cum}, $mm^3\ g^{-1}$	1520	1840	900	1040	676	940
SSA, $m^2\ g^{-1}$	7	3.6	0.7	1.8	5.3	9.3
Average pore diameter, μm	0.9	2	5	2.3	0.5	0.4
Median pore diameter, μm	20	26	43	30	8.6	20

The amount of micropores and mesopores in wood fractions is low, corresponding to results of Reyes et al. [41]. This could be accounted for by the submicroscopic pore system within the cell wall, small apertures within the resin canals and pits [47, 48]. The range of mesopores complies with the apertures of the pits which have an average diameter of 200 nm and

continuous canals within the epithelium tissue [49]. The average pore size of the high lignin containing bark and branches varied only slightly during $scCO_2$ extraction. The extraction of needles resulted in a larger percentage of micro- and mesopores, leading to the specific surface area increase. The higher cumulative pore volume of wood fractions after extraction is caused by the high content of micropores with poorer accessibility as reported by Plötze and Niemz [23]. The results indicate that the wood extraction affects the pore size and volume only slightly.

3.2. Particle size and shape

The particle size and shape of non-treated wood fractions and samples after $scCO_2$ extraction were analyzed by CAMSIZER XT instrument. The results of the particle characterization study indicate nearly similar particle size of all wood fractions, as shown in the supplemental material (Figure S-3). The particle shape of samples was characterized using the sphericity (SPHT) and width/length ratio (b/l) parameters. The wood fractions obtained cylindrical or rectangular shapes (SPHT = 0.5-0.8; b/l ratios = 0.5-0.7). It seems that the needles are more elongated (b/l $\approx$ 0.5) than other wood fractions. The bark samples showed the smallest changes in particle size and shape in the extraction process. The results of particles > 0.25 mm in terms of shape description were considered as non-representative due to the low presence of particles in this fraction. The effect of $scCO_2$ extraction is overall negligible on the particle size and shape of scots pinewood fractions.

3.3. Extractives yields

Total amounts of extractives are shown in Figure 5.

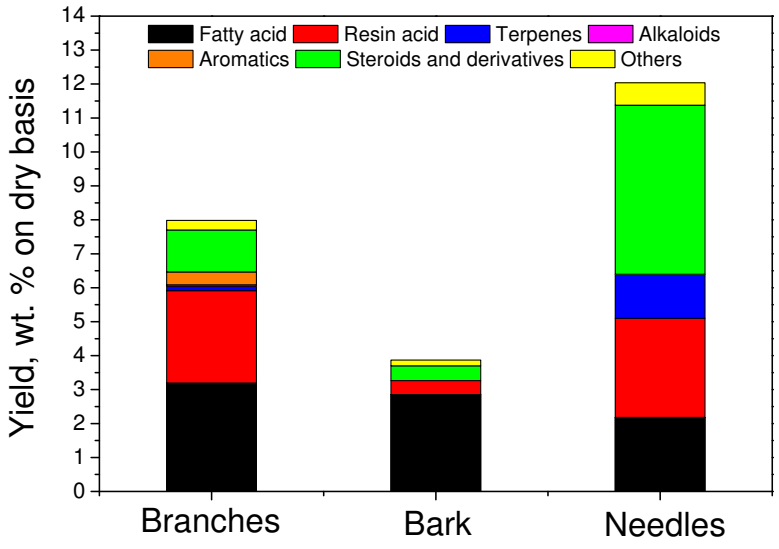

Figure 5: Yields of extractives from Soxhlet extraction of needles, bark and branches.

The largest amount of extractives (11 wt.%, db) was determined in needles, whereas the extractives content was significantly lower in branches (about 7 wt.%, db) and bark (about 3.7 wt.%, db). The Soxhlet extraction of needles led to significantly greater yields of steroids and derivatives, terpenes and other extractives than the extraction of branches and bark. The extraction of needles and branches gave similar yields of resin acids which were greater than the yields from bark extraction.

3.4. Biochar characterization

3.4.1. Product yields

The mass balances of the slow pyrolysis experiments with respect to measured solid residue (char) and major liquid products (water and organic

fraction), dependent on the heat treatment temperature, are shown in Figure 6.

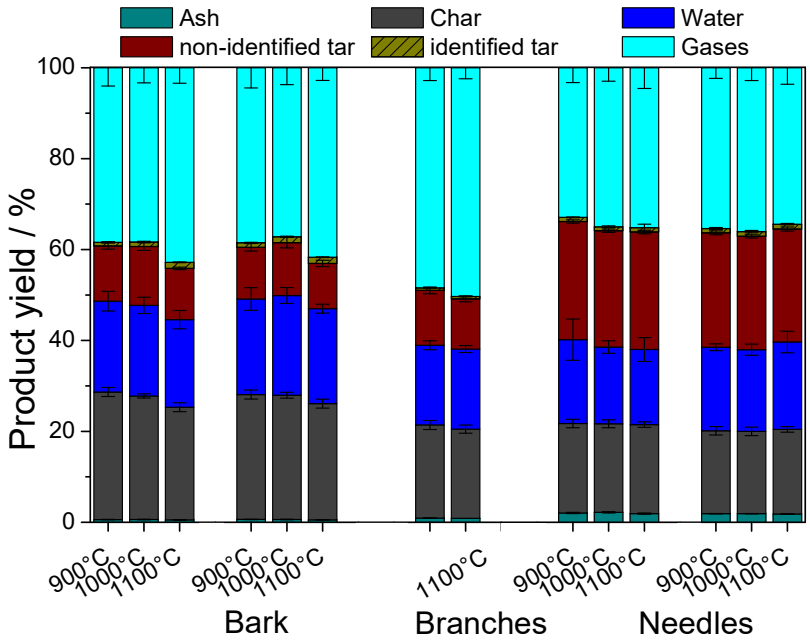

Figure 6: Tar and char yields (wt. % relative to the original biomass) of needles, bark and branches, reacted at 900-1100°C in the slow pyrolysis reactor. The total yield of char is separated in ash and organic matters. The total yield of tar is separated in organic fraction and water content. The error bars characterize the deviations between the total yields of products.

The amount of gaseous species was not measured in the present study, but estimated by the difference from the mass balance. The mass balances represent an average of two measurements. The char yields from pyrolysis of needles, bark and branches were similar at 900, 1000 and 1100°C. The differences in product yields of non-treated wood fractions and samples after $scCO_2$ extraction were small. The char yield from pyrolysis of needles was

lower than that from pyrolysis of bark and vice versa with the liquid product yields due to the higher lignin content and lower amounts of extractives in bark. This observation was confirmed by the similarly lower char yields of branches and needles compared to that of bark. In contrast, the liquid product yields of bark and branches generated at 1100°C were similar due to low content of remaining extractives after $scCO_2$ treatment.

3.4.2. Tar analysis

The identification of individual tar compounds was based on the present results of GC-MS analysis, PAH pattern recognized in the literature and comparison with the reference chromatograms of external standards. The identified tar compounds with the relevant information were listed in the supplemental material (Table S-3). Figure 7 shows the change in the yields of tar from pyrolysis of non-treated needles, branches and bark and fractions after $scCO_2$ extraction in the range from 900 to 1100°C. The pyrolysis of both non-treated and $scCO_2$ extracted bark gave a greater tar yield compared to other wood fractions. The yield of identified tar from non-treated branches showed the lowest (5.5 mg g^{-1}-sample), whereas the yield of identified tar from $scCO_2$ extracted bark was the greatest (13.5 mg g^{-1}-sample). In general, the tar yields of non-treated wood fractions were lower than the tar yields from pyrolysis of $scCO_2$ extracted samples. This may also show that the presence of resin or fatty acids in pinewood could decrease tar formation during pyrolysis.

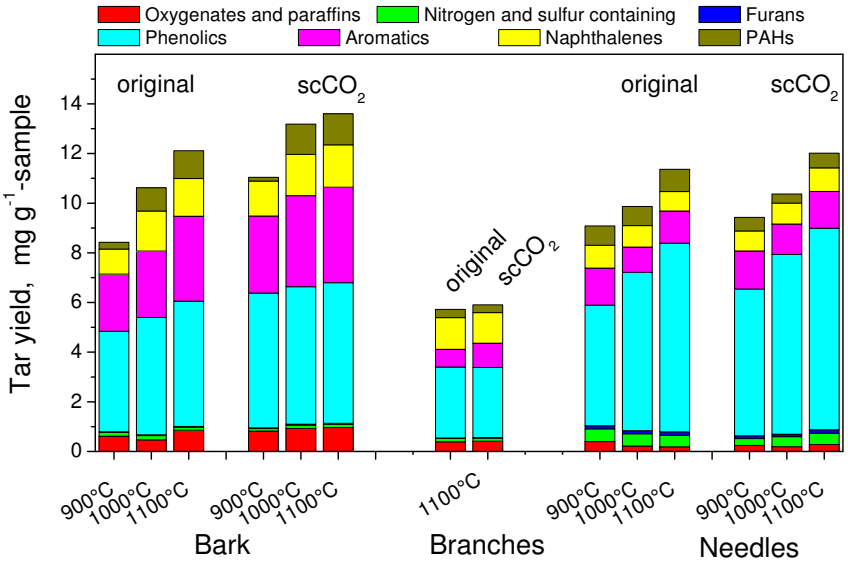

Figure 7: Tar yields (mg g^{-1} on dry basis) of non-treated needles, bark and branches and wood fractions after $scCO_2$ extraction.

Moreover, greater yields of aromatic, naphthalenes, oxygenates and paraffins were observed in tar from bark pyrolysis, whereas needles tar obtained greater concentrations of phenolics, furans, nitrogen and sulfur containing compounds compared to tars from pyrolysis of bark and branches. The tar yields increased with the increased heat treatment temperature. In pyrolysis of bark, the tar yields increased due to the greater yields of aromatic compounds, whereas tar yields in pyrolysis of needles increased due to the increase in concentration of naphthalenes.

3.4.3. Thermogravimetric analysis

Figure 8 shows differential weight loss curves (DTG) for the 40 % volume fraction CO_2 gasification of solid residues from pyrolysis.

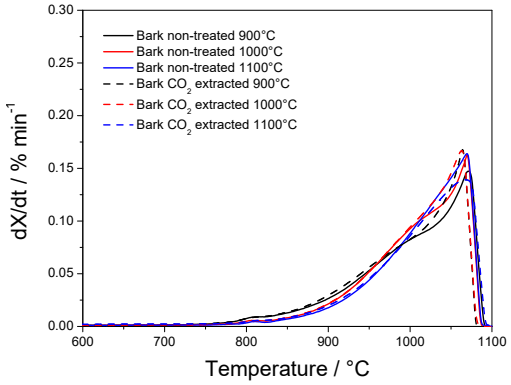

8(a): Bark

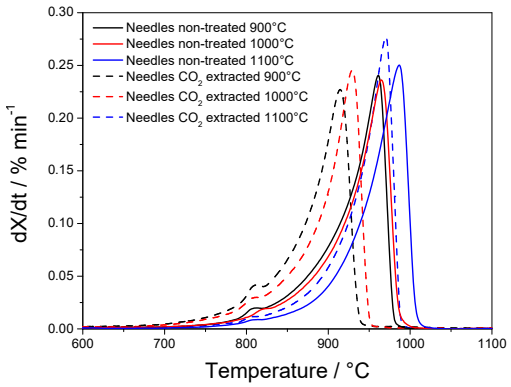

8(b): Needles

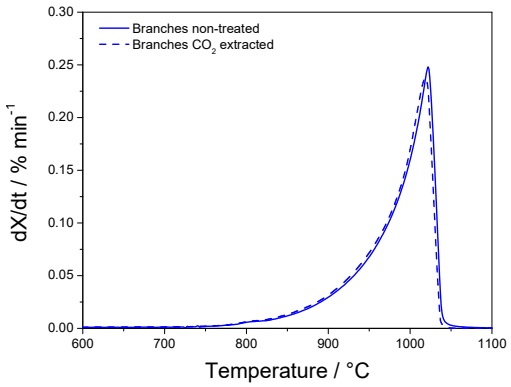

8(c): Branches

Figure 8: DTG curves of char from non-treated bark, needles and branches and $scCO_2$ wood samples pyrolyzed at 900, 1000, and 1100°C and further reacted in 20 % volume fraction CO_2 + 80 % volume fraction N_2.

The DTG curves show a single broad peak in CO_2 gasification, indicating a heterogeneous char mixture with respect to the composition and particle size as suggested by Russell et al. [50]. The maximal reaction rates of chars of non-treated and $scCO_2$ bark and branches were similar at nearly 1065 and 1020°C, whereas the maximum reaction rate of char from pyrolysis of $scCO_2$ extracted needles at 900 and 1000°C was about 100°C greater than that of char from non-treated needles. Moreover, the char of non-treated needles from pyrolysis at 1100°C was slightly less reactive than the char of $scCO_2$ extracted needles.

3.4.4. Dielectric measurements

The relative dielectric constant ε' and dielectric loss tangent tan δ of non-treated original biomass, $scCO_2$ treated wood fractions and chars are shown in Figure 9. The dielectric constant smoothly decreased with frequency. Therefore, the frequency-dependence behavior for all char samples is largely in agreement with that for activated carbon and coal chars [32, 51]. The ε' of char samples increased with the increased heat treatment temperature during pyrolysis. The dielectric properties of prepared chars were greater compared to all raw biomass samples which could indicate that the carbon structure in these chars have changed dramatically after pyrolysis. The loss of moisture and oxygen-containing function groups in biomass skeleton could lead to a greater C/O ratio that increased as the heat treatment temperature increased. The CO_2 extraction of wood led to even higher C/O ratio biomass to start with and hence higher dielectric properties were observed for $scCO_2$ treated chars compared to untreated ones at the same heat treatment temperature. The results also indicate an increase in content and structure

ordering of carbon in generated chars had occurred as the heat treatment temperature increased, as reported by Alias et al. [52].

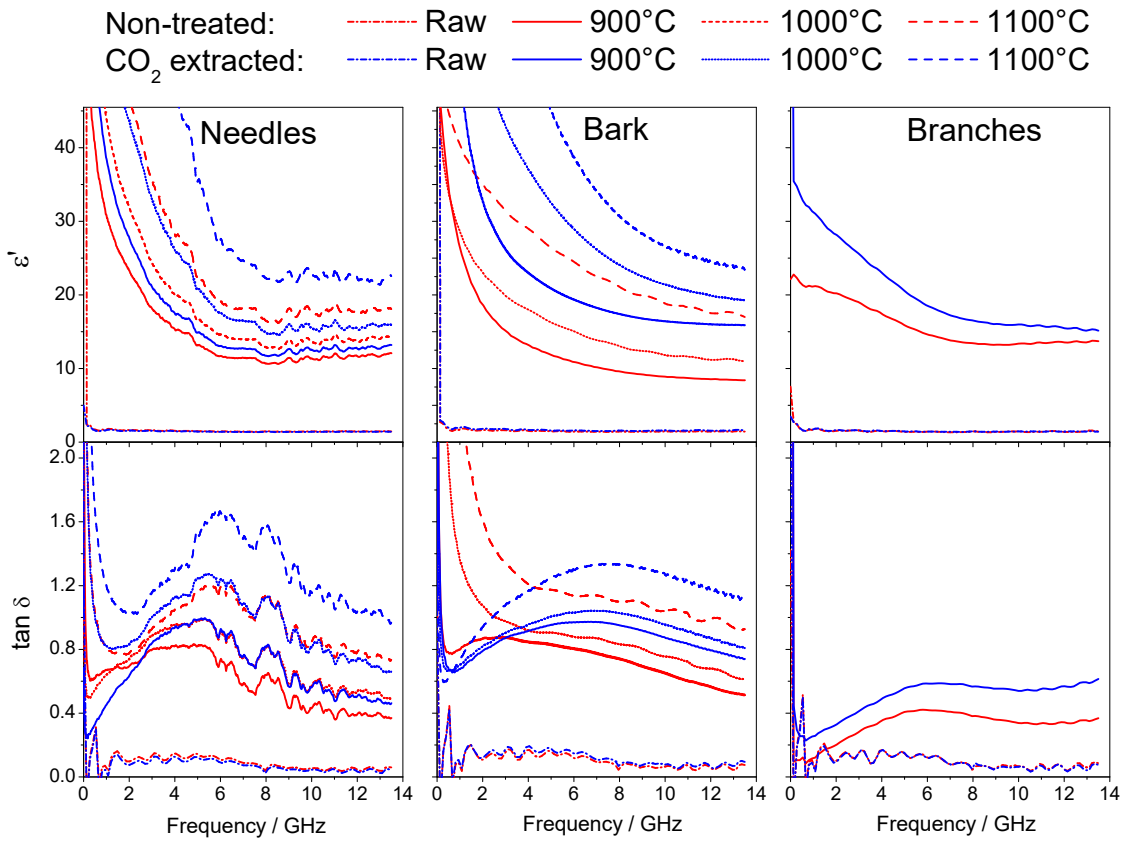

Figure 9: Dielectric constant ε' and dielectric loss tangent tan δ of non-treated original biomass, scCO$_2$ treated wood fractions and chars.

The heat treatment of biomass enhance the dielectric losses and therefore more heat is generated inside biomass char, indicating that biochar is a microwave prone material [51]. Figure 9 shows that the tan δ values of chars range from 0.4 to 1.6 at the maximum frequency and are greater than that

of biomass due to the increase in a surface area and carbon content with the heat treatment.

4. Discussion

The pyrolysis experiments showed that the differences in wood fraction composition exerted greater influence on the yields and composition of pyrolysis products, dielectric properties and intrinsic reactivity of char samples than heat treatment temperature or supercritical extraction. The yields of char and liquid products were similar during pyrolysis of non-treated wood fractions and samples after $scCO_2$ extraction. The high-ash containing needles are rich in calcium, potassium, and phosphorus. The high level of alkali metals in biomass catalyzes the conversion of bridges into char, promoting faster devolatilization rates and surpressing tar formation, leading to greater char yields [53, 54]. Thus, based on ash content alone it might be expected that the liquid product yield is greater than during pyrolysis of bark and branches. However, pyrolysis of low ash-containing bark showed a greater char yield and formed less liquid products than during pyrolysis of needles. This is due to the greater lignin content (46.5 wt. %, db) in bark compared to other wood fractions (27 to 29 wt. %, db). In addition, the lower extractives content in branches (8 wt.%, db) than in needles (12 wt.%, db) led to formation of less liquid products.

The results of this study showed that the $scCO_2$ extraction had also less influence on the density, particle size and shape of wood fractions. An innovative approach was developed to characterize the biomass porosity and density using XμCT technique. The 3D imaging analysis using XμCT technique and

mercury intrusion porosimetry showed that the non-treated wood fractions are less porous than samples after $scCO_2$ extraction. In general, all wood fractions contain more macropores than micro- and mesopores ranging from 90 to 97 %. Lignin mainly contributes to the porosity of biochars and activated carbons [55]. Bark particles showed a greater micro-/mesoporosity and lower macroporosity than needles and branches particles. This is due to the greater lignin content in bark fraction with the more porous surface structure than other lignocellulosic compounds [56]. The differences in surface properties and distribution of lignocellulosic compounds in wood fractions could also lead to greater extractives yields during $scCO_2$ extraction of needles, confirming the previous results of Backlund [57]. The greater yields of resin acids, steroids and terpenes were found in $scCO_2$ extracted needles due to the greater porosity, larger average pore size and less fibrous structure compared to other wood fractions. The differences in lignocellulosic composition had also a strong impact on the yield and composition of tar during pyrolysis. The high yields of naphthalene, PAHs, phenolic and aromatic compounds were observed in liquid products from bark pyrolysis which were attributed to greater lignin content compared to other wood fractions. The low lignin-containing needles and branches formed less PAHs and aromatic compounds during pyrolysis, confirming the previous results of Yu et al. [58]. Interestingly, greater yields of naphthalene were found in tar of needles that has greater content of extractives compared to other wood fractions. The heat treatment temperature and $scCO_2$ extraction had a significant impact on the tar yields, leading to the increase in naphthalene, PAHs, aromatic and phenolic fractions with the greater temperature. The increase in heat treatment

temperature led to the increase in hydrogen concentration that promotes the hydrocracking process of tar fragments into smaller tar molecules and methane and thus, more naphthalene is formed [59]. The overall effect of $scCO_2$ extraction on the physical properties of wood is negligible. However, the isolation of waxes and terpenes by $scCO_2$ extraction can lead to changes in the allocation of remaining extractives and other lignocellulosic compounds in the wood cell wall and thus, enhance the release of tar compounds during pyrolysis of extracted wood fraction [60]. The isolation of extractives by $scCO_2$ extraction could also lead to the allocation of alkali metals in the wood cell wall and formation of greater concentrations of water-soluble alkali during pyrolysis [61]. The present results showed that the alkali compounds increased the reactivity of needle char generated at temperatures $< 1100°C$. The extractives content in the original wood and yield of extractives after Soxhlet pre-treatment was greater in needles compared to other wood fractions. Therefore, the effect of $scCO_2$ extraction on the allocation of alkali metal and lignocellulosic compounds was greater in needles extraction compared to that of other wood fractions. Overall, the $scCO_2$ extraction had also an impact on the dielectric properties of wood char. In general, the ε' values of wood chars varied from 8 to 25, approaching dielectric properties of activated carbons (20-40) [62]. The increase in heat treatment temperature led to the formation of more ordered carbon in char structure [25]. Breaking of aliphatic hydrocarbon groups and formation of large polyaromatic structures result in stacking of aromatic carbon rings in char samples [63]. Thus, conduction losses would be experienced in chars due to the π-electron conjugation within the ordered carbon domains which experience higher dielectric

properties. Stronger carbon-carbon π-bonds could be formed between compressed polyaromatic carbon layers at high temperatures, whereas the π-bond localized electron in turbostratic char structure contributes to dielectric permittivity through the high polarization [64, 65]. The results indicate that bark char was more dipolar than needles and branches char obtained from pyrolysis at 1100°C. This is due the greater lignin content in original bark compared to other wood fractions, as reported by Ben et al. [66]. The hydroxyl groups are strongly polarized with high hydrophilic properties. The high content of non-polar groups in lignin fibers and polar groups in pinewood bark results in the dipole formation and thus, better dielectric properties of bark char. Moreover, the alkali rich needles and branches could decrease the orientation of polarization in the carbonaceous char matrix and thus, decrease the dielectric constants of needles and branches char samples [67]. The dielectric constants of $scCO_2$ treated char samples were slightly greater than that of char samples from non-treated biomass. The differences in the dielectric properties of chars from non-treated biomass and $scCO_2$ extracted wood fractions were related to the differences either in density of original wood, stacking of aromatic rings in the char, type of oxygen functional group (i.e. OH, CHO, ether, COOH) or moisture content, consistent with the previous results of Ramasamy et al. [68]. The $scCO_2$ extracted wood fractions are more dense than the non-treated pinewood and thus, more polar groups can accompany dielectric polarization, improving the dielectric properties of original wood and chars [69].

Importantly from a technological standpoint, the $scCO_2$ extraction does not have any negative impact on the biochar properties. The present results

clearly demonstrate that high heat treatment temperature and high lignin content in biomass improve the dielectric properties of biochar and increase the char graphitization approaching the properties of fossil-based metallurgical coke [70]. Moreover, the alkali compounds have a negligible influence on the CO_2 reactivity of mostly all biochar samples which will reduce the electric power required for smelting [71].

5. Conclusion

Different pinewood fractions were converted into renewable biochar by pyrolysis treatment. The novelty of this work relies on the fact that the high heat treatment temperatures and high lignin content in biomass improve the dielectric properties and increase graphitization of biochar. The pretreatment using $scCO_2$ extraction of wood allows to extract more than half of value-added compounds without any significant influence on the physical properties of original wood and on the yield of solid biochars. However, the presence of extractives in original pinewood showed properties which decrease the formation of tar during slow pyrolysis. Under properly selected treatment conditions (e.g. $> 1100°C$), biochars can be produced from a mixture of different low quality wood fractions with reactivity and dielectric properties approaching that of fossil-based metallurgical coke and with the low content of liquid products, including naphthalene, PAHs, aromatic and phenolic fractions. The finding of this study emphasizes the potential use of biocarbon-based reductants in the ferroalloy industries, with concomitant reduction in CO_2 emissions.

Acknowledgements

The authors gratefully acknowledge financial support from FORMAS (CETEX project), Kempe Foundation, Björn Wahlströms, and Jernkontoret Stiftelsen. The authors acknowledge the facilities and technical support of Gundula Stein from GNF Berlin Adlershof e.V. Dr. Daniel Eriksson from Swedish University of Agricultural Sciences in Umeå is acknowledged for the preparation of pinewood fractions. We are grateful to the plant cell wall and carbohydrate analytical facility at UPSC/SLU, supported by Bio4Energy and TC4F for the GC-MS analysis. The authors acknowledge the facilities and technical support of Dr. Junko Takahashi-Schmidt at Umeå Plant Science Centre.

References

[1] Pardo de Donlebun JPA, The EU enlargement in 2004: analysis of the forestry situation and perspectives in relation to the present EU and Sweden. Skogsstyrelsen National Board of Forestry. Jönköping: Sweden; 2003 October Report No. ISSN1100-0295 .

[2] de Jong J, Akselsson C, Berglund H, Egnell G, Gerhardt K, Lönnberg L and etc., Consequences of an increased extraction of forest biofuel in Sweden. Swedish Energy Agency. Eskilstuna: Sweden; 2014 September Report No. ISSN1403-1892 .

[3] Attard TM, Arshadi M, Nilsson C, Budarin VL, Valencia-Reyes E, Clark JH and etc., Impact of supercritical extraction on solid fuel wood pellet

properties and off-gassing during storage, Green Chem 18 (9) (2016) 2682–90.

[4] Hill K, Fats and oils as oleochemical raw materials, Pure Appl Chem 72 (7) (2000) 1255–64.

[5] Ruston NA, Commercial uses of fatty acids, J Am Oil Chem Soc 29 (11) (1952) 495–8.

[6] Gill I, Valivety R, Polyunsaturated fatty acids: 1. Occurrence, biological activities and applications, Trends Biotech 15 (10) (1997) 401–9.

[7] White K, Lorenz N, Potts T, Penney WR, Babcock R, Hardison A and etc., Production of biodiesel fuel from tall oil fatty acids via high temperature methanol reaction, Fuel 90 (11) (2011) 3193–9.

[8] Arshadi M, Hunt AJ, Clark JH, Supercritical fluid extraction (SFE) as an effective tool in reducing auto-oxidation of dried pine sawdust for power generation, RSC Adv 2 (2012) 1806–9.

[9] Smith SM, Sahle Demessie E, Morrell JJ, Levien KL, Spliethoff H, Ng H, Supercritical fluid (SCF) treatment: its effect on bending strength and stiffness of ponderosa pine sapwood, Wood Fiber Sci 25 (2) (1993) 119–23.

[10] Hakkila P, Utilization of residual biomass, Springer, 1989.

[11] Lestander TA, Lindeberg J, Eriksson D, Bergsten U, Prediction of Pinus sylvestris clear-wood properties using NIR spectroscopy and biorthogo-

nal partial least squares regression, Can J Forest Research 38 (7) (2008) 2052–62.

[12] Gustafsson G, Heartwood and lightwood formation in Scots pine - A physological approach. PhD thesis, Swedish University of Agricultural Sciences, 2001.

[13] Backlund I, Cost-effective Cultivation of Lodgepole Pine for Biorefinary Applications. PhD thesis, Swedish University of Agricultural Sciences, 2013.

[14] Koch P, Lodgepole pine in North America: Nonwood products characterization of tree parts, Forest Prod Soc, 1996.

[15] Werkelin J, Skrifvars BJ, Zevenhoven M, Holmbom B, Huppa M, Chemical forms of ash-forming elements in woody biomass fuels, Fuel 89 (2010) 481–93.

[16] Oasmaa A, Kuoppala E, Gust S, Solantausta Y, Fast pyrolysis of forestry residue. 1. Effect of Extractives on Phase Separation of Pyrolysis Liquids, Energy Fuels 17 (1) (2003) 437–43.

[17] Myeong S, Han SH, Shin SJ, Analysis of Chemical Compositions and Energy Contents of Different Parts of Yellow Poplar for Development of Bioenergy Technology, J Korean For Soc 99 (5) (2010) 706–10.

[18] Joffre T, Girlanda O, Forsberg F, Sahlén F, Sjödahl M, Gamstedt EK, A 3D in-situ investigation of the deformation in compressive loading in the thickness direction of cellulose fiber mats, Cellulose 22 (2015) 2993–3001.

[19] Forsberg F, Mooser R, Arnold M, Hack E, Wyss P, 3D micro-scale deformations of wood in bending: Synchrotron radiation μCT data analyzed with digital volume correlation, J Struct Biol 164 (2008) 255–62.

[20] Forsberg F, Sjödahl M, Mooser R, Hack E, Wyss P, Full Three-Dimensional Strain Measurements on Wood Exposed to Three-Point Bending: Analysis by Use of Digital Volume Correlation Applied to Synchrotron Radiation Micro-Computed Tomography Image Data, Strain 46 (2010) 47–60.

[21] Gamble JF, Terada M, Holzner C, Lavery L, Nicholson SJ, Timmens P and etc., Application of X-ray microtomography for the characterisation of hollow polymer-stabilised spray dried amorphous dispersion particles, Int J Pharma 510 (2016) 1–8.

[22] Otsu N, A Threshold Selection Method from Gray-Level Histograms, IEEE Transactions on systems, man, and cybernetics 9 (1) (1979) 62–6.

[23] Plötze M, Niemz P, Porosity and pore size distribution of different wood types as determined by mercury intrusion porosimetry, Europ J Wood Wood Product 69 (4) (2011) 649–57.

[24] Yin J, Song K, Lu Y, Zhao G, Yin Y, Comparison of changes in micropores and mesopores in the wood cell walls of sapwood and heartwood, Wood Sci Technol 49 (2015) 987–1001.

[25] Surup GR, Heidelmann M, Kofoed Nielsen H, Trubetskaya A, Characterization and reactivity of charcoal from high temperature pyrolysis (800–1600°C), Fuel 235 (2019) 1544–1554.

[26] Trubetskaya A, Poyraz Y, Weber R, Wadenbäck J, Secondary comminution of wood pellets in power plant and laboratory-scale mills, Fuel Process Tech 160 (2017) 216–27.

[27] Trubetskaya A, Beckmann G, Wadenbäck J, Holm JK, Velaga SP, Weber R, One way of representing the size and shape of biomass particles in combustion modeling, Fuel 206 (2017) 675–83.

[28] R-Development-Core-Team, R: A Language and Environment for Statistical Computing, http://www.R-project.org/ .

[29] Tolu J, Gerber L, Boily JF, Bindler R, High-throughput characterization of sediment organic matter by pyrolysis-gas chromatography/mass spectrometry and multivariate curve resolution: A promising analytical tool in (paleo)limnology, Anal Chim Acta 880 (2015) 93–102.

[30] Gerber L, Eliasson M, Trygg J, Moritz T, Sundberg B, Multivariate curve resolution provides a high-throughput data processing pipeline for pyrolysis-gas chromatography/mass spectrometry, J Anal Appl Pyrolysis 95 (2012) 95–100.

[31] MS-SEARCH, NIST Mass Spectrometry Data Center: NIST/EPA/NIH Mass Spectral Database, http://chemdata.nist.gov .

[32] Liu H, Xu L, Yan J, Fan B, Qiao X, Yang Y, Effect of coal rank on structure and dielectric properties of chars, Fuel 153 (2015) 249–56.

[33] Sluiter A, Hames B, Ruiz R, Scarlata C, Sluiter J, Templeton D et al., Determination of Structural Carbohydrates and Lignin in Biomass.

Golden (CO): National Renewable Energy Laboratory; 2011 July Report No. NREL/TP-510-42618. Contract No.: DE-AC36-08-GO28308 .

[34] Willför S, Hemming J, Leppänen AS, Analysis of extractives in different pulps - Method development, evaluation, and recommendations. Finland: Åbo Akademi University, Laboratory of Wood and Paper Chemistry; 2004-2009 Report No. B1 of the EU COST E41 action "Analytical tools with applications for wood and pulping chemistry" .

[35] Hames B, Ruiz R, Scarlata C, Sluiter J, Sluiter A, Preparation of Samples for Compositional Analysis. Golden (CO): National Renewable Energy Laboratory; 2011 June Report No. NREL/TP-510-42620. Contract No.: DE-AC36-99-GO10337 .

[36] Thammasouk K, Tandjo D, Penner MH, Influence of Extractives on the Analysis of Herbaceous Biomass, J Agric Food Chem 45 (1997) 437–43.

[37] Weber E, Fernandex M, Hoffman W, Wapner P, Comparison of X-Ray Micro-Tomography Measurements of Densities and Porosity to Traditional Techniques for Carbon-Carbon Composites, Defense Tech Inform Center, 2009.

[38] Erdogan ST, Simple Estimation of the Surface Area of Irregular 3D Particles, J Mat Civil Eng 28 (8) (2016) 1–10.

[39] Hamdi SE, Delisee C, Malvestio J, Da Silva N, Le Duc A, Beaugrand J, X-ray computed microtomography and 2D image analysis for morphological chracterization of short lignocellulosic fibers raw materials: A benchmark survey, Composites: Part A 76 (2015) 1–9.

[40] Brewer CE, Chuang VJ, Masiello CA, Gonnermann H, Gao X, Dugan B and etc., New approaches to measuring biochar density and porosity, Biomass Bioenergy 66 (2014) 176–85.

[41] Reyes T, Bandyopadhyay SS, McCoy BJ, Extraction of Lignin from Wood with Supercritical Alcohols, The J Supercrit Fluids 2 (1989) 80–4.

[42] Pfriem A, Zauer M, Wagenführ A, Alteration of the pore structure of spruce (*Picea abies* (L.) K)arst.) and maple (*Acer pseudoplatanus* L.) due to thermal treatment as determined by helium pycnometry and mercury intrusion porosimetry, Holzforschung 63 (2009) 94–8.

[43] Kollmann F, Technologie des Holzes und der Holzwerkstoffe. Band I (in German), Springer, 1951.

[44] Moura MJ, Ferreira PJ, Figueiredo MM, Mercury intrusion porosimetry in pulp and paper technology, Powder Tech 160 (2005) 61–6.

[45] Zauer M, Hempel S, Pfriem A, Mechtcherine V, Wagenführ A, Investigations of the pore-size distribution of wood in the dry and wet state by means of mercury intrusion porosimetry, Wood Sci Technol 48 (2014) 1229–40.

[46] Wagenführ R, Holzatlas, Hanser, 2000.

[47] Schneider A, Wagner L, Bestimmung der Porengrößvenverteilung in Holz mit dem Quecksilber-Porosimeter, Holz Roh Werst 32 (1974) 216–24.

[48] Schneider A, Beitrag zur Porositätanalyse von Holz mit dem Quecksilber-Porosimeter, Holz Roh Werst 37 (1979) 295–302.

[49] Liese W, Fahnenbrock M, Elektromikroskopische Untersuchungen über den Bau der Hoftüpfel, Holz Roh Werkst 10 (1952) 197–201.

[50] Russell NV, Beeley TJ, Man CK, Gibbins JR, Williamson J, Development of TG measurements of intrinsic char combustion reactivity for industrial and research purposes, Fuel Process Tech 57 (2) (1998) 113–30.

[51] Atwater JE, Wheeler RR, Complex permittivities and dilectric relazation of granular activated carbons at microwave frequencies between 0.2 and 26 GHz, Carbon 41 (2003) 1801–7.

[52] Alias N, Zaini MAA, Kamaruddin MJ, Relationships between dielectric properties and characteristics of impregnated and activated samples of potassium carbonate- and sodium hydroxide-modified palm kernel shell for microwave-assisted activation, Carbon letters 24 (2017) 62–72.

[53] Niksa S, Predicting the rapid devolatilization of diverse forms of biomass with bio-Flashchain, Proc Combust Inst 28 (2) (2000) 2727–33.

[54] Nik-Azar M, Hajaligol MR, Sohrabi M, Dabir B, Mineral matter effects in rapid pyrolysis of beechwood, Fuel Process Technol 51 (1-2) (1997) 7–17.

[55] Cagnon B, Py X, Guillot A, Stoeckli F, Chambat G, Contributions of hemicellulose, cellulose and lignin to the mass and the porous proper-

ties of chars and steam activated carbons from various lignocellulosic precursors, Biores Tech 100 (1) (2009) 292–8.

[56] Chatterjee S, Saito T, Lignin-Derived Advanced Carbon Materials, ChemSusChem 8 (2015) 3941–58.

[57] Backlund I, Arshadi M, Hunt AJ, McElroy CR, Attard TM, Bergsten U, Extractive profiles of different lodgepole pine (*Pinus contorta*) fractions frown under a direct seeding-based silvicultural regime, Ind Crops Products 58 (2014) 220–9.

[58] Yu H, Zhang Z, Li Z, Chen D, Characteristics of tar formation during cellulose, hemicellulose and lignin gasification, Fuel 118 (2014) 250–6.

[59] Zhang YL, Luo YH, Wu WG, Zhao SH, Long YF, Heterogeneous Cracking Reaction of Tar over Biomass Char, Using Naphthalene as Model Biomass Tar, Energy Fuels 28 (2014) 3129–37.

[60] Reverchon E, Supercritical fluid extraction and fractionation of essential oils and related products, J Supercrit Fluids 10 (1997) 1–37.

[61] Trubetskaya A, Jensen PA, Jensen AD, Umeki K, Kling J, Glarborg P and etc., Effects of Several Types of Biomass Fuels on the Yield, Nanostructure and Reactivity of Soot from Fast Pyrolysis at High Temperatures, Appl Energy 171 (2016) 468–82.

[62] Ellison C, McKeown MS, Trabelsi S, Boldor D, Dielectric Properties of Biomass/Biochar Mixtures at Microwave Frequencies, Energies 10 (502) (2017) 1–12.

[63] Solomon PR, Carangelo RM, FT-IR analysis of coal: 2. Aliphatic and aromatic hydrogen concentration, Fuel 67 (7) (1988) 949–59.

[64] Selim MM, El-Nabarawy TA, Ghazy TM, Farid T, The relation between the adsorption characteristics of polar organic compounds (alcohols and acids) and their orientation polarization on activated carbon, Carbon 19 (3) (1981) 161–5.

[65] Fornies-Marquina JM, Martin JC, Martinez JP, Miranda JL, Romero C, Dielectric characterization of coals, Can J Phys 81 (3) (2003) 599–610.

[66] Ben AI, Arous M, Kallel A, Effect of maleic anhydride on dielectric properties of natural fiber composite, J Electrostat 72 (2014) 156–60.

[67] Shinoj S, Visvanathan R, Panigrahi S, Kochubabu M, Oil palm fiber (OPF) and its composites: a review, Ind Crops Prod 33 (2011) 7–22.

[68] Ramasamy S, Moghtaderi B, Dielectric Properties of Typical Australian Wood-Based Biomass Materials at Microwave Frequency, Energy Fuels 24 (2010) 4534–48.

[69] Sahin H, Ay N, Dielectric properties of hardwood species at microwave frequencies, J Wood Sci 50 (2004) 375–80.

[70] Surup GR, Heidelmann M, Schubert D, Deike R, Foppe M, Trubetskaya A and etc., The effect of ffedstock origin and temperature on the structure and reactivity of char from pyrolysis at 1300–2800°C, Fuel 235 (2019) 306–16.

[71] Sahajwalla V, Dubikova M, Khanna R, Reductant characterisation and selection: implications for ferroalloys processing, 10^{th} Int Ferroalloys Congress INFACON X. Transformation through Technology 68 (2004) 351–62.

4.5 Charcoal pelleting

Characterization of charcoal composite pellets for the use in ferroalloy industries

Gerrit Ralf Surup[a], Henrik Kofoed Nielsen[a], Marius Großarth[b], Rüdiger Deike[b], Jan Van den Bulcke[c], Pierre Kibleur[c], Iván Josipovic[d], Elena Yazhenskikh[e], Sergey Beloshapkin[f], James J. Leahy[f], Anna Trubetskaya[g,*]

[a]*Department of Engineering Sciences, University of Agder, 4879 Grimstad, Norway*
[b]*Chair of Metallurgy for Iron and Steel Production, University of Duisburg-Essen, 47119 Duisburg, Germany*
[c]*Laboratory of Wood Technology - Woodlab, Gent University, 9000, Gent, Belgium*
[d]*Department of Physics and Astronomy, Gent University, 9000, Gent, Ireland*
[e]*Institute of Energy and Climate Research, Jülich Research Centre, 52428 Jülich, Germany*
[f]*Bernal Center, University of Limerick, Castletroy, Ireland*
[g]*School of Engineering and Ryan Institute, National University of Ireland Galway, Galway, Ireland*

Abstract

This study investigates the effect of heat treatment temperature on the properties of charcoal composite pellets used for the reduction of ferroalloys. The heavy molecular fraction of biooil was used as a binder for the charcoal ore pellet preparation. The effect of heat treatment temperature on the pellet shrinkage was related to the degree of reduction that varied among feedstocks and ore composition. The devolatilization of a binding agent resulted in an increase of charcoal inner pore volume, whereas biooil formed a solidified carbonaceous structure between the charcoal particles and thus, increased the pellet mechanical strength. In addition, the results showed that the size

*Corresponding author. anna.trubetskaya@nuigalway.ie

and shape of charcoal pellets were not affected by the biooil devolatilization. Manganese composite pellets were characterized by the loss of mechanical stability during pyrolysis, whereas the structure and composition of silica composite pellets remained unaffected by heat treatment temperatures $<$ 1650°C. The findings of this work show the potential use of biooil as a binder for the charcoal composite pellet use in ferroalloy industries. The composite pellets are suitable to pre-reduce the manganese-ore in low temperature zones of an industrial furnace, and the charcoal pellets can be used as an alternative bed material. However, the CO_2 high reactivity may create challenges during the direct replacement of metallurgical coke with the bio-reductants.
Keywords:

---

1. Introduction

Metallurgy is one of the most energy intensive industries, which is responsible for about 10 % of the global anthropogenic CO_2 emissions [1, 2]. The use of biomass and its derivatives as CO_2 neutral reduction agents in metallurgical processes can be a possible solution to decrease emissions. One of the challenges to use charcoal in metallurgical processes is related to the fragility and generation of large amounts of fine particles during transportation and storage. The mechanical strength of charcoal can be improved through pelletization or briquetting [3, 4]. In ferroalloy industries, manganese ore pellets must be sintered at higher temperatures to provide a mechanical stability that is similar to that of iron ore pellets [5]. The addition of wood dust and dolomite is known to increase the required sintering temperature of the ore pellets and thus, broadly used in iron and manganse alloy produc-

tion [4–7]. The use of pellets from charcoal-ore blends is known to reduce the electricity demand and increase the yield of elemental manganese [8]. The metallurgical production nowadays is based on the use of fossil-based fuels because the use of charcoal-ore pellets in the reduction process can increase the overall power consumption by 72-152 kWh per tonne FeMn and will increase the cost of a reduction process [7].

The properties of charcoal pellets can be affected by the feedstock, particle size and pelletization process. A constant pellet size improves the porosity of shrinking pellet during the heat treatment leading to the stable operation of a furnace [9]. The high porosity of a charcoal pellet affects the mechanical strength and degree of pre-reduction, whereas the shape factor and size of a carbonaceous pellet have a strong influence on the segregation and gas permeability during the ore reduction [7]. The early stages of the reduction process depend on the mass transfer between the solid carbon and metal oxide [10]. Thus, small carbon charge results in a high pre-reduction of ore metals and decreased heat treatment temperature, which might also affect the temperature in a coke bed [7, 11]. In addition, fine charcoal particles can lead to a poor gas permeability in the burden. Similar problems can occur when the melting temperature is below the reduction temperature and no contact between the molten metal-oxide and the coke bed exists [6]. Moreover, the melting temperature of minerals can affect furnace temperature zones [7], whereas an increased content of acid oxides can decrease the melting temperature of ore metals [12]. The charcoal composition can also affect the ore reduction, whereas an optimum carbon level for the direct reduction of iron ore composite pellets is required to be below the stoichiometric amount of carbon

required for the reduction [13]. Charcoal pellets with the high carbon content could lead to the high volatile matter release, resulting in an increased porosity and formation of cracks during material reduction [13, 14]. In addition, the low mechanical stability, high reactivity and shrinkage of charcoal particles might create challenges for the stable furnace operation [15, 16]. The reduction of charcoal composite pellets results in a significant change of the pellet properties and shape in ferroalloy industries [17, 18]. In previous studies, a dilatation of iron composite pellets was observed in the temperature range from 900 to 1000°C, whereas a shrinkage occurred in the temperature range from 1100 to 1200°C [19, 20]. In addition, the swelling of iron composite pellets at temperatures below 1100°C was correlated to the transition from iron oxide to the elemental metal [3]. The volume of composite pellets can also change due to the increase of temperature gradient that is affected by exothermic and endothermic reactions in the pellet during reduction [3, 21]. However, literature data is scarce that describes the effect of charcoal properties and composition on resulting composite pellet properties that impact metallurgical applications, adding uncertainty to the use of bio-reductants as an approach to increase yields of manganese or silicon during reduction of metal oxides.

In summary, renewable charcoal pellets have potential as environmentally benign replacements to fossil-based composite pellets used in ferroalloys production, but knowledge of relationships between operating conditions, charcoal and binder composition and elemental metal yield is limited. In this study, the impacts of charcoal composition on the density, thermal conductivity and elemental metal yields during reduction in a high temperature

furnace were investigated. The specific objectives of this study were to: (1) understand the influence of reduction process on properties of charcoal composite pellets and (2) determine the degree of charcoal composite pellet reduction changing its properties to levels that are suitable for application in ferroalloy industries.

2. Materials and methods

2.1. Raw biomass characterization

Norway spruce (*Picea abies*) and sessile oak (*Quercus petraea*) were chosen for the charcoal composite pellet study. The age of the Norway spruce was 39 years, whereas oak was 46 years. Feedstock selection was based on the differences in ash composition and plant cell compounds (cellulose, hemicellulose, lignin, extractives) of softwood and hardwood. Norway spruce is low in ash and with lower potassium and calcium contents than oak, whereas oak is low in lignin content. Both spruce and oak samples were chipped by a disc chipper to 5-20 mm and dried at 60°C before storage. Prior to the wood characterization, biomass samples were divided into six equal fractions using a riffler. A vibrating EFL2000 sieve shaker (ENDECOTTS, United Kingdom) comprising ten sieves ranging from 2 to 20 mm in opening size and a bottom pan (< 2 mm) was used (EN ISO 17827-2:2016) to determine the particle size distribution.

2.2. Charcoal characterization

Charcoal samples from Norway spruce and sessile oak were generated from woodchips in the slow pyrolysis reactor at 500, 700, 900, 1100 and

1300°C. The charcoal samples were crushed to a fine powder in a mortar with a ceramic pestle and used for heating microscopy and thermogravimetric analysis tests. Charcoal sample from Norway spruce produced at 900°C was chosen for the reduction in high temperature furnace. Biooil from the slow pyrolysis experiments was chosen as the binding agent. Prior to pelletization, the water fraction of biooil was removed by vacuum distillation (300 mbar and 80°C) and the residue (tar) was used as a binder. A compact hot pellet press (MTI Corporation, USA) was used, that consists of a metal cylinder with a press channel, a backstop and a split furnace. Charcoal pellets were made from charcoal particles, tar binder and water in the wt.% ratio of 60:30:10. Composite pellets were prepared from the high pure manganese ore (Eramet AS, Norway) and charcoal in the wt.% ratio of 66:34, whereas microsilica particles (Elkem AS, Norway) were mixed with the charcoal in the wt.% ratio of 50:50. Pellets with a diameter and height of 3 mm were pressed by a manual pellet press tool (Hesse instruments, Germany). About 3 g of the mixture was pressed at 130 MPa into pellets with a diameter of 12 mm and a height of about 20 mm. Once the pellet was pressed, the backstop was removed and the pellet was extruded from the steel die. The pellets were dried at 30°C overnight in a drying chamber and stored in sealed plastic containers.

2.3. High-temperature furnace

The charcoal was treated in a vacuum induction furnace (max. 60 kW, max. 10 kHz) with a chamber volume of 0.5 m^3. The heating vessel consists of a three-part crucible with an outer alumina crucible (outer diameter: 130 mm, inner diameter: 110 mm, height: 300 mm), a middle carbon crucible

(outer diameter: 90 mm, inner diameter: 50 mm, height: 145 mm) and an inner glass carbon crucible (outer diameter: 50 mm, inner diameter: 38 mm, height: 125 mm), as shown previously [22]. The three-part crucible was positioned in an induction coil. The gap between the alumina crucible and the carbon crucible was filled up with a carbon felt. A carbon felt disc (diameter: 110 mm, height: 30 mm) between the bottom of the alumina and carbon crucibles was used for the high-temperature protection. The pellets were placed in the glassy carbon crucible. The pellet temperature was measured by thermocouples type S about 5 mm above each pellet. Prior to the experiment, the chamber was evacuated and filled with argon. The chamber was continuously purged by argon at a defined flow rate of 20 l min^{-1}. The formation of carbon monoxide was monitored by a gas emission analyser VARIO Luxx (MRU, Germany). The sample was heated to 900°C at a heating rate of 100°C min^{-1} and further heated at 10°C min^{-1} to 1650°C and kept at that temperature for 2 h. After the heating program was finished, the sample was cooled to room temperature at a negative heating rate of 30°C min^{-1} and stored in sealed plastic containers.

2.4. Solid product analysis

2.4.1. Thermogravimetric analysis

The reactivity of the milled charcoal and charcoal pellets were analyzed by exposing samples to a reactive gas consisting of 10, 20, 60 and 100 % volume fraction CO_2 in a thermogravimetric instrument TGA/DSC 1 STARe System (Mettler Toledo, USA). Nitrogen was used as the inert gas to reduce the volume fraction of the CO_2. In each experiment, 5 mg were loaded into an Al_2O_3 crucible. The charcoal samples were firstly heated to 110°C and

kept for 30 min isothermally for drying. The dried samples were subsequently heated to 1100°C at a constant heating rate of 10°C min^{-1} and kept at the final temperature for 30 min. The reaction threshold is the temperature that corresponds to the appearance of the sample mass decrease [23]. Simultaneous non-isothermal thermogravimetric measurements of charcoal were carried out in N_2 to determine the mass loss of incompletely reacted charcoal pellets.

2.4.2. Heating microscope

The silhouettes of charcoal pellets were investigated in inert atmosphere using a heating microscope EM-201-17 (Hesse Instrument, Germany), as shown in Figure 1.

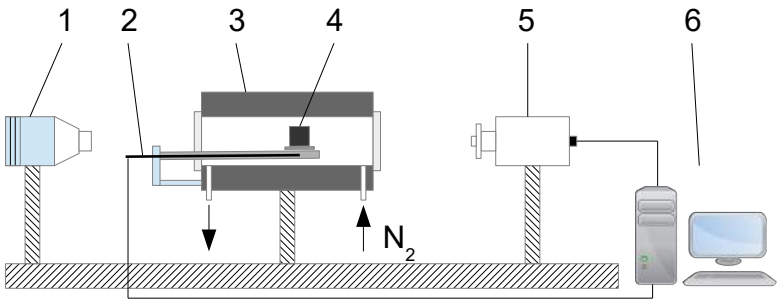

Figure 1: Heating microscope includes the following parts: 1. Light source, 2. Thermocouple type S, 3. Heating chamber, 4. Charcoal pellet sample, 5. Camera, 6. Computer.

Charcoal pellets with a diameter and height of 3 mm were used for the experiments. The charcoal pellets with an edge length of 3 or 4 mm were placed in a center of the sample plate above the tip of the thermocouple. The heating chamber was continuously purged by nitrogen at a constant

rate of 500 ml min^{-1}, which was controlled by a flowmeter HFC-202 (Teledyne, USA). The samples were heated to 500°C at a constant heating rate of 30°C min^{-1} and further heated at a heating rate of 10°C min^{-1} to the final temperature, where the samples were kept for 30 min.

2.4.3. Electrical resistivity

Electrical conductivity measurements were performed using a 34470A 7 1/2 Digit Multimeter (Keysight Technologies, USA). The connection between the four probes of the source meter and microelectrodes was established using a socket. Two adjacent electrodes were connected to the voltmeter (Fluke, USA), whereas the other two electrodes were connected to the current source (ISO-Tech IPS 3303) (constant current) of the source meter, as it was reported by Sun et al. [24]. A charcoal pellet was connected by four different electrodes to the source meter based on the van der Pauw electrode geometry [25]. The electrical conductivity was determined according to equation 1:

$$\sigma = \frac{L}{R \cdot A} \tag{1}$$

In equation 1, σ is the electrical conductivity, A is the cross-sectional area, L is the length of the resistor, and R is the resistance between Ti-Au electrodes.

2.4.4. Microscopy

The surface properties of charcoal composite pellets were investigated using a digital microscope VHX-500F (Keyence, Germany), whereas the cross-sections of samples were analyzed using an optical microscope DM4000 M LED (Leica, Germany). Prior to the analysis, the composite pellets were embedded in the conductive polymer Technovit® 5000 (Kulzer Technik, Germany). SEM/EDS analysis of the char was conducted on a high-resolution

field emission microscope SU-70 (Hitachi, Japan) under high vacuum in order to understand structural properties and composition of ferroalloys and charcoal pellets. The elemental mapping was performed on four different areas of interest for the manganese oxides and quartz charcoal pellets.

2.4.5. Thermodynamic calculations

Thermodynamic calculations were performed using the computational package FactSage [26]. The commercial database FToxid combined with the dataset FactPS for pure substances along with the new GTOX oxide database (Research Center Juelich and GTT-Technologies, Germany) [27] combined with the commercial database for pure substances (SGPS) were used for the equilibrium calculations under defined conditions (chemical composition of a system, temperature, pressure). All available phase relations were taken into account by calculation: the Gibbs energy of a system is minimized in order to find the equilibrium state. The results were obtained for equilibrium conditions only, the possible kinetic effects are not considered.

2.5. X-ray diffraction

The crystalline constituents of charcoal and charcoal composite pellets were characterized using an Empyrean X-ray diffractometer with a copper tube, a quartz monochromator (CuKα1 radiation, $\lambda = 1.54056$ Å), using an imaging strip covering 100° as a detector for 4 h. The diffractometer was operated in transmission mode with the sample placed on tape in a thin layer and placed on a rotating disc-holder. The phase analyses were done in the Crystallographica Search-Match software (Version 3,1,0,0) and the ICDD PDF4 database. The multiple phase fitting of the PXRD patterns

and crystallite size analysis were carried out with the WINPOW Rietveld software. The refined backgrounds have been subtracted in the displayed PXRD patterns.

2.5.1. X-ray microtomography

The charcoal pellets were scanned using the HECTOR X-ray CT system [28, 29] at the Ghent University Centre for X-ray Tomography (UGCT, www.ugct.ugent.be). The HECTOR system was developed and built by the Radiation Physics group of the UGCT in collaboration with TESCAN XRE, (www.XRE.be, part of the TESCAN ORSAY HOLDING a.s.), formerly known as XRE, a UGCT spin-off company. More specifically, a Region Of Interest (ROI) of an untreated and treated pellet before and after heat treatment was scanned without subsampling, thus avoiding any artifacts due to the sample manipulation. The X-ray tube voltage and tube power were 70 kV and 10 W, respectively. 2401 projections were collected, with an exposure time of 1 s, over a sample rotation of 360°, resulting in a total scan time of 1 h. The volumes were reconstructed using the Octopus Reconstruction software [30], licensed by XRE, and the spatial resolution in terms of approximate voxel pitch was 3.5μm. The reconstructed pellet structure corresponds to a cylinder with a diameter of 6.7 mm and a height of 5.9 mm. In order to calculate the porosity within the pellet volume, segmentation was carried out by thresholding using Otsu's method as a first estimate but further fine-tuned visually [31]. Image analysis was carried out using Octopus Analysis, formerly known as Morpho+ [32], while the 3D visualizations were performed with VGStudio MAX3.2 (Volume Graphics GmbH, Germany).

3. Results and discussion

3.1. Biomass characterization

The ultimate and proximate analysis of oak and spruce was carried out at Eurofins Lidköping and shown in Table 1.

Table 1: Proximate, ultimate and ash analyses of feedstocks.

Fuel	Norway spruce	Oak
Proximate analysis		
Moisture, (wt. % as received)	8.6	7.6
Ash at 550 °C, (wt. % dry basis)	0.8	1.6
Volatiles, (wt. % dry basis)	80.6	82.6
Fixed carbon content (wt. % dry basis)	18.6	15.8
HHV, (MJ kg^{-1})	20.3	19.3
LHV, (MJ kg^{-1})	18.5	17.5
Ultimate analysis, (wt. %, dry basis)		
C	53.2	50.6
H	6.1	6.1
N	0.1	0.2
S	0.06	0.02
Cl	0.04	0.02
Ash compositional analysis, (mg kg^{-1} on dry basis)		
Al	40	20
Ca	2300	3600
Fe	200	50
K	800	1500
Mg	250	300
Na	<50	<50
P	200	250
Si	550	550
Ti	50	50

The compositional analysis of biomass (cellulose, hemicellulose, acid-soluble lignin, acid-insoluble lignin, and extractives) was conducted by Celig-

nis Analytical according to NREL technical reports [33–35] and Thammasouk et al. [36], and is shown in Table 2.

Table 2: Composition of Norway spruce and oak, calculated in percentage based on dry basis (wt. %).

Biomass	**Cellulose**	**Hemicellulose**	**Lignin**		**Extractives**
			acid insoluble	**acid soluble**	
Norway spruce	37.8	25	27.9	0.7	7.8
Oak	36.7	18.7	19.4	2.5	11

3.2. Product yields

The original spruce and oak charcoal pellets and charcoal composite pellets from pyrolysis at temperatures ranging from 500 to 1300°C were reacted in a heating microscope in order to study the pellet behaviour at high temperatures. The mass losses from tests using heating microscopy were recorded at 1200°C. In addition, the mass losses of manganese and quartz charcoal pellets were determined in the high-temperature furnace at 1550 and 1650°C, as shown in Figure 2. The results showed that the mass loss from secondary pyrolysis of both spruce and oak charcoal pellets decreased with increasing primary pyrolysis temperature, from about 55 % for charcoal produced at 500°C to 11 % for charcoal generated at 1300°C. In general, the mass loss of original charcoal pellets was greater than the mass loss of secondary heat treated charcoal particles that decreased from about 22 % for charcoal produced at 500°C to 6 % for charcoal generated at 1300°C [22]. The greater mass loss of charcoal pellets compared to the mass loss of original charcoal particles was attributed to the high content of binder and water in a pellet.

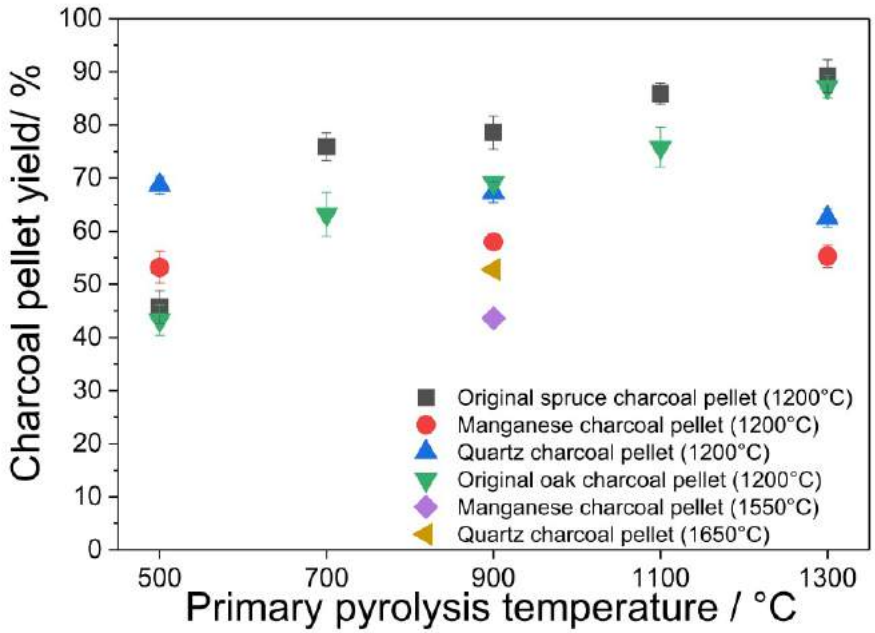

Figure 2: Charcoal pellet yields (%) from pyrolysis in a heating microscope and high-temperature furnace.

In addition, the pellet from charcoal produced at 1300°C showed the greatest solid yield, indicating the enhanced coke formation from reacting biooil in a charcoal matrix. This was related to the increase in porosity of charcoal that was caused by the progressive removal of volatiles from pores, and the physical and chemical condensation of the remaining skeletal charcoal structure with increasing heat treatment temperature [37, 38]. Thus, the charcoal particles with the greater porosity had a stronger tendency to trap reacting biooil in voids than the charcoal produced at heat treatment temperatures below 1300°C, confirming previous results of Veksha et al. [39]. The solid pellet yields of composite pellets remained similar for the charcoal produced at 500, 900 and 1300°C, indicating a competition between

devolatilization and reduction reactions. In addition, the solid yields of composite pellets were lower than the solid yields of original charcoal pellets. This is also probably due to competing reduction and devolatilization reactions in pyrolysis of charcoal composite pellets [40].

3.3. Gas evolution

The gas evolution of composite pellets is shown in Figure 3.

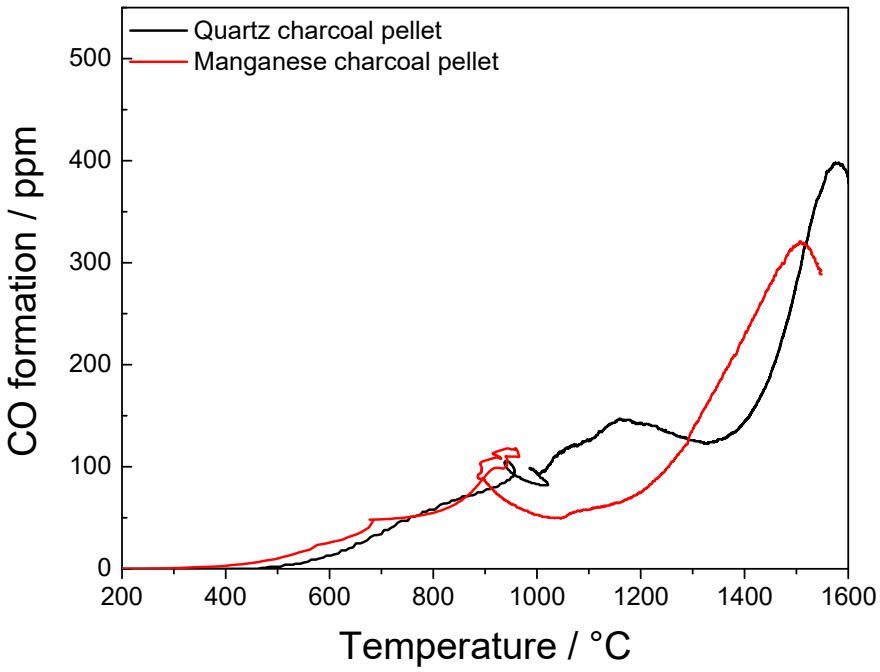

Figure 3: CO evolution of manganese and quartz charcoal pellets during pyrolysis.

The gas evolution at temperatures below 1000°C was related to the biooil devolatilization and decomposition. The CO formation in pyrolysis of manganese charcoal pellets was observed at 1020°C with the maximum yield

at 1480°C, confirming previous results of Tangstad et al. [7, 41]. The melting point of manganese oxides increased with the decreased oxidation state of manganese in the temperature range from 535°C (MnO_2) to 1945°C (MnO), whereas the elemental manganese has a melting point of 1246°C [42]. Thus, the high oxidation states of manganese can melt and faster react with the carbonaceous matrix of charcoal than the low manganese oxidation states during the reduction. The CO formation during reduction of quartz charcoal pellets began at 1330°C with the maximum yield at 1580°C. In the present study, the temperature for the maximum CO yield was 100°C lower than temperatures reported in previous studies [43]. The decrease in temperature required for the maximum CO formation during charcoal pellet conversion into the elemental metals emphasize a key role of feedstock on the reduction of ferroalloys.

3.4. Charcoal pellet reactivity

Figure 4 shows the differential weight loss curves for the 100 % volume fraction CO_2 gasification of spruce and oak charcoal pellets with a diameter of 3 mm. The DTG curves show a double peak in CO_2 gasification, indicating a heterogeneous char mixture with respect to the composition that leads to the differences in reactivity of two constituents with less reactive carbon structure. The maximal reaction rates of spruce charcoal pellets varied from 950 to 1010°C. The maximum reaction rate of oak charcoal pellets ranged from 930 to 1010°C, indicating a minor effect of feedstock origin on the char reactivity. The maximum reaction rates of spruce and oak charcoal pellets reacted at 1300°C were the highest and nearly identical.

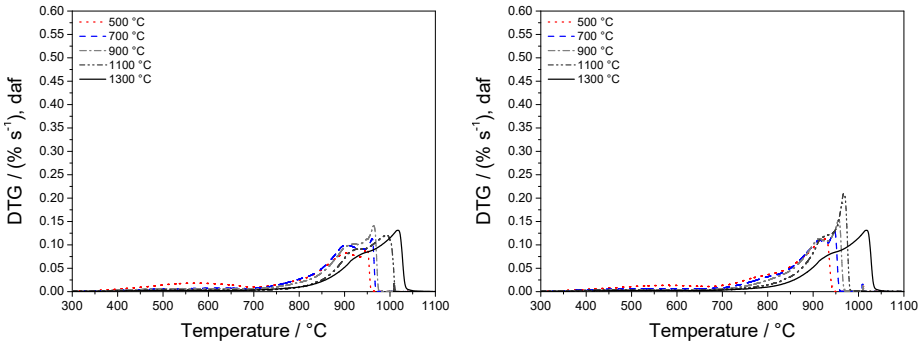

4(a): Spruce pellets

4(b): Oak pellets

Figure 4: DTG curves of charcoal pellets generated from (a) spruce and (b) oak and reacted in 100 % volume fraction CO_2.

In general, the maximum reaction rates of charcoal pellets were similar to the reaction rates of secondary heat treated biooil-charcoal blends from previous studies [22]. The results show that differences in heat treatment temperature have more influence on charcoal reactivity than the feedstock composition. Moreover, the present results indicated that the gas permeability between the charcoal particles was not affected by pelletizing process and addition of biooil as a binder. The devolatilization of water and light molecular compounds in biooil might increase the porosity inside the pellets approching the porosity of bulk charcoal material that was confirmed by the optical microscopy below.

3.5. Electrical resistivity

The electrical resistivity of charcoal composite pellets was studied after compression, drying and secondary heat treatment (SHT) in the high temperature furnace. The results were summarized in Table 3.

Table 3: Electrical resistivity of manganese oxide or quartz charcoal pellets.

	After pressing		After drying		After SHT	
Material	Ωm	σ	Ωm	σ	Ωm	σ
MnO charcoal pellet	1.7	0.4	1.1	0.26	0.34	0.1
Quartz charcoal pellet	0.38	0.035	1.1	0.44	0.44	0.13

The electrical resistivity of manganese oxide charcoal pellets decreased from 1.7 to 0.35 Ωm, whereas the electrical resistivity of quartz charcoal pellets remained unchanged ($\approx 0.4\,\Omega$m). In comparison, the electrical resistivity of original charcoal pellets increased from 0.8 to 1.5 Ωm after the heat treatment [22]. Howeover, the electrical conductivity of original charcoal particles decreased from 1.5 to 0.01 Ωm in the temperature range from 700 to 900°C and kept nearly constant for the heat treatment up to 1300°C, emphasizing the importance of temperature in the range above 900°C.

3.6. Pellet shrinkage

Figure 5 shows silhouette areas of original charcoal pellets from spruce and oak and charcoal manganese oxide pellets using the heating microscope at temperatures up to 1200°C. The charcoal pellets were shrinking when the primary pyrolysis temperature was surpassed. The distillation of biooil resulted in a dilatation of oil and solid coke formation. Interestingly, no swelling was observed on the surface of charcoal pellets in the boiling range. The results indicated that the incomplete pyrolysis was progressing even when the heat treatment temperature surpassed the final temperature of primary pyrolysis. Moreover, the evaporation of light molecular species from biooil had no influence on the particle size and shape of charcoal pellets.

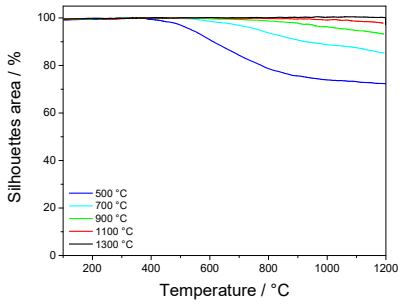

5(a): Original spruce pellets

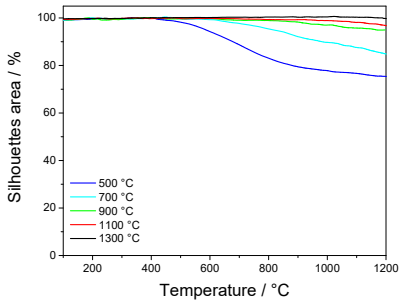

5(b): Original oak pellets

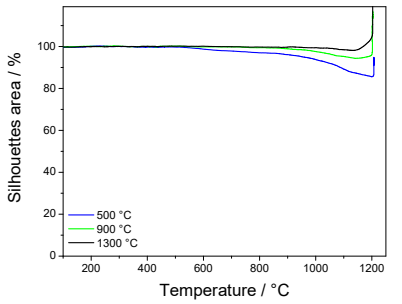

5(c): Spruce manganese oxide charcoal pellet

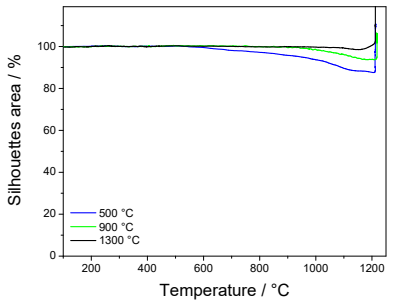

5(d): Oak manganese oxide charcoal pellet

Figure 5: Percentage of silhouette area changes of original wood pellet and charcoal manganese oxide pellets in nitrogen atmosphere using heating microscopy at temperatures up to 1200°C.

A dilatation of manganese oxide charcoal pellets was observed when the sample reached the final temperature of 1200°C. The pellets formed whiskers at the outer surface when the temperature was increased to 1300°C and residence time of 30 min, as shown in the supplemental material (Figure S-4). The structural changes were not observed at temperatures greater than 1300°C during experiments in the high temperature furnace. Thus, the present results showed that the manganese ore was reduced to the elemen-

tal manganese and further reacted to manganese(II) nitride at temperatures below 1300°C, confirming the previous observations of Lyutaya et al. [44].

3.7. Thermodynamic calculations with FactSage

The equilibrium calculations of charcoal composite pellets were performed to investigate the formation of slag phases. The thermodynamic calculations showed that silicon carbides, silicon oxides, carbon and gas were the dominating phases formed during quartz charcoal pellet reduction, as shown in Figure 6. The manganese carbides were found along with silicates in manganese composite pellets. The thermodynamic calculations showed that liquid elemental manganese, manganese carbide (C_3Mn_7) and liquid manganese oxides (MnO) were the dominating phases formed during pyrolysis of MnO containing charcoal pellets in the temperature range from 1200 to 1300°C. The previous studies showed the formation of manganese carbides in the temperature range from 800 to 1300°C [45], whereas manganese oxides and liquid oxides were formed at temperatures greater than 1200°C [46]. The C_6Mn_{23} compound was formed for MnO/C ratios greater than 1/1.3, whereas C_3Mn_7 and carbon were formed during reduction with the larger carbon excess ratios [47]. The equilibrium calculations showed that C_3Mn_7 can be formed at temperatures up to 1400°C, whereas the dissociation of manganese carbides into liquid manganese alloys and graphite can occur at temperatures above 1300°C through peritectic reactions [48]. The MnO/C ratios lower than 1/1.3 provide sufficient amount of carbon that completely reduces manganese alloys based on the XRD results from previous studies [48]. In the present study, the formation of manganese carbides during reduction can be related to the slow cooling rate [49].

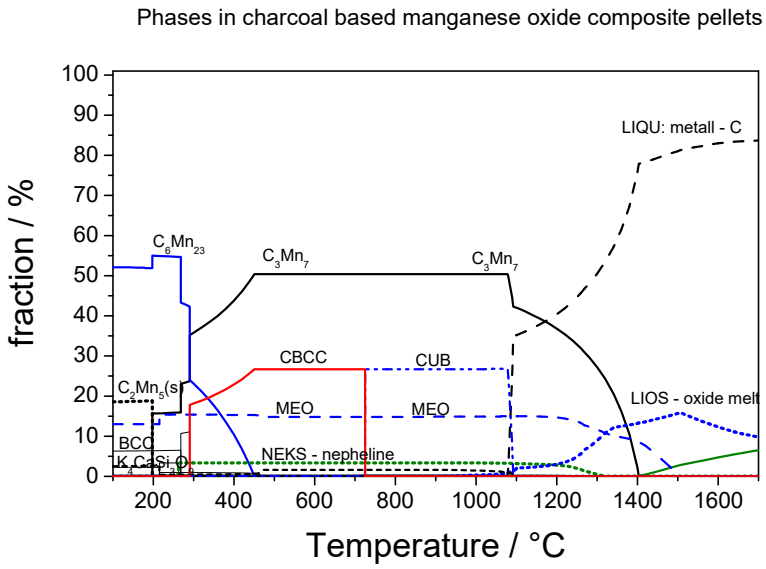

6(a): Manganese ore composite pellet

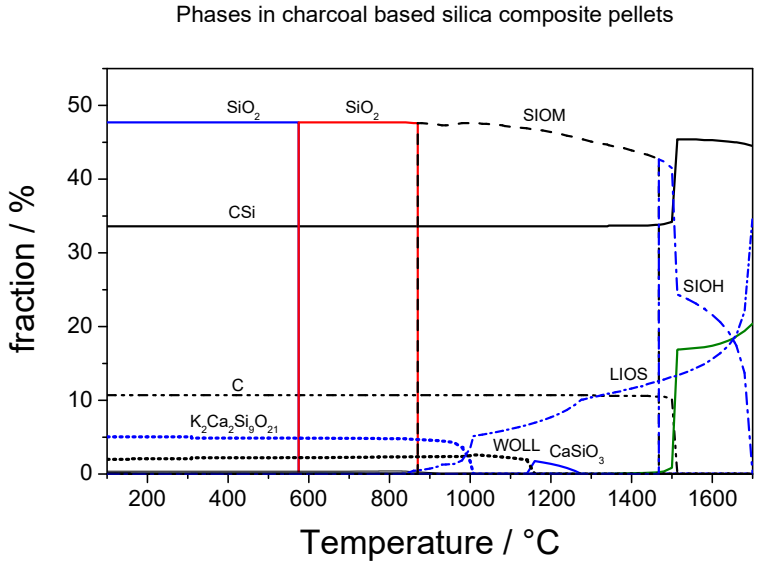

6(b): Silica composite pellet

Figure 6: Output results of FactSage calculation using GTOX database with the main inorganic components of charcoal composite pellets with MnO or quartz particles after heat treatment at 1650°C. The following abbreviations were used MEO (blend of MnO, FeO and CaO), LIOS (oxide melt), CBCC and CUB (manganese solid solution phases), BCC (iron solid solution phase), SIOM (solid solution based on $SiO_{2,tridymite}$), SIOH (solid solution based on $SiO_{2,cristobalite}$) and WOLL (wollastanite).

3.8. X-ray diffraction

The XRD analysis of original spruce indicated the formation of crystalline pattern correlated to the cellulose structure, as shown in Figure 7.

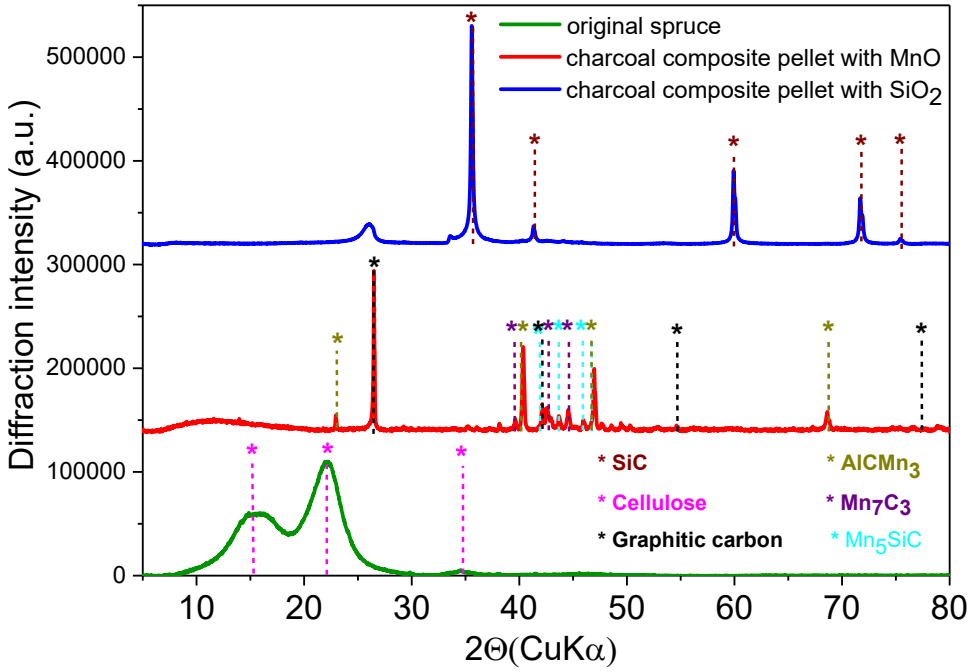

Figure 7: XRD measurements of original spruce, spruce charcoal pellet with MnO particles or with quartz particles after heat treatment.

The broad reflections at 15, 22.5 and 35° show the development of a crystalline phase, where the c axis of the crystal is parallel to the cellulose chain axis [50]. The XRD results showed that charcoal pellets with MnO particles exhibit reflections from graphitic carbon indicating the progress in graphitization with the increasing heat treatment temperature. In addition, charcoal pellets with MnO particles contain reflections from orthorhom-

bic manganese carbides (Mn_5SiC and Mn_7C_3) and cubic manganese carbide (Mn_3AlC), whereas charcoal quartz pellets contain sharp and narrow reflections from silicon carbide [51, 52]. The formation of silicon carbides during high-temperature pyrolysis of charcoal quartz pellets is related to the decomposition of charcoal carbon on quartz particles [43].

3.9. Microscopy

The external surface structure of manganese charcoal pellet after reduction was studied using microscopy, as shown in Figure 8.

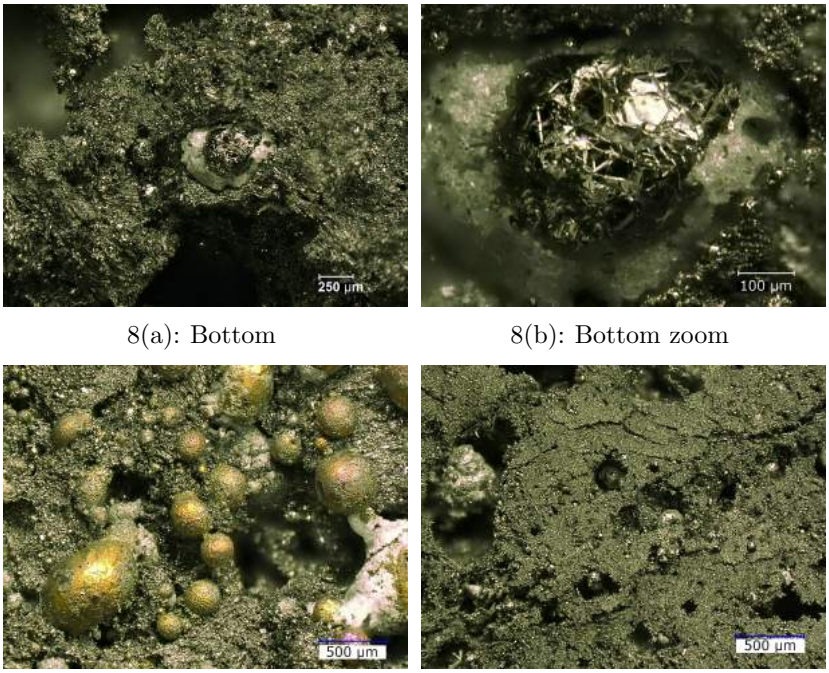

8(a): Bottom 8(b): Bottom zoom

8(c): Top 8(d): Side

Figure 8: Optical microscopy of manganese composite pellets at the bottom, at the top and on side pellet locations.

The structural changes of composite charcoal pellet after reduction were investigated at the top, bottom and side locations. Figure 8(a) shows that the porosity of manganese alloy particles increased after heat treatment. In addition, Figure 8(b) shows the formation of a metal skeleton with the large voids that probably contained manganese carbides due to the high amount of carbon detected during SEM-EDS analysis. The original structure of charcoal particles was only observed at locations where manganese oxide particles were not incorporated, as shown in Figures 8(c)-8(d).

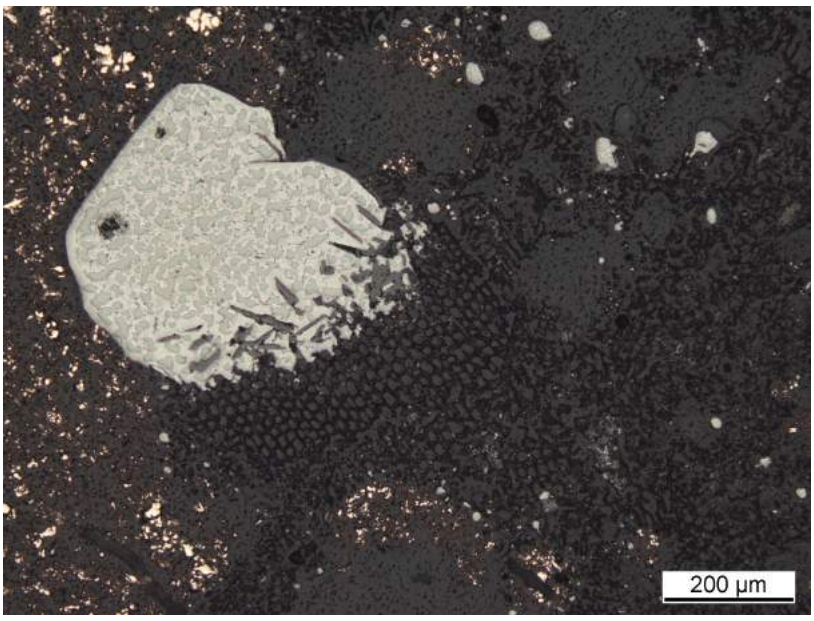

Figure 9: Cross section of the manganese charcoal pellet.

Figure 9 shows the cross section of manganese charcoal pellets. The high temperature reduction of manganese oxides led to the formation of large voids inside the particle, which were filled with the reacting charcoal material. Moreover, Figure 9 indicates the formation of different liquefied metal

phases. The dissolution of the carbon into the metal slag was observed at the boundary layer between slag and charcoal particles, as observed in the previous studies [53]. Figure 10 shows that the structure of quartz charcoal pellets remained unchanged after the reduction at 1650°C. The charcoal structure can visually separated from the unreacted quartz particles. However, an additional solid carbon structure was formed inside the charcoal structure during the reduction. This was related to the formation of silicon carbides during the reduction. The previous studies showed that SiO gas could react with the solid carbon at temperatures above 1512°C according to reaction 2 [54].

$$SiO(g) + 2C = SiC(s) + CO(g) \tag{2}$$

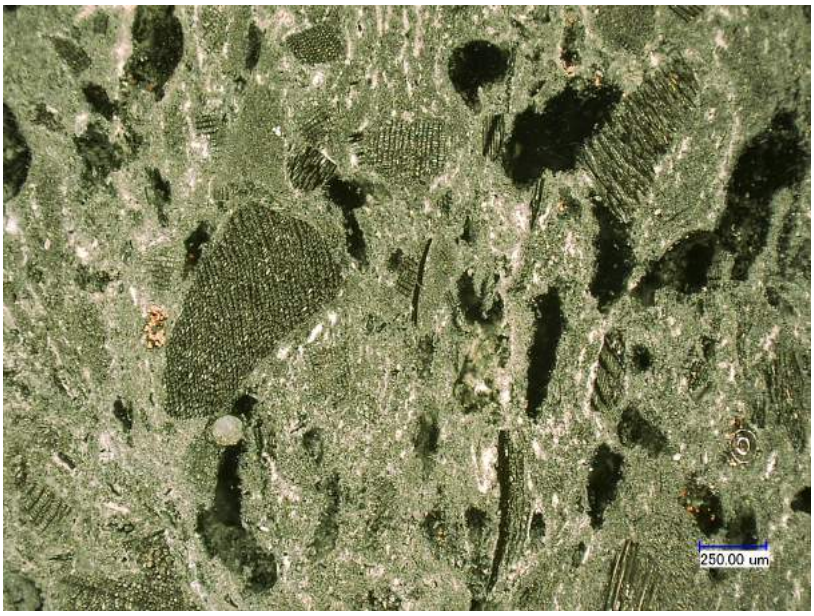

Figure 10: Optical microscopy of quartz charcoal pellets.

The additional layer of silicon carbides could block the pellet surface for

the further consecutive reactions, resulting in a reduced formation of CO at 1650°C [55].

The elemental composition of charcoal composite pellets is summarized in the supplemental material (Table S-3). The mapping areas of the SEM-EDS analysis were schematically shown in the supplemental material (Figure S-5 and Figure S-6). Results of elemental analysis using the SEM-EDS technique showed that iron, aluminum and silicon were detected in the reduced manganese oxide charcoal pellet. The metal skeleton was embedded into the carbonaceous charcoal matrix, whereas oxygen was mainly observed in the charcoal enriched spots. Moreover, the high amounts of carbon and manganese suggested that manganese oxides were reduced to manganese and manganese carbides during high temperature treatment. The elemental analysis of reduced quartz charcoal pellets indicated that the composition remained only slightly changed during the reduction due to the high oxygen content in the charcoal particles. However, the high mass loss of quartz charcoal pellets (47 %) indicated the decomposition of charcoal and biooil and the reduction of quartz based on the results above 3.2.

3.10. X-ray microtomography

Figure 11 shows the 2D and 3D cross-sectional slices obtained from XμCT measurements for non-treated and heat treated charcoal pellets. The characteristic features of charcoal particles are observed for all scanned samples. The spatial resolution of 3.5 μm is sufficient for observing most features of the charcoal particles and binder, providing physically reasonable structural assessments. The XμCT images indicated that charcoal particles in heat treated pellets were more porous than charcoal particles in untreated

pellets. The greater level of voids, obtained with the pellet treatment than in non-treated pellets reflects the greater porosity of treated charcoal pellets. The increased porosity from 0.5 to 1.4 % with the temperature treatment in the charcoal pellets was mostly related to the volatile release in the heat treatment.

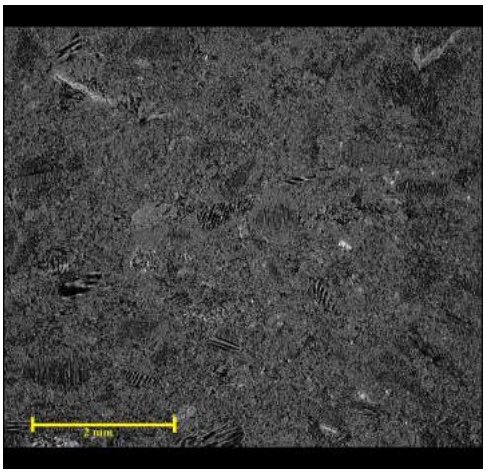

11(a): 2D projection of non-treated pellet

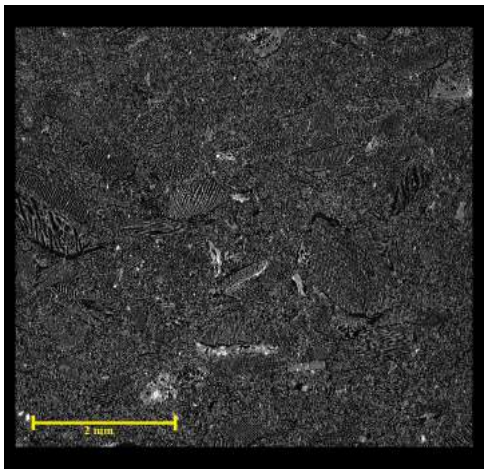

11(b): 2D projection of heat treated pellet

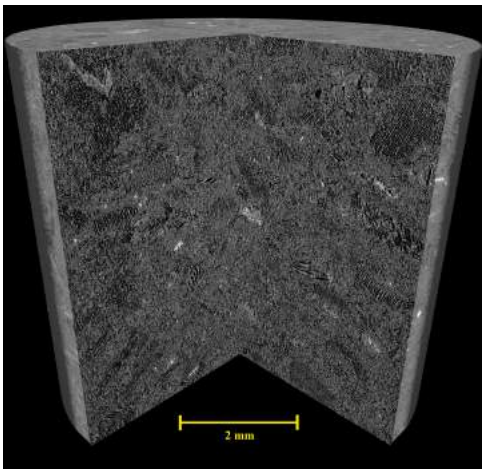

11(c): 3D projection of non-treated pellet

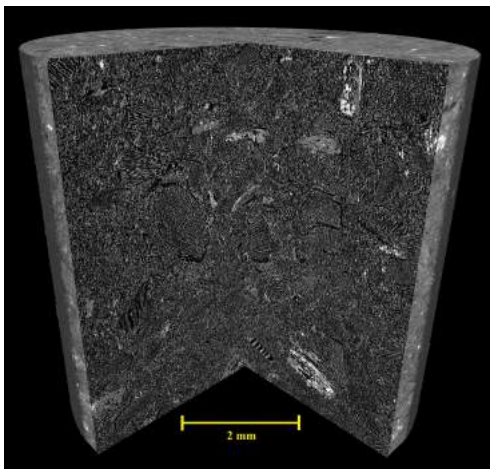

11(d): 3D projection of heat treated pellet

Figure 11: XμCT imaging analysis of non-treated and heat treated charcoal pellets.

The XμCT images indicated that solid manganese oxide particles melt and formed large voids during the reduction of charcoal composite pellets, as shown in Figure 12.

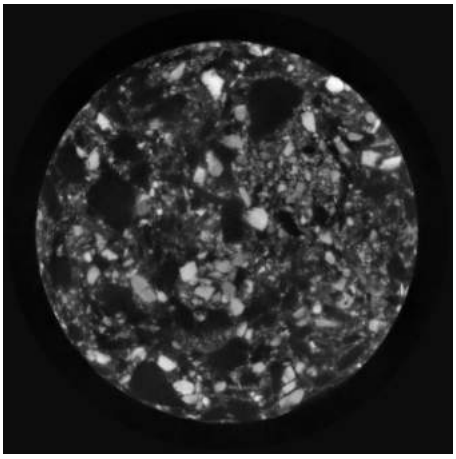

12(a): 2D projection of raw Mn charcoal pellet

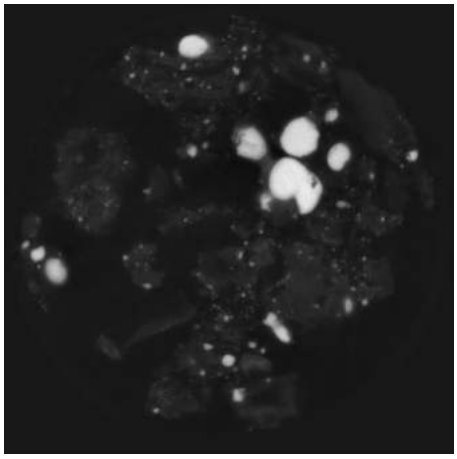

12(b): 2D projection of heat treated Mn charcoal pellet

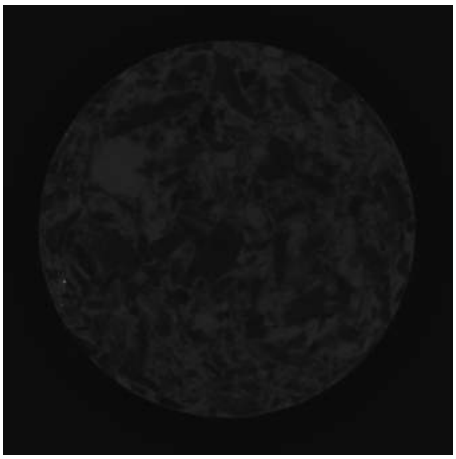

12(c): 2D projection of raw SiO_2 charcoal pellet

12(d): 2D projection of heat treated SiO_2 charcoal pellet

Figure 12: XμCT imaging analysis of raw and heat treated manganese or quartz charcoal pellets.

The low level of voids in the carbonaceous matrix of charcoal pellets after reduction reflects the reaction of manganese oxide and organic charcoal matter into the elemental manganese, manganese carbides, etc. In addition, the increased porosity from 50.1 to 84.7 % in the manganese charcoal pellets was mostly related to the transformation of manganese oxides to the elemental manganese and released gaseous products during the reduction. The XμCT images indicated that quartz particles in charcoal composite pellets remained unchanged in terms of the shape and size, corresponding to the optical microscopy results. In addition, quartz particles remained solid and the border between quartz particles and charcoal matrix is visible indicating less transformations during the quartz charcoal pellet reduction than during the heat treatment of manganese charcoal pellets.

4. Conclusion

The novelty of this work relies on the fact that the solid yield, electrical resistivity and conversion of ferroalloys to the elemental metals can be improved by the addition of biooil as a binder to the charcoal composite pellets. Softwood and hardwood were converted into renewable carbonaceous reductants using pyrolysis treatment. The experiments in the heating microscope and high-temperature furnace showed that the solid yields were greater during reduction of original charcoal pellets than during pyrolysis of charcoal composite pellets. The addition of biooil increased the porosity of charcoal composite pellets and thus, enhanced the gas permeability and competition of devolatilization and reduction reactions in pyrolysis. Moreover, the addition of biooil did not have any influence on the size and shape of a

charcoal composite pellet, leading to the negligible changes in the pellet mechanical stability. The charcoal pellets obtained a similar reactivity to the charcoal-biooil blends and thus, remained more reactive than fossil-based coke. In addition, the biooil showed properties of a binder that increased the electrical resistance of manganese charcoal pellets and did not influence the electrical properties of quartz charcoal pellets. This indicates a major effect of ferroalloy origin on the pellet electrochemical properties. The findings of this study emphasize the potential use of biocarbon-based composite pellets in the ferroalloy industry with concomitant improvement in charcoal transportation and storage.

Acknowledgements

The authors gratefully acknowledge financial support from Elkem AS, Saint Gobain Ceramic Materials AS, and Eramet Norway AS.

References

[1] Steinfeld A, High-temperature solar thermochemistry for CO_2 mitigation in the extractive metallurgical industry, Energy 22 (2) (1997) 311–6.

[2] Balomenos E, Panias D, Paspaliaris I, Energy and Exergy Analysis of the Primary Aluminum Production Processes: A Review on Current and Future Sustainability, Mineral Process Extrac Metal Review 32 (2) (2011) 69–89.

[3] Nascimento RC, Mourao MB, Capocchi JDT, Reduction-swelling behaviour of pellets bearing iron ore and charcoal, Can Metall Quart 37 (5) (1998) 441–8.

[4] Dutta SK, Iron ore–coal composite pellets/briquettes as new feed material for iron and steelmaking, Mat Sci Eng Int J 1 (2017) 10–3.

[5] Olsen SE, Tangstad M, Lindstad T, Production of Manganese Ferroalloys, Tapir Akademisk Forlag, 2007.

[6] Lintumaa T, Krogerus H, Jokinen P, Factors affecting the reducibility of sintered chromite pellets and chromite lump ore, INFACON XI, New Delhi, India (2007) 75–84.

[7] Tangstad M, Leroy D, Ringdalen E, Behaviour of agglomerates in ferromanganese production, Infacon XII, Hensinki, Finland (2010) 457–66.

[8] Yoshikoshi H, Takeuchi O, Miyashita T, Kuwana T, Kishikawa K, Development of Composite Cold Pellet for Silico-Manganese Production, Transactions ISIJ 24 (6) (1984) 492–7.

[9] Use of sintered pellets in production of high carbon ferrochrome, 2007.

[10] Zhang B, Xue Z, Kinetics Analyzing of Direction Reduction on Manganese Ore Pellets Containing Carbon, IJNM 2 (2013) 116–20.

[11] Jayakumari S, Tangstad M, Carbon materials for silicomanganese reduction, Infacon XIV, Kiev, Ukraine (2015) 374–81.

[12] Brynjulfsen T, Tangstad M, Melting and reduction of manganese sinter and pellets, Infacon XIII, Almaty, Kazakhstan (2013) 137–47.

[13] Mishra S, Roy GG, Effect of Amount of Carbon on the Reduction Efficiency of Iron Ore-Coal Composite Pellets in Multi-layer Bed Rotary Hearth Furnace (RHF), Metall Mat Trans B 47 (4) (2016) 2347–56.

[14] Kasai E, Kitajima T, Kawaguchi T, Carbothermic Reduction in the Combustion Bed Packed with Composite Pellets of Iron Oxide and Coal, ISIJ Int 40 (9) (2000) 842–9.

[15] Mašlejová A, Utilization of biomass in ironmaking, Metal (2013) 122–7.

[16] Papadikis K, Gu S, Bridgwater AV, CFD modelling of the fast pyrolysis of biomass in fluidised bed reactors: Modelling the impact of biomass shrinkage, Chem Eng J 149 (1-3) (2009) 417–27.

[17] Sah R, Dutta SK, Effects of Binder on the Properties of Iron Ore-Coal Composite Pellets, Min Process Extr Met Rev 31 (2) (2010) 73–85.

[18] Pal J, Ayyandurai A, Ammasi A, Hota SK, Koranne VM, Venugopalan T, Improving reducibility of iron ore pellets by optimization of physical parameters, J Min Metall Sect B Metall 53 (2016) 1–10.

[19] Seaton CE, Foster JS, Velasco J, Structural Changes Occurring during Reduction of Hematite and Magnetite Pellets Containing Coal Char, Transactions ISIJ 23 (6) (1983) 497–503.

[20] Yunos NFM, Aziz NA, Ismail AN, Idris MA, Reduction Behaviour of Iron Ores by Agricultural Waste Chars, Mat Sci Forum 819 (2015) 31–6.

[21] Seaton CE, Foster JS, Velasco J, Reduction Kinetics of Hematite and Magnetite Pellets Containing Coal Char, Transactions ISIJ 23 (6) (1983) 490–6.

[22] Surup GR, Vehus T, Eidem PA, Trubetskaya A, Nielsen HK, Characterization of renewable reductants and charcoal-based pellets for the use in ferroalloy industries, Energy 167 (2019) 337–45.

[23] Suopajärvi H, Kemppainen A, Haapakangas J, Fabritius T, Extensive review of the opportunities to use biomass-based fuels in iron and steelmaking processes, J Clean Prod 148 (2017) 709–34.

[24] Sun L, Wang J, Bonaccurso E, Conductivity of individual particles measured by a microscopic four-point-probe method, Sci Rep 3 (2013) 1–5.

[25] van der Pauw LJ, A Method of Measuring Specific Resistivity and Hall Effect of Discs of Arbitrary Shape, Philips Res Rep 13 (1) (1958) 1–9.

[26] Bale CW, Belisle E, Chartrand P, Decterov SA, Eriksson G, Gheribi AE and etc., FactSage thermochemical software and databases, 2010-2016, Calphad 54 (2016) 35–53.

[27] Hack K, Jantzen T, Müller M, Yazhenskikh E, Wu G, A novel thermodynamic database for slag systems and refractory materials, Proceedings 5th Int Congress Sci Tech Steelmaking, ICS Dresden (2012) 1–15.

[28] Dierick M, Van Loo D, Masschaele B, Boone M, Van Hoorebeke L, A LabVIEW based generic CT scanner control software platform, J X-ray Sci Technol 18 (4) (2010) 451–61.

[29] Masschaele B, Dierick M, Van Loo D, Boone MN, Brabant L, Pauwels E and etc., HECTOR: A 240kV micro-CT setup optimized for research, J Phys Conf Ser 463 (1) (2013) 1–4.

[30] Vlassenbroeck J, Dierick M, Masschaele B, Cnudde V, Van Hoorebeke L, Jacobs P, Software tools for quantification of X-ray microtomography at the UGCT, Proceedings 5th Int Congress Sci TechSteelmaking, ICS Dresden (2012) 1–15.

[31] Otsu N, A Threshold Selection Method from Gray-Level Histograms, IEEE Transactions on systems, man, and cybernetics 9 (1) (1979) 62–6.

[32] Brabant L, Vlassenbroeck J, De Witte Y, Cnudde V, Boone MN, Dewanckele J and etc., Three-dimensional analysis of high-resolution X-ray computed tomography data with Morpho+, MICROSC MICROANAL 17 (2011) 252–63.

[33] Sluiter A, Hames B, Ruiz R, Scarlata C, Sluiter J, Templeton D et al., Determination of Structural Carbohydrates and Lignin in Biomass. Golden (CO): National Renewable Energy Laboratory; 2011 July Report No. NREL/TP-510-42618. Contract No.: DE-AC36-08-GO28308 .

[34] Willför S, Hemming J, Leppänen AS, Analysis of extractives in different pulps - Method development, evaluation, and recommendations. Finland: Åbo Akademi University, Laboratory of Wood and Paper Chemistry; 2004-2009 Report No. B1 of the EU COST E41 action "Analytical tools with applications for wood and pulping chemistry" .

[35] Hames B, Ruiz R, Scarlata C, Sluiter J, Sluiter A, Preparation of Samples for Compositional Analysis. Golden (CO): National Renewable Energy Laboratory; 2011 June Report No. NREL/TP-510-42620. Contract No.: DE-AC36-99-GO10337 .

[36] Thammasouk K, Tandjo D, Penner MH, Influence of Extractives on the Analysis of Herbaceous Biomass, J Agric Food Chem 45 (1997) 437–43.

[37] Kumar M, Gupta RC, Influence of carbonization conditions on physical properties of Acacia and Eucalyptus wood chars, Trans Ind Inst Met 46 (6) (1993) 345–52.

[38] Brewer CE, Chuang VJ, Masiello CA, Gonnermann H, Gao X, Dugan B and etc., New approaches to measuring biochar density and porosity, Biomass Bioenergy 66 (2014) 176–85.

[39] Veksha A, McLaughlin H, Layzell DB, Hill JM, Pyrolysis of wood to biochar: Increasing yield while maintaining microporosity, Biores Tech 153 (2014) 173–9.

[40] Abdel Halim KS, Bahgat M, Morsi MB, El-Barawy K, Pre-reduction of manganese ores for ferromanganese industry, Ironmak Steelmak 38 (4) (2011) 279–84.

[41] Sesen FE, Practical reduction of manganese oxide, Int J Chem Eng Appl 1 (1) (2017) 1–2.

[42] Staffansson LI, On the Mn-MnS phase diagram, Met Mat Trans B 7 (1) (1976) 131–4.

[43] Li F, Tangstad M, Solheim I, Quartz and carbon black pellets for silicon production, Infacon XIV, Kiev, Ukraine (2015) 390–401.

[44] Lyutaya MD, Goncharuk AB, Manganese nitrides, Sov Powder Metall 16 (3) (1977) 208–12.

[45] Akil C, Geveci A, Optimization of Conditions to Produce Manganese and Iron Carbides from Denizli-Tavas Manganese Ore by Solid State Reduction, Turkish J Eng Env Sci 32 (2008) 125–31.

[46] Yastreboff M, Ostrovski O, Ganguly S, Carbothermic Reduction of Manganese from Manganese Ore and Ferromanganese Slag, Infacon VIII, Beijing, China (1998) 263–70.

[47] Kononov R, Ostrovski O, Ganguly S, Carbothermic solid state reduction of manganese ores, Infacon XI, New Delhi, India (2007) 258–67.

[48] Shin HK, Lee BD, Lee HS, Lee YE, Mechanism of carbothermic reduction of Mn oxide powder, Infacon XIII, Almaty, Kazakhstan (2013) 621–9.

[49] Grimsley WD, See JB, King RP, Mechanism and rate of reduction of Mamatwan manganese ore fines by carbon, S African Inst Mining Metal 78 (3) (1977) 51–62.

[50] French AD, Idealized powder diffraction patterns for cellulose polymorphs, Cellulose 21 (2) (2014) 885–96.

[51] Schwarz RR, McCallum D, Analysis of Ferrosilicon and Silicon Carbide by an X-ray Fluorescence Fusion Method - An X-ray Diffraction Investigation of the Preliminary Oxidation, Anal Comm 34 (1997) 165–9.

[52] Moustafa SF, Morsi MB, Alm El-Din A, Formation of silicon carbide from rice hulls, Can Metall Quar 36 (5) (1997) 355–8.

[53] Braga RS, Takano C, Mourao MB, Prereduction of self-reducing pellets of manganese ore, Ironmak Steemak 34 (4) (2007) 279–84.

[54] Monsen B, Kolbeinsen L, Prytz S, Myrvågnes V, Tang K, Possible use of natural gas for silicon of ferrosilicon production, Infacon XIII, Almaty, Kazakhstan (2013) 467–78.

[55] Pistorius PC, Reductant selection in ferro-alloy production: The case for the importance of dissolution in the metal, J South African Inst Min Met 102 (1) (2002) 33–6.

Chapter 5

Summary discussion

Article I contains the results on pyrolysis product yields and composition of charcoal from softwood and hardwood reacted in the temperature range from 500 to 1300 °C. In addition, the effects of an additional or second heat treatment at 700, 1000, 1300 and 1600 °C and biooil conditioning were studied. Articles II and III describe the properties of charcoal samples which reacted at temperatures up to 2800 °C. In Article IV the influence of a pretreatment, i.e. supercritical CO_2 extraction on the product yields and composition was discussed. Article V provides the results on physical properties of charcoal based pellets and charcoal pelletilizing process using biooil as a binding agent and presents the results on the characterization of charcoal composite pellets during the high-temperature reduction. In the present chapter, the main findings, uncertainties, limitations and transferability to the use of other biomaterials as CO_2 neutral reductants are discussed and further suggestions are made for the use of charcoal composite pellets in ferroalloy industries.

5.1 High temperature treatment

Renewable reductants have to fulfill the requirements of ferroalloy industries before they can replace fossil coke. Knowledge of material inputs and reduction process parameters is important because the product composition is highly affected by the time-temperature history and feedstock origin. In the present study, the properties of charcoal from high-temperature pyrolysis were investigated at a heating rate of 10 °C min^{-1}. The effects of heat treatment temperature and feedstock origin were discussed with respect to the charcoal yield, fixed carbon yield and volatile matter content.

5.1.1 Primary heat treatment of wood

The use of charcoal as a CO_2 neutral reductant in ferroalloy industries depends on such properties as mechanical stability, reactivity and particle size. Metallurgical grade char-

coal with a required carbon content ≥ 85 wt.% can be produced at temperatures greater than 750 °C under slow heating pyrolysis conditions [1–3]. However, the volatile matter content and reactivity of charcoal create challenges in the replacement of fossil coke. In the present study, the charcoal yield from pyrolysis of spruce and oak decreased with the increasing heat treatment temperature, from about 29 to 22 % for spruce and from 27 to 20 % for oak in the temperature range from 500 to 1300 °C. Likewise, the fixed carbon yield decreased from 23.6 to 21 % and 21.7 to 17.9 % respectively for spruce and oak charcoal in the same temperature range. The carbon content increased from about 83 to 93 % for the produced spruce charcoal and from 79 to 89 % for oak charcoal, indicating the removal of hydrogen and oxygen compounds. However, the volatile matter content at a heat treatment temperature of 1300 °C was still about 5 wt.% or more than 3 times larger than for metallurgical coke. The yields of biooil in pyrolysis of oak increased slightly from 33 to 38 % in the temperature range from 500 to 900 °C and remained constant at greater temperatures, whereas similar yields of biooil were observed during pyrolysis of spruce. The water content in spruce biooil was 5 % points greater than the water content in the biooil from oak pyrolysis under same conditions. The product yields of charcoal and biooil were similar during pyrolysis of non-treated biomass and biomass after $scCO_2$ extraction. Thus, the removal of value added components prior to the primary pyrolysis can enhance the overall economics without negative affects on the biomass feed. High level of alkali metals can promote faster devolatilisation rates, suppressing the formation of biooil and catalyze the formation of char, leading to greater char yields [4, 5]. However, the pyrolysis of spruce resulted in a greater charcoal yield than the pyrolysis of oak. Likewise, a greater charcoal yield was obtained during pyrolysis of low ash containing bark compared to pyrolysis of needles and branches. The greater charcoal yield of spruce and bark was attributed to the greater lignin content than in original oak. The lower content of extractives in spruce (7.8 %) than in oak (11 %) led to the formation of less tar organic products. A similar tendency was obsered for branches (8 wt.% extractable) and needles (12 wt.% extractable). The results of this study showed that the biomass composition had a minor influence on the product composition, whereas the influence of the ash can be neglected.

5.1.2 Secondary heat treatment of charcoal

Charcoal pellets using biooil as a binder and the charcoal samples and were subjected to a secondary heat treatment. The additional pyrolysis led to the further decrease in a fixed carbon yield of both charcoal samples with the increased temperature from 700 to 1600 °C. The proximate analysis showed that the additional mass loss was mainly caused by the release of remaining volatile matter, in which the carbon content of the

remaining charcoal was further increased. It was noted that the fixed carbon content of both spruce and oak charcoal samples produced at temperatures above 700 °C increased after the secondary heat treatment at 700 and 1000 °C, indicating a char stabilization in the secondary heat treatment at lower temperatures. The carbon content of charcoal increased with the increased temperature to 94 %, whereas the volatile matter decreased to 2.5 wt.%. The properties of charcoal samples after secondary heat treatment were similar to the charcoal properties from primary pyrolysis. The final solid yield after the secondary heat treatment can be affected by differences in the lignocellulosic composition of biomass, ash content and ash composition, primary heat treatment temperature and secondary heat treatment temperature. The results showed that the total ash content of spruce and oak samples from pyrolysis in the temperature range up to 1600 °C remained unchanged. Only the total calcium content of charcoal decreased by 25 and 50 % during pyrolysis of spruce and oak in the temperature range between 800 and 1200 °C. Thus, the ash content does not have a significant influence on the charcoal yield and composition.

5.1.3 Biooil conditioning

Biooil was further treated using distillation, co-pyrolysis with wood and biooil-charcoal blend distillation. The distillation of biooil to 450 °C resulted in a coke formation of about 30 % of its organic fraction, corresponding to approximately 7 % points of the biomass input. On the other hand, the co-pyrolysis of biooil and biooil-charcoal distillation increased the charcoal yield by ≥ 4 % points constant at 700, 900 and 1100 °C, indicating a catalytic effect of the solid matrix on the tar decomposition. The similar solid increase at 700, 900 and 1100 °C indicate that the no tar decomposition occurred in this temperature range. The biooil analysis has shown that the feedstock had only minor influence on the biooil composition. The carbon content after co-pyrolysis was increased by ≥ 2 % points compared to primary pyrolysis, indicating that the formed coke consists mainly of carbon. In addition, the volatile matter content of the charcoal was more than 2 % points lower compared to the charcoal from primary heat treatment. The results indicate that the composition of wood changed prior to the pyrolysis process. Pyrolytic acids in the biooil can be used to remove alkali and alkaline earth metals from biomass, in which an increased production of anhydrosugars was reported [6, 7]. The mineral matter of the original biomass can catalyze primary and secondary pyrolysis reactions, such as dehydration and char forming reactions [8–10]. The increased sugars and sugar derivatives are formed at the cost of carbonyls and phenolic compounds after the acid leaching [7]. However, a similar coke formation was obtained for post-distillation of the biooil-charcoal blend. Thus, some coke forming precursors can be stabilized before repolymerization. Wu et al. reported that the coke formation of acid-treated biooil in alcohol is lower compared to

water [11]. No clear correlation between the removal of mineral matter and the formation of sugars and sugar derivatives by leaching was found in literature [7]. In this thesis, the distillation of biooil-charcoal blends resulted in a 1-2 % points greater volatile matter content than in co-pyrolysis of biooil and biomass. The carbon content of the solid product was slightly lower than for the biooil co-pyrolysis, indicating a larger fraction of hydrogen und oxygen groups in the repolymerized charcoal matrix. Thus, the co-pyrolysis of biooil and biomass results in a predominance of secondary reactions and the formation of more cross-linked charcoal fractions compared to the biooil-charcoal distillation. However, both biooil conditioning processes led to the formation of an additional carbon layer on the charcoal surface, confirming the results of Elkasabi et al. [12]. In summary, the post distillation enables the usage of biooil as a binding agent in pellet production.

5.2 Morphology and nanostructure

The morphology and nanostructure of charcoal can affect the reactivity, electrical resistivity and gas permeability. The nanostructure and CO_2 reactivity of charcoal are interrelated properties. The present results showed that the nanostructure of charcoal samples was strongly affected by the heat treatment temperature of primary and secondary heat treatment. The porosity of both oak and spruce charcoal samples increased with the increasing heat treatment temperature in the temperature range from 300 to 700 °C [13]. The charcoal porosity at greater temperatures slightly varied among spruce and oak samples. Spruce charcoal was less micro- and mesoporous compared to oak charcoal, indicating a strong influence of the wood species on the porosity. The specific surface area of spruce and oak charcoal at 800 °C was 9 and 8 times respectively larger than the charcoal produced at 1600 °C. The charcoal samples produced at temperatures $\leq$ 1600 °C exhibited shorter graphene layers and less crystalline structure than in coal chars, indicating a larger fraction of amorphous carbon compared to coal chars [14]. The oak and spruce charcoal samples heat treated at 1600 °C showed differences in the nanostructure, whereas the oak charcoal was more graphitic. Thus, oak graphene layers were straight and long compared to spruce. This is due to the catalytic effect of alkali metals on the devolatilisation reactions of charcoal at high temperatures (1000-1600 °C) [15, 16]. Oak charcoal exhibited a nanostructure similar to glassy carbon [17] with the graphene layers which have a similar interplanar distance to graphite. However, the charcoal produced in the temperature range from 1000 to 1600 °C mostly consisted of non-graphitizing carbons [18–20]. The spruce charcoal exibited a heterogeneous structure of amorphous carbon and nano-crystalline graphite. The lower oxygen content in oak charcoal enhanced the coalescence of crystallites and led to a higher degree of graphitization [21]. Oxygen containing

functional groups in the charcoal were located at the edges of aromatic layers which can hinder the alignment of graphene layers during the heat treatment [20]. This thesis showed that the graphitization of all charcoal samples increased significantly with the increased heat treatment temperature. Charcoal samples from pyrolysis at 1300 and 1600 °C mostly contained amorphous carbon with a minor presence of nano-crystalline graphite. The structure resembled carbon black based on the results of Raman spectroscopy. At heat treatment temperatures of 2400 and 2800 °C the mean separation distance of graphene segments was similar to graphite (0.335 nm), indicating the importance of very high heat treatment temperatures for the graphitization of carbon. However, the nanostructure of alfalfa straw charcoal heat treated at 2800 °C was less graphitic and more porous than woody charcoal. In addition, charcoal samples from wood contained more than 100 layers of straight graphene segments, whereas only 30 to 50 layers were obtained for the alfalfa straw charcoal. The long and straight graphene layers of alfalfa charcoal suggest that an increase in heat treatment temperature can result in a further graphitization and formation of additional graphene segments. The high heat treatment temperatures led to the formation of a graphitized carbon structures in comparison to the carbon structure proposed by Franklin [18].

5.3 Charcoal pellets

Spruce charcoal was mixed with biooil and manganese ore or silica respectively to produce charcoal composite pellets. Charcoal pellets and charcoal composite pellets were investigated to understand the effect of secondary heat treatment on the final properties, i.e. mechanical stability, shape and reactivity. The water free fraction of biooil was used as a binder in a charcoal pelletizing process. The heat treatment at 450 °C increased the hardness of the pellet from 450 to 490 N, which was similar to that of alfalfa straw pellets using hydrated lime as binder [22]. The biooil formed a coke structure between the charcoal particles and increased the hardness and electrical resistivity of the charcoal pellet. The latter increased from 0.8 to 1.5 Ωm after the secondary heat treatment, indicating the loss of conductive components during evaporation. The electrical resistivity of charcoal particles varied from 0.01 to 0.03 Ωm and was similar to that of metallurgical coke ($\leq 0.01\,\Omega$m) [23]. This emphasizes the importance of charcoal pelletizing process with the biooil to improve the electrical properties of charcoal pellets, respectively. Moreover, this indicates that the heat treatment improves the mechanical strength and electrical resistivity of charcoal pellets for the use in ferroalloy industries. The durability of charcoal pellets decreased from 98.4 to 95.7 % after the secondary heat treatment, whereas the standard requirements for the high quality wood pellet durability are ≥ 97.5 % [24].

Thus, the improvement of charcoal pellet durability using an additional binder or different concentration of tar organic fraction was proposed for the further studies. The addition of biooil as a binder increased the porosity of the charcoal pellets after the secondary heat treatment, whereas devolatilisation of light biooil fraction enhanced the gas permeability in the pellet. The CO_2 reactivity of the charcoal pellet was similar to that of biooil-charcoal blend distillation and thus, pelletizing with the biooil as a binder did not affect the charcoal reactivity. However, the reactivity remained greater than that of fossil-based coke. In addition, the enhanced gas permeability improved the mass transfer in charcoal composite pellets, leading to an improved pre-reduction of manganese charcoal pellets. The pellet size and shape remained constant for the heat treatment temperatures less the primary pyrolysis temperature, emphasizing a dominating role of primary pyrolysis temperatures in the minimization of pellet shrinkage effect. The addition of biooil had less influence on the charcoal composite pellet size, leading to the negligible changes in the mechanical stability. This indicated the potential of charcoal pellet use in ferroalloy industries, whereas the pelletizing of charcoal with the biooil as a binder can improve the charcoal properties for transportation and storage.

5.4 Charcoal reactivity

The CO_2 reactivity of charcoal can be affected by differences in feedstock origin and process conditions, such as ash composition, carbon chemistry, nanostructure, heat treatment temperature and residence time. Based on the higher ash content, it might be expected that oak charcoal should be more reactive than spruce charcoal. However, the reactivity of both charcoal samples was similar and thus, the effect of ash content and composition had only a minor effect on the reactivity under slow heating conditions ($10\,^{\circ}C\ min^{-1}$). The derivative thermogravimetry (DTG) curve of spruce charcoal showed a double peak in CO_2 gasification, whereas oak charcoal samples exhibited a triple peak after biooil conditioning. The multi-peaks indicate the presence of a heterogeneous charcoal mixture with respect to its composition. Spruce and oak charcoal from primary pyrolysis exhibited a maximum reaction rate that varied from 800 to $1030\,^{\circ}C$, whereas the maximum reaction rate of spruce charcoal generated at 700 and $900\,^{\circ}C$ and oak charcoal generated from 700 to $1100\,^{\circ}C$ took place at about $960\,^{\circ}C$. The results indicate that differences in the heat treatment temperature have more influence on the charcoal reactivity than the wood species. The distillation of the biooil-charcoal blend resulted in a shift to lower reaction temperatures. The same trend was observed for charcoal pellets, indicating an increase in CO_2 gasification reactivity after the distillation of biooil with the charcoal. This might be due to the cross-linking of hydroxyl groups with carbonyls, increasing the molecular

weight of the residue [25]. In comparison, the maximum reaction rate of both charcoal samples from co-pyrolysis of biomass and biooil resulted in a shift to greater temperatures, indicating the decrease in CO_2 gasification reactivity. However, both biooil conditioning routes showed only a small influence on the CO_2 reactivity, confirming the results of Veksha et al. [26]. The maximum reaction rate of charcoal samples produced at 500 °C was shifted by about 60 °C to greater temperatures by the secondary heat treatment at 1000, 1300 and 1600 °C. This indicates a consecutive pyrolysis of the original charcoal structure in the secondary heat treatment. However, it was observed that the CO_2 reactivity of charcoal samples pyrolyzed at ≥ 700 °C remained nearly unchanged after the secondary heat treatment. The additional heat treatment at temperatures > 1000 °C affected the reactivity of charcoal samples less than the co-pyrolysis and biooil distillation. However, the maximum reaction rate from primary pyrolysis samples at 1300 °C was shifted to about 40 °C lower temperatures after the secondary heat treatment at 1300 and 1600 °C. Spruce charcoal from pyrolysis at 800 °C was four times more reactive than charcoal from pyrolysis at 1600 °C, whereas the specific surface area of charcoal at 1600 °C was 9 times smaller. Oak charcoal generated at 800 °C was two times more reactive with an eight times greater surface area compared to charcoal prepared at 1600 °C. This indicates that the influence of the surface area on the CO_2 reactivity is small. Spruce and pinewood charcoal generated at 1600 °C were about 40 and 60 times respectively more reactive than metallurgical coke. The co-pyrolysis of biooil with pinewood charcoal at 1600 °C can lead to the formation of less reactive charcoal by the to the formation of carbon deposits on the charcoal matrix during pyrolysis [27, 28]. However, this charcoal was still about 15 times more reactive than metallurgical coke. The thermal decomposition of the biooil can generate radicals that penetrate into the charcoal structure and promote the formation of small ring structures that later transform into larger PAH compounds [29, 30]. The PAH compounds can decrease the CO_2 reactivity[31]. The overall reaction rates of charcoal samples from the secondary heat treatment at 2400 and 2800 °C were of the same order of magnitude and similar to metallurgical coke. This result clearly demonstrates that the heat treatment temperature becomes the dominating factor governing CO_2 reactivity when the secondary heat treatment is conducted at temperatures greater than 2400 °C. This emphasizes that the heat treatment temperature is the most important parameter for the charcoal to approach the CO_2 reactivity of metallurgical coke.

Bibliography

[1] A. Adrados, A. Lopez-Urionabarrenechea, J. Solar, J. Requies, I. De Marco, and J.F. Cambra. Upgrading of pyrolysis vapours from biomass carbonization. *J ANAL APPL PYROL*, 103:293–299, 2013.

[2] M.J. Antal, W.S.L. Mok, G. Varhegyi, and T. Szekely. Review of methods for improving the yield of charcoal from biomass. *ENERG FUEL*, 4(3):221–225, 1990.

[3] J. Bourke, M. Manley-Harris, C. Fushimi, K. Dowaki, T. Nunoura, and M.J. Antal. Do All Charcoals Have the Same Chemical Structure? 2. A Model of the Chemical Structure of Carbonized Charcoal. *IND ENG CHEM RES*, 46(18):5954–5967, 2007.

[4] S. Niksa. Predicting the rapid devolatilization of diverse forms of biomass with bio-flashchain. *PROC COMBUST INST*, 28(2):2727–2733, 2000.

[5] M. Nik-Azar, M.R. Hajaligol, M. Sohrabi, and B. Dabir. Mineral matter effects in rapid pyrolysis of beechwood. *FUEL PROCESS TECHNOL*, 51(1-2):7–17, 1997.

[6] S.R.G. Oudenhoven, A.G.J. van der Ham, H. van den Berg, R.J.M. Westerhof, and S.R.A. Kersten. Using pyrolytic acid leaching as a pretreatment step in a biomass fast pyrolysis plant: Process design and economic evaluation. *BIOMASS BIOENERG*, 95:388–404, 2016.

[7] H. Persson, E. Kantarelis, P. Evangelopoulos, and W. Yang. Wood-derived acid leaching of biomass for enhanced production of sugars and sugar derivatives during pyrolysis: Influence of acidity and treatment time. *J ANAL APPL PYROL*, 127:329–334, 2017.

[8] C. A. Zaror and D. L. Pyle. The pyrolysis of biomass: A general review. *P INDIAN AS-ENG SCI*, 5(4):269, Dec 1982.

[9] K. Raveendran, A. Ganesh, and K.C. Khilar. Influence of mineral matter on biomass pyrolysis characteristics. *FUEL*, 74(12):1812–1822, 1995.

[10] C. Di Blasi, C. Branca, and G. D'Errico. Degradation characteristics of straw and washed straw. *THERMOCHIM ACTA*, 364(1):133–142, 2000.

[11] L. Wu, X. Hu, S. Wang, D. Mourant, Y. Song, T. Li, and et al. Formation of coke during the esterification of pyrolysis bio-oil. *RSC ADV*, 6:86485–86493, 2016.

[12] Y. Elkasabi, A.A. Boateng, and M.A. Jackson. Upgrading of bio-oil distillation bottoms into biorenewable calcined coke. *BIOMASS BIOENERG*, 81:415–423, 2015.

[13] C.E. Brewer, V.J. Chuang, C.A. Masiello, H. Gonnermann, X. Gao, and Dugan, B. and et al. New approaches to measuring biochar density and porosity. *BIOMASS BIOENERG*, 66:176–185, 2014.

[14] T. Beeley, J. Crelling, J. Gibbins, R. Hurt, M. Lunden, C. Man, and et al. Transient high-temperature thermal deactivation of monomaceral-rich coal chars. *In: 26th SYMP COMB INST*, pages 3103–3110, 1996.

[15] T. Hata, K. Ishimaru, M. Fujisawa, P. Bronsveld, T. Vystavel, J. De Hosson, and et al. Catalytic graphitization of wood-based carbons with alumina by pulse current heating. *FULLER NANOTUB CAR N*, 13:435—-445, 2005.

[16] M.T. Johnson and K.T. Faber. Catalytic graphitization of three dimensional wood-derived porous scaffolds. *J MATER RES*, 26(1):18—25, 2011.

[17] G.M. Jenkins, K. Kawamura, and L.L. Ban. Formation and structure of polymeric carbons. *PROC R SOC Lond A*, 327:501—517, 1972.

[18] R.E. Franklin and J.T. Randall. Crystallite growth in graphitizing and non-graphitizing carbons. *P ROY SOC LOND A MAT*, 209(1097):196–218, 1951.

[19] A. Oberlin. Carbonization and graphitization. *CARBON*, 22(6):521–541, 1984.

[20] F. Kurosaki, K. Ishimaru, T. Hata, P. Bronsveld, E. Kobayashi, and Y. Imamura. Microstructure of wood charcoal prepared by flash heating. *CARBON*, 41(15):3057–3062, 2003.

[21] A. Trubetskaya, P.A. Jensen, J.D. Jensen, M. Steibel, H. Spliethoff, and P. Glarborg. Influence of fast pyrolysis conditions on yield and structural transformation of biomass chars. *FUEL PROCESS TECHNOL*, 140:205–214., 2015.

[22] N. Kaliyan and R.V. Morey. Factors affecting strength and durability of densified biomass products. *BIOMASS BIOENERG*, 33(3):337–359, 2009.

[23] P.A. Eidem, M. Tangstad, and J.A. Bakken. Determination of electrical resistivity of dry coke beds. *MATER TRANS B*, 39(1):7–15, 2008.

[24] A. Abedi, H. Cheng, and A.K. Dalai. Effects of natural additives on the properties of sawdust fuel pellets. *ENERG FUEL*, 32(2):1863–1873, 2018.

[25] S. Laurichesse and L. Avérous. Chemical modification of lignins: Towards biobased polymers. *PROG POLYM SCI*, 39(7):1266–1290, 2014.

[26] A. Veksha, H. McLaughlin, D.B. Layzell, and J.M. Hill. Pyrolysis of wood to biochar: Increasing yield while maintaining microporosity. *BIORESOUR TECHNOL*, 153:173–179, 2014.

[27] W.G. Appleby, J.W. Gibson, and G.M. Good. Coke formation in catalytic cracking. *IND ENG CHEM PROCESS DES DEV*, 1(2):102–110, 1962.

[28] R. Coll, J. Salvado, X. Farriol, and D. Montane. Steam reforming model compounds of biomass gasification tars: conversion at different operating conditions and tendency towards coke formation. *FUEL PROCESS TECHNOL*, 74:19–31, 2001.

[29] H.-L. Tay, S. Kajitani, S. Zhang, and C.-Z. Li. Effects of gasifying agent on the evolution of char structure during the gasification of Victorian brown coal. *FUEL*, 103:22–28, 2013.

[30] D.M. Keown, J.-I. Hayashi, and C.-Z. Li. Drastic changes in biomass char structure and reactivity upon contact with steam. *FUEL*, 87:1127–1132, 2008.

[31] D. Feng, Y. Zhao, Y. Zhang, and S. Sun. Effects of H_2O and CO_2 on the homogeneous conversion and heterogeneous reforming of biomass tar over biochar. *INT J HYDROGEN ENERG*, 42(18):13070–13084, 2017.

Chapter 6

Conclusion

Biomass pyrolysis at high heat treatment temperatures and slow heating rates was investigated in a laboratory scale reactor and pilot plant high-temperature furnaces. The effects of wood origin and process parameters on the pyrolysis product yields, structure, morphology of charcoal and CO_2 reactivity of charcoal-based pellets were investigated for the use of renewable reducing agents in ferroalloy industries. Such operating parameters as the primary heat treatment temperature (500-1300 °C), secondary heat treatment temperature (700-2800 °C), biooil conditioning (recycling and distillation) and CO_2 concentration (10-100 vol.%) were varied in the present study. The wood species (Norway spruce and sessil oak) were used as local fuels, whereas beechwood, pinewood, wheat straw and alfalfa straw were supplied from Sweden and Denmark.

The results showed that the charcoal yield decreased with increasing temperature from 29 to 22 % and 27 to 20 % for spruce and oak in the temperature range from 500 to 1300 °C, whereas the fixed carbon yield of charcoal was nearly constant at primary heat treatment temperatures up to 900 °C. However, the heat treatment temperatures greater than 900 °C led to the further decrease in the fixed carbon yield. Likewise, the carbon content increased with increasing heat treatment temperature, indicating the removal of oxygen and hydrogen containing species. Spruce charcoal showed a greater fixed carbon yield than oak charcoal, due to the higher carbon content in original spruce. However, the spruce charcoal exhibited a greater oxygen content, whereas the ash content of oak charcoal was twice greater than that of spruce charcoal. The biooil yield in pyrolysis of oak increased slightly in the temperature range from 500 to 900 °C and remained constant at higher temperatures, whereas the biooil content of spruce was almost similar for the pyrolysis temperatures above 500 °C. However, the water content of spruce biooil was about 5 % points greater compared to oak pyrolysis. The secondary heat treatment of charcoal samples further decreased the charcoal yield by the partial removal of volatiles and thus, resulted in the carbon content increase. A volatile matter content of charcoal was similar

to that of metallurgical coke due to the secondary heat treatment at 1600 °C, emphasizing the importance of high heat treatment temperatures on the charcoal structure. However, the fixed carbon yield decreased with increasing secondary heat treatment temperature and thus, decreased the efficiency of the process. Biooil co-pyrolysis and charcoal-biooil distillation increased the fixed carbon yield by about 4 % points at 700, 900 and 1100 °C, indicating that the feedstock had no influence on the char forming product yields in the biooil. However, the volatile matter increased by the post distillation more than by biooil recycling. In addition, the pre-treatment of biomass by supercritical CO_2 ($scCO_2$) extraction enabled the extraction of more than half of value-added compounds without any significant influence on the charcoal yields.

The reactivity of charcoal samples was investigated in CO_2 gasification. The results showed that the heat treatment temperature and CO_2 concentration affected the reactivity more than the biooil conditioning, biomass origin, ash content and composition. The threshold temperature in CO_2 increased for both wood species irrespective of the CO_2 concentration from about 670 to 830 °C. A threshold temperature of charcoal was similar to that of metallurgical coke (850 °C) when the wood species were reacted at 1300 °C. However, the CO_2 reactivity of charcoal from pyrolysis at 1300 °C was greater than reactivity of fossil reducing agents. The influence of heat treatment temperature on the CO_2 reactivity of charcoal was less pronounced during wood pyrolysis at temperatures < 1600°C, whereas the effect of CO_2 concentration become more influencing. The maximum reaction rate in non-steady experiments was shifted to greater temperatures with increasing heat treatment temperatures, whereas the increasing CO_2 concentrations resulted in the shift to lower temperatures. However, the maximum reaction rate of charcoal after the secondary heat treatment at 1300 and 1600 °C was shifted to temperatures about 40 °C lower compared to the charcoals produced at 1300 °C in the primary pyrolysis. It was shown that the reactivities of charcoal from pyrolysis at temperatures of 2400 to 2800 °C were similar to those of metallurgical coke, emphasizing the importance of graphitizing temperatures on the reactivity and structure of charcoal. The maximum reaction rate was shifted to lower temperatures after the charcoal-biooil blend distillation, indicating an increase in CO_2 gasification reactivity, whereas the co-pyrolysis of biomass and biooil resulted in the opposite trend. The results indicate that high heat treatment temperatures are essential for the achievement of metallurgical coke reactivity. The ash composition influenced the charcoal reactivity less than the heat treatment temperature. In general, the ash content of charcoal increased during pyrolysis, whereas the calcium content decreased with increasing heat treatment temperature. The greater pyrolysis temperatures resulted in the ordering of charcoal carbonaceous matrix. The oak charcoal from pyrolysis at 1600°C contained long and flat graphene layers and interplanar dis-

tances which were similar to graphite and thus, the oak charcoal was more ordered than the spruce charcoal. The TEM analysis showed that charcoal had structural characteristics of non-graphitizing carbon. Thus, increasing heat treatment temperature increased the graphitization of charcoal structure, leading to the charcoal reactivity that is nearly similar to that of low reactive metallurgical coke. The more ordered structure of charcoal also affected its electrical properties. The electrical resistivity decreased with increasing heat treatment temperatures. The electrical resistivity of charcoal from pyrolysis at 900 °C and ≥ 1300 °C decreased to 30 mΩm and 10 mΩm. Thus, the electrical resistivity of both oak and spruce charcoal samples generated at high heat treatment temperatures was similar to metallurgical coke. Likewise, the dielectric losses were enhanced with increasing heat treatment temperature. In addition, greater electrical resistivity of charcoal was achieved by pelletizing of charcoal particles using bioooil as a binder agent.

The separation of the water phase increased the organic fraction of the binder, resulting in an increased density of charcoal based pellets. The ratio of 65:30 of charcoal to biotar was used to produce pellets with acceptable mechanical properties. However, the durability of charcoal pellets decreased after the secondary heat treatment from 98 to 95 %, whereas the hardness increased from 455 to 490 N. Thus, charcoal based pellets have a mechanical stability similar to alfalfa straw pellets. By the second heat treatment the biooil decomposed and formed a polycyclic aromatic coke structure between the charcoal particles with similar properties to the charcoal. The reactivity of charcoal-based pellets was similar to that of heat treated charcoal-biooil blend, indicating that pelleting does not affect the reactivity towards CO_2 due to the devolatilization of the light fraction inside the pellet. Charcoal based pellets provided a stable shape until the primary pyrolysis temperature was surpassed. Thus, the devolatilization of light biooil components does not cause a dilatation or contraction of the pellet, while the consecutive pyrolysis result in a further shrinkage of the particles. Therefore, a high primary heat treatment temperature is required for charcoal pellet and biocoke production.

Manganese ore composite pellets on the other hand exhibited a shrinkage at temperatures above 1050 °C, in which the mechanical stability decreased by the reduction of manganese oxide. Large internal void fractions were formed around the metal and slag by the high-temperature pyrolysis. The short distance between the charcoal and the metal oxide improve the mass transfer of CO and CO_2 between the particles. In addition, the large contact area enhances the dissolution of the carbon into the slag. Both effects increase the value of renewable charcoal based pellets for the use in ferroalloy industries.

In summary, the heat treatment temperature had the greatest influence on the final pellet yield, in which the pelleting with biooil showed the greatest influence on the electrical resistivity at temperatures greater than 900 °C. The effect of heat treatment temperature

on charcoal particles was stronger at low and intermediate heat treatment temperatures before the basic structural units reorganized and coalesced. The electrical resistivity of particles from both charcoal samples was similar to metallurgical coke (10 mΩm) when a heat treatment temperature of $\geq 1300\,^{\circ}$C was applied. The electrical resistivity can be increased to 500-1500 mΩm by pelleting the comminuted charcoal with biooil as a binder. The production of charcoal based pellets with biooil as a binder showed great promise to produce renewable reducing agents with a high resistivity and low CO_2 reactivity.

Chapter 7

Suggestions for future work

In the present work, the results showed that biooil can be used as a binding agent and the coke forming compounds in the biooil are suitable precursors for the production of thermally stable charcoal-based pellets. Therefore, further studies on the optimization of operating conditions for the production of biooil and charcoal-based pellets are recommended. In addition, the yield of biooil from biomass pyrolysis is low for the cost efficient charcoal-based pellet production. In the present study, the mechanical and electrical properties of charcoal from pyrolysis at 900 °C were investigated. However, in order to understand the interactions of charcoal with biooil (liquid pyrolysis fraction) on the industrial scale, a wider range of heat treatment temperatures and blending ratios must be considered. This will give a new knowledge on the interaction of charcoal surface and biooil properties. The biooil-charcoal blend may improve the wettability of the charcoal surface. It was previously hypothesized that the coke forming compounds of the biooil can stabilize the charcoal particles. Further studies on the determination of yields and compositions of liquid and gaseous pyrolysis by-products may give a new knowledge on the reactions of functional groups which affect biooil aging and coking.

The differences in CO_2 reactivity were related to the structural changes of charcoal after primary and secondary heat treatment. In order to understand the catalytic effect of alkali metals on the CO_2 reactivity of charcoal-based pellets, further studies on the high ash containing feedstocks and waste materials are recommended. Charcoal leaching or doping prior to pelletizing can be used to adjust the ash content and composition of the final product. The precise description of the ash intrusion into the charcoal structure and the chemical bonds are needed to describe the catalytic reactions. In the present study, the lower bio-pitch yields from the charcoal-biooil distillation compared to the distillation of pure biooil indicated the catalytic effect of alkali metals on the charcoal reactivity. In addition, knowledge on the CO_2 reactivity of biooil-charcoal blends remains limited. Therefore, the characterization of charcoal surface using Nuclear Magnetic Resonance

(NMR) spectroscopy and X-ray photoelectron spectroscopy (XPS) is required to understand the structural changes of charcoal.

Finally, in the present work, the mechanical stability and electrical resistivity of charcoal-based pellets were only analyzed at room temperature conditions. In the future investigations, the properties of charcoal pellets should be studied at high temperatures. Due to the reduction reactions in the manganese composite pellets, the results indicate that the presence of carbon in these pellets can potentially inhibit the coke bed replacement. However, the manganese charcoal-based pellets have also the potential to improve the reduction of the manganese-oxide due to the high electrical resistance in the furnace. Moreover, the properties of ore charcoal-based pellets are recommended to study at temperatures which are relevant to the industrial furnaces. Finally, the kinetic model of slow pyrolysis at high temperatures can be established to predict the yield and composition of charcoal and other by-products. The implementation of secondary reactions taking place in gas phase could improve the model accuracy. A wider range of experimental data can be included in the model to improve the optimization tool for the prediction of reaction kinetics.

Appendix A

Appendices

A.1 Supplemental materials article 1

Characterization of renewable reductants and charcoal-based pellets for the use in ferroalloy industries

Contribution of the authors

Gerrit Ralf Surup planned the majority of the study, developed a reactor for the charcoal production and performed the pyrolysis experiments.
Tore Vehus supported the work on the tar characterization.
Per-Anders Eidem consulted the work on the mechanical strength and conductivity measurements of pellets.
Anna Trubetskaya supported on the manuscript structuring and did the manuscript proof-reading. She has also participated in the experimental work on the pellet properties and analysis of tar properties.
Henrik Kofoed Nielsen provided extensive comments to the manuscript, grant writing for the PhD project and assistance with the construction of the instruments.

Characterization of renewable reductants and charcoal-based pellets for the use in ferroalloy industries

Gerrit Surup[a,*], Tore Vehus[a], Per-Anders Eidem[c], Anna Trubetskaya[b,**], Henrik Kofoed Nielsen[a]

[a]*Department of Engineering Sciences, University of Agder, 4879 Grimstad, Norway*
[b]*Mechanical Engineering Department, National University of Ireland Galway, Galway, Ireland*
[c]*Department of Material Sciences and Chemistry, SINTEF Helgeland, 8626 Mo i Rana, Norway*

S-1. Methodology

S-1.1. Particle size distribution

The results are presented as a cumulative particle size distribution, based on volume (Q_3). The cumulative particle size distribution is described in EN ISO 9276-1:1998, and is defined as

$$Q_3(x_{Ma\,min,m}) = \sum_{i=1}^{m} \overline{q_3}(x_{Ma\,min,i})\Delta x_{Ma\,min,i}, \tag{1}$$

where $\overline{q_3}$ is the area of the histogram. The results of a particle size analysis are also presented as a frequency distribution over $x_{Ma\,min}$, based on volume (q_3), so that

$$q_3(x_{Ma\,min}) = \frac{dQ_3(x_{Ma\,min})}{dx_{Ma\,min}}. \tag{2}$$

The characteristic diameters from sieving were defined based on three sizes within the entire population: d10, d50, d90. The d50 value is the median

*Corresponding author email: gerrit.surup@uia.no
**Corresponding author email: anna.trubetskaya@nuigalway.ie

particle size within the population, with 50 % of the population greater than this size, and 50 % smaller than this size. Similarly, 10 % of the population is smaller than the d10 size; while 90 % of the population is smaller than the d90 size [1]. All measurements were conducted in triplicate to establish repeatability which exceeded 95 % confidence intervals. The measurement inaccuracy from sieving analysis was mainly caused by weighing errors.

S-2. Results

Figure S-1 shows a Van Krevelen plot of original spruce and oak samples and their charcoals from co-pyrolysis with the recycled tar at temperatures from 700 to 1100°C and residual solid material after distillation of tar and charcoal mixture. The results indicate that the oxygen and hydrogen content in all charcoal samples from co-pyrolysis with the recycled tar decreases with the higher heat treatment temperature. The spruce charcoal after co-pyrolysis with the recycled tar contained less carbon and more oxygen than oak charcoal. The oxygen content in charcoal samples after co-pyrolysis and distillation treatments remained greater than that of metallurgical coke.

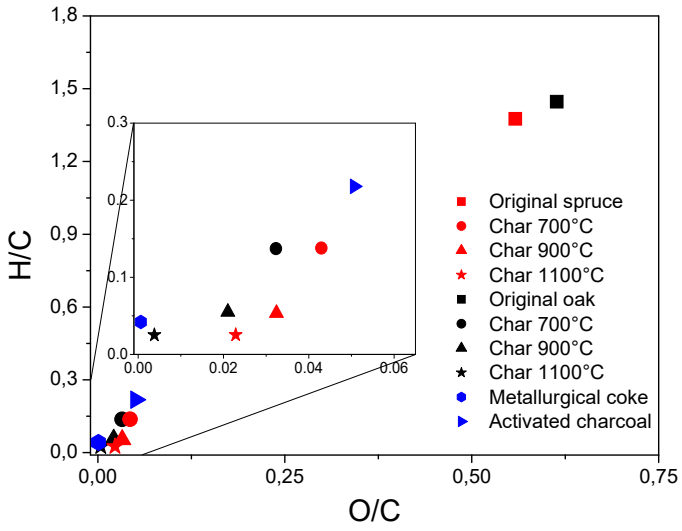

1(a): Co-pyrolysis of charcoal with recycled tar

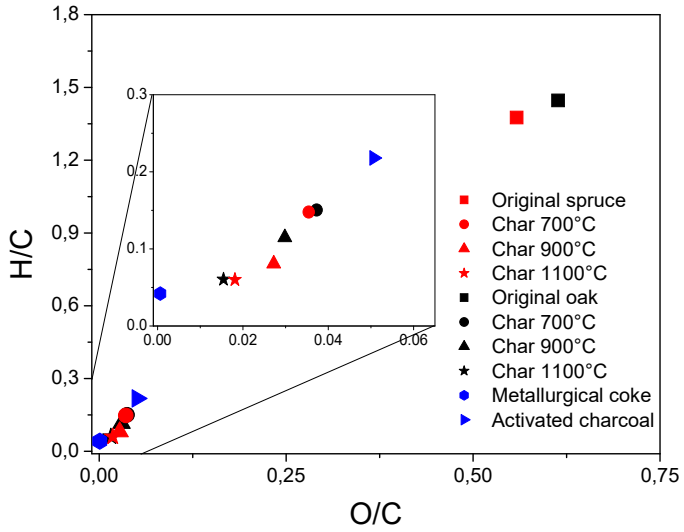

1(b): Distillation

Figure S-1: Van Krevelen plot of original spruce and oak samples and their charcoals from co-pyrolysis with the recycled tar at temperatures from 700 to 1100°C and residual solid material after distillation of tar and charcoal mixture compared to elemental composition of metallurgical coke and activated charcoal.

Figure S-2 shows a Van Krevelen plot of spruce and oak charcoal samples from additional heat treatment at 700, 1000, 1300 und 1600°C. The carbon and oxygen content in spruce and oak charcoal samples decreases only slightly with the additional heat treatment at 700°C compared to the primary charcoal, as shown in the main manuscript. It was observed that additional pyrolysis of both samples at temperatures > 1000°C leads to elemental composition of charcoal with more carbon and less hydrogen approaching that of fossil-based metallurgical coke.

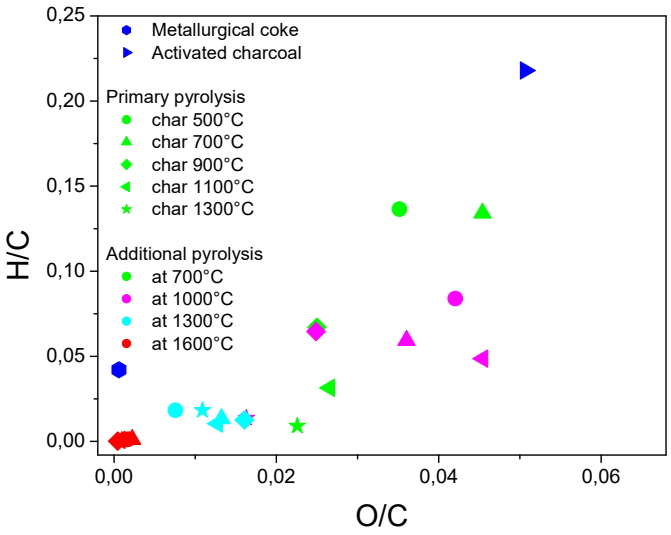

2(a): Spruce charcoal

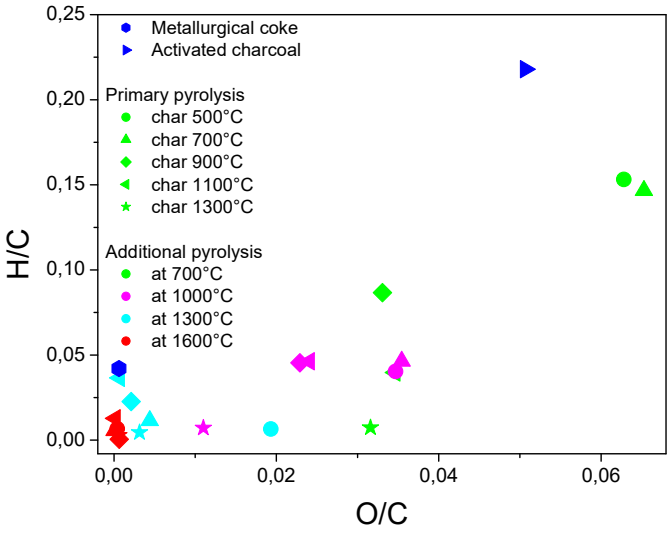

2(b): Oak charcoal

Figure S-2: Van Krevelen plot of spruce and oak charcoals prepared at 500, 700, 900, 1100 and 1300°C and additional heat treated at temperatures 700, 1000, 1300 und 1600°C compared to elemental composition of metallurgical coke and activated charcoal.

S-2.1. Particle size characterization

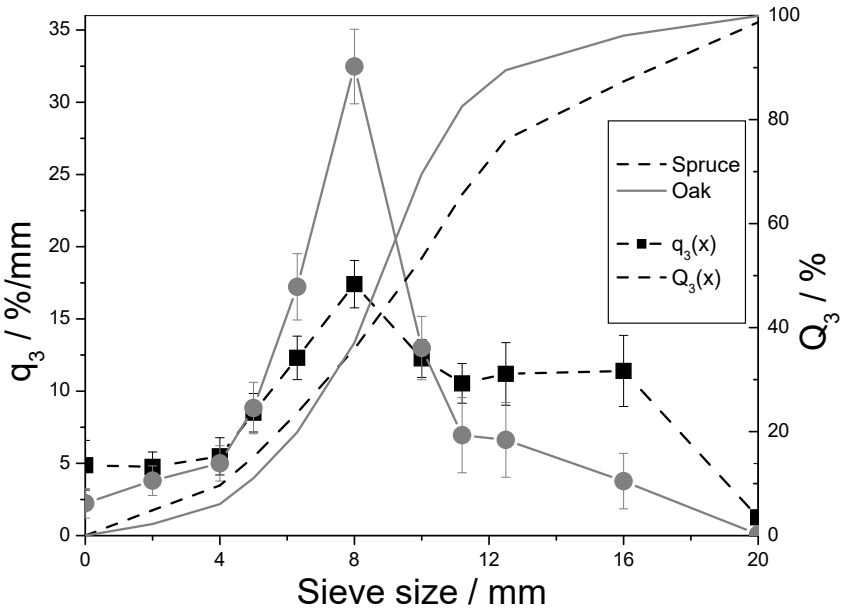

Figure S-3: Cumulative particle size distribution Q_3 and particle size distribution q_3, based on volume, for original spruce and oak samples characterized by the sieving.

S-2.2. Char reactivity

Figure S-4 shows differential weight loss curves (DTG) for the 100 % volume fraction CO_2 gasification of spruce and oak char samples from co-pyrolysis and distillation treatments.

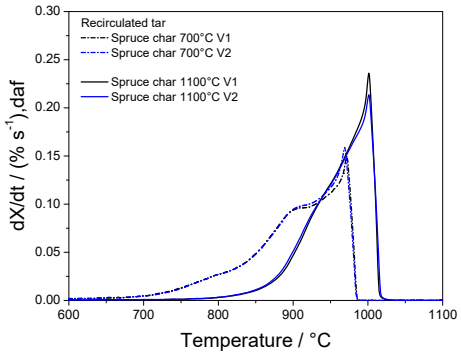

4(a): Co-pyrolysis of spruce charcoal

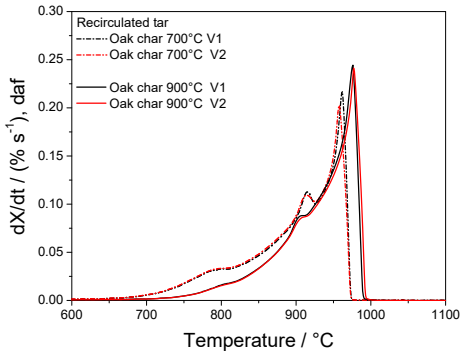

4(b): Co-pyrolysis of oak charcoal)

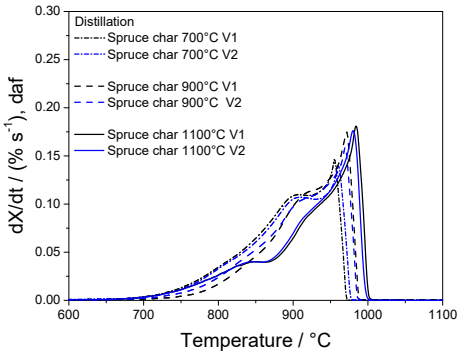

4(c): Distillation of spruce charcoal

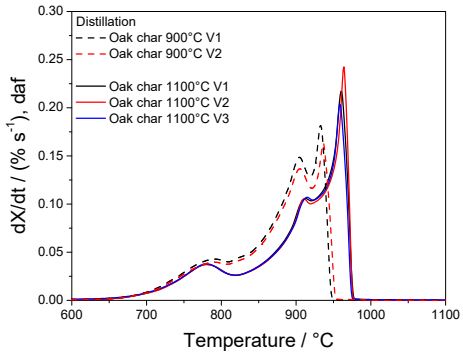

4(d): Distillation of oak charcoal

Figure S-4: Repeatability of DTG curves of spruce and oak charcoal from co-pyrolysis and distillation treatments reacted in 100 % volume fraction CO_2.

Figure S-5 shows differential weight loss curves (DTG) for the 100 % volume fraction CO_2 gasification of spruce and oak char samples after additional heat treatment at 1000, 1300, and 1600°C.

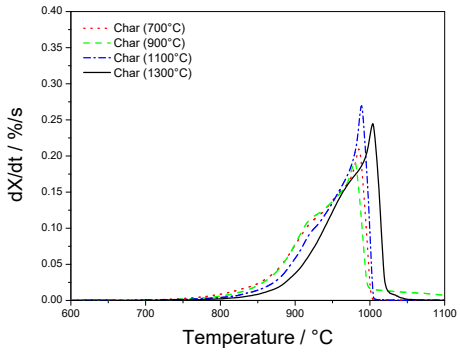

5(a): Spruce char (1000°C)

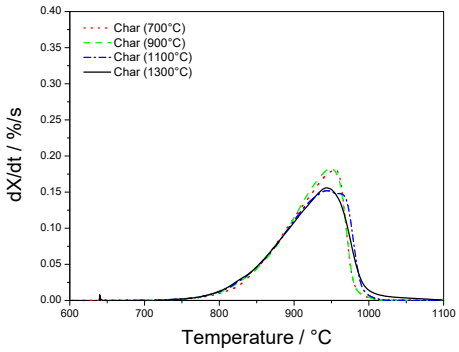

5(b): Spruce char (1300°C)

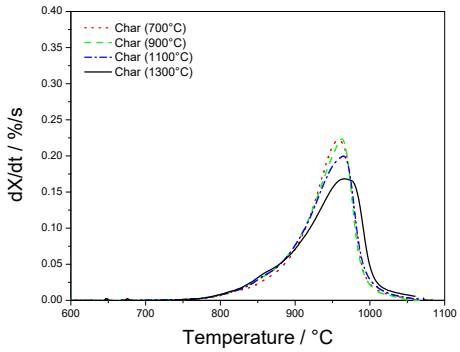

5(c): Spruce char (1600°C)

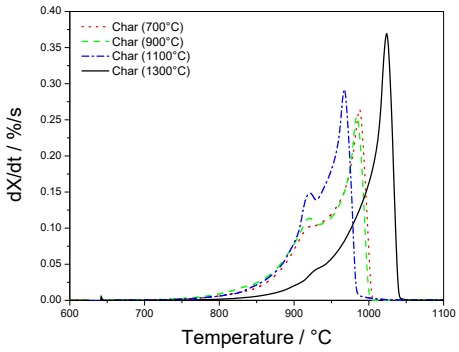

5(d): Oak char (1000°C)

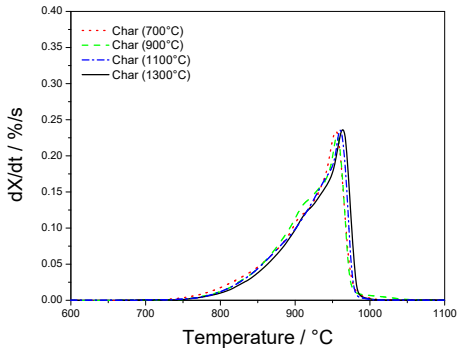

5(e): Oak char (1300°C)

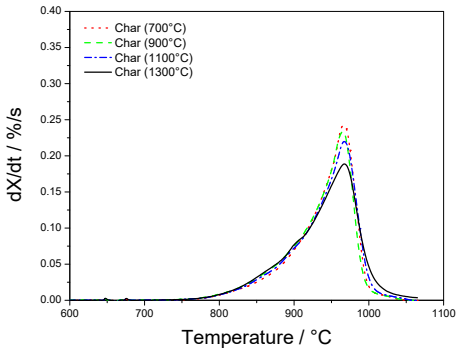

5(f): Oak char (1600°C)

Figure S-5: DTG curves of original spruce and oak and their chars from additional heat treatment at 1000, 1300, and 1600°C reacted in 100 % volume fraction CO_2.

S-3. Mass balances and CO_2 reactivity

Table S-1: Product yield, proximate and ultimate analysis (db) and CO_2 reactivity of spruce and oak after primary heat treatment.

	Spruce					**Oak**				
Heat treatment temperature (°C)	500	700	900	1100	1300	500	700	900	1100	1300
Char yield, (g_{char} $g_{biomass}{}^{-1}$)	29.1	26.2	25.0	23.7	22.3	27.2	23.5	21.9	20.5	19.7
Proximate and ultimate analysis (wt. % dry basis)										
Ash at 550°C	1.92	2.10	2.01	2.22	2.20	4.60	5.59	6.25	6.42	4.96
Fixed carbon	80.5	88.0	89.3	91.0	93.2	78.5	84.0	84.0	86.5	89.2
Volatiles	17.6	9.65	8.4	6.6	4.4	16.9	10.5	9.7	7.0	5.7
C	82.8	84.9	88.7	92.3	92.9	80.7	88.4	88.1	88.6	90.6
H	2.88	1.10	0.84	0.49	0.16	2.79	1.07	0.46	0.17	0.16
N	0.33	0.32	0.51	0.27	0.34	0.81	0.58	0.50	0.90	0.78
O	12.7	11.6	7.92	4.73	4.4	11.1	9.91	6.75	3.91	3.54
Reactivity in 100 % CO_2										
Threshold temperature (°C)	670	700	719	751	829	667	677	724	777	822
Peak temperature (°C)	964	969	983	1002	1011	953	974	969	968	1010
Reaction rate (% min^{-1})	10.3	11.0	11.8	15.1	17.0	14.5	17.5	17.2	22.0	28.4

Table S-2: Product yield, proximate and ultimate analysis (db) and CO_2 reactivity of spruce and oak after co-pyrolysis with recirculated tar and distillation.

	Recirculated tar			Distillation		
Heat treatment temperature (°C)	700	900	1100	700	900	1100
Spruce charcoal						
Char yield (g_{char} $g_{biomass}{}^{-1}$)	29.9	29.3	27.6	30.1	29.2	27.7
Proximate and ultimate analysis (wt. % dry basis)						
Ash at 550°C	3.24	2.83	2.57	2.65	2.09	2.57
Fixed carbon	92.0	93.2	93.1	88.9	91.6	92.6
Volatile matter	4.72	4.05	4.28	8.45	6.51	4.82
C	90.4	92.4	93.9	90.9	94.7	95.6
H	1.04	0.41	0.19	0.72	0.19	0.06
N	0.10	0.38	0.50	1.31	0.91	0.92
O	5.18	3.99	2.86	4.41	2.08	0.83
Reactivity in 100 % CO_2						
Peak temperature (°C)	984	998	1004	970	971	984
Reaction rate (% min^{-1})	11.3	11.8	18.3	8.78	9.97	10.86
Oak charcoal						
Char yield (g_{char} $g_{biomass}{}^{-1}$)	29.0	27.9	25.6	29.1	28.3	26.9
Proximate and ultimate analysis (wt. % dry basis)						
Ash at 550°C	3.00	3.64	4.58	4.52	4.60	4.83
Fixed carbon	86.0	87.3	90.2	86.2	86.8	87.0
Volatile matter	6.19	4.54	4.58	9.24	7.97	7.37
C	91.3	92.1	94.7	86.7	90.1	93.4
H	1.04	0.42	0.20	1.09	0.86	0.28
N	0.71	1.28	1.64	0.79	0.64	1.00
O	3.93	2.58	0.48	6.93	3.58	0.39
Reactivity in 100 % CO_2						
Peak temperature (°C)	962	987	1008	941	936	962
Reaction rate (% min^{-1})	12.1	14.2	15.4	10.3	10.	13.8

Table S-3: Product yield, proximate and ultimate analysis after secondary heat treatment of spruce and oak charcoal at 700 and 1000°C.

	Spruce charcoal					**Oak charcoal**				
Primary heat treatment temperature (°C)	500	700	900	1100	1300	500	700	900	1100	1300
Secondary heat treatment at 700°C										
Char yield ($g_{char}\ g_{biomass}{}^{-1}$)	24.7	25.3	24.3	23.5	22.0	24.6	23.8	22.9	21.5	20.2
Proximate and ultimate analysis (wt. % dry basis)										
Ash at 550°C	2.00	2.19	2.30	2.30	2.38	5.02	5.05	4.90	4.42	4.78
Fixed carbon	92.2	93.6	94.2	94.1	95.0	90.2	90.3	92.3	92.6	92.5
Volatile matter	5.75	4.19	3.50	3.60	2.57	4.81	4.69	2.85	3.01	2.71
C	90.1	90.3	92.3	92.0	94.2	85.8	86.5	90.4	89.6	90.8
H	1.02	1.01	0.52	0.24	0.07	1.10	1.06	0.65	0.30	0.06
N	2.27	0.93	1.86	2.32	0.89	1.09	0.55	0.10	0.96	0.33
O	4.22	5.47	3.07	3.26	2.84	7.19	7.52	3.98	4.13	3.82
Reactivity in 100 % CO_2										
Peak temperature, °C	967	969	968	995	992	949	951	966	977	995
Reaction rate (% min^{-1})	12.1	12.5	14.4	17.1	19.7	14.6	17.6	19.9	23.4	28.2
Secondary heat treatment at 1000°C										
Char yield ($g_{char}\ g_{biomass}{}^{-1}$)	23.7	23.0	23.4	22.2	21.9	23.3	22.7	21.8	20.5	20.2
Proximate and ultimate analysis (wt. % dry basis)										
Ash at 550°C	3.39	2.79	2.74	2.66	2.83	5.47	4.93	6.62	6.37	5.08
Fixed carbon	91.2	93.4	92.2	93.7	93.3	90.7	91.1	88.1	88.9	92.5
Volatile matter	5.37	3.82	4.99	3.53	3.86	3.85	3.95	5.28	4.74	2.38
C	90.3	91.4	92.1	91.3	94.9	89.3	89.6	90.4	89.6	91.7
H	0.63	0.45	0.50	0.37	0.11	0.30	0.35	0.34	0.35	0.06
N	0.06	0.97	1.60	0.18	0.08	1.18	0.94	1.06	0.86	0.33
O	5.06	4.39	3.06	5.53	2.06	4.13	4.23	2.76	2.87	1.34
Reactivity in 100 % CO_2										
Peak temperature (°C)	976	990	984	1003	1008	988	991	987	971	1015
Reaction rate (% min^{-1})	14.0	14.7	12.7	19.5	17.3	17.0	18.9	20.4	22.3	29.2

Table S-4: Product yield, proximate and ultimate analysis after secondary heat treatment of spruce and oak charcoal at 1300 and 1600°C.

	Spruce charcoal					**Oak charcoal**				
Primary heat treatment temperature (°C)	500	700	900	1100	1300	500	700	900	1100	1300
Secondary heat treatment at 1300°C										
Char yield ($g_{char}\ g_{biomass}{}^{-1}$)	22.9	22.6	22.3	21.3	21.0	22.2	20.5	19.7	19.0	18.7
Proximate and ultimate analysis (wt. % dry basis)										
Ash at 550°C	2.72	2.75	2.85	3.02	3.03	6.26	6.31	6.82	5.96	5.40
Fixed carbon	94.2	95.0	94.6	94.6	94.4	91.2	91.5	90.7	91.7	92.0
Volatile matter	2.65	2.22	2.55	2.40	2.61	2.56	2.14	2.45	2.33	2.55
C	95.8	95.0	95.8	95.2	95.6	91.8	93.3	92.6	93.2	93.2
H	0.15	0.11	0.10	0.08	0.15	0.05	0.09	0.17	0.28	0.04
N	0.05	0.21	0.27	0.32	0.12	0.37	0.05	0.34	0.08	0.09
O	0.97	1.68	1.01	1.62	1.39	2.37	0.55	0.26	0.08	0.4
Reactivity in 100 % CO_2										
Peak temperature (°C)	931	956	950	950	950	958	950	963	965	964
Reaction rate (% min^{-1})	10.6	10.4	11.2	9.3	9.5	16.0	17.8	16.4	16.6	17.0
Secondary heat treatment at 1600°C										
Char yield ($g_{char}\ g_{biomass}{}^{-1}$)	22.4	22.0	21.9	21.0	20.2	20.7	20.2	20.2	19.5	18.7
Proximate and ultimate analysis (wt. % dry basis)										
Ash at 550°C	2.20	2.35	2.19	2.33	2.49	5.99	5.40	5.60	5.63	5.65
Fixed carbon	97.3	97.2	97.3	97.2	97.2	93.5	94.2	93.9	93.9	94.0
Volatile matter	0.49	0.44	0.53	0.48	0.35	0.47	0.42	0.52	0.46	0.34
C	96.6	96.6	96.3	96.5	96.0	92.5	90.6	91.5	91.4	90.9
H	0.014	0.018	0.003	0.006	0.008	0.051	0.042	0.004	0.098	0.022
N	1.06	0.93	1.51	1.07	1.38	1.39	3.95	2.78	2.81	3.37
O	0.17	0.14	0.02	0.11	0.10	0.05	0.01	0.08	0.02	0.07
Reactivity in 100 % CO_2										
Peak temperature (°C)	959	966	964	965	961	966	967	967	968	967
Reaction rate (% min^{-1})	13.5	13.2	11.6	10.1	13.5	15.8	16.0	14.6	14.6	13.3

References

[1] Tannous K, Lam PS, Sokhansanj S, Grace JR, Physical properties for flow characterization of ground biomass from Douglas Fir Wood, Part Sci Technol 31 (2012) 291–300.

A.2 Supplemental materials article 2

Characterization and reactivity of charcoal from high temperature pyrolysis (800-1600 °C)

Contribution of the authors

Gerrit Ralf Surup planned the majority of the study, developed a reactor for the charcoal production and performed the pyrolysis and CO_2 reactivity experiments.
Markus Heidelmann performed the TEM imaging of all char samples and contributed to the data processing using Gatan software and further description of the results in the manuscript.
Anna Trubetskaya supported on the manuscript structuring, managed the correspondence among co-authors and did the manuscript proof-reading. She has also performed the reactivity measurements for TGA measurements >1100 °C.
Henrik Kofoed Nielsen provided extensive comments to the manuscript, grant writing for the PhD project and assistance with the introduction and conclusion of the manuscript.

Characterization and reactivity of charcoal from high temperature pyrolysis (800-1600°C)

Gerrit Ralf Surup[a], Henrik Kofoed Nielsen[a], Markus Heidelmann[b], Anna Trubetskaya[c,*]

[a]*Department of Engineering Sciences, University of Agder, 4879 Grimstad, Norway*
[b]*Interdisciplinary Center for Analytics on the Nanoscale, University of Duisburg-Essen, 47057 Duisburg, Germany*
[c]*Mechanical Engineering Department, National University of Ireland Galway, Galway, Ireland*

S-1. TEM analysis

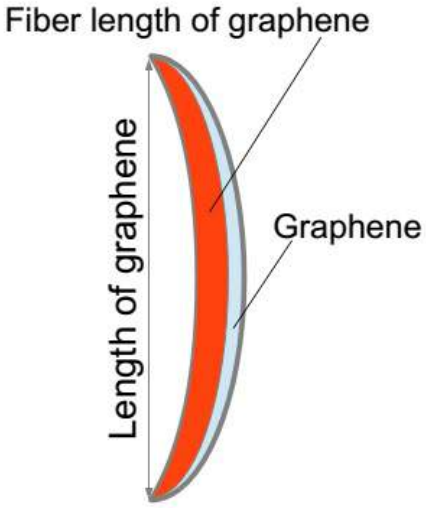

Figure S-1: Graphene fiber length and length used for the curvature calculation.

*Corresponding author. anna.trubetskaya@nuigalway.ie

S-2. Char reactivity

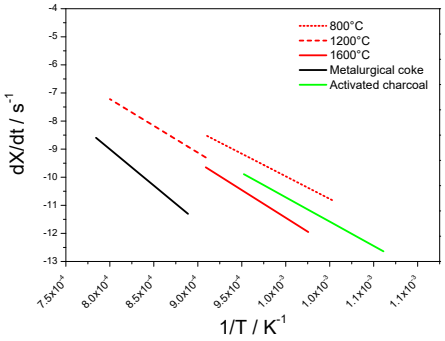

2(a): Spruce char (20 % CO_2 + 80 % N_2)

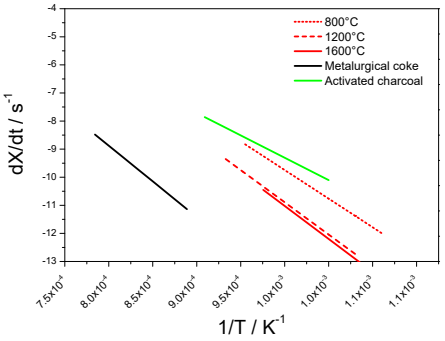

2(b): Spruce char (100 % CO_2)

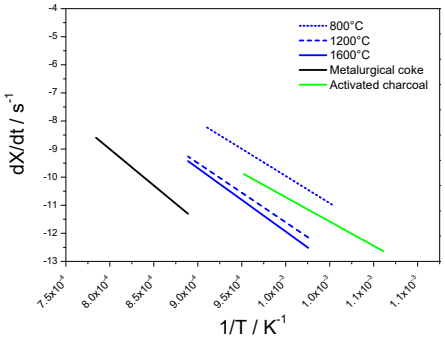

2(c): Oak char (20 % CO_2 + 80 % N_2)

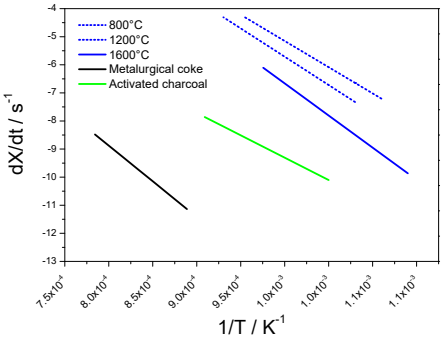

2(d): Oak char (100 % CO_2)

Figure S-2: Arrhenius plot of CO_2 reactivity of activated charcoal, metallurgical coke, Norway spruce and oak chars from pyrolysis at 800, 1200, and 1600°C reacted in 20 % volume fraction CO_2 + 80 % volume fraction N_2 and in 100 % CO_2.

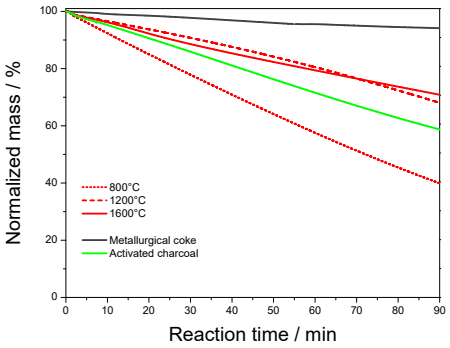

3(a): Spruce char (20 % CO_2 + 80 % N_2)

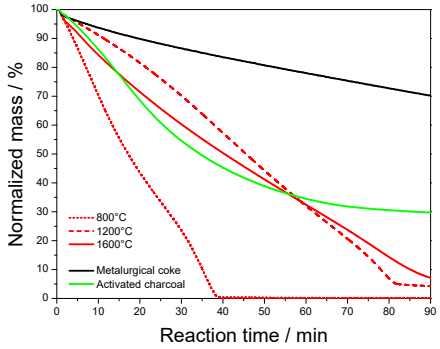

3(b): Spruce char (100 % CO_2)

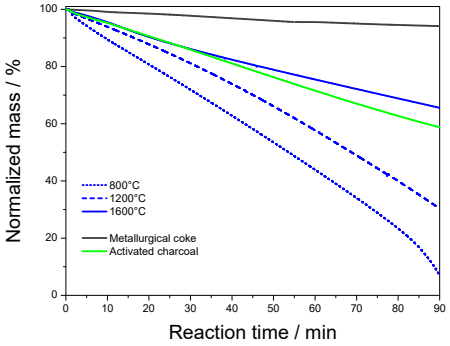

3(c): Oak char (20 % CO_2 + 80 % N_2)

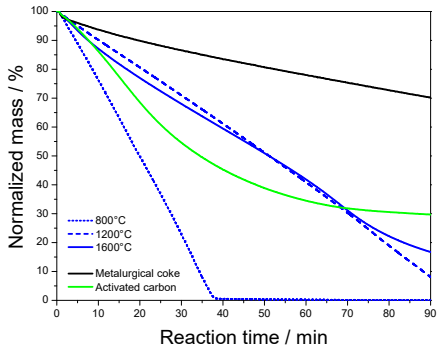

3(d): Oak char (100 % CO_2)

Figure S-3: Thermogravimetric analysis of activated charcoal, metallurgical coke, Norway spruce and oak chars from pyrolysis at 800, 1200, and 1600°C reacted in 20 % CO_2 + 80 % N_2 and 100 % CO_2. The normalized mass is shown over the reaction time (min).

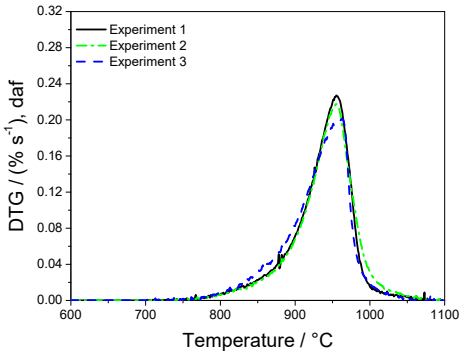

4(a): Spruce char (1600°C; 100 % CO_2)

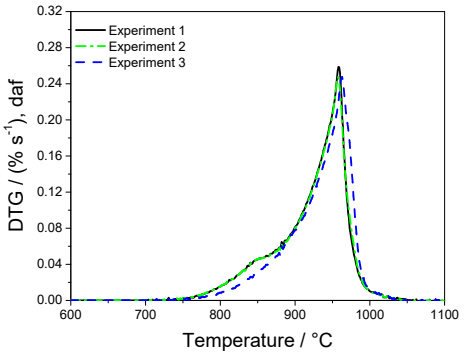

4(b): Oak char (1600°C; 100 % CO_2)

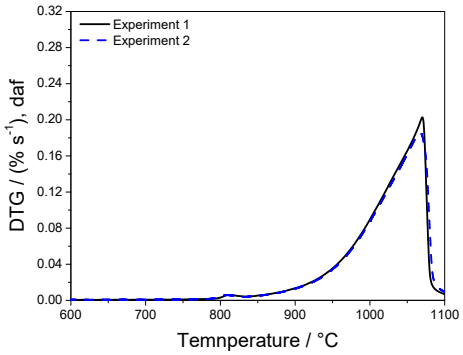

4(c): Spruce char (1200°C; 20 % CO_2 + 80 % N_2)

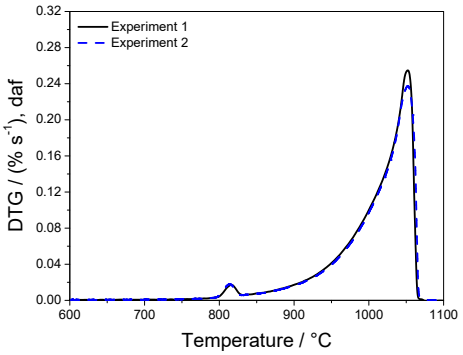

4(d): Oak char (1200°C; 20 % CO_2 + 80 % N_2)

Figure S-4: Repeatability of DTG curves of oak and spruce char samples from pyrolysis at 1600°C reacted in 100 % volume fraction CO_2 and oak and spruce char samples from pyrolysis at 1200°C reacted in 20 % volume fraction CO_2 + 80 % volume fraction N_2.

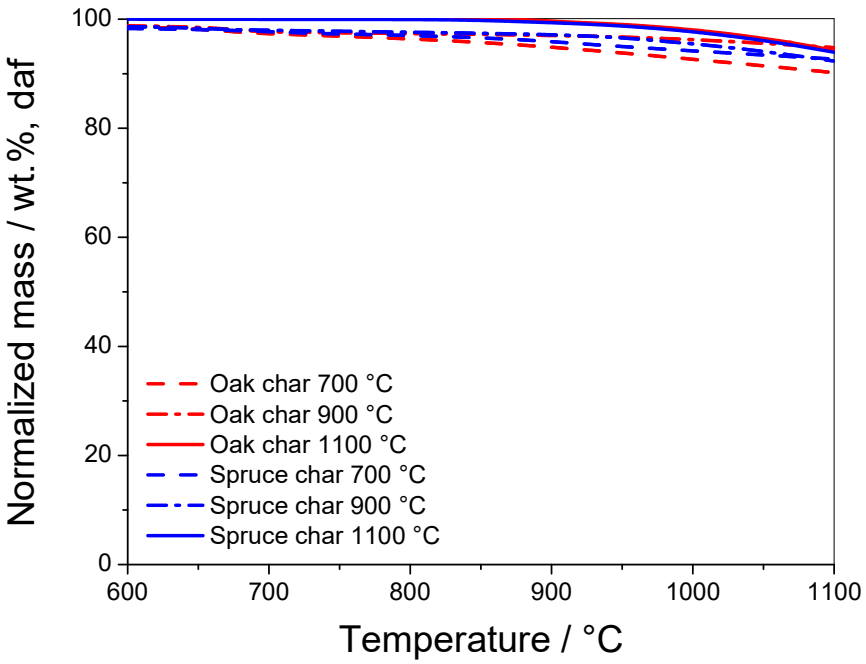

Figure S-5: Thermogravimetric analysis in 100 % volume fraction N_2 flow of spruce and oak chars from pyrolysis at 800, 1200 and 1600°C.

Table S-1: Kinetic parameters for CO_2 reactivity of metallurgical coke, activated charcoal, chars from Norway spruce and oak reacted in 20 % volume fraction CO_2 + 80 % volume fraction N_2.

E_a	A_i	r_{max} at 1000°C
kJ mol^{-1}	s^{-1}	s^{-1}
Norway spruce		
Char from pyrolysis at 800°C		
134	$4.6 \cdot 10^2$	$1.5 \cdot 10^{-3}$
Char from pyrolysis at 1200°C		
159	$3.1 \cdot 10^3$	$1 \cdot 10^{-3}$
Char from pyrolysis at 1600°C		
164	$4.1 \cdot 10^3$	$1 \cdot 10^{-3}$
Oak		
Char from pyrolysis at 800°C		
161	$1.2 \cdot 10^4$	$3 \cdot 10^{-3}$
Char from pyrolysis at 1200°C		
176	$1.4 \cdot 10^4$	$1 \cdot 10^{-3}$
Char from pyrolysis at 1600°C		
188	$4.3 \cdot 10^4$	$1 \cdot 10^{-3}$
Metallurgical coke		
144	$7.4 \cdot 10^2$	$4.1 \cdot 10^{-3}$
Charcoal		
215	$1.2 \cdot 10^5$	$4 \cdot 10^{-2}$

Table S-2: Kinetic parameters for CO_2 reactivity of metallurgical coke, activated charcoal, chars from Norway spruce and oak reacted in 100 % CO_2.

E_a	A_i	r_{max} at 1000°C
kJ mol^{-1}	s^{-1}	s^{-1}
Norway spruce		
Char from pyrolysis at 800°C		
170	$4.2{\cdot}10^{4}$	$4.6{\cdot}10^{-3}$
Char from pyrolysis at 1200°C		
191	$1.7{\cdot}10^{5}$	$2.6{\cdot}10^{-3}$
Char from pyrolysis at 1600°C		
196	$2.7{\cdot}10^{5}$	$2.6{\cdot}10^{-3}$
Oak		
Char from pyrolysis at 800°C		
155	$7.4{\cdot}10^{5}$	0.3
Char from pyrolysis at 1200°C		
168	$1.9{\cdot}10^{6}$	0.2
Char from pyrolysis at 1600°C		
190	$1.1{\cdot}10^{7}$	0.2
Metallurgical coke		
161	$7.8{\cdot}10^{3}$	$4{\cdot}10^{-2}$
Charcoal		
211	$9.4{\cdot}10^{4}$	0.1

The influence of convective flow on the mass transfer inside the crucible was assumed to be negligible, and so mass transport occurs by molecular diffusion only. The mass transfer of product gases on the reaction was neglected, and the temperature within the char layer was assumed uniform. Furthermore, it was assumed that the char particles were distributed equally in the TG crucible. The maximal reaction rate (r_{max}) measured by the thermogravimetric instrument is shown as the first derivative (DTG) at the maximal temperature in Figure 2 of the main manuscript. The mass transfer (r_{diff}) of CO_2 transfer to the surface of the soot particle bed was estimated

in Table S-3. The mass transfer (% min^{-1}) of CO_2 transfer to the surface of the char particle bed was estimated as shown in equation 1:

$$r_{diff} = \frac{A_{cr} \cdot D_{AB} \cdot 60 \cdot M_c \cdot C_B}{L_{cr} \cdot m_{TG,s}} \cdot 100 \tag{1}$$

In equation 1, M_c is molar carbon weight, L_{cr} and A_{cr} are height and area of a thermogravimetric crucible, $m_{TG,s}$ is the initial sample weight. The diffusion coefficient (D_{AB}) was obtained from correlation of Chapman and Enskog [1]. C_B is the bulk concentration of CO_2 in the inlet gas (N_2) and calculated in equation 2:

$$C_B = \frac{p \cdot y_{bulk}}{R \cdot T} \tag{2}$$

In equation 2, y_{bulk} is the mole fraction of the reacting gas in the bulk (CO_2), and p is the total pressure.

Table S-3: The diffusion rate was calculated at the relevant peak temperature of the TG experiment in 20 % or 100 % volume fraction CO_2, and compared with the reaction rate (r_{max}) measured by the thermogravimetric instrument and shown in Figure 2 of the manuscript as the first derivative (DTG) at the maximal temperature.

Char type	Peak temperature*	D_{AB}	r_{diff}	r_{max}/r_{diff}
	°C	$m^2\ s^{-1}$	% min^{-1}	
20 % CO_2 + 80 % N_2				
Spruce char (800°C)	1031	$2{\cdot}10^{-4}$	26	0.4
Spruce char (1200°C)	1069	$2.1{\cdot}10^{-4}$	25	0.5
Spruce char (1600°C)	1024	$2{\cdot}10^{-4}$	26	0.2
Oak char (800°C)	1022	$2{\cdot}10^{-4}$	26	0.4
Oak char (1200°C)	1050	$2{\cdot}10^{-4}$	26	0.6
Oak char (1600°C)	1082	$2.1{\cdot}10^{-4}$	25	0.3
100 % CO_2				
Spruce char (800°C)	980	$1.8{\cdot}10^{-4}$	135	0.1
Spruce char (1200°C)	1005	$1.9{\cdot}10^{-4}$	132	0.1
Spruce char (1600°C)	958	$1.8{\cdot}10^{-4}$	137	0.1
Oak char (800°C)	982	$1.8{\cdot}10^{-4}$	134	0.1
Oak char (1200°C)	996	$1.9{\cdot}10^{-4}$	133	0.1
Oak char (1600°C)	961	$1.8{\cdot}10^{-4}$	137	0.1

*Relevant peak temperature of the thermogravimetric experiment

L_{cr} is 4 mm and crucible diameter is 5 mm

The reaction rate of spruce and oak chars obtained from pyrolysis at 800, 1200, and 1600°C determined isothermally by the thermogravimetric instrument at 850°C in 20 % or 100 % volume fraction CO_2 is shown in Table S-4 using mass loss data from Figure S-6.

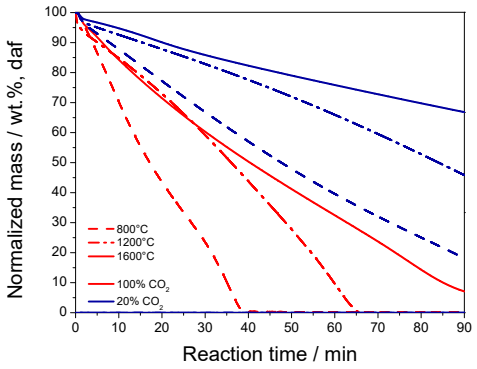

6(a): Spruce char

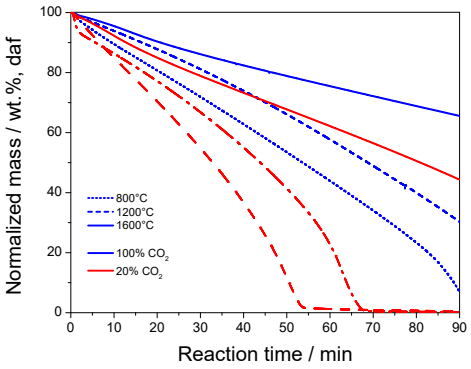

6(b): Oak char (1600°C)

Figure S-6: Influence of CO_2 concentration (20 and 100 % CO_2) on the reaction rate measured by the thermogravimetric instrument at 850°C of oak char generated at 800, 1200, and 1600°C.

Table S-4: The reaction rate (% min^{-1}) of spruce and oak obtained from pyrolysis at 800, 1200, and 1600°C measured in thermogravimetric instrument at 850°C in 20 or 100 % volume fraction CO_2.

Sample	CO_2 concentration, %	Heat treatment temperature, °C		
		800	1200	1600
Spruce	20	1.050	0.528	0.339
Spruce	100	2.969	1.458	1.009
Oak	20	1.462	0.935	0.604
Oak	100	2.612	1.788	1.134

The reaction rate of CO_2 gasification ($r_{850°C}$) is represented by means of the Arrhenius equation in equation 3 [2, 3]:

$$r_{850°C} = -A_i \cdot exp\left(\frac{-E_a}{R \cdot T}\right) \cdot \left(1 - \frac{m_p}{m_{p0}}\right) \cdot {p_{CO_2}}^n \quad (3)$$

In equation 3, p_{CO_2} is the partial pressure of CO_2, m_{p_0} is the initial mass of char, m_p the mass of char at time t, n is the reaction order. When n = 1 was used in the calculation, it is expected that the reaction rate decreases with the decrease in CO_2 concentration from 100 to 20 % linearly [4, 5]. However, the decrease in CO_2 concentration from 100 to 20 % led to the decrease in reaction rate by factor of 2.5 for spruce char and by factor of 1.82 for oak char. Moreover, the reaction order n was calculated by the method of least squares for both char samples using the data from Table S-4. The calculation showed that the reaction orders for spruce and oak chars are different (0.571 for spruce char and 0.372 for oak char). The reaction rate and partial pressure could not be linearly correlated for both n=1 and n=0.571; 0.372. Thus, the intrinsic reaction rate depends on the CO_2 concentration.

S-3. Pore size distributions

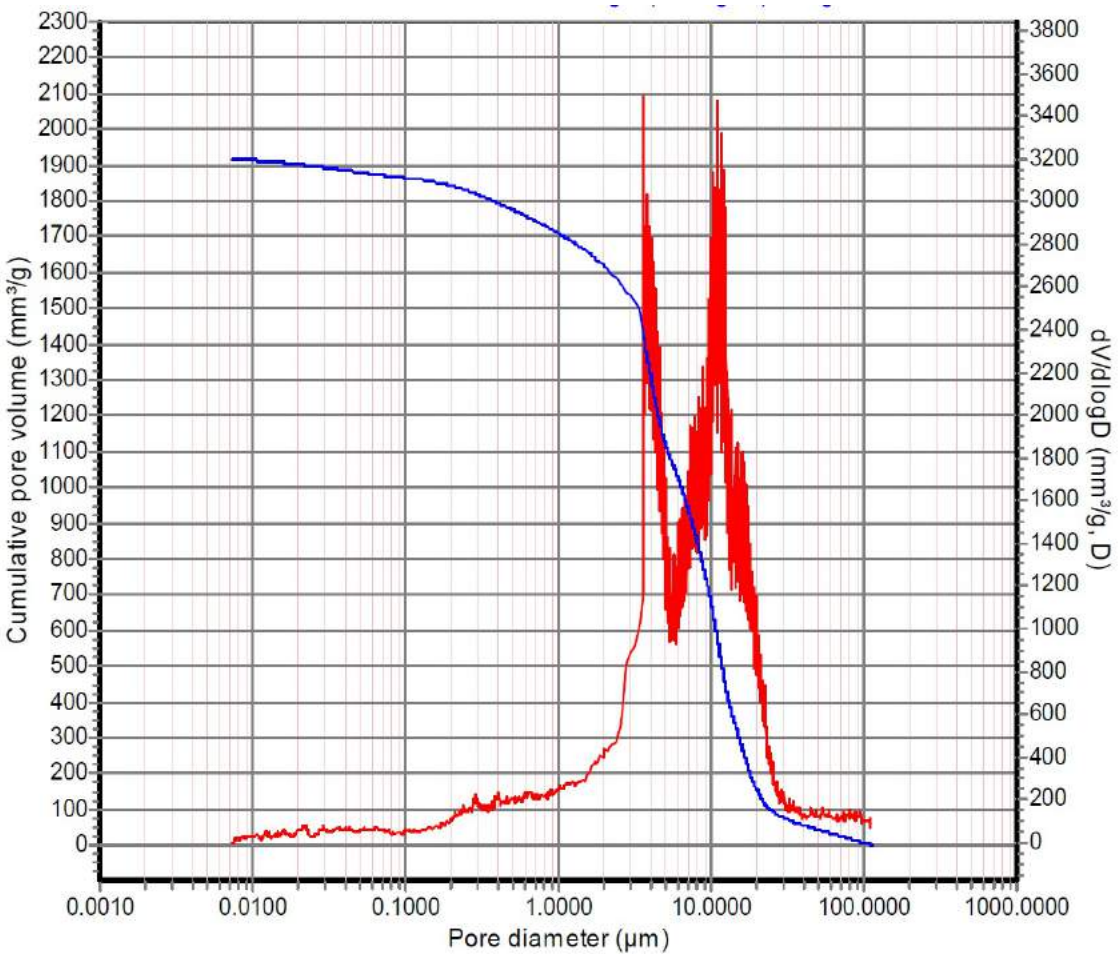

Figure S-7: Cumulative pore volume (mm^3 g^{-1}) and pore size distribution, dV/dlogD (mm^3 g^{-1}, D) of Norway spruce char generated at 800°C.

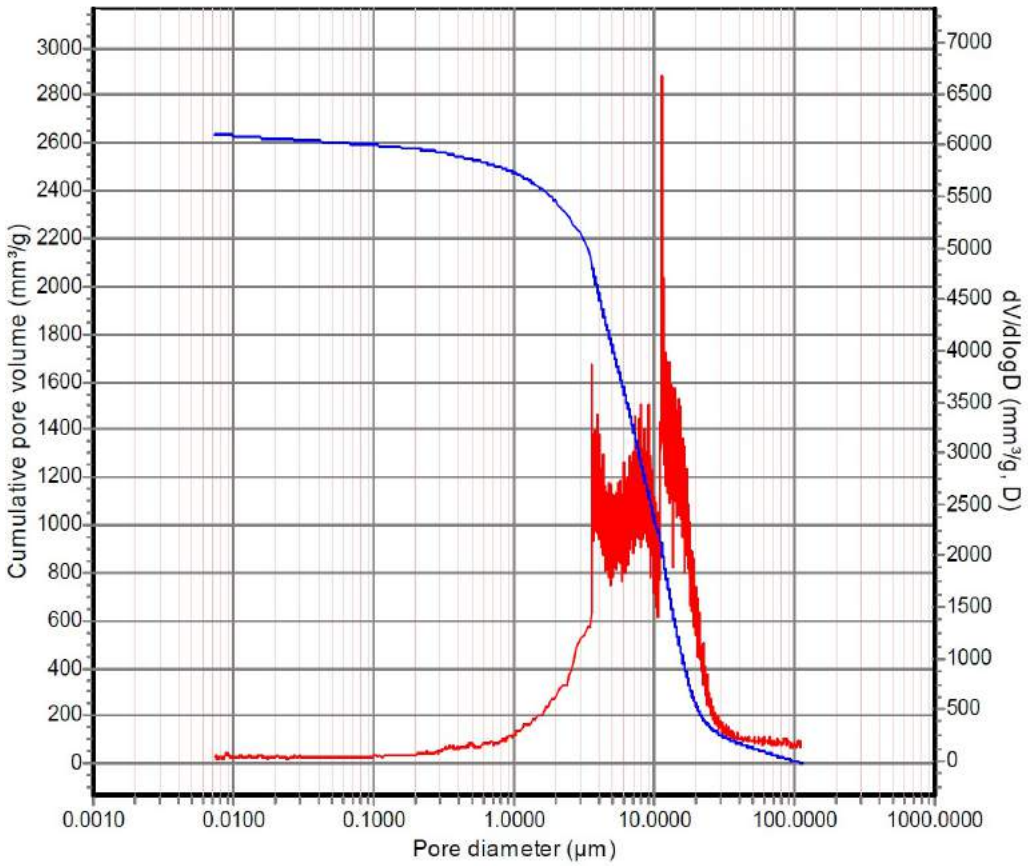

Figure S-8: Cumulative pore volume (mm^3 g^{-1}) and pore size distribution, dV/dlogD (mm^3 g^{-1}, D) of Norway spruce char generated at 1200°C.

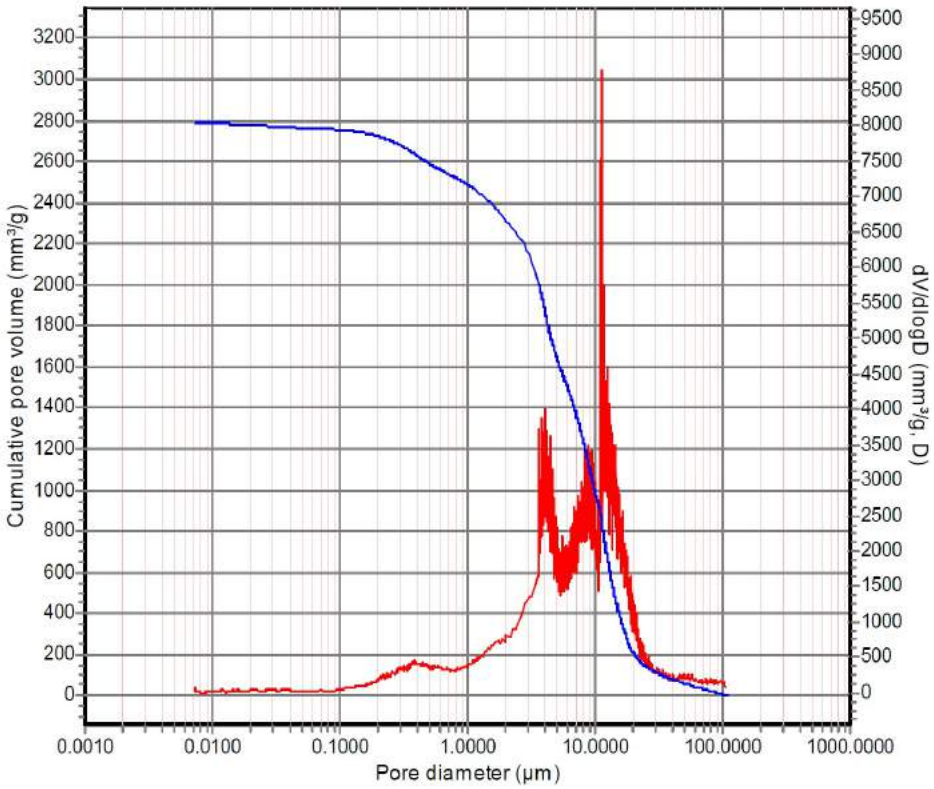

Figure S-9: Cumulative pore volume (mm^3 g^{-1}) and pore size distribution, dV/dlogD (mm^3 g^{-1}, D) of Norway spruce char generated at 1600°C.

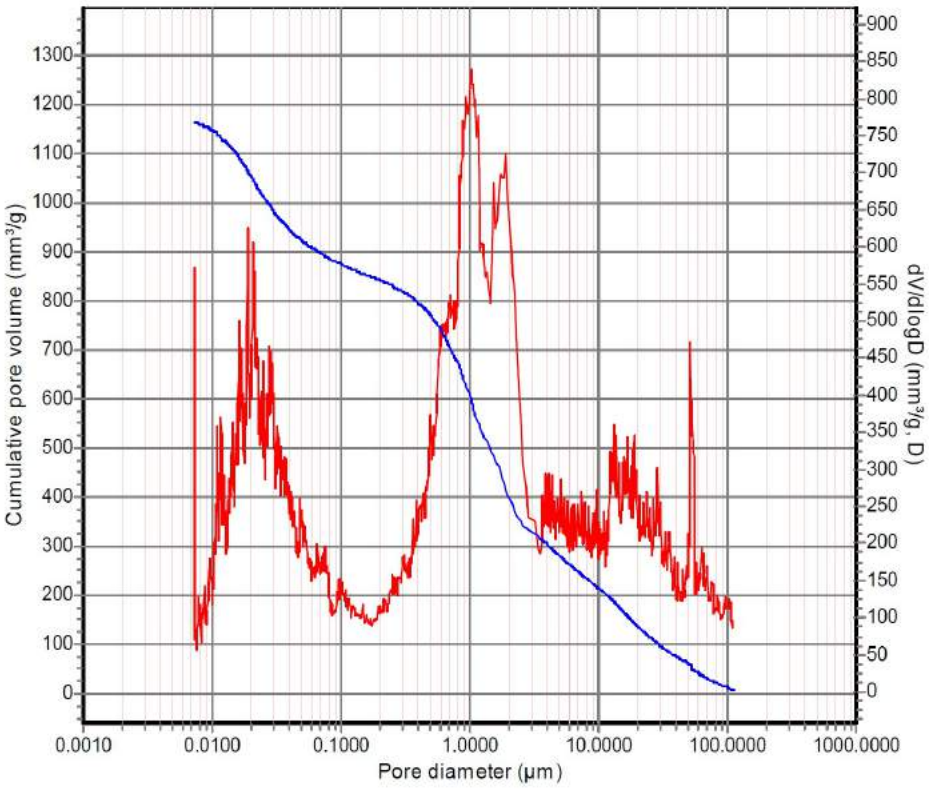

Figure S-10: Cumulative pore volume (mm^3 g^{-1}) and pore size distribution, dV/dlogD (mm^3 g^{-1}, D) of oak char generated at 800°C.

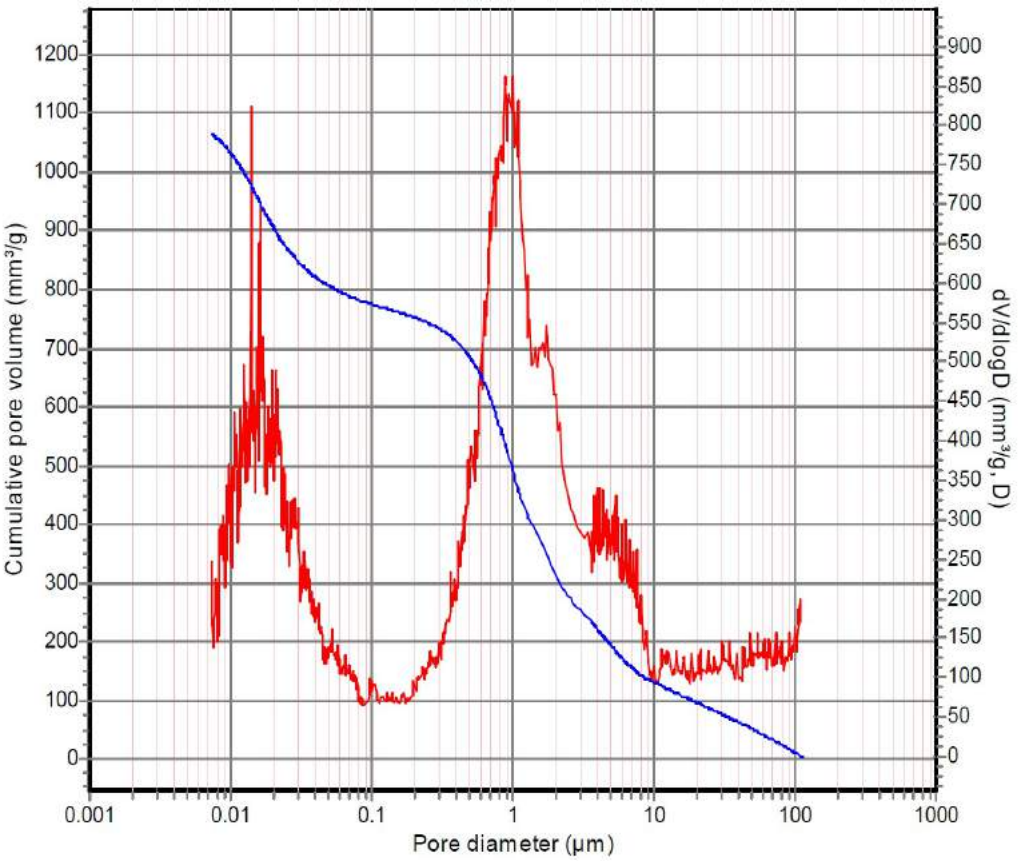

Figure S-11: Cumulative pore volume (mm^3 g^{-1}) and pore size distribution, dV/dlogD (mm^3 g^{-1}, D) of oak char generated at 1200°C.

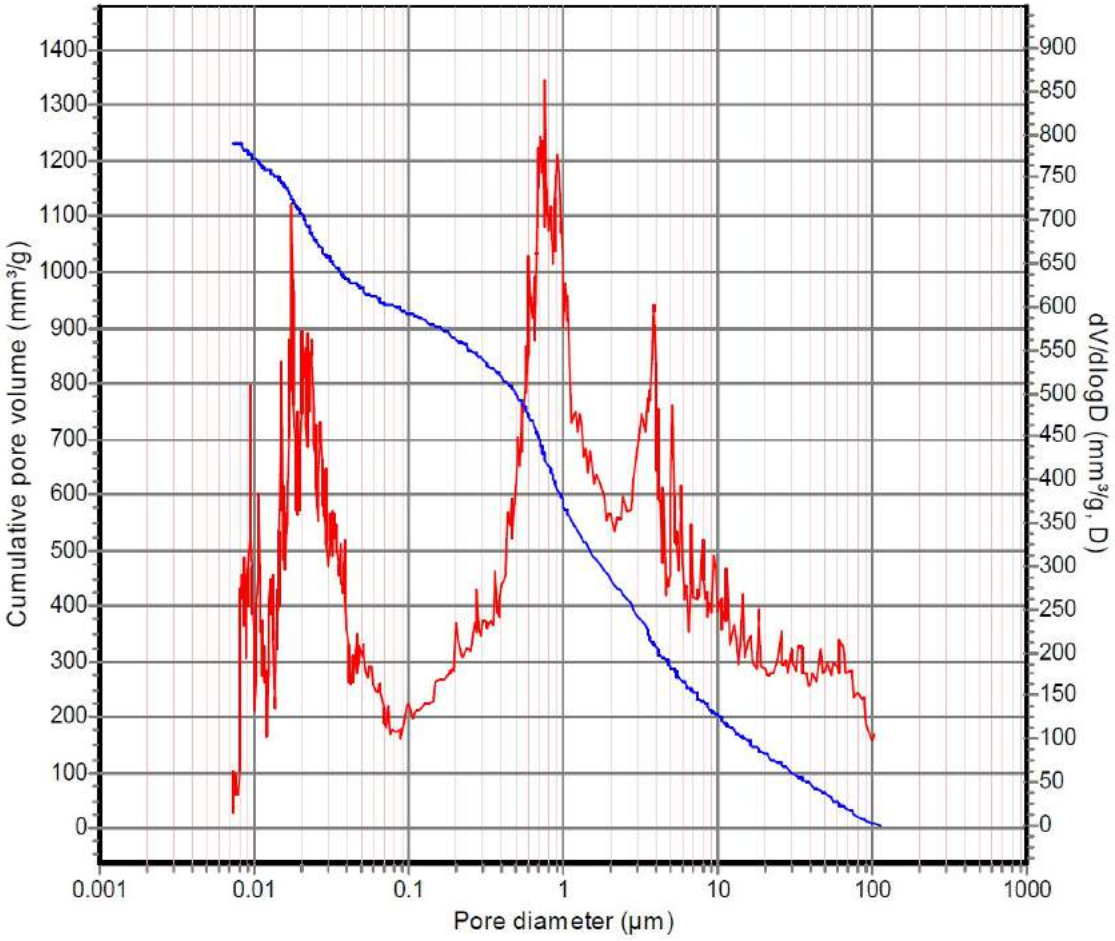

Figure S-12: Cumulative pore volume (mm^3 g^{-1}) and pore size distribution, dV/dlogD (mm^3 g^{-1}, D) of oak char generated at 1600°C.

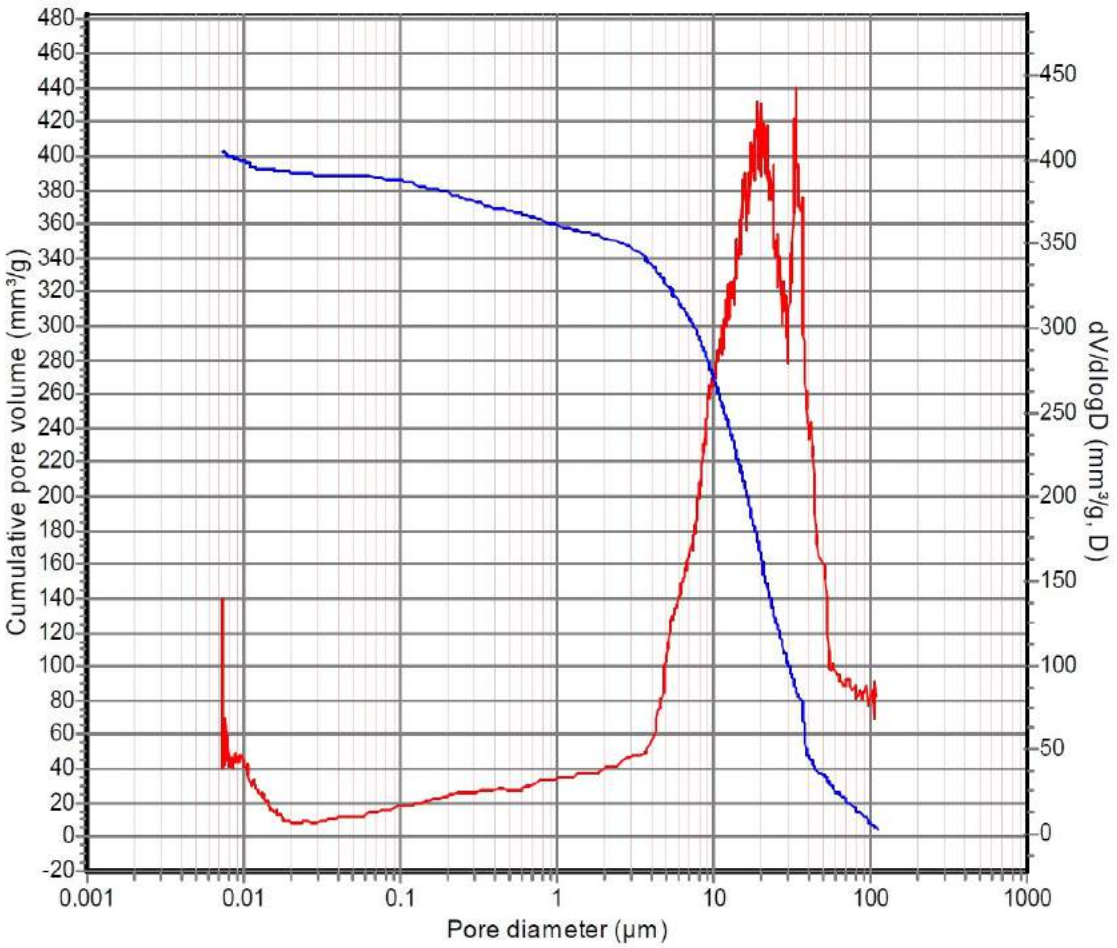

Figure S-13: Cumulative pore volume (mm^3 g^{-1}) and pore size distribution, dV/dlogD (mm^3 g^{-1}, D) of metallurgical coke.

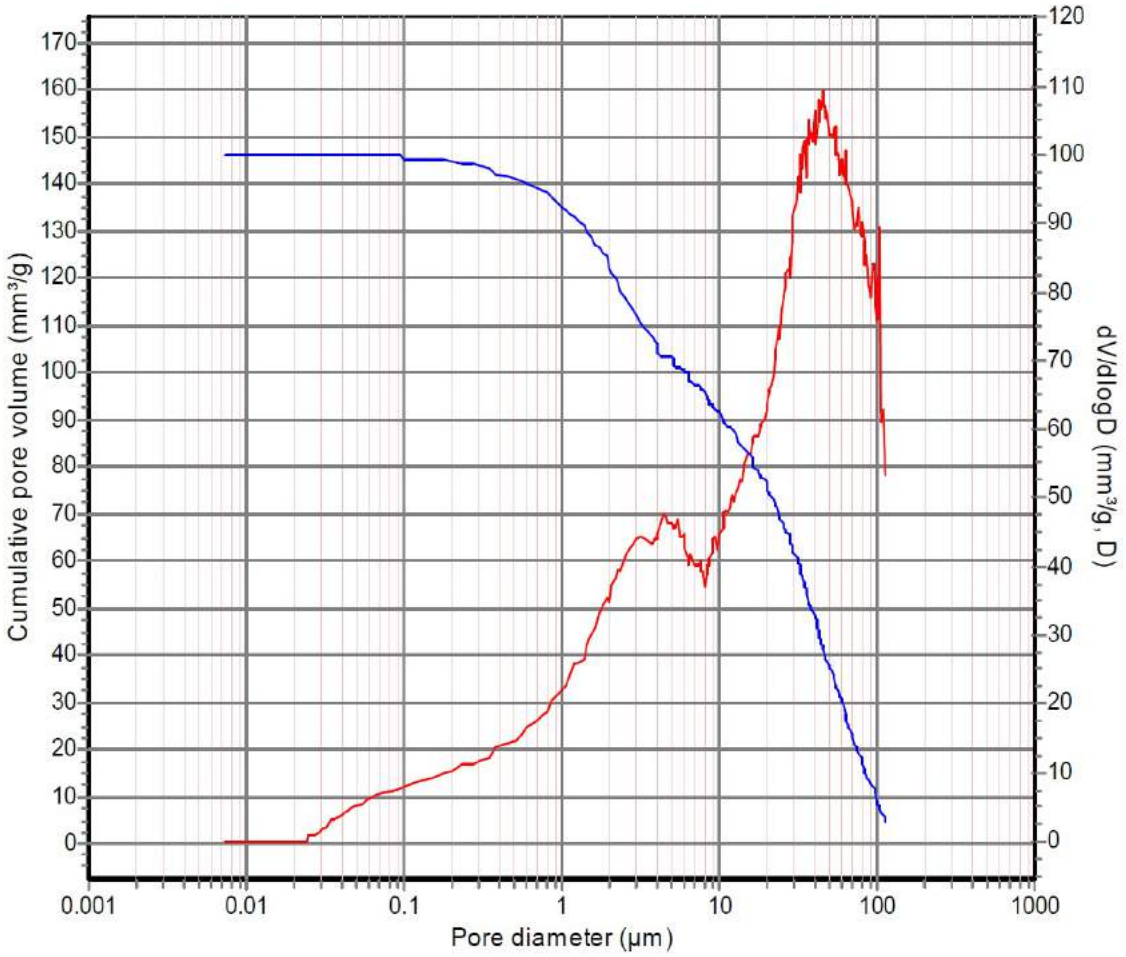

Figure S-14: Cumulative pore volume ($mm^3\ g^{-1}$) and pore size distribution, dV/dlogD ($mm^3\ g^{-1}$, D) of activated charcoal.

S-4. N_2 adsorption measurements

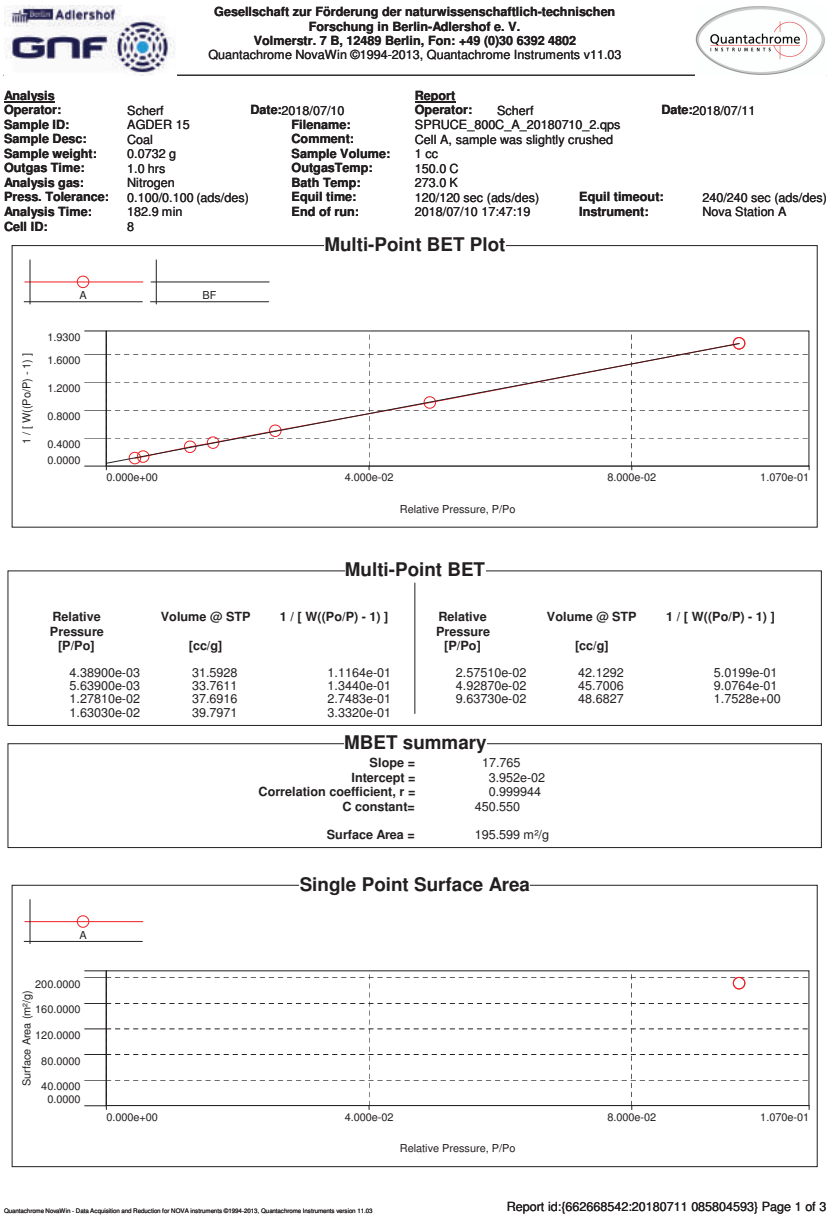

Figure S-15: N_2 adsorption measurements of Norway spruce char generated at 800°C.

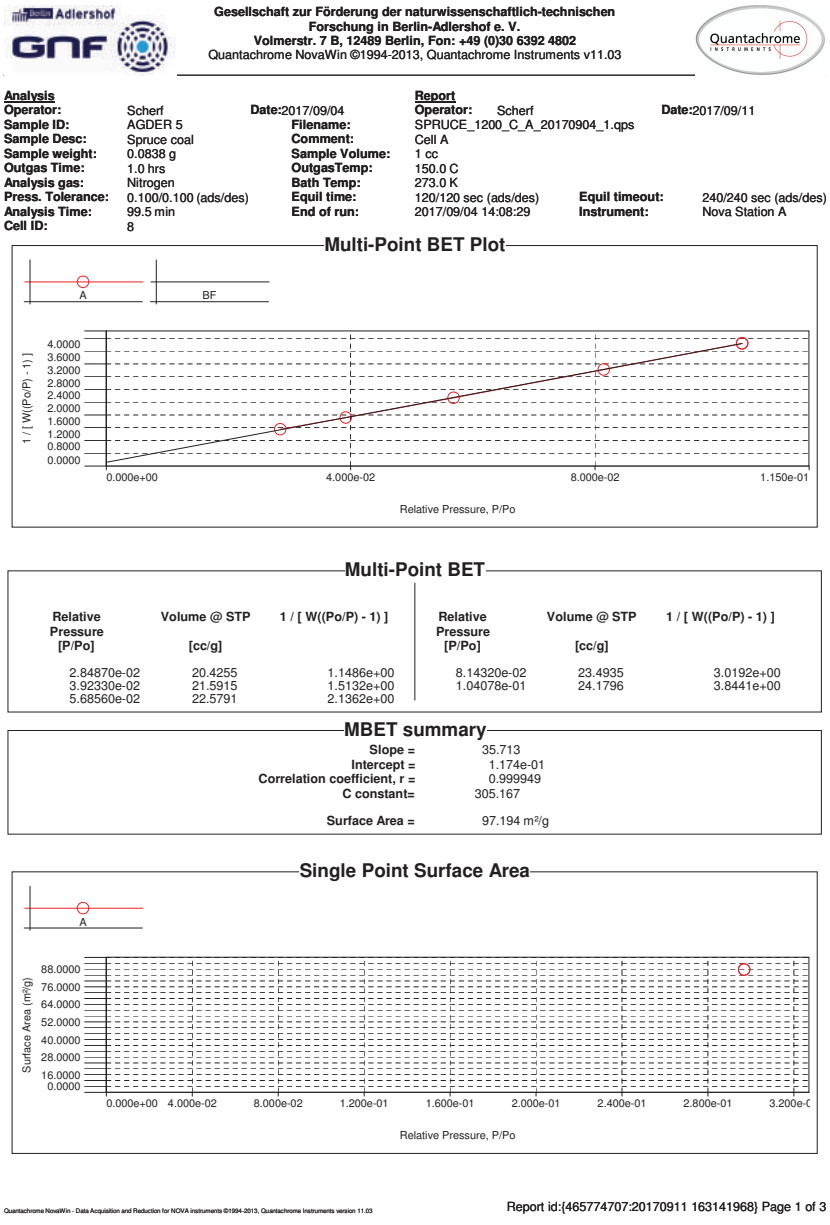

Figure S-16: N_2 adsorption measurements of Norway spruce char generated at 1200°C.

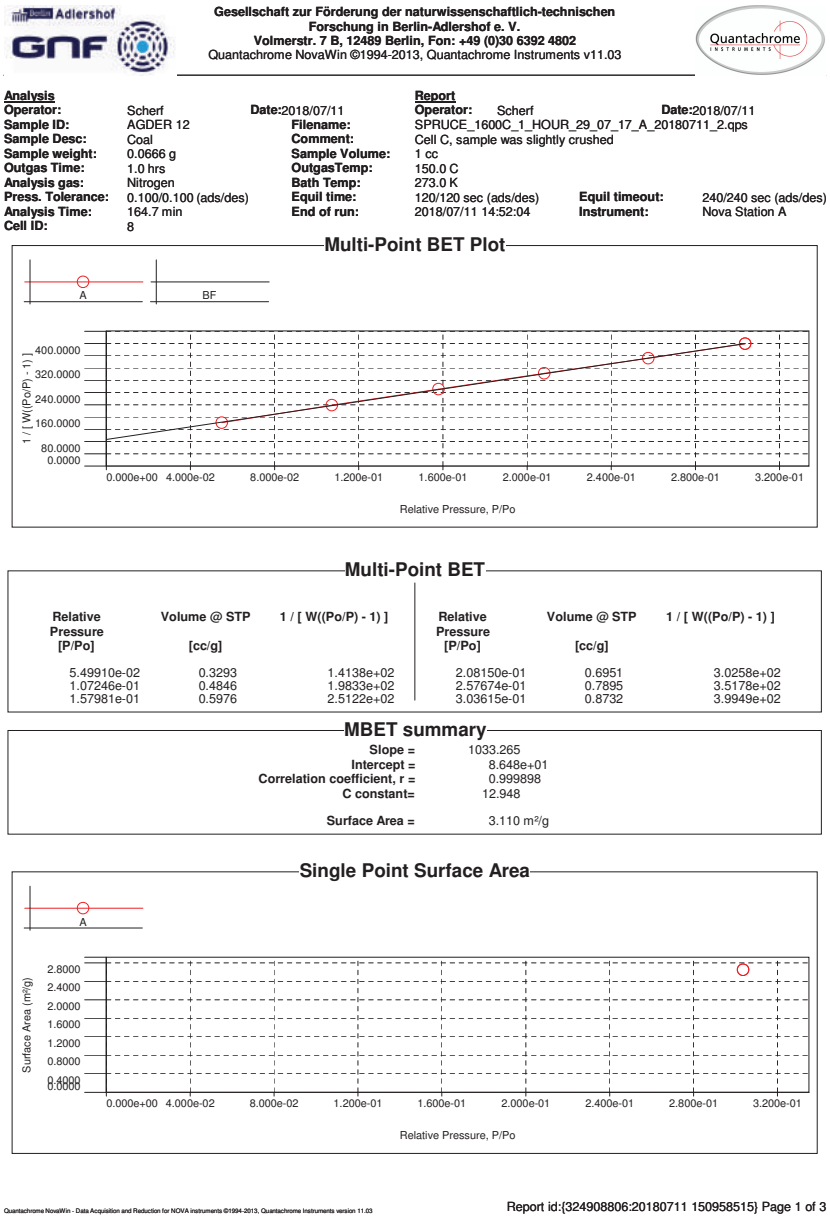

Figure S-17: N_2 adsorption measurements of Norway spruce char generated at 1600°C.

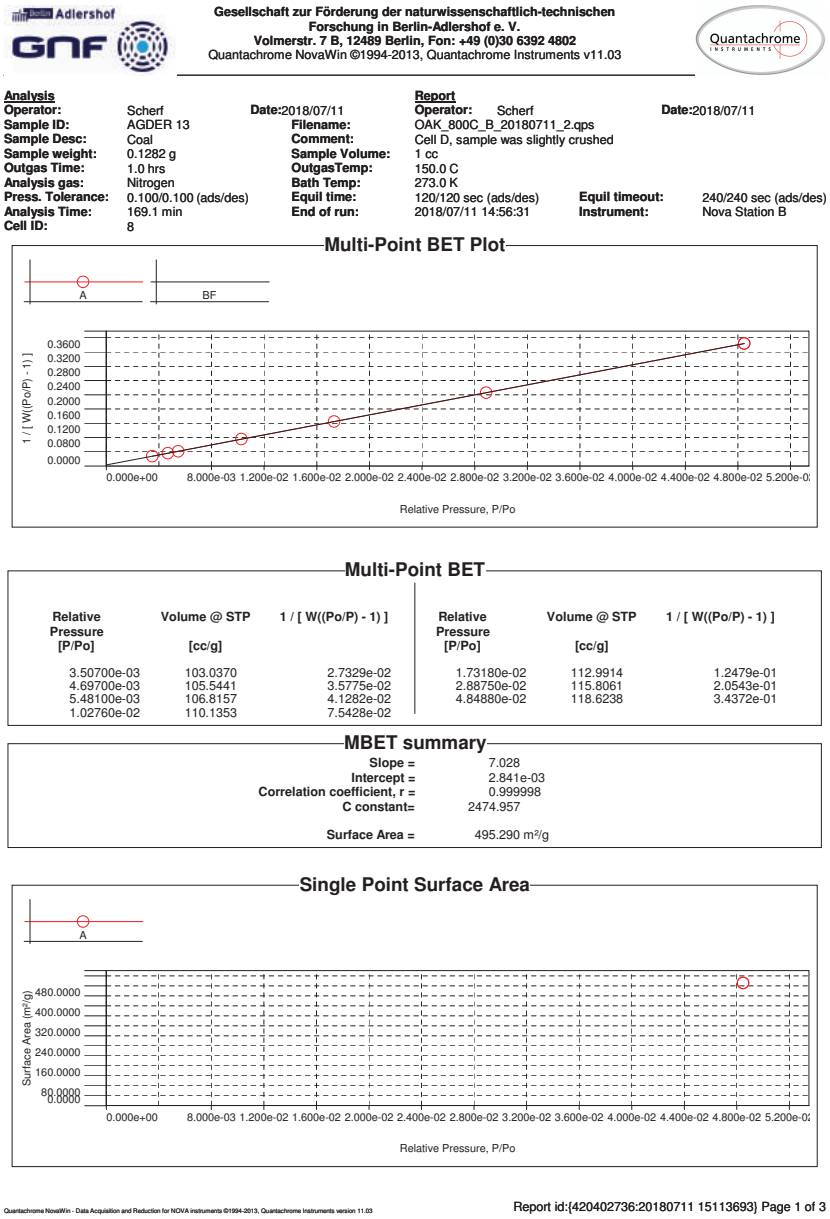

Figure S-18: N_2 adsorption measurements of oak char generated at 800°C.

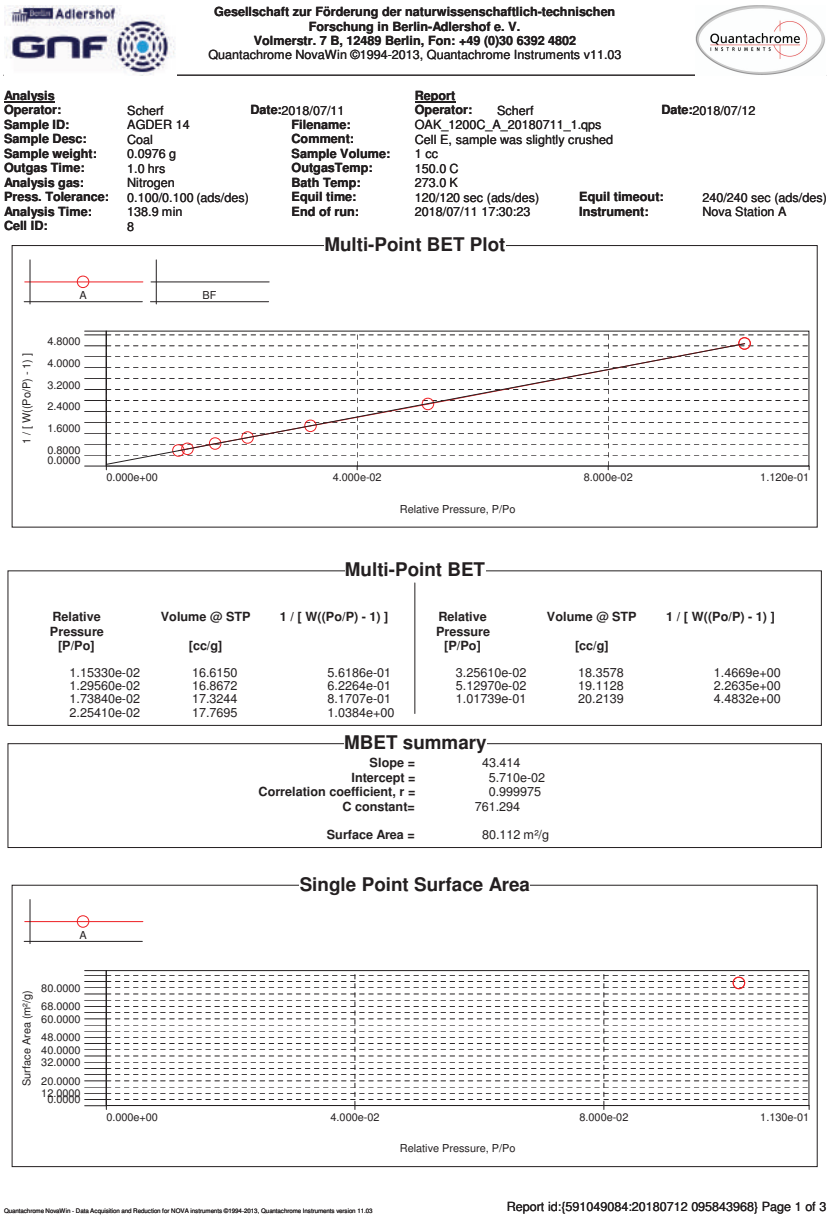

Figure S-19: N_2 adsorption measurements of oak char generated at 1200°C.

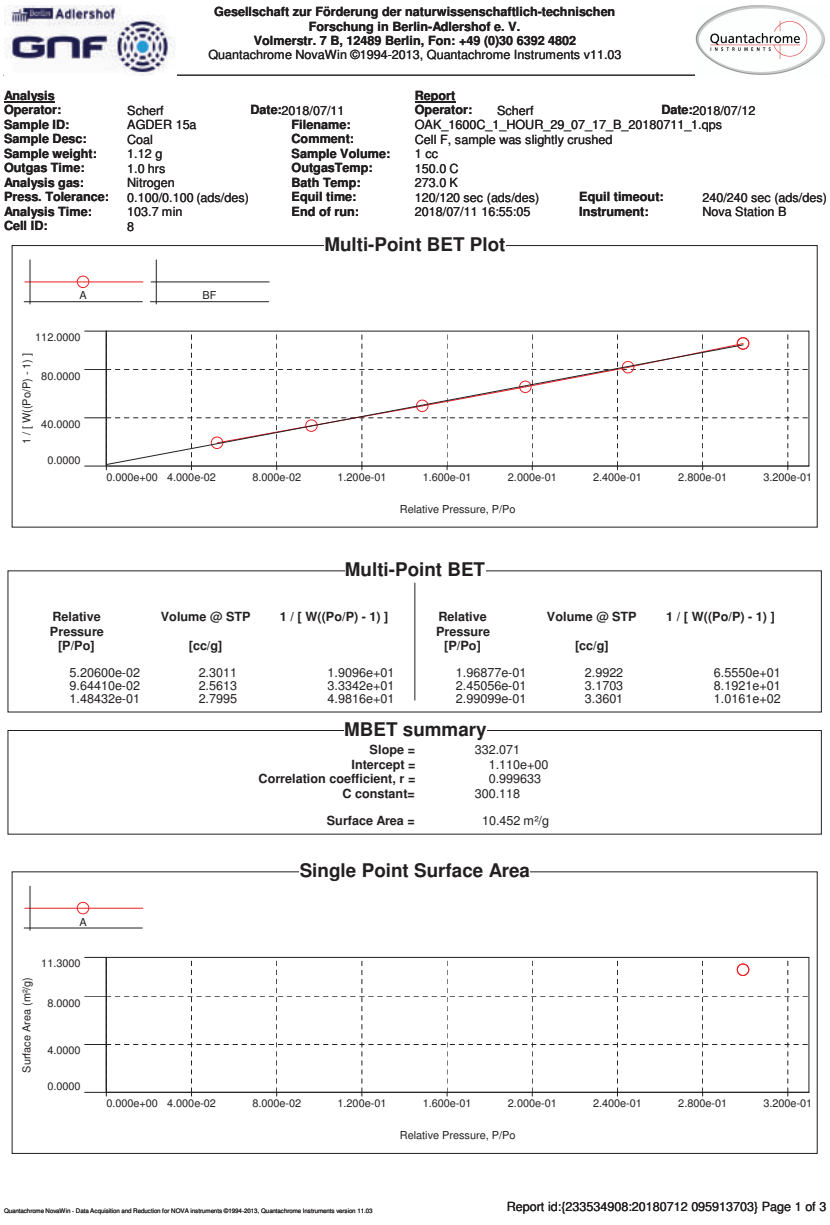

Figure S-20: N_2 adsorption measurements of oak char generated at 1600°C.

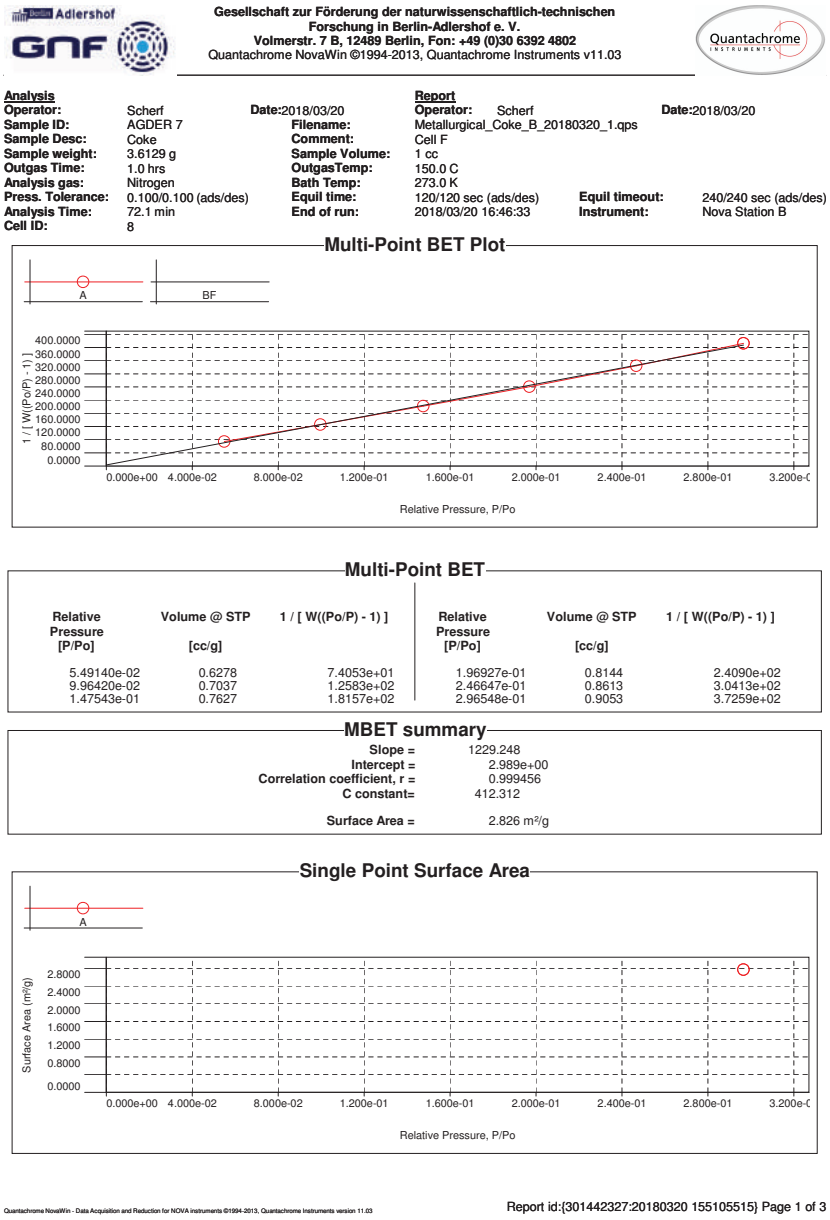

Figure S-21: N_2 adsorption measurements of metallurgical coke.

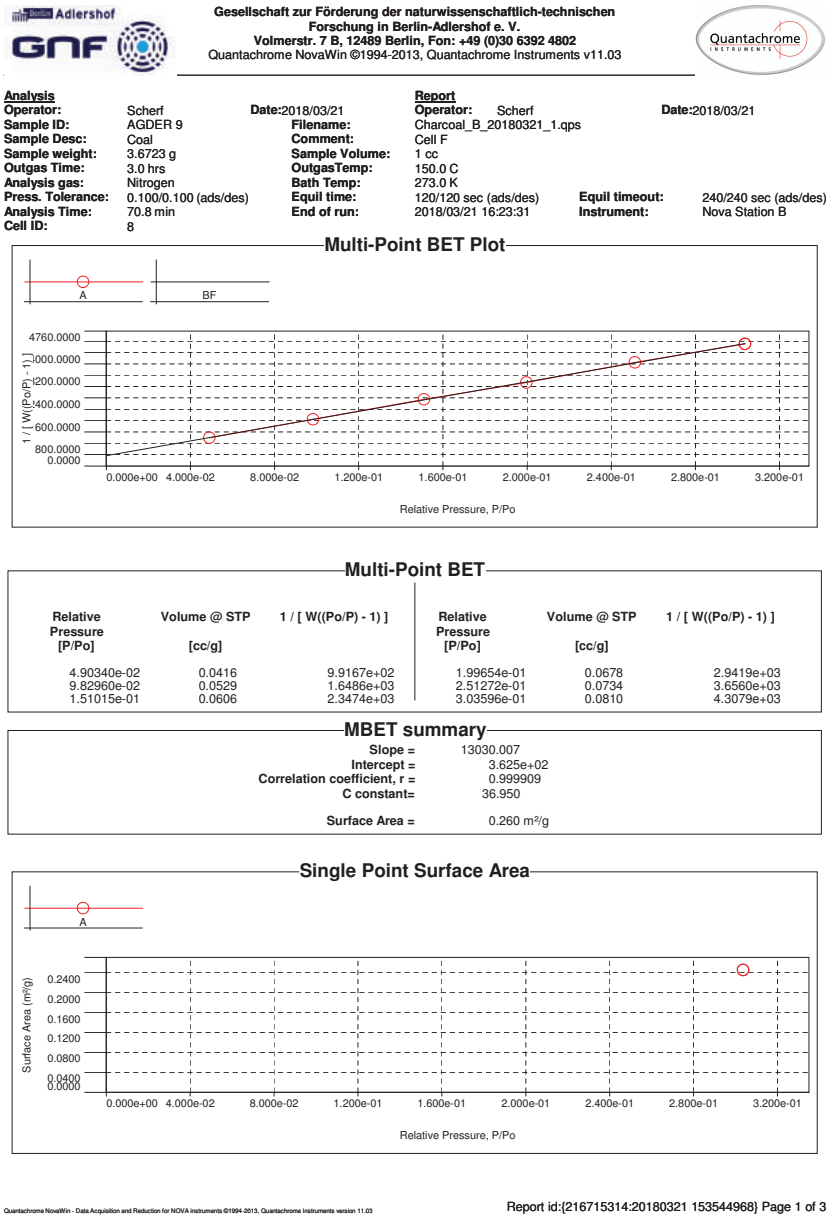

Figure S-22: N_2 adsorption measurements of activated charcoal.

S-5. Raman spectroscopy

S-5.1. Raman spectra processing

Table S-5: Raman spectroscopic data for Norway spruce and oak char samples related to the peak position, relative peak area and peak width (FWHM).

	Norway spruce char			Oak char		
	800°C	1200°C	1600°C	800°C	1200°C	1600°C
Peak position (cm^{-1})						
S_L	1071	1070	1072	1074	1074	1070
S	1197	1199	1198	1181	1199	1198
D_S	1274	1255	1275	1264	1252	1277
D	1340	1345	1340	1340	1340	1342
A_1	1432	1442	1410	1460	1434	1420
A_2	1550	1546	1550	1534	1535	1545
G_G	1570	1571	1571	1571	1570	1570
G_L	1594	1589	1602	1594	1588	1590
D'	1610	1610	1621	1614	1617	1620
Relative peak area						
S_L	0.09	0.05	0.14	0.3	0.13	0.1
S	1.6	2.1	0.5	1.6	0.8	0.8
D_S	1.3	0.8	0.7	1.5	0.2	1
D	3.9	6.8	3.9	5.1	3.5	4.7
A_1	2.2	1.6	3.4	3.1	0.9	2.4
A_2	3.3	4.4	1.3	1.2	2	1.4
G_G	0.6	0.2	1.4	1.1	0.3	1.3
G_L	1.6	3	2.1	2.1	1.6	2.7
D'	0.01	0.15	0.08	0.7	0.2	0.6
FWHM (cm^{-1})						
S_L	63.9	39.4	72.5	95.6	72.4	69.3
S	142.1	166.3	111.6	119.1	131.7	139.8
D_S	103.2	88.1	69.7	104.5	62.6	74.4
D	113.3	109.6	66.9	125.1	114.5	65.9
A_1	117.6	88.1	207.6	131.7	100.6	141.6
A_2	137.3	130.6	67.4	77.7	133.8	75.9
G_G	58.9	34.1	40.3	54.8	51.1	41.1
G_L	53.7	60.4	42.4	64.5	61.2	43.6
D'	23	28.8	16.7	80.7	38.5	31.7

Table S-6: Raman spectroscopic data for Norway spruce and oak char samples related to the integrated peak area ratios (A_{S_L}/A_{G_L} and A_D/A_{G_L}) and mean crystal size in the a-direction (L_a).

	Norway spruce char			Oak char		
	800°C	1200°C	1600°C	800°C	1200°C	1600°C
Integrated peak area ratios						
A_D/A_{G_L}	2.35	2.26	1.9	2.5	2.3	1.7
A_{S_L}/A_{G_L}	0.06	0.02	0.06	0.13	0.08	0.04
Mean crystal size in the a-direction						
L_a (Å)	1.9	1.9	2.3	1.7	1.9	2.6

S-6. Ash compositional analysis

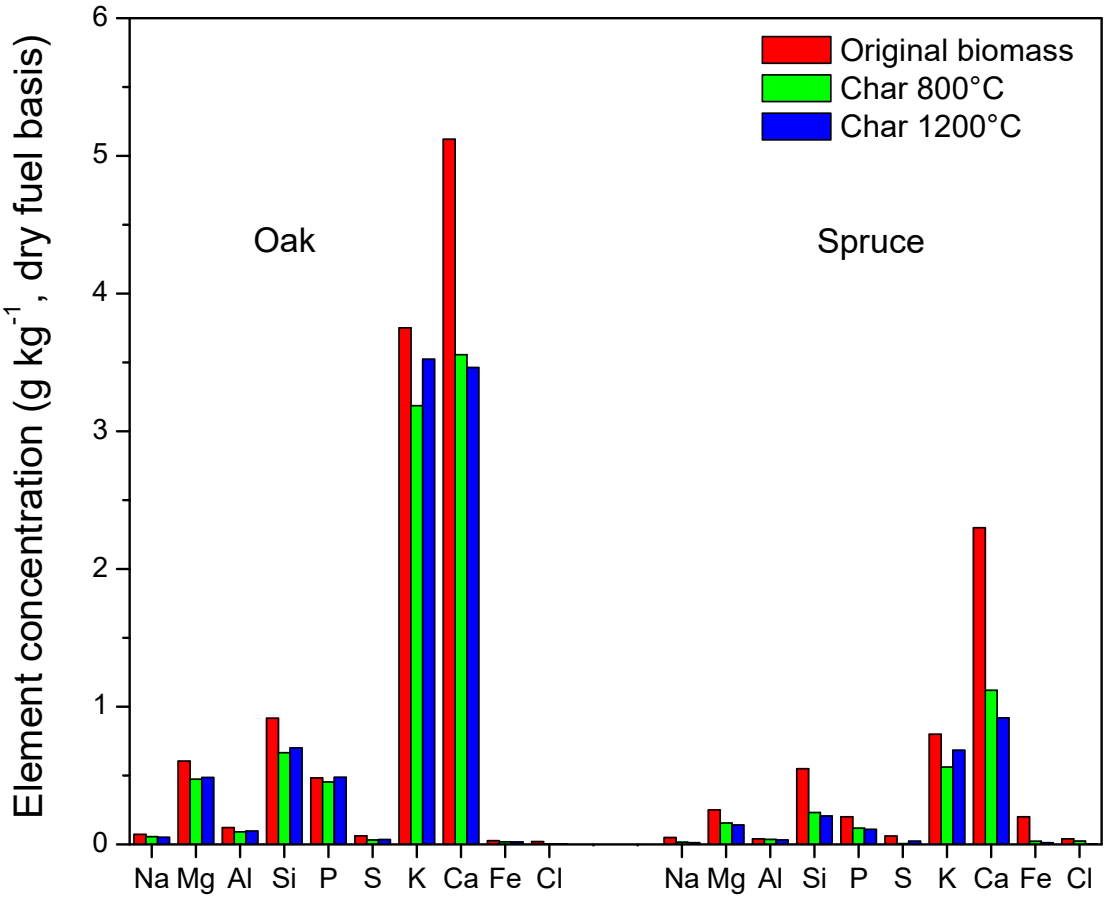

Figure S-23: Ash compositional analysis of original oak and spruce, and their chars from pyrolysis at 800 and 1200°C which is shown in g kg^{-1} on the dry ash basis of original biomass.

[1] Poling BE, Prausnitz JM, O'Connell J, The properties of Gases and Liquids, McGRAW-HILL, 2000.

[2] Seo DK, Lee SK, Kang MW, Hwang J, Yu TU, Gasification reactivity of biomass chars with CO_2, Biomass Bioenergy 34 (2010) 1946 – 53.

[3] Agirre I, Griessacher T, Rösler G, Antrekowitsch J, Production of charcoal as an alternative reducing agent from agricultural residues using a semi-continuous semi-pilot scale pyrolysis screw reactor, Fuel Process Tech 106 (2013) 114–21.

[4] Prigiobbe V, Polettini A, Baciocchi R, Gas–solid carbonation kinetics of Air Pollution Control residues for CO_2 storage, Chem Eng J 148 (2009) 270–8.

[5] Calo JM, Perkins MT, A heterogeneous surface model for the "steady-state" kinetics of the boudouard reaction, Carbon 25 (3) (1987) 395–407.

A.3 Supplemental materials article 3

The effect of feedstock origin and temperature on the structure and reactivity of char from pyrolysis at 1300-2800 °C

Contribution of the authors

Gerrit Ralf Surup planned the majority of the study, developed a reactor for the charcoal production and performed the pyrolysis experiments and manuscript writing.
Markus Heidelmann performed the TEM imaging of all char samples and contributed to the data processing using Gatan software and further description of the results in the manuscript.
Manuel Foppe supported with the experiments in a high-temperature furnace including gas measurements and data processing of experiments at University of Duisburg-Essen.
Daniel Schubert optimized the high-temperature furnace at University of Duisburg-Essen, calibrated all sensors and participated in the TEM microscopy data processing including Gatan software calibration.
Prof. Rüdiger Deike provided the financial support for the furnace construction, consulted the authors regarding the furnace use and experimental plan and also participated in the manuscript writing.
Anna Trubetskaya supported on the manuscript structuring, managed the correspondence among co-authors and did the manuscript proof-reading. She also performed TGA reactivity measurements >1100 °C.

The effect of feedstock origin and temperature on the structure and reactivity of char from pyrolysis at 1300-2800°C

Gerrit Ralf Surup[a], Manuel Foppe[b], Daniel Schubert[b], Rüdiger Deike[b], Markus Heidelmann[c], Michael T Timko[d], Anna Trubetskaya[e,*]

[a]*Department of Engineering Sciences, University of Agder, 4879 Grimstad, Norway*
[b]*Chair of Metallurgy for Iron and Steel Production, University of Duisburg-Essen, 47119 Duisburg, Germany*
[c]*Interdisciplinary Center for Analytics on the Nanoscale, University of Duisburg-Essen, 47057 Duisburg, Germany*
[d]*Chemical Engineering Department, Worcester Polytechnic Institute, 01609 Worcester, MA, USA*
[e]*Mechanical Engineering Department, National University of Ireland, H91TK33 Galway, Ireland*

*Corresponding author. anna.trubetskaya@nuigalway.ie

Preprint submitted to Fuel *July 14, 2018*

S-1. TEM analysis

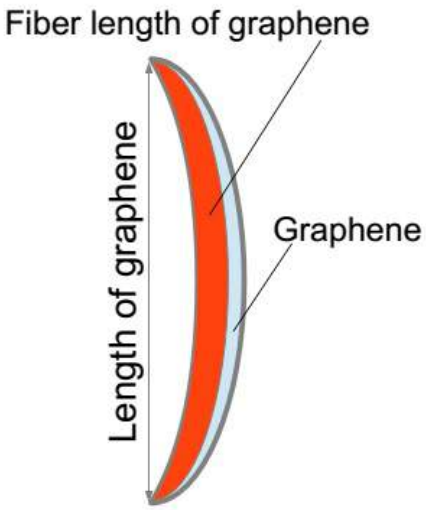

Figure S-1: Graphene fiber length and length used for the curvature calculation.

S-2. Char reactivity

S-2.1. Oxidation reactivity measurements

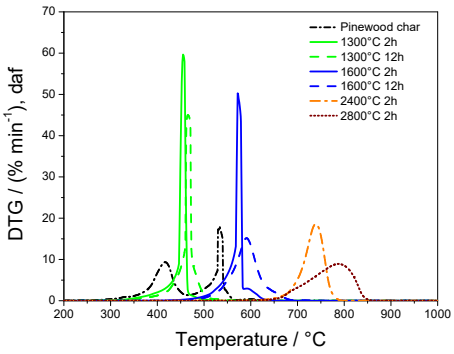

2(a): Pinewood char

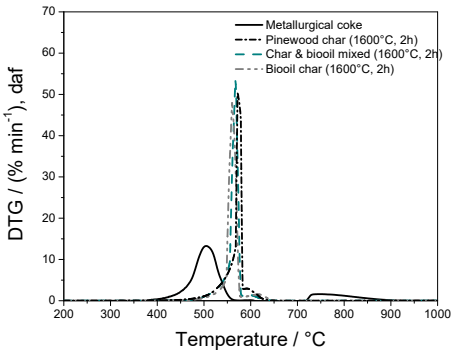

2(b): Reacted biooil with pinewood char

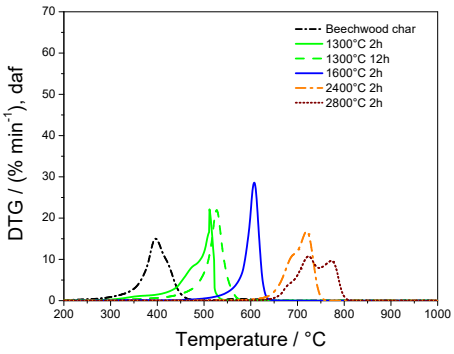

2(c): Beechwood char

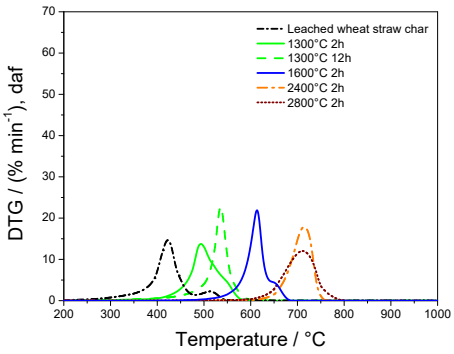

2(d): Leached wheat straw char

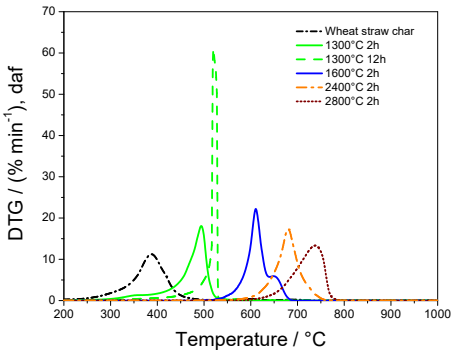

2(e): Wheat straw char

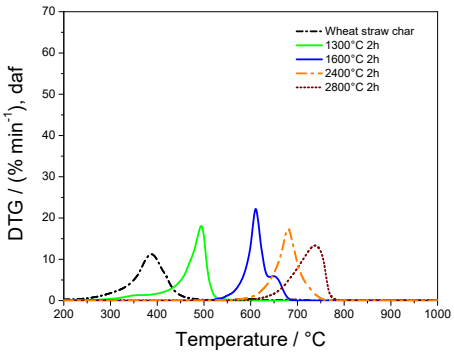

2(f): Alfalfa straw char

Figure S-2: (a),(c)-(f) DTG curves of pinewood, beechwood, leached wheat straw, wheat straw, alfalfa straw char from pyrolysis at 1300, 1600, 2400, and 2800°C for 2 and 12 h and (b) DTG curves of pinewood char, mixed pinewood char with biooil, reacted biooil from pyrolysis at 1600°C for 2 h and metallurgical coke and reacted in 5 % volume fraction O_2 + 95 % volume fraction N_2.

S-2.2. Arrhenius plot of O_2 and CO_2 reactivity

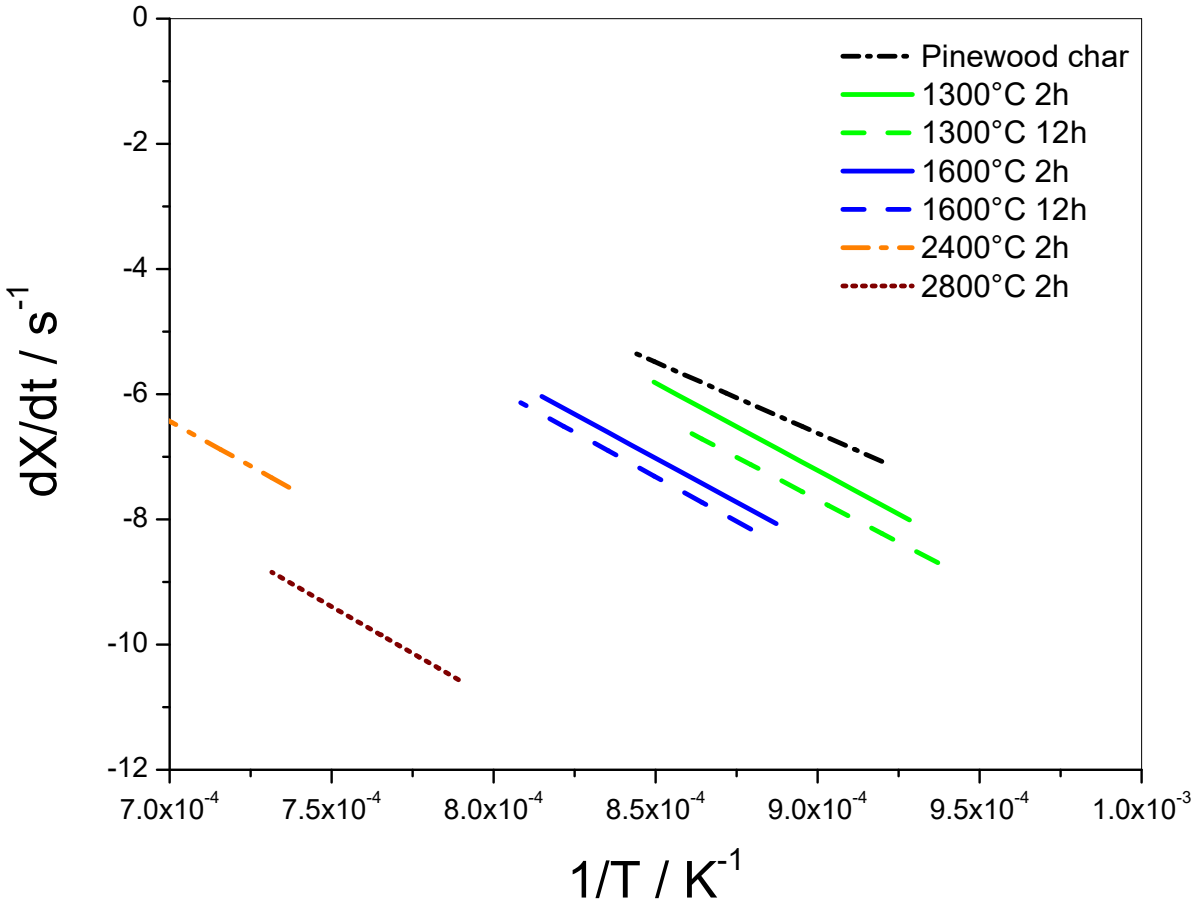

Figure S-3: Arrhenius plot of CO_2 reactivity of pinewood char reacted in 40 % volume fraction CO_2 + 60 % volume fraction N_2.

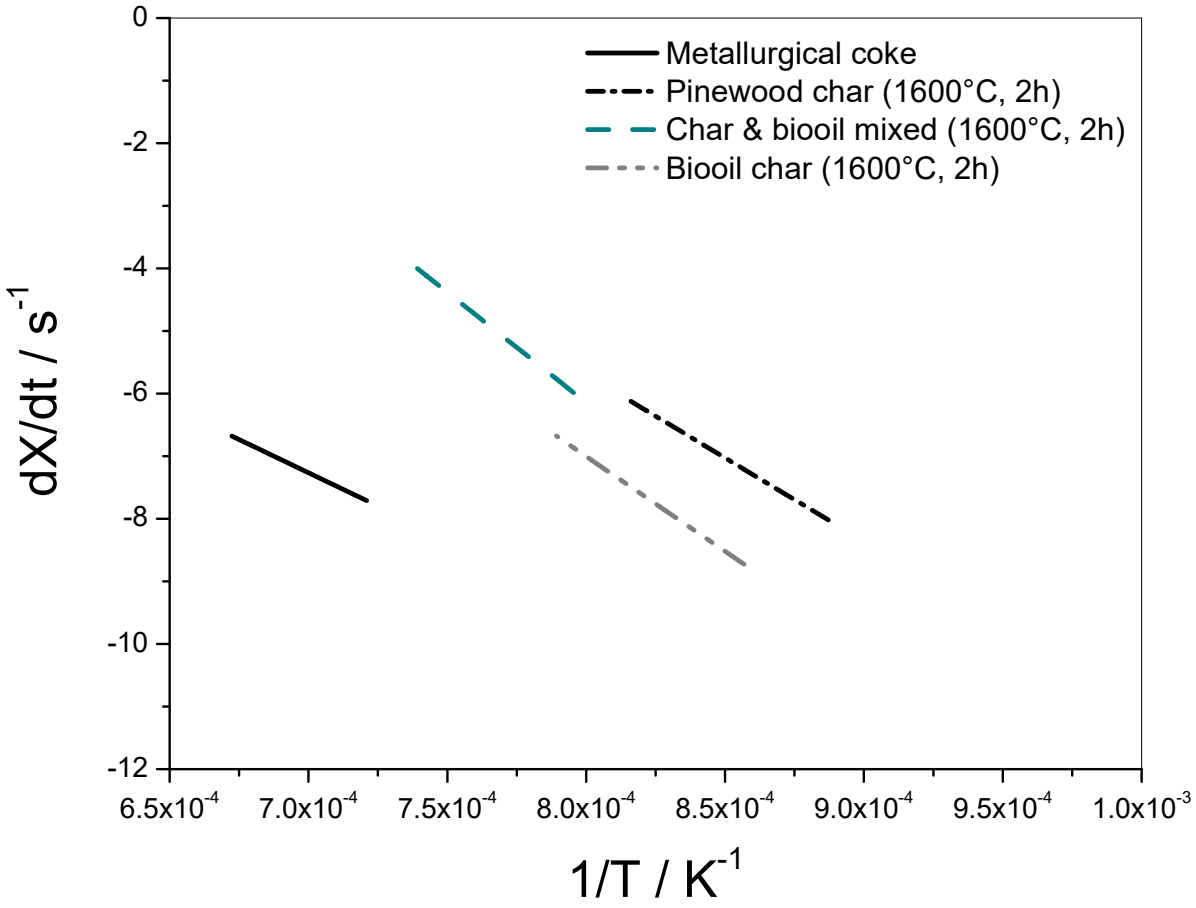

Figure S-4: Arrhenius plot of CO_2 reactivity of biooil char and mixed biooil with pinewood char reacted in 40 % volume fraction CO_2 + 60 % volume fraction N_2.

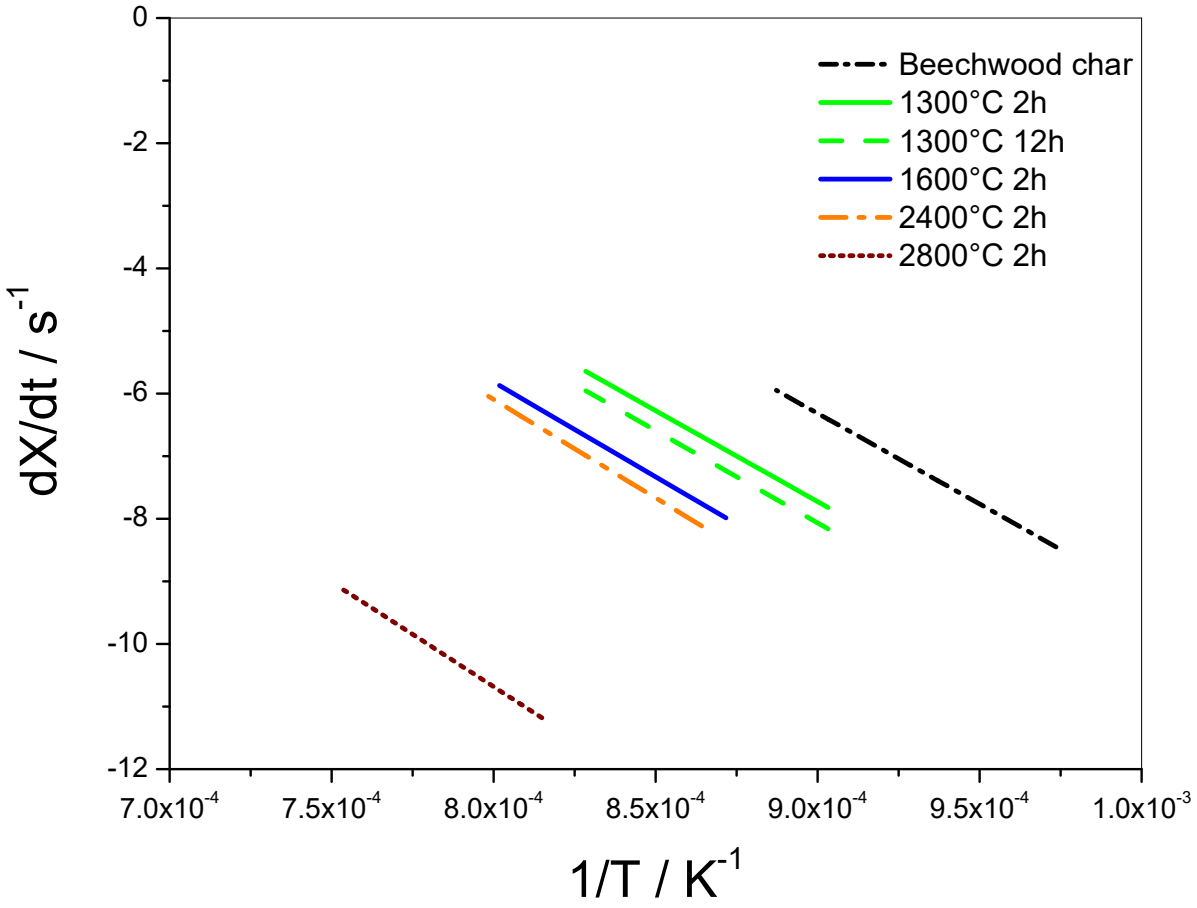

Figure S-5: Arrhenius plot of CO_2 reactivity of beechwood char reacted in 40 % volume fraction CO_2 + 60 % volume fraction N_2.

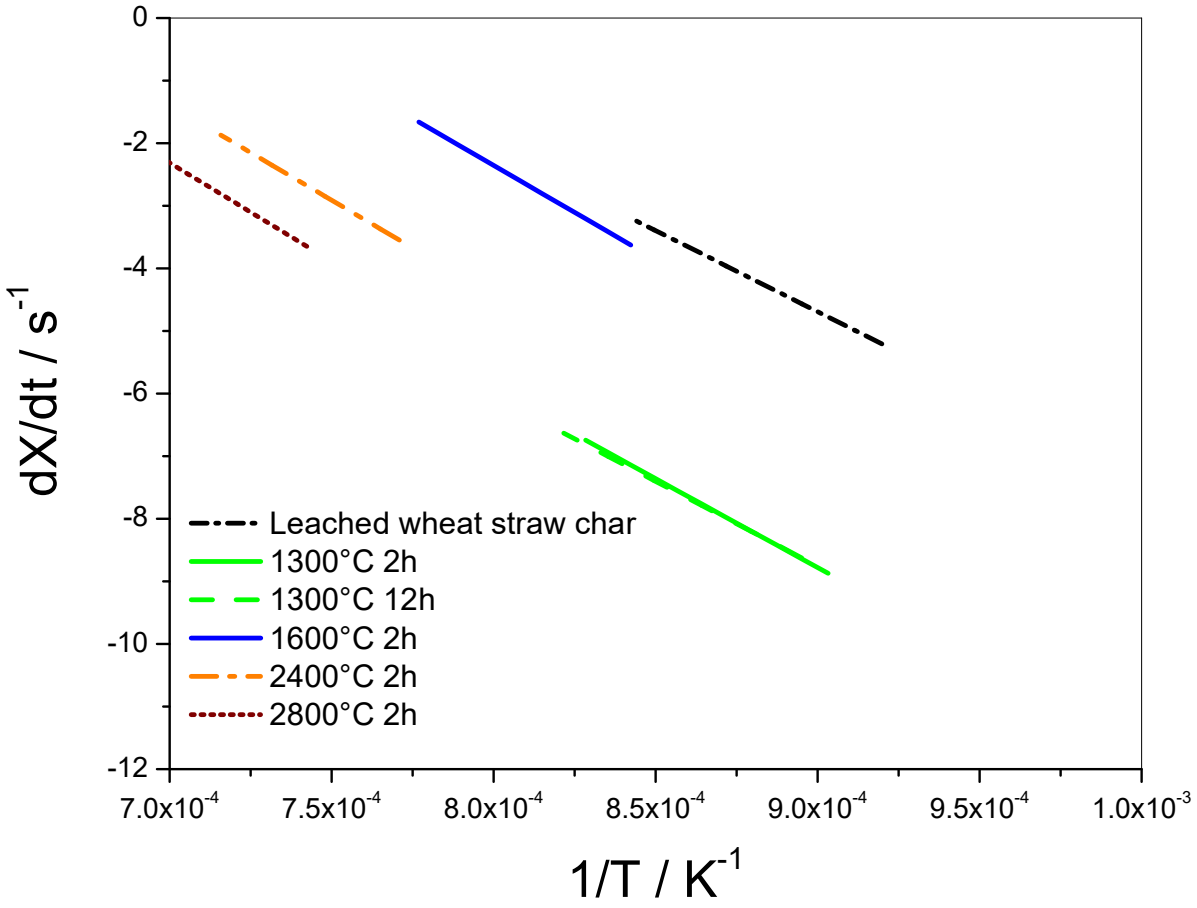

Figure S-6: Arrhenius plot of CO_2 reactivity of leached wheat straw char reacted in 40 % volume fraction CO_2 + 60 % volume fraction N_2.

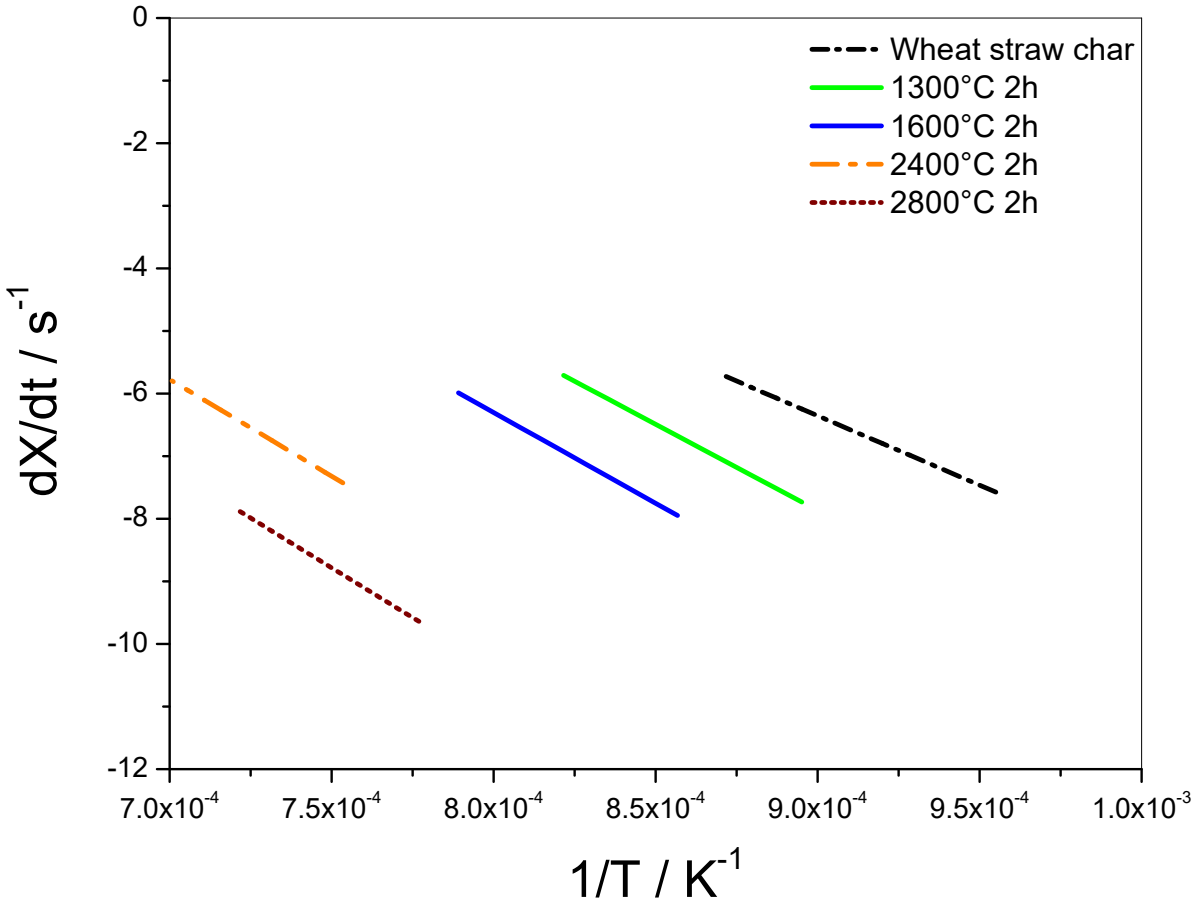

Figure S-7: Arrhenius plot of CO_2 reactivity of wheat straw char reacted in 40 % volume fraction CO_2 + 60 % volume fraction N_2.

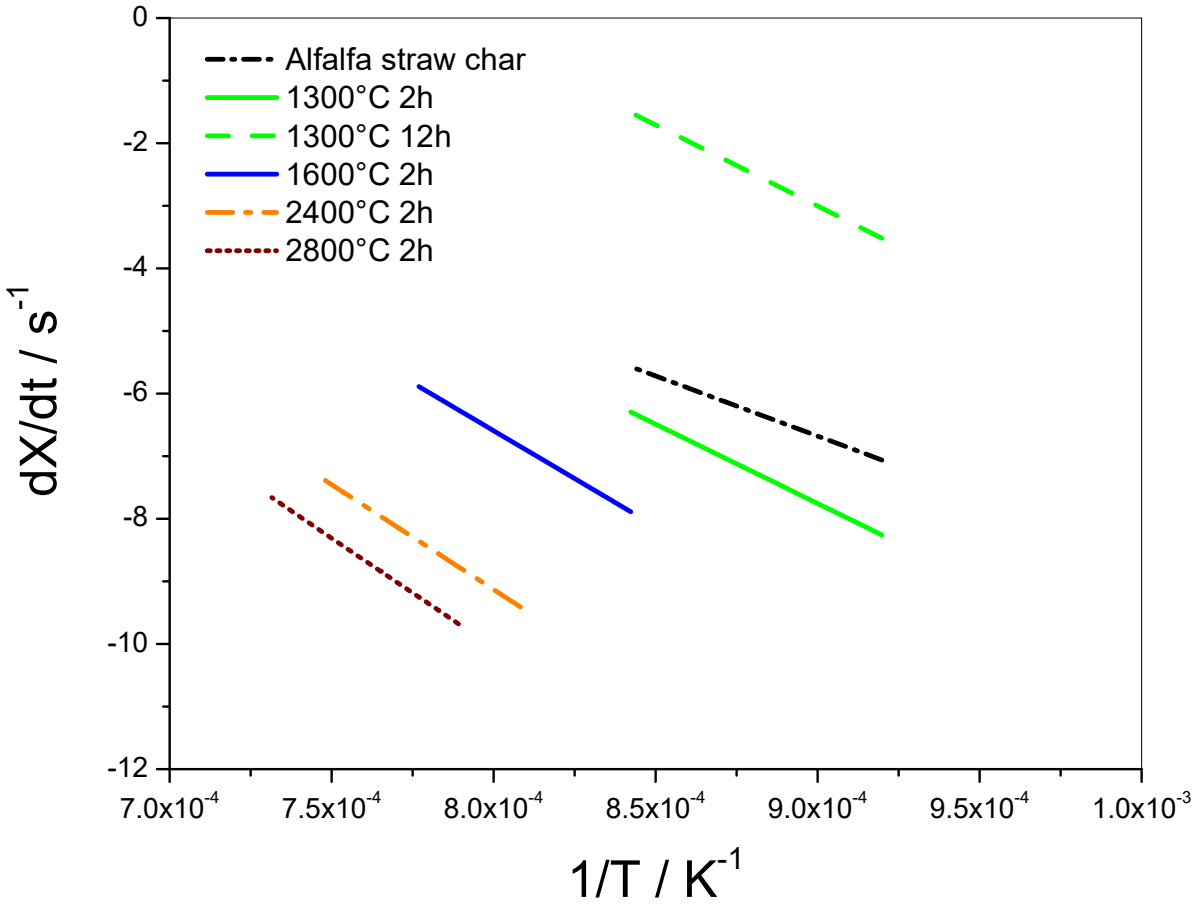

Figure S-8: Arrhenius plot of CO_2 reactivity of alfalfa straw char reacted in 40 % volume fraction CO_2 + 60 % volume fraction N_2.

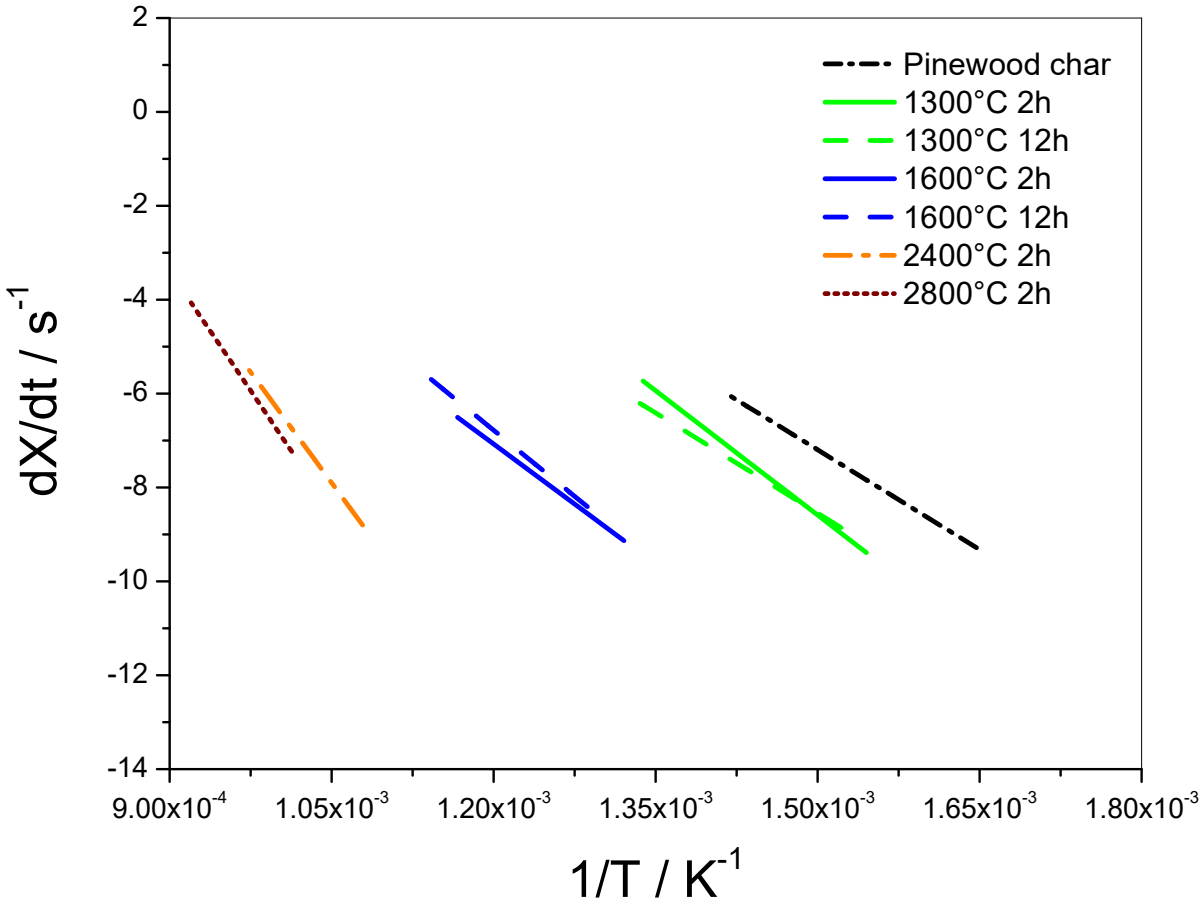

Figure S-9: Arrhenius plot of O_2 reactivity of pinewood char reacted in 5 % volume fraction O_2 + 95 % volume fraction N_2.

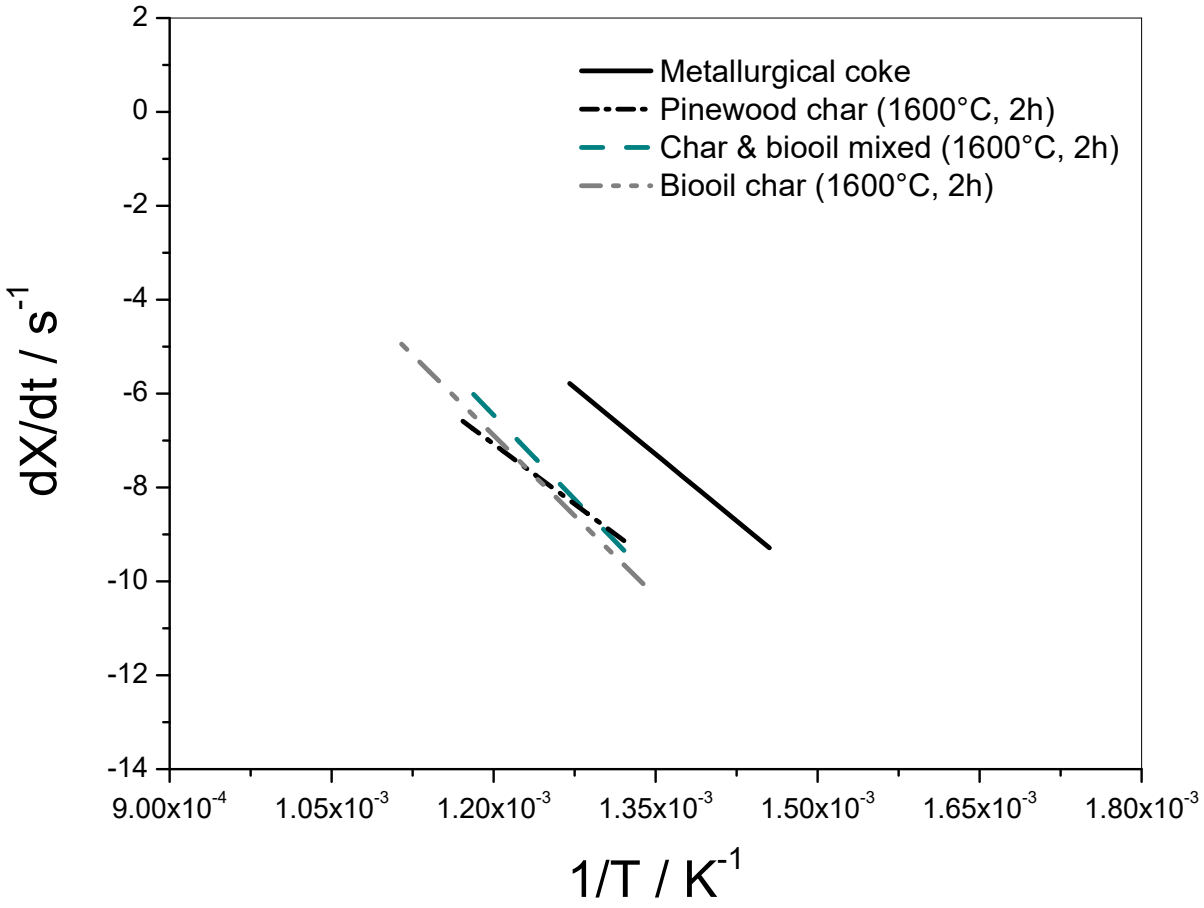

Figure S-10: Arrhenius plot of O_2 reactivity of biooil char and mixed biooil with pinewood char reacted in 5 % volume fraction O_2 + 95 % volume fraction N_2.

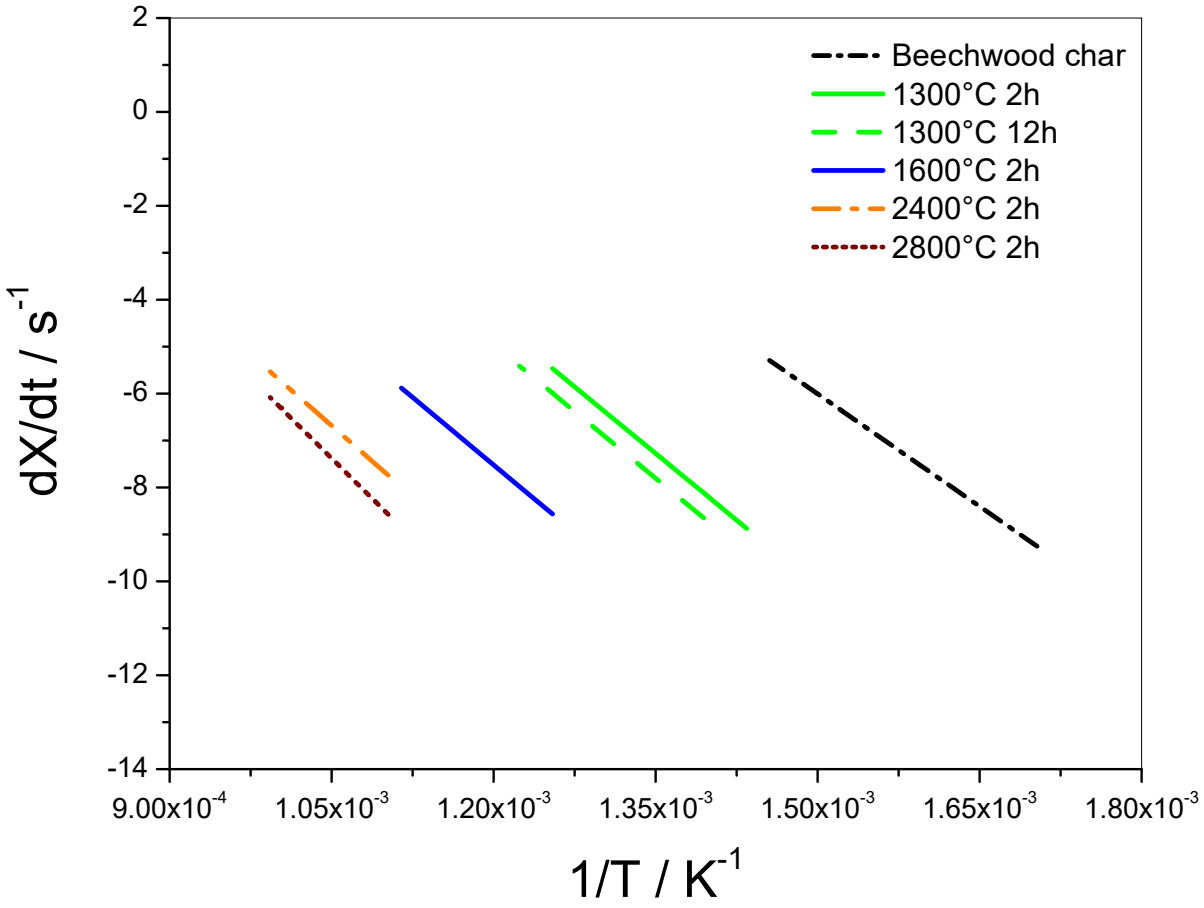

Figure S-11: Arrhenius plot of O_2 reactivity of beechwood char reacted in 5 % volume fraction O_2 + 95 % volume fraction N_2.

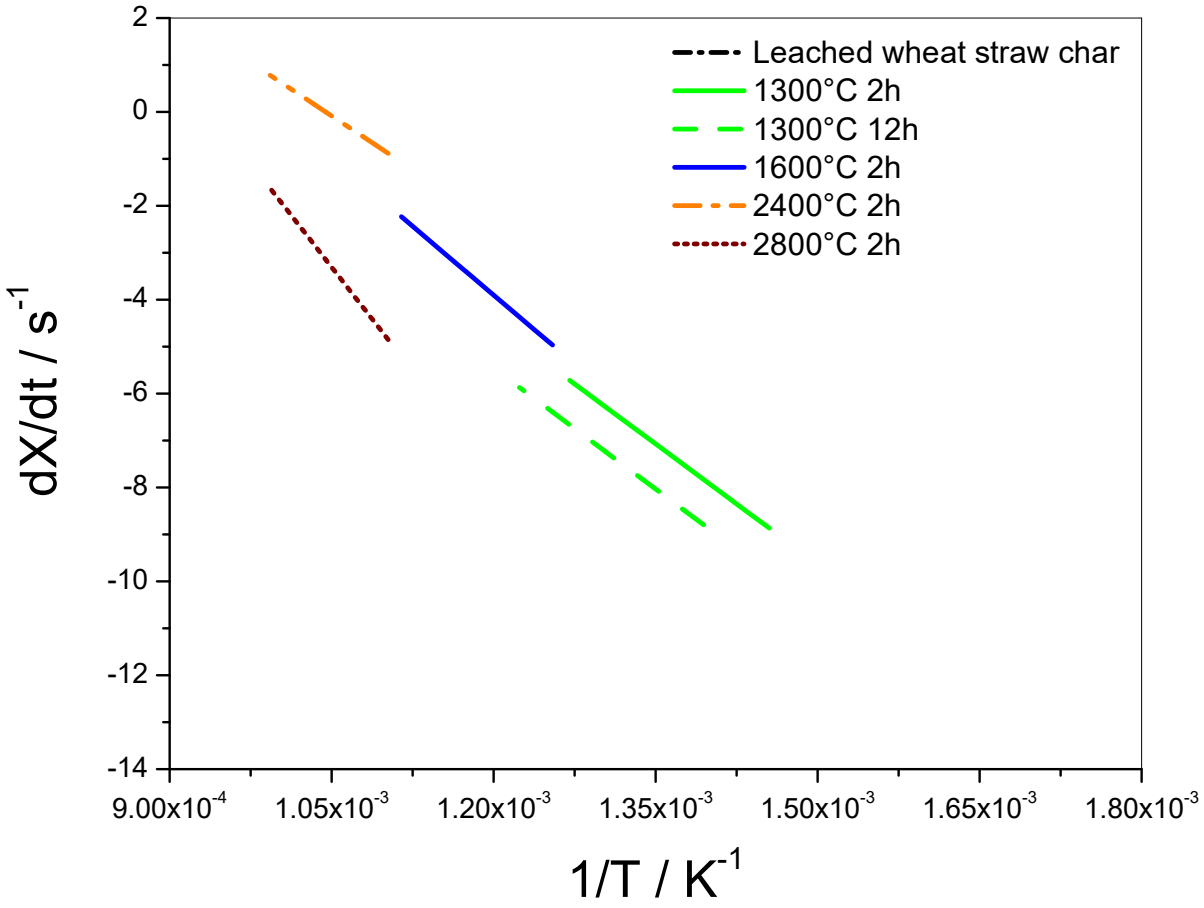

Figure S-12: Arrhenius plot of O_2 reactivity of leached wheat straw char reacted in 5 % volume fraction O_2 + 95 % volume fraction N_2.

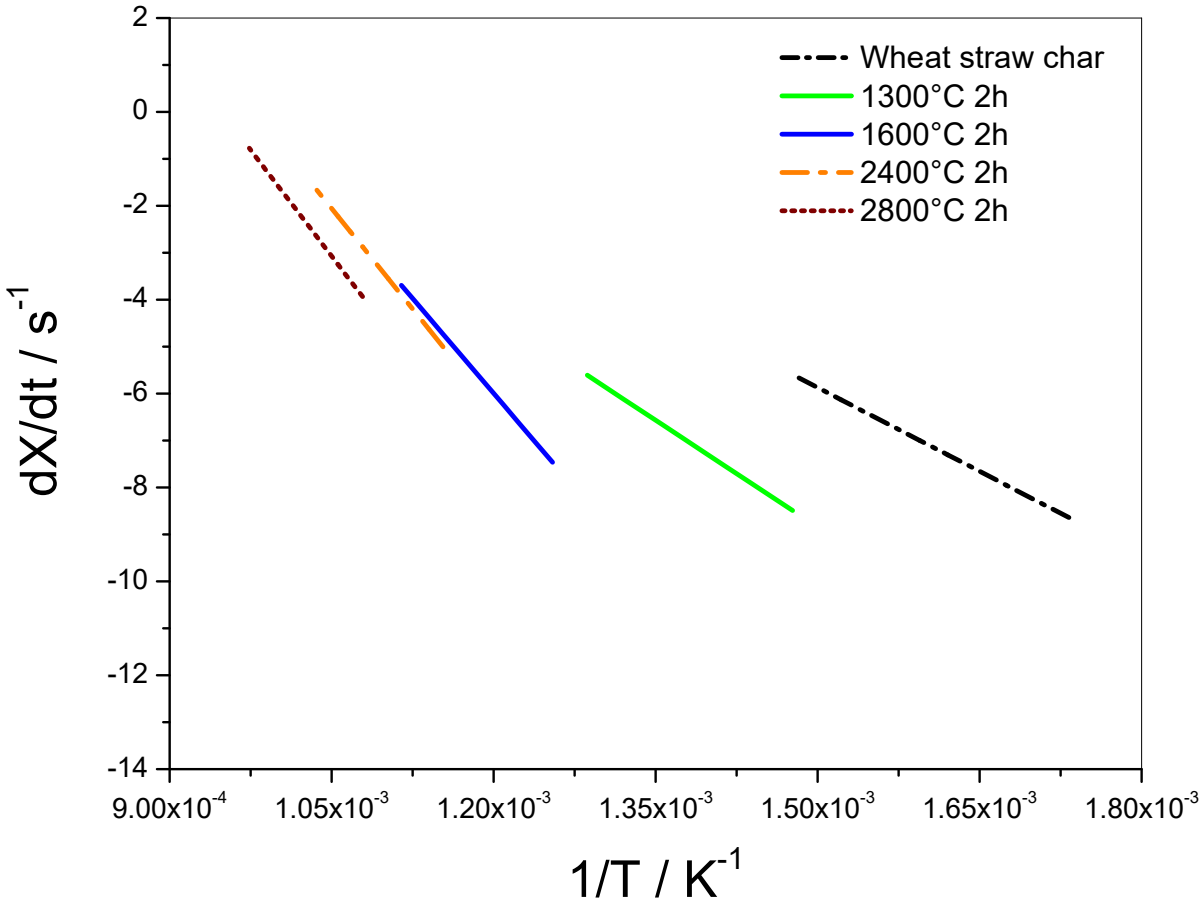

Figure S-13: Arrhenius plot of O_2 reactivity of wheat straw char reacted in 5 % volume fraction O_2 + 95 % volume fraction N_2.

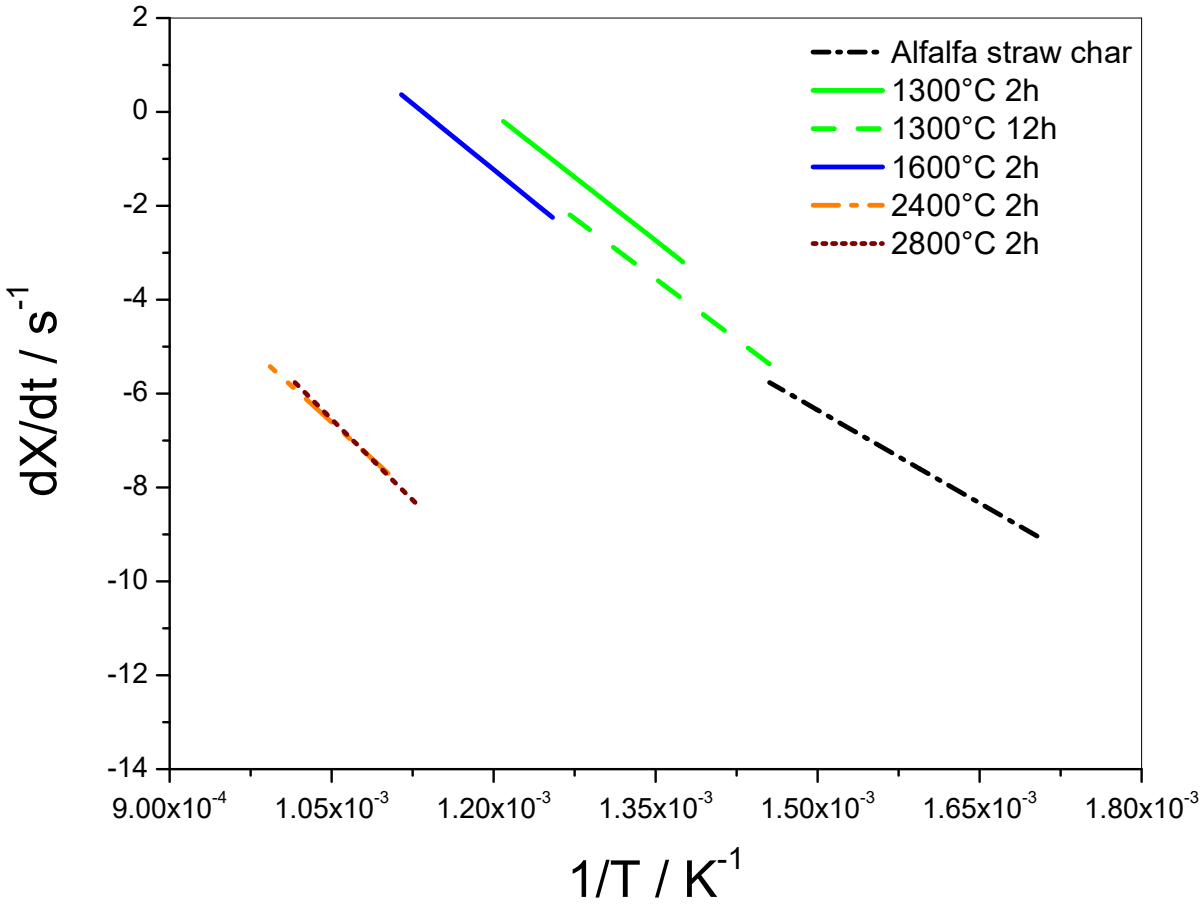

Figure S-14: Arrhenius plot of O_2 reactivity of alfalfa straw char reacted in 5 % volume fraction O_2 + 95 % volume fraction N_2.

Table S-1: Kinetic parameters for O_2 reactivity of pinewood chars, biooil char, and mixed biooil with pinewood char in 5 % volume fraction O_2 + 95 % volume fraction N_2.

E_a	A	r_{max} at 600°C
kJ mol^{-1}	s^{-1}	s^{-1}
Pinewood char		
Non-treated pinewood char		
118	$1.3{\cdot}10^{6}$	0.1
1300°C, 2 h		
147	$6{\cdot}10^{7}$	0.1
1300°C, 12 h		
118	$3.6{\cdot}10^{5}$	$3{\cdot}10^{-2}$
1600°C, 2 h		
142	$7{\cdot}10^{5}$	$2{\cdot}10^{-3}$
1600°C, 12 h		
155	$6.6{\cdot}10^{6}$	$3{\cdot}10^{-3}$
2400°C, 2 h		
261	$8{\cdot}10^{10}$	$2{\cdot}10^{-5}$
2800°C, 2 h		
282	$7{\cdot}10^{11}$	$8{\cdot}10^{-6}$
Biooil char (1600°C, 2 h)		
198	$4{\cdot}10^{9}$	$6{\cdot}10^{-3}$
Mixed biooil with pinewood char (1600°C, 2 h)		
191	$9{\cdot}10^{8}$	$4{\cdot}10^{-3}$
Metallurical coke		
157	$9{\cdot}10^{7}$	$3{\cdot}10^{-2}$

Table S-2: Kinetic parameters for O_2 reactivity of beechwood and alfalfa straw chars in 5 % volume fraction O_2 + 95 % volume fraction N_2.

E_a	A	r_{max} at 600°C
kJ mol^{-1}	s^{-1}	s^{-1}
Beechwood char		
Non-treated beechwood char		
133	$6.4 \cdot 10^7$	0.7
1300°C, 2 h		
157	$9 \cdot 10^7$	$3 \cdot 10^{-2}$
1300°C, 12 h		
158	$6 \cdot 10^7$	$2 \cdot 10^{-2}$
1600°C, 2 h		
160	$6 \cdot 10^6$	$2 \cdot 10^{-3}$
2400°C, 2 h		
168	$2 \cdot 10^6$	$2 \cdot 10^{-4}$
2800°C, 2 h		
190	$2 \cdot 10^7$	$7 \cdot 10^{-5}$
Alfalfa straw char		
Non-treated alfalfa straw char		
110	$7 \cdot 10^5$	0.2
1300°C, 2 h		
143	$3.4 \cdot 10^8$	1
1300°C, 12 h		
150	$8.7 \cdot 10^8$	1
1600°C, 2 h		
156	$2 \cdot 10^9$	1
2400°C, 2 h		
173	$4.2 \cdot 10^6$	$2 \cdot 10^{-4}$
2800°C, 2 h		
191	$4.3 \cdot 10^7$	$2 \cdot 10^{-4}$

Table S-3: Kinetic parameters for O_2 reactivity of leached wheat straw and wheat straw chars in 5 % volume fraction O_2 + 95 % volume fraction N_2.

E_a	A	r_{max} at 600°C
kJ mol^{-1}	s^{-1}	s^{-1}
Leached wheat straw char		
Non-treated leached wheat straw char		
126	$8{\cdot}10^{6}$	0.2
1300°C, 2 h		
142	$8{\cdot}10^{6}$	$3{\cdot}10^{-2}$
1300°C, 12 h		
143	$8.4{\cdot}10^{6}$	$2.4{\cdot}10^{-2}$
1600°C, 2 h		
163	$1.1{\cdot}10^{8}$	$2.2{\cdot}10^{-2}$
2400°C, 2 h		
246	$1{\cdot}10^{12}$	$2.2{\cdot}10^{-3}$
2800°C, 2 h		
258	$5{\cdot}10^{12}$	$2{\cdot}10^{-3}$
Wheat straw char		
Non-treated wheat straw char		
99	$1.6{\cdot}10^{5}$	0.2
1300°C, 2 h		
126	$1{\cdot}10^{6}$	$3{\cdot}10^{-2}$
1600°C, 2 h		
224	$2.8{\cdot}10^{11}$	$1{\cdot}10^{-2}$
2400°C, 2 h		
237	$1.3{\cdot}10^{12}$	$1{\cdot}10^{-2}$
2800°C, 2 h		
251	$3{\cdot}10^{12}$	$3{\cdot}10^{-3}$

Table S-4: Kinetic parameters for CO_2 reactivity of pinewood chars, biooil char, and mixed biooil with pinewood char in 40 % volume fraction CO_2 + 60 % volume fraction N_2.

E_a	A	r_{max} at 1000°C
kJ mol^{-1}	s^{-1}	s^{-1}
Pinewood char		
Non-treated pinewood char		
189	$1{\cdot}10^{6}$	$1.7{\cdot}10^{-2}$
1300°C, 2 h		
232	$6{\cdot}10^{7}$	$1.8{\cdot}10^{-2}$
1300°C, 12 h		
226	$2{\cdot}10^{7}$	$1{\cdot}10^{-1}$
1600°C, 2 h		
233	$2{\cdot}10^{7}$	$5.5{\cdot}10^{-3}$
1600°C, 12 h		
237	$2{\cdot}10^{7}$	$4.2{\cdot}10^{-3}$
2400°C, 2 h		
238	$8.3{\cdot}10^{5}$	$1{\cdot}10^{-4}$
2800°C, 2 h		
248	$4.3{\cdot}10^{5}$	$2.9{\cdot}10^{-5}$
Biooil char (1600°C, 2 h)		
242	$2.1{\cdot}10^{7}$	$2.5{\cdot}10^{-3}$
Mixed biooil with pinewood char (1600°C, 2 h)		
252	$3.2{\cdot}10^{7}$	$1.4{\cdot}10^{-3}$
Metallurical coke		
224	$1.4{\cdot}10^{5}$	$9.3{\cdot}10^{-5}$

Table S-5: Kinetic parameters for CO_2 reactivity of beechwood and alfalfa straw chars in 40 % volume fraction CO_2 + 60 % volume fraction N_2.

E_a	A	r_{max} at 1000°C
kJ mol^{-1}	s^{-1}	s^{-1}
Beechwood char		
Non-treated beechwood char		
241	$3.8{\cdot}10^{8}$	$5{\cdot}10^{-2}$
1300°C, 2 h		
242	$1{\cdot}10^{8}$	$1.2{\cdot}10^{-2}$
1300°C, 12 h		
246	$1.1{\cdot}10^{8}$	$9{\cdot}10^{-3}$
1600°C, 2 h		
251	$9.6{\cdot}10^{7}$	$4.6{\cdot}10^{-3}$
2400°C, 2 h		
262	$9.6{\cdot}10^{6}$	$1.8{\cdot}10^{-4}$
2800°C, 2 h		
278	$9.3{\cdot}10^{6}$	$3.7{\cdot}10^{-5}$
Alfalfa straw char		
Non-treated alfalfa straw char		
160	$4.2{\cdot}10^{4}$	$1.1{\cdot}10^{-2}$
1300°C, 2 h		
211	$3.4{\cdot}10^{6}$	$7.8{\cdot}10^{-3}$
1300°C, 12 h		
216	$3.4{\cdot}10^{6}$	$4.8{\cdot}10^{-3}$
1600°C, 2 h		
254	$5{\cdot}10^{7}$	$6.4{\cdot}10^{-4}$
2400°C, 2 h		
279	$4.9{\cdot}10^{7}$	$1.8{\cdot}10^{-4}$
2800°C, 2 h		
291	$6.1{\cdot}10^{7}$	$7.1{\cdot}10^{-5}$

Table S-6: Kinetic parameters for CO_2 reactivity of leached wheat straw and wheat straw chars in 40 % volume fraction CO_2 + 60 % volume fraction N_2.

E_a	A	r_{max} at 1000°C
kJ mol^{-1}	s^{-1}	s^{-1}
Leached wheat straw char		
Non-treated leached wheat straw char		
215	$1.3{\cdot}10^{8}$	0.2
1300°C, 2 h		
236	$1.9{\cdot}10^{7}$	$4{\cdot}10^{-3}$
1300°C, 12 h		
226	$6.4{\cdot}10^{6}$	$3.5{\cdot}10^{-3}$
1600°C, 2 h		
249	$4.6{\cdot}10^{7}$	$2.7{\cdot}10^{-3}$
2400°C, 2 h		
253	$1.2{\cdot}10^{6}$	$5.2{\cdot}10^{-5}$
2800°C, 2 h		
262	$2.6{\cdot}10^{6}$	$4.5{\cdot}10^{-5}$
Wheat straw char		
Non-treated wheat straw char		
184	$8.1{\cdot}10^{5}$	$2.2{\cdot}10^{-2}$
1300°C, 2 h		
229	$2.2{\cdot}10^{7}$	$9{\cdot}10^{-3}$
1600°C, 2 h		
241	$5.3{\cdot}10^{7}$	$7.6{\cdot}10^{-3}$
2400°C, 2 h		
257	$8{\cdot}10^{6}$	$2.2{\cdot}10^{-4}$
2800°C, 2 h		
265	$3.5{\cdot}10^{6}$	$5{\cdot}10^{-5}$

S-3. Raman spectroscopy

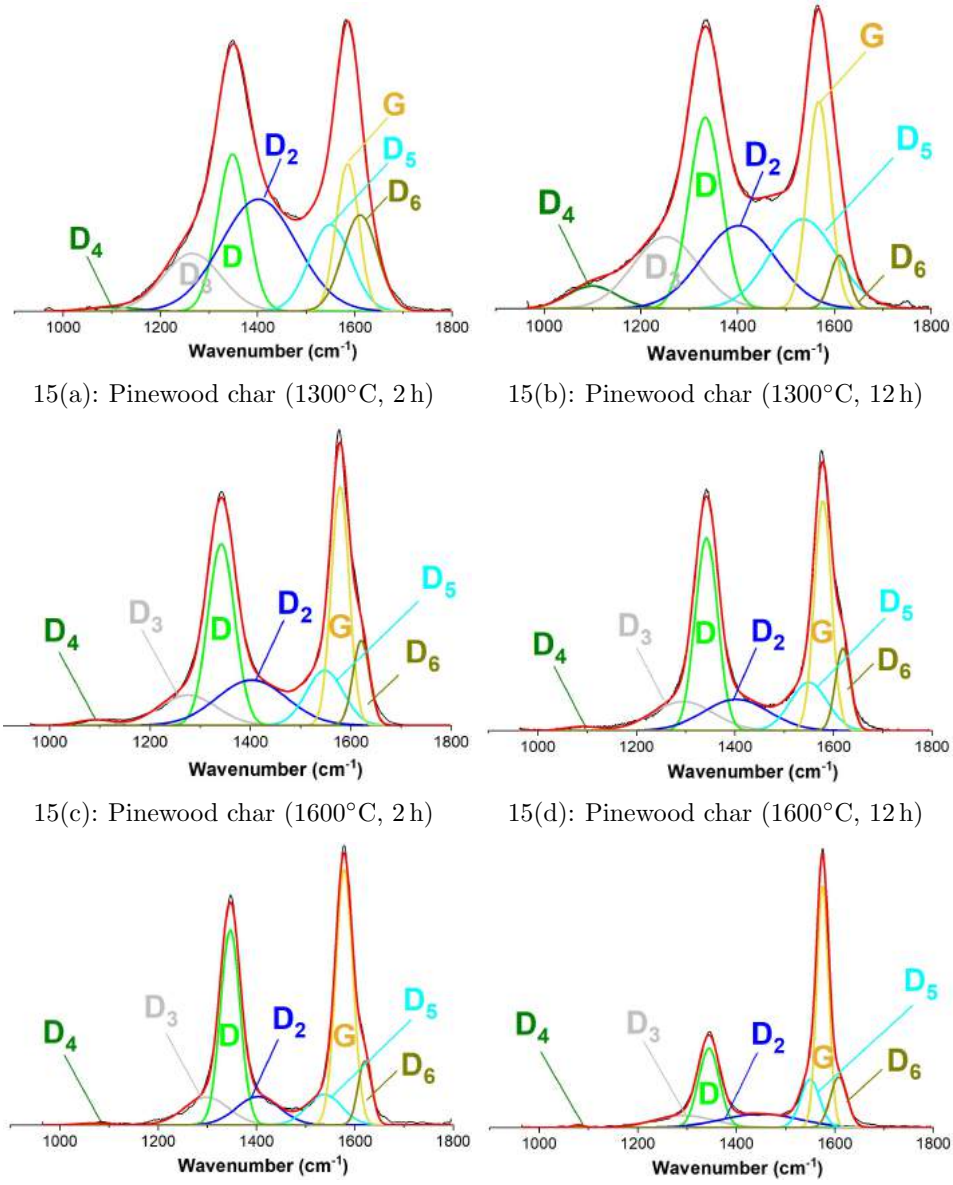

15(a): Pinewood char (1300°C, 2 h)

15(b): Pinewood char (1300°C, 12 h)

15(c): Pinewood char (1600°C, 2 h)

15(d): Pinewood char (1600°C, 12 h)

15(e): Pinewood char (2400°C, 2 h)

15(f): Pinewood char (2800°C, 2 h)

Figure S-15: Deconvolution of Raman spectrum of pinewood chars from pyrolysis at 1300 and 1600 for 2 and 12 h, and at 2400 and 2800°C for 2 h.

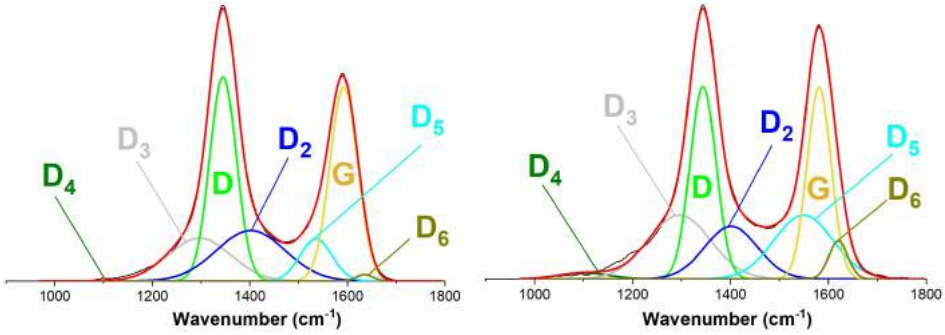

16(a): Biooil char

16(b): Mixed biooil and pinewood char

Figure S-16: Deconvolution of Raman spectrum of biooil char and reacted mixture of biooil and char from pyrolysis at 1600°C for 2 h.

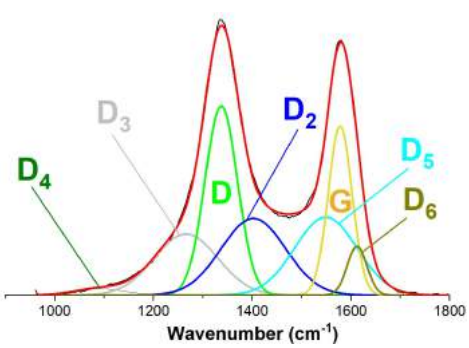

17(a): Beechwood char (1300°C, 2 h)

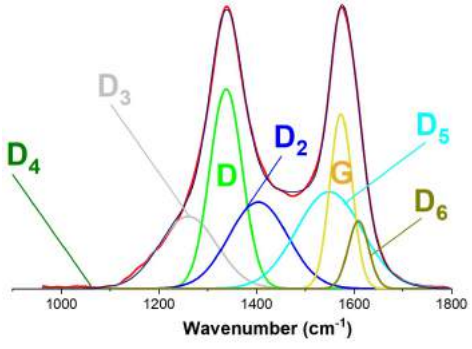

17(b): Beechwood char (1300°C, 12 h)

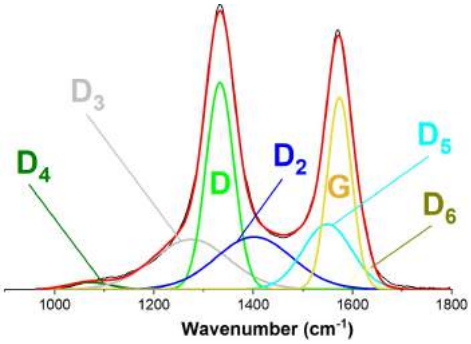

17(c): Beechwood char (1600°C, 2 h)

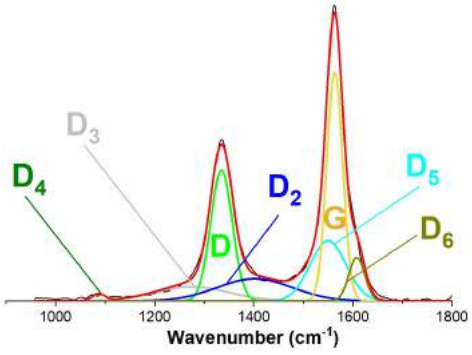

17(d): Beechwood char (2400°C, 2 h)

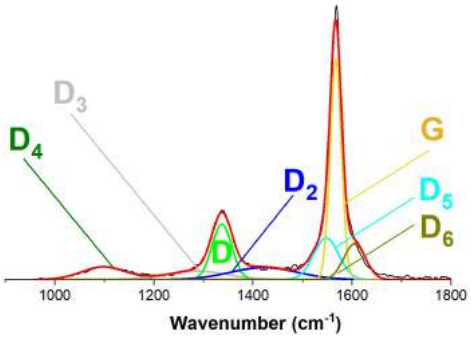

17(e): Beechwood char (2800°C, 2 h)

Figure S-17: Deconvolution of Raman spectrum of beechwood chars from pyrolysis at 1300°C for 2 and 12 h, and at 1600, 2400 and 2800°C for 2 h.

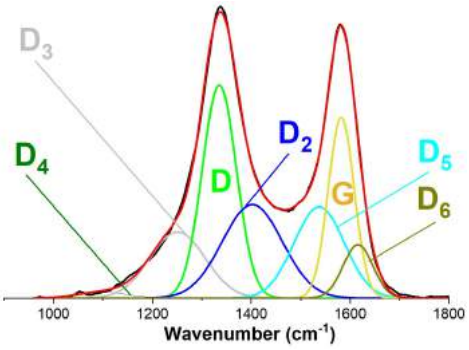

18(a): Leached wheat straw char (1300°C, 2 h)

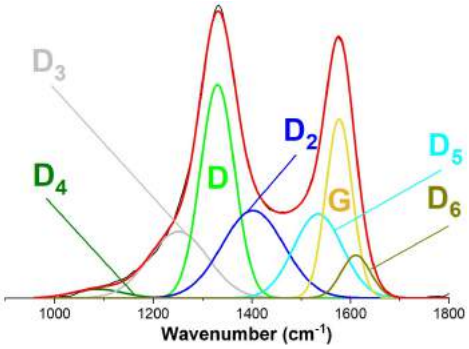

18(b): Leached wheat straw char (1300°C, 12 h)

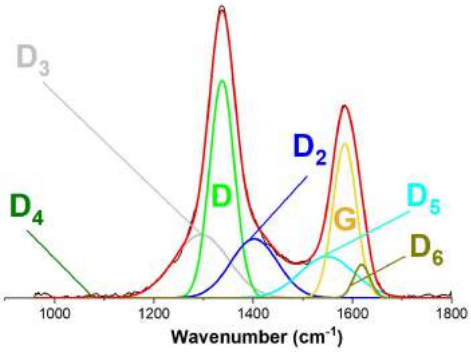

18(c): Leached wheat straw char (1600°C, 2 h)

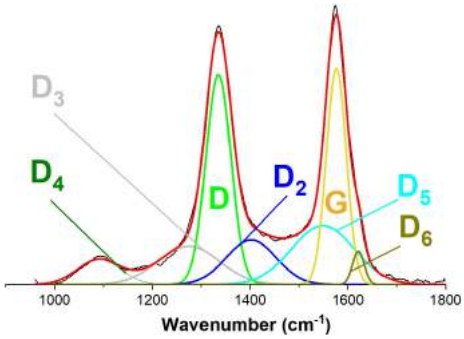

18(d): Leached wheat straw char (1600°C, 12 h)

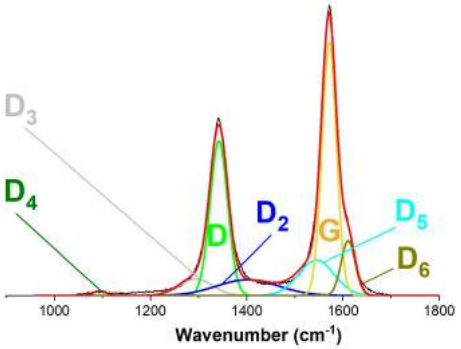

18(e): Leached wheat straw char (2400°C, 2 h)

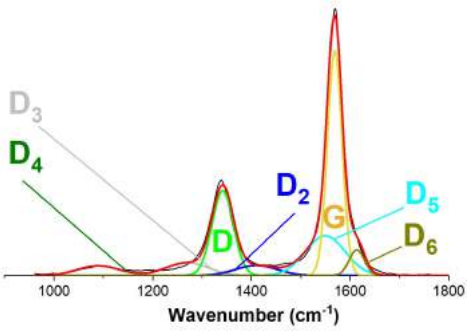

18(f): Leached wheat straw char (2800°C, 2 h)

Figure S-18: Deconvolution of Raman spectrum of leached wheat straw chars from pyrolysis at 1300 and 1600°C for 2 and 12 h, and at 2400 and 2800°C for 2 h.

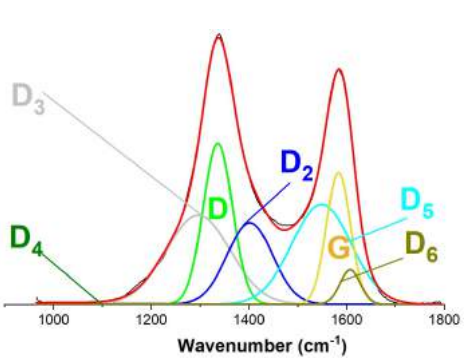

19(a): Wheat straw char (1300°C, 2 h)

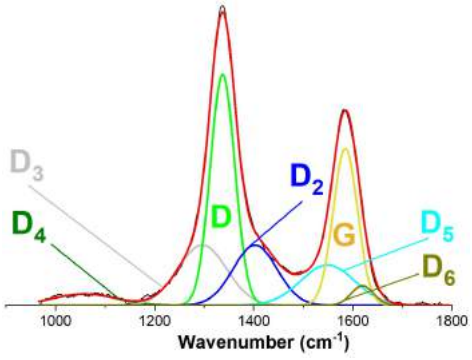

19(b): Wheat straw char (1600°C, 2 h)

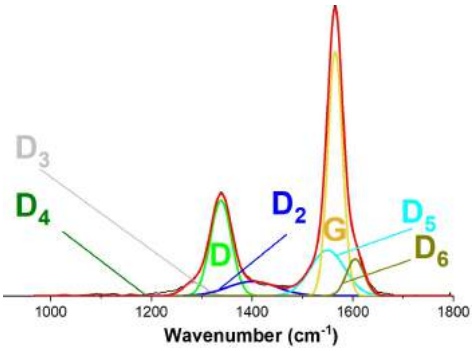

19(c): Wheat straw char (2400°C, 2 h)

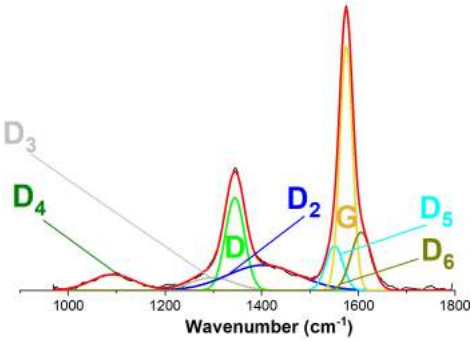

19(d): Wheat straw char (2800°C, 2 h)

Figure S-19: Deconvolution of Raman spectrum of wheat straw chars from pyrolysis at 1300 and 1600°C for 2 and 12 h, and at 2400 and 2800°C for 2 h.

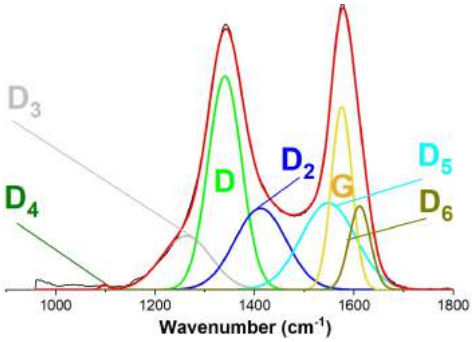

20(a): Alflafa straw char (1300°C, 2 h)

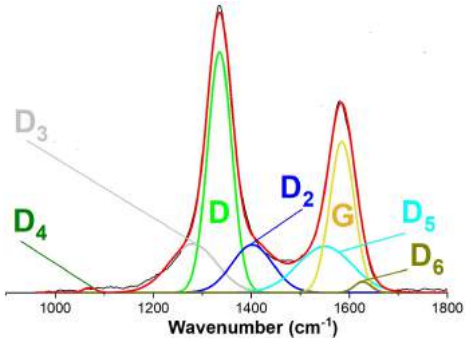

20(b): Alfalfa straw char (1300°C, 12 h)

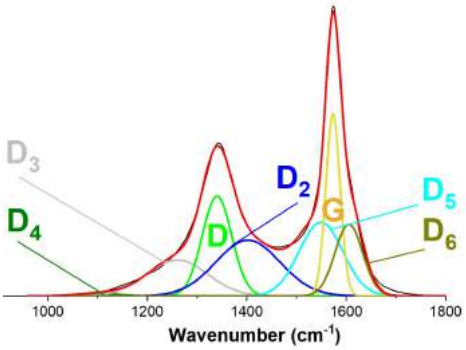

20(c): Alfalfa straw char (1600°C, 2 h)

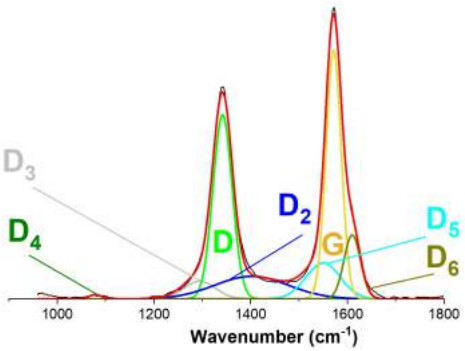

20(d): Alfalfa straw char (2400°C, 2 h)

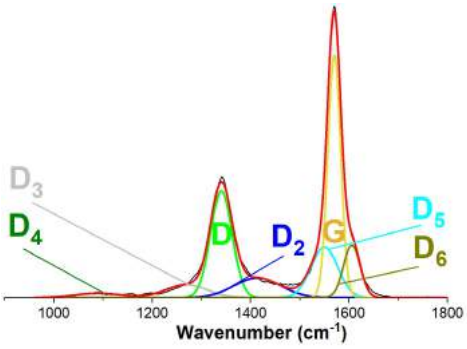

20(e): Alfalfa straw char (2800°C, 2 h)

Figure S-20: Deconvolution of Raman spectrum of alfalfa straw chars from pyrolysis at 1300°C for 2 and 12 h, and at 1600, 2400 and 2800°C for 2 h.

S-3.1. Raman spectra processing

Table S-7: Raman spectroscopic data for pinewood char samples related to the peak position, relative peak area, peak width (FWHM), integrated peak area ratio (A_D/A_G) and mean crystal size in the a-direction (L_a).

	1300°C, 2 h	1300°C, 12 h	1600°C, 2 h	1600°C, 12 h	2400°C, 2 h	2800°C, 2 h
Peak position (cm^{-1})						
D_4	1099	1099	1090	1090	1070	1079
D_3	1266	1252	1275	1295	1298	1295
D	1349	1333	1342	1342	1347	1345
D_2	1402	1402	1402	1403	1404	1450
D_5	1549	1535	1548	1550	1538	1550
G	1585	1568	1579	1578	1578	1575
D_6	1611	1610	1621	1619	1620	1608
Relative peak area						
D_4	0.2	0.9	0.2	0.2	0.1	0.1
D_3	2.7	3.7	1.8	2.1	1.6	1.2
D	3.9	4.8	5.2	5.1	4.9	2.9
D_2	6.9	4.8	3.4	2.4	1.6	1.8
D_5	2.9	4.6	2.2	2.1	1.4	1.6
G	2.7	3.7	4.5	4.6	5.6	5.1
D_6	2.7	0.8	1.5	1.5	1.1	1.5
FWHM (cm^{-1})						
D_4	122.1	120.3	80.8	80.2	76	30
D_3	140.5	160	134	145	107	141
D	74.1	79	63.1	53	47	50
D_2	183.9	180	164.1	156	104	180
D_5	100.4	160.8	86.9	88	83	46
G	54.8	55.9	41.8	40.8	41	28
D_6	84.4	45.6	39	35.8	33	40
Integrated peak area ratio						
A_D/A_G	1.4	1.3	1.2	1.1	0.9	0.6
Mean crystal size in the a-direction						
L_a (Å)	3.1	3.4	3.6	4	4.8	7.3

Table S-8: Raman spectroscopic data for biooil char and mixed biooil with pinewood char samples from pyrolysis at 1600°C for 2 h related to the peak position, relative peak area, peak width (FWHM), integrated peak area ratio (A_D/A_G) and mean crystal size in the a-direction (L_a).

	biooil char	mixed biooil with pinewood char
Peak position (cm^{-1})		
D_4	1099	1099
D_3	1298	1296
D	1345	1344
D_2	1402	1401
D_5	1536	1549
G	1593	1581
D_6	1635	1620
Relative peak area		
D_4	0.01	0.3
D_3	2.8	3.8
D	5.7	4.8
D_2	3.6	2.7
D_5	1.4	3.6
G	5.7	4.4
D_6	0.1	0.7
FWHM (cm^{-1})		
D_4	10	120.7
D_3	150	150
D	64.6	62.7
D_2	166.1	127.8
D_5	77.1	142.2
G	67.3	58.1
D_6	40.7	45.4
Integrated peak area ratio		
A_D/A_G	1	1.1
Mean crystal size in the a-direction		
L_a (Å)	4.4	4

Table S-9: Raman spectroscopic data for beechwood char samples related to the peak position, relative peak area, peak width (FWHM), integrated peak area ratio (A_D/A_G) and mean crystal size in the a-direction (L_a).

	1300°C, 2 h	1300°C, 12 h	1600°C, 2 h	2400°C, 2 h	2800°C, 2 h
Peak position (cm^{-1})					
D_4	1071	1099	1070	1087	1098
D_3	1261	1260	1275	1275	1288
D	1337	1338	1333	1335	1337
D_2	1403	1404	1402	1402	1422
D_5	1550	1549	1550	1550	1548
G	1575	1573	1574	1563	1567
D_6	1608	1609	1623	1608	1605
Relative peak area					
D_4	0.2	0.01	0.3	0.1	1
D_3	3.1	3.4	3.5	1.4	0.9
D	5.1	5.2	5.4	3.7	1.9
D_2	5.5	4.1	3.7	2.2	1.5
D_5	3.3	5.1	3	2.9	1.8
G	2.6	3.1	4.4	4.8	4.4
D_6	1.8	1.1	0.4	0.9	1.4
FWHM (cm^{-1})					
D_4	120.8	30.9	98	30	105.7
D_3	159	140	180	177	141.1
D	77.2	78.5	67	51.1	47.2
D_2	180.2	142	180	180	161.2
D_5	119.2	159	116	85.2	59.9
G	51	53.7	58	37.8	27
D_6	55.2	49.7	39.8	38	51.3
Integrated peak area ratio					
A_D/A_G	2	1.7	1.2	0.8	0.4
Mean crystal size in the a-direction					
L_a (Å)	2.2	2.6	3.6	5.5	10.9

Table S-10: Raman spectroscopic data for leached wheat straw char samples related to the peak position, relative peak area, peak width (FWHM), integrated peak area ratio (A_D/A_G) and mean crystal size in the a-direction (L_a).

	1300°C, 2 h	1300°C, 12 h	1600°C, 2 h	1600°C, 12 h	2400°C, 2 h	2800°C, 2 h
Peak position (cm^{-1})						
D_4	1099	1088	1071	1091	1095	1090
D_3	1251	1251	1296	1275	1295	1270
D	1336	1331	1338	1336	1342	1342
D_2	1402	1403	1402	1402	1402	1410
D_5	1537	1535	1549	1549	1545	1550
G	1582	1577	1585	1577	1571	1569
D_6	1616	1611	1619	1622	1611	1614
Relative peak area						
D_4	0.2	0.4	0.02	1.1	0.1	0.7
D_3	2.9	3.1	3.5	2.5	0.8	0.9
D	5.7	5.8	5.5	5.5	4.1	3.2
D_2	4.4	4.3	2.8	2.3	1.4	0.7
D_5	3.6	3.2	2.3	3.8	1.9	2.7
G	3.7	3.7	3.7	4.5	5.6	5.8
D_6	1.3	1	0.6	0.4	1.1	0.7
FWHM (cm^{-1})						
D_4	120	120	20	104	30	100
D_3	132.2	142	130	148	80	100
D	81.5	81.7	59	60.4	43	51.1
D_2	143.3	148.3	111.1	120	150	100
D_5	120	116.9	129.6	151	86.4	94.2
G	61.8	63.1	55.5	48	35.9	34.8
D_6	71.2	70	38.8	28.1	34.4	36.1
Integrated peak area ratio						
A_D/A_G	1.5	1.5	1.5	1.4	0.7	0.6
Mean crystal size in the a-direction						
L_a (Å)	2.9	2.9	2.9	3.1	6.2	7.3

Table S-11: Raman spectroscopic data for wheat straw char samples related to the peak position, relative peak area, peak width (FWHM), integrated peak area ratio (A_D/A_G) and mean crystal size in the a-direction (L_a).

	1300°C, 2 h	1600°C, 2 h	2400°C, 2 h	2800°C, 2 h
Peak position (cm^{-1})				
D_4	1070	1059	1057	1092
D_3	1297	1296	1285	1298
D	1337	1337	1338	1345
D_2	1402	1403	1401	1403
D_5	1549	1549	1550	1550
G	1584	1585	1565	1575
D_6	1607	1619	1605	1606
Relative peak area				
D_4	0.3	0.7	0.1	1.1
D_3	5	3	0.4	0.9
D	4.2	5.7	3	2.8
D_2	3.3	2.7	1.1	2.8
D_5	5.2	2.2	2.4	1.2
G	2.8	3.9	5.4	4.8
D_6	0.6	0.4	1	1.8
FWHM (cm^{-1})				
D_4	148.2	149.7	120	106
D_3	154.8	115.4	50	106
D	70.5	58.1	49	46.7
D_2	110	104.2	115	172.8
D_5	143.4	128.4	80.4	41.7
G	57.8	57.9	34.5	30.9
D_6	49.3	53	41	48.9
Integrated peak area ratio				
A_D/A_G	1.5	1.5	0.6	0.6
Mean crystal size in the a-direction				
L_a (Å)	2.9	2.9	7.3	7.3

Table S-12: Raman spectroscopic data for alfalfa straw char samples related to the peak position, relative peak area, peak width (FWHM), integrated peak area ratio (A_D/A_G) and mean crystal size in the a-direction (L_a).

	1300°C, 2 h	1300°C, 12 h	1600°C, 2 h	2400°C, 2 h	2800°C, 2 h
Peak position (cm^{-1})					
D_4	1099	1070	1099	1079	1090
D_3	1263	1281	1261	1295	1270
D	1341	1336	1340	1342	1341
D_2	1413	1402	1403	1402	1414
D_5	1549	1550	1549	1550	1550
G	1576	1585	1574	1571	1570
D_6	1612	1627	1605	1610	1606
Relative peak area					
D_4	0.03	0.07	0.1	0.1	0.3
D_3	2.3	2.6	2.3	0.7	0.8
D	6.1	6.5	3.2	4.7	3.6
D_2	3.6	2.2	3.9	2.2	1.5
D_5	4.1	2.8	3.5	1.6	2.1
G	3.2	4.2	2.8	5	4.9
D_6	1.5	0.2	2.1	1.4	1.4
FWHM (cm^{-1})					
D_4	20	30	101	30	113
D_3	118	115.1	142.2	76.4	100
D	79.2	58.2	69.8	47.1	51.6
D_2	122.1	98.8	152.5	180	112
D_5	129.7	131.4	103	83.4	63.8
G	48.9	59	33.8	37.4	30.7
D_6	50.2	40	65.3	40.3	40
Integrated peak area ratio					
A_D/A_G	1.9	1.5	1.1	0.9	0.7
Mean crystal size in the a-direction					
L_a (Å)	2.3	2.9	4	4.8	6.2

S-4. Nanostructure

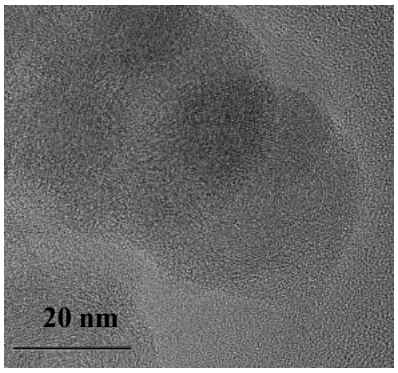

21(a): Beechwood char (1300°C, 2 h)

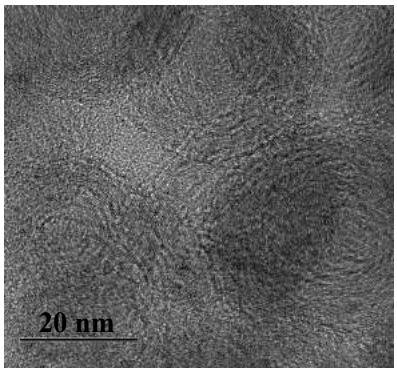

21(b): Beechwood char (1300°C, 12 h)

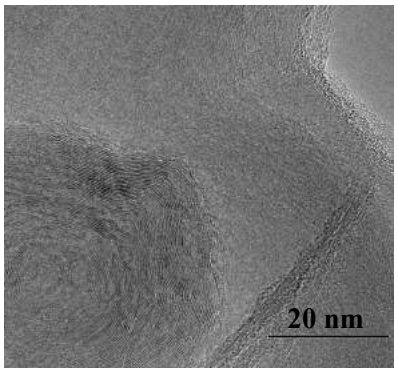

21(c): Beechwood char (1600°C, 12 h)

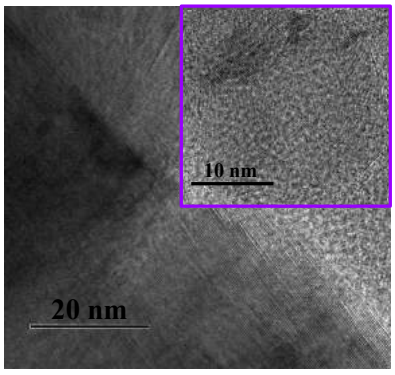

21(d): Beechwood char (2400°C, 2 h)

Figure S-21: TEM images of beechwood char reacted at 1300°C for 2 h and 12 h, 1600 for 12 h and 2400°C for 2 h. In Figure 21(d) the nano-crystalline graphitic ring is shown in the purple rectangle.

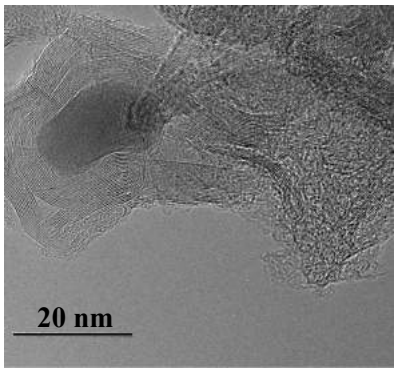

22(a): Leached wheat straw char (1300°C, 2 h)

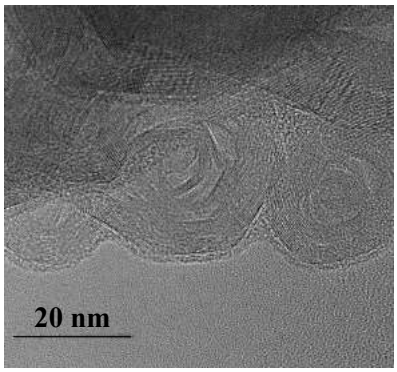

22(b): Leached wheat straw char (2400°C, 2 h)

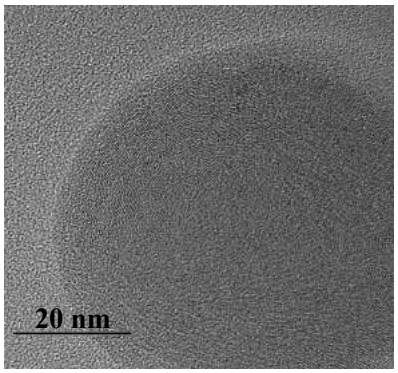

22(c): Wheat straw char (1300°C, 2 h)

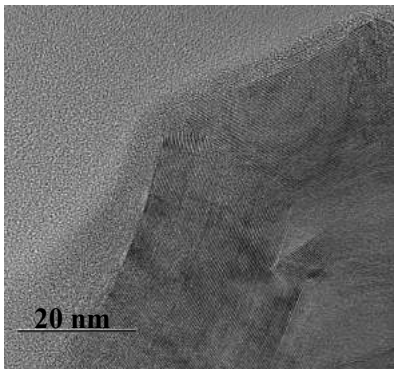

22(d): Wheat straw char (2400°C, 2 h)

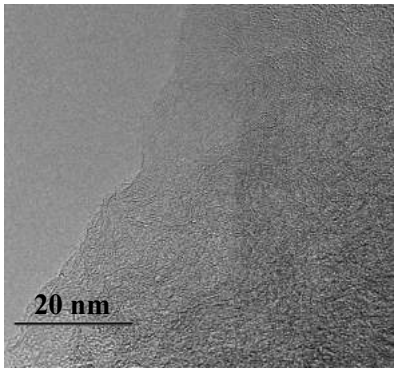

22(e): Alfalfa straw char (1300°C, 2 h)

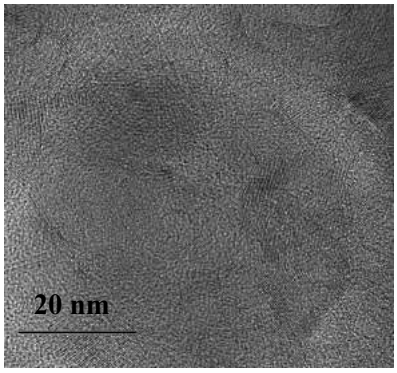

22(f): Alfalfa straw char (2400°C, 2 h)

Figure S-22: TEM images of leached wheat straw, wheat straw, alfalfa straw char reacted at 1300 and 2400°C for 2 h.

S-5. Discussion

Table S-23 summarizes the maximal reaction rates at 600°C during oxidation of pinewood, beechwood, leached wheat straw, wheat straw, and alfalfa straw chars from pyrolysis at 1300, 1600, 2400 and 2800°C for 2 h or 12 h that are shown versus relative area ratio A_D/A_G.

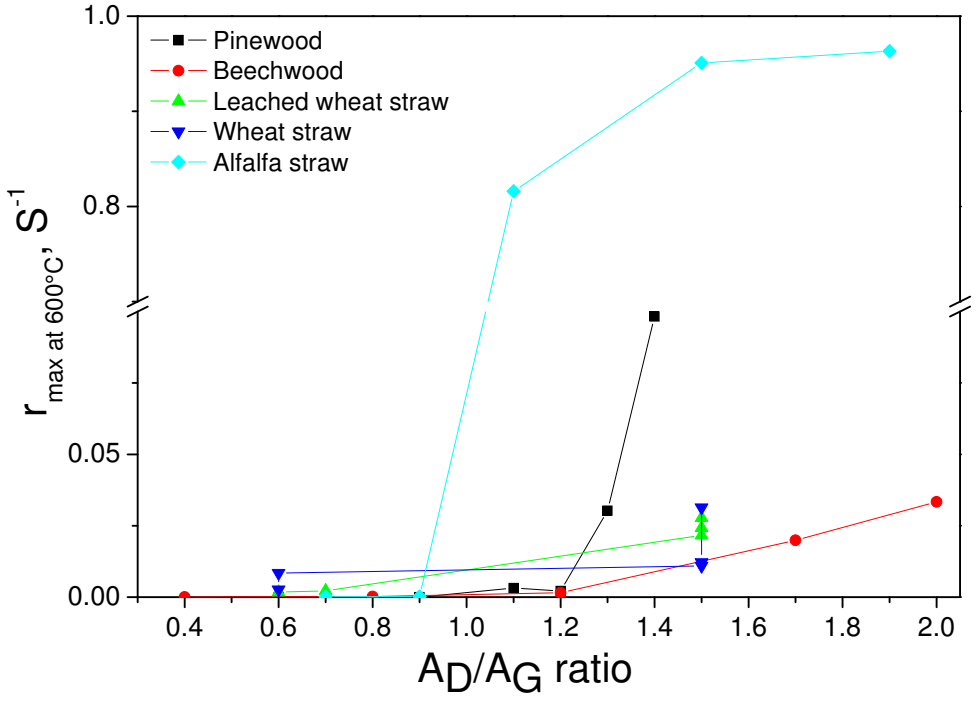

Figure S-23: Maximal reaction rate at 600°C (results from Tables S-1-S-3) during oxidation versus A_D/A_G ratio of pinewood, beechwood, leached wheat straw, wheat straw, alfalfa straw chars from pyrolysis at 1300, 1600, 2400 and 2800°C for 2 or 12 h (results from Figures S-15-S-20).

A.4 Supplemental materials article 4

The effect of wood composition and supercritical CO_2 extraction on biochar pro-duction in ferroalloy industries

Contribution of the authors

Gerrit Ralf Surup planned the majority of the study, developed a reactor for the charcoal production and also performed all pyrolysis experiments and manuscript writing.
Andrew J Hunt participated in the development of the supercritical extractor and performed experiments which pointed that the use of CO_2 is the most beneficial method for the removal of fatty and resin acids.
Thomas Attard constructed the small scale extraction setup and performed the supercritical extraction experiments.
Vitaliy L Budarin performed the pore size, porosity and density measurements of non-treated and fractions after supercritical CO_2 extraction.
Fredrik Forsberg performed the microtomography characterization of needles, data processing and setting a new method for the sample holding during the real measurements.
Mehrdad Arshadi participated in the selection of feedstocks, manual preparation of feedstocks that includes milling, chipping and pulverization.
Victor Abdelsayed constructed a setup for the dielectric properties measurements of charcoal and performed the experiments.
Dushyant Shekhawat participated in the dielectric properties measurements and has tested the instrument using different point methods. He has also actively supported in the data processing and description of dielectric properties in the manuscript.
Anna Trubetskaya supported on the manuscript structuring, managed the correspondence among co-authors and did the manuscript proof-reading. She has participated in the tar measurement using GC-FID.

The effect of wood composition and supercritical CO_2 extraction on biochar production in ferroalloy industries

Gerrit Ralf Surup[a], Andrew J Hunt[b], Thomas Attard[c], Vitaliy L Budarin[c], Fredrik Forsberg[d], Mehrdad Arshadi[e], Victor Abdelsayed[f,g], Dushyant Shekhawat[f], Anna Trubetskaya[i,h,*]

[a]*Department of Engineering Sciences, University of Agder, 4879, Grimstad, Norway*
[b]*Materials Chemistry Research Center, Department of Chemistry and Center of Excellence for Innovation in Chemistry, Faculty of Science, Khon Kaen University, 123 Mittraparb Road, 40002, Khon Kaen, Thailand*
[c]*Department of Chemistry, The University of York, Heslington, York, YO10 5DD, UK*
[d]*Department of Engineering Sciences and Mathematics, Luleå University of Technology, 97187, Luleå, Sweden*
[e]*Department of Forest Biomaterials and Technology, Swedish University of Agricultural Sciences, 90183, Umeå, Sweden*
[f]*National Energy Technology Laboratory, Morgantown, WV 26507, USA*
[g]*AECOM, Morgantown, WV 26507, USA*
[h]*School of Engineering and Ryan Institute, National University of Ireland Galway, Galway, Ireland*
[i]*Department of Chemical Sciences, University of Limerick, V94 T9PX, Limerick, Ireland*

[*]Corresponding author. anna.trubetskaya@nuigalway.ie

Preprint submitted to Journal of Cleaner Production *March 19, 2019*

S-1. Original biomass characterization

Table S-1: Proximate, ultimate and ash analyses of the non-treated bark from large diameter Scots pinewood and bark after CO_2 supercritical extraction.

Fuel	**Original bark**	**Bark after CO_2 extraction**
Proximate and ultimate analysis (% on dry basis)		
Moisture[a]	9	8
Ash (550 °C)	0.6	0.5
Volatiles	71.6	70.9
HHV[b]	21.8	21.3
LHV[b]	20.6	20.1
C	54.7	54.5
H	5.5	5.4
O	38.8	39.4
N	0.3	0.2
S	0.02	0.02
Ash compositional analysis (mg kg^{-1} on dry basis)		
Cl	< 0.01	0.01
Al	250	300
Ca	1200	1300
Fe	60	60
K	800	900
Mg	200	200
Na	10	10
P	150	150
Si	350	300
Ti	2	3

[a] wt. % (as received) [b] in MJ kg^{-1}

S-2. Elemental analysis

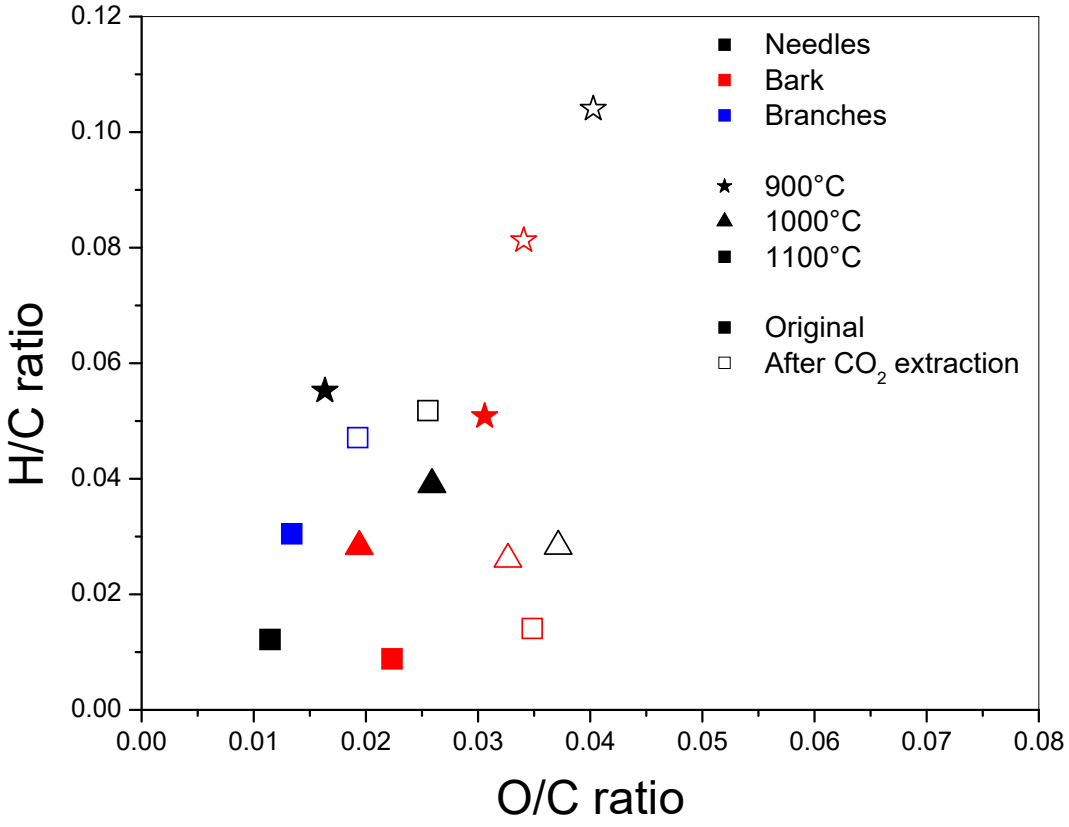

Figure S-1: Van Krevelen plot of original wood fractions, samples after $scCO_2$ extraction and their chars.

S-3. Ash compositional analysis

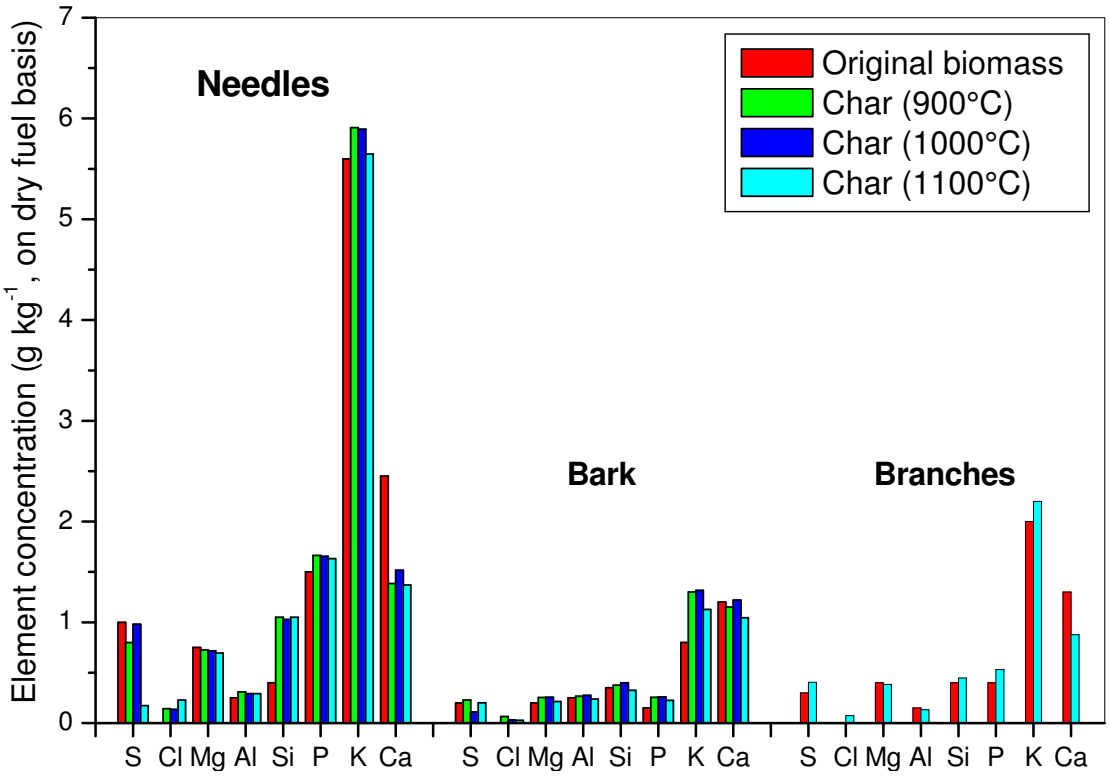

Figure S-2: Ash compositional analysis of original needles, bark and branches and wood fractions after $scCO_2$ extraction and their chars from pyrolysis at 900, 1000 and 1100°C which is shown in g kg^{-1} on the dry ash basis of original biomass.

S-4. 2D dynamic imaging analysis

S-4.1. Methodology

Particle shadows were captured by two cameras, namely a zoom camera, designed for the analysis of smaller particles, and a basic-camera that was

able to detect larger particles. The projected area of the particles was analyzed by the CAMSIZER XT 6.3.10 software (Retsch Technology, Germany). Fine biomass particles tend to agglomerate which makes it difficult to detect the true geometric dimensions of each individual particle. Therefore, the particle agglomerates were separated without destroying the primary particles by air pressure dispersion. The Martin diameter is a chord length that divides the projected particle area into two equal halves [1]. The minimal Martin diameter ($x_{Ma,min}$) is determined from the smallest Martin diameter of the particle projection [2], and represents a particle width based on the assumption of a biomass particle to be thinner than its width in the diffusion process of a combustion modeling. The Feret diameter is a distance between two tangents placed perpendicular to the measurement direction [1]. The Feret maximal diameter is the longest Feret diameter of all measured Feret diameters of a particle [2], and the longest measurable diameter $x_{Fe,max}$ is the largest diameter to fulfill the assumption that the length of a particle has to be larger than its width. The results are presented as a cumulative particle size distribution, based on volume (Q_3). The cumulative particle size distribution is described in EN ISO 9276-1:1998, and is defined as

$$Q_3(x_{Ma\,min,m}) = \sum_{i=1}^{m} \overline{q_3}(x_{Ma\,min,i})\Delta x_{Ma\,min,i}, \tag{1}$$

where $\overline{q_3}$ is the area beneath the histogram. The results of a particle size analysis are also presented as a frequency distribution over $x_{Ma\,min}$, based on volume (q_3), so that

$$q_3(x_{Ma\,min}) = \frac{dQ_3(x_{Ma\,min})}{dx_{Ma\,min}}. \tag{2}$$

5

The particle size distributions obtained from the 2D dynamic imaging were defined based on three sizes within the entire population: d10, d50, d90. The d50 value is the median particle size within the population, with 50 % of the population greater than this size, and 50 % smaller than this size. Similarly, 10 % of the population is smaller than the d10 size; while 90 % of the population is smaller than the d90 size [3]. All measurements were conducted in triplicate to establish repeatability which was better than 95 % confidence intervals.

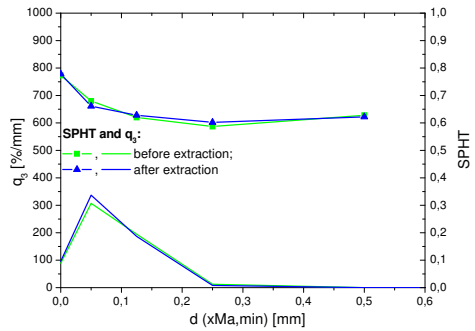

3(a): SPHT and q_3 of needles

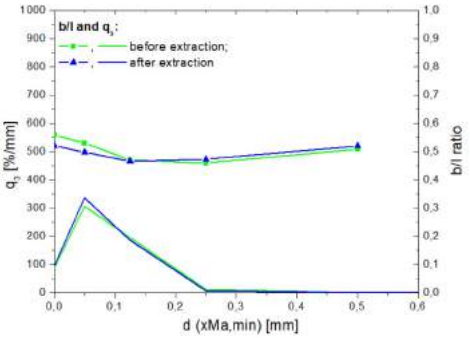

3(b): b/l and q_3 of needles

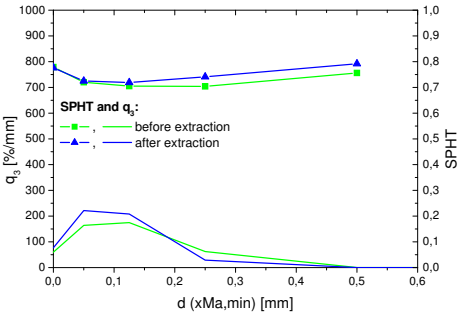

3(c): SPHT and q_3 of bark

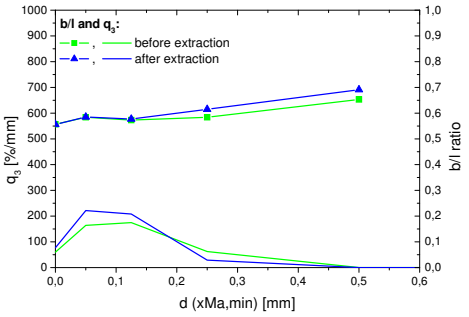

3(d): b/l and q_3 of bark

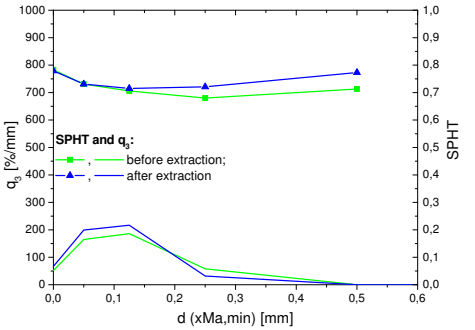

3(e): SPHT and q_3 of branches

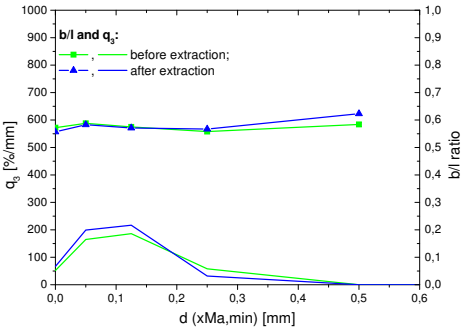

3(f): b/l and q_3 of branches

Figure S-3: Particle frequency distribution (q_3), sphericity (SPHT) and width/length ratio (b/l) of non-treated wood fractions and samples after supercritical CO_2 extraction: (a-b) bark from small diameter and large diameter pinewood logs; (c-d) branches and stumps; (e-f) needles and cones.

S-5. Pore size distributions

Pore volume and size. The pore volume can be derived from the quantity of intruded mercury. The pore size distribution is determined according to the Washburn equation [4]:

$$D_p = -\frac{4\gamma cos\Theta}{p} \tag{3}$$

In equation 3, Θ is assumed to be equal to 141° [5] and γ is equal to 0.48 N m^{-1} [6]. The median pore diameter (D_{md}) is defined as the pore diameter at which 50 % of total intrusion was reached. The average pore diameter (D_{pa}) is calculated, assuming that all pores are cylindrical, in equation 4:

$$D_{pa} = -\frac{4V_{cum}}{SSA} \tag{4}$$

The cumulative pore volume distribution is calculated in equation 5:

$$V_{cum}(D) = \frac{-dV_p}{dlogD_p} \tag{5}$$

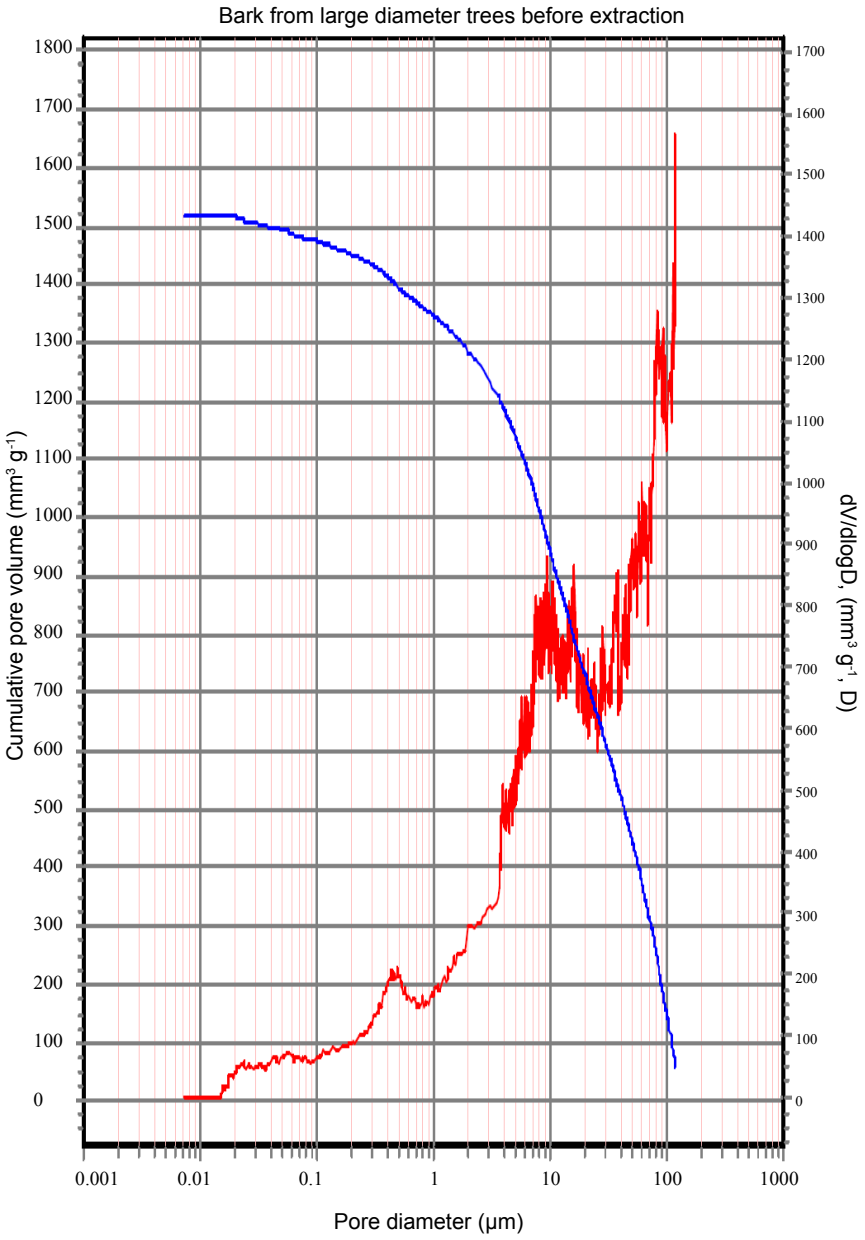

Figure S-4: Cumulative pore volume (mm^3 g^{-1}) and pore size distribution, dV/dlogD (mm^3 g^{-1}, D) of bark before extraction.

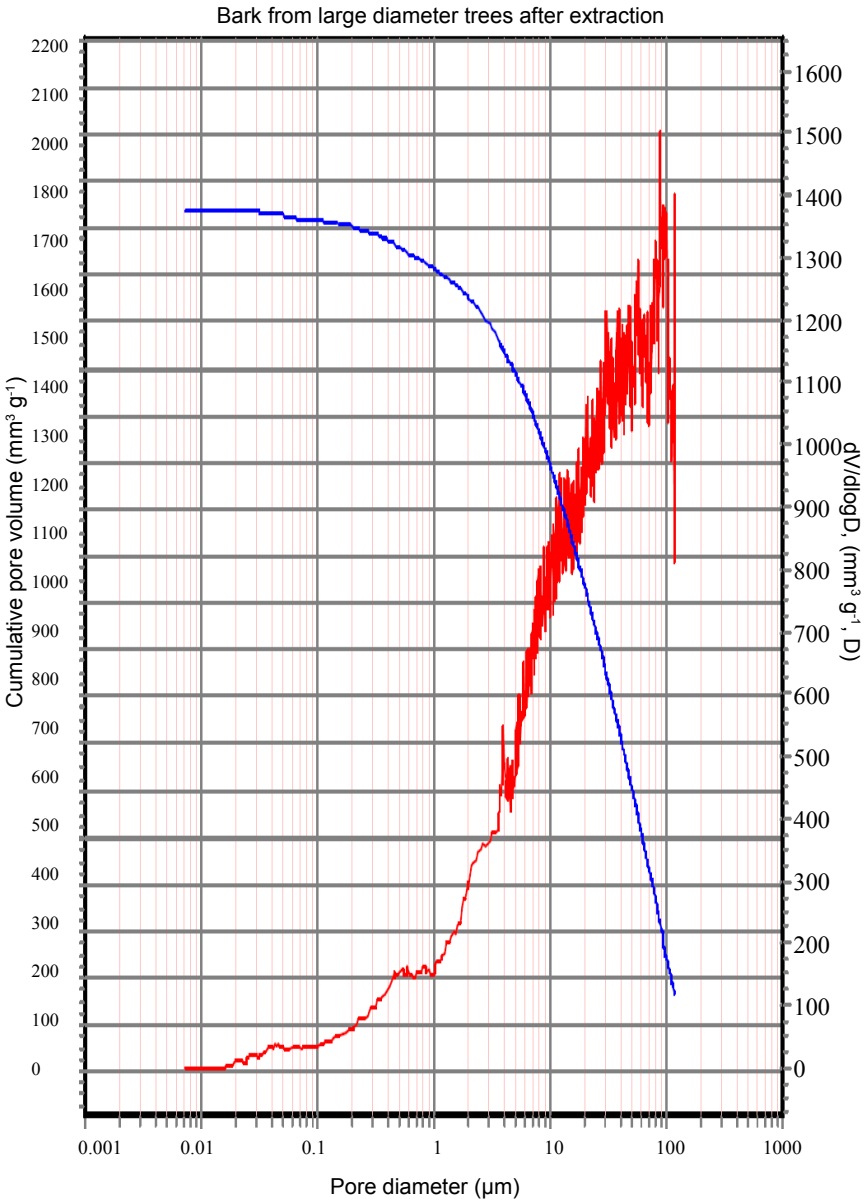

Figure S-5: Cumulative pore volume (mm^3 g^{-1}) and pore size distribution, dV/dlogD (mm^3 g^{-1}, D) of bark after extraction.

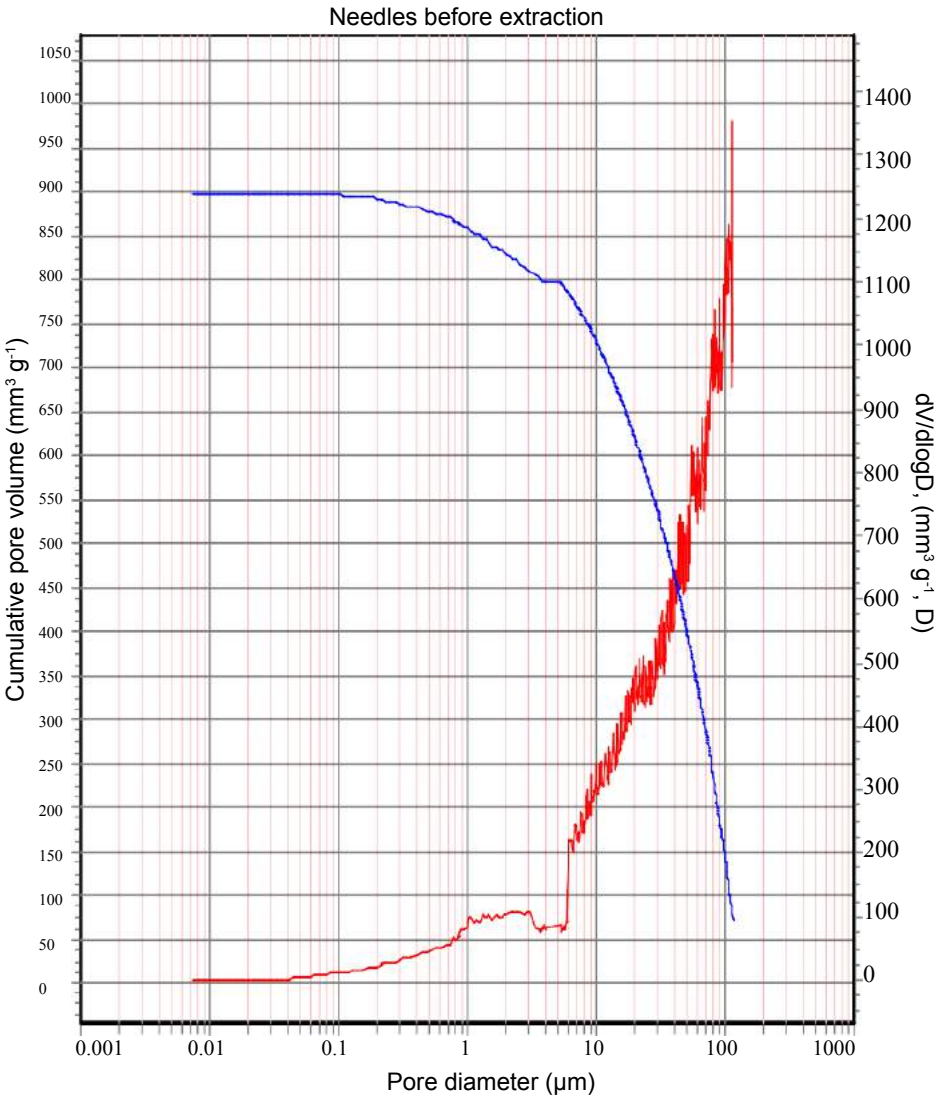

Figure S-6: Cumulative pore volume (mm^3 g^{-1}) and pore size distribution, dV/dlogD (mm^3 g^{-1}, D) of needles before extraction.

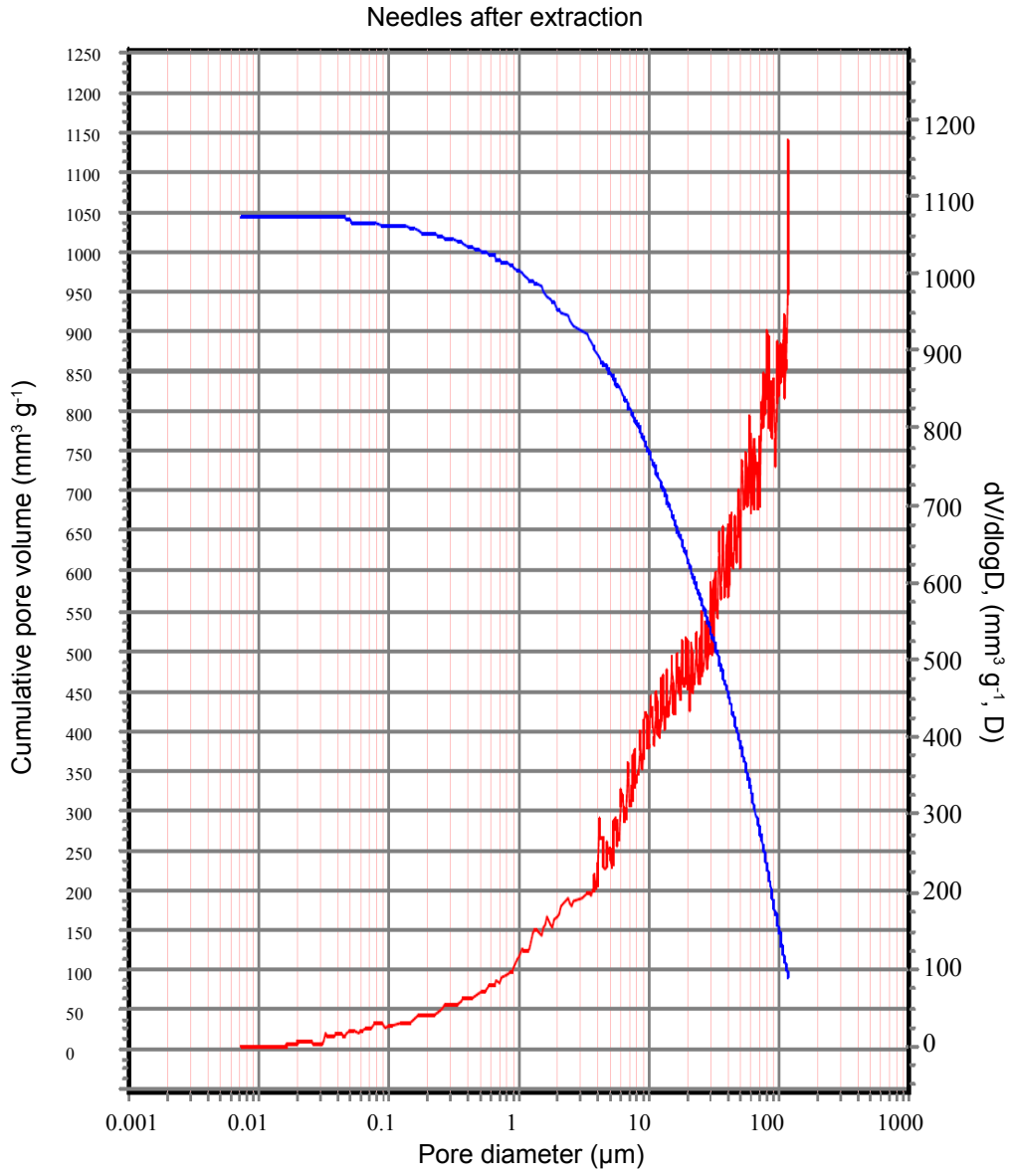

Figure S-7: Cumulative pore volume (mm^3 g^{-1}) and pore size distribution, dV/dlogD (mm^3 g^{-1}, D) of needles after extraction.

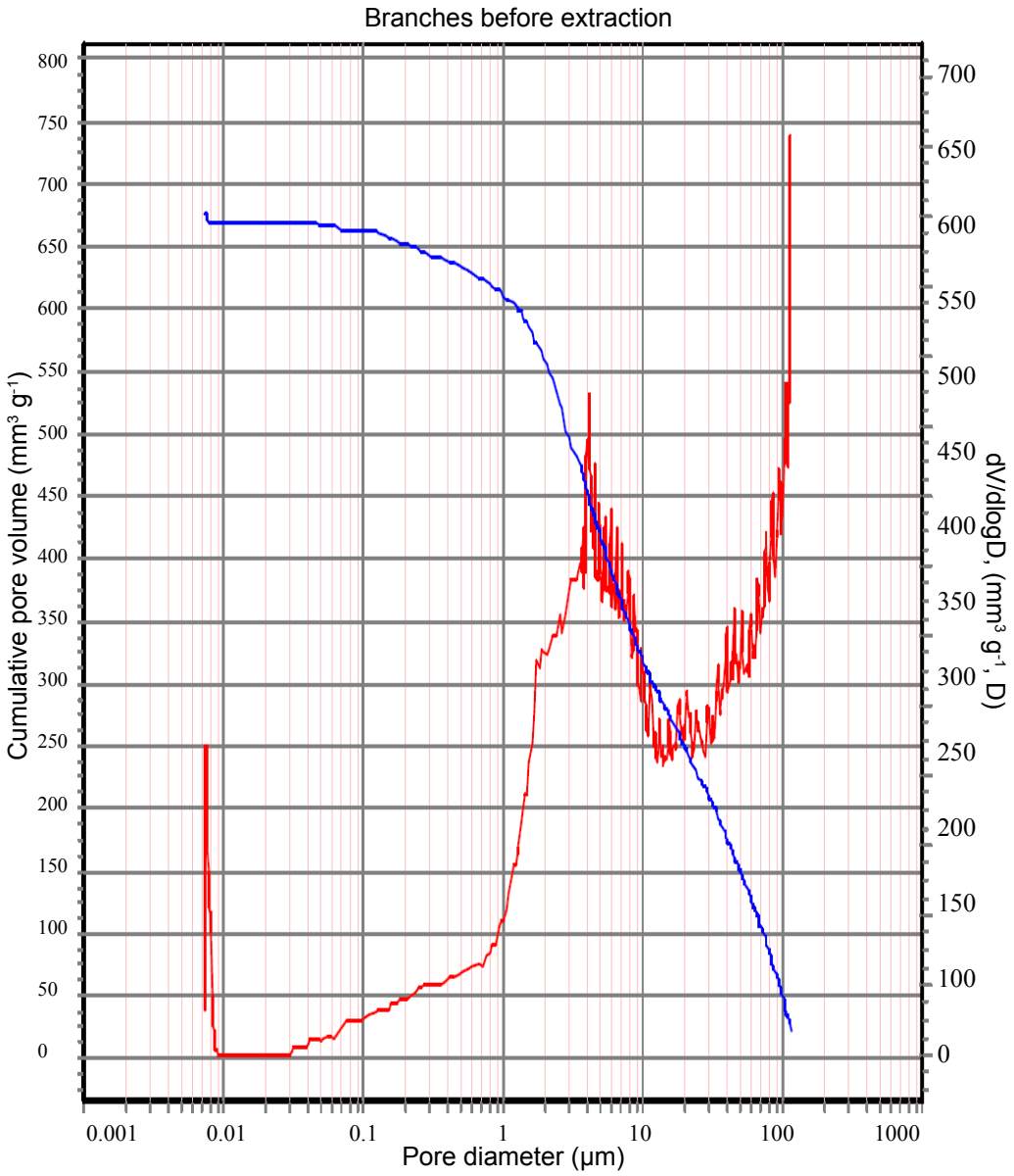

Figure S-8: Cumulative pore volume (mm^3 g^{-1}) and pore size distribution, dV/dlogD (mm^3 g^{-1}, D) of branches before extraction.

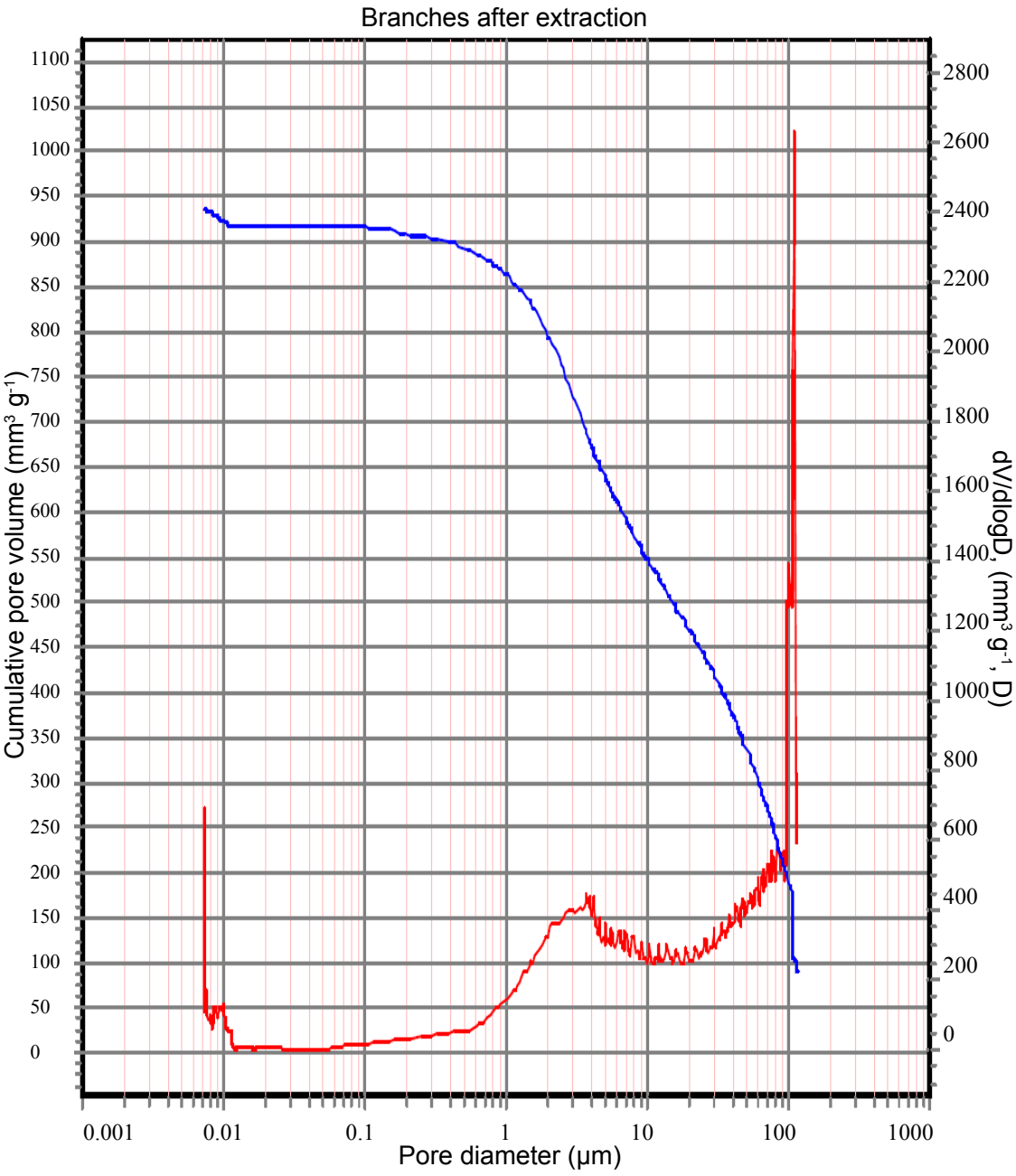

Figure S-9: Cumulative pore volume (mm^3 g^{-1}) and pore size distribution, dV/dlogD (mm^3 g^{-1}, D) of branches after extraction.[14]

S-6. X-ray microtomography

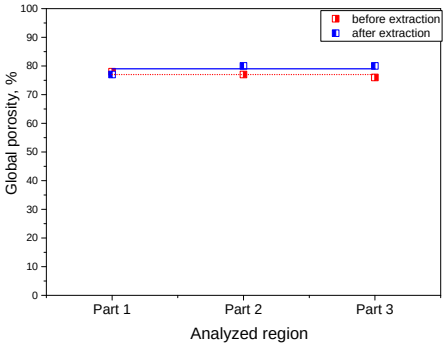

10(a): Global porosity

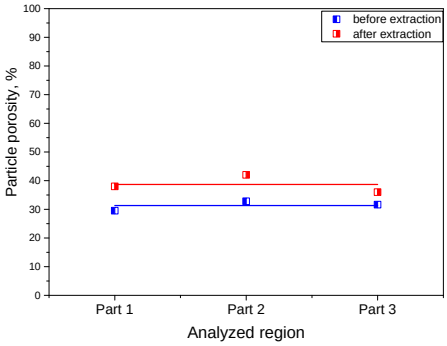

10(b): Particle porosity

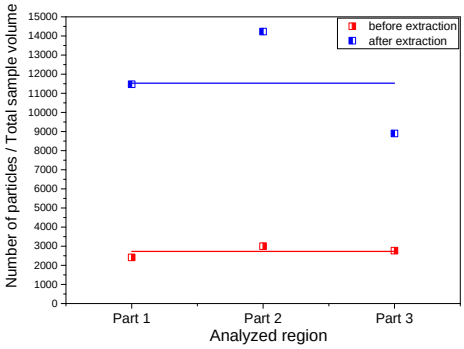

10(c): Number of particles/volume

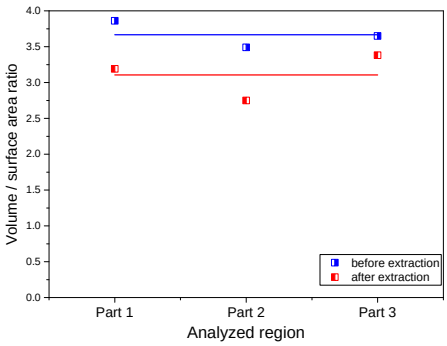

10(d): Particle volume/surface area

Figure S-10: The XμCT quantitative analysis of non-treated pinewood needles and fraction after $scCO_2$ extraction: (a) global porosity; (b) particle porosity; (c) number of particles/volume, and (d) particle volume/area ratio.

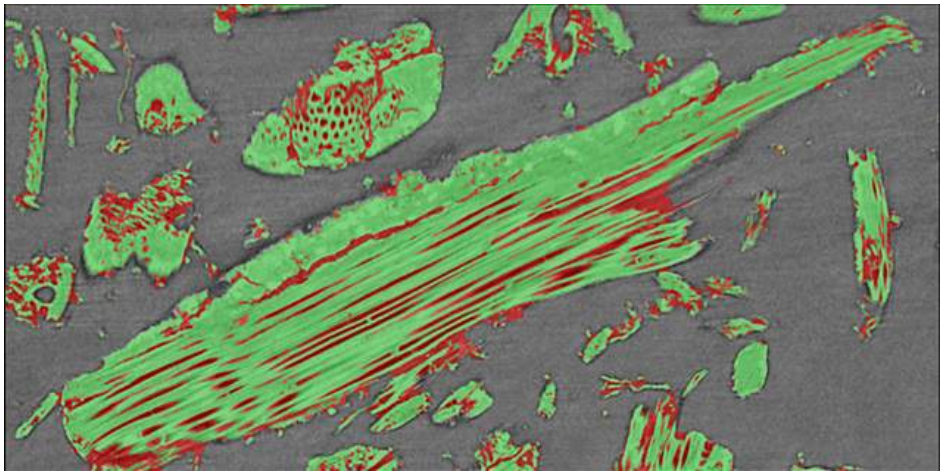

Figure S-11: The μCT particle porosity analysis of non-treated pinewood needles.

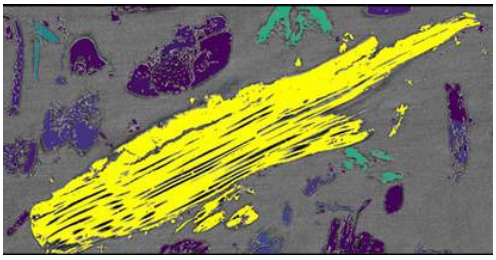

12(a): Non-treated needles

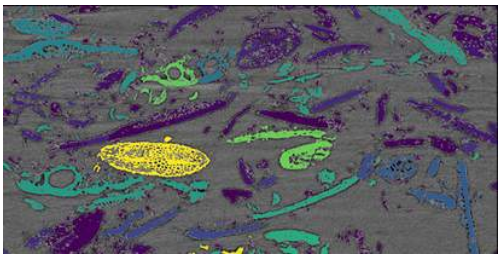

12(b): Needles after $scCO_2$ extraction

Figure S-12: The XμCT particle number pro total masked particle volume (total voxel = 6.5 mm^3) analysis of non-treated pinewood needles and fraction after $scCO_2$ extraction.

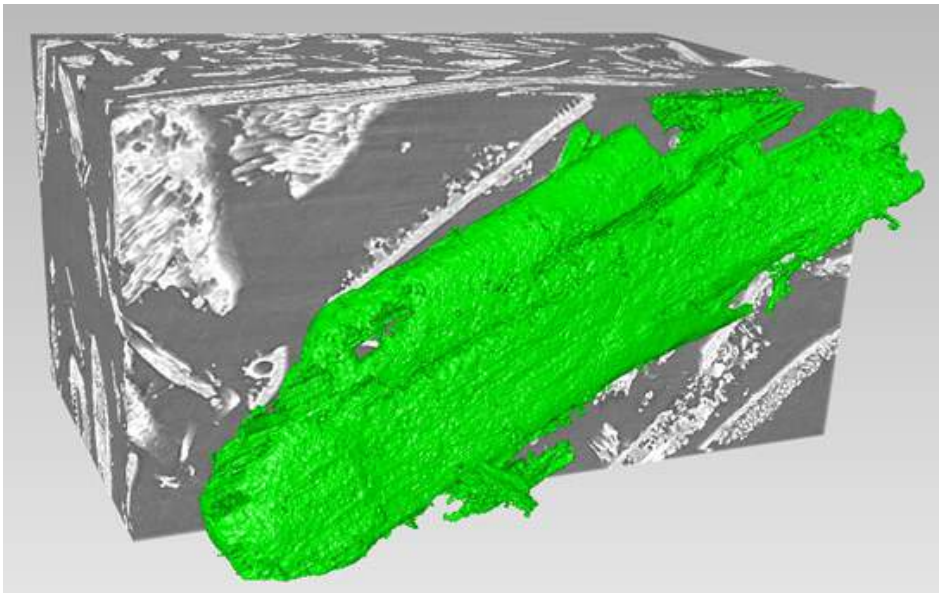

Figure S-13: The μCT particle volume analysis of non-treated pinewood needles.

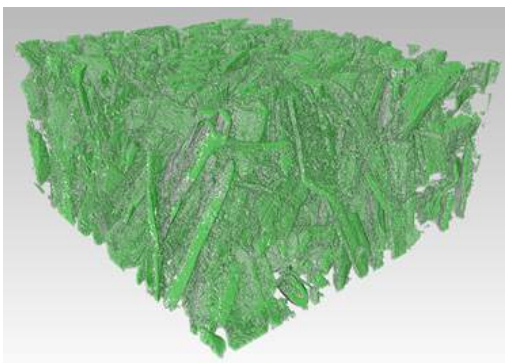

14(a): Non-treated needles

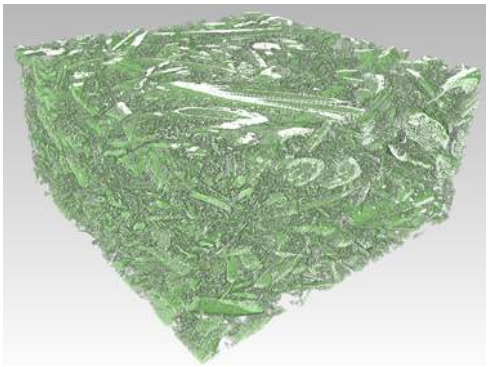

14(b): Needles after $scCO_2$ extraction

Figure S-14: The volume-to-surface area ratio calculation approach of non-treated pinewood needles and fraction after $scCO_2$ extraction using XμCT instrument.

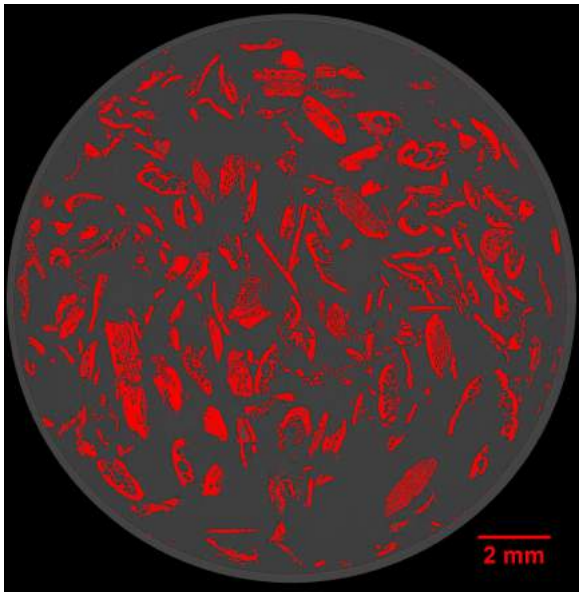

15(a): Non-treated needles

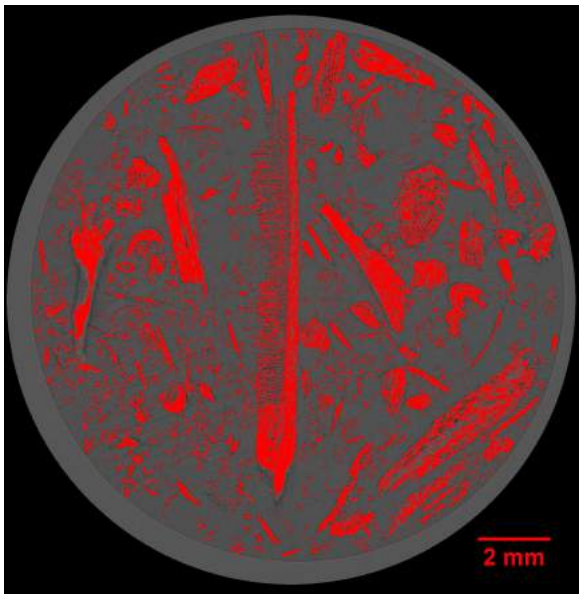

15(b): Needles after $scCO_2$ extraction

Figure S-15: The 2D visualized images from XμCT analysis of non-treated needles and fraction after CO_2 extraction using ImageJ software.

S-7. Arrhenius plot of CO_2 char reactivity

Table S-2: Kinetic parameters for CO_2 reactivity of char from non-treated bark, needles and branches and $scCO_2$ wood samples pyrolyzed at 900, 1000, and 1100°C and further reacted in 20 % volume fraction CO_2 + 80 % volume fraction N_2.

Temperature	E_a	A	r_{max} at 600°C
°C	kJ mol^{-1}	s^{-1}	s^{-1}
Char from non-treated bark			
900	156	$2.4 \cdot 10^5$	$1.7 \cdot 10^{-3}$
1000	173	$1.1 \cdot 10^6$	$1 \cdot 10^{-4}$
1100	187	$3.8 \cdot 10^6$	$6.7 \cdot 10^{-4}$
Char from $scCO_2$ extracted bark			
900	157	$2.9 \cdot 10^5$	$1.8 \cdot 10^{-3}$
1000	176	$1.5 \cdot 10^6$	$9.5 \cdot 10^{-4}$
1100	192	$6.9 \cdot 10^6$	$6.7 \cdot 10^{-4}$
Char from non-treated needles			
900	197	$4.9 \cdot 10^7$	$2.5 \cdot 10^{-3}$
1000	198	$4.7 \cdot 10^7$	$2.2 \cdot 10^{-3}$
1100	210	$1 \cdot 10^8$	$1.1 \cdot 10^{-3}$
Char from $scCO_2$ extracted needles			
900	185	$2.9 \cdot 10^7$	$6.2 \cdot 10^{-3}$
1000	188	$3.2 \cdot 10^7$	$4.6 \cdot 10^{-3}$
1100	207	$1.1 \cdot 10^8$	$1.6 \cdot 10^{-3}$
Char from non-treated branches			
1100	192	$1.1 \cdot 10^7$	$1 \cdot 10^{-3}$
Char from $scCO_2$ extracted branches			
1100	191	$1.1 \cdot 10^7$	$1 \cdot 10^{-3}$

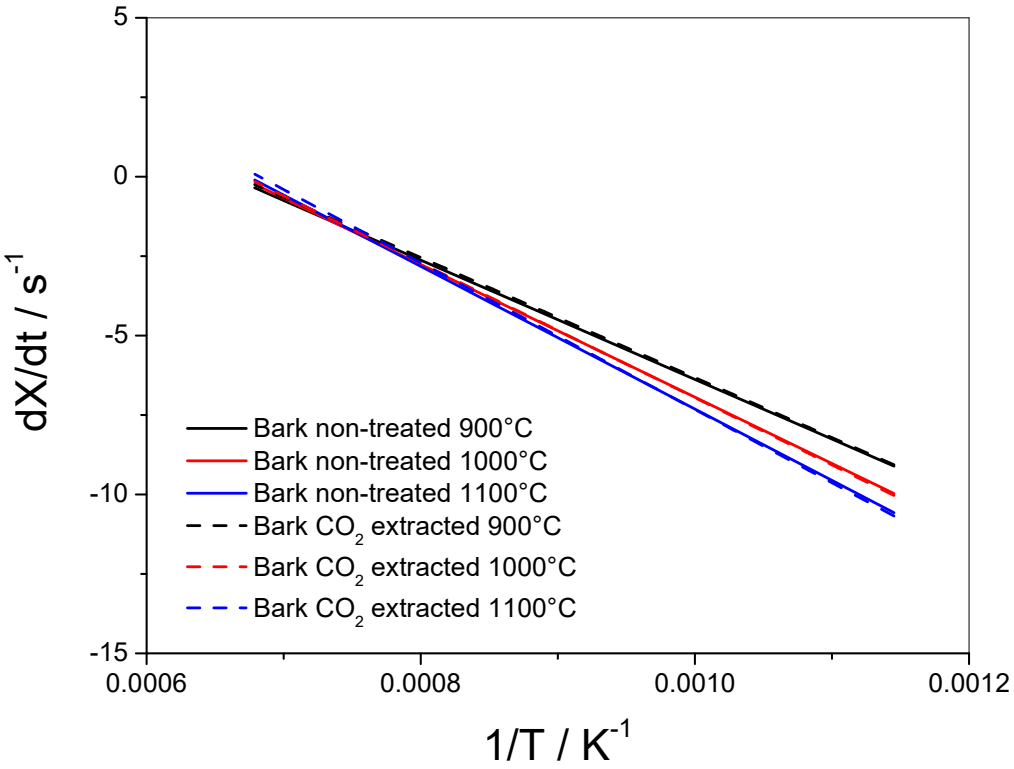

Figure S-16: Arrhenius plot of CO_2 reactivity of char from non-treated bark and $scCO_2$ extracted wood fraction reacted in 20 % volume fraction CO_2 + 80 % volume fraction N_2.

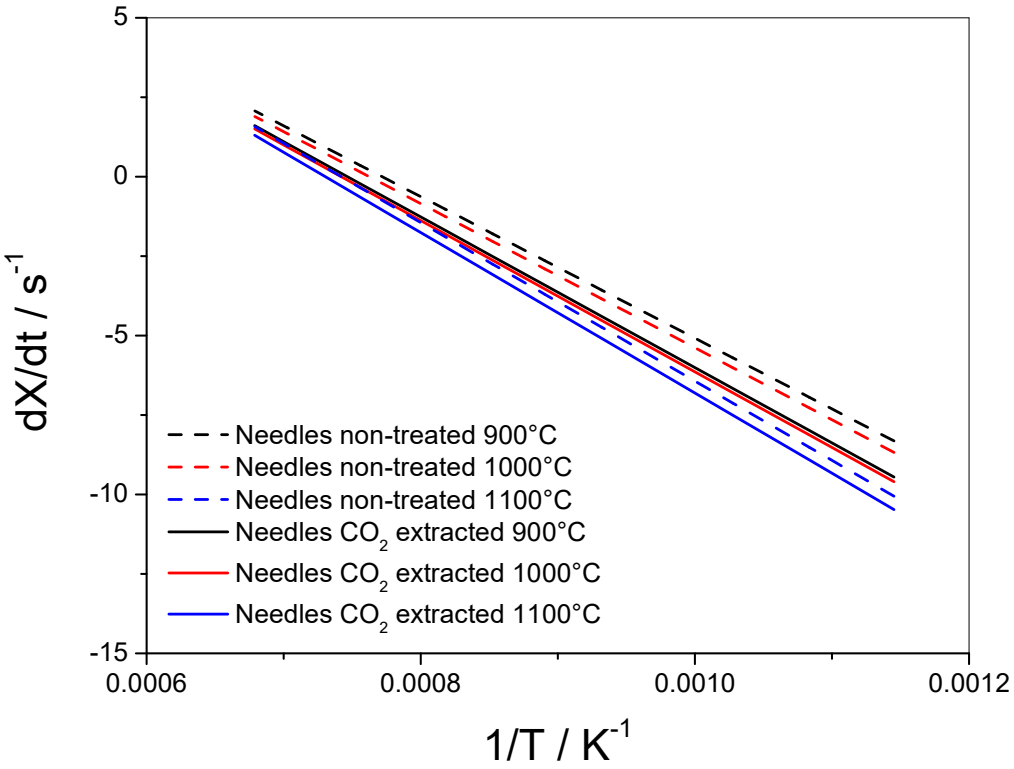

Figure S-17: Arrhenius plot of CO_2 reactivity of char from non-treated needles and $scCO_2$ extracted wood fraction reacted in 20 % volume fraction CO_2 + 80 % volume fraction N_2.

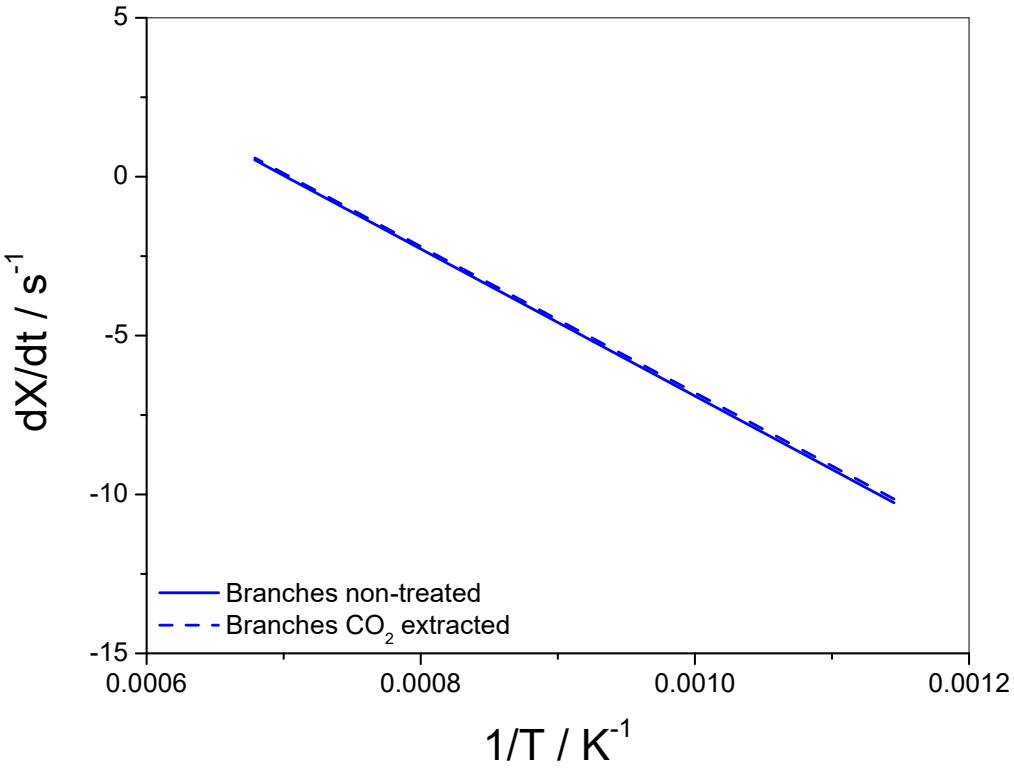

Figure S-18: Arrhenius plot of CO_2 reactivity of char from non-treated branches and $scCO_2$ extracted wood fraction reacted in 20 % volume fraction CO_2 + 80 % volume fraction N_2.

S-8. Characterization and quantitation of tar compounds

The identification of individual tar compounds was based on the present results of GC-MS analysis, PAH pattern recognized in the literature and comparison with the reference chromatograms of external standards. The identified tar compounds with the relevant information were listed in Table S-3. Forty five compounds in the pyrolysis tar have been quantified and grouped for the quantification.

Table S-3: List of indentified tar compounds with the CAS number, empirical formula, molecular weight and retention time and external standards with the manufacturer, catalog numbers and concentrations (μg ml^{-1}).

No	Compounds	CAS no.	Formula	MW	Cat. no./solv.	Producer	Conc.	RT
							μg ml^{-}1	min
1	Acetonitrile	75-05-8	C_2H_3N	41.05	S-145/Me	SPEX	1000	6.18
2	Benzene	71-43-2	C_6H_6	78.11	CRM47505/Me	S-A	2000	6.30
3	Toluene	108-88-3	C_7H_8	92.14	CRM47505/Me	S-A	2000	9.04
4	2-Methylthiophene	554-14-3	C_5H_6S	98.17	S-3982/Me	SPEX	1000	10.01
5	3-Methylthiophene	616-44-4	C_5H_6S	98.17	S-2576/Me	SPEX	1000	10.27
6	Pyrrole	109-97-7	C_4H_4NH	67.09	12776/Me	S-A	1000	10.72
7	Ethylbenzene	100-41-4	C_8H_{10}	106.17	CRW47505/Me	S-A	2000	15.79
8	Styrene	100-42-5	C_8H_8	104.15	40669/Me	S-A	5000	16.87
9	1,2,4-Trimethylbenzene	95-63-6	C_9H_{12}	120.19	S-3720/Me	SPEX	1000	22.74
10	α-Methylstyrene	98-83-9	C_9H_{10}	118.18	S-2560/Me	SPEX	1000	23.64
11	Dimethyl Malonate	108-59-8	$C_5H_8O_4$	132.12	12777/Me	S-A	1000	24.7
12	1,2,3-Trimethylbenzene	526-73-8	C_9H_{12}	120.19	S-3717/Me	SPEX	1000	26.18
13	Phenol	108-95-2	C_6H_5OH	94.11	40063/Me	S-A	5000	26.5
14	Benzaldehyde	100-52-7	C_7H_6O	106.12	S-402/Me	SPEX	1000	27.02
15	2-Methylphenol	95-48-7	C_7H_8O	108.14	S-2545/Me	SPEX	1000	32.67
16	1-Phenyl-1-propyne	673-32-5	C_9H_8	116.16	12774/Me	S-A	1000	33.55
17	3-Methylphenol	108-39-4	C_7H_8O	108.14	S-2540/Me	SPEX	1000	34.99
18	Phenyl acetate	122-79-2	$C_8H_8O_2$	136.1	S-3046/Me	SPEX	1000	36.84
19	3-Methylbenzofuran	21535-97-7	C_9H_8O	132.16	1956.16/IO	C	1000	37.25
20	2-Methylbenzofuran	4265-25-2	C_9H_8O	132.16	S-2461/Me	SPEX	1000	37.53
21	2,6-Dimethylphenol	576-26-1	$C_8H_{10}O$	122.17	S-1662/Me	SPEX	1000	38.11
22	Naphthalene	91-20-3	$C_{10}H_8$	128.17	PAH Mix 3/Me	S-A	1000	46.77
23	4-Vinylphenol	2628-17-3	C_8H_8O	120.15	S-4692/Me	SPEX	1000	49.37
24	Quinoline	91-22-5	C_9H_7N	129.16	S-3245/Me	SPEX	1000	56.07
25	1-Methylnaphthalene	90-12-0	$C_{11}H_{10}$	142.2	PAH Mix 3/Me	S-A	1000	58.33
26	1-Indanone	83-33-0	C_9H_8O	132.16	10719.9/T	C	1000	60.44
27	Indole	120-72-9	C_8H_7N	117.15	S-2260/Me	SPEX	1000	62.07
28	Biphenyl	92-52-4	$C_{12}H_{10}$	154.21	48161/Me	S-A	2000	64.61
29	2,6-Dimethylnaphthalene	581-42-0	$C_{12}H_{12}$	156.22	S-1640/Me	SPEX	1000	64.87
30	1,3-Dimethylnaphthalene	575-41-7	$C_{12}H_{12}$	156.22	S-1631/Me	SPEX	1000	67.01
31	Biphenylene	259-79-0	$C_{12}H_8$	152.19	12778/Me	S-A	1000	71.35
32	Acenaphthene	83-32-9	$C_{12}H_{10}$	154.2	PAH Mix 3/Me	S-A	1000	74.92

No	Compounds	CAS no.	Formula	MW	Cat. no./solv.	Producer	Conc.	RT
33	Dibenzofuran	132-64-9	$C_{12}H_8O$	168.19	40261/Me	S-A	5000	76.69
34	Fluorene	86-73-7	$C_{13}H_{10}$	166.22	PAH Mix 3/Me	S-A	200	80.84
35	2-Methylfluorene	1430-97-3	$C_{14}H_{12}$	180.25	0351.14/T	C	1000	84.85
36	4-Methylfluorene	1556-99-6	$C_{14}H_{12}$	180.25	1091.14/IO	C	1000	85.57
37	Phenanthrene	85-01-8	$C_{14}H_{10}$	178.23	PAH Mix 3/Me	S-A	100	88.06
38	Anthracene	120-12-7	$C_{14}H_{10}$	178.23	PAH Mix 3/Me	S-A	100	88.22
40	1-Methylphenanthrene	832-69-9	$C_{15}H_{11}$	192.26	S-2535/Me	SPEX	1000	90.96
41	4H-Cyclopenta[def]phenanthrene	203-64-5	$C_{15}H_{10}$	190.25	S-1035/Me	SPEX	1000	91.04
42	2-Phenylnaphthalene	612-94-2	$C_{16}H_{12}$	204.27	1956.16/IO	C	1000	91.63
43	Fluoranthene	206-44-0	$C_{16}H_{10}$	202.26	PAH Mix 3/Me	S-A	100	92.04
44	Pyrene	129-00-0	$C_{16}H_{10}$	202.25	PAH Mix 3/Me	S-A	100	92.91
45	2-Methylpyrene	3442-78-2	$C_{17}H_{12}$	216.28	S-3858/MC	SPEX	1000	97.51

S-A: Sigma-Aldrich, USA
SPEX: SPEX CertiPrep, USA
C: Chiron, Norway
Me: Methanol
T: Toluene
MC: Methylchloride
IO: Isooctane

References

[1] Stiess M, Mechanische Verfahrenstechnik 1 (in German), Springer, 1992.

[2] Merkus HG, Particle Size Measurements, Springer, 2009.

[3] Tannous K, Lam PS, Sokhansanj S, Grace JR, Physical properties for flow characterization of ground biomass from Douglas Fir Wood, Part Sci Technol 31 (2012) 291–300.

[4] Washburn EW, Note on a method of determining the distribution of pore sizes in a porous material, Proc Natl Acad Sci 7 (1921) 115–6.

[5] Junghaus K, Niemz P, Bächle F, Untersuchungen zum Einfluess der thermischen Vergütung auf die Porosität von Fichtenholz, Holz Roh Werkst 63 (3) (2005) 243–4.

[6] Plötze M, Niemz P, Porosity and pore size distribution of different wood types as determined by mercury intrusion porosimetry, Europ J Wood Wood Product 69 (4) (2011) 649–57.

A.5 Supplemental materials article 5

Characterization of charcoal-based composite pellets for the use in ferroalloy industries

Contribution of the authors

Gerrit Ralf Surup planned the majority of the study, developed a reactor for the charcoal production and also performed all pyrolysis experiments and manuscript writing.
Henrik Kofoed Nielsen provided extensive comments to the manuscript and assisted with the ash heating microscopy assembly.
Marius Großarth supported the experimental work using a high-temperature furnace.
Prof. Rüdiger Deike consulted and assisted the optical microscopy analysis and also participated in the writing article section related to the microscopy.
Jan Van den Bulcke participated in the microtomography scans and development of a procedure how to characterize different phases in a pellet.Pierre Kibleur evaluated the microtomography data and wrote a software for the data processing of such complex three phase structure. He has also provided the data for the porosity fraction calculation.
Pierre Kibleur evaluated the microtomography data and wrote a software for the data processing of such complex three phase structure. He has also provided the data for the porosity fraction calculation.
Elena Yazhenskikh conducted the Factsage calculations and also processed the data.
Michael Müller assisted with the Factsage calculation and consulted regarding the choice of the Factsage subpackage for the simulation of thermal equilibrium at such high temperatures.
James J Leahy conducted the proof-reading of the manuscript.
Anna Trubetskaya supported on the manuscript structuring, managed the correspondence among co-authors and did the manuscript proof-reading.

Characterization of charcoal composite pellets for the use in ferroalloy industries

Gerrit Ralf Surup[a], Henrik Kofoed Nielsen[a], Marius Großarth[b], Rüdiger Deike[b], Jan Van den Bulcke[c], Pierre Kibleur[c], Michael Müller[e], Mirko Ziegner[e], Elena Yazhenskikh[e], Sergey Beloshapkin[f], James J. Leahy[f], Anna Trubetskaya[g,*]

[a]*Department of Engineering Sciences, University of Agder, 4879 Grimstad, Norway*
[b]*Chair of Metallurgy for Iron and Steel Production, University of Duisburg-Essen, 47119 Duisburg, Germany*
[c]*Laboratory of Wood Technology - Woodlab, Gent University, 9000, Gent, Belgium*
[d]*Department of Physics and Astronomy, Gent University, 9000, Gent, Ireland*
[e]*Institute of Energy and Climate Research, Jülich Research Centre, 52428 Jülich, Germany*
[f]*Bernal Center, University of Limerick, Castletroy, Ireland*
[g]*School of Engineering and Ryan Institute, National University of Ireland Galway, Galway, Ireland*

S-1. Pellet shrinkage

The silhouette of the charcoal pellets (heat treated at 900°C) and manganese composite pellets in N_2 and CO_2 at a flow rate of 500 ml min^{-1} are shown in Figure S-1. It can be noted that no shrinkage is observed at temperatures below the heat treatment temperature, whereas a consecutive shrinkage occurred at higher temperatures. At temperatures above 1000°C, the manganese composite pellets began to shrink, whereas whiskers formed at temperatures above 1200°C, as shown in Figure S-2.

*Corresponding author. anna.trubetskaya@nuigalway.ie

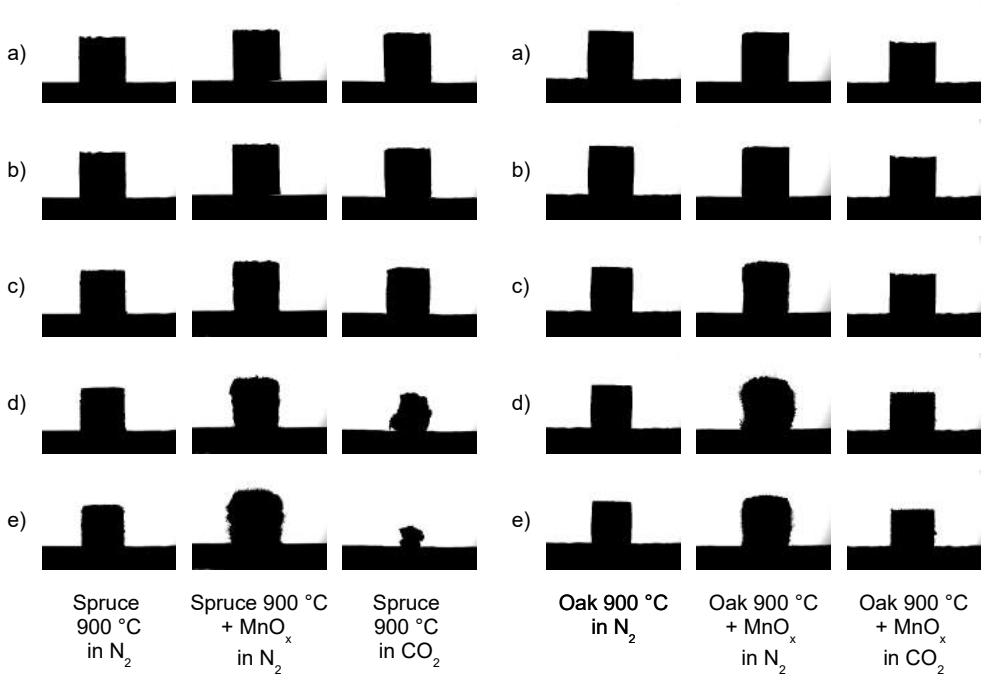

1(a): Spruce 1(b): Oak

Figure S-1: Silhouette of the spruce pellets at a) 100°C; b) 900°C; c) 1000°C; d) 1200°C; e) heating program finished

2(a): Charcoal pellet

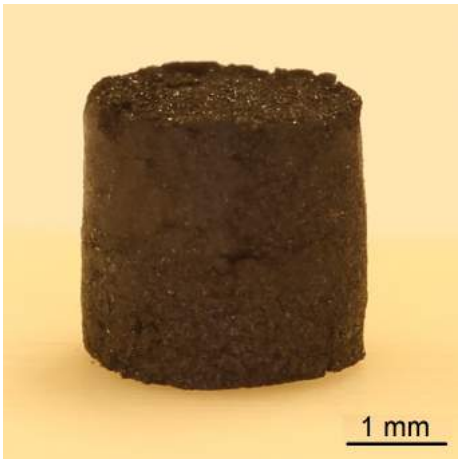

2(b): Heat treated pellet

2(c): MnO composite pellet at 1200 °C

2(d): MnO composite pellet at 1300 °C

Figure S-2: (a,b) Charcoal pellets before and after heat treatment and (c,d) Manganese composite pellets after heat treatment at 1200 and 1300°C.

The composite pellets in CO_2 did not develop whiskers, indicating the fully conversion of the carbon material before the reduction temperature was reached.

S-2. Microscopy

The elemental composition of reduced charcoal composite pellets was investigated using the SEM-EDS technique and summarized in Tables S-1-S-3.

Table S-1: Elemental composition of manganese composite pellets from SEM-EDS analysis.

	Mapping 1	Mapping 2	Mapping 3	Mapping 4
Element	wt.%			
C	64.4	69.8	75.6	60.2
Mn	23.9	19.5	2.0	28.9
O	3.1	7.7	8.6	4.3
Fe	5.6	1.1	0.3	3.4
Cu	0.5	0.4	12.7	1.6
Al	1.4	0.7	0.2	0.9
Si	0.7	0.4	0.2	0.4
Cl	0.1	0.4	0.3	0.2

Table S-2: Elemental composition of reduced quartz charcoal pellets from SEM-EDS analysis.

	Mapping 1	Mapping 2	Mapping 3	Mapping 4
element	wt.%			
C	71.8	69.3	64.7	54.8
O	19.6	20.1	23.4	28.7
Si	8.1	9.2	11.5	16.1

Table S-3: Elemental composition of reduced manganese oxides or quartz charcoal pellets from SEM-EDS analysis.

	MnO charcoal pellet		Quartz charcoal pellet	
Element	wt.%	σ	wt.%	σ
C	67.5	6.7	65.2	7.5
Mn	18.6	11.7		
O	5.9	2.6	23.0	4.2
Fe	2.6	2.4		
Cu	3.8	6.0		
Al	0.8	0.5		
Si	0.4	0.2	11.2	3.5
Cl	0.3	0.1	0.2	0.1

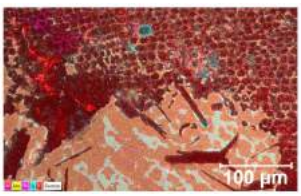

3(a): Mapping 1

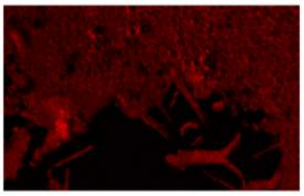

3(b): Carbon

3(c): Manganese

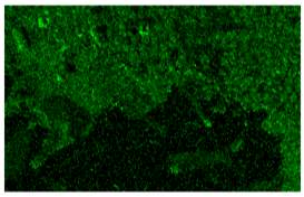

3(d): Oxygen

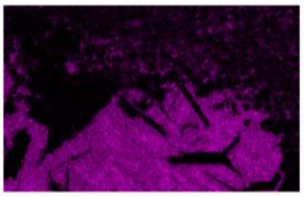

3(e): Iron

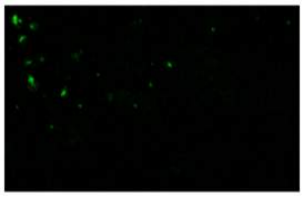

3(f): Copper

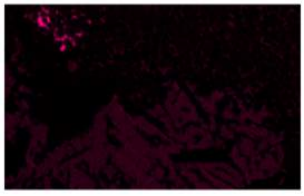

3(g): Aluminum

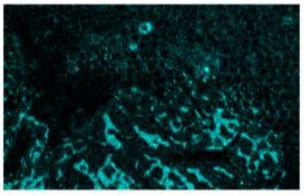

3(h): Silicon

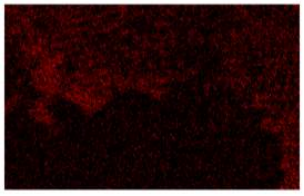

3(i): Chlorine

Figure S-3: EDS mapping image of the manganese composite pellets at spot 1.

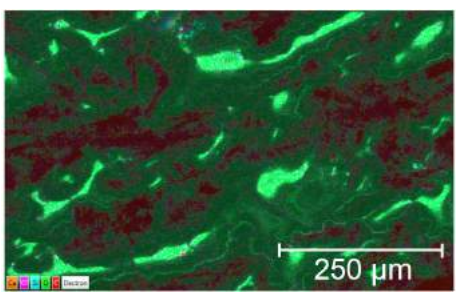

4(a): Mapping Si

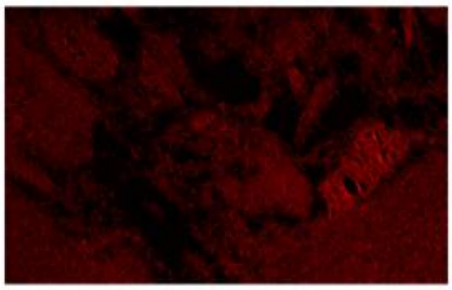

4(b): Carbon

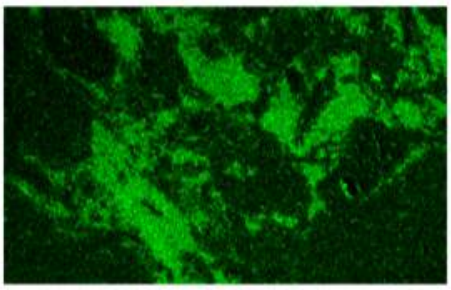

4(c): Oxygen

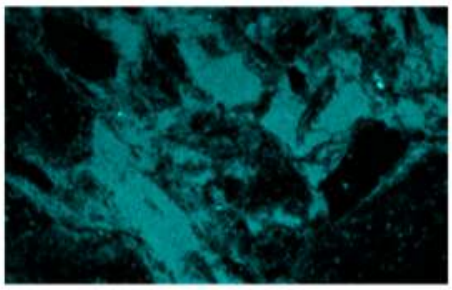

4(d): Silicon

Figure S-4: EDS mapping image of the silica composite pellets at spot 1.

S-3. Biomass shrinkage

Figure S-5 shows the shrinkage of softwood and hardwood cubes in the temperature range between 100 and 900°C, in which the growing directions (i.e. upright (x-y) and horizontal (y-z)) are stated for softwood and the influence of the main wood structures (heartwood, sapwood and bark) for hardwood. The shrinkage of the wood pellets occurs at temperatures above 240°C. No swelling was observed in the investigated temperature range at slow heating conditions.

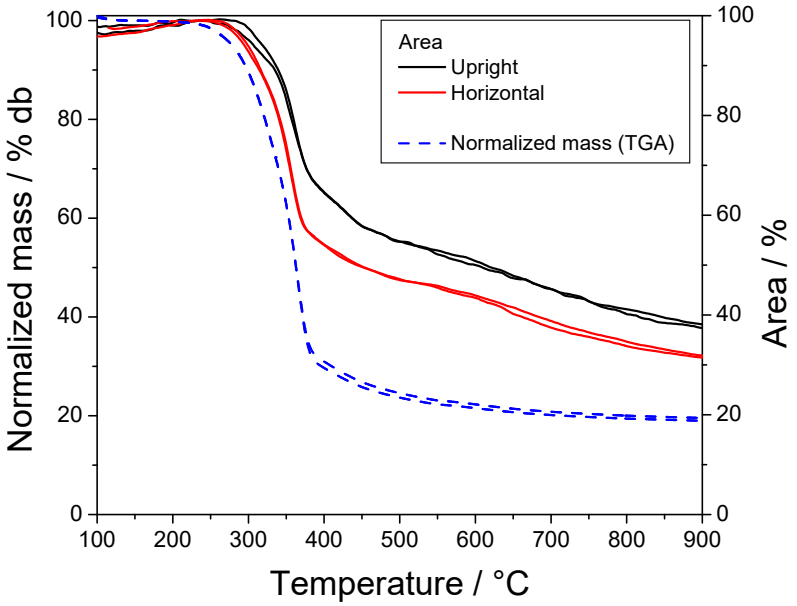

5(a): Softwood

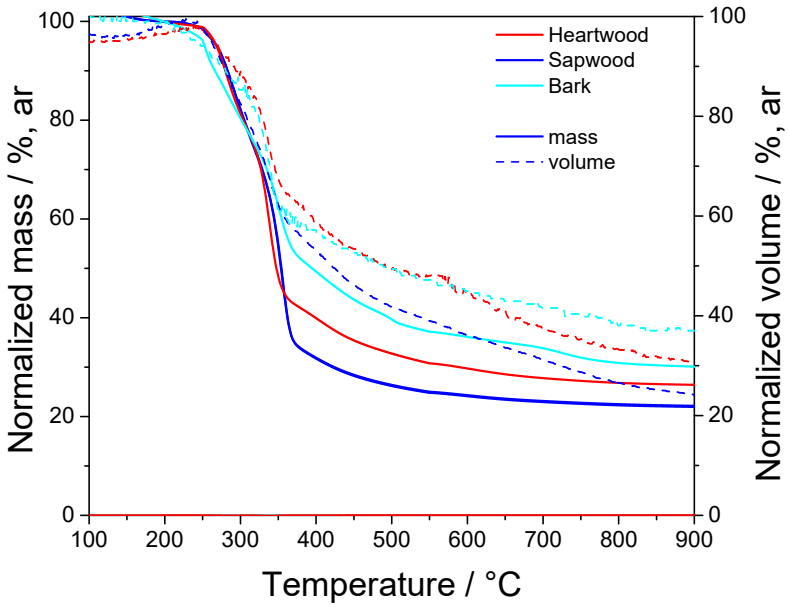

5(b): Hardwood

Figure S-5: Particle shrinkage and mass loss of: (a) softwood cubes and (b) hardwood cubes in the temperature range between 100 and 900°C.

The shrinkage of the biomass particles can be correlated to the mass loss by the release of volatile matter measured in TGA. The particle contraction at 900°C in growing direction (longitudinal) was about 25 to 35 % and less intense than the shrinkage in transverse directions, where a shrinkage of 40 to 50 % was observed. The mass loss in the temperature range between 400 and 900°C was more distinct than the volume contraction. Thus, the density of the charcoal samples is lower compared to the origin wood samples, whereas the porosity is larger. Weber and Quicker summarized that the porosity of charcoal samples increased from 53 % to about 72 % at heat treatment temperatures of 850°C [1]. The porosity by skeleton density was investigated for the heat treatment temperature of 800°C to 78.5 % and 68.5 % for spruce and oak [2]. The true density of charcoal samples increases with increasing temperature [3, 4] from about 1400 kg m^{-3} to 1950 kg m^{-3} and is at most at pyrolysis temperatures of about 1000°C [3, 5].

Simultaneous thermogravimetric measurements were carried out in N_2 to determine the mass loss of the cubes. The relative density of the charcoal samples was calculated by dividing the normalized mass by the normalized volume of the cubes and is shown in Figure S-6. The relative density was normalized to a temperature of 200°C before the main pyrolysis reactions occurred. First, the density of the charcoal samples decreased to about 65 % at 375°C of the original density, where the density kept nearly stable to 550°C. At temperatures above 550°C the relative density increased to about 85 % of the original density at 900°C. The results indicate that a larger content of extractables in the heartwood is beneficial at heat treatment temperatures below 700°C. However, the relative difference of the different wood origin

was negligible.

The envelope density of the pyrolyzed charcoal cubes was evaluated at room temperature. The particle size of the pyrolyzed charcoal cubes was analyzed by a caliper with a readability of 0.01 mm, and the belonging mass was determined on a microbalance (Perkin Elmer, USA) with a readability of 1 μg. The average envelope density was 320 kg m^3 for the softwood charcoal, respectively 570 kg m^3 for the hardwood charcoal.

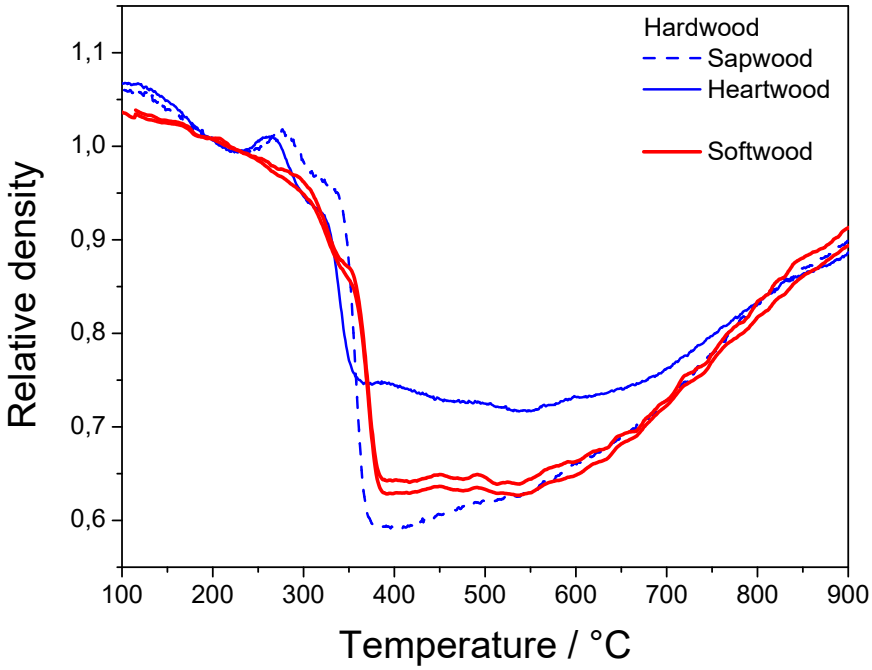

Figure S-6: Calculated envelope density of softwood and hardwood in a temperature range of 100 to 900°C.

References

[1] Weber K, Quicker P, Properties of biochar, Fuel 217 (2018) 240–61.

[2] Surup GR, Nielsen HK, Heidelmann M, Trubetskaya A, Characterization and reactivity of charcoal from high temperature pyrolysis (800–1600°c), Fuel 235 (2019) 1544–54.

[3] Hu Q, Yang H, Yao D, Zhu D, Wang X, Shao J, etc., The densification of bio-char: Effect of pyrolysis temperature on the qualities of pellets, Biores Technol 200 (2016) 521–7.

[4] Brewer CE, Chuang VJ, Masiello CA, Gonnermann H, Gao X, Dugan B, etc., New approaches to measuring biochar density and porosity, Biomass Bioenergy 66 (2014) 176–85.

[5] Hussein A, Larachi F, Ziegler D, Alamdari H, Effects of heat treatment and acid washing on properties and reactivity of charcoal, Biomass Bioenergy 90 (2016) 101–13.

A.6 Biooil

The distillation curve of biooil investigated in the TGA system by heating the water free fraction of the biooil at 5 °C min^{-1} to the final temperature of 450 °C is shown in Figure A.1. The boiling curve for spruce biooil was shifted to higher temperature compared to oak biooil, indicating a larger molecules in the spruce biooil. However, the final bio-pitch content of oak was higher compared to spruce biooil and pinewood flash pyrolysis oil. The results show that up to 30 % of the water free biooil can be converted into the solid residue. The pitch content was evaluated in an atmospheric distillation carried out to a heating mantle temperature of 450 °C, in which the pitch content corresponded to 7 % points of both initial biomass. However, due to heat losses at the thermocouple, no distillation curve was completely measured in the distillation.

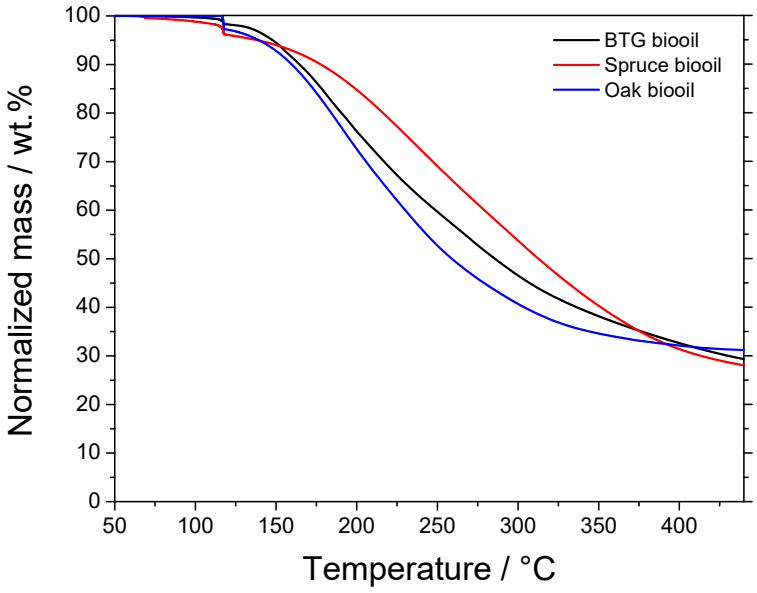

Figure A.1: Distillation curve of spruce and oak biooil compared to flash pyrolysis oil from BTG

The solid residue of the biooil distillation was investigated by the Jeol JSM-6400 Scanning Microscope and is shown in Figure A.2. The biopitch exhibited a porous structure similar to the charcoal, but less structured and with larger pores.

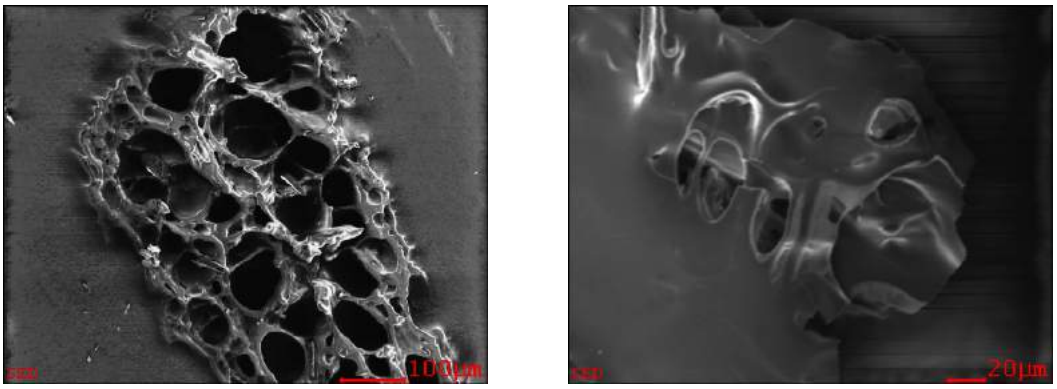

(a) Biopitch particle (b) Closeup

Figure A.2: SEM images of the solid residue from biooil distillation

The FID signal of spruce and oak biooil after biooil conditioning are shown in Figure A.4. The results indicate that the biooil composition after distillation and recycling are similar for both biomass feedstocks in the temperature range between 700 and 1100 °C. However, the biooil from primary pyrolysis caused noise, leading to a FID signal which was not stable for analysis. It is hypothesized that the biopitch was formed by the reactive compounds, stabilizing the in the mixture.

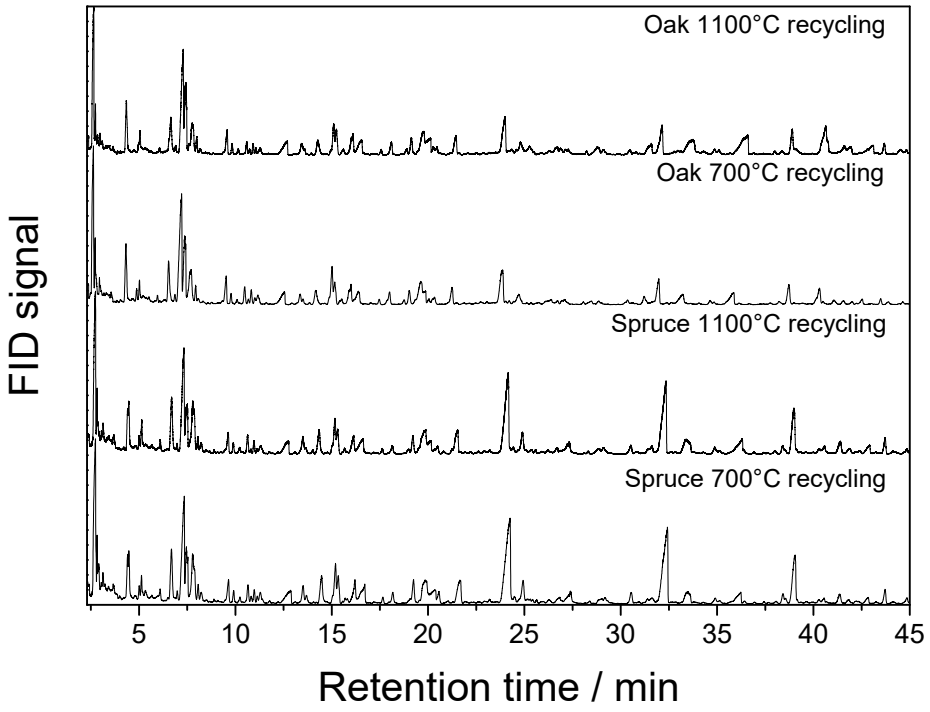

(a) Biooil recycling

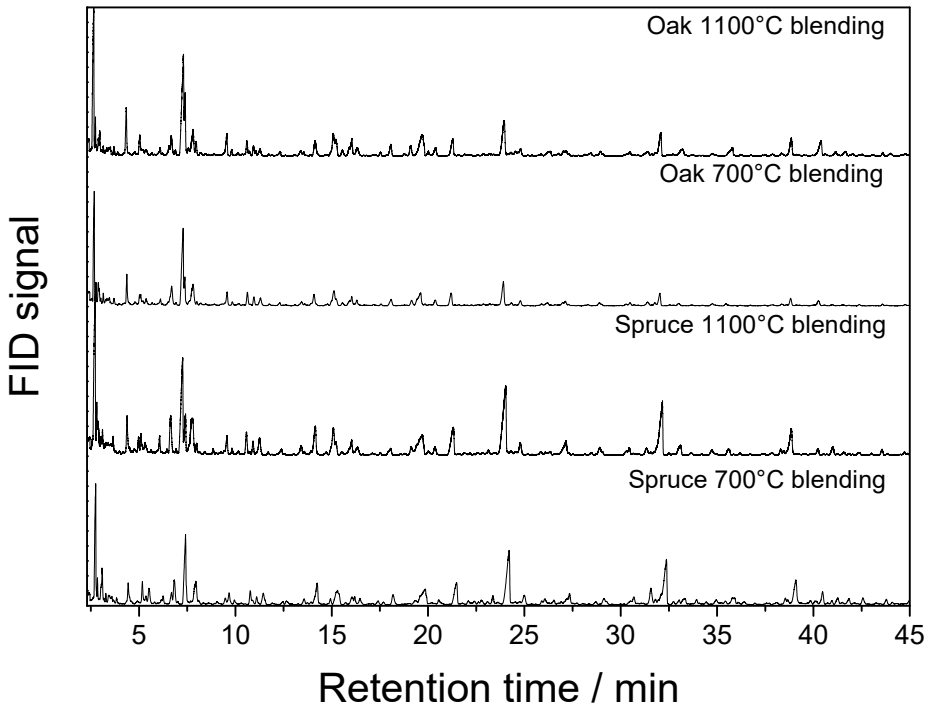

(b) Biooil-biochar blend distillation

Figure A.3: FID signal for (a) recycled biooil and (b) biooil-charcoal blend distillation for oak and spruce charcoal produced at 700 and 1100 °C

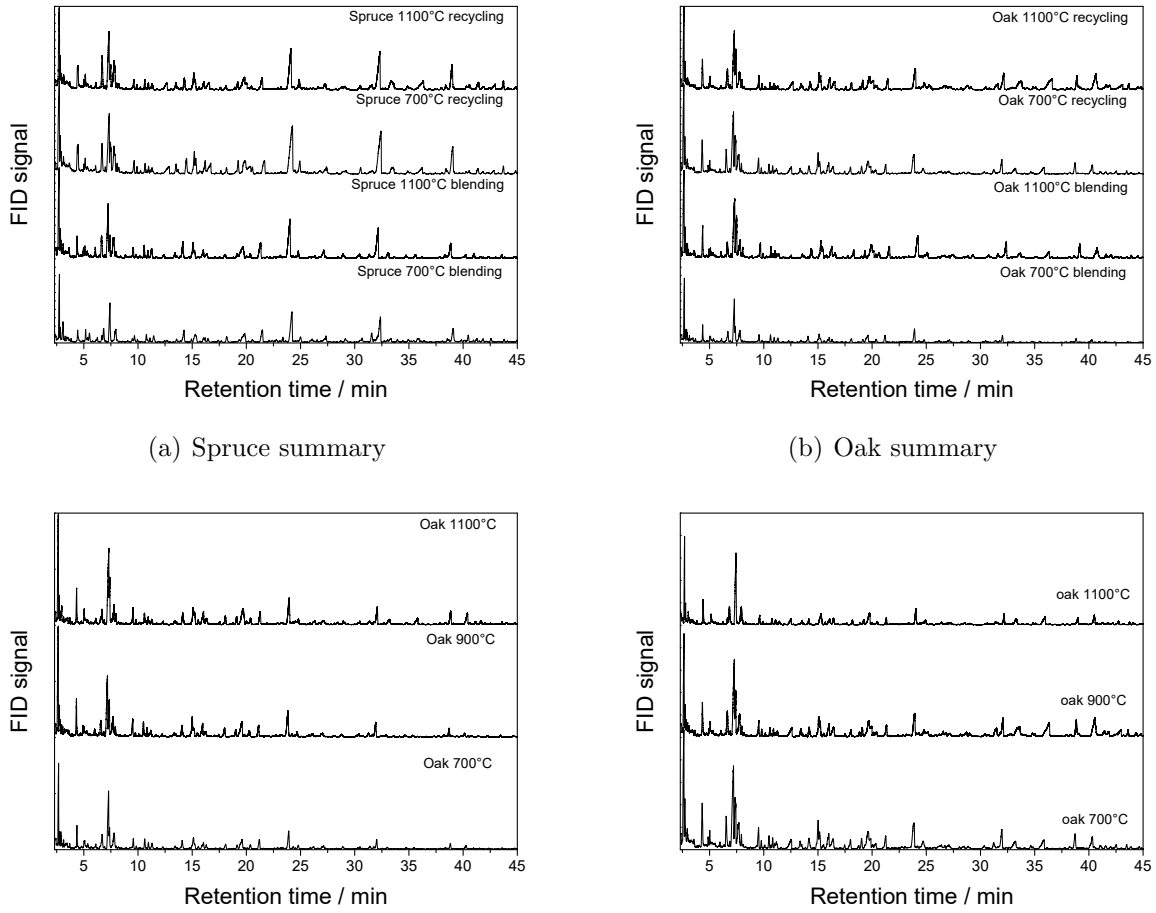

(a) Spruce summary

(b) Oak summary

(c) Oak blend distillation

(d) Oak biooil recycling

Figure A.4: Summary of the FID signals of (a) spruce and (b)-(d) oak charcoal produced at 700, 900 and 1100 °C

A.7 Solvent extraction

Condensed biooil on the charcoal surface was investigated in a Soxhlet apparatus. Water and acetone were used as solvents, whereas the weight difference of the dried charcoal samples before and after extraction was intended to estimate the condensed biooil content. However, no weight difference was observed for heat treatment temperatures above 500 °C of both biomass, indicating no condensation of the biooil on the charcoal matrix.

A.8 Charcoal-metallurgical coke blending

Figure A.5 shows the differential weight loss curves (DTG) for charcoal and metallurgical coke in air (21 vol.% O_2). Charcoal and metallurgical coke were blended with a ratio of 0:1, 1:3, 1:1, 3:1 and 1:0, corresponding to 0 %, 25 %, 50 %, 75 % and 100 % charcoal. The

peak reaction temperature of charcoal and metallurgical coke were 625 °C for charcoal, respectively 825 °C for metallurgical coke. It can be noted that the temperature of maximum reaction rate of both peaks shifted to lower temperature for increasing blending ratio, as shown in Figure A.5.

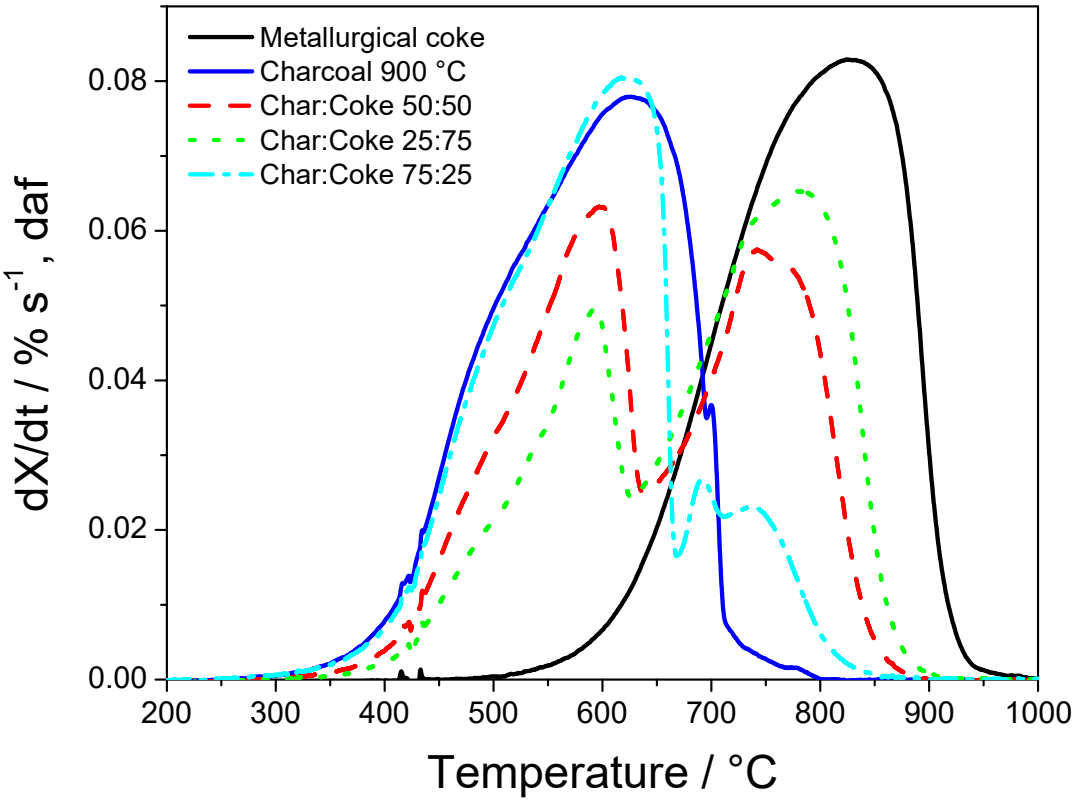

Figure A.5: DTG curves of charcoal-metallurgical coke blends